frontiers | Research Topics

Low-carbon oriented improvement strategy for flexibility and resiliency of multi-energy systems

Edited by
Yumin Zhang, Lu Zhang, Rufeng Zhang, Hao Wang and Shuai Yao

Published in
Frontiers in Energy Research

ISSN 1664-8714
ISBN 978-2-8325-5437-1
DOI 10.3389/978-2-8325-5437-1

About Frontiers

Frontiers is more than just an open access publisher of scholarly articles: it is a pioneering approach to the world of academia, radically improving the way scholarly research is managed. The grand vision of Frontiers is a world where all people have an equal opportunity to seek, share and generate knowledge. Frontiers provides immediate and permanent online open access to all its publications, but this alone is not enough to realize our grand goals.

Frontiers journal series

The Frontiers journal series is a multi-tier and interdisciplinary set of open-access, online journals, promising a paradigm shift from the current review, selection and dissemination processes in academic publishing. All Frontiers journals are driven by researchers for researchers; therefore, they constitute a service to the scholarly community. At the same time, the *Frontiers journal series* operates on a revolutionary invention, the tiered publishing system, initially addressing specific communities of scholars, and gradually climbing up to broader public understanding, thus serving the interests of the lay society, too.

Dedication to quality

Each Frontiers article is a landmark of the highest quality, thanks to genuinely collaborative interactions between authors and review editors, who include some of the world's best academicians. Research must be certified by peers before entering a stream of knowledge that may eventually reach the public - and shape society; therefore, Frontiers only applies the most rigorous and unbiased reviews. Frontiers revolutionizes research publishing by freely delivering the most outstanding research, evaluated with no bias from both the academic and social point of view. By applying the most advanced information technologies, Frontiers is catapulting scholarly publishing into a new generation.

What are Frontiers Research Topics?

Frontiers Research Topics are very popular trademarks of the *Frontiers journals series*: they are collections of at least ten articles, all centered on a particular subject. With their unique mix of varied contributions from Original Research to Review Articles, Frontiers Research Topics unify the most influential researchers, the latest key findings and historical advances in a hot research area.

Find out more on how to host your own Frontiers Research Topic or contribute to one as an author by contacting the Frontiers editorial office: frontiersin.org/about/contact

Low-carbon oriented improvement strategy for flexibility and resiliency of multi-energy systems

Topic editors

Yumin Zhang — Shandong University of Science and Technology, China
Lu Zhang — China Agricultural University, China
Rufeng Zhang — Northeast Electric Power University, China
Hao Wang — Monash University, Australia
Shuai Yao — Cardiff University, United Kingdom

Citation

Zhang, Y., Zhang, L., Zhang, R., Wang, H., Yao, S., eds. (2024). *Low-carbon oriented improvement strategy for flexibility and resiliency of multi-energy systems*. Lausanne: Frontiers Media SA. doi: 10.3389/978-2-8325-5437-1

Table of contents

frontiers | Frontiers in Energy Research

TYPE Original Research
PUBLISHED 24 October 2023
DOI 10.3389/fenrg.2023.1291552

OPEN ACCESS

EDITED BY
Rashid Mehmood,
King Abdulaziz University, Saudi Arabia

REVIEWED BY
Zhixuan Gao,
China Electric Power Research Institute (CEPRI), China
Zecheng Li,
State Grid Ningxia Electric Power Research Institute, China
Peng Chen,
Huairou Laboratory, China

*CORRESPONDENCE
Zhengzhong Gao,
skdgzz@163.com

RECEIVED 09 September 2023
ACCEPTED 09 October 2023
PUBLISHED 24 October 2023

CITATION
Feng C, Ye P, Gao Z, Jiang H, Zang X and Zhang X (2023), A novel distributing–collecting on-line insulation monitoring system and line selection technology for the DC supply system. *Front. Energy Res.* 11:1291552. doi: 10.3389/fenrg.2023.1291552

A novel distributing–collecting on-line insulation monitoring system and line selection technology for the DC supply system

Chen Feng, Pingfeng Ye, Zhengzhong Gao*, Haiyang Jiang, Xiangyu Zang and Xiangxing Zhang

College of Electrical Engineering and Automation, Shandong University of Science and Technology, Qingdao, China

At present, the power supply system of 5G base stations is a micro smart grid, it generally uses 240 V DC power supply with multiple branches, and leakage accidents will threaten personal and property safety, so it is vital to identify the fault line accurately and remove the faults rapidly. In this paper, the leakage phenomenon of transmission lines in the HVDC power supply system of a 5G communication base station is studied. To address the issue of multi-branch line leakage diagnosis and line selection in the 240 V DC system, a new distributed DC insulation monitoring and fault line selection technology and system are proposed. The distributed DC insulation monitoring line selection technology is used to collect the leakage current of each branch by setting a unique single-core DC leakage transformer and process the signal primarily. In addition, a high-resistance bridge switchgear is added to the bus bar. According to different leakage currents caused by the imbalance of the bridge before and after the switch, the insulation resistance of electrodes to the ground is calculated accurately, which solves the problem that the current technology cannot judge the fault of the positive and negative electrodes to the ground at the same time. Through both simulation and prototype experiments, the feasibility of this technology and system device in line insulation monitoring and line selection of the HVDC communication base station power supply system is verified.

KEYWORDS

insulation monitoring system, leakage phenomenon, fault line selection, grounding selection for DC system, simulation and prototype experiments

1 Introduction

Currently, a high-voltage DC power supply system with a voltage level of 240 V is widely used as equipment in a signal system, transformer substation, and communication station because of the complicated environment (Hellgren, 2004; Li, 2012; Chen, 2018a). As these DC power supply systems include many branches and loads, when the line insulation drops, it is easy to cause grounding, short circuit, and other faults, endangering personal safety or equipment safety. Therefore, it is necessary to have a corresponding insulation monitoring device, which can give early warning and lock the fault location quickly.

At present, the integral insulation monitoring and protection technology is adopted in the power supply of communication station usually. However, it is impossible to select and locate the faulty branch accurately. The existing insulation monitoring methods with the function of fault branch selection include the balance-bridge method and signal injection method. However, there are also many problems in these methods. For the balance-bridge method of fault line selection, it is necessary to set the bridge's parameters accurately, according to the system type (Huang et al., 2019). If the value of the bridge parameter is low, the insensitivity of the insulation monitoring system will cause an inaccuracy of the fault judgment. On the contrary, if the value of the bridge parameter is high, the test data will have large deviation and the equipment maintenance cost will increase. Furthermore, it is difficult to detect the simultaneous decline of positive and negative insulation resistances to the ground with current technology (Luo et al., 2016). In order to detect the insulation state of each electrode, switchable bridges need to be installed in each branch. This bridge has caused the line-to-ground insulation resistance to drop actually. For each additional bridge, the equivalent value of the ground resistance will be doubled, and the risk of personal electric shock will increase accordingly (Jiang and Ji, 2009; Yin et al., 2012; Rybski et al., 2015). At the same time, on one hand, the active power leakage current sensor installed in the branch is costly; on the other hand, it is ineffective to detect all kinds of insulation faults. The signal injection method is greatly affected by the electrical distribution parameters, and it is impossible to judge the insulation drop in the complicated environment (Yow-Chyi and Chen-You, 2012; Olszowiec, 2017).

To solve these issues, a distributing–collecting online insulation monitoring system is proposed. It adopts the single-core DC-type current transformers settled in each branch to collect the micro-current after the insulation fault. Ground insulation monitoring and line selection can also be realized under various insulation faults. This paper mainly includes the following aspects: the principle and technology of leakage protection are analyzed, and the sensor suitable for the distributed acquisition system is studied. The advantages and disadvantages of current leakage protection technology are compared and analyzed. A novel distributing–collecting on-line insulation monitoring system is proposed, which is more suitable for the DC transmission system of communication base stations and the use of remote electrical equipment. The hardware structure and algorithm principle of the proposed system are developed and designed. It is best to build the analog communication base station of the DC transmission system using MATLAB software verification and prototype verification, carry out experimental verification, and analyze the results to verify the effectiveness of the system device.

2 Method

2.1 Personal electrical safety issues and insulation monitoring settings

With reference to the provisions of China's electrical safety regulations (GB/T 13870.2-2016), the human body safety current in the DC system is no more than 50 mA, i.e., when the current flowing through the human body is below 50 mA, it is not life-threatening, and people who are subjected to an electric shock can react in time and avoid continuous injury (Dawalibi et al., 1990). For the DC power supply system, it is stipulated that the product of the human electric shock current and the action time is not more than 30 mA s. By imitating the safety parameters of the AC system, the safety parameter for the DC system can be stipulated as 50 mA s. According to China's human body safety current standard, adult men's threshold to get rid of the electric shock should be no more than 10 mA (Roberts, 2009; Zhao et al., 2017; Zhenbin et al., 2021).

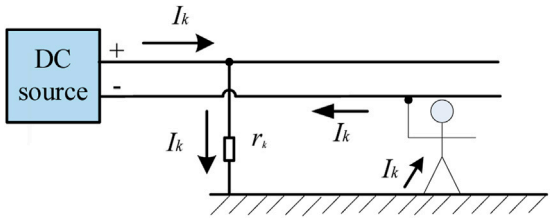

FIGURE 1
DC personal electric shock safety diagram.

As shown in Figure 1, the line in the figure represents the line of the general DC power supply system. When a person touches the positive pole or negative pole of the line and the insulation of the other pole drops, an electric shock accident will occur.

Generally, the resistance of the human body r_{bady} is regarded as 1 kΩ, and the voltage level of the DC power supply system for the communication system is 240 V.

$$I_k = \frac{U_0}{r_k + r_{\text{bady}}}. \tag{1}$$

Calculated by Eq. 1, when the insulation resistance r_k of the line (positive or negative pole) drops to 3.8 kΩ, if the person happens to touch the other pole (negative or positive pole) of the line, the current flowing through the person is 50 mA (human body safety current for the DC system). When the insulation resistance of the line drops to 24 kΩ, the current flowing through the body is 9.6 mA (the threshold current to get rid of the electric shock).

In order to guarantee the human safety and ensure certain reliability, the current flowing through a person must be controlled under 50 mA. Since the communication system powered by the DC power supply system is generally installed in a high tower, there is a great danger of muscle suppression caused by an electric shock. Therefore, for avoiding an electric shock and enabling people to get rid of the electric shock in time, it is recommended to set the tripping operation setting as 28 kΩ (1.2 times of 24 kΩ).

2.2 Distributed online insulation monitoring system

2.2.1 The structure of a distributed online insulation monitoring system

Aiming at the deficiency of the existing insulation monitoring system, this paper proposes a distributed online insulation monitoring

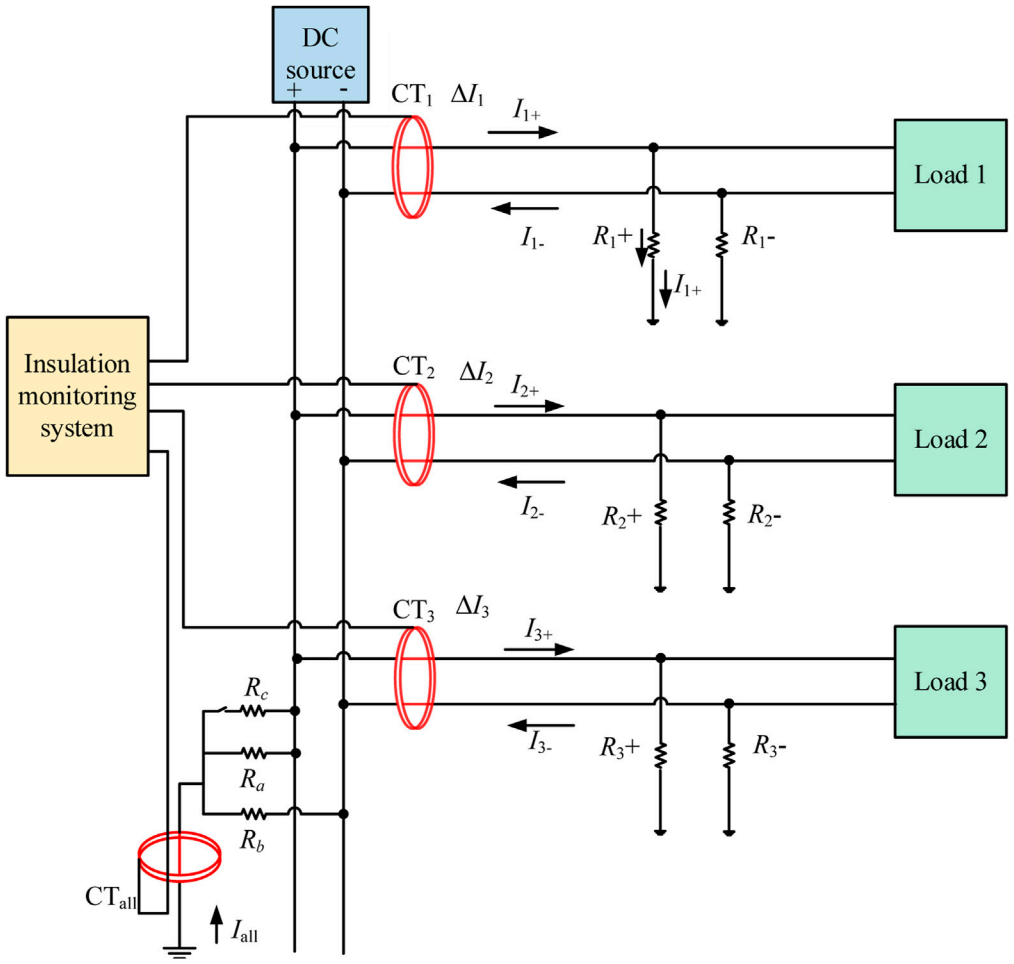

FIGURE 2
Distributed online insulation monitoring system.

system. Figure 2 displays the distributed insulation monitoring system. The whole system consists of a centralized central processing unit and a dedicated DC residual current transformer distributed in each branch. Positive and negative cable currents in each branch pass through the special DC residual current transformer proposed in this paper at the same time, and the residual current of each branch is extracted using the principle of the current magnetic field effect canceling each other in the positive and negative cables for insulation monitoring. All control signal transmission, signal collection, and processing are integrated in the central processing unit of the distributed insulation monitoring device. The central processing unit uniformly sends out the control signal, controls, and modulates the special DC transformer to collect the signal, and the collected signal is uniformly processed by the central processing unit. CT_1, CT_2, … CT_n are DC insulation monitoring transformers installed in each branch, and CT_{all} is the DC insulation monitoring transformer, which is installed at the bus with a high resistance to ground. R_{1+}, R_{1-}, R_{2+}, R_{2-} … R_{n+}, and R_{n-} are the insulation resistances of each branch. R_a and R_b are the balanced high resistance to the ground of the bus.

The entire system consists of a central processing unit and DC residual current transformers distributed over the branches. The transformer collects residual current of each branch for insulation monitoring by the principle that the magnetic field created by current in different directions cancels each other out.

2.2.2 Distributed online insulation monitoring transformer

By studying the existing magnetic modulation current transformers, a new insulation monitoring transformer is presented, which is more durable, precise, economical, and practical. The existing magnetic modulation current transformers are all active transformers; they usually require a control circuit, and a signal processing and amplifying circuit in them. An alternating current signal is added to the magnetic core, so the direct current of the DC power system can be extracted on the secondary side of the transformer. The current transformer is shown in Figure 3 (Chen and Sun, 2018; Xie et al., 2016; M; Shi et al., 2022).

The principle of the transformer is as follows: first, the central processing unit sends out the AC control signal, which is injected into the magnetic ring of the transformer. The acquisition coil transmits the collected signal back to the signal processing module of the central processing unit. Through signal processing, the DC component is extracted (Wang et al., 2020; Li et al., 2015). As shown in Figure 3, when the AC signal is injected into the injection

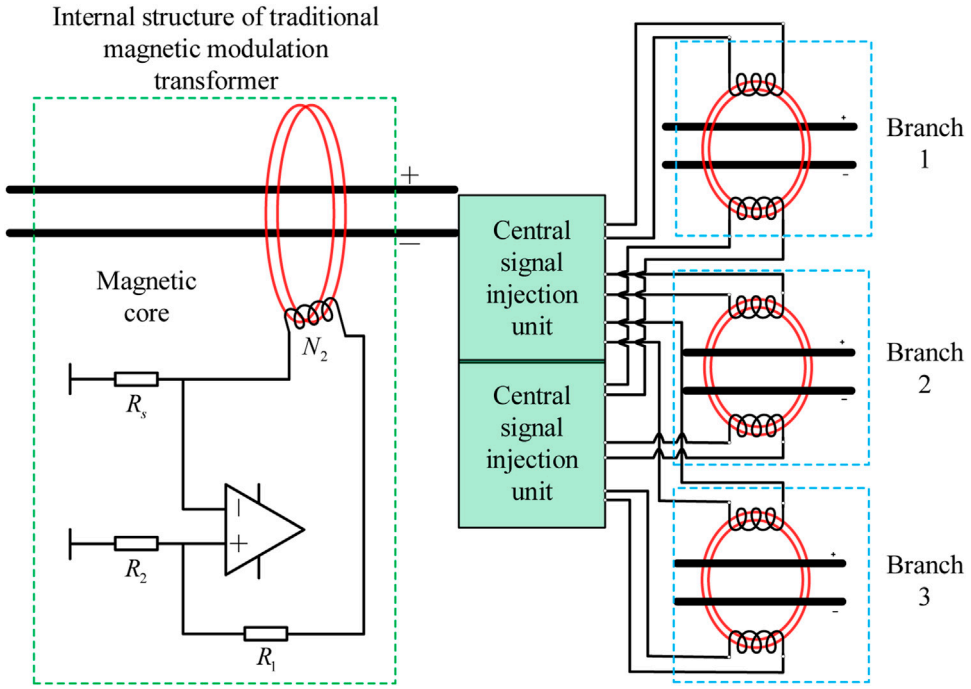

FIGURE 3
Traditional magnetic modulation and improved distributed modulation transformers.

coil on the magnetic ring in the transformer, the AC signal generates an alternating magnetic field in the magnetic ring. The line under test passes through the center of the magnetic core. If the line under test contains a DC signal, the DC signal will generate a magnetic field offset in a fixed direction in the magnetic ring. The acquisition coil collects the signals generated by the combined action of AC and DC signals on the magnetic field, and the injected magnetic field is changed by the bias of the DC magnetic field (Zhao et al., 2012; Chen et al., 2019). The collected signal is processed to obtain the DC current of the line under test. In order to further reduce the cost, the central processing unit of the insulation monitoring system is proposed to inject ac control signals into the transformers of each branch, control the magnetic-modulated current transformer to extract the dc current, and collect the residual current of each branch by the central processing unit so as to judge the insulation decline state. This method does not require the transformer of each branch to install the control circuit, and signal processing and amplification circuit separately and greatly reduces the cost of the transformer; the control signal is uniformly sent by the central processing unit, reducing the error and improving the reliability of insulation monitoring.

The development board of arm STM32F103 selected in this paper is equipped with three 12-bit ADC converters, with an AD sampling rate up to 1 MHz. Because the ADC converter can only collect 0–3.3 V voltage signal and the transformer secondary side current signal is given, we need to regulate the transformer secondary side of current signal, as shown in Figure 4. After current voltage conversion, the in-phase amplifier, pressure limiting protection, signal processing steps, such as isolation, and low pass filtering can be collected to the transformer secondary side current signal, to arm for analysis and calculation.

2.2.3 Analysis and determination for the insulation fault

In view of the possibility of each cable in the complex DC power system having an insulation drop, the distributed insulation monitoring system can realize the real-time online monitoring of the insulation state of each branch in the system.

Figure 2 shows high-resistance grounding in the DC power supply system. If the grounding fault or insulation degradation occurs in the positive pole of branch 1, there is leakage current I_{1+}, which flows into the earth and flows back to the negative pole through high-resistance grounding of the bus; at this time, the current of branch 1 is increased and $\Delta I_1 > 0$. Transformer 1 of branch 1 can collect the DC leakage current in real-time and upload it to the central processing unit.

Figure 2 shows R_a and R_b are the high resistance of neutral point grounding bus, communication equipment in the 240V power supply system. The resistance value is generally set to 200 kΩ. R_{n+} and R_{n-} are the positive and negative insulation resistance of the n branch. The cable-related parameters show the system of intact cable insulation resistance of approximately 40 MΩ. Taking branch n as an example, Figure 5 shows the simplified circuit. R_a, R_b, R_{n+}, and R_{n-} constitute the bridge balance. When no insulation drop occurs, R_{n+} is equal to R_{n-}, R_a is equal to R_b, and the bridge becomes balanced, and $\Delta I_n = I_{n+} - I_{n-} = 0$.

When a single-terminal ground fault occurs, the positive insulation resistance R_{n+} in branch n decreases, the negative resistance R_{n-} remains unchanged, and the bridge is unbalanced. The leakage current flows from the positive electrode through the positive insulation resistance R_{n+} into the earth and flows back to the negative electrode from the bus high resistance R_b to form a circuit. At this point, the measured current of the branch n CT_n is

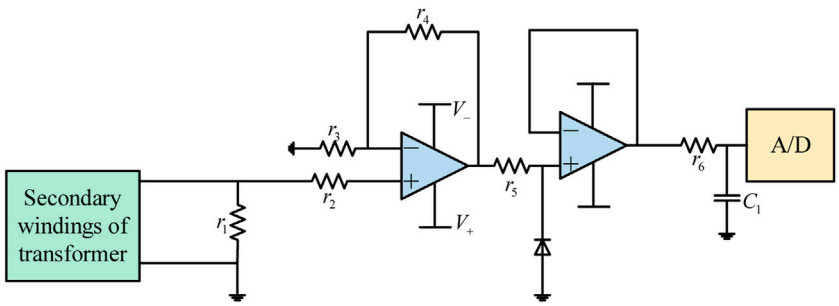

FIGURE 4
Signal conditioning circuit.

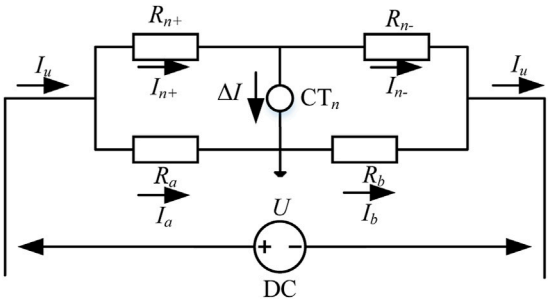

FIGURE 5
Equivalent circuit of the single-pole grounding fault.

$\Delta I_n = I_{n+} - I_{n-} \neq 0$. Since the negative resistance R_{n-} is unchanged, $I_{n-} \approx 0$; it is negligible, so $\Delta I_n = I_{n+}$.

According to the Kirchhoff's voltage law (Quintela et al., 2009),

$$U = R_a I_a + R_b (\Delta I_n + I_a), \tag{2}$$

$$R_{n+} = \frac{R_a I_a}{I_{n+}} = \frac{R_a [U - R_b \Delta I_n]}{I_{n+}}. \tag{3}$$

Because the anode voltage U is observed to be 240 V, high-resistance R_a and R_b are 200 kΩ; the drain-current value ΔI_n is obtained from the transformer CTn, and the value of positive insulation resistance R_{n+} can be obtained.

Similarly, if the negative monopole insulation drops, the negative insulation resistance R_{n-} in the branch n drops, the positive resistance R_{n+} remains unchanged, the bridge is unbalanced, and the leakage current flows from the negative electrode through the negative insulation resistance R_{n-} into the earth and flows from the bus high-resistance R_a back to the positive electrode to form a circuit, which is opposite to the positive insulation decreasing leakage current. At this point, the current measured by CTn in branch n is $\Delta I_n^{'}$. $\Delta I_n^{'} = I_{n+} - I_{n-} \neq 0$. Since the positive resistor R_{n+} is unchanged, $I_{n+} \approx 0$; it is negligible, so $\Delta I_n^{'} = I_{n-}$.

$$U = R_b I_b + R_a \left(\Delta I_n^{'} + I_b\right), \tag{4}$$

$$R_{n-} = \frac{R_b I_b}{I_{n-}} = \frac{R_b [U - R_a \Delta I']}{\Delta I_n^{'} (R_a + R_b)}. \tag{5}$$

Because the anode voltage U is considered to be 240V, high-resistance R_a and R_b are obtained to be 200 kΩ, the leakage current value ΔI_n is obtained by CT$_n$, by substituting Eq. 5, and the value of negative insulation resistance R_{n-} can be obtained.

Section 2.1 has been demonstrated that the insulation resistance alarm value should be greater than 28 k.

Therefore, the set values for the insulation monitoring system are $R_n \geq 2.8 \times 10^4 \Omega$. It can be found that the positive electrode-to-earth insulation fault and the negative electrode-to-earth insulation fault measure the opposite current direction when the monopole insulation fault occurs. Then, the calculation shows that the insulation resistance is less than the setting value when $|\Delta I_n| \leq 5.26 \times 10^{-4}$A. Therefore, when the system branch transformer detects leakage current $|\Delta I_n| > 5.26 \times 10^{-4}$A, the system raises an alarm and through ΔI_n direction to determine the positive or negative insulation fault.

The monitoring principle analysis and formula derivation for the single-terminal grounding fault are mentioned previously. This principle can also be extended to realize the on-line monitoring function for insulation of one or more branches at the same time. It is only necessary to calculate the insulation resistance of each branch individually.

However, in the DC power supply system, in addition to the monopole insulation drop, there are also single-branch double-stage insulation drop faults. Because the aforementioned principles are derived from the monopole insulation drop, it is not applicable to the case of the anode and cathode simultaneous drop. Therefore, the balanced resistance switching principle is adopted in this paper, that is, a resistance switching device is added to the high-resistance connection of the distribution bus to realize the monitoring technology of this kind of fault. Figure 6 shows that a new resistance R_c and switching device are added to the positive pole of the bus. The switching device is selected to be closed every 5 s for a duration of 1 minute before disconnecting. Its simplified equivalent circuit diagram is shown in Figure 6.

In Figure 6, the initial state of switch K is state 1. R_a and R_b are the high resistances at the neutral point of the bus; R_c is the switchable high resistance, which is used to change the state of the bridge; R_{n+} and R_{n-} are, respectively, the insulation resistance values of positive and negative pole cables in branch n; and ΔI_n is the leakage current, $\Delta I_n = I_{n+} - I_{n-}$. U_2 is the negative electrode-to-earth voltage, which is the terminal voltage of R_b or R_{n-}.

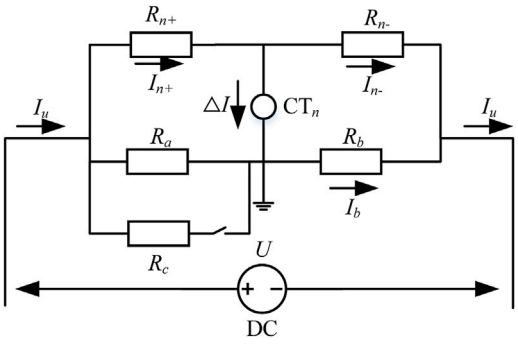

FIGURE 6
Equivalent circuit diagram.

If the positive and negative pole wires of branch n suffer from insulation decline at the same time, the equation under state 1 can be obtained according to the following circuit principle:

$$\frac{U}{R_a//R_{n+} + R_b//R_{n-}} = \frac{U_2}{R_b//R_{n-}}, \tag{6}$$

$$U_2 = (I_a + \Delta I_n)R_b, \tag{7}$$

$$U_2 = U - I_a R_a. \tag{8}$$

Combining Eqs 7, 8, we observe that

$$I_a = \frac{U - \Delta I_n R_b}{R_a + R_b}, \tag{9}$$

$$U_2 = \frac{R_b(U + \Delta I_n R_b)}{R_a + R_b}. \tag{10}$$

Switch K is closed, followed by state 2; $\Delta I_n^{'}$ is the leakage current at state 2, where $\Delta I_n^{'} = I_{n+}^{'} - I_{n-}^{'}$. $U_2^{'}$ is the negative electrode-to-earth voltage, that is, the terminal voltage of R_b or R_{n-} can be obtained according to the following circuit principle:

$$\frac{U}{R_a//R_c//R_{n+} + R_b//R_{n-}} = \frac{U_2^{'}}{R_b//R_{n-}}, \tag{11}$$

$$U_2 = \left(I_a^{'} + \Delta I_n^{'}\right)R_b, \tag{12}$$

$$U_2^{'} = U - I_a^{'} R_a. \tag{13}$$

Combining Eqs 12, 13, we observe that

$$I_{ac} = \frac{U - \Delta I_n^{'} R_b}{R_a//R_c + R_b}, \tag{14}$$

$$U_2^{'} = \frac{R_b\left(U + \Delta I_n^{'} R_b\right)}{R_a//R_c + R_b}. \tag{15}$$

Combining Eqs 6, 11, we observe that

$$R_{n+} = \frac{1}{\frac{R_a//R_c}{R_a R_b} \times \frac{\left(U - \Delta I_n^{'} R_b\right)(R_a + R_b)}{\left(U + \Delta I_n^{'} \times R_a//R_c\right)(R_a + R_b) - (U + \Delta I_n R_a)\left(R_a//R_c + R_b\right)}}, \tag{16}$$

$$R_{n-} = \frac{1}{\frac{R_a^2(R_a + R_b)}{R_b^2(U + \Delta I_n R_a)(R_a + R_b)} \times \frac{(U - \Delta I_n R_b)\left(U - \Delta I_n^{'} R_b\right)}{\left(U + \Delta I_n^{'} \times R_a//R_c\right)(R_a + R_b) - (U + \Delta I_n R_a)\left(R_a//R_c + R_b\right)}}. \tag{17}$$

Because R_a, R_b, and R_c are known for 200 kΩ, U is the negative voltage on both ends as its value is 240 V, and $\Delta I_n^{'}$ and ΔI_n can be measured using a branch transformer, which can calculate the value of insulation resistance R.

Therefore, when the transformer of the branch and the transformer of the high-resistance side of the bus bar detect leakage current, the decrease in the conductor insulation resistance value can be determined in real time, according to the direction and size of the leakage current of the positive and negative branches. If the value is less than the setting value, the system will give an alarm and produce corresponding actions. Compared to the probability that both poles of a branch have an insulation decrease, a single-pole insulation fault is more likely to happen. So, it is necessary to allocate time for monitoring each fault in a reasonable way. Table 1 shows the time allocation for switch K switching to monitor two faults. The resistance switching device is the switch K shown in Figure 2.

The switching frequency of switch K is 6 s/time. If switch K is closed, the bridge is unbalanced, and the system is efficient to detect the condition that the insulation resistance of the positive and negative poles is decreased to the same value at the same time. Furthermore, if the switch is turned off, a single-pole insulation decrease could be detected in this mode.

3 Results

3.1 Simulation of the single-electrode grounding fault

The Simulink model based on MATLAB is shown in Figure 7.

First, the state of the power supply system during normal operation is simulated and analyzed. When the insulation is well, the insulation resistance of each branch is approximately 40 MΩ. The results show that the leakage current measured by each transformer is 0.

The second step is to simulate monopole to ground insulation descent. Branch 1 is set as the faulty branch. In order to ensure the diversity and comprehensiveness of the simulation, it is assumed that the grounding resistance of the branch with an insulation fault is 100 kΩ, 75 kΩ, 50 kΩ, 28 kΩ, and 8 kΩ. When the monopole insulation drops in the positive or negative insulation, the leakage current value is equal, and the current direction is opposite. It can be determined whether the positive insulation or the negative insulation decreases by the current direction. Therefore, only the positive insulation decreases are simulated.

As shown in Figure 8, the comparison between the simulation results and the calculation formula shows the relationship between the leakage current and insulation resistance when different monopole-to-ground insulation resistance values are simulated. The curve in the figure is the formula of calculating insulation resistance by leakage current in Section 2 of this paper.

When the monopole-to-the ground insulation fault occurs, the smaller the monopole-to-the ground insulation resistance is, the greater the leakage current will be. The simulation results are in perfect agreement with the calculated results. Through comparison, it can be seen that the formula proposed in this paper can accurately

10.3389/fenrg.2023.1291552

TABLE 1 Time allocation of switch K.

Condition of K	Switching cycle of K (s)	Monitoring mode
Closed	1	Balanced insulation decreases in two poles of the branch
Broken	5	Single-pole insulation decreases

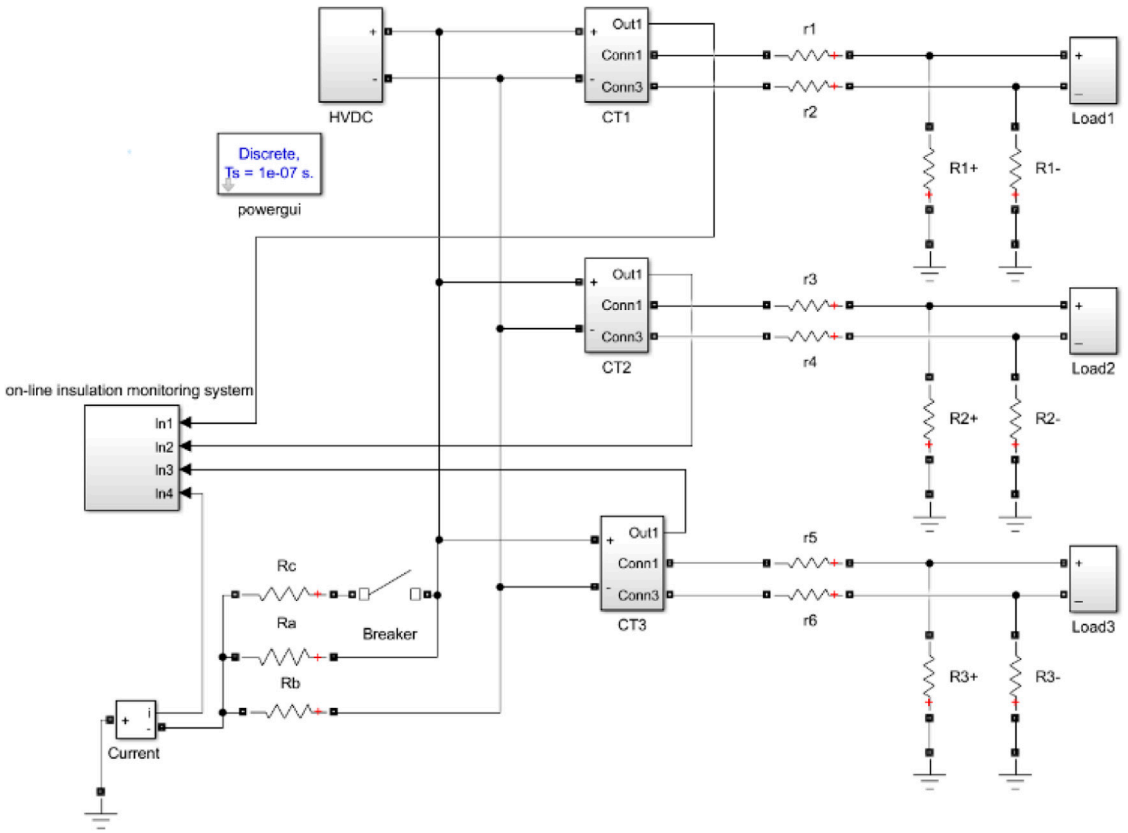

FIGURE 7
Simulation mode of the distributed insulation monitoring system.

calculate the insulation resistance for the monopole insulation decline.

If there is insulation degradation in multiple branches at the same time, there will be leakage current in all branches with an insulation fault and the high-resistance grounding bus-bar. Therefore, it could recognize insulation degradation in all branches through this technology.

3.2 Simulation of the multi-electrode grounding fault

In the third step, the insulation of the anode and cathode drops at the same time. In the simulation figure, the branch containing Rc contains a circuit breaker to simulate the two states of bridge resistance before and after switching (before the cut is state 1 and after the cut is state 2). In order to carry out a comprehensive analysis, the following positive and negative insulation resistance values are selected: 150 kΩ, 100 kΩ, 75 kΩ, 50 kΩ, 28 kΩ, and 8 kΩ. Leakage current ΔI under state 1 and leakage current $\Delta I'$ under state 2 were measured, and the data were drawn in the three-dimensional coordinate system, as shown in red dots in Figures 9, 10, respectively, for the simulation results. In the figure, x axis and y axis represent positive and negative insulation resistance, respectively. The z-axis in the two figures shows the leakage current ΔI under state 1 and the leakage current $\Delta I'$ under state 2. Eqs 18, 19 were recorded into the coordinate system, as shown in the surface in Figure 9. When the positive and negative insulation resistances were given different values, the leakage current ΔI under state 1 and the leakage current $\Delta I'$ under state 2 were shown.

In state 1, the greater the difference between the positive electrode-to-ground insulation resistance and the negative electrode-to-ground insulation resistance is, the greater the

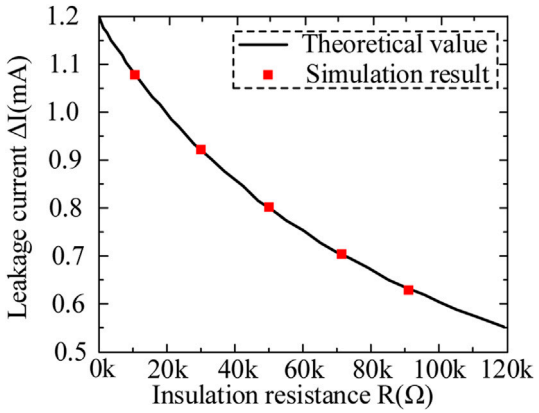

FIGURE 8
Simulation results and the calculation formula.

leakage current value will be, and the direction is related to the insulation resistance at the poles. When $R_{n+} > R_{n-}$, the leakage current is negative; when $R_{n+} < R_{n-}$, the leakage current is positive; and when $R_{n+} = R_{n-}$, the leakage current is 0. At this point, it is impossible to judge the insulation resistance to the ground, so the bridge resistance needs to be switched to state 2. In state 2, it can be seen that due to the imbalance of high resistance of bus grounding, when the positive electrode-to-earth insulation resistance is much greater than the negative electrode-to-earth insulation resistance, the leakage current value is the maximum, and the leakage current is negative. When $R_{n+} \times R_b = R_{n-} \times R_{a//c}$, the leakage current is 0 due to the bridge balance.

It can be seen from the comparison that the formula proposed in this paper can accurately calculate the insulation resistance of the anode and cathode for the simultaneous decline of the anode and cathode insulation.

3.3 Analysis of the experiment

In order to test the proposed distributed insulation monitoring system in this paper, an experimental setup was built, and a prototype device of the system was made for experiments. Figures 11 and 12 shows the experimental setup of insulation monitoring system proposed in this paper. Eight branches can be collected and calculated simultaneously. Figure 11 shows the central processing module of the system in this paper, whose function is to transmit the detection control signal, process the collected signal, calculate the insulation resistance, and complete the alarm or transmit the result to the upper computer. As shown in Figure 12, the signal acquisition module passes the positive and negative poles of each branch through the center of the current transformer at the same time.

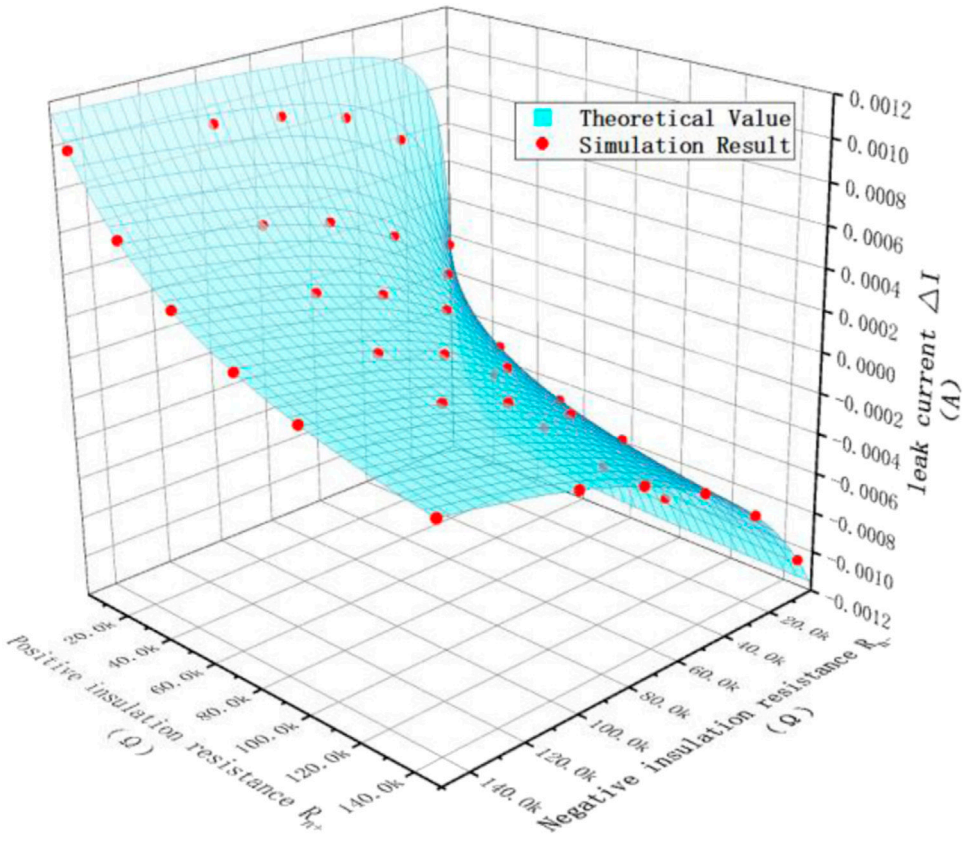

FIGURE 9
Simulation results are compared with the theoretical values under state 1.

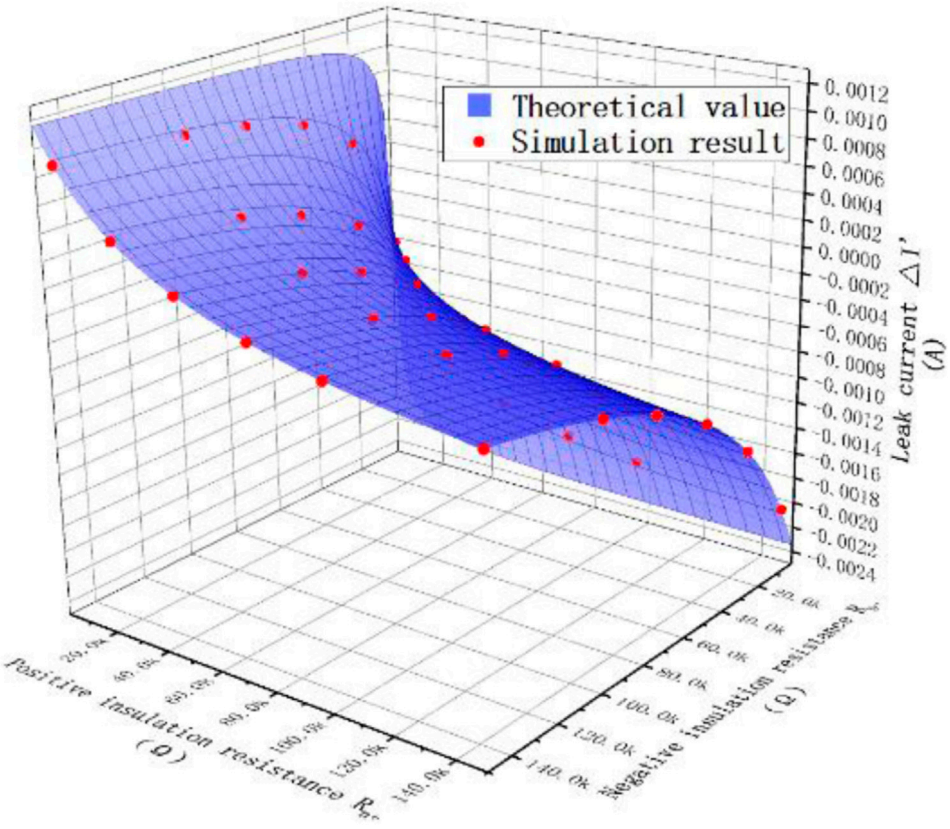

FIGURE 10
Simulation results are compared with the theoretical values under state 2.

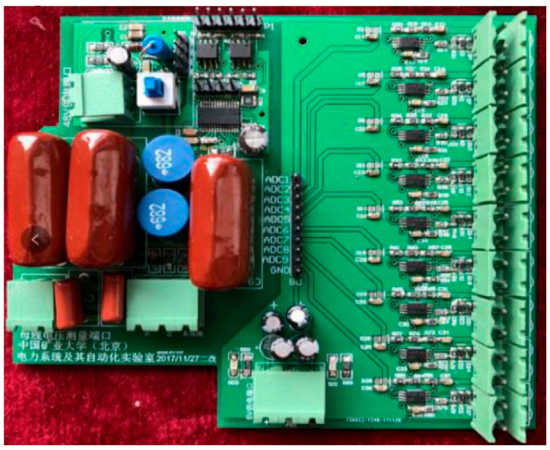

FIGURE 11
Central processing module of the system.

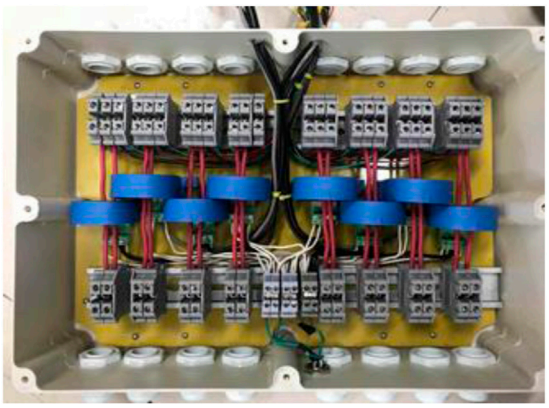

FIGURE 12
Transformer connection situation.

The current transformer sends the acquisition signal to the A/D acquisition module of the central processing module and to the oscilloscope used in the experiment. The positive and negative lines of one branch are simultaneously passed through the single-core DC current transformer. The transformer is powered by the central processing module, and the range is ± 10uA~2 mA. The circuit of the transformer is shown in Figure 13.

First, the single insulation drop detection was verified. In order to carry out a comprehensive analysis, three branches were selected for the failure test. For each branch, first, the negative insulation resistance was kept unchanged, and the positive electrode was

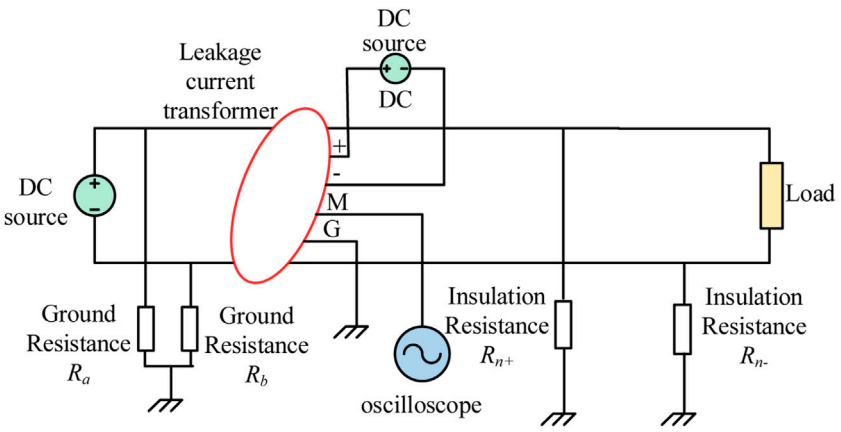

FIGURE 13
Experimental equivalent circuit.

TABLE 2 Simulation and theoretical parameter table of multi-branch cable insulation monitoring.

Positive insulation resistance/KΩ	Negative insulation resistance/ KΩ	State 1 leakage current ΔI/mA	State 2 leakage current ΔI′/mA	Calculated value of positive insulation resistance/KΩ	Calculated value of negative insulation resistance/KΩ	Positive insulation resistance error rate	Negative insulation resistance error rate
150	150	0	−0.280	153	151	2%	0.66%
150	28	−0.662	−1.331	150.2	28	0.1%	0%
100	28	−0.539	−1.232	100.2	28.2	0.2%	0.7%
100	75	−1.116	−0.522	101	75.8	1%	1.06%
75	50	−0.120	−0.062	76.5	51	2%	2%
75	28	−1.674	−1.12	75.4	28.3	0.5%	1%
50	50	0	−0.436	51	51	2%	2%
28	50	0.288	−0.071	27.3	48.7	−2.5%	−2.6%
28	8	−0.631	−1.46	28.3	8.08	1%	1%
8	28	0.627	−0.36	27.8	7.99	0.71%	1.25%

connected to the ground, 100 kΩ, 75 kΩ, 50 kΩ, 28 kΩ, and 8 kΩ. Multiple measurements of leakage current ΔI are averaged. Figure 14 shows the comparison between the experimental results and theoretical calculations. The error bar represents experimental data, and the curves are theoretical values. It is observed that the lower the insulation resistance to ground is, the smaller the resulting error will be.

It can be seen from this that the designed prototype can accurately determine and calculate the single pole-to-ground insulation resistance drop fault.

Then, the condition of positive and negative insulation resistances falling simultaneously was verified, the system bus contained switching resistance R_c, the resistance value of positive and negative insulation resistances to the ground was changed, and the leakage current ΔI before switching and $\Delta I'$ after switching was recorded. As shown in the following table, the calculated insulation parameter and its error for system with multi-branch insulation degradation are shown in Table 2.

The comparison between the calculated insulation parameters and the theoretical insulation parameters shows that the monitoring error of the system will gradually increase with the decrease in the difference of positive and negative line insulation resistances. However, the error of insulation resistance calculated by the system based on distributed selection is less than ± 3%, which fully meets the basic requirements of the system. Therefore, this principle can be applied to online insulation monitoring for all kinds of degradation.

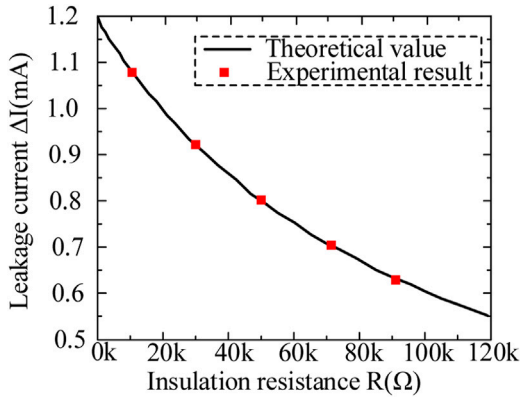

FIGURE 14
Comparison experimental results and theoretical calculation of the single branch.

4 Conclusion

Based on the analysis of the existing problems of the leakage protection technology for DC power supply systems in domestic and abroad, and focus on the insulation degradation fault of the DC power system in the communication station, this paper proposes an on-line insulation monitoring system based on distributed selection. This system can realize online insulation monitoring, and can quickly and accurately diagnose the faulty branch with insulation degradation, single-line grounding fault, and the grounding fault of the remote equipment shell

Through experiments and simulations, the conclusions are as follows:

(1) When the monopole-to-ground insulation drops, the smaller the monopole-to-ground insulation resistance is, the greater the leakage current will be. The simulation and experiment basically agree with the calculation results, which prove that the formula proposed in this paper can calculate the insulation resistance accurately.
(2) When both positive and negative insulation resistances are decreased, in state 1, the larger the difference between the positive pole-to-ground insulation resistance and the negative pole-to-ground insulation resistance is, the larger the leakage current value will be, and the direction is related to the insulation resistance at the poles. When $R_{n+} > R_{n-}$, the leakage current is negative; when $R_{n+} < R_{n-}$, the leakage current is positive; and when $R_{n+} = R_{n-}$, the leakage current is 0. At this point, it is impossible to judge the insulation resistance to the ground, so the bridge resistance needs to be switched to state 2. In state 2, it can be seen that due to the imbalance of high resistance of bus grounding, when the positive electrode-to-earth insulation resistance is much greater than the negative electrode-to-earth insulation resistance, the leakage current value is the maximum, and the leakage current is negative. When $R_{n+} \times R_b = R_{n-} \times R_{a//c}$, the leakage current is 0 because of the bridge balance. The simulation results are in good agreement with the calculated values, which proves the theory proposed in this paper. Compared with the calculated results, the experimental results have some errors; the error rate is less than 3%, in line with the general engineering standards. Therefore, it is shown that the distributed DC insulation on-line monitoring technology proposed in this paper can accurately complete the calculation and fault judgment of the positive and negative insulation resistances of each branch.

Data availability statement

The original contributions presented in the study are included in the article/Supplementary Material; further inquiries can be directed to the corresponding author.

Author contributions

CF: methodology and writing—original manuscript. PY: data curation, and writing—review and editing. ZG: resources, supervision, and writing—review and editing. HJ: formal analysis, and writing—review and editing. XZa: investigation, and writing—review and editing. XZh: writing—review and editing.

Funding

The authors declare that no financial support was received for the research, authorship, and/or publication of this article.

Conflict of interest

The authors declare that the research was conducted in the absence of any commercial or financial relationships that could be construed as a potential conflict of interest.

Publisher's note

References

Chen, Y. (2018a). Research on common DC current detection technolog. *Low. Volt. Appar.* 22, 82–86. doi:10.16628/j.cnki.2095-8188.2018.22.015

Chen, Y., and Sun, J. (2018). Research on residual current protection device with DC component detectio. *Electr. Energy Manag. Technol.* 14, 37–41. doi:10.16628/j.cnki.2095-8188.2018.14.007

Chen, Z., Li, H., Liu, L., Xiang, L., and Bai, B. (2019). DC bias treatment of hybrid type transformer based on magnetic flux modulation mechanism. *IEEE Trans. Magnetics* 55 (6), 1–4. doi:10.1109/tmag.2019.2903566

Dawalibi, F. P., Southey, R. D., and Baishiki, R. S. (1990). Validity of conventional approaches for calculating body currents resulting from electric shocks. *IEEE Trans. Power Deliv.* 5 (2), 613–626. doi:10.1109/61.53063

Hellgren, O. (2004). "A key to expanding older DC systems with new equipment," in *Intelec 2004. 26th annual international telecommunications Energy conference*, 241–247. doi:10.1109/INTLEC.2004.1401473

Huang, Y., Qin, J., Liu, N., Huang, H., Zhang, J., Bi, L., et al. (2019). Differential current method of unbalanced bridge with double bridge arm for DC insulation detection. *Electr. Energy Manag. Technol.* 11, 57–61. doi:10.16628/j.cnki.2095-8188.2019.11.011

Jiang, J., and Ji, H. (2009). "Study of insulation monitoring device for DC system based on four-switch combination," in *2009 international conference on computational intelligence and software engineering*, 1–4. doi:10.1109/CISE.2009.5363460

Li, H. (2012). Application analysis of high voltage DC power supply system (240V) in a test project. *Intelec* 2012, 1–7. doi:10.1109/INTLEC.2012.6374511

Li, K., Niu, F., Wu, Y., Wang, Y., Dai, Y., Wang, L., et al. (2015). Nonlinear current detection based on magnetic modulation technology. *IEEE Trans. Magnetics* 51 (11), 1–4. Art no. 4004804. doi:10.1109/tmag.2015.2446134

Luo, Z., Ren, X., Yang, H., Cai, G., Qing, C., and Luo, Y. (2016). "Research on the insulation monitoring devices for DC power system based on the detection technology of DC bus to grounding capacitance," in *2015 2nd international forum on electrical engineering and automation*, 117–120. doi:10.2991/ifeea-15.2016.24

Olszowiec, P. (2017). Influence of insulation monitoring devices on the operation of DC control circuits. *Power Technol. Engineeing* 6 (50), 653–656. doi:10.1007/s10749-017-0768-1

Quintela, F. R., Redondo, R. C., Melchor, N. R., and Redondo, M. (2009). A general approach to Kirchhoff's Laws. *IEEE Trans. Educ.* 52 (2), 273–278. doi:10.1109/te.2008.928189

Roberts, D. (2009). 50-V shock hazard threshold. *IEEE Trans. Industry Appl.* 46 (1), 102–107. doi:10.1109/TIA.2009.2036541

Rybski, R., Kaczmarek, J., and Kontorski, K. (2015). Impedance comparison using unbalanced bridge with digital sine wave voltage sources. *IEEE Trans. Instrum. Meas.* 64 (12), 3380–3386. doi:10.1109/TIM.2015.2444255

Shi, M., Miao, H., Fei, J., Ge, X., Xiao, X., Wu, F., et al. (2022). "The development of DC leakage current monitoring device," in *2022 IEEE 5th international electrical and Energy conference (CIEEC)* (Nangjing, China: IEEE).

Wang, S., Li, H., Liu, Q., Huang, Q., and Liu, Y. (2020). "Design of a DC residual current sensor based on the improved DC component method," in *2020 IEEE power & Energy society general meeting (PESGM)* (Canada: Montreal, QC), 1–5.

Xie, Z., Han, S., and Wang, L. (2016). "The magnetic modulation of DC transformer core characteristics analysis," in *2016 3rd international conference on information science and control engineering (ICISCE)*, 1433–1438. doi:10.1109/ICISCE.2016.306

Yin, G., Liu, Y., Xu, H., Li, M., and Li, J. (2012). "The new DC system insulation monitoring device based on phase differences of magnetic modulation," in *2012 international conference on systems and informatics (ICSAI2012)*, 585–658. doi:10.1109/ICSAI.2012.6223065

Yow-Chyi, L., and Chen-You, L. (2012). Insulation fault detection circuit for ungrounded DC power supply systems. *SENSORS* 2012, 1–4. doi:10.1109/ICSENS.2012.6411550

Zhao, H., Xiao, X., and Sun, Q. (2017). Identifying electric shock in the human body via α dispersion. *IEEE Trans. Power Deliv.* 33 (3), 1107–1114. doi:10.1109/TPWRD.2017.276616

Zhao, X., Li, L., Lu, J., Cheng, Z., and Lu, T. (2012). Characteristics analysis of the square laminated core under DC-biased magnetization by the fixed-point harmonic-balanced FEM. *IEEE Trans. magnetics* 48 (2), 747–750. doi:10.1109/tmag.2011.2174776

Zhenbin, C., Weiya, C., Xiangyu, C., Qiao, H., Lu, H., and Qiu, N. (2021). A new method of insulation detection on electric vehicles based on a variable forgetting factor recursive least squares algorithm. *IEEE Access* 9, 73590–73607. doi:10.1109/access.2021.3079332

Nomenclature

Parameter

r_{bady}	Resistance of the human body
r_k	Insulation resistance
U_0	Voltage level of the DC power supply system for the communication system
CT_n	DC insulation monitoring transformers installed in branch n
CT_{all}	DC insulation monitoring transformer which is installed at the bus with high resistance to ground
R_{n+}/R_{n-}	Insulation resistance of branch n
R_a/R_b	Balanced high resistance to ground of the bus
U	Anode voltage
R_n	Set values for the insulation monitoring system
R_c	New resistance and switching device to the positive pole of the bus
K	Initial state of the switch

Variable

I_k	Current flowing through the body
I_{1+}	Leakage current
ΔI_n	Current increment of branch n
$\Delta I_n^{'}$	Current measured by CTn in branch n
U_2	Negative electrode-to-earth voltage
ΔI	Leakage current

frontiers | Frontiers in Energy Research

TYPE Original Research
PUBLISHED 08 November 2023
DOI 10.3389/fenrg.2023.1289275

OPEN ACCESS

EDITED BY
Shuai Yao,
Cardiff University, United Kingdom

REVIEWED BY
Haixiang Zang,
Hohai University, China
Tong Zhang,
Cardiff University, United Kingdom

*CORRESPONDENCE
Shutan Wu,
wushutan@seu.edu.cn

RECEIVED 05 September 2023
ACCEPTED 16 October 2023
PUBLISHED 08 November 2023

CITATION
Zhu L, Wu S, Liu H, Wang Q and Tang Y (2023), Spatio-temporal load migration potential of data centers: Evaluation and application.
Front. Energy Res. 11:1289275.
doi: 10.3389/fenrg.2023.1289275

Spatio-temporal load migration potential of data centers: Evaluation and application

Lei Zhu, Shutan Wu*, Haoyu Liu, Qi Wang and Yi Tang

School of Electrical Engineering, Southeast University, Nanjing, China

The wide distribution of data centers and the delay tolerance of computing tasks endow data center loads with adjustable characteristics in both temporal and spatial dimensions. Due to the characteristics of abundant spatiotemporal flexibility, data centers can participate in the optimization of power system operation and regulation. To quantify this flexibility, this paper proposes a spatiotemporal load migration potential evaluation model. Meanwhile, a data center energy management strategy is combined with the characteristics of spatiotemporal load migration, which deeply exploits the migration potential through the spatiotemporal redistribution of delay-tolerant tasks, as well as server ON/OFF scheduling and CPU operating frequency scaling across different spatial locations. A case study demonstrates that adopting the proposed approach considering an energy management strategy can effectively improve the load migration potential of data centers. The migration characteristics of data centers have great application prospects in reducing carbon emissions and enhancing operational flexibility.

KEYWORDS

data centers, spatio-temporal load migration, potential evaluation, energy management strategy, flexibility

1 Introduction

The gradual replacement of traditional thermal power sources with high-penetration renewable energy sources poses a significant challenge to power systems in dealing with multidimensional uncertainties. The inadequate regulation capacity on the power generation side necessitates the participation of flexible resources on the load side in power dispatching, thereby improving the flexibility of power systems (Han et al., 2022). For example, energy storage systems (Ma et al., 2022) and temperature-controlled loads (Song et al., 2022) are commonly used to adjust the temporal distribution of loads to alleviate peak power demand and decrease the power supply pressure on the power generation side. With the continuous advancement of digital infrastructure construction, new types of spatially distributed resources (e.g., data centers (DCs), communication base stations, and electric vehicles) have emerged to provide novel solutions for power load adjustment. These resources can intercommunicate through various wide-area networks (i.e., computation networks (Chen et al., 2021a), communication networks (Fan et al., 2021) and transportation networks (Yuan et al., 2022)) to indirectly realize the spatial migration of power energy.

The surge in demand for data processing is prompting cloud service operators to build more geographically distributed DCs, with the aim of achieving low-latency and highly reliable services, which makes DCs emerge as major electricity consumers (Martijn and Fons, 2021). According to reports, the electricity consumption of DCs

reached approximately 3% of the total amount globally in 2016 (Danilak, 2017), and it is still doubling every 4 years (Long et al., 2022). In some metropolises, such as Beijing in China, the power load capacity occupied by DCs has already accounted for 8% of the total power load capacity in 2021. Given the rapid expansion of data centers at the spatiotemporal scale and migration level, it is of great importance to fully exploit the adjustment potential of DC loads in power systems.

Current research on utilizing the adjustment capability of DCs can be primarily categorized into two levels. That is, temporal level and spatial level. At the temporal level, the workloads of DCs with low delay sensitivity can be shifted to alternate working hours to alleviate the power load pressure at a specific time. This characteristic enables DCs to be integrated into demand response (Kwon, 2020) to improve frequency quality (Fu et al., 2020) or smooth power fluctuation (Yang et al., 2018), similar to traditional interruptible power loads.

What sets DCs apart is their capacity to migrate workloads spatially, thereby reducing power loads in specific locations to achieve regulation objectives (Wang et al., 2022). Therefore, the spatial load migration capability of geo-distributed data centers is more effective in power dispatch. There have been relevant studies on the application of spatial load migration by DCs for power system regulation purposes. In terms of operational stability, DCs can flexibly adjust the spatial distribution of power loads to diminish voltage violations (Chen et al., 2021b), relieve network congestion (Chen et al., 2021c) and reduce peak loads (Guo et al., 2021a). In terms of operational economy, existing studies achieved the optimal comprehensive operation cost of power systems (Gu et al., 2015) and renewable energy consumption (Yang et al., 2022) through spatial scheduling in DCs. In terms of resilience enhancement, DCs can be dispatched in pre-event prevention (Liu et al., 2022), during-event emergency control (Yu et al., 2015) and post-event restoration (Liu et al., 2019) to reduce power loss after extreme events. The benefits of DCs as spatiotemporal flexible resources for participating in power grid scheduling have been demonstrated in the abovementioned literature. However, the differentiation of the spatiotemporal load migration (STLM) potential of DCs in different scenarios has not been considered. It is imperative to quantitatively evaluate the STLM potential of DCs to devise more effective grid regulation strategies tailored to different scenarios, but this issue remains unexplored in current research.

The STLM potential of DCs is primarily derived from the redistribution of workloads, which is heavily influenced by the energy management strategies implemented within the DCs. By employing energy management strategies, internal equipment in data centers can effectively reduce energy consumption and thereby enhance the STLM potential of DCs. Some energy-saving technologies and strategies have been studied, such as dynamic voltage/frequency scaling (DVFS) (Wang et al., 2017), dynamic cluster server configuration (DCSC) (Li et al., 2012), and the collaborative control method of information technology (IT) systems and cooling systems (Fu et al., 2020; Lyu et al., 2021), achieving the optimization goal of minimum total energy consumption. However, there is a paucity of research that integrates internal energy management strategies with external migration schemes. Inadequate energy management strategies can amplify the burden on DC task processing and increase the power supply pressure on the power systems, ultimately resulting in a significant reduction in the STLM potential of DCs.

This paper proposes a quantitative approach for evaluating the STLM potential of DCs, which provides a basis for devising diverse power scheduling strategies. Meanwhile, the DVFS-DCSC technique, coupled with an energy management mechanism, is adopted to further enhance the STLM potential of DCs. Then, an application model of a day-ahead scheduling strategy considering the STLM potential of DCs is proposed, and the flexibility and economic efficiency of power systems are significantly improved. The major contributions of this paper are as follows.

1) An STLM potential evaluation model is established to quantify the migration loads of urban DCs in different scenarios, which evaluates the STLM potential by spatiotemporal workload redistribution.
2) An energy management strategy is applied in the proposed potential evaluation model to further exploit the STLM potential of DCs, and server ON/OFF scheduling and CPU operating frequency selection are optimized to maximize the STLM potential.
3) A workload optimization scheduling strategy considering customer satisfaction is established to ensure the quality of service (QoS) of DCs and avoid workload accumulation. The STLM ability of tasks with different service-level agreements (SLAs) is also analyzed in this case.
4) A day-ahead scheduling method that integrates the STLM of DCs with DVFS-DCSC technology is proposed based on the proposed evaluation model. The carbon emissions and the CPU utilization are better optimized compared with the conventional scheduling strategy.

The remainder of this paper is organized as follows. The theoretical basis of DCs' spatiotemporal flexibility is introduced in Section 2. The DC model and STLM potential evaluation model are established in Sections 3, 4, respectively. In Section 5, case studies on the STLM potential evaluation of DCs and day-ahead scheduling strategies considering energy management strategies are carried out, and the results are displayed and discussed accordingly. Section 6 gives a brief conclusion.

2 Theoretical basis of DC STLM potential

The coupling architecture of the computation network and power system is shown in Figure 1. The DC load exhibits high flexibility in both the temporal and spatial dimensions. The prioritization of workloads and the emerging trend of cloud interconnectivity among DCs endow them with the capability of STLM. Therefore, the spatiotemporal workload redistribution among DCs is the basis for them to participate in the STLM of power loads.

Many studies have been performed on temporal load migration, which will not be discussed in detail. This section focuses on spatial load migration, which refers to a scheduling method that involves either shedding loads at some locations or migrating loads that ought to exist in one center to other centers (Wang et al., 2022). The migration potential of spatially flexible loads can be assessed

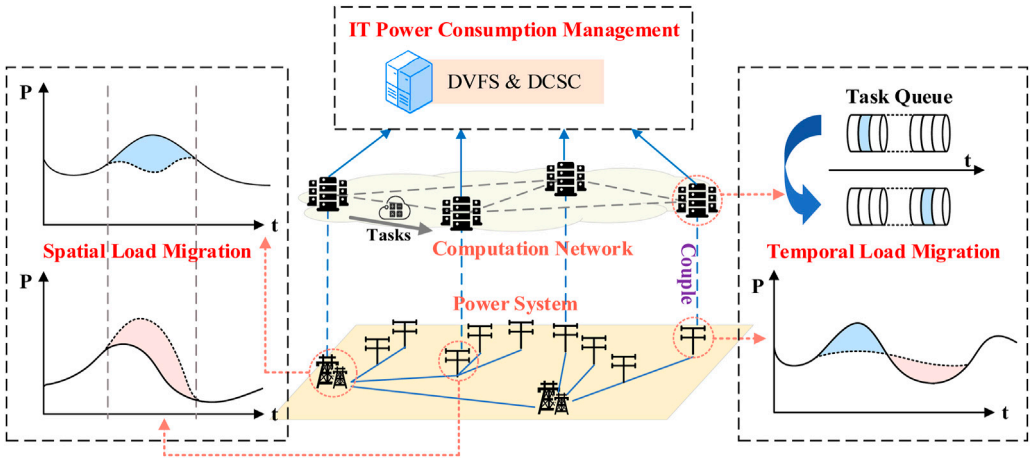

FIGURE 1
Coupling architecture of the computation network and power network.

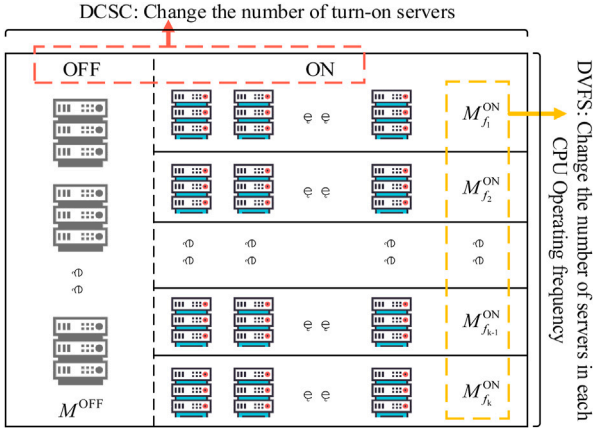

FIGURE 2
DVFS-DCSC energy management strategy.

quantitatively from various perspectives, including the temporal scale, spatial scale, and migration level. The temporal scale determines the response speed of load migration, the spatial scale determines the coverage range of load migration, and the migration level determines the extent to which migration scheduling can contribute to overall system performance. Regional DCs achieve spatial interconnection via backbone optical networks, whose extremely high transmission speeds and minimal delay rates of merely 0.02 ms/km (Zhou et al., 2016) enable rapid load migration across timescales ranging from seconds to hours. In addition, the optical fiber network also has the characteristics of high bandwidth and strong reliability, facilitating the interconnection not only of local distribution network DCs but also of transnational DCs. Hence, the spatial range of data load migration can span several kilometers to several thousand kilometers. To accommodate the ever-increasing data business requirements, modern large-scale DCs must be capable of sustaining loads that can measure in the tens of megawatts, thereby necessitating migration levels spanning from hundreds of kilowatts to tens of megawatts.

The STLM potential of DCs is related to many factors, including the number and capacity of fiber links connected to them, their workload processing capacity, and the number of tasks assigned to each time period. However, the potential relying on only the spatiotemporal redistribution of workloads is relatively limited, and the STLM potential of DCs can be further enhanced through optimization of their energy management strategies. DVFS is an efficient and feasible energy management technology for DCs, improving the utilization of a server via discrete adjustments to CPU operating voltage or frequency, thereby reducing the power consumption. Meanwhile, DCSC reduces total cluster power consumption by consolidating the load on a subset of machines and turning off the rest during low workload periods (Guo et al., 2021b). Adopting the DVFS-DCSC energy management strategy, as seen in Figure 2, can not only reduce the target DCs' energy consumption but also improve the ability of other DCs to undertake workloads, thus further enhancing the STLM potential of the target DC.

3 Modeling and characteristics of DCs

Considering the factors affecting the DCs' STLM, the models of DC power consumption, DVFS technology, DCSC technology, optical network power consumption, workloads and QoS are established in this section.

3.1 Power consumption model of DC

The DC is mainly composed of IT equipment, cooling equipment and distribution equipment, and the energy consumption of DC can be expressed as (1). Among them, the IT equipment energy consumption accounts for the largest

proportion of the total energy consumption, which has the widest range of changes. As the core element of IT equipment, servers are the key equipment for massive data computing and processing, which accounts for the largest proportion of IT equipment energy consumption. Therefore, it can be used to represent the total energy consumption of IT equipment, as shown in (2). In the typical server power consumption model, the part of the CPU changes the most, and the power consumption of other components, such as memory, hard disk and network, can be regarded as approximately constant (Jin et al., 2020). Therefore, the power consumption model of a single server can be represented by the superposition of fixed power and dynamic power, which is expressed as (3).

$$P^{\mathrm{DC}} = P^{\mathrm{IT}} + P^{\mathrm{CO}} + P^{\mathrm{EL}} \tag{1}$$

$$P^{\mathrm{IT}} = M^{\mathrm{ser}} \cdot P^{\mathrm{ser}} \tag{2}$$

$$p^{\mathrm{ser}} = p^{\mathrm{ser}}_{\mathrm{fixed}} + p^{\mathrm{ser}}_{\mathrm{dyna}} \tag{3}$$

where P^{DC} denotes the power consumption of the DC; P^{IT} denotes the power consumption of IT equipment; P^{CO} denotes the power consumption of cooling equipment; and P^{EL} denotes the power consumption of distribution equipment. M^{ser} is the number of servers owned by the data center; P^{ser} is the power consumption of the servers. $p^{\mathrm{ser}}_{\mathrm{fixed}}$ and $p^{\mathrm{ser}}_{\mathrm{dyna}}$ denote the fixed power and dynamic power of the servers, respectively.

The cooling energy consumption P^{CO} depends on the amount of heat generated by servers, and the heat is almost entirely derived from the computing energy consumption (Liu et al., 2018). In DCs, the energy consumption of cooling and distribution systems can be estimated based on the typical power usage effectiveness (PUE). PUE is defined as the energy consumption ratio of the entire DC to the IT equipment, so P^{DC} can be expressed as (4).

$$P^{\mathrm{DC}} = \mathrm{PUE} \cdot P^{\mathrm{IT}} \tag{4}$$

3.2 DVFS model of DC

For the status of DC operation, there are many DCs with redundant server configurations and low CPU utilization in most time periods. DVFS changes the power consumption of the DC by discretely adjusting the CPU operating voltage or frequency. To facilitate actual operation, this paper only considers the adjustment of the CPU operating frequency f and sets several suitable frequencies for selection, as shown in (5). Each operating frequency has a corresponding server processing capacity, which is proportional to this frequency. The dynamic power of the server is related to the third power of the CPU operating frequency. The higher the CPU operating frequency is, the stronger the ability to process the workloads, although the consequence of energy consumption greatly increases. The CPU utilization can be calculated by the ratio of the capacity needed for task processing to the server processing capacity, as shown in (6–8). When f is constant, $p^{\mathrm{ser}}_{\mathrm{dyna}}$ is proportional to U, which is described in (9). For processing the same number of tasks, the CPU consumes less energy under a lower frequency. Therefore, the frequency can be reduced in the period of fewer workloads to improve the CPU utilization and decrease the DC energy consumption.

$$f \in \{f^{\mathrm{CPU}}_1, f^{\mathrm{CPU}}_2, \cdots, f^{\mathrm{CPU}}_{k-1}, f^{\mathrm{CPU}}_k\} \tag{5}$$

$$\boldsymbol{U} = \frac{\lambda}{\mu} \tag{6}$$

$$\boldsymbol{\lambda} = \frac{L}{M^{\mathrm{ser}}} \tag{7}$$

$$\boldsymbol{L} = \sum_{task \epsilon TASK} M^{\mathrm{process}}_{task} \cdot \gamma^{task} \tag{8}$$

$$P^{\mathrm{ser}}_{\mathrm{dyna}} = A^{\mathrm{ser}} \cdot f^3 \cdot U \tag{9}$$

where f^{CPU} denotes the working frequency of the CPU. U is the CPU utilization rate; λ is the tasks processed by a server during unit time; μ is the processing capacity of a server. A^{ser} denotes the dynamic power consumption coefficient of a server; L denotes the total load that the DC needs to process; $M^{\mathrm{process}}_{task}$ denotes the total number of processed tasks; γ^{task} denotes the CPU capacity required to process one task; $TASK$ is a set of task types.

According to the abovementioned analysis, DVFS can be applied to enhance the STLM potential of DCs. The DCs to which migration terminates can increase f to undertake more tasks, while the DCs from which migration originates can decrease f to reduce energy consumption, which can further expand the DC migration load. Given that DVFS can be executed within a few milliseconds (Li et al., 2012), it represents a viable strategy for scheduling within temporal scales ranging from seconds to hours.

3.3 DCSC model of DCs

On the one hand, adjusting the dynamic power of the server has a good energy-saving effect on the DC. On the other hand, the fixed power of the server is also a part that cannot be ignored. The spatial migration of power loads in DCs is achieved through the spatiotemporal redistribution of workloads. This part has limited migration potential and cannot cope well with extreme situations such as large power shortages in power systems. Although the fixed power cannot freely change the spatial distribution of power loads through data load redistribution among DCs such as the dynamic power, local DCs can shut down the current idle servers while simultaneously activating new servers elsewhere within the network to tackle increased workload demand. Therefore, it can be considered that the fixed power of servers also has the ability of spatial migration. In other words, the ON/OFF operation of geographically distributed servers transforms fixed power into a schedulable spatial resource. Since the cooling energy consumption of the DC depends on the heat generated by the IT equipment, it will also change with the regulation of the IT equipment for a constant PUE, thereby reducing the total energy consumption and greatly improving the STLM potential of DCs.

To prolong the service life of the servers as much as possible, the servers should avoid frequent ON/OFF operation, thereby setting a minimum ON/OFF time to force them to maintain at least for a period before becoming another state, as shown in (10). The ON/OFF operation of a server is a second-level delay process, so DCSC is more suitable as a minute-level or hour-level scheduling method.

$$\begin{aligned} &I_{t_1} = 1, I_{t_2} = 0, I_{t_3} = 1 \\ &\forall t_1 < t_2 < t_3, t_2 - t_1 \geq MD, t_3 - t_2 \geq MD \end{aligned} \tag{10}$$

where I_t denotes the operating state of a server at time t, 1 represents ON, 0 represents OFF, and *MD* denotes the minimum ON/OFF time of a server.

3.4 Power consumption model of optical networks

The interconnection communication network that DCs rely on is generally composed of backbone optical networks, which have large transmission capacity, extremely fast transmission speed and much lower delay. For typical optical networks, the energy consumption can be generated by an IP layer, an optical–electric–optical layer and a wavelength-division multiplexing layer (Zhang et al., 2015). The networks' energy consumption is jointly borne by the source node and destination node (Deylamsalehi et al., 2018), assuming that the source node and the destination node bear half of the network energy consumption.

Referring to the power consumption model of the server, a simplified power consumption model of the optical network can also be expressed as the superposition of fixed power and dynamic power (Dayarathna et al., 2016). The fixed power is the elementary energy consumption of the communication equipment, which is unrelated to network traffic. The dynamic power is the energy consumption of the network transmission and is related to the network traffic (Sun et al., 2013). Furthermore, the bandwidth and traffic within optical networks can be likened to the processing capacity and workload demand of CPUs in servers. The power consumption of the optical fiber link (i, j) is shown in (11), and (12) represents the power consumption of network element (NE) node i.

$$P_{ij}^{\text{net}} = p_{\text{fixed}}^{\text{net}} + l_{ij} \cdot p_{\text{dyna}}^{\text{net}} \tag{11}$$

$$P_i^{\text{net}} = \frac{1}{2} \sum_{j:\ (i,j)\in E} P_{ij}^{\text{net}} \tag{12}$$

where P_{ij}^{net} denotes the power consumption of link (i, j) and $p_{\text{fixed}}^{\text{net}}$ and $p_{\text{dyna}}^{\text{net}}$ denote the fixed power and dynamic power of the optical fiber network, respectively. l_{ij} is the traffic of link (i, j); E is the set of optical fiber links. $\sum_{j:\ (i,j)\in E} P_{ij}^{\text{net}}$ represents the sum of the power consumption of all links connected to node i.

3.5 Models of workloads and QoS

When exploring the DCs' STLM potential, it is necessary to find an appropriate trade-off strategy between adjusting the power consumption of IT equipment and meeting the users' requirements for QoS. The workload can be divided into delay-sensitive tasks and delay-tolerant tasks according to the SLA (Cupelli et al., 2018). Delay-sensitive tasks, such as live broadcast, real-time payment and real-time measurement, need to be processed immediately after the arrival of the tasks at t_{ar}, and thus, they are not suitable to be migrated to other DCs for processing as spatially flexible resources. In contrast, delay-tolerant tasks, such as image processing and scientific computing, only need to be completed before the deadline $t_{\max}$. The QoS constraints are shown in (13), where $\Delta t_{\text{tr,qu}}$ denotes the queuing waiting time for migration, Δt_{tr} denotes the needed time for task migration, $\Delta t_{\text{pro,qu}}$ denotes the waiting time for processing in the queue, and Δt_{pro} denotes the needed time for task processing. As shown in Figure 3, different types of tasks have different SLAs for the deadline of completion, which can vary from a few minutes to several hours, so they have great spatiotemporal flexibility. After migration to other DCs at t_{ar}', the tasks can be stored in the hard disk without immediate processing. Consequently, the time points t_{mig} and t_{st} for migration and processing can be freely selected to achieve the optimal operation strategy.

$$\Delta t_{\text{tr,qu}} + \Delta t_{\text{tr}} + \Delta t_{\text{pro,qu}} + \Delta t_{\text{pro}} \le t_{\max} \tag{13}$$

To avoid the backlogs being processed near $t_{\max}$, a task-scheduling optimization strategy considering customer satisfaction is established. The variation in customer satisfaction with waiting time is not completely linear but rather a nonlinear curve. Prolonged wait times lead to reduced customer perception, ultimately resulting in a diminishing marginal rate of satisfaction. Positive values denote satisfaction, whereas negative values imply dissatisfaction. Since all tasks need to be strictly processed before $t_{\max}$ according to the SLA, the negative part of the curve is not considered. The cosine distributed time satisfaction function is truncated from the part of the cosine function curve, which is expressed as (14). The curve changes little around the thresholds L_i and U_i, and the slope of the middle part of the curve is larger. Let U_i be $t_{\max}$, and let L_i be set as a reasonable value. To enable the tasks to be completed under the conditions of achieving high time satisfaction, the average customer satisfaction can be set to be greater than a certain fixed value.

$$S(t) = \begin{cases} 1, t \in [0, L_i] \\ 0.5 + 0.5\cos\left(\dfrac{\pi}{U_i - L_i} \cdot \left(t - \dfrac{U_i + L_i}{2}\right) + \dfrac{\pi}{2}\right), t \in [L_i, U_i] \end{cases} \tag{14}$$

To clarify the completion of each batch task in each time period, matrix A is established as shown in (15). A is a T-order sparse matrix, and its lower-left corner and upper-right corner are composed of zero elements. The zero elements in the lower-left corner indicate that the tasks arriving at t cannot be processed ahead of t, and the zero elements in the upper-right corner indicate that the number of tasks violating SLAs is none, which meets the maximum response time constraints of QoS. The average value of customer satisfaction $\overline{S_{task}}$ can be defined as the ratio between the total satisfaction and the total number of tasks processed, which can be calculated in (16) and (17).

$$A = \begin{bmatrix} M_{task,11}^{\text{fin}} & M_{task,12}^{\text{fin}} & M_{task,13}^{\text{fin}} & \cdots & M_{task,1t_{\text{task}}^{\max}}^{\text{fin}} & 0 & 0 & \cdots & 0 \\ 0 & M_{task,21}^{\text{fin}} & M_{task,22}^{\text{fin}} & \cdots & M_{task,2(t_{\text{task}}^{\max}-1)}^{\text{fin}} & M_{task,2t_{\text{task}}^{\max}}^{\text{fin}} & 0 & \cdots & 0 \\ \vdots & & \vdots & & \vdots & \vdots & & & \vdots \\ 0 & \cdots & 0 & M_{task,(T-t_{\text{task}}^{\max})1}^{\text{fin}} & M_{task,(T-t_{\text{task}}^{\max})2}^{\text{fin}} & M_{task,(T-t_{\text{task}}^{\max})3}^{\text{fin}} & \cdots & M_{task,(T-t_{\text{task}}^{\max})t_{\text{task}}^{\max}}^{\text{fin}} & 0 \\ 0 & \cdots & 0 & 0 & M_{task,(T-t_{\text{task}}^{\max}+1)1}^{\text{fin}} & M_{task,(T-t_{\text{task}}^{\max}+1)2}^{\text{fin}} & \cdots & M_{task,(T-t_{\text{task}}^{\max}+1)(t_{\text{task}}^{\max}-1)}^{\text{fin}} & M_{task,(T-t_{\text{task}}^{\max}+1)t_{\text{task}}^{\max}}^{\text{fin}} \\ 0 & \cdots & 0 & 0 & 0 & M_{task,(T-t_{\text{task}}^{\max}+2)1}^{\text{fin}} & \cdots & M_{task,(T-t_{\text{task}}^{\max}+2)(t_{\text{task}}^{\max}-2)}^{\text{fin}} & M_{task,(T-t_{\text{task}}^{\max}+2)(t_{\text{task}}^{\max}-1)}^{\text{fin}} \\ \vdots & & \vdots & \vdots & \vdots & \vdots & & \vdots & \vdots \\ 0 & \cdots & 0 & 0 & 0 & 0 & 0 & M_{task,(T-1)1}^{\text{fin}} & M_{task,(T-1)2}^{\text{fin}} \\ 0 & \cdots & 0 & 0 & 0 & 0 & 0 & 0 & M_{task,T1}^{\text{fin}} \end{bmatrix} \tag{15}$$

$$\bar{S}_{task} = \frac{\sum_{t=1}^{t_{task}^{\max}} M_{task,t}^{\text{fin}} \cdot S_{task}(t)}{\sum_{t=1}^{t_{task}^{\max}} M_{task,t}^{\text{fin}}} \tag{16}$$

$$M_{task,t}^{\text{fin}} = \sum_{a=1}^{T+1-t} M_{task,a(t+a-1)}^{\text{fin}} \tag{17}$$

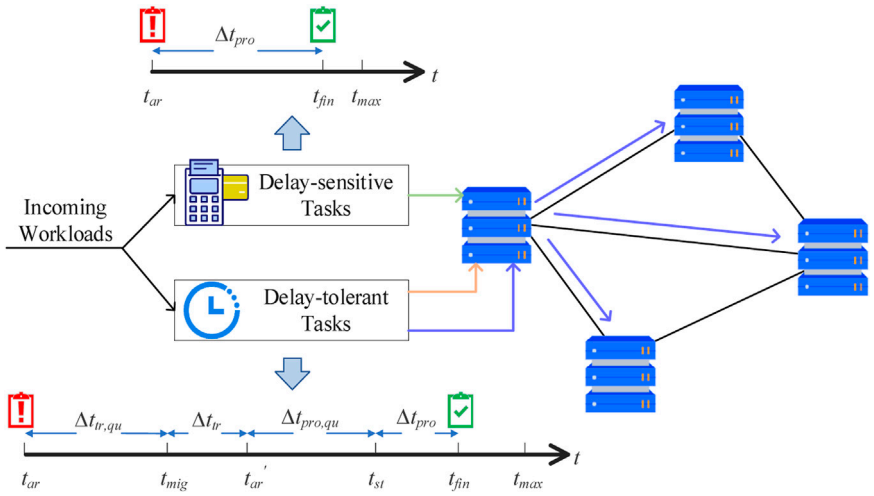

FIGURE 3
IT workload models with different delay tolerances.

where $M^{\text{fin}}_{task,ab}$ denotes the number of tasks received at time a and finished in period (b-1, b]; $t_{task}{}^{\max}$ denotes the deadline of completion time for *task*; $S_{task}(t)$ denotes the satisfaction value of completing the task in period (t-1, t); and $M^{\text{fin}}_{task,t}$ denotes the number of all tasks finished in period (t-1, t].

4 Potential evaluation model of the DCs' STLM

The above models can be applied to the STLM potential evaluation of DCs, and the corresponding objective functions and constraints are set in the section.

4.1 Objective function of STLM potential evaluation

Considering the energy management strategy, optical network allocation, and QoS, the potential evaluation model of the DCs' STLM is established. To obtain the maximum STLM of region i, the minimum sum of the power consumption of the DC and NE in region i at time T is taken as the objective function, as expressed in (18) and (19).

$$\min P^{\text{total}}_{i} = \sum_{t=1}^{T}\left(P^{\text{DC}}_{i,t} + P^{\text{net}}_{i,t}\right) \tag{18}$$

where

$$\begin{cases} P^{\text{DC}}_{i,t} = \text{PUE}_i \cdot \left[M^{\text{ON}}_{i,t} \cdot p^{\text{ser}}_{\text{fixed}} \right. \\ \left. + \sum_{k\in K}\left(\dfrac{\sum_{task\in TASK} M^{\text{process}}_{i,k,t,task} \cdot \gamma^{task}}{\mu_{i,k}} \cdot A^{\text{ser}} \cdot f^{3}_{i,k} \right) \right] \\ P^{\text{net}}_{i,t} = \dfrac{1}{2} \sum_{j:\ (i,j)\in E} \left(p^{\text{net}}_{\text{fixed}} + l_{ij,t} \cdot p^{\text{net}}_{\text{dyna}} \right) \end{cases} \tag{19}$$

4.2 Constraints of STLM potential evaluation

4.2.1 Constraint of power balance

(20) and (21) ensure that the regional power systems meet the real-time balance of power, and the power supply of the grid is less than its maximum output.

$$P^{\text{PV}}_{i,t} + P^{\text{grid}}_{i,t} = P^{\text{Load}}_{i,t} + P^{\text{DC}}_{i,t} + P^{\text{net}}_{i,t} \tag{20}$$

$$P^{\text{grid}}_{i,t} \le P_{i,\text{grid}}{}^{\max} \tag{21}$$

where $P^{\text{PV}}_{i,t}$ and $P^{\text{Load}}_{i,t}$ denote the predicted value of PV generation and power load in area i at time t; $P^{\text{DC}}_{i,t}$, $P^{\text{net}}_{i,t}$ and $P^{\text{grid}}_{i,t}$ denote the power consumption of DC/NE/grid in area i at time t, respectively; and $P_{i,\text{grid}}{}^{\max}$ denotes the upper limit of output power of grid region i.

4.2.2 Constraint of DCSC in DCs

(22) and (23) indicate that the number of servers ON cannot exceed the total number of servers owned by DCs, and to handle the tasks beyond the plan well, maintaining a certain minimum number of active servers is imperative. (24) and (25) calculate the number of newly ON/OFF servers at time t. (26–29) calculate the number of servers that can be turned ON/OFF at time t based on the minimum ON/OFF time, thus providing (30) and (31) with the upper limit of the number of servers that can be turned ON/OFF, avoiding the loss of serving life of servers due to the frequent ON/OFF operation.

$$M_i = M^{\text{ON}}_{i,t} + M^{\text{OFF}}_{i,t} \tag{22}$$

$$M_{i,\text{ON}}{}^{\min} \le M^{\text{ON}}_{i,t} \le M_i \tag{23}$$

$$M^{\text{offon}}_{i,t} = \frac{M^{\text{ON}}_{i,t} - M^{\text{ON}}_{i,t-1} + \left| M^{\text{ON}}_{i,t} - M^{\text{ON}}_{i,t-1} \right|}{2} \tag{24}$$

$$M^{\text{onoff}}_{i,t} = \frac{\left| M^{\text{ON}}_{i,t} - M^{\text{ON}}_{i,t-1} \right| - M^{\text{ON}}_{i,t} + M^{\text{ON}}_{i,t-1}}{2} \tag{25}$$

for $1 \le t \le MD_i$

$$M^{\text{onable}}_{i,t} = M_i - M^{\text{ON}}_{i,t} - \sum_{n=1}^{t} M^{\text{onoff}}_{i,n} \tag{26}$$

$$M_{i,t}^{\text{offable}} = M_i - M_{i,t}^{\text{OFF}} - \sum_{n=1}^{t} M_{i,n}^{\text{offon}} \tag{27}$$

for $MD_i + 1 \le t \le T$

$$M_{i,t}^{\text{onable}} = M_i - M_{i,t}^{\text{ON}} - \sum_{n=t-MD_i+1}^{t} M_{i,n}^{\text{onoff}} \tag{28}$$

$$M_{i,t}^{\text{offable}} = M_i - M_{i,t}^{\text{OFF}} - \sum_{n=t-MD_i+1}^{t} M_{i,n}^{\text{offon}} \tag{29}$$

for $1 \le t \le T$

$$\mathbf{0} \le M_{i,t}^{\text{onoff}} \le M_{i,t}^{\text{offable}} \tag{30}$$

$$\mathbf{0} \le M_{i,t}^{\text{offon}} \le M_{i,t}^{\text{onable}} \tag{31}$$

where $M_{i,t}^{\text{ON}}$ and $M_{i,t}^{\text{OFF}}$ denote the number of servers ON/OFF in DC i at time t; $M_{i,t}^{\text{offon}}$ and $M_{i,t}^{\text{onoff}}$ denote the number of newly ON/OFF servers in DC i at time t; and $M_{i,t}^{\text{onable}}$ and $M_{i,t}^{\text{offable}}$ denote the number of servers that can be turned on/off in DC i at time t.

4.2.3 Constraint of DVFS in DCs

(32) represents the number of servers operating at each operating frequency after adopting DVFS technology. (33) forces the average CPU utilization of servers at each operating frequency to be less than an upper limit, which avoids CPU saturation and is conducive to stable hardware operation.

$$M_{i,t}^{\text{ON}} = \sum_{k \in K} M_{i,k,t}^{\text{ON}} \tag{32}$$

$$\sum_{task \in TASK} M_{i,k,t,task}^{\text{process}} \cdot \gamma^{task} \le {U_{i,k}}^{\max} \cdot M_{i,k,t}^{\text{ON}} \cdot \mu_{i,k} \tag{33}$$

where ${U_{i,k}}^{\max}$ denotes the upper limit of the CPU utilization rate.

4.2.4 Constraint of QoS

To reduce the impact on the processing plans of other DCs, this part only redistributes the receiving tasks of the source DC i temporally and spatially. (34–36) enforce that all types of tasks must be completed within a designated maximum response time according to the SLAs while dictating the relationship between the number of tasks received by and processed at destination DCs.

$$\sum_{k \in K} M_{i,k,t,task}^{\text{process}} = M_{i,t,task}^{\text{process}} \tag{34}$$

for $1 \le t \le T - {t_{task}}^{\max} + 1$, $\forall task \in DU$

$$\sum_{n=1}^{t} M_{i,n,task}^{\text{in}} \le \sum_{n=1}^{{t_{task}}^{\max}+t-1} \sum_{m=1}^{N} M_{m,n,task}^{\text{process}} \le \sum_{n=1}^{{t_{task}}^{\max}+t-1} M_{i,n,task}^{\text{in}} \tag{35}$$

for $1 \le t \le T$, $\forall task \in DU$

$$\sum_{n=1}^{t} \sum_{m=1, m \ne i}^{N} M_{m,n,task}^{\text{process}} \le \sum_{n=1}^{t} \sum_{m=1, m \ne i}^{N} M_{m,n,task}^{\text{mig}} \le \sum_{n=1}^{t} \left(M_{i,n,task}^{\text{in}} - M_{i,n,task}^{\text{process}} \right) \tag{36}$$

where $M_{i,t,task}^{\text{process}}$ denotes the total number of tasks processed by DC i in time period t; DU is the set of delay-tolerant tasks; N is the number of DCs in the network; $M_{i,n,task}^{\text{in}}$ denotes the number of tasks allocated to DC i by the front-end server in time period n; and $M_{m,n,task}^{\text{mig}}$ denotes the number of tasks that migrated to DC m in time period n.

(37) makes the average customer satisfaction of each type of task greater than a preestablished threshold, which not only shortens the waiting time for processing tasks but also avoids the accumulation of unprocessed workloads.

$$\bar{S}_{task} \ge S_c, \forall task \in DU \tag{37}$$

where S_c is the satisfaction requirement of customers.

4.2.5 Constraints of optical network transmission

(38–40) explain the condition that task migration should satisfy for optical network traffic. (38) is the constraint of NE node traffic conservation, which represents the number of tasks that the network switching equipment i transmits to node j. When the tasks migrate from DC i to DC j, if node i is the migration destination, the net number of tasks received by DC i is $M_{i,t,task}^{\text{mig}}$. If node i is neither a migration source nor a destination, no task migrates into DC i, which is connected to NE i. If the node is a source, the number of tasks received by DC i is equal to the negative number of tasks migrated into other DCs. (39) and (40) calculate the occupied bandwidth of link (i, j) at time t and limit the maximum optical network traffic.

$$\sum_{j:\ (i,j) \in E} M_{ij,t}^{task} - \sum_{j:\ (j,i) \in E} M_{ji,t}^{task} = \begin{cases} -\sum_{m=1, m \ne i}^{N} M_{m,t,task}^{\text{mig}} (s \to d), i = s \\ 0, i \ne s \cap i \ne d \\ M_{i,t,task}^{\text{mig}} (s \to d), i = d \end{cases} \tag{38}$$

$$l_{ij,t} = \sum_{task \in DU} \left(M_{ij,t}^{task} + M_{ji,t}^{task} \right) \cdot \beta^{task}, (i, j) \in E \tag{39}$$

$$\mathbf{0} \le l_{ij,t} \le {l_{ij}}^{\max}, (i, j) \in E \tag{40}$$

where $M_{ij,t}^{task}$ denotes the number of tasks migrated from NE i to NE j at time period t; β^{task} denotes the bandwidth required to migrate one task; and ${l_{ij}}^{\max}$ denotes the maximum bandwidth of link (i,j).

4.3 Day-ahead scheduling model considering the STLM potential of DCs

The proposed spatiotemporal migration model of DCs considering DVFS-DCSC technology can be applied to not only the potential evaluation but also the day-ahead scheduling strategy of multi-DCs. The day-ahead scheduling takes the minimum carbon emissions of all DCs and NEs as the objective function, and the tasks in each DC can be redistributed temporally and spatially. Therefore, the constraint can be adjusted as (41):

$$\min C = \sum_{t=1}^{T} \left[e \cdot \sum_{i=1}^{N} \left(P_{i,t}^{\text{DC}} + P_{i,t}^{\text{net}} \right) \cdot \Delta t \right] \tag{41}$$

where C is the total carbon emissions of all DCs and NEs in time period T and e is the CO2 emission density.

5 Case study

As shown in Figure 4, the urban distribution network with six DCs is used for the case study. Region 1 is a light-industrial area,

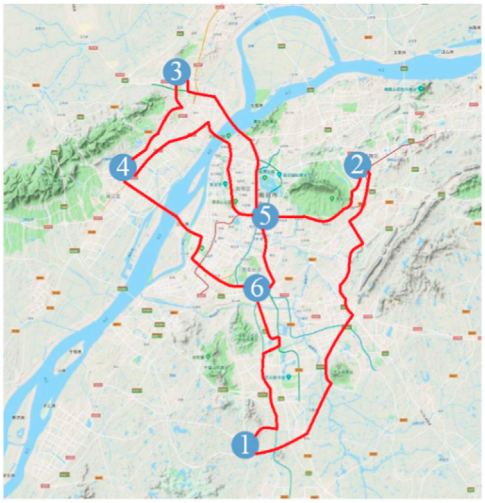

FIGURE 4
The urban DC network with six DCs.

regions 2 and 6 are residential areas, region 3 is a heavy-industrial area, and regions 4 and 5 are commercial areas. The weather conditions of each region are the same, and the loads and PV generation are shown in Figure A1 in the Appendix. The number of tasks allocated to each DC in each time period is shown in Figure A2 in the Appendix. The delay-tolerant tasks handled by DCs account for 60% of the total tasks, and there are seven types of tasks. The capacity needed for processing, the bandwidth needed for migration, the proportion and the maximum response time for each type of task are shown in Figure A3 in the Appendix. Each DC adopts the same type of server, and the relevant parameters of the DC are presented in Table 1. Each DC must maintain the activation of a minimum of 50% of its servers. A case study of the STLM potential evaluation and day-ahead scheduling of DCs is solved in MATLAB 2021a using Gurobi 9.5.1 to demonstrate the validity of the proposed model.

5.1 STLM potential evaluation of DCs considering the DVFS-DCSC energy management strategy

To quantify the maximum STLM potential of the DC to deal with certain emergency situations such as load shortages, the proposed method is used to evaluate the STLM potential.

5.1.1 Migration results

The power spatiotemporal changes in each DC before and after migration are shown in Figures 5A, B. Without loss of generality, the STLM characteristics and effects of DC1 are discussed in detail, and the following conclusions can be drawn:

1) After adopting the DVFS-DCSC STLM method, the migration effect of DC1 is obvious. During the valley period of task processing, DC1 operates with the minimum number of needed activated servers, resulting in minimal power variation. Conversely, during the peak period of task processing, the migration capacity of DC1 is limited by the optical network capacity and the processing capacity of other DCs, resulting in small power peaks.
2) The total number of tasks processed by all DCs before and after migration adheres to conservation. However, the power consumption reduction of DC1 is nonconservative with the power consumption increase of other DCs responsible for processing the migrated tasks. This is because the server's dynamic power is proportional to the cube of the CPU operating frequency. Given identical processing tasks, higher frequencies result in greater power consumption.

The case study compares the migration effect of three scheduling strategies: time-domain migration, STLM and STLM considering the DVFS-DCSC energy management strategy. Figure 6 shows the power curve of DC1 after adopting various control strategies. The results show that the power consumption of DC1 with the STLM mechanism is reduced by 32.83% compared to that of only time-domain migration. However, the DVFS-DCSC method not only reduces the power consumption of DC1 but also improves the ability to bear the workload of other DCs. As shown in this figure, adopting the STLM mechanism considering the DVFS-DCSC energy management strategy proposed in this paper, compared with the STLM mechanism and time-domain migration mechanism alone, the power consumption of DC1 is reduced by 37.96% and 58.33%, respectively. Therefore, the STLM potential of DCs can be significantly enhanced through the proposed method.

5.1.2 Migration and processing of delay-tolerant tasks

Figures 7A, B display the migration and processing plans of DC1's delay-tolerant tasks. The comparison between the two figures reveals some incongruities in the tasks processed and received by destination DCs during the same time period. This difference arises due to the tasks' inherent tolerance for delays, whereby they may be temporarily stored in the hard disks of servers with no immediate processing needed and subsequently dispatched for processing at an optimal time. Figure 7A shows that the number of tasks migrated from DC1 in each period changes roughly according to its original plan of task arrival, but the overall change is not large. This is because DC1 has only two links connected to other DCs, and its migration potential is limited by the bandwidth of links (1,2) and (1,6). For example, at 14:50, the tasks are almost all migrated to DC2 and DC3. At this time, links (1,2) and (1,6) have no idle transmission capacity, with the consequence that more tasks cannot be migrated outside. DC5 has four links connected to other DCs, so its STLM potential is more considerable than that of DC1.

5.1.3 Influence of migration on the server operating state

For a single DC, the change in the operating state of each server is the direct cause of the change in the power consumption.

TABLE 1 Parameters of DC.

Parameters	Value
Base power consumption of a server $p_{\text{fixed}}^{\text{ser}}$ (W)	53
CPU optional operating frequency f_k (GHz)	{1, 1.5, 2, 2.7, 3}
Processing capacity corresponding to each operating frequency μ_k	{5, 7.5, 10, 13.5, 15}
A^{ser}(W/GHz^3)	6.5
Upper limit of CPU utilization $U^{\max}$	0.9
PUE	1.3
Number of servers in each DC M_i	{4, 5, 4, 4, 5, 4}*10^4
Base power consumption of an optical network link $p_{\text{fixed}}^{\text{net}}$ (W)	1720
Dynamic power consumption of an optical network link $p_{\text{dyna}}^{\text{net}}$ (W/Gbps)	12.8
Bandwidth of each link $l^{\max}$ (Gbps)	400
MD (min)	30
CO_2 Emission Intensity e (t/MWh)	0.85
Customer satisfaction requirement S_c	0.6

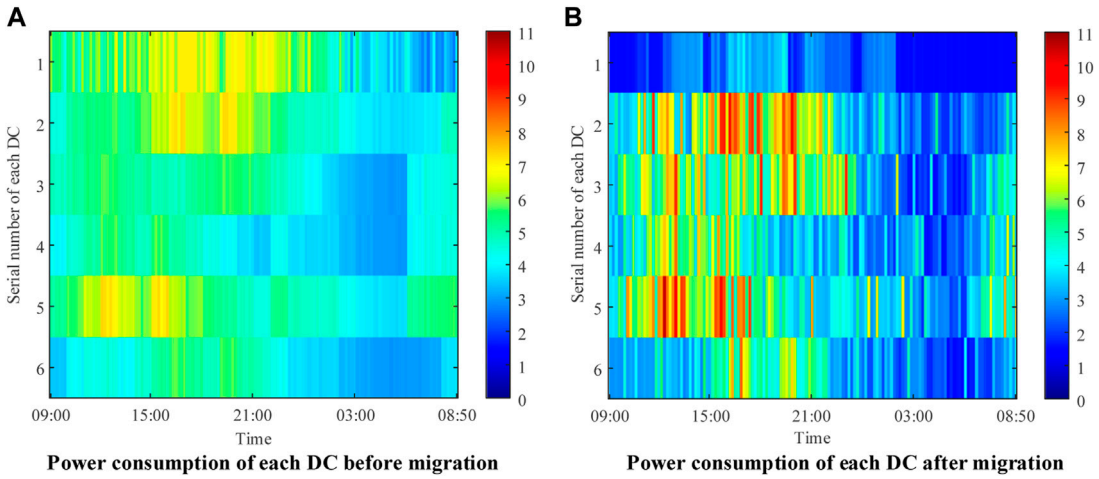

FIGURE 5
Comparison results before and after migration.

The DVFS-DCSC STLM mechanism changes the CPU operating frequency and the number of active servers in each DC to enhance the STLM potential of DCs. The number of servers turned on by each DC is shown in Figure 8. As exemplified by DC1 and DC5, their server operating status and frequency are shown in Figures 9A, B, respectively. At the peak time of task processing, almost all servers are turned on by each DC. At the valley of task processing, to reduce power consumption, the servers turned on by DC1 and 5 are mostly under operating frequency f_1, and a small part is under other frequencies. During peak hours, the migration capacity of DC1 is limited, and some tasks that cannot be migrated outside need to be handled locally. Therefore, more servers are turned on and operate under the operating frequency f_2. DC5 is in a heavy-load state after receiving the tasks migrated from DC1, and many servers are under operating frequency f_5, which makes its power consumption at a rather high level.

5.1.4 Total power consumption before and after load migration

As shown in Figure 10, after adopting this method to maximize the STLM potential of DC1 (as shown by the blue line), the total power consumption of all DCs and NEs decreases compared to the pre-migration stage without an energy management strategy, depicted by the pink line. This reduction occurs because the energy consumption modes of all DCs are optimized during the

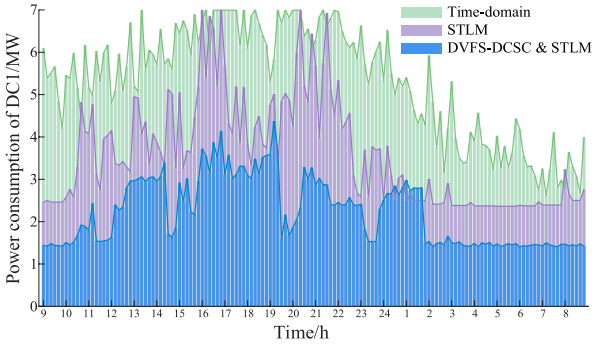

FIGURE 6
Comparison results under different migration methods.

migration process. However, if all DCs have already adopted the DVFS-DCSC method for energy consumption optimization before migration (as shown by the yellow line), the total power consumption after migration will be considerably higher than that before migration. This implies that maximizing the STLM potential of DCs will involve certain economic sacrifices and may lead to increased carbon emissions within the entire DC network. This is because in the peak period of task processing, the destination DCs are already heavily burdened with their own processing workloads. At this time, to continue processing tasks from DC1, more servers must be turned on, and the CPU operating frequency must be scaled to a higher level. The tasks that can be processed by DC1 under a lower operating frequency can only be completed under a higher operating frequency in other destination DCs, which explains why the overall energy consumption will increase after migration. Therefore, to ensure the overall economy and low-carbon emissions, grid operators should retain part of the STLM potential when formulating the demand response scheme. The remaining STLM potential can be exploited and applied in emergency dispatching scenarios.

5.2 Day-ahead scheduling strategy for minimum carbon emissions

5.2.1 Scheduling results

The total carbon emissions of all DCs and optical networks before and after DVFS-DCSC & STLM scheduling are compared, as shown in Figure 11. Compared with the time-domain migration method and DVFS-DCSC technology alone, the total carbon emissions are reduced by 32.92% and 10.21%, respectively, after adopting the proposed method.

As displayed in Figure 12, after scheduling with the DVFS-DCSC STLM, the average utilization rate of the CPU is increased from 39.89% to 83.14%, which effectively reduces the number of redundant servers and total power consumption. Most of the time after migration, the average utilization rate of CPU has reached more than 70%. For the moment of low utilization, even if there are fewer workloads allocated for processing, the number of servers each DC turns on must exceed the minimum requirement.

5.2.2 Influence of migration on the server operating state

To illustrate the impact of the proposed scheduling scheme on the operating state of the server, we take the 7th type of task (with the maximum response time of 8 h shown in Figure A3 in Appendix) as an example and obtain the processing results in each time period according to matrix *An* in Eq. 13, which is shown in Figure 13. In this figure, each row represents the batch processing plan of the incoming tasks at one point, and each column represents the number and composition of tasks completed at each time, which indicates that this type of task has a great ability for temporal migration. That is, we can

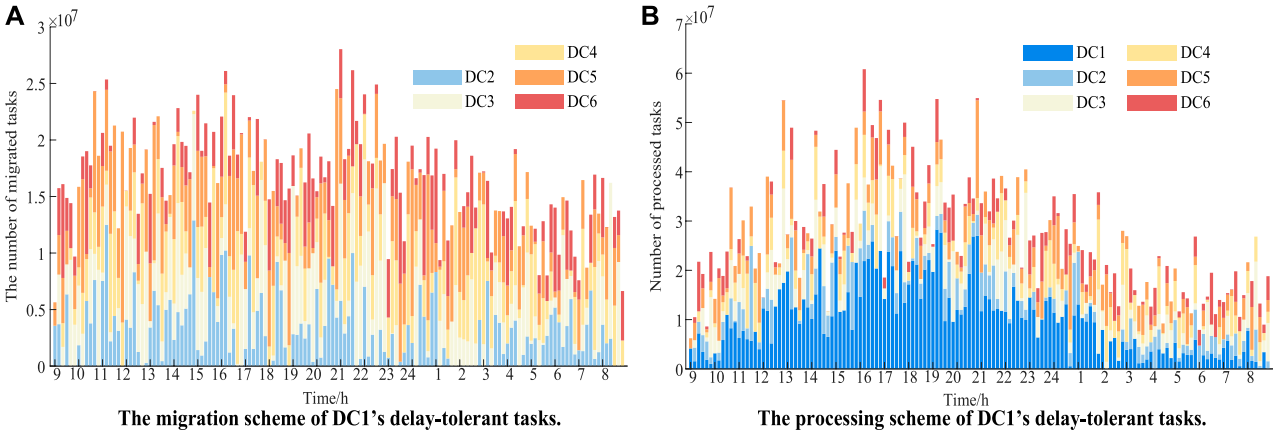

FIGURE 7
The migration and processing schemes of DC1's delay-tolerant tasks.

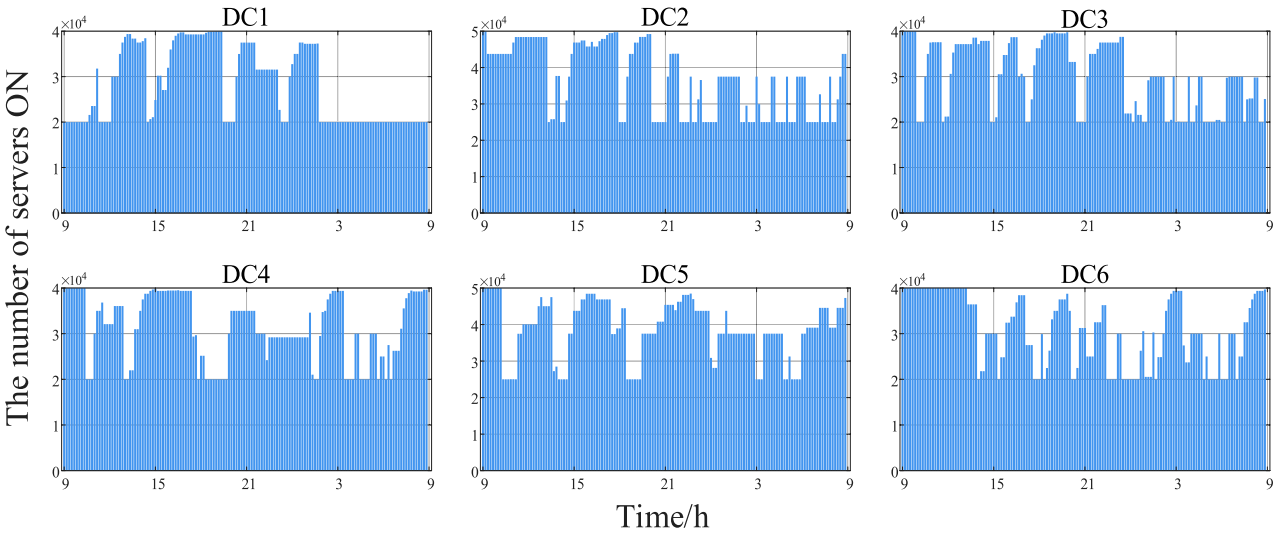

FIGURE 8
The number of active servers in each DC in each period.

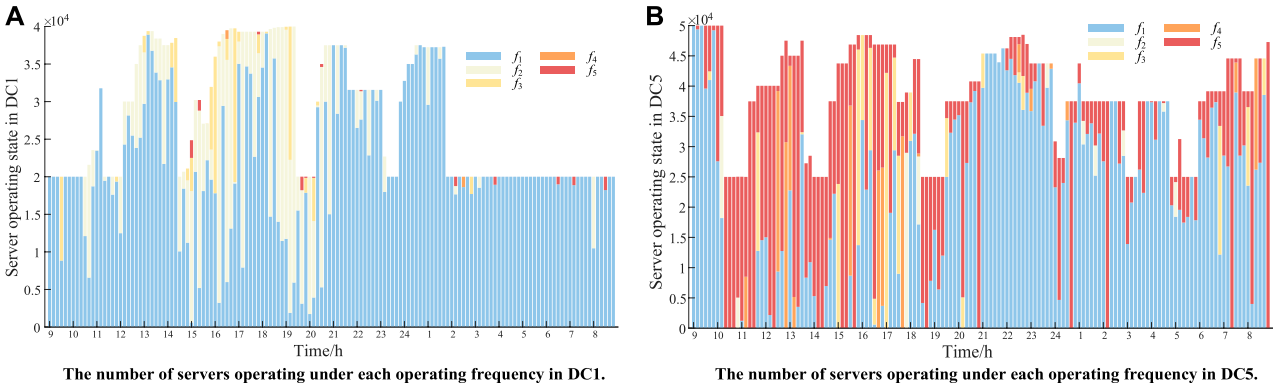

FIGURE 9
The number of servers operating under each operating frequency in DC1 and DC5.

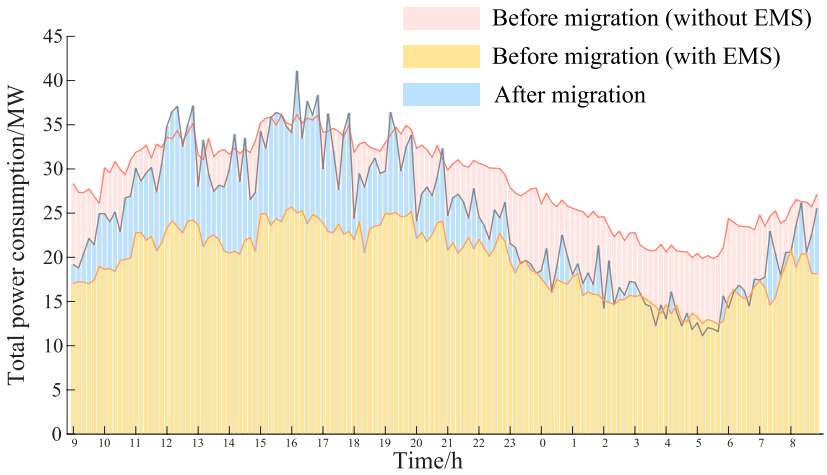

FIGURE 10
The total power consumption of DCs and NEs before and after migration.

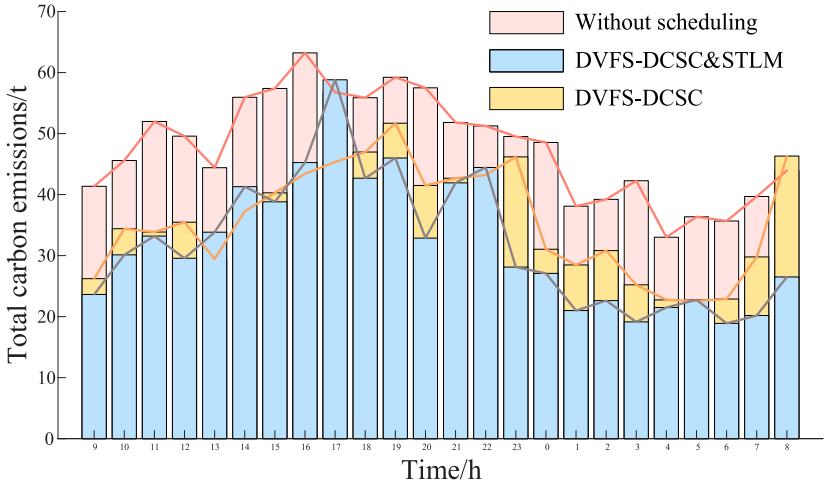

FIGURE 11
Comparison results of total carbon emissions before and after migration.

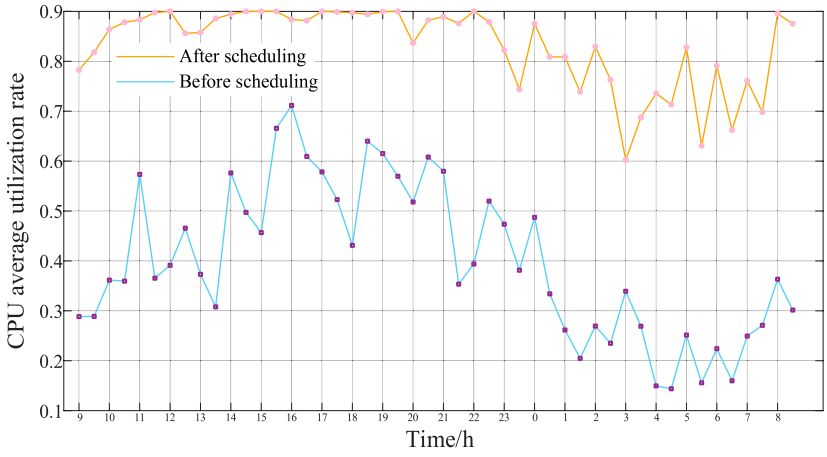

FIGURE 12
Comparison results of the CPU average utilization rate before and after scheduling.

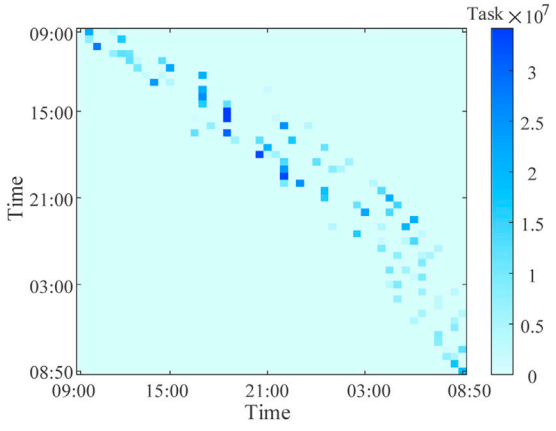

FIGURE 13
Processing results of the 7th type of task in each time period.

intuitively obtain the temporal migration results of different delay-tolerant tasks in this scheduling scheme.

However, the delay-tolerant tasks with a long time of t_{max}, such as 4 h or 8 h, account for a small proportion. That is, the overall ability for time-domain (temporal) migration of all tasks is relatively weak. Meanwhile, due to the unobvious spatiotemporal differences in the task arrangement among DCs, the purpose of the STLM in day-ahead scheduling is to spread the tasks handled by each DC equitably, thereby minimizing the number of active servers and maintaining low-frequency server operation as much as possible. In each time period, the number of active servers in each DC is shown in Figure 14. As exemplified by DC1 and DC5, in contrast to the case study of potential evaluation, the server operating states of these two DCs are relatively close, are shown in Figures 15A, B, respectively. Since the task allocation plan of DC1 has more tasks than those of other DCs and other DCs are already in heavy loads during the peak of task processing, it is not necessary to migrate more tasks but to process them locally.

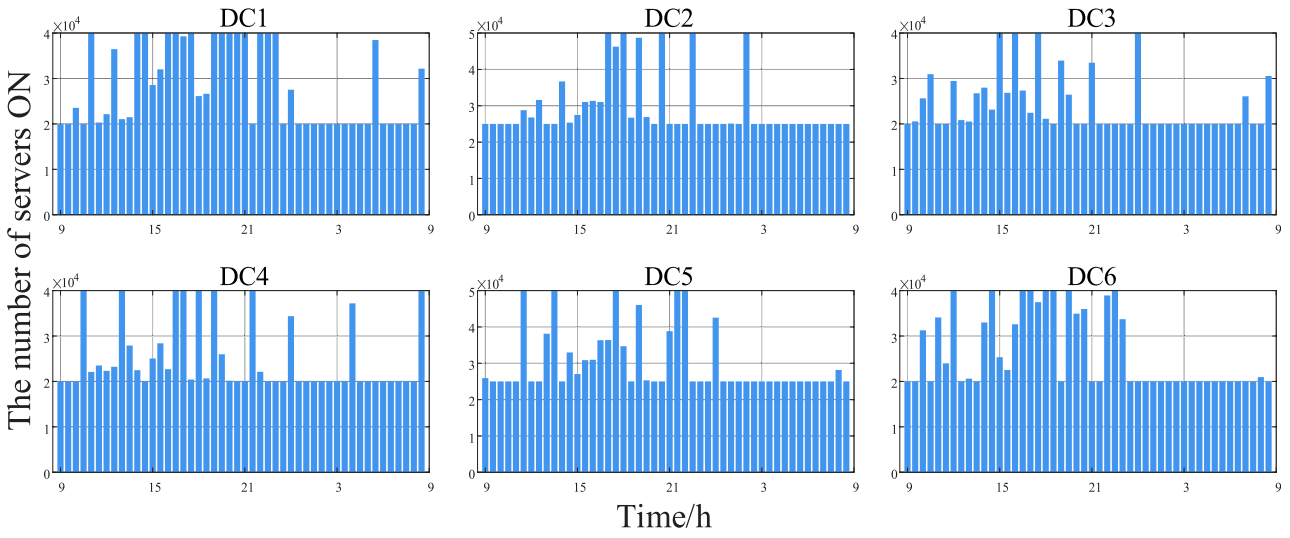

FIGURE 14
The number of active servers in each DC in each time period.

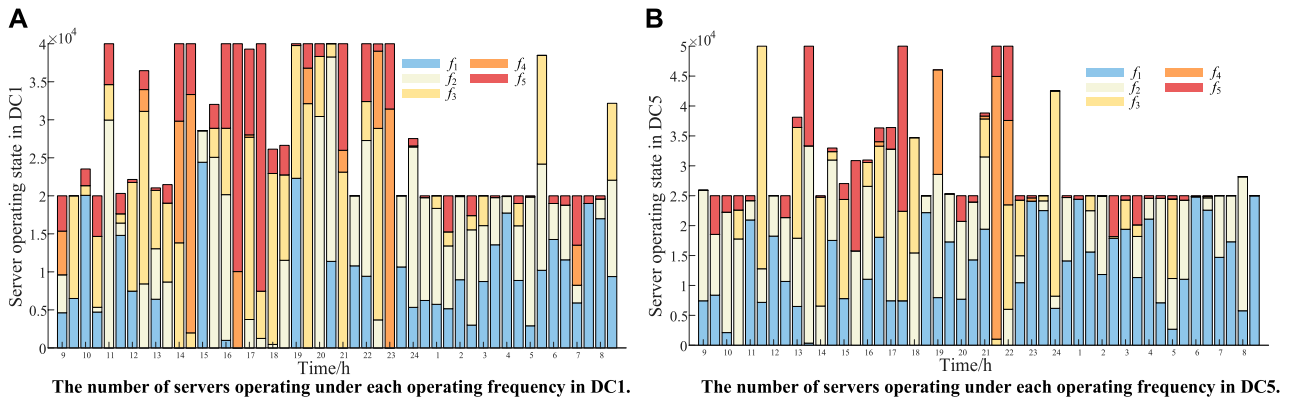

FIGURE 15
The number of servers operating under each operating frequency in DC1 and DC5.

6 Conclusion

Due to the great spatiotemporal flexibility of data loads, this paper proposes an approach to evaluate the STLM potential of DCs. The proposed model is further applied to the day-ahead scheduling of urban DCs, minimizing daily carbon emissions. The case study verifies the effectiveness of the STLM model and energy management strategy. The following conclusions are drawn:

1) The spatiotemporal redistribution of delay-tolerant tasks, as well as server ON/OFF scheduling and CPU operating frequency scaling in different spatial locations, provides DCs with STLM potential.
2) Due to the operating characteristics of the servers, the utilization of STLM potential is often accompanied by increased energy consumption, which comes at the cost of the economy of the entire system. However, in an emergency, DCs need to provide power support with maximum STLM potential, regardless of the economy.
3) In the day-ahead scheduling of urban DCs, in contrast to emergency control, the purpose of the STLM is to spread the tasks handled by each DC evenly in space, reducing the number of servers turned on and increasing the proportion of servers that operate under low frequencies.

The STLM potential evaluation model of DCs and the proposed day-ahead scheduling scheme provide a novel approach to exploring spatiotemporal flexible resources. Considering the significant differences between DCs and other forms of spatially flexible loads, subsequent research must be undertaken to devise a

collaborative scheduling strategy for managing diverse spatially flexible loads.

Data availability statement

The original contributions presented in the study are included in the article/supplementary material, further inquiries can be directed to the corresponding author.

Author contributions

LZ: Conceptualization, Data curation, Formal Analysis, Writing–original draft. SW: Data curation, Investigation, Methodology, Validation, Writing–original draft. HL: Methodology, Resources, Software, Visualization, Writing–original draft. QW: Methodology, Project administration, Supervision, Writing–review and editing. YT: Supervision, Writing–review and editing.

Funding

The author(s) declare that no financial support was received for the research, authorship, and/or publication of this article.

Conflict of interest

The authors declare that the research was conducted in the absence of any commercial or financial relationships that could be construed as a potential conflict of interest.

Publisher's note

All claims expressed in this article are solely those of the authors and do not necessarily represent those of their affiliated organizations, or those of the publisher, the editors and the reviewers. Any product that may be evaluated in this article, or claim that may be made by its manufacturer, is not guaranteed or endorsed by the publisher.

References

Chen, M., Gao, C., Li, Z., Shahidehpour, M., Zhou, Q., Chen, S., et al. (2021a). Aggregated model of data network for the provision of demand response in generation and transmission expansion planning. *IEEE Trans. Smart Grid* 12 (1), 512–523. doi:10.1109/tsg.2020.3015475

Chen, M., Gao, C., Shahidehpour, M., and Li, Z. (2021c). Incentive-compatible demand response for spatially coupled internet data centers in electricity markets. *IEEE Trans. Smart Grid* 12 (3), 3056–3069. doi:10.1109/tsg.2021.3053433

Chen, S., Li, P., Ji, H., Yu, H., Yan, J., Wu, J., et al. (2021b). Operational flexibility of active distribution networks with the potential from data centers. *Appl. Energy* 293, 116935. doi:10.1016/j.apenergy.2021.116935

Cupelli, L., Schütz, T., Jahangiri, P., Fuchs, M., Monti, A., and Müller, D. (2018). Data center control strategy for participation in demand response programs. *IEEE Trans. Ind. Inf.* 14 (11), 5087–5099. doi:10.1109/tii.2018.2806889

Danilak, R. (2017). *Why energy is a big and rapidly growing problem for data centers*. Boston, MA, USA: Forbes Technology Council.

Dayarathna, M., Wen, Y., and Fan, R. (2016). Data center energy consumption modeling: a survey. *IEEE Commun. Surv. Tut* 18 (1), 732–794. doi:10.1109/comst.2015.2481183

Deylamsalehi, A., Davis, D. A. P., Afsharlar, P., Bahrami, M., Chen, W., and Vokkarane, V. M. (2018). Using machine learning to balance energy cost and emissions in optical networks. *J. Opt. Commun. Netw.* 10 (10), D72–D83. doi:10.1364/jocn.10.000d72

Fan, H., Wang, H., Xia, S., Li, X., Xu, P., and Gao, Y. (2021). Review of modeling and simulation methods for cyber physical power system. *Front. Energy Res.* 9, 642997. doi:10.3389/fenrg.2021.642997

Fu, Y., Han, X., Baker, K., and Zuo, W. (2020). Assessments of data centers for provision of frequency regulation. *Appl. Energy* 277, 115621. doi:10.1016/j.apenergy.2020.115621

Gu, L., Zeng, D., Barnawi, A., Guo, S., and Stojmenovic, I. (2015). Optimal task placement with QoS constraints in geo-distributed data centers using DVFS. *IEEE Trans. Comput.* 64 (7), 2049–2059. doi:10.1109/tc.2014.2349510

Guo, C., Luo, F., Cai, Z., Dong, Z.-Y., and Zhang, R. (2021a). Integrated planning of internet data centers and battery energy storage systems in smart grids. *Appl. Energy* 281, 116093. doi:10.1016/j.apenergy.2020.116093

Guo, C., Xu, K., Shen, G., and Zukerman, M. (2021b). Temperature-aware virtual data center embedding to avoid hot spots in data centers. *IEEE Trans. Green Commun. Netw.* 5 (1), 497–511. doi:10.1109/tgcn.2020.3015234

Han, H., Wei, T., Wu, C., Xu, X., Zang, H., Sun, G., et al. (2022). A low-carbon dispatch strategy for power systems considering flexible demand response and energy storage. *Front. Energy Res.* 10, 883602. doi:10.3389/fenrg.2022.883602

Jin, C., Bai, X., Yang, C., Mao, W., and Xu, X. (2020). A review of power consumption models of servers in data centers. *Appl. Energy* 265, 114806. doi:10.1016/j.apenergy.2020.114806

Kwon, S. (2020). Ensuring renewable energy utilization with quality of service guarantee for energy-efficient data center operations. *Appl. Energy* 176, 115424. doi:10.1016/j.apenergy.2020.115424

Li, J., Li, Z., Ren, K., and Liu, X. (2012). Towards optimal electric demand management for internet data centers. *IEEE Trans. Smart Grid* 3 (1), 183–192. doi:10.1109/tsg.2011.2165567

Liu, H., Liu, B., Yang, L. T., Lin, M., Deng, Y., Bilal, K., et al. (2018). Thermal-aware and DVFS-enabled big data task scheduling for data centers. *IEEE Trans. Big Data* 4 (2), 177–190. doi:10.1109/tbdata.2017.2763612

Liu, S., Zhao, T., Liu, X., Li, Y., and Wang, P. (2022). Proactive resilient day-ahead unit commitment with cloud computing data centers. *IEEE Trans. Ind. Appl.* 58 (2), 1675–1684. doi:10.1109/tia.2022.3145761

Liu, Y., Lei, S., and Hou, Y. (2019). Restoration of power distribution systems with multiple data centers as critical loads. *IEEE Trans. Smart Grid* 10 (5), 5294–5307. doi:10.1109/tsg.2018.2880255

Long, S., Li, Y., Huang, J., Li, Z., and Li, Y. (2022). A review of energy efficiency evaluation technologies in cloud data centers. *Energy Build.* 260, 111848. doi:10.1016/j.enbuild.2022.111848

Lyu, J., Zhang, S., Cheng, H., Yuan, K., Song, Y., and Fang, S. (2021). Optimal sizing of energy station in the multienergy system integrated with data center. *IEEE Trans. Ind. Appl.* 57 (2), 1222–1234. doi:10.1109/tia.2021.3054607

Ma, M., Huang, H., Song, X., Peña-Mora, F., Zhang, Z., and Chen, J. (2022). Optimal sizing and operations of shared energy storage systems in distribution networks: a bi-level programming approach. *Appl. Energy* 307, 118170. doi:10.1016/j.apenergy.2021.118170

Martijn, K., and Fons, W. (2021). Usage impact on data center electricity needs: a system dynamic forecasting model. *Appl. Energy* 291, 116798. doi:10.1016/j.apenergy.2021.116798

Song, Y., Chen, F., Xia, M., and Chen, Q. (2022). The interactive dispatch strategy for thermostatically controlled loads based on the source-load collaborative evolution. *Appl. Energy* 309, 118395. doi:10.1016/j.apenergy.2021.118395

Sun, G., Anand, V., Liao, D., Lu, C., Zhang, X., and Bao, N. H. (2013). Power-efficient provisioning for online virtual network requests in cloud-based data centers. *IEEE Syst. J.* 9 (2), 427–441. doi:10.1109/jsyst.2013.2289584

Wang, H., Wang, Q., Tang, Y., and Ye, Y. (2022). Spatial load migration in a power system: concept, potential and prospects. *Int. J. Electr. Power Energy Syst.* 140, 107926. doi:10.1016/j.ijepes.2021.107926

Wang, S., Qian, Z., Yuan, J., and You, I. (2017). A DVFS based energy-efficient tasks scheduling in a data center. *IEEE Access* 5, 13090–13102. doi:10.1109/access.2017.2724598

Yang, T., Jiang, H., Hou, L., and Geng, Y. (2022). Study on carbon neutrality regulation method of interconnected multi-datacenter based on spatio-temporal dual-dimensional computing load migration. *Proc. CSEE* 42 (1), 164–177. doi:10.13334/j.0258-8013.pcsee.210485

Yang, T., Zhao, Y., Pen, H., and Wang, Z. (2018). Data center holistic demand response algorithm to smooth microgrid tie-line power fluctuation. *Appl. Energy* 231, 277–287. doi:10.1016/j.apenergy.2018.09.093

Yu, L., Jiang, T., and Cao, Y. (2015). Energy cost minimization for distributed Internet data centers in smart microgrids considering power outages. *IEEE Trans. Parallel Distrib. Syst.* 26 (1), 120–130. doi:10.1109/tpds.2014.2308223

Yuan, Q., Ye, Y., Tang, Y., Liu, Y., and Strbac, G. (2022). A novel deep-learning based surrogate modeling of stochastic electric vehicle traffic user equilibrium in low-carbon electricity-transportation nexus. *Appl. Energy* 315, 118961. doi:10.1016/j.apenergy.2022.118961

Zhang, J., Zhao, Y., Yu, X., Zhang, J., Song, M., Ji, Y., et al. (2015). Energy-efficient traffic grooming in sliceable-transponder-equipped IP-Over-Elastic optical networks [invited]. *J. Opt. Commun. Netw.* 7 (1), 142–152. doi:10.1364/jocn.7.00a142

Zhou, Z., Liu, F., Zou, R., Liu, J., Xu, H., and Jin, H. (2016). Carbon-aware online control of geo-distributed cloud services. *IEEE Trans. Parall Distr Syst.* 27 (9), 2506–2519. doi:10.1109/tpds.2015.2504978

Appendix

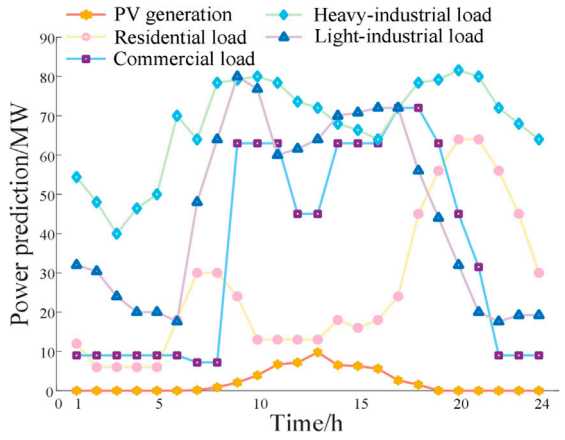

FIGURE A1
PV generation and loads of an urban power system.

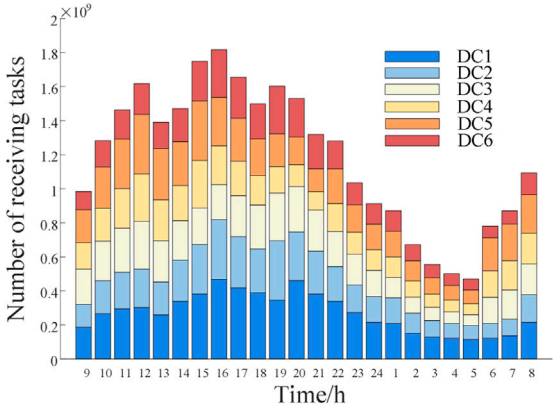

FIGURE A2
Number of workloads in each DC in each time period.

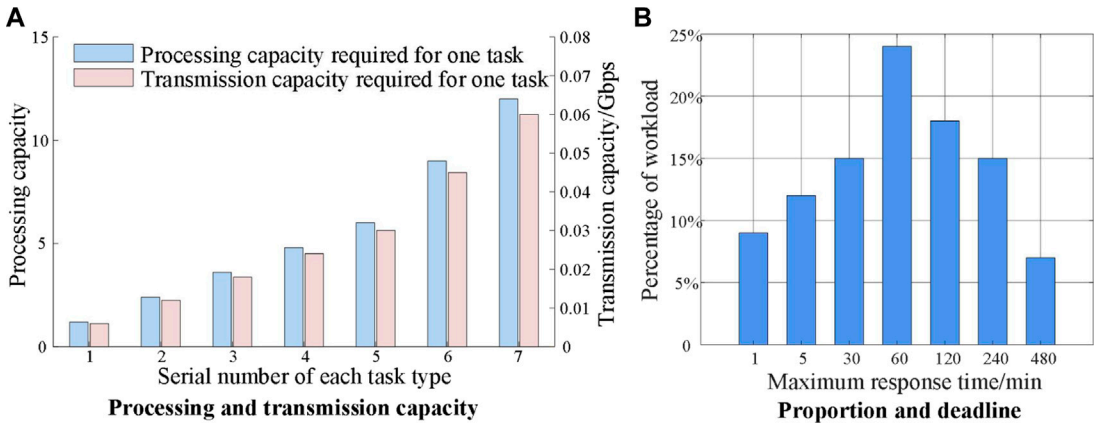

FIGURE A3
Parameters of each type of task.

Nomenclature

Abbreviations

DC	Data center
STLM	Spatiotemporal load migration
DVFS	Dynamic voltage/frequency scaling
DCSC	Dynamic cluster server configuration
IT	Information technology
PUE	Power usage effectiveness
NE	Network element
SLA	Service-level agreement
QoS	Quality of service
EMS	Energy management strategy

Parameters

A^{ser}	Dynamic power consumption coefficient of a server
PUE_i	Power usage effectiveness of DC i
$p^{ser}_{fixed}/p^{net}_{fixed}$	Base power consumption of a server/fiber link
$P^{PV}_{i,t}/P^{Load}_{i,t}$	Predicted value of PV generation and power load in area i at time t
M_i	Number of servers in DC i
$M_{i,ON}{}^{min}$	Minimum number of servers required to be ON in DC i
MD	Minimum ON/OFF time of a server
U	CPU utilization rate
L	Total load that the DC needs to process
γ^{task}	CPU capacity needed of processing one *task*
λ	Tasks processed by a server during unit time
$M^{process}_{task}$	Total number of processed tasks
f_k	CPU operating frequency of a server under operating status k
μ_k	Processing capacity of a server under f_k
U^{max}	Upper limit of CPU utilization
$P_{i,grid}{}^{max}$	Upper limit of output power of grid region i
$t_{task}{}^{max}$	Deadline of completion time for *task*
S_c	Customer satisfaction requirement
$M^{in}_{i,t,task}$	Number of incoming tasks in DC i at time t
β^{task}	Bandwidth needed of migrating one *task*
$l_{ij}{}^{max}$	Maximum bandwidth of link (i,j)
E	Set of the optical fiber links
$K/TASK/DU/E$	Set of CPU operating status/task types/delay-tolerant task types/links
e	CO2 emission intensity

Variables

$P^{DC}_{i,t}/P^{net}_{i,t}/P^{grid}_{i,t}$	Power consumption of DC/NE/grid in area i at time t
$M^{ON}_{i,t}/M^{OFF}_{i,t}$	Number of servers ON/OFF in DC i at time t
$p^{ser}_{dyna}/p^{net}_{dyna}$	Dynamic power consumption of a server/fiber link
$U_{i,k,t}$	Average CPU utilization of servers under f_k in DC i at time t
$M^{offon}_{i,t}/M^{onoff}_{i,t}$	Number of newly ON/OFF servers in DC i at time t
$M^{onable}_{i,t}/M^{offable}_{i,t}$	Number of servers can be turned on/off in DC i at time t
$M^{ON}_{i,k,t}$	Number of servers under f_k in DC i at time t
$M^{mig}_{i,t,task}$	Number of tasks migrated to DC i at time t
$\Delta t_{tr,qu}/\Delta t_{tr}/\Delta t_{pro,qu}/\Delta t_{pro}$	Queuing waiting time/needed time for task migration/ waiting time for processing in the queue/needed time for task processing
P^{net}_{ij}	Power consumption of the link (i, j)
$M^{task}_{ij,t}$	Number of tasks migrated from NE i to NE j at time t
$M^{fin}_{task,ab}$	Number of tasks finished in $(b\text{-}1, b]$ periods coming at time a
$M^{fin}_{task,t}$	Number of all tasks finished in $(t\text{-}1, t]$ periods
$\overline{S_{task}}$	Average customer satisfaction

frontiers | Frontiers in Energy Research

TYPE Original Research
PUBLISHED 10 November 2023
DOI 10.3389/fenrg.2023.1295070

OPEN ACCESS

EDITED BY
Rufeng Zhang,
Northeast Electric Power University, China

REVIEWED BY
Xiangjun Zeng,
China Three Gorges University, China
Zaiyu Chen,
Nanjing University of Science and Technology, China
Junjun Xu,
Nanjing University of Posts and Telecommunications, China

*CORRESPONDENCE
Shaomei Zhang,
zsmphys@sdust.edu.cn

RECEIVED 15 September 2023
ACCEPTED 16 October 2023
PUBLISHED 10 November 2023

CITATION
Zhang W, Zhang S, Zhang Y, Xu G and Mao H (2023), A KRR-UKF robust state estimation method for distribution networks.
Front. Energy Res. 11:1295070.
doi: 10.3389/fenrg.2023.1295070

A KRR-UKF robust state estimation method for distribution networks

Wei Zhang[1], Shaomei Zhang[2]*, Yongchen Zhang[3], Guang Xu[1] and Huizong Mao[3]

[1]Zhuhai XJ Electric Co, Ltd, Zhuhai, China, [2]College of Electronic and Information Engineering, Shandong University of Science and Technology, Qingdao, China, [3]College of Electrical Engineering and Automation, Shandong University of Science and Technology, Qingdao, China

State estimation is an integral component of energy management systems. Employing a state estimation methodology that is both accurate and resilient is essential for facilitating informed decision-making processes. However, the complex scenarios (unknown noise, low data redundancy, and reconfiguration) of the distribution network pose new challenges for state estimation. In the context of this study, we introduce a state estimation technique known as the kernel ridge regression and unscented Kalman filter. In normal conditions, the non-linear correlation among data and unknown noise increases the difficulty of modeling the distribution network. Thence, kernel ridge regression is developed to map the data into high-dimensional space that transforms the non-linear problem into linear formulations base on the data rather the complicate grid model, which improves model generalization performance and filters out unknown noises. In addition, with the unique prediction correction mechanism of the Kalman method, the kernel ridge regression-mapped state value can be revised by the measurement, which further enhances model accuracy and robustness. During abnormal operating conditions and taking into account the presence of faulty data within the measurement system, we initiate the use of a long short-term memory network and combined convolutional neural network (CNN) model, referred to as the ATT-CNN-GRU. This model is utilized for the prediction of pseudo-measurements. Subsequently, we use an outlier detection method known as ordering points to identify the clustering structure to effectively identify and substitute erroneous data points. Cases on the IEEE-33 bus system and 109-bus system from a city in China show that the method has superior accuracy and robustness.

KEYWORDS

deep learning, kernel ridge regression, outlier detection method, state estimation, unscented Kalman filter

1 Introduction

Power system state estimation (PSSE), playing a key role in safety monitoring (Samuelsson et al., 2006) and optimal dispatching (Bai et al., 2016), is a necessary data support for the energy management system (EMS) (Guo et al., 2014; Zhao et al., 2019a). However, the information uploaded via grid measurement equipment exists as bad data and unknown noise, which severely restricted the performance of state estimation (Du et al., 2010). Hence, there is an urgent need for a more effective state estimation method.

In general, the state estimation techniques could be broadly classified into parameter methods represented by the Kalman filter (KF) (Zadeh et al., 2010; Rosenthal et al., 2017) and data-driven methods such as machine learning (Weng et al., 2016; Mestav et al., 2019a). The KF determines the best estimate of state using the forecast-correction mode, and this superior feature inspires many scholars to focus on the estimation algorithms under the KF framework (Kalman, 1960). In the work of Ghahremani et al. (2016), an extended Kalman filter method utilizing PMU was introduced to identify and estimate the system state and unidentified variables inputs when the noise is assumed to be Gaussian. The method was further developed by Zhao (2018), which combined the H∞ and extended Kalman filter (HEKF). The HEKF model parameters are improved by considering the effect of uncertainties (varying generator transient reactance, uncertain inputs, and noise statistics) on the dynamic model of the system. Moreover, it is effective when the noise statistics and transient reactance are unknown. Zhao et al. (2019b), to improve accuracy and accelerate convergence, introduced a comprehensive and robust dynamic state estimation framework that leverages the unscented Kalman filter (UKF) and the ability to deal with (Ji et al., 2021) weak observation dynamic variables, which enhances filter performances against bad data. These aforementioned methods improve the performance of the Kalman-like algorithms, but such methods are restricted in practical applications because most of the noise in the actual power system may not follow the Gaussian distribution.

To address the aforementioned problems, a generalized maximum likelihood UKF(GM-UKF) estimation approach was introduced by Zhao et al. (2018), which can improve data redundancy and filter bad data, and the undetermined Gaussian and non-Gaussian noises are also filtered out by the generalized maximum likelihood-estimator, which enhanced the filter effectiveness and robustness. Dang et al. (2020) presented a minimum error entropy UKF (MEE-UKF), which exhibits the robustness and validity with respect to multimodal distribution noises. In conclusion, Kalman-like methods use prediction equations to correct measuring equations and are widely used in industry. However, the parameter model behaves very differently when choosing different parameter combinations, and the flexibility of these methods may be limited or even fail to converge. In addition, the calculation speed and accuracy still need to be improved.

The difficulties posed by these issues have necessitated the exploration of data-driven approaches, which utilize historical data for offline training and real-time data for online state estimation. The data-driven methods may have an excellent performance if the dataset is sufficient. The deep neural network (DNN) was proposed by Mestav et al. (2018); it learns the probability distribution of grid data to estimate the state online, which results in better robustness and accuracy. This method was further developed by Zhang et al. (2019); a deep recurrent neural network is utilized to forecast the state by leveraging the long-term non-linear correlations embedded within the historical data. This approach has notably enhanced the accuracy of estimation. Netto et al. (2018) introduced a robust, data-driven Kalman filter incorporating the generalized maximum likelihood Koopman operator (GM-KKF) to expedite convergence speed. Compared with the Kalman filter, the Koopman operator using a batch-mode regression formulation improves nearly one-third in terms of the computation speed. In the work of Mestav et al. (2018), Bayesian state estimation was trained by the DNN, and the DNN can overcome computation complexity in Bayesian estimation, which has robustness for bad data and missing data. It is noted that some time series algorithms can also handle missing and abnormal data, which was proposed in our previous work (Ji et al., 2021). The long short-term memory (LSTM) method is combined with the outlier detection technology to predict the outlier, thus improving the robustness of the filter, which proves that the time series prediction method can be applied in PSSE. Furthermore, we notice that the convolutional neural network combined with the attention mechanism (ATT-CNN) can also filter data feature via convolutional operation (Kollias et al., 2021). However, none of these studies have focused on the estimation performance in the presence of network reconfiguration or reduced redundancy of measurements in practical application.

This paper introduces a robust method for power system state estimation built upon the kernel ridge regression and unscented Kalman filter (KRR-UKF). This approach makes several key contributions, which are given as follows.

(1) A data-driven KRR approach is first developed in power system state estimation. Considering the data correlation in PSSE is non-linear and complicated, which is hard to be solved using the linear ridge regression method, the kernel trick is applied to map data into linear space, which can auto-adjust the model based on the input data rather the mechanism model parameters and express the data relation precisely and insensitive to unknown noises. Thereby, reconstructing state transition and measuring models in the UKF can improve the robustness and accuracy of PSSE notably.
(2) An improved deep learning model the ATT-CNN-GRU is first proposed to provide pseudo-measurements. The ATT module can calculate the attention weights of the input data and assist the CNN to obtain local features and filter noise, and then, the selected valuable features are passed to the gated recurrent unit (GRU) for establishing a more suitable model for the relevant data, which can accelerate computation speed and improve accuracy compared with LSTM.
(3) An ordered point to identify the cluster structure (OPTICS) outlier detection method is presented to detect outliers, which is less sensitive to noise and the changes of parameters, allowing us to identify outliers accurately and quickly.

In Section 2, the KRR algorithm is described. The KRR-UKF is described in Section 3. A novel time series model through the ATT-CNN-GRU is depicted in Section 4, which ensures robustness in the case of abnormal data. The robustness and wide applicability of the estimator are tested in Section 5. Finally, conclusions are derived in Section 6.

2 Kernel ridge regression

The main task of PSSE in the distribution network (DN) is to obtain the voltage and phase information synchronously when giving the relevant measurement information and pseudo-measurements of

a distribution network; the formulation of state and measurement equations at time t are expressed as follows:

$$x_t = O_t x_{t-1} + w_t, \tag{1}$$

$$z_t = f(x_t) + v_t. \tag{2}$$

In an actual scenario, the measurement information is acquired using a smart meter, PMU that is susceptible to the unknown noises w_t, and the state equations are also corrupted by process noise v_t; these noises are usually assumed to follow Gaussian. However, due to the channel communication noise, ambient temperature, and diverse system operating conditions, the process and measurement noise are always not Gaussian-distributed. Therefore, in order to filter out the unknown noise in the system, the key issue is how to establish the noise w_t and v_t models properly. With this regard, Eq. 1 and 2 can be built based on the KRR method to perform SE in the distribution network. Based on that, we make the assumption that there exist n nodes and l lines within the DN, which can be depicted by a graph $\mathcal{G}$ = {N, L, N = 1,2 … N}, the total dataset count is designated as M, and the DN measurements set at bus n and line nm at time t are denoted by $z^n = \{P_t^n, Q_t^n, P_t^{nm}, Q_t^{nm}, t = 1, 2, 3\cdots M\}$. Let the voltage at the bus n be defined as $x_t^n = V_t^n \angle \theta_t^n$. Then, the measurements and state sets are assumed as $Z = \{z^n, n \in N\}$ and $X^n = \{x_1^n, x_2^n \cdots x_t^n, t = 1, 2, \cdots M\}$, respectively, to collect the DN information. The set is considered the state estimation set for bus n, with $Y = \{y^n, n \in N\}$ representing the state estimation dataset.

2.1 Ridge regression

According to the ridge regression method (Hoerl et al., 1970), the ridge regression model can be set as $f(W) = W^{\mathrm{T}}X$ with $W^{\mathrm{T}} = (w_1, w_2 \cdots w_{\mathrm{n}})^{\mathrm{T}}$, and the cost function is given as follows:

$$L(W) = \sum_{i=1}^{n} \left\| w_i^T x_i - y_i \right\|_2^2, \tag{3}$$

where ${w_i}^{\mathrm{T}} x_i$ is the weighted training sample of voltage information and y_i is the corresponding estimation, and we assume the estimated value is

$$W_1 = \mathrm{argmin} L(W). \tag{4}$$

Considering that there may be insufficient power state information in practical, due to which matrix W might become invertible or model overfitting might occur, the regularization framework $\mathrm{argmin}[L(W) + \eta P(W)]$ is introduced, and the estimated value of W1 can be given as follows:

$$W_t = \left(X^T X + \eta^{-1} T\right)^{-1} X^T Y, \tag{5}$$

where the estimated value W1 is the sum of a generalized non-negative semidefinite matrix and a diagonal matrix. As the sum is positive definite, W1 is reversible, which can suppress overfitting.

2.2 Kernel ridge regression

KRR is a powerful machine learning method used to capture the connection between output and input datasets. The kernel method can map the measurement or state information into high-dimensional space; thus, all data are replaced by their feature vector: $X \to \hat{X}, Y \to \hat{Y}$; then, according to wood bury matrix identity (Murphy, 2012),

$$\left(E - FH^{-1}G\right)^{-1} FH^{-1} = E^{-1}F\left(H - GE^{-1}F\right)^{-1}, \tag{6}$$

where H-1 = η-1 I, F = $\hat{X}$, G = $-\hat{X}$, and E = I, and W1 can be restated as follows:

$$W_1 = \hat{X}^T \left(\eta I + \hat{X}\hat{X}^T\right)^{-1} \hat{Y}. \tag{7}$$

Equation 7 can be further restated as follows:

$$W_1 = \sum_{i=0}^{n} \alpha_i \hat{X}, \alpha = \left(\hat{X}\hat{X}^{\mathrm{T}} + \eta I\right)^{-1} \hat{Y}. \tag{8}$$

Therefore, when a new state data $\hat{X}\star$ is added to the dataset, the predicted value can be computed by projecting it to solution W1 as follows:

$$Y\star = W_1^{\mathrm{T}} \hat{X}\star = X^{\mathrm{T}} \hat{X} \left(X^{\mathrm{T}} X + \eta I\right)^{-1} \hat{Y} = \kappa\left(\hat{X}\right)\left(K + \eta I\right)^{-1} \hat{Y}, \tag{9}$$

where $\kappa(\hat{X}) = K(X, \hat{X})$ and K is the kernel function. In this paper, the radial basis function is selected as follows:

$$K\left(X, \hat{X}\right) = \exp\left(-\frac{\left\|X - \hat{X}\right\|^2}{2\sigma^2}\right). \tag{10}$$

For the parameter selection issues, the five-fold cross validation can be used to optimize the kernel ridge regression convergence speed and accuracy (Arlot et al., 2010).

3 Kernel ridge regression and unscented Kalman filter

The state estimation model denoted by Eq. 1 and Eq. 2 can be reformed as follows:

$$X_{t+1} = g(X_t) + q_t, \tag{11}$$

$$Z_{t+1} = f(X_{t+1}) + p_t. \tag{12}$$

The state variables X_{t} and $X_{\mathrm{t+1}}$ include the amplitude and phase of voltage, which are passed through by the transition function g; besides, the measurements $Z_{\mathrm{t+1}}$ contain real and reactive power flow measurements of relevant node and branch, which are passed through by the measuring function f. q_{t} and p_{t} are the noises following Gaussian distribution. However, the functions g and f are non-linear functions, and the estimation after passing the state or measurement through these two functions is no longer Gaussian. So, to effectively use the Kalman filter for *a posteriori* probability estimation, the UKF uses the unscented transformation method to simulate real distribution of the dataset.

The transition and the measuring functions g and f can be replaced by the KRR model so as to learn the covariances of the unknown noise in measurement and state information. A set of state–measurement relations needs to be identified to form the training data of KRR. In the transition model, $x_{t\text{-}1}$ is mapped to state transition $\Delta x = x_t\text{-}x_{t\text{-}1}$, and the state x_t can be calculated by combining the previous state transition. In the measuring model, state x_t is mapped to measurement z_t. Then, the formulations of the

training sets in transition and the measuring functions are shown as follows:

$$\begin{cases} m_f = \{x_{t-1}, \Delta x\} \\ m_g = \{z_t, x_t\} \end{cases}. \tag{13}$$

KRR approximates the functions g and f, and they are denoted by $\hat{\mathrm{K}}^f$ and $\hat{\mathrm{K}}^g$, respectively. Thus, (11) and (12) are rewritten as follows:

$$x_t = \hat{\mathrm{K}}^f\left(m_f\right) + \varepsilon_t, \tag{14}$$

$$z_t = \hat{\mathrm{K}}^g\left(m_g\right) + \delta_t, \tag{15}$$

where the noises ε_t are distributed following a mean of 0 Gaussian distribution *co-variance* $\hat{\mathrm{K}}^f(m_f)$ and $\hat{\mathrm{K}}^g(m_g)$. To further remove the impacts of the non-Gaussian noise, we use an approximate parametric system model (Julier et al., 2000), and (14) and (15) are rewritten as follows:

$$x_t^{'} = \hat{\mathrm{K}}^f\left(m_f\right) + \hat{\varepsilon}_t + \hat{f}\left(\hat{m}_f\right), \tag{16}$$

$$z_t^{'} = \hat{\mathrm{K}}^g\left(m_g\right) + \hat{\delta}_t + \hat{g}\left(\hat{m}_g\right), \tag{17}$$

where $\hat{m}_f = \left\{x_{t-1}, x_t - \hat{\mathrm{K}}^f(m_f)\right\}$, $\hat{m}_g = \left\{x_t, z_t - \hat{\mathrm{K}}^g(m_g)\right\}$, $\hat{\varepsilon}_t \sim N(0, \hat{f}(\hat{m}_f))$, and $\hat{\delta}_t \sim N(0, \hat{g}(\hat{m}_g))$. The sigma points can be given by the following equation:

$$\begin{cases} \gamma = \sqrt{(n+\lambda)} \\ \chi_{t-1} = \left(\mu_{t-1}, \mu_{t-1} + \gamma\sqrt{\theta_{t-1}}, \mu_{t-1} - \gamma\sqrt{\theta_{t-1}}\right) \end{cases}, \tag{18}$$

where μ_{t-1} and θ_{t-1} are the mean and covariance of $x_t^{'}$, respectively. The sigma nodes are calculated using the KRR transition model.

$$\vec{\chi}_t^i = \hat{\mathrm{K}}^f\left(\chi_{t-1}^i\right). \tag{19}$$

The average and variance of the transition noise Q_t can be acquired through the predictive in KRR at the prior mean sigma point.

$$Q_t = \hat{\mathrm{K}}^f\left(\mu_{t-1}, \hat{m}_f\right), \tag{20}$$

$$\begin{cases} \hat{\mu}_t = \sum_{i=1}^{2N} w_m^i \vec{\chi}_t^i \\ \hat{\theta}_t = \sum_{i=1}^{2N} w_c^i \left(\vec{\chi}_t^i - \hat{\mu}_t\right)\left(\vec{\chi}_t^i - \hat{\mu}_t\right)^T + Q_t. \end{cases} \tag{21}$$

Then, the new sigma points are given as follows:

$$\hat{\chi}_t = \left(\hat{\mu}_t, \hat{\mu}_t + \gamma\sqrt{\hat{\theta}_t}, \hat{\mu}_t - \gamma\sqrt{\hat{\theta}_t}\right). \tag{22}$$

We can obtain the predicted measurements using the KRR model, and the resultant sigma points are applied for calculating the mean values $\hat{z}_t$ and S_t along with their associated uncertainties.

$$\begin{cases} \hat{z}_t^i = \hat{\mathrm{K}}^g\left(\hat{\chi}_t^i\right) \\ \hat{z}_t = \sum_{i=1}^{2N} w_m^i \hat{z}_t^{\mathrm{i}} \end{cases}, \tag{23}$$

$$\begin{cases} R_t = \hat{\mathrm{K}}^g\left(\mu_{t-1}, \hat{m}_g\right) \\ S_t = \sum_{i=1}^{2N} w_c^i \left(\hat{z}_t^{\mathrm{i}} - \hat{z}_t\right)\left(\hat{z}_t^{\mathrm{i}} - \hat{z}_t\right)^T + R_t \end{cases}, \tag{24}$$

where R_t is the measurement noise. We can compute the Kalman gain K_t and use it to update the state estimate.

$$\begin{cases} \hat{\theta}_t^{x,z} = \sum_{i=1}^{2N} w_c^i \left(\hat{X}_t^i - \hat{\mu}_t\right)\left(\hat{z}_t^i - \hat{z}_t\right)^T \\ K_t = \hat{\theta}_t^{x,z} S_t^{-1} \end{cases}, \tag{25}$$

$$\begin{cases} \mu_t = \hat{\mu}_t + K_t\left(z_t - \hat{z}_t\right) \\ \theta_t = \hat{\theta}_t - K_t S_t K_t^T \end{cases}. \tag{26}$$

The KRR-UKF inherits the advantages of the UKF for linearization and can automatically adjust the model and learn the noise characteristics in the data. The non-parametric model can analyze samples directly without prior assumptions about the sample dataset, if less training data are available; to put it differently, the KRR that is built with more input data offers more accurate result. In addition, to save time cost, a parallel computing algorithm is casted to accelerate calculation speed (Ko et al., 2007).

4 Robust power system state estimation

Abnormal measurements (Zhang et al., 2020) seriously affect the collection and analysis of user electricity consumption information, so data detection and replacement are extremely necessary.

4.1 ATT-CNN-GRU prediction

4.1.1 ATT

The attention mechanism (ATT) abstracts the weight information of historical time series data by calculating the influence weight of each input data separately and performs weighted average processing on all information weight factors, so as to realize the adaptive weight distribution and enhance the predictive precision of the algorithm. It is assumed that the ATT mechanism is used to calculate attention distribution between voltage data V= (v_1, v_2 … v_i, i = 1 .. n-1) with timescales from 1 to n-1 and voltage data v_n at time n. First, the correlation between each historical voltage data V and v_n is computed through the utilization of the score function s. Then, the outcome is normalized using the *SoftMax* function, and the attention distribution of VN at each historical voltage input is obtained. The formula of α_i is given as follows:

$$a_i = SoftMax\left(s\left(v_i, v_n\right)\right) = \frac{\exp\left(s\left(v_i, v_n\right)\right)}{\sum_{i=1}^{n} \exp\left(s\left(v_i, v_n\right)\right)}. \tag{27}$$

Finally, we weighted the historical voltage data based on the obtained attention distribution to get the input information that the next CNN model should focus on.

$$Att = \sum_{i=1}^{n-1} \alpha_i v_i. \tag{28}$$

4.1.2 CNN

Since the state information is recorded in chronological order that has a robust correlation, the CNN can be employed to extract relevant characteristics from the historical operation data (Wu et al., 2022). With the superiority of convolutional operations of the CNN,

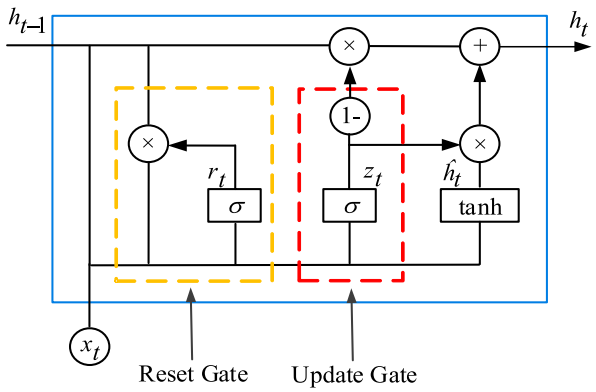

FIGURE 1
Structure of the GRU

it is possible to perform a more advanced and abstract representation of unprocessed data (Jensen et al., 2017).

The convolutional layer performs convolutional operations on the information in receptive field by designing convolutional kernels of appropriate size to abstractly represent the raw data. The feature map C with input S of the convolutional layer can be represented as follows:

$$C = P(S \otimes W_c + b_c), \tag{29}$$

where ⊗ is the convolutional operation, the rectified linear unit (ReLU) (Hara et al., 2015) is selected, and P is the activation function.

There are two types of pooling layers, namely, max-pooling and mean-pooling. In this paper, the choice is made to use max-pooling. This operation preserves robust features while discarding weaker ones. Additionally, it aids in the reduction of the number of parameters to mitigate the risk of overfitting.

In this paper, the CNN is harnessed to capture the features within the raw data and eliminate noise and unstable elements by multi-dimensional data mining. The processed and relatively stable data are passed into the LSTM network as a whole for long-term sequence prediction.

4.1.3 GRU

The GRU is a variant of the LSTM algorithm. Compared with traditional LSTM (Hochreiter et al., 1997), the GRU simplifies the network structure by reducing the gate function and greatly improves the operational efficiency. By introducing the gate function, we can mine the time sequence regularity of relatively long interval and delay. The structure of the GRU is shown in Figure 1.

In period t, the GRU receives input from two external sources, namely, the present state $x_t^{'}$ and the concealed state h_{t-1}. The operational workflow of the GRU can be segregated into two distinct steps.

4.1.3.1 Reset gate

This gate function reduces the risk of gradient explosion in the model by dropping some information about the data that is not relevant to the prediction moment and deciding how much information needs to be saved.

$$r_t = \sigma\left(W_r\left[h_{t-1}, x_t^{'}\right]\right). \tag{30}$$

4.1.3.2 Update gate

The reset gate has the same structure as the t update gate and determines the degree to which the low-weight information is forgotten and how much memory is retained to update to the current cell.

$$u_t = \sigma\left(W_u\left[h_{t-1}, x_t^{'}\right]\right). \tag{31}$$

The newly updated memory content utilizes the reset gate to preserve information related to the past and calculate the Hadamard product (*) of the reset gate r_t and $[h_{t-1}, x_t^{'}]$. The Hadamard results will be summed and passed to the hyperbolic tangent activation function (tanh). Thence, h_t retains the influence of historical data on the current prediction and regulates the influx of input data by employing gating mechanisms, deciding what information should be propagated to the subsequent unit, avoiding the gradient disappearance problem.

$$\begin{cases} \hat{h}_t = \tanh\left(W_{\hat{h}} \cdot [r_t * (h_{t-1}, x_t)]\right) \\ h_t = (1 - u_t) * h_{t-1} + u_t * \hat{h}_t \end{cases}. \tag{32}$$

4.1.4 ATT-CNN-GRU

The ATT-CNN is employed to find time series data patterns, which are imported as a whole into the GRU model for long time series prediction to improve prediction stability, and the steps are given as follows.

1. Data pre-processing: The data are normalized and then split into next sets according to the GRU model training method (Sutskever et al., 2013).
2. ATT-CNN unit: The pre-processed data are distinguished from their strong and weak features. The weak features are removed, and the strong features are extracted as the next unit input.
3. GRU unit: Utilizing the output from the preceding unit as input to construct the time series prediction model.
4. Output: Exporting the results of ATT-CNN-GRU prediction.

More training details can be found in the work of Vinvals et al. (2015), where the ATT-CNN-GRU is used to fast predict the state vector. Next, an OPTICS-based abnormal detection method is first introduced and combined with the ATT-CNN-GRU to handle the outliers.

4.2 Abnormal data detection and replacement

After obtaining the predicted state value, the corresponding measurement data can be obtained through the power flow equation (PF) (Tinney et al., 1967).

$$\begin{cases} P_t^n = V_t^n \sum_{n=1}^{N} V_t^m \left(G^{nm} \cos\theta_t^{nm} + B^{nm} \sin\theta_t^{nm}\right) \\ Q_t^n = V_t^n \sum_{n=1}^{N} V_t^m \left(G^{nm} \sin\theta_t^{nm} - B^{nm} \sin\theta_t^{nm}\right) \\ P_t^{nm} = V_t^{n,2} G^{nm} - V_t^n V_t^m G^{nm} \cos\theta_t^{nm} - V_t^n V_t^m G^{nm} \sin\theta_t^{nm} \\ Q_t^{nm} = -V_t^{n,2} B^{nm} - V_t^n V_t^m B^{nm} \sin\theta_t^{nm} + V_t^n V_t^m B^{nm} \cos\theta_t^{nm} \end{cases}. \tag{33}$$

For outliers such as missing and error measurements, the anomaly detection method is applied to deal with these outliers.

OPTICS is a commonly used detection algorithm, which can efficiency discover the oddly shape cluster. OPTICS creates a neighborhood $N_\varepsilon(z_i^*)$ of radius ε for each z_i^*, and there should be no less than *MinPts* data points in the neighborhood, where z_i^* is the new input measurement at time *i*. Some definitions are given as follows.

Directly density-reachable: If the new measurements z_i^* and z_j^* satisfy $z_i^* \in N_\varepsilon(z_j^*)$ and $card(N_\varepsilon(z_j^*)) \geq MinPts$, then z_i^* is considered to be reachable by z_j^* density directly, and z_j^* is regarded as ***core object***, where the $card(N_\varepsilon(z_j^*))$ denotes the quantity of elements contained in the set $N_\varepsilon(z_j^*)$.

Density-reachable: For the dataset $z_r^*, z_{r+1}^*, \cdots, z_{r+s}^*$, if $z_i^* i \in [r, r+s-1]$ can be reachable by z_{i+1}^* density directly, then z_i^* is density-reachable from z_{i+1}^*.

Density-connected: If z_i^* and z_j^* are reachable by z_k^* density directly, then z_i^* and z_j^* are density-connected.

Core distance: The minimum neighborhood radius that makes z_i^* a ***core object*** can be expressed as follows:

$$cd(z) = \begin{cases} d(z, N_\varepsilon^a(z)), & \text{if} \quad |N_\varepsilon(z)| \geq MinPts \\ undefined, & \text{if} \quad |N_\varepsilon(z)| < MinPts \end{cases}, \tag{34}$$

where $N_\varepsilon^a(z)$ denotes the data $N_\varepsilon(z)$ that is the *ath* nearest neighbor to the data *z*, and *z* is the *core object*.

4.2.1 Reachability distance

The reachability distance is given as follows:

$$rd(z_i^*, z_j^*) = \begin{cases} undefined & \text{if} \quad card(N_\varepsilon(z_i^*)) \leq MinPts \\ \max\left(cd(z_j^*), d(z_i^*, z_j^*)\right) & \text{if} \quad card(N_\varepsilon(z_i^*)) \geq MinPts \end{cases}, \tag{35}$$

where $rd(z_i^*, z_j^*)$ is the minimum distance at which z_i^* can be reachable by z_j^* density directly, and z_j^* is a *core object*.

In practical applications, the dispatch center only needs to import historical data into our KRR-UKF method and perform modeling and then collect real-time data to perform real-time filtering. Meanwhile, the model can also expand the training set based on the actual production data to optimize the filter. The specific flow of the robust KRR-UKF at time *t* is shown in Figure 2.

The selection of parameters ε and *MinPts* can be found in the work of Ankerst et al. (1999). The OPTICS and ATT-CNN-GRU are used to handle the outliers, which consist of the following steps.

1. Computing reachability distance: Data z_i in new measurement dataset *Z* are selected randomly as the current object, and then, the reachability distance of all other measurements in *Z* is calculated with respect to the current object.
2. Marking the data: Data with the smallest reachability distance from the current object are found, and then, the current object is replaced with that set of data and is marked as processed.
3. Getting the smallest reachability distance: The reachable distances of the unprocessed data from the current object are calculated in turn, and if any of these reachable distances is smaller than the reachable distance calculated in step 2, then the corresponding data are replaced with the current object. If not, the current object remains unchanged.
4. Iteration: Steps 2 and 3 are repeated until all data in *Z* have been processed.
5. Classifying the data: The calculated reachable distance ε' of each data is compared with ε; if $\varepsilon' < \varepsilon$, then the reachable distance is meaningful, and the corresponding data are considered normal. Otherwise, it is marked as outlier.
6. Predicting the state: The predicted measurements in period *t* of node *n* can be computed via the ATT-CNN-GRU.
$$\hat{z}^n = \left\{\hat{P}_t^n, \hat{Q}_t^n, \hat{P}_t^{nm}, \hat{Q}_t^{nm}\right\}. \tag{36}$$
7. Outlier replacement: If the input data are marked as outliers, the corresponding measurements are replaced by (39).

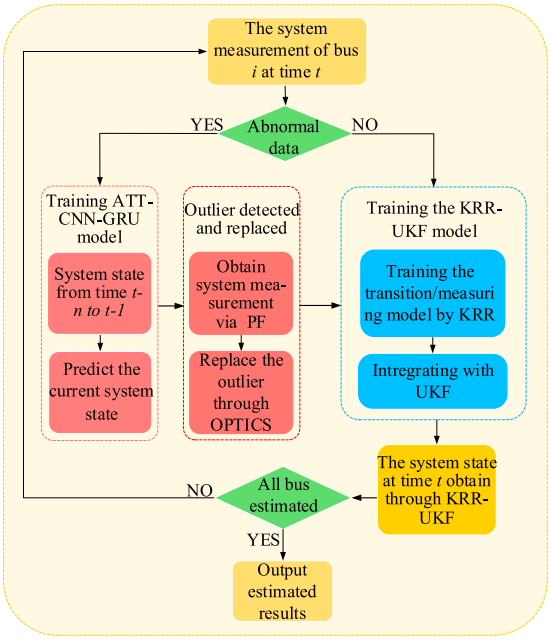

FIGURE 2
Flow chart of the robust KRR-UKF method.

5 Case studies

Simulations are carried on a IEEE 33-bus system and a realistic 109-bus system from a city in China to verify the robustness under different circumstances. The ATT-CNN-GRU and KRR-UKF models are developed using PYTHON on the NVIDIA GTX-1660TI with 16 GB RAM. The system state and measurement dataset are obtained from the MATPOWER toolkit. We use the mean absolute error (MAE) and root mean squared error (RMSE) (Hossain et al., 2020).

5.1 IEEE 33-bus system

The load data on Belgian grid of 2020 are selected to generate 8,760 measurement state sets, in which a total of 4,000 sets of data

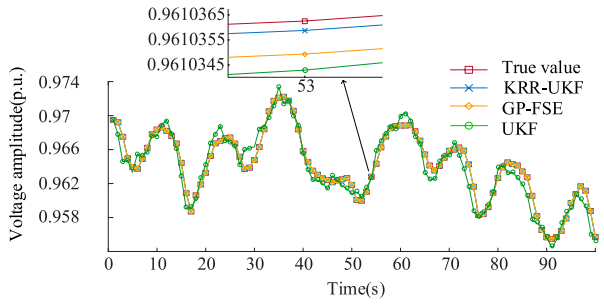

FIGURE 3
Filtering result of node 6 of three algorithms.

are randomly selected as the training set. The load data of 2021 on Belgian grid are used to generate 8,760 data as the test set.

5.2 Scenario 1: with only Gaussian noise

We assume that the noise follows the Gaussian distribution. We compare the UKF with the KRR-UKF and GP-FSE (Ji et al., 2021) under ideal conditions. It is noted that in the existing references on PSSE based on Kalman filtering, in this section, Gaussian noise with a mean value of 0 and a variance of 10^{-6} is added into the sample data, and the filter performance of the three algorithms is shown in Figure 3.

As shown in Figure 3, under the ideal conditions, there is a substantial disparity between the estimated state obtained through UKF and the true value. Furthermore, we can see from Figure 3, as data-driven algorithms, the KRR-UKF and GP-FSE have a better prediction performance than the UKF, and the difference between the estimated state via the KRR-UKF and the actual value is exceedingly minute. This is because kernel ridge regression is a powerful non-parametric tool that has the capability to acquire noise characteristics and smoothing parameters from the training data; thus, it is also deduced that the accuracy of GP-FSE is slightly inferior to the method we have introduced.

To intuitively demonstrate the effectiveness of these filters, the MAE and RMSE of the KRR-UKF are shown in Figure 4A. In addition, to further illustrate the robustness of our methods, Gaussian noise characterized by a mean of 0 and a variance of and 10^{-4} is added to the sample data.

Figure 4 illustrated the MAE and RMSE of the KRR-UKF algorithm maintained at the range of 10^{-5}–10^{-6} under different noises. The proposed KRR maps the non-linear correlation into high dimension for precisely tracking data characteristics. Then, the five-fold cross-validation method also assigns more appropriate parameters to the noise data for optimizing the estimated results. As displayed in Figure 4A, the data-driven approach we propose exhibits remarkable accuracy and stability, and Figure 4B shows that the proposed method still has excellent prediction accuracy when the noise covariance is increased to 10^{-4}. Furthermore, the RMSE is more sensitive to predicting abnormal values, but the RMSE of the KRR-UKF estimation results remains at 10^{-6} under different noise levels, which demonstrates that the method has good robustness to the Gaussian noise.

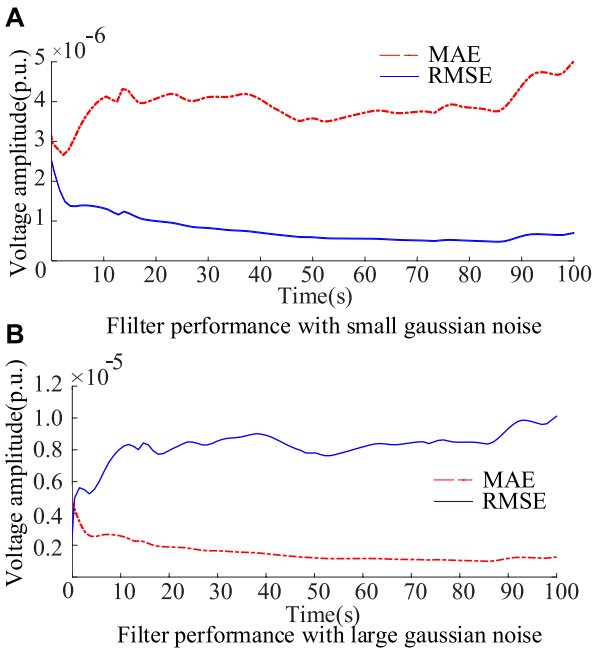

FIGURE 4
KRR-UKF performance on node 6. **(A)** MAE and RMSE of the KRR-UKF with small Gaussian of noise **(B)** MAE and RMSE of the KRR-UKF with large Gaussian of noise.

5.3 Scenario 2: with non-Gaussian noise

To test KRR-UKF performances under different non-Gaussian noises, the weights are 0.95 and 0.05, the bimodal Gaussian noise with covariance matrices of 10^{-6} I and 10^{-5} I is added. The KRR-UKF has the ability to assign higher weight to the predicted value information with small deviation, thus filtering out non-Gaussian noise data.

In Figure 5 (a), when the degree of noise deviating from the Gaussian distribution increases, the proposed KRR-UKF still maintains the estimation performance similar to scenario 1, and its MAE and RMSE can be kept at 10^{-6} and 10^{-5}, respectively, which proves that the method can filter non-Gaussian noises. In order to showcase the robustness of the KRR-UKF approach, Laplace noise and Cauchy noise are added, the covariance matrix of Laplace is 10^{-5} I, and the location parameter and scale location parameter are 0 and $10^{-5}I$, respectively.

In Figure 5, the MAE of the KRR-UKF filter increases slightly, and the error remains at 10^{-5}, which indicates that the proposed KRR-UKF is robust to different non-Gaussian noises. To fully verify the robustness of the KRR-UKF, noises that further deviate from the Gaussian distribution are added to the datasets of the KRR-UKF and GP-FSE, the bimodal Gaussian noise covariance matrices of the two models are 10^{-6} I and 10^{-4} I, respectively; and the noise weight ratio is gradually changed from 0.95/0.05 to 0.5/0.5, with a step size of 0.05.

In Table 1, both methods show an increase in MAE as the deviation of non-Gaussian noise grows and finally remains at the order of 10^{-4}, but due to the lack of correction of predict equation, the MAE of GP-FSE has nearly tripled, and its RMSE increases to 1.190×10^{-4}, which means the instability of GP-FSE increases further. However, the kernel ridge regression method can optimize the parameters; thus, enabling the model adapts the unknown noise exactly and corrects the estimation results more

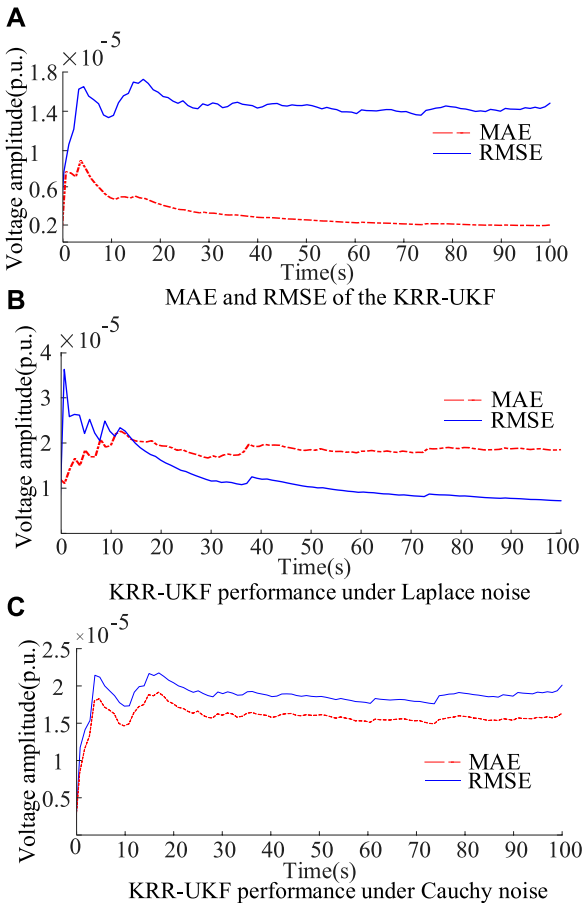

FIGURE 5
Filtering performance of node 6 in non-Gaussian of noise. **(A)** In small noise, **(B)** under Laplace noise, and **(C)** under Cauchy noise.

TABLE 1 Performance of the two algorithms under different weight noises.

Weight ratio	KRR-UKF	GP-FSE	KRR-UKF	GP-FSE
	MAE	MAE	RMSE	RMSE
0.95/0.05	1.221×10^{-5}	1.192×10^{-5}	1.231×10^{-5}	1.428×10^{-5}
0.9/0.1	5.474×10^{-5}	6.921×10^{-5}	2.221×10^{-5}	1.442×10^{-5}
0.85/0.15	8.758×10^{-5}	7.083×10^{-5}	2.612×10^{-5}	3.098×10^{-5}
0.8/0.2	8.948×10^{-5}	1.211×10^{-4}	3.642×10^{-5}	6.281×10^{-5}
0.75/0.25	1.007×10^{-4}	1.574×10^{-4}	2.943×10^{-5}	6.270×10^{-5}
0.7/0.3	1.331×10^{-4}	3.551×10^{-4}	4.804×10^{-5}	8.018×10^{-5}
0.65/0.35	1.642×10^{-4}	3.903×10^{-4}	5.307×10^{-5}	7.821×10^{-5}
0.6/0.4	2.026×10^{-4}	4.026×10^{-4}	5.625×10^{-5}	9.026×10^{-5}
0.55/0.45	1.354×10^{-4}	5.091×10^{-4}	6.760×10^{-5}	9.778×10^{-5}
0.5/0.5	1.880×10^{-4}	5.129×10^{-4}	8.857×10^{-5}	1.190×10^{-4}

accurately. The RMSE of the proposed method fluctuates between 5.857×10^{-5} and 1.231×10^{-5}, which demonstrates that the proposed KRR-UKF has good robustness and stronger stability.

TABLE 2 Performances of the KRR-UKF using different datasets.

Dataset	MAE	RMSE	Time (s)
$\{V^n\}$-$\{P^n\}$	6.958×10^{-5}	3.898×10^{-5}	0.021
$\{V^n\}$-$\{P^n, Q^n\}$	6.272×10^{-5}	3.463×10^{-5}	0.026
$\{V^n\}$-$\{P^n, Q^n, P^{nm}\}$	5.133×10^{-5}	2.726×10^{-5}	0.027
$\{V^n\}$-$\{P^n, Q^n, P^{nm}, Q^{nm}\}$	4.341×10^{-5}	2.203×10^{-5}	0.031

5.4 Scenario 3: with reduced measurement redundancy

The proposed KRR-UKF method uses the historical data to model the measuring equation in certain topology network; the ratio between the number of measurement quantities and state quantities is defined as measurement redundancy, which is crucial to determine the result of state estimation. The historical data used in this model include nodal voltage, phase angle (V, θ), nodal active and reactive power (P, Q), and associated branch (P^{nm}, Q^{nm}). We take the voltage of bus 18 as the test state consistent with scenario 2. The 100s estimated results are compared with the calculated value using PF under noiseless condition.

In Table 2, as the measurement redundancy increases, the MAE and RMSE gradually decline, which is due to the facts that more measurement information can be used to eliminate the influence of bad data and errors. The parallel computing method can compute the state mapped values of multiple measurements simultaneously, so when the redundancy increases, there is no significant increase in consumption time. When the redundancy reaches 4, the time consumption of the KRR-UKF only increased 33% and remained in the order of milliseconds, indicating that the proposed method can work properly with reduced measurement redundancy.

5.5 Scenario 4: under network reconfiguration

To demonstrate the proposed filter performances when the topology network changes, we take node 24 as an example. Table 3 gives two network structures, and the topology changes from structure A to structure B at 50s. Half of the KRR-UKF training set comes from structure A and half from topology B.

The performance under the condition of small Gaussian noise is plotted in Figure 6.

In Figure 6, the voltage amplitude estimated by the KRR-UKF aligns closely with the actual value. It should be noted that the proposed KRR-UKF can model only based on the input data, free from the limitations of the mechanism model. Thus, when the topology network changes at 50s, both RMSE and MAE can be maintained at around 10^{-5}. It can be inferred that the approach is capable of performing under network reconfiguration by simply expanding the training set, which is sufficient to deal with the topological changes in the distribution network.

TABLE 3 Two different structures of the IEEE-33 system.

Index	Open switches
Structure A	S33, S34, S35, S36, and S37
Structure B	S7, S9, S14, S32, and S37

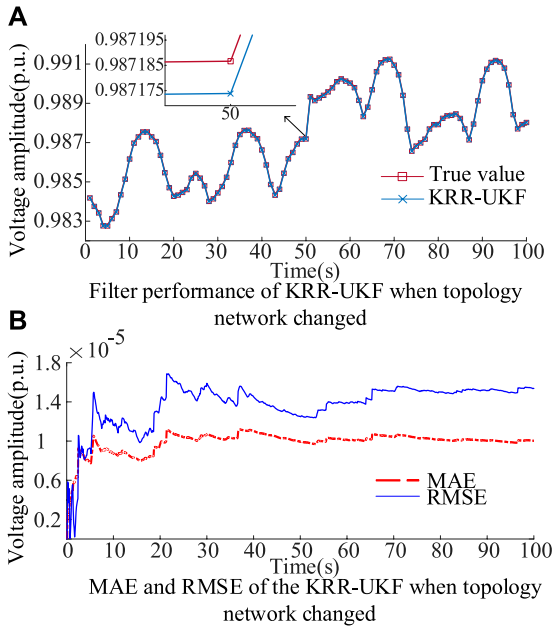

FIGURE 6
Filtering performance of node 24 when topology changes. **(A)** Filter performance of the KRR-UKF when the topology network changed. **(B)** MAE and RMSE of the KRR-UKF when the topology network changed.

5.6 Scenario 5: with abnormal or missing data

Due to communication channel interruption, flicker, and abnormal data transmission problems in the data acquisition system, abnormal or missing data may occur. To demonstrate the feasibility of using the ATT-CNN-GRU for outlier replacement, this section takes the voltage of node 11 as an example. This paper sets up two cases.

Case 1. assumed that 30% of the active power is abnormal in the measurement data of node 11, and the gross error is 15%.

Case 2. assumed that there are 20% missing in the measurement data of node 11.

The OPTICS clustering algorithm is applied to detect and label outliers, and then, the proposed ATT-CNN-GRU is used to predict and replace the abnormal measurements. The model tuning mainly includes the number of convolutional layers, and the voltage estimation results of different layers are shown in Table 4.

In Table 1, the estimation accuracy and estimation efficiency of the CNN are optimal for a number of layers of 2. We list the voltage prediction results of ATT-CNN-LSTM and the ATT-CNN-GRU with the same structure in Table 5 to substantiate the effectiveness. Comparing with ATT-CNN-LSTM, the prediction accuracy and stability of the ATT-CNN-GRU improved by 12.51% and 16.39%, respectively, because our method optimizes parameter structure and integrates global and local features to avoid losing necessary feature data. Thence, the time required to predict the data reduces consumption of time by 14.75% compared with ATT-CNN-LSTM, which proves that the method can accurately and efficiently replace the bad data. Therefore, the ATT-CNN-GRU is selected to handle outliers, and the filtering results of the KRR-UKF after ATT-CNN-GRU replacing the anomalous data are shown in Figure 7.

In Figure 7A, the MAE of the KRR-UKF maintained at 10^{-5}, through the ATT-CNN module, the improved GRU can extract coarse-grained features from the fine-grained features in data. To a certain extent, it can solve the problems of memory loss and gradient dispersion induced by excessively long steps in the GRU, which provides the proposed method with accurate measurement data for filtering. From the results of Figure 7 (b), the filtering curve fluctuates very slightly and ensures filtering accuracy.

In Table 6, the WLS has the least calculation time, but the estimation accuracy is the worst. Nevertheless, the KRR-UKF uses improved LSTM algorithms for data replacement, so there will be time loss when abnormal conditions occur, and still has milli-second calculation time, which fulfills the criteria for achieving real-time state estimation accuracy.

The KRR-UKF also displays relatively heightened estimation accuracy under abnormal conditions with an RMSE of 3.4×10^{-5}, which is nearly 33% accurate than a GP-FSE. Hence, the KRR-UKF emerges as a relatively optimal choice for real-time state estimation in the IEEE 33-bus system.

5.7 109-bus system from a city in China

In this section, a 109-bus distribution network system from a city in China is selected for a practical application test. We obtained the operation data in August 2020, randomly selected 2,880 groups as the training set, and used 2,880 groups of data in August 2021 as

TABLE 4 Estimation results for different numbers of convolutional layers.

Number of layers	MAE	RMSE	Execution time (ms)
1	4.509×10^{-4}	2.585×10^{-4}	14.79
2	9.903×10^{-5}	8.021×10^{-5}	15.54
3	2.119×10^{-4}	1.067×10^{-4}	15.92
4	2.031×10^{-4}	9.852×10^{-5}	17.23

TABLE 5 Comparison of forecast results of different algorithms.

Predicted duration (s)	Algorithms	MAE	RMSE	Execution time (s)
1,000	ATT-CNN-GRU	8.048×10^{-5}	6.103×10^{-5}	1.856
	ATT-CNN-LSTM	9.199×10^{-5}	7.612×10^{-5}	2.177

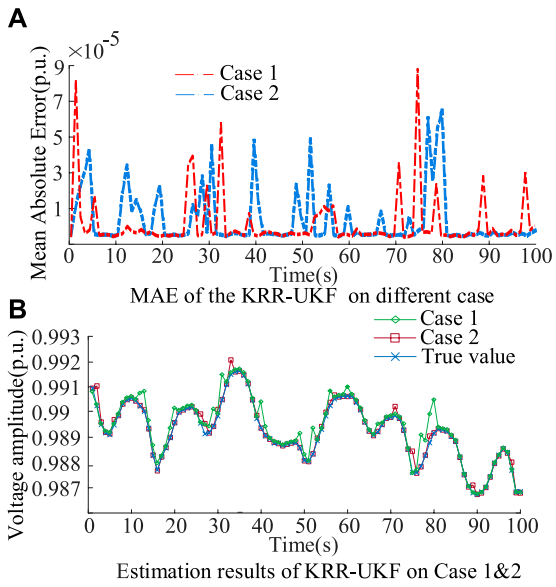

FIGURE 7
Filtering performance for node 11. **(A)** MAE of the KRR-UKF in case 1&2. **(B)** estimation results of KRR-UKF in case 1&2.

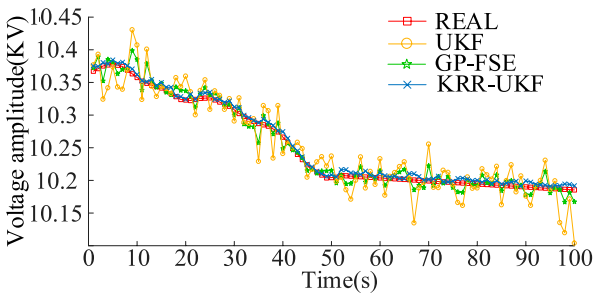

FIGURE 8
Filtering performance of different algorithms.

the testing dataset. We randomly choose 20% data from the test set for exception handling, in which 10% data are replaced by 0 value and 10% data are randomly reduced by 15%. The estimation results of the KRR-UKF, GP-FSE, and UKF under normal conditions are shown in Figure 8.

As shown in Figure 8, the filtering curves UKF fluctuate, and the accuracy decreases due to unknown noise, which is affected by unknown noise and has many deviation points. However, the KRR-UKF can maintain the same trend as the true value in general.

In Table 7, comparing with the simulation result in scenario 1, the accuracy of the UKF is greatly reduced due to the unknown noise. The GP-FSE model is affected by non-Gaussian noise in training data and lack of predictive steps to correct it. The error increases to 10^{-3}. However, the KRR-UKF still shows favorable performance, whose RMSE is 3.22×10^{-4}. The calculation time of the KRR-UKF is 0.292 s, which also fulfills the requirements of real time state estimation. In

TABLE 6 RMSE and computing time of different algorithms.

Index	Algorithm	Normal	Abnormal
RMSE	WLS	7.1×10^{-3}	--
	UKF	5.4×10^{-4}	7.8×10^{-3}
	CSS (Prasad et al., 2017)	2.6×10^{-4}	--
	Method in the work of Kong et al. (2022)	3.8×10^{-4}	--
	GP-FSE	7.5×10^{-6}	4.5×10^{-5}
	KRR-UKF	5.1×10^{-6}	3.4×10^{-5}
Time (ms)	WLS	2.1	--
	UKF	29.4	28.9
	CSS (Prasad et al., 2017)	--	--
	Method in the work of Kong et al. (2022)	19.1	--
	GP-FSE	32.51	39.24
	KRR-UKF	46.56	40.21

TABLE 7 Comparison of different filters.

Indicator	UKF	GP-FSE	KRR-UKF
MAE	6.22×10^{-2}	4.91×10^{-3}	1.09×10^{-4}
RMSE	5.41×10^{-2}	1.29×10^{-3}	3.18×10^{-4}
Time (s)	0.128	0.271	0.292

conclusion, the proposed KRR-UKF has sufficient accuracy and robustness that can be applied in practical engineering.

6 Conclusion

In this paper, a KRR-UKF method, which can improve the exactitude and robustness of state estimation, is proposed. The test results prove that the proposed KRR-UKF method can filter unknown noise in the power system, and the ATT-CNN-GRU can enhance the accuracy of the predicting outlier, as well as in the conditions of topology network changes or reduced measurement redundancy. Furthermore, the performances of the KRR-UKF method are only related to the dataset; that is to say, there is no need to consider the actual physical model. Moreover, compared to existing algorithms, the KRR-UKF exhibits significant enhancements in both estimation accuracy and computational efficiency.

Although the KRR-UKF shows extraordinary performances on state estimation, when the system is in three-phase unbalanced states, the results of state estimation may become worse. Furthermore, the method introduced in this paper necessitates a considerable volume of historical operational data for model training, imposing a slightly higher requirement on data accuracy without considering the placement of measurement equipment and acquisition accuracy in real industry. Further verification of the feasibility of application to industry is still required.

Data availability statement

The data analyzed in this study are subject to licenses/restrictions: The source of the dataset is the project provider, which is not convenient to disclose. Requests to access these datasets should be directed to SZ, zsmphys@sdust.edu.cn.

Author contributions

WZ: data curation, supervision, and writing–original draft. SZ: conceptualization, methodology, resources, and writing–review and editing. YZ: investigation and writing–original draft. GX: formal analysis and writing–original draft. HM: validation and Writing–original draft.

Conflict of interest

WZ and GX were employed by Zhuhai XJ Electric Co., Ltd.

The remaining authors declare that the research was conducted in the absence of any commercial or financial relationships that could be construed as a potential conflict of interest.

Publisher's note

All claims expressed in this article are solely those of the authors and do not necessarily represent those of their affiliated organizations, or those of the publisher, the editors, and the reviewers. Any product that may be evaluated in this article, or claim that may be made by its manufacturer, is not guaranteed or endorsed by the publisher.

References

Ankerst, M., Breunig, M. M., Kriegel, H. P., and Sander, J. (1999). OPTICS: ordering points to identify the clustering structure. *ACM Sigmod Rec.* 28 (2), 49–60. doi:10.1145/304181.304187

Arlot, S., and Celisse, A. (2010). A survey of cross-validation procedures for model selection. *Stat. Surv.* 4. doi:10.1214/09-ss054

Bai, X., Qu, L., and Qiao, W. (2016). Robust AC optimal power flow for power networks with wind power generation. *IEEE Trans. Power Syst.* 31, 4163–4164. doi:10.1109/tpwrs.2015.2493778

Dang, L., Chen, B., Ma, W., and Ren, P., (2020). Robust power system state estimation with minimum error entropy unscented Kalman filter. *IEEE Trans. Instrum. Meas.* 69, 8797–8808. doi:10.1109/tim.2020.2999757

Du, Q., Bo, Z., Dong, Y., and Luo, X. S. (2010). Effect of noise on erosion of safe basin in power system. *Nonlinear Dyn.* 61, 477–482. doi:10.1007/s11071-010-9663-0

Ghahremani, E., and Kamwa, I. (2016). Local and wide-area PMU-based decentralized dynamic state estimation in multi-machine power systems. *IEEE Trans. Power Syst.* 31, 547–562. doi:10.1109/tpwrs.2015.2400633

Guo, L., Liu, W., Li, X., Liu, Y., Jiao, B., Wang, W., et al. (2014). Energy management system for stand-alone wind-powered-desalination microgrid. *IEEE Trans. Smart Grid* 7 (2), 1–1087. doi:10.1109/tsg.2014.2377374

Hara, K., Saito, D., and Shouno, H. (2015). "Analysis of function of rectified linear unit used in deep learning," in International Joint Conference on Neural Networks 2015, Killarney, Ireland, July 12–16, 2015, 1–8.

Hochreiter, S., and Schmidhuber, J. (1997). Long short-term memory. *Neural Comput.* 9 (8), 1735–1780. doi:10.1162/neco.1997.9.8.1735

Hoerl, A. E., and Kennard, R. W. (1970). Ridge regression: biased estimation for nonorthogonal problems. *Technometrics* 12 (1), 55–67. doi:10.1080/00401706.1970.10488634

Hossain, M., and Mahmood, H. (2020). Short-term photovoltaic power forecasting using an LSTM neural network and synthetic weather forecast. *IEEE Access* 8, 172524–172533. doi:10.1109/access.2020.3024901

Jensen, S. K., Pedersen, T. B., and Thomsen, C. (2017). Time series management systems: a survey. *IEEE Trans. Knowl. Data Eng.* 29, 2581–2600. doi:10.1109/tkde.2017.2740932

Ji, X., Yin, Z., Zhang, Y., Wang, M., Zhang, X., Zhang, C., et al. (2021). Real-time robust forecasting-aided state estimation of power system based on data-driven models. *Int. J. Electr. Power and Energy Syst.* 125, 106412. doi:10.1016/j.ijepes.2020.106412

Julier, S., Uhlmann, J., and Durrant-Whyte, H. F. (2000). A new method for the nonlinear transformation of means and covariances in filters and estimators. *IEEE Trans. Automatic Control* 45 (3), 477–482. doi:10.1109/9.847726

Kalman, R. E. (1960). *A new approach to linear filtering and prediction problems.*

Ko, J., Klein, D. J., and Fox, D. (2007). "Gaussian processes and reinforcement learning for identification and control of an autonomous blimp," in Proceedings 2007 IEEE International Conference on Robotics and Automation, Roma, Italy, 14 April 2007, 742–747.

Kollias, D., and Zafeiriou, S. (2021). Exploiting Multi-CNN features in CNN-RNN based dimensional emotion recognition on the OMG in-the-Wild dataset. *IEEE Trans. Affect. Comput.* 12 (12), 595–606. doi:10.1109/taffc.2020.3014171

Kong, X., Zhang, X., Zhang, X., Wang, C., Chiang, H. D., and Li, P. (2022). Adaptive dynamic state estimation of distribution network based on interacting multiple model. *IEEE Trans. Sustain. Energy* 13 (2), 643–652. doi:10.1109/tste.2021.3118030

Mestav, K. R., Luengo-Rozas, J., and Tong, L. (2018). "State estimation for unobservable distribution systems via deep neural networks," in 2018 IEEE Power and energy Society General Meeting (PESGM), Portland, Oregon, 5-10 August 2018, 1–5.

Mestav, K. R., Luengo-Rozas, J., and Tong, L. (2019b). Bayesian state estimation for unobservable distribution systems via deep learning. *IEEE Trans. Power Syst.* 34, 4910–4920. doi:10.1109/tpwrs.2019.2919157

Mestav, K. R., and Tong, L. (2019a). "State estimation in smart distribution systems with deep generative adversary networks," in 2019 IEEE International Conference on Communications, Control, and Computing Technologies for Smart Grids, Beijing, China, October 2019, 1–6.

Murphy, K. P. (2012). *Machine learning: a probabilistic perspective*. Massachusetts, United States: Mit Press.

Netto, M., and Mili, L. (2018). A robust data-driven Koopman Kalman filter for power systems dynamic state estimation. *IEEE Trans. Power Syst.* 33, 7228–7237. doi:10.1109/tpwrs.2018.2846744

Prasad, S., and Vinod Kumar, D. M. (2017). Hybrid fuzzy charged system search algorithm-based state estimation in distribution networks. *Eng. Sci. Technol.* 20 (3), 922–933. doi:10.1016/j.jestch.2017.04.002

Rosenthal, W. S., Tartakovsky, A. M., and Huang, Z. (2017). Ensemble kalman filter for dynamic state estimation of power grids stochastically driven by time-correlated mechanical input power. *IEEE Trans. Power Syst.* 33 (4), 3701–3710. doi:10.1109/tpwrs.2017.2764492

Samuelsson, O., Hemmingsson, M., Nielsen, A. H., Pedersen, K., and Rasmussen, J. (2006). Monitoring of power system events at transmission and distribution level. *IEEE Trans. Power Syst.* 21, 1007–1008. doi:10.1109/tpwrs.2006.873014

Sutskever, I. (2013). *Training recurrent neural networks*. Toronto on Canada: University of Toronto.

Tahmasebi, P., and Hezarkhani, (2011). Application of a modular feedforward neural network for grade estimation. *Nat. Resour. Res.* 20, 25–32. doi:10.1007/s11053-011-9135-3

Tinney, W. F., and Hart, C. E. (1967). Power flow solution by Newton's method. *IEEE Trans. Power Apparatus Syst.*, 1449–1460. PAS-86. doi:10.1109/tpas.1967.291823

Vinyals, O., Toshev, A., and Bengio, S. (2015). "Show and tell: a neural image caption generator," in Proceedings of the IEEE Conference on Computer Vision and Pattern Recognition. 2015, Boston, Massachusetts, 7-12 June 2015, 3156–3164.

Weng, Y., Negi, R., Faloutsos, C., and Ilic, M. D. (2016). Robust data-driven state estimation for smart grid. *IEEE Trans. Smart Grid* 8 (4), 1956–1967. doi:10.1109/tsg.2015.2512925

Wu, H., Xu, Z., and Wang, M. (2022). Unrolled spatiotemporal graph convolutional network for distribution system state estimation and forecasting[J]. *IEEE Trans. Sustain. Energy* 14 (1), 297–308. doi:10.1109/TSTE.2022.3211706

Zadeh, R. A., Ghosh, A., and Ledwich, G. (2010). Combination of Kalman filter and least-error square techniques in power system. *IEEE Trans. Power Deliv.* 25, 2868–2880. doi:10.1109/tpwrd.2010.2049276

Zhang, H., Yu, T., Wang, W., Jiao, W., Chen, W., Zhong, Q., et al. (2020). Characterization of volatile profiles and marker substances by HS-spme/GC-MS during the concentration of coconut jam. *Deep Reinf. Learn.* 9, 347–364. doi:10.3390/foods9030347

Zhang, L., Wang, G., and Giannakis, G. B. (2019). Real-time power system state estimation and forecasting via deep unrolled neural networks. *IEEE Trans. Signal Process.* 67 (15), 4069–4077. doi:10.1109/tsp.2019.2926023

Zhao, J. (2018). Dynamic state estimation with model uncertainties using H_∞ extended kalman filter. *IEEE Trans. Power Syst.* 33, 1099–1100. doi:10.1109/tpwrs.2017.2688131

Zhao, J., and Mili, L. (2018). A robust generalized-maximum likelihood unscented Kalman filter for power system dynamic state estimation. *IEEE J. Sel. Top. Signal Process.* 12, 578–592. doi:10.1109/jstsp.2018.2827261

Zhao, J., Mili, L., and Gomez-Exposito, (2019b). Constrained robust unscented kalman filter for generalized dynamic state estimation. *IEEE Trans. Power Syst.* 34, 3637–3646. doi:10.1109/tpwrs.2019.2909000

Zhao, J., Qi, J., Huang, Z., Meliopoulos, A. P. S., Gomez-Exposito, A., Netto, M., et al. (2019a). Power system dynamic state estimation: motivations, definitions, methodologies, and future Work. *IEEE Trans. Power Syst.* 34, 3188–3198. doi:10.1109/tpwrs.2019.2894769

Nomenclature

11.1 Indices

i	Index of node
n/m	Index of branch
t	Index of time

11.2 Sets

N	Set of all bus
S	Training data
W	Set of weight
X	Set of state
Y	Set of estimation
Z	Set of measurement

11.3 Parameters

$b_c \in \mathbb{R}^d$	Biases vector of convolution
$b_i \in \mathbb{R}^d$	Biases vector of the input stage
$b_f \in \mathbb{R}^d$	Biases vector of the forget stage
$b_o \in \mathbb{R}^d$	Biases vector of the output stage
$b_m \in \mathbb{R}^d$	Biases vector of the current state
c_t	Cell state in prior t
h_{t-1}	Hidden state in prior t
I	Unit matrix
q_t	Process noises that follow Gaussian
p_t	Measurement noises that follow Gaussian
w_t	Process noises
v_t	Measurement noises
$W_r \in \mathbb{R}^{d\times 2d}$	Weighted matrices of the reset state
$W_u \in \mathbb{R}^{d\times 2d}$	Weighted matrices of the update state
$W_{\hat{h}} \in \mathbb{R}^{d\times 2d}$	Weighted matrices of the output state
$O \in \mathbb{R}^{d\times 2d}$	Weighted matrices of the transition function
X_k	Reactance of branch k
ζ	Trend vector in period t
η	Hyperparameter of the regularization function

11.4 Variables

B_t^{nm}	Susceptance of branch nm in period t
C	Mapped output of convolution
G_t^{nm}	Conductance of branch nm in period t
P_t^n	Active power of bus n in period t
P_t^{nm}	Active power of branch nm in period t
Q_t^n	Reactive power of bus n in period t
Q_t^{nm}	Reactive power of branch nm in period t
V_t^n	Voltage magnitude of bus n in period t
θ_t^n	Phase angle of bus n in period t
θ_t^{nm}	Phase angle difference between bus n and m in period t
Υ^i	Output of the transition function

11.5 Functions

$f(\cdot)$	Measuring function
$g(\cdot)$	Transition function
$L(\cdot)$	Cost function
$P(\cdot)$	Regularization function
σ	Active function tanh

frontiers | Frontiers in Energy Research

TYPE Original Research
PUBLISHED 22 November 2023
DOI 10.3389/fenrg.2023.1326068

OPEN ACCESS

EDITED BY
Shuai Yao,
Cardiff University, United Kingdom

REVIEWED BY
Wei Liu,
Nanjing University of Science and Technology, China
Shuxin Tian,
Shanghai University of Electric Power, China

*CORRESPONDENCE
Minjian Cao,
tycmj_scholar@163.com

RECEIVED 22 October 2023
ACCEPTED 07 November 2023
PUBLISHED 22 November 2023

CITATION
Cao M, Hu Z and Cai J (2023), Optimal scheduling of pumped storage hydropower plants with multi-type of units in day-ahead electricity market considering water head effects. *Front. Energy Res.* 11:1326068. doi: 10.3389/fenrg.2023.1326068

Optimal scheduling of pumped storage hydropower plants with multi-type of units in day-ahead electricity market considering water head effects

Minjian Cao[1]*, Zechun Hu[1] and Jilin Cai[2]

[1]Department of Electrical Engineering, Tsinghua University, Beijing, China, [2]College of Electrical Engineering and Control Science, Nanjing Tech University, Nanjing, China

Pumped-storage hydropower plant (PSHP) is a type of valuable energy storage system and a flexible resource to the modern power system with increasing renewable energy integration. As independent market participants, a PSHP can participate in both the energy market and frequency regulation market to maximize its revenue and contribution to the secure and economic operation of the power system. In some PSHPs, both fixed-speed and variable-speed units are installed to improve the flexibility, especially when operating in the pumping mode. However, it's difficult to deal with the nonlinear relationships among power, flow, and water head in pumping and generating modes. This paper proposes iterative solution methods for scheduling the PSHP by considering the relationship between power and flow at different water heads for different types of units. The scheduling problem is established as a scenario-based optimization formulation by considering PSHP's participation in both the energy market and frequency regulation market. In each iteration, the optimal dispatch model is formulated as a Mixed Integer Linear Programming (MILP) problem. Case studies are performed and simulation results validate the effectiveness of the model and the iterative solution methods.

KEYWORDS

pumped-storage hydropower plant, water head effects, scenario-based optimization, fixed-speed units, variable-speed units

1 Introduction

The large-scale development of renewable energy, such as wind and solar, is very important to achieve the targets of carbon neutrality (Outlook, 2020; Stančin et al., 2020). However, the volatile and intermittent characteristic of renewable energy generation brings great challenges to power balance of power systems (Cai et al., 2019). Energy storage systems, especially pumped storage hydropower plants (PSHP), will play a key role in the future power systems with very high penetration of renewable power generation.

Currently, pumped-storage hydropower units can be divided into fixed-speed units and variable-speed units. Compared to variable-speed units, fixed-speed units are mature and used in most pumped storage hydropower plants worldwide (Yang and Yang, 2019; Vasudevan et al., 2021). Meanwhile, with the development of AC excitation technology, power can be adjusted for variable speed units in pumping mode. In addition, variable-speed units can generate a lower percentage of the rated power in comparison to fixed-speed units,

which means that variable-speed units have a stronger power regulation capability to cope with future large-scale renewable energy output fluctuations and renewable energy consumption.

In the US and some regions in Europe, PSHPs can participate in the local electricity market as independent players. The PSHPs can pump water to store energy when the electricity tariff is low, while generating to get profits during periods with high electricity price (Kim et al., 2021; Liu et al., 2021). Therefore, the PSHP declares its generating and pumping curve in the day-ahead market according to the forecast electricity price and receives the revenue as a price-taker. In Emmanuel and Denholm (2022), a modified price-taker model with a market feedback function is established to simulate the impact of increased storage including PSHP. A market participation strategy and schedule for a PSHP with hydraulic short-circuit technology are proposed using a price-taker model presented in Kwon et al. (2021). However, with the development of pumped storage unit technology and the improvement of the electricity market, pumped storage power plants can participate not only in the energy market, but also in the regulation and reserve market (Chazarra et al., 2017). In Chazarra et al. (2017), a scheduling model is established for a closed-loop PSHP participating in both the energy and secondary regulation market. Besides, using variable-speed units also makes it possible to get profits from the regulation market, when units operate in pumping mode (Rayati et al., 2022). By establishing an accurate model for PSHPs, PSHPs can be dispatched effectively, contributing to improving the overall benefits of PSHPs.

In the previous research, studies related to the optimal scheduling of PSHPs were mostly based on the constant head model, which means PSHPs were considered to maintain a constant head in operation. With this assumption, power shows a linear relationship with the flow in pumping and generating modes. In Bruninx et al. (2015); Moradi et al. (2017); Li et al. (2018); Abdelshafy et al. (2020); He et al. (2020), different coefficients are used to describe the linear relationship between the power and flow in pumping mode and generating mode. The pumping and generating constraints with corresponding coefficients are included in the optimization model. In fact, many PSHPs are head-sensitive plants, meaning the actual pumping and generating power of the pumped storage units is influenced by the combination of the head and flow. In order to dispatch PSHPs more effectively, it is necessary to establish an optimal dispatch model for PSHPs reflecting the nonlinear relationship of "power-flow-water head" for both fixed-speed and variable-speed units in pumping and generating modes.

Some researchers proposed linearized methods to accurately demonstrate the relationship between the flow and power under different hydraulic heads (Su et al., 2019; Toubeau et al., 2019; Wang et al., 2021; Yuan et al., 2021). In Toubeau et al. (2019), nonlinear pump/turbine head-dependent curves are modeled and linearized to decrease the endogenous uncertainties in the models. In Su et al. (2019); Wang et al. (2021), the MILP formulation is used to model the hydropower plants, which can give an approximate model to demonstrate the model of plants with nonlinear and non-convex features. However, it takes a long time or cannot get the optimal solution, when the PSHP contains multiple units or too many linearized constraints with a large number of binary variables included in the model to give a better approximation. Besides, the different operating characteristics of variable-speed and fixed-speed units make it difficult to optimize the scheduling of pumped storage power plants with multi-type of units.

Two major contributions have been made in this paper. One of the contributions is to propose an optimal day-ahead dispatch method for a PSHP containing multi-type of units considering the effect of hydraulic heads. The optimization objective is to maximize the revenue of PSHPs in the energy market and the regulation market. Nonlinear characteristics among the "power-flow-water head" of fixed-speed and variable-speed units are considered to establish a more realistic model for the PSHP. The other contribution is to propose an iterative method for solving the optimal scheduling model of the PSHP considering the influence of hydraulic effects. A heuristic-based acceleration method is proposed to improve the effectiveness of the computational results. The proposed method significantly shortens the solution time compared to directly solving complicated linearized models and gives a better approximation solution for the model. Therefore, it is more practical for the proposed algorithm to be used in engineering.

The remaining of this paper is organized as follows. Section 2 establishes the day-ahead dispatch model to maximize the revenues for the PSHP in the energy market and regulation market. Section 3 introduces the mathematical formulation of the fixed-speed and variable-speed units in both pumping and generating states. Section 4 describes the iteration strategy for optimal scheduling. Several cases are conducted in Section 5 to validate the correctness and effectiveness of the method of the proposed methods. Finally, conclusions are drawn in Section 6.

2 Basic day-ahead dispatch model for a PSHP containing multi-type units

In contrast to a fixed-speed unit, the pumping power of a variable-speed unit can be changed in the pumping mode. Therefore, a PSHP containing multi-type of units can participate in energy and frequency regulation with higher flexibility. By optimizing the generating and pumping power of units, it is possible for the PSHP's operator to get more revenue by fully making use of the multiple units. Considering the participation of PSHP in both energy and frequency regulation markets, we construct the basic day-ahead self-scheduling model for a PSHP to maximize the expected total revenue in this section.

In the model, the PSHP is regarded as a price-taker of the electricity markets, and the uncertainties of demand for frequency regulation are also considered. The nonlinear characteristics of "power-flow-water head" for the fixed-speed and variable-speed units in the PSHP are modeled and elaborated in the next section.

2.1 Objective function

The objective function includes the revenues of PSHP trading in energy market R^e and the regulation market R^r, as well as the startup/shutdown cost of the pump C^{PH}.

$$\max \quad \sum_{t} \sum_{\omega \in \Omega} \alpha_{\omega} \left(R^{e}_{\omega,t} + R^{r}_{\omega,t} \right) - C^{PH}_{t} \tag{1}$$

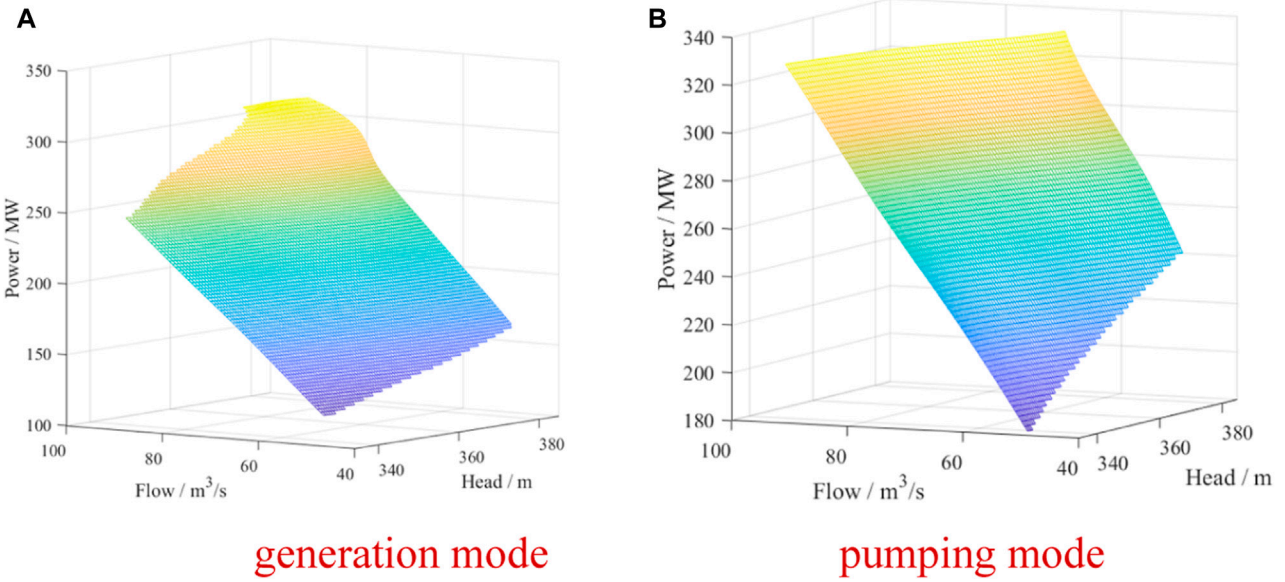

FIGURE 1
Nonlinear relationship among water head, flow and power for a variable-speed unit. **(A)** generation mode, **(B)** pumping mode.

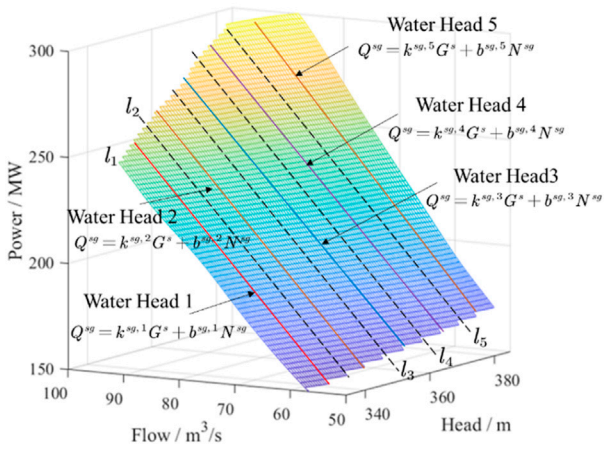

FIGURE 2
Typical water heads and the corresponding function for fixed-speed units in generating mode.

$$R^{e}_{\omega,t} = \left(G^{se}_{\omega,t} + G^{ve}_{\omega,t} - P^{se}_{t} - P^{ve}_{\omega,t}\right)\Delta t \cdot \lambda^{e}_{t} \tag{2}$$

$$R^{r}_{\omega,t} = \left(G^{sr}_{\omega,t} + G^{vr}_{\omega,t} + P^{vr}_{\omega,t}\right) \cdot \left(\lambda^{rp}_{t} + m\lambda^{re}_{t}\right)\Delta t \tag{3}$$

$$C^{PH}_{t} = C^{su}N^{su}_{t} + C^{sd}N^{sd}_{t} + C^{vu}N^{vu}_{t} + C^{vd}N^{vd}_{t} \tag{4}$$

Eq. 2 represents the revenues of PSHP with fixed-speed and variable units in the energy market. Eq. 3 depicts the revenues of the PSHP from the regulation market. The payment of regulation services consists of a capacity payment and a performance-based payment. The former payment indicates the opportunity costs of enabled capacities, while the latter reflects the contribution to the frequency regulation. As uncertainties exist in the Automatic Generation Control (AGC) signal, a scenario-based optimization objective function is established to consider the uncertainty of the AGC signals. Eq. 4 shows the total startup and shutdown cost of the PSHP at time *t*.

2.2 Constraints

$$N^{sp}_{t+1} = N^{sp}_{t} + N^{su}_{t} - N^{sd}_{t} \tag{5}$$

$$N^{vp}_{t+1} = N^{vp}_{t} + N^{vu}_{t} - N^{vd}_{t} \tag{6}$$

$$N^{sp}_{t}, N^{su}_{t}, N^{sd}_{t}, N^{vp}_{t}, N^{vu}_{t}, N^{vd}_{t} \geq 0 \tag{7}$$

$$\sum_{t} N^{su}_{t}(k) + N^{sd}_{t}(k) \leq A \cdot N_{s} \tag{8}$$

$$\sum_{t} N^{vu}_{t}(k) + N^{vd}_{t}(k) \leq A \cdot N_{v} \tag{9}$$

$$0 \leq P^{state}_{t} + G^{state}_{t} \leq 1 \tag{10}$$

$$0 \leq N^{sg}_{t} \leq N_{s}G^{state}_{t} \tag{11}$$

$$0 \leq N^{sp}_{t} \leq N_{s}P^{state}_{t} \tag{12}$$

$$0 \leq N^{vg}_{t} \leq N_{v}G^{state}_{t} \tag{13}$$

$$0 \leq N^{vp}_{t} \leq N_{v}P^{state}_{t} \tag{14}$$

$$0 \leq N^{sg}_{t} \leq N_{s} - N^{sp}_{t-1} \tag{15}$$

$$0 \leq N^{vg}_{t} \leq N_{v} - N^{vp}_{t-1} \tag{16}$$

Constraints (5–7) show the number of units in the pump state in operation. Constraints (8, 9) limit the number of times that units can switch between the pump state and the generation state. Constraint (10) guarantees that the PSHP cannot pump and generate at the same time. The number of units in operation should be less than the total number of units by constraints (11–14). Besides, units are not

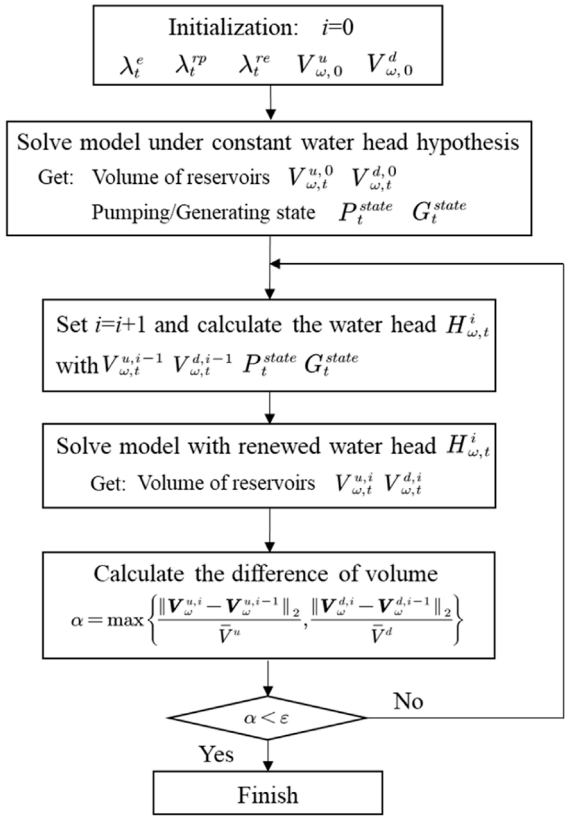

FIGURE 3
Flowchart of the iteration method.

allowed to change from pump state to generation state between adjacent dispatch periods according to constraints (15–16).

$$P_t^{se} = N_t^{sp} \cdot \bar{P}^{sp} \tag{17}$$

$$G_{\omega,t}^{s,\exp} = G_{\omega,t}^{se} + s_{\omega,t}^{up/dw} G_{\omega,t}^{sr} \tag{18}$$

$$0 \le G_{\omega,t}^{sr} \le \bar{G}_{\omega,t}^{sg} - G_t^{se} \tag{19}$$

$$0 \le G_{\omega,t}^{sr} \le G_{\omega,t}^{se} - \underline{G}_{\omega,t}^{sg} \tag{20}$$

$$G_{\omega,t}^{v,\exp} = G_{\omega,t}^{ve} + s_{\omega,t}^{up/dw} G_{\omega,t}^{vr} \tag{21}$$

$$0 \le G_{\omega,t}^{vr} \le \bar{G}_{\omega,t}^{vg} - G_{\omega,t}^{ve} \tag{22}$$

$$0 \le G_{\omega,t}^{vr} \le G_{\omega,t}^{ve} - \underline{G}_{\omega,t}^{vg} \tag{23}$$

$$P_{\omega,t}^{v,\exp} = P_{\omega,t}^{ve} - s_{\omega,t}^{up/dw} P_{\omega,t}^{vr} \tag{24}$$

$$0 \le P_{\omega,t}^{vr} \le \bar{P}_{\omega,t}^{vp} - P_{\omega,t}^{ve} \tag{25}$$

$$0 \le P_{\omega,t}^{vr} \le P_{\omega,t}^{ve} - \underline{P}_{\omega,t}^{vp} \tag{26}$$

Constraints (17–26) show the pumping and generating power constraints for fixed-speed and variable-speed units in the PSHP. The pumping and generating power for each unit should be within the feasible operating region. As the PSHP participates in the regulation market, the expected pump and generation power is limited by constraints (18, 21, 24). The operating power is the sum of the pump and generation power participating in the day-ahead market and the actual power participating in the regulation market.

$$V_{\omega,t}^u = V_{\omega,t-1}^u - Q_{\omega,t}^g \cdot \Delta t + Q_{\omega,t}^p \cdot \Delta t \tag{30}$$

$$V_{\omega,t}^d = V_{\omega,t-1}^d + Q_{\omega,t}^g \cdot \Delta t - Q_{\omega,t}^p \cdot \Delta t \tag{31}$$

$$\bar{V}^u \ge V_t^u \ge \underline{V}^u \tag{32}$$

$$\bar{V}^d \ge V_t^d \ge \underline{V}^d \tag{33}$$

$$\Delta V_{\max} \ge V_{T_{all}}^u - V_0^u \ge -\Delta V_{\max} \tag{34}$$

The volume constraints of the upper and the lower reservoirs are shown in constraints (30–34). Constraints (30, 31) represent the volume balance of the PSHP between dispatch periods. In operation, the amount of water stored in the reservoir should not exceed the reservoir capacity. Besides, the daily volume change should be limited by constraint (34) to guarantee the reservoir's starting volume of the next day.

3 An improved model for the nonlinear "power-flow-water head" characteristics of PSHP

In Section 2, a general day-ahead scheduling model is established for PSHP. However, the model does not include detailed constraints to describe the relationship between the water flow and the power for the fixed-speed and variable-speed units. In this section, an improved mathematical model for the units are established considering the nonlinear relationship among power, flow, and water head.

3.1 Overview of the traditional constant water head (CWH) model

This is the most commonly used model in the previous studies, but it has an obvious error as the hydraulic effects on the power and flow are not considered. Under the constant water head hypothesis, the power is approximately proportional to the flow.

$$Q_{\omega,t}^g = \frac{1}{\eta_g \cdot \rho_0 \cdot g \cdot h_0} \left(G_{\omega,t}^{s,\exp} + G_{\omega,t}^{v,\exp}\right) \tag{35}$$

$$Q_{\omega,t}^p = \frac{\eta_p}{\rho_0 \cdot g \cdot h_0} \left(P_t^{se} + P_{\omega,t}^{v,\exp}\right) \tag{36}$$

Equations (35) and (36) indicate the linear relationship between the water flow and the generating/pumping power of the PSHP. The water head is assumed to maintain as h_0 in operation. However, the water head varies with the volume of the reservoirs, leading to the inaccuracy of the model.

3.2 An improved linearized model based on a cluster of typical water heads (ACTWH)

In operation, the variation of the water head influences the flow and the pumping/generating power. Usually, the detailed parameters can be obtained through experiments before the unit is put into operation.

Figure 1 shows the nonlinear relationship among water head, flow, and power for a variable-speed unit in generating/pumping

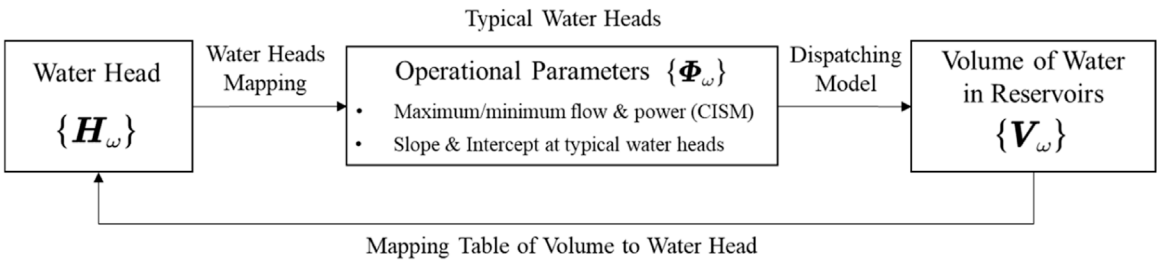

FIGURE 4
Iterative searching process for the optimal dispatch results.

mode, separately. In order to maintain the operating life of the unit up to the design life, there are restrictions on the operating zone of the unit in generating/pumping modes. Without loss of generality, this section constructs a pumping and generating model for the units considering the water head effects according to references (Wood et al., 2013; Mousavi et al., 2019; Alvarez, 2020). The data used can be found at https://pan.baidu.com/s/14QUJkkbEkAr10JZ7XhvUFA?pwd=1111. In real application, the model parameters can be replaced based on experimental data during the optimization.

For the fixed-speed units in generation mode and variable-speed units in generating/pumping mode, the power is approximately proportional to the flow at the same water head. A series of linear functions reflecting the relationship between power and flow can be established by choosing a cluster of water heads at equal distances as shown in Figure 2.

The function of the power varying with flow at any water head can be represented by the linear function at the nearest typical water heads. For example, when the water head is between l_1 and l_2 in Figure 2, the relationship between power and flow can be represented by the line named Water Head 1. Assuming that the water head is close to the jth typical water head at time k under scenario ω, the constraints for the units in generating/pumping mode can be represented by

$$Q_{\omega,t}^{sg} = k_t^{sg,j} G_{\omega,t}^{s,\exp} + b_t^{sg,j} N_{\omega,t}^{sg} \tag{37}$$

$$Q_t^{sp} = b_t^{vg,j} N_t^{sp} \tag{38}$$

$$Q_{\omega,t}^{vg} = k_t^{vg,j} G_{\omega,t}^{v,\exp} + b_t^{vg,j} N_t^{vg} \tag{39}$$

$$Q_{\omega,t}^{vp} = k_t^{vp,j} P_{\omega,t}^{v,\exp} + b_t^{vp,j} N_t^{vp} \tag{40}$$

$$\underline{Q}^{j,sg} \cdot N_t^{sg} \le Q_{\omega,t}^{sg} \le \bar{Q}^{j,sg} \cdot N_t^{sg} \tag{41}$$

$$\underline{G}^{j,sg} \cdot N_t^{sg} \le G_{\omega,t}^{sg} \le \bar{G}_i^{j,sg} \cdot N_t^{sg} \tag{42}$$

$$\underline{Q}^{j,vg} \cdot N_t^{vg} \le Q_{\omega,t}^{vg} \le \bar{Q}^{j,vg} \cdot N_t^{vg} \tag{43}$$

$$\underline{G}^{j,vg} \cdot N_t^{vg} \le G_{\omega,t}^{vg} \le \bar{G}^{j,vg} \cdot N_t^{vg} \tag{44}$$

$$\underline{Q}^{j,vp} \cdot N_t^{vp} \le Q_{\omega,t}^{vp} \le \bar{Q}^{j,vp} \cdot N_t^{vp} \tag{45}$$

$$\underline{P}^{j,vp} \cdot N_t^{vp} \le P_{\omega,t}^{vp} \le \bar{P}^{j,vp} \cdot N_t^{vp} \tag{46}$$

$$\underline{V_j}^{u} \le V_{\omega,t}^{u} \le \bar{V}_j^{u} \tag{47}$$

Equations (37)–(40) show the linearized function of flow varying with power at typical water head j in hour t under scenario ω for the fixed-speed and variable-speed units in generating/pumping mode, respectively. Constraints (41–46) demonstrate the upper and lower limits of the power and flow for fixed-speed and variable-speed units in the generation/pumping state. Constraint (47) shows the volume limits of upper reservoir.

4 Customized iterative solution method for the ACTWH based PSHP

The optimal scheduling model for a PSHP with multi-type of units is established based on the ACTWH idea in Sections 2, 3. The objective function of the model is (1), and the constraints of the model are composed of (5)-(34) and (37)-(47). In this model, the indices of the water heads at each hour in (37)-(47) are hyper-parameters, which influences the choice of the solution method.

One solution method is to reformulate the ACTWH-based model as an MILP problem by the Big M technique. In this case, the model can be directly solved by commercial solvers, and details are given in the Appendix. However, there is a dilemma when using the Big M technique based direct solution method (DSM): 1) increasing the typical water heads introduce many auxiliary binary variables and relevant constraints, which significantly increases the complexity and solution time of the model; 2) a small number of typical water heads are unable to precisely reflect the nonlinear relationship between power and flow at different water heads.

4.1 Design of the customized iterative solution method (CISM)

To relieve the bottleneck of DSM, CISM is designed in this section to shorten the solution time and improve the practicability of the ACTWH-based model for PSHPs. The procedures are detailed below and illustrated by Figure 3.

Firstly, the volume of reservoirs (i.e., $V_{\omega,t}^{u,0}$ and $V_{\omega,t}^{d,0}$) and pumping/generating state (i.e., P_t^{state} and G_t^{state}) are calculated by solving the dispatch model of PSHPs under CWH hypothesis, where the objective function is (1) and the constraints include Constraints (5)–(36). This is a simple MILP model and can be rapidly solved by commercial solvers. Set the iteration counter $i = 1$, and the iteration begins.

In the ith iteration, according to $V_{\omega,t}^{u,i-1}$, $V_{\omega,t}^{d,i-1}$, P_t^{state} and G_t^{state} obtained above, the water heads at each hour in daily operation $H_{\omega,t}^{i}$ can be renewed by referring to the design parameters of the PSHP.

TABLE 1 Total revenues of PSHP for different model.

	SMCWHH	CISM	DSM
Revenues in Energy Market (M¥)	1.17	1.15	1.78
Revenues in Regulation Market (M¥)	3.12	2.24	2.30
Startup/Shutdown Cost (M¥)	0.05	0.05	0.05
Total Profits (M¥)	4.24	3.34	4.03
Solving Time(s)	87.6	184.9	15,123

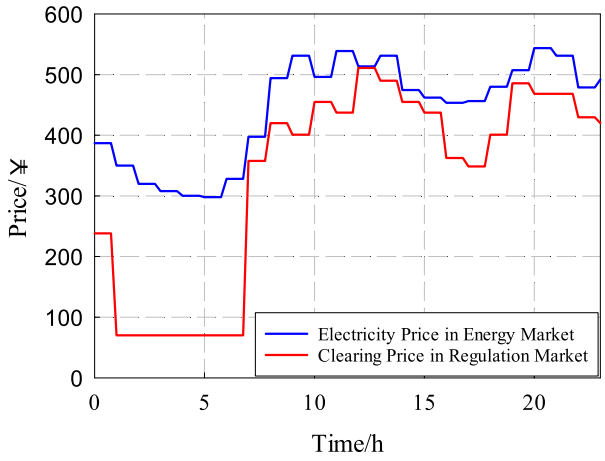

FIGURE 5
Clearing price in energy and regulation market.

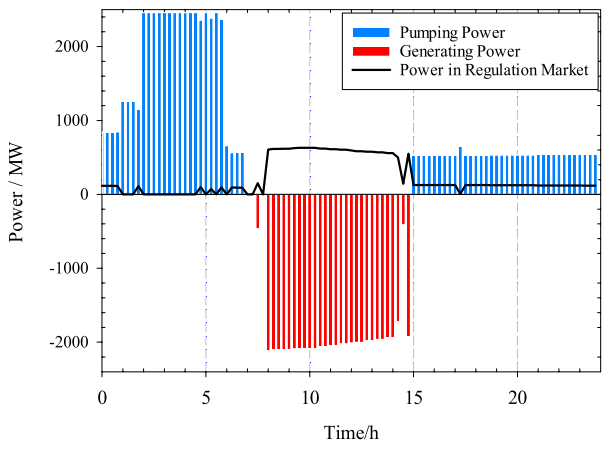

FIGURE 6
Operation results of PSHP with CISM under scenario 5.

Then the renewed water heads $H^{i}_{\omega,t}$ are introduced into the dispatch model composed of (1), (5)-(34) and (37)-(47) to uniquely determine the hyper-parameter j in constraints (37)–(47). By solving the renewed dispatch model, the updated $V^{u,i}_{\omega,t}$ and $V^{d,i}_{\omega,t}$ are obtained. The iteration continues until the relative errors of $V^{u,i}_{\omega,t}$ and $V^{d,i}_{\omega,t}$ are less than the predefined gap, otherwise run to the (i+1)-th iteration and set $i = i$+1.

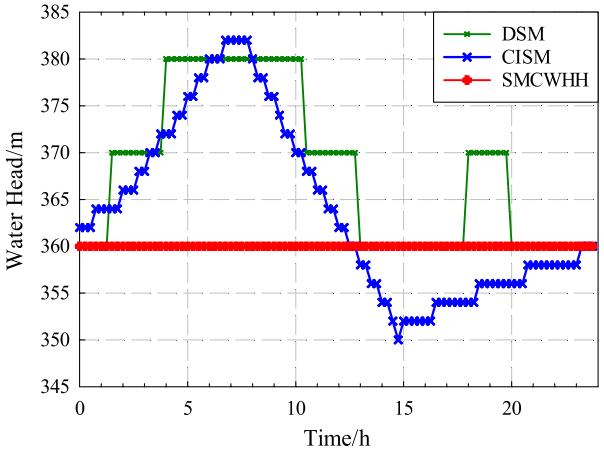

FIGURE 7
Water head profiles under scenario 5 with different solution methods.

Finally, the results of the last iteration are the optimal dispatch strategy considering the effects of the water heads.

With CISM, the renewal of water heads is decoupled with the optimization of the ACTWH-based model, and the auxiliary binary variables and constraints in DSM are all eliminated, which reduce the complexity and solution time.

4.2 Proof of CISM by deduction from the fixed-point view

The iteration of CISM can be described by the interaction between the $\boldsymbol{H}_{\omega}$, $\boldsymbol{\Phi}_{\omega}$ and $\boldsymbol{V}_{\omega}$ presented in Figure 4. Each box in Figure 4 represents some key state variables, and links between boxes stand for the corresponding decision processes formulated above, which constitute one closed directed loop.

For such interacted models, the optimal solutions should make them reach optimality simultaneously, which is not guaranteed. Hence, we adopt the fixed-point theory to analyze whether the solutions exist or not.

First, we define some mappings according to the logic in Figure 4:

- $\{\boldsymbol{\Phi}_{\omega}\} = M_{\mathrm{WH}}(\{\boldsymbol{H}_{\omega}\})$: According to the proposed ACTWH idea, with the water head $\boldsymbol{H}_{\omega}$ given, mapping M_{WH} determines the parameters of the linear function at the typical water heads, which are denoted by $\{\boldsymbol{\Phi}_{\omega}\}$. It is illustrated by Figure 2 that M_{WH} is constructed by a mapping function instead of an optimization process, so its feasibility is ensured. Besides, the mapping in Figure 2 is obviously continuous because the variation of $\{\boldsymbol{H}_{\omega}\}$ falling in the domain cannot cause step changes in $\{\boldsymbol{\Phi}_{\omega}\}$.
- $\{\boldsymbol{V}_{\omega}\} = M_{\mathrm{DM}}(\{\boldsymbol{\Phi}_{\omega}\})$: Mapping M_{DM} represents the optimal dispatch model of a PSHP participating in energy and frequency regulation markets, which is an optimal power

TABLE 2 Total revenues of PSHP with different number of variable-speed units.

	Number of variable-speed units					
	0	1	2	3	4	5
Revenue in Energy Market (M¥)	1.20	1.23	1.15	1.00	0.41	0.47
Revenue in Regulation Market (M¥)	1.65	1.87	2.24	2.58	3.37	3.50
Start-up Cost (M¥)	0.05	0.05	0.05	0.05	0.04	0.04
Total Revenue (M¥)	2.80	3.05	3.34	3.53	3.74	3.93

TABLE 3 Total revenues of PSHP in different operation mode.

	Regular mode	HSC mode
Revenue in Energy Market (M¥)	1.15	0.73
Revenue in Regulation Market (M¥)	2.24	2.99
Start-up Cost (M¥)	0.05	0.05
Total Revenue (M¥)	3.34	3.67

flow problem. M_{DM} can also be seen as continuous because: 1) $\boldsymbol{\Phi}_\omega$ is regard as constant parameters instead of optimization variables; 2) $\boldsymbol{V}_\omega$ is not composed of the dual variables of the binding constraints in the optimal dispatch model, so there are no step changes in $\boldsymbol{V}_\omega$ with respect to the variation of $\boldsymbol{\Phi}_\omega$.

- $\{\boldsymbol{H}_\omega\} = M_{VH}(\{\boldsymbol{V}_\omega\})$: Once the volumes of water in the upper and the lower reservoirs $\boldsymbol{V}_\omega$ are known, the corresponding water levels of the two reservoirs can be easily derived. The difference between the two water levels is the value of the water head $\boldsymbol{H}_\omega$, so the mapping between $\boldsymbol{V}_\omega$ and $\boldsymbol{H}_\omega$ (i.e., M_{VH}) is obviously a continuous function, whose feasibility is also ensured like M_{WH}.

Then the loop in Figure 4 can be described by mapping M_{whole} defined as follows:

$$\{\boldsymbol{H}_\omega\} = M_{whole}(\{\boldsymbol{H}_\omega\}) = M_{VH}(M_{DM}(M_{WH}(\{\boldsymbol{H}_\omega\}))) \tag{48}$$

With the water head space A defined as

$$A = \left\{\{\boldsymbol{H}_w\} \middle| \boldsymbol{H}_w{}^{min} \le \boldsymbol{H}_w \le \boldsymbol{H}_w{}^{max}\right\}, \tag{49}$$

it can be seen that M_{whole} is a self-mapping $A \to A$. Since the mappings M_{WH}, M_{DM}, and M_{VH} are continuous, composite mapping M_{whole} is also continuous.

Due to the continuity, convexity and compactness of A, the fixed point is proved to exist in A according to the Brouwer fixed point theorem (Kellogg et al., 1976), which is the solution to the interacted optimization problem shown in Figure 4. Such fixed-point problem can be commonly solved by the iterative method, which we have given in Figure 4.

5 Case studies

5.1 Simulation settings and parameters

A PSHP with 7 fixed-speed units and 2 variable-speed units is used to perform the case study, with the goal of maximizing its total revenue. The rated power of the fixed-speed units is 300 MW, while the counterpart of variable-speed units is 330 MW. The operation characteristics of the units are shown in Figure 1. Bath County PSHP is chosen to carry out the case studies, and the relationship between the volume and the water head is proportionally scaled by referring to Shisanling PSHP, China. The basic parameters of Bath County PSHP given in (Cao et al., 2021) are used.

The interval between two adjacent typical water heads is 10 m, while the counterpart for a cluster of water heads is 2 m. At each chosen water head, the power approximately shows a linear relationship to the flow. Therefore, the discretized model of the "power-flow-water head" for units can be used to optimize the operation of PSHP. The time interval is 15 min in daily operation, while the bidding power in the regulation market remains the same in an hour.

The forecast prices for energy and regulation are from (Kazempour et al., 2009). The RegA-type regulation signals of PJM market for a whole year are used to establish the energy demand for frequency regulation (Zhang et al., 2018; Cheng et al., 2023; Zhou et al., 2024). The energy demand for frequency regulation are calculated by averaging regulation signals in every 15 min, and the k-means clustering method is used to generate 10 scenarios to represent the potential frequency regulation requirements. The probability of scenarios ranges between 0.8% and 47.1%. Besides, according to historical statistical data, the average regulation mileage is 2.75 (Xia et al., 2016).

The models are solved by using GUROBI 9.1.0 solver and CVX toolbox in MATLAB environment (Grant and Boyd, 2014). Besides, numerical simulations are performed on a laptop containing an Intel Core i7-4700MQ CPU with 2.4 GHz and 16 GB of RAM.

5.2 Simulation results

The objective of the model is to maximize the profits of the PSHP with multi-type of units. According to the simulation results, the solution time of DSM is significantly longer than that of the other methods. This subsection compares the optimization results solved by three solution methods, including Solution Method under CWH Hypothesis (SMCWHH), DSM and CISM.

Table 1 shows the operational results of PSHP under different solution methods. According to the results, the PSHP can get more profits from the regulation market than the energy market. SMCWHH is the fastest solution method, and the total profit is also the largest. In fact, since the water head increases in pump

mode, more energy needs to be cost. Besides, the actual generation power declines with the decrease of water head, which further leads to a decrease in revenue. Therefore, more profit is expected to be gotten for SMCWHH, which is an error for the solution method.

Figure 5 demonstrates the clearing price in the energy and regulation market (Kazempour et al., 2009). According to Figure 5, the electricity price is low between 0:00 and 7:00. The total pumping and generating power of PSHP with CISM under scenario 5 is shown in Figure 6. The units pump when the electricity is low, while generating when the electricity is high. For the fixed-speed units, the units can only participate in the regulation market in generation mode. When the PSHP generates power, more power can participate in the regulation market to get more profits.

Figure 7 shows the water head profiles calculated by different solution methods. In daily operation, the water heads with the volume of water stored in the reservoirs. Besides, the change in water heads has an effect on the power and flow. For the constant water head model, the water heads remain the same in daily operations, causing errors to some extent. Since the relationship between power and flow at different heads can be better approximated, the model solved by CISM can give the closest solution to the actual operation.

5.3 Discussions

Sensitivity analyses are performed by setting the different number of variable-speed units in the subsection. Besides, this part also shows the change of revenue of PSHP, when the PSHP is working in the hydraulic short-circuit mode.

5.3.1 Impact of the number of variable-speed units on simulation results

Assuming the total number of units is 9 in the PSHP, Table 2 compares the effect of different variable-speed units on the profits of the PSHP by setting the number of variable-speed units from 0 to 5. According to Table 2, the revenue of the PSHP is mainly from the regulation market. As the generating power of variable-speed units can change in a wider range at the same water head compared to the fixed-speed units and its pumping power can also be changed in pumping mode, a PSHP with more variable-speed units can gain more revenue from the regulation market.

5.3.2 Impact of hydraulic short-circuit (HSC) mode for PSHP

In HSC mode, PSHP can pump and generate simultaneously. Although the efficiency of the HSC mode is less than the regular mode, the power of PSHP can be regulated within a wider range under the HSC mode. Table 3 demonstrates the operation results of PSHP in the regular and HSC mode. When the PSHP works in HSC mode, it loses 0.42 M¥ in the energy market. However, working in HSC mode also makes the PSHP gain 0.75 M¥ more in the regulation market than the PSHP working in the regular mode. According to Table 3, the PSHP can gain more profits from the regulation market in HSC mode.

6 Conclusion

This paper proposes an optimal scheduling method for the PSHP with variable-speed and fixed-speed units considering variable head effects. The objective is to maximize the profits of the PSHP by participating in the energy and regulation markets. The nonlinear relationship of power and flow for the variable-speed and fixed-speed units is established in detail by considering the water head effects. Besides, two iteration solution methods for revising the water head are proposed to optimize the operation of multi-type of units in PSHP. The numerical results show that the scheduling results are closer to the actual operation than the results under the assumption of constant water head. The iteration solution method considering a cluster of water heads can give the most practical solution with less time. Moreover, the PSHP can get more profits by installing more variable-speed units or by operating in short-circuit mode. Besides, PSHP is expected to participate in the intra-day market to further improve the flexibility of the power systems, so its two-stage dispatch model considering the water head effects is among our future work.

Data availability statement

The original contributions presented in the study are included in the article/Supplementary Material, further inquiries can be directed to the corresponding author.

Author contributions

MC: Conceptualization, Data curation, Formal Analysis, Funding acquisition, Investigation, Methodology, Project administration, Resources, Supervision, Validation, Visualization, Writing–original draft. ZH: Conceptualization, Investigation, Software, Writing–review and editing. JC: Conceptualization, Formal Analysis, Supervision, Writing–original draft, Writing–review and editing.

Funding

The author(s) declare financial support was received for the research, authorship, and/or publication of this article. This work was supported in part by the National Natural Science Foundation of China under Grant 52107105.

Conflict of interest

The authors declare that the research was conducted in the absence of any commercial or financial relationships that could be construed as a potential conflict of interest.

Publisher's note

References

Abdelshafy, A. M., Jurasz, J., Hassan, H., and Mohamed, A. M. (2020). Optimized energy management strategy for grid connected double storage (pumped storage-battery) system powered by renewable energy resources. *Energy* 192, 116615. doi:10.1016/j.energy.2019.116615

Alvarez, G. E. (2020). Operation of pumped storage hydropower plants through optimization for power systems. *Energy* 202, 117797. doi:10.1016/j.energy.2020.117797

Bruninx, K., Dvorkin, Y., Delarue, E., Pandžić, H., D'haeseleer, W., and Kirschen, D. S. (2015). Coupling pumped hydro energy storage with unit commitment. *IEEE Trans. Sustain. Energy* 7 (2), 786–796. doi:10.1109/tste.2015.2498555

Cai, J., Xu, Q., Cao, M., and Yang, B. (2019). A novel importance sampling method of power system reliability assessment considering multi-state units and correlation between wind speed and load. *Int. J. Electr. Power & Energy Syst.* 109, 217–226. doi:10.1016/j.ijepes.2019.02.019

Cao, M., Hu, Z., Meng, Y., Cai, F., and Duan, X. (2021). Day-ahead optimal dispatching strategy for flexible HVDC transmission system including pumped storage hydro plant and renewable energy generation. *Automation Electr. Power Syst.* 45 (15), 36–44. doi:10.7500/AEPS20330331010

Chazarra, M., Pérez-Díaz, J. I., and García-González, J. (2017). Optimal joint energy and secondary regulation reserve hourly scheduling of variable speed pumped storage hydropower plants. *IEEE Trans. Power Syst.* 33 (1), 103–115. doi:10.1109/tpwrs.2017.2699920

Cheng, L., Zang, H., Wei, Z., and Sun, G. (2023). Secure multi-party household load scheduling framework for real-time demand-side management. *IEEE Trans. Sustain. Energy* 14 (1), 602–612. doi:10.1109/tste.2022.3221081

Emmanuel, M. I., and Denholm, P. (2022). A market feedback framework for improved estimates of the arbitrage value of energy storage using price-taker models. *Appl. Energy* 310, 118250. doi:10.1016/j.apenergy.2021.118250

Grant, M., and Boyd, S. (2014). *CVX: matlab software for disciplined convex programming, version 2.1*.

He, J., Sun, B., Jia, Q., Xu, F., Liu, L., and Gao, B. (2020). "Research on intraday rolling optimal dispatch including pumped storage power station," in 2020 International Conference on Intelligent Computing, Automation and Systems (ICICAS), Chongqing, China, December 29-31, 2022 (IEEE), 261–265.

Kazempour, S. J., Hosseinpour, M., and Moghaddam, M. P. (2009). "Self-scheduling of a joint hydro and pumped-storage plants in energy, spinning reserve and regulation markets," in 2009 IEEE Power & Energy Society General Meeting, Calgary, Alberta, Canada, 26-30 July 2009 (IEEE), 1–8.

Kellogg, R. B., Li, T.-Y., and Yorke, J. (1976). A constructive proof of the brouwer fixed-point theorem and computational results. *SIAM J. Numer. Anal.* 13 (4), 473–483. doi:10.1137/0713041

Kim, H. J., Sioshansi, R., and Conejo, A. J. (2021). Benefits of stochastic optimization for scheduling energy storage in wholesale electricity markets. *J. Mod. Power Syst. Clean Energy* 9 (1), 181–189. doi:10.35833/mpce.2019.000238

Kwon, J., Levin, T., and Koritarov, V. (2021). "Optimal market participation of pumped storage hydropower plants considering hydraulic short-circuit operation," in 2020 52nd North American Power Symposium (NAPS), Tempe, Arizona, USA, 11-13 April 2021 (IEEE), 1–6.

Li, J., Wang, S., Liu, Y., and Fang, J. (2018). A coordinated dispatch method with pumped-storage and battery-storage for compensating the variation of wind power. *Prot. control Mod. power Syst.* 3, 1–14. doi:10.1186/s41601-017-0074-9

Liu, Y., Wu, L., Yang, Y., Chen, Y., and Bo, R. (2021). Secured reserve scheduling of pumped-storage hydropower plants in ISO day-ahead market. *IEEE Trans. Power Syst.* 36 (6), 5722–5733. doi:10.1109/tpwrs.2021.3077588

Moradi, J., Shahinzadeh, H., and Khandan, A. (2017). A cooperative dispatch model for the coordination of the wind and pumped-storage generating companies in the day-ahead electricity market. *Int. J. Renew. Energy Res.* 7 (4), 2057–2067. doi:10.20508/ijrer.v7i4

Mousavi, N., Kothapalli, G., Habibi, D., Khiadani, M., and Das, C. K. (2019). An improved mathematical model for a pumped hydro storage system considering electrical, mechanical, and hydraulic losses. *Appl. energy* 247, 228–236. doi:10.1016/j.apenergy.2019.03.015

Outlook, I. G. R. (2020). *Energy transformation 2050*. Masdar City, United Arab Emirates: International Renewable Energy Agency IRENA.

Rayati, M., Sheikhi, A., Ranjbar, A. M., and Sun, W. (2022). Optimal equilibrium selection of price-maker agents in performance-based regulation market. *J. Mod. Power Syst. Clean Energy* 10 (1), 204–212. doi:10.35833/mpce.2019.000559

Stančin, H., Mikulčić, H., Wang, X., and Duić, N. (2020). A review on alternative fuels in future energy system. *Renew. Sustain. Energy Rev.* 128, 109927. doi:10.1016/j.rser.2020.109927

Su, C., Cheng, C., Wang, P., Shen, J., and Wu, X. (2019). Optimization model for long-distance integrated transmission of wind farms and pumped-storage hydropower plants. *Appl. Energy* 242, 285–293. doi:10.1016/j.apenergy.2019.03.080

Toubeau, J., Grève, Z. D., Goderniaux, P., Vallée, F., and Bruninx, K. (2019). Chance-constrained scheduling of underground pumped hydro energy storage in presence of model uncertainties. *IEEE Trans. Sustain. Energy* 11 (3), 1516–1527. doi:10.1109/tste.2019.2929687

Vasudevan, K. R., Ramachandaramurthy, V. K., Venugopal, G., Ekanayake, J. B., and Tiong, S. K. (2021). Variable speed pumped hydro storage: a review of converters, controls and energy management strategies. *Renew. Sustain. Energy Rev.* 135, 110156. doi:10.1016/j.rser.2020.110156

Wang, S., Liu, J., Chen, H., Bo, R., and Chen, Y. (2021). Modeling state transition and head-dependent efficiency curve for pumped storage hydro in look-ahead dispatch. *IEEE Trans. Power Syst.* 36 (6), 5396–5407. doi:10.1109/tpwrs.2021.3084909

Wood, A. J., Wollenberg, B. F., and Sheble, G. B. (2013). *Power generation, operation, and control*. New Jersey, United States: John Wiley & Sons.

Xia, R., Hu, Z., Wu, L., and Liu, H. (2016). Joint operation optimization of wind-storage union with energy storage participating frequency regulation. *Power Syst. Technol.* 40 (8), 2251–2257. doi:10.13335/j.1000-3673.pst.2016.08.001

Yang, W., and Yang, J. (2019). Advantage of variable-speed pumped storage plants for mitigating wind power variations: integrated modelling and performance assessment. *Appl. Energy* 237, 720–732. doi:10.1016/j.apenergy.2018.12.090

Yuan, W., Wang, X., Su, C., Cheng, C., and Wu, Z. (2021). Stochastic optimization model for the short-term joint operation of photovoltaic power and hydropower plants based on chance-constrained programming. *Energy* 222, 119996. doi:10.1016/j.energy.2021.119996

Zhang, H., Hu, Z., Munsing, E., Moura, S. J., and Song, Y. (2018). Data-driven chance-constrained regulation capacity offering for distributed energy resources. *IEEE Trans. Smart Grid* 10 (3), 2713–2725. doi:10.1109/tsg.2018.2809046

Zhou, Y., Li, X., Han, H., Wei, Z., Zang, H., Sun, G., et al. (2024). Resilience-oriented planning of integrated electricity and heat systems: a stochastic distributionally robust optimization approach. *Appl. Energy* 353, 122053. doi:10.1016/j.apenergy.2023.122053

Appendix: Direct Soution Method (DSM) under Typical Water Head

The dispatch model based on ACTWH proposed in Section II and III can be reformulated as an MILP model as follows.

Firstly, to ensure that the water head at any hour is represented by only one typical water head, we add an equality constraint (48).

$$\sum_{j=1}^{H_c} L_{\omega,t}^{j} = 1 \tag{A1}$$

where all $L_{\omega,t}^{j}$ is an 0–1 variable, and only one of them can take 1 in hour t. If $L_{\omega,t}^{j}$ is 1, the water head in scenario ω in hour t is represented by typical water head j.

Then, with the introduction of $L_{\omega,t}^{j}$, constraints (37)–(46) can be reformulated as

$$-\mathrm{M}\left(1-L_{\omega,t}^{j}\right) \le Q_{\omega,t}^{sg} - \left(k^{sg,j}G_{\omega,t}^{sg} + b^{sg,j}N_t^{sg}\right) \le \mathrm{M}\left(1-L_{\omega,t}^{j}\right) \tag{A2}$$

$$-\mathrm{M}\left(1-L_{\omega,t}^{j}\right) + \underline{Q}^{j,sg}\cdot N_t^{sg} \le Q_{\omega,t}^{sg} \le \mathrm{M}\left(1-L_{\omega,t}^{j}\right) + \bar{Q}^{j,sg}\cdot N_t^{sg} \tag{A3}$$

$$-\mathrm{M}\left(1-L_{\omega,t}^{j}\right) + \underline{G}^{j,sg}\cdot N_t^{sg} \le G_{\omega,t}^{sg} \le \mathrm{M}\left(1-L_{\omega,t}^{j}\right) + \bar{G}_i^{j,sg}\cdot N_t^{sg} \tag{A4}$$

$$-\mathrm{M}\left(1-L_{\omega,t}^{j}\right) \le Q_{\omega,t}^{sp} - b^{sp,j}N_t^{sp} \le \mathrm{M}\left(1-L_{\omega,t}^{j}\right) \tag{A5}$$

$$-\mathrm{M}\left(1-L_{\omega,t}^{j}\right) \le Q_{\omega,t}^{vg} - \left(k^{vg,j}G_{\omega,t}^{vg} + b^{vg,j}N_t^{vg}\right) \le \mathrm{M}\left(1-L_{\omega,t}^{j}\right) \tag{A6}$$

$$-\mathrm{M}\left(1-L_{\omega,t}^{j}\right) + \underline{Q}^{j,vg}\cdot N_t^{vg} \le Q_{\omega,t}^{vg} \le \mathrm{M}\left(1-L_{\omega,t}^{j}\right) + \bar{Q}^{j,vg}\cdot N_t^{vg} \tag{A7}$$

$$-\mathrm{M}\left(1-L_{\omega,t}^{j}\right) + \underline{G}^{j,vg}\cdot N_t^{vg} \le G_{\omega,t}^{vg} \le \mathrm{M}\left(1-L_{\omega,t}^{j}\right) + \bar{G}^{j,vg}\cdot N_t^{vg} \tag{A8}$$

$$-\mathrm{M}\left(1-L_{\omega,t}^{j}\right) \le Q_{\omega,t}^{vp} - \left(k^{vp,j}P_{\omega,t}^{vp} + b^{vp,j}N_t^{vp}\right) \le \mathrm{M}\left(1-L_{\omega,t}^{j}\right) \tag{A9}$$

$$-\mathrm{M}\left(1-L_{\omega,t}^{j}\right) + \underline{Q}^{j,vp}\cdot N_t^{vp} \le Q_{\omega,t}^{vp} \le \mathrm{M}\left(1-L_{\omega,t}^{j}\right) + \bar{Q}^{j,vp}\cdot N_t^{vp} \tag{A10}$$

$$-\mathrm{M}\left(1-L_{\omega,t}^{j}\right) + \underline{P}^{j,vp}\cdot N_t^{vp} \le P_{\omega,t}^{vp} \le \mathrm{M}\left(1-L_{\omega,t}^{j}\right) + \bar{P}^{j,vp}\cdot N_t^{vp} \tag{A11}$$

where a large number M called Big M is introduced to coordinate a series of exclusive constraints at different typical water heads. When $L_{\omega,t}^{j}$ is 1, the power and flow should be limited within the allowable range at water head j, and the flow shows a linear relationship with the power. When $L_{\omega,t}^{j}$ is 0, all of the constraints are relaxed.

$$L_{\omega,t}^{j}\cdot \underline{V_j}^{u} \le V_{\omega,t}^{u,j} \le L_{\omega,t}^{j}\cdot \bar{V}_j^{u} \tag{A12}$$

$$\sum_{j=1}^{H_c} V_{\omega,t}^{u,j} = V_{\omega,t}^{u} \tag{A13}$$

Constraints (A12)-(A13) are supplementary volume constraints for the upper reservoir in operation. As the volume of reservoir is equally divided by the typical water heads, the actual volume at each moment can only be in one of these intervals. When $L_{\omega,t}^{j}$ is 1, it means the volume in scenario ω in hour t is within the range from $\underline{V_j}^{u}$ to $\bar{V}_j^{u}$. Otherwise, the volume is not within the interval.

According to the reformulation above, the model solved by the direct method is constructed as:

1) The objective function is shown as (1);
2) The constraints consist of Constraints (5)–(34) and (A1)–(A13). In theory, such an MILP problem can be directly solved by commercial solvers, which is not elaborated here.

Nomenclature

1 Set and Index

i	Index for times of iteration
j	Index for typical water head
t	Index for hour t
ω	Index for scenario
Ω	Index for set of all scenarios
sp,sg	Index for fixed-speed units in pumping/generating mode
vp,vg	Index for variable-speed units in pumping/generating mode
se,ve	Index for power in energy market for fixed-speed/variable-speed units
sr,vr	Index for power in regulation market for fixed-speed/variable-speed units
CWH	Index for the optimization model under constant water head hypothesis

2 Constant and Parameters

g	Gravitational acceleration, in m/s^2
ρ_0	Water density, in kg/m^3
α_ω	Probability of the scenario ω
A	Total startup/shutdown time of the units in a day
C^{su}, C^{sd}	Startup and shutdown cost for the fixed-speed units, in ¥
C^{vu}, C^{vd}	Startup and shutdown cost for the variable-speed units, in ¥
m	average mileage
N_s, N_v	Number of fixed-speed and variable units
$\mathbf{h_0}$	Average water head, in m
H_c	Total number of typical water heads
λ_t^e	Electricity tariff of energy market in hour t, in ¥/MWh
λ_t^{rp}	Electricity tariff of regulation capacity, in ¥/MW.
λ_t^{re}	Electricity tariff of regulation mileage, in ¥/MWh
$\bar{p}^{(\cdot)}$, $\underline{p}^{(\cdot)}$	Maximum/Minimum rated pumping power for units, in MW.
$\bar{g}^{(\cdot)}$, $\underline{g}^{(\cdot)}$	Maximum/Minimum rated generating power for units, in MW.
$\bar{p}^{(\cdot)j}$, $\underline{p}^{(\cdot)j}$	Maximum/Minimum pumping power for units at water head j, in MW.
$\bar{g}^{(\cdot)j}$, $\underline{g}^{(\cdot)j}$	Maximum/Minimum generating power for units at water head j, in MW.
$k^{(\cdot)j}$	Slope of the linear function mapping power to flow for units at water head j
$b^{(\cdot)j}$	Intercept of the linear function mapping power to flow for units at water head j
$s_t^{up/dw}$	Upward/Downward average regulation signal in hour t
Δt	Time interval
T_{all}	Total number of time intervals in a day
$\bar{V}^u$, $\underline{V}^u$	Maximum/Minimum volume of upper reservoir
$\bar{V}^d$, $\underline{V}^d$	Maximum/Minimum volume of lower reservoir
$\Delta V_{\max}$	Allowable change of the volume of the reservoir

3 Variables

P_t^{state}, G_t^{state}	Binary variables for pumping/generating state in hour t
$L_{\omega,t}^j$	Binary variables for showing water head position in scenario ω in hour t
N_t^{su}, N_t^{sd}	Number of startup/shutdown fixed-speed units
N_t^{vu}, N_t^{vd}	Number of startup/shutdown variable-speed units
$N_t^{(\cdot)}$	Number of units in operation in hour t
$P_t^{(\cdot)}$	Pumping power in hour t, in MW.
$G_t^{(\cdot)}$	Generating power in hour t, in MW.
$G_t^{s,\exp}$	Expectation value of generating power of fixed-speed units participating in electricity market in hour t, in MW
$G_t^{v,\exp}$, $P_t^{v,\exp}$	Expectation value of generating/pumping power of variable-speed units participating in electricity market in hour t, in MW
V_t^u, V_t^d	Volume of upper/lower reservoir in hour t, in m^3
$Q_t^{(\cdot)}$	Pumping/Generating flow for units in hour t, in m^3/s
$R_{\omega,t}^e$, $R_{\omega,t}^r$	Total revenues of PSHP in energy market/regulation market in scenario ω in hour t

frontiers | Frontiers in Energy Research

TYPE Original Research
PUBLISHED 29 November 2023
DOI 10.3389/fenrg.2023.1321384

OPEN ACCESS

EDITED BY
Yumin Zhang,
Shandong University of Science and Technology, China

REVIEWED BY
Zhiyi Chen,
RMIT University, Australia
Sheng Chen,
Hohai University, China
Congyue Zhang,
Southeast University, China

*CORRESPONDENCE
Ning Ji,
ningji599@163.com

RECEIVED 14 October 2023
ACCEPTED 15 November 2023
PUBLISHED 29 November 2023

CITATION
Wu Y, Ren G, Jiang B, Dai W, Ji N and Chen X (2023), Attentive multi-scale aggregation based action recognition and its application in power substation operation training.
Front. Energy Res. 11:1321384.
doi: 10.3389/fenrg.2023.1321384

Attentive multi-scale aggregation based action recognition and its application in power substation operation training

Yi Wu[1], Gang Ren[1], Bing Jiang[2], Wei Dai[3], Ning Ji[1]* and Xi Chen[1]

[1]Technican Training Center of State Grid Jiangsu Electric Power Co., Ltd., Suzhou, China, [2]College of Automation and College of Artificial Intelligence, Nanjing University of Posts and Telecommunications, Nanjing, China, [3]State Grid Jiangsu Electric Power Co., Ltd., Nanjing, China

With the rapid development of the power system and increasing demand for intelligence, substation operation training has received more attention. Action recognition is a monitoring and analysis system based on computer vision and artificial intelligence technology that can automatically identify and track personnel actions in video frames. The system accurately identifies abnormal behaviors such as illegal operations and provides real-time feedback to trainers or surveillance systems. The commonly adopted strategy for action recognition is to first extract human skeletons from videos and then recognize the skeleton sequences. Although graph convolutional networks (GCN)-based skeleton-based recognition methods have achieved impressive performance, they operate in spatial dimensions and cannot accurately describe the dependence between different time intervals in the temporal dimension. Additionally, existing methods typically handle the temporal and spatial dimensions separately, lacking effective communication between them. To address these issues, we propose a skeleton-based method that aggregates convolutional information of different scales in the time dimension to form a new scale dimension. We also introduce a space-time-scale attention module that enables effective communication and weight generation between the three dimensions for prediction. Our proposed method is validated on public datasets NTU60 and NTU120, with experimental results verifying its effectiveness. For substation operation training, we built a real-time recognition system based on our proposed method. We collected over 400 videos for evaluation, including 5 categories of actions, and achieved an accuracy of over 98%.

KEYWORDS

substation operation, skeleton-based action recognition, multi-scale aggregation, attention mechanism, spatio-temporal fusion

1 Introduction

Substations are an essential part of power systems and their safe operation is crucial to ensure the reliability of power supply. The safety awareness and standardized operation of substation operators are important factors to ensure the safe operation of substations. Therefore, incorporating artificial intelligence especial action recognition technology into substation operation training can effectively improve the safety awareness and standardized operation level of substation operators, thereby ensuring the safe operation of substations.

For example, dangerous or erroneous action of substation operators can be identified and warned.

In order to recognize action, skeleton data can first be extracted from a video sequence and then recognized. This approach has the advantage of fast processing speed and avoidance of interference from changes in background and lighting in the video.

However, action recognition based on skeleton data remains a challenging task, as it not only requires modeling the spatial domain (between joint points) but also better describing temporal features. Early studies used manually designed features to process skeleton data, but these features had limited expressive power and could not describe complex actions. In recent years, deep learning methods, especially those based on graph convolutional networks (GCN), have achieved superior performance. The human skeleton can be considered a graph structure composed of joint points and natural connections between them, making skeleton data suitable for modeling in the spatial domain (between joint points). However, GCN cannot be used for time domain modeling. Existing methods for recognizing GCN-based classes typically use traditional one-dimensional convolution to describe temporal features, but due to the varying length of dependency between moments, the kernel size has a significant impact on recognition accuracy. Additionally, these methods often alternately process spatial and temporal information, resulting in insufficient interaction between the temporal and spatial dimensions and unable to fully explore the inherent connections between time and space.

To address these issues, we propose in this paper a time-domain multi-scale information aggregation method for human skeleton-based action recognition. In order to accurately capture the dependency between varying length moments, the convolution results of multiple time-domain convolutional kernels are aggregated at a new scale dimension, producing a four-dimensional tensor including time, space, feature channels, and scale. To enable the network to automatically select important features, this paper proposes a time-space-scale fusion attention mechanism that fully integrates information across different dimensions to produce a scale-sensitive attention weight to reweight the original feature tensor. The method is validated on two publicly available datasets: NTU60 and NTU120. We have deployed our method at substation operation training locations, building a real-time behavior recognition system. We collected more than 400 video sequences, including five different action categories, with an overall recognition rate of 98%.

2 Related works

Computer vision has been increasingly applied in the power system due to its ability to analyze large amounts of data and detect anomalies. By analyzing video footage or sensor data, computer vision algorithms can identify potential issues in the power grid such as damaged equipment, broken wires, or other hazards that could lead to outages or safety concerns. For example, the system in (Chan et al., 2004) was able to conduct automatically intruder detection, fire alarm zone detection and substation meter reading in power substations. Automatic busbar detection from images can be conducted in (Chen et al., 2015). Mobile robots for electric power substation equipment's inspection was surveyed in (Allan and Beaudry, 2014; Lu et al., 2017; Dong et al., 2023). Automatic safety helmet detection for operators was achieved in (Li et al., 2017). In this paper, we focus on the actions of substation operators and develop algorithms to automatically identify their actions, providing a basis for subsequent analysis of the standardization and safety of their actions.

For skeleton-based action recognition, early methods employed manually designed features (Vemulapalli et al., 2014; Weng et al., 2017), with limited generalization ability and unable to extend to recognizing various complex actions. With the development of deep learning, methods based on recurrent neural networks (RNN), specifically long short-term memory networks (LSTM) were proposed to model the time domain (Du et al., 2015; Liu et al., 2016; Zhang et al., 2017). With the introduction of graph convolutional networks (GCN) and their superior performance, more and more research has been conducted based on GCN.

Graph neural networks (GNNs) (Wu et al., 2020) can handle graph data with arbitrary topology, and have been extensively studied in recent years. In these studies, graph convolutional networks (GCNs) were first introduced as the first-order approximation of local spectral convolutions (Kipf and Welling, 2016), due to their simple mean neighborhood aggregator, they are widely used for processing various graph data, including human skeleton data. However, existing methods for skeleton-based action recognition based on GCNs (Yan et al., 2018; Li et al., 2019; Cheng et al., 2020; Shi et al., 2020) tend to focus on improving the information processing in the spatial domain, while using a single one-dimensional convolution with a fixed receptive field in the temporal domain. This makes the network unable to model complex temporal dependencies and separate the time and spatial domains, resulting in limited exchange of information between them. To address these issues, this paper proposes a multi-scale time-domain information fusion network that effectively models complex relationships in the temporal domain, and a time-space-channel-scale fusion mechanism that fully communicates the four different data dimensions.

3 Proposed method

3.1 Method overview

The overall framework of the proposed method is shown in Figure 1. After three-dimensional (or two-dimensional) skeleton data goes through a series of spatial-temporal processing units, it passes through fully connected layers and obtains classification results by using the softmax function. Each spatial-temporal processing unit consists of two parts: a spatial processing unit and a temporal processing unit. The spatial processing unit is conducted by adaptive graph convolution (AGCN), while the temporal processing unit is the core of our method, which consists of multi-scale convolutional aggregation and space-time-scale fusion attention mechanism (STSA). In this method, the number of spatial-temporal processing units is set to 10.

3.2 Multi-scale aggregation

To overcome the problem of single receptive field in temporal convolution and difficulty in describing complex temporal

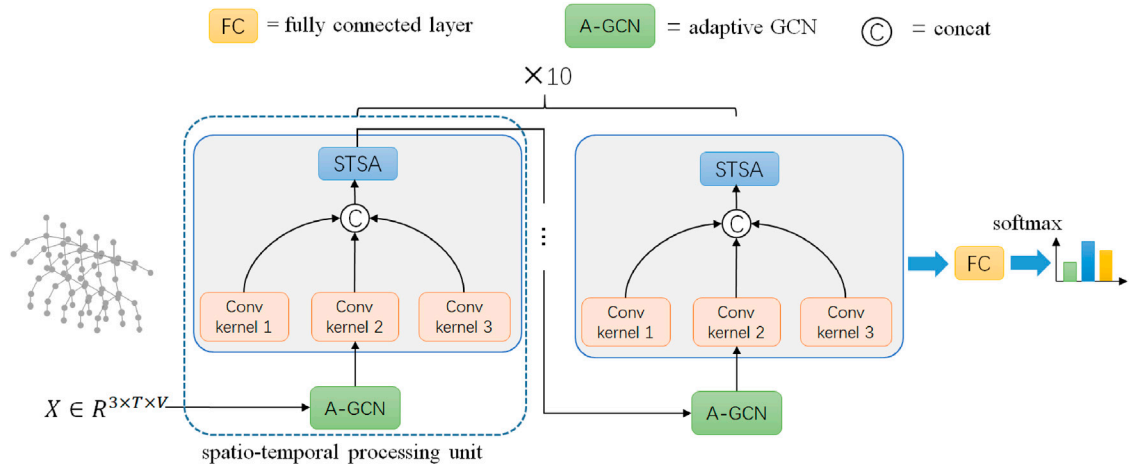

FIGURE 1
Overall architecture of the proposed method.

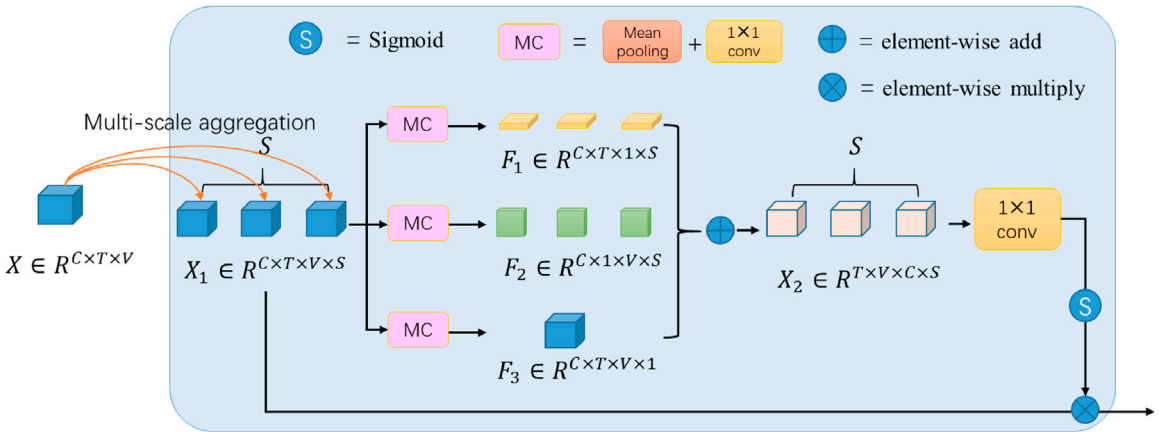

FIGURE 2
Diagram of space-time-scale fusion attention.

TABLE 1 Performance evaluation on NTU RGB + D dataset compared with other methods.

Method (year)	Cross-sub (%)	Cross-view (%)
ST-GCN (Yan et al., 2018)	81.5	88.3
2s-AGCN (Shi et al., 2019)	88.5	95.1
Dynamic-GCN (Ye et al., 2020)	91.5	96.0
Adaptive-ST-GCN (Chen et al., 2021a)	91.5	96.0
MSTGCN (Chen et al., 2021b)	91.5	96.6
EfficientGCN-B4 (Song et al., 2022)	90.8	**96.7**
GSTLN (Dai et al., 2023)	91.9	96.6
Proposed	**92.1**	96.5

The bold values are the maximum values.

TABLE 2 Performance evaluation on NTU RGB + D 120 dataset compared with other methods.

Method (year)	Cross-sub (%)	Cross-set (%)
ST-GCN (Yan et al., 2018)	70.7	73.2
2s-AGCN (Shi et al., 2019)	82.9	84.9
Dynamic-GCN (Ye et al., 2020)	87.3	88.6
Adaptive-ST-GCN (Chen et al., 2021a)	88.4	88.3
MSTGCN (Chen et al., 2021b)	87.5	88.8
EfficientGCN-B4 (Song et al., 2022)	88.7	88.9
GSTLN (Dai et al., 2023)	88.1	89.3
Proposed	**88.9**	**89.7**

The bold values are the maximum values.

TABLE 3 Results of ablation experiments.

Method	Cross-sub (%)
Kernels: 3, 5, 7	88.6
Kernels: 3, 5, 7, 9	88.7
Kernels: 5, 7, 9, 11	88.8
Kernels: 5, 7, 9	**88.9**
Kernels: 7, 9, 11	88.7
Kernels: 7, 9, 11	88.7
w/o STSA	88.3
Fusion time-scale	88.3
Fusion space-time	88.6
Fusion space-scale	88.5

The bold values are the maximum values.

dependencies, we propose in this paper a multi-scale convolutional aggregation method. The effectiveness of using multiple convolutional kernels to obtain different receptive fields has been validated in previous works. However, in these works, the results of multiple convolutional kernels are usually added or connected to achieve the purpose of multi-scale information aggregation. In this way, the importance of information at multiple scales is the same, making it difficult for the network to adaptively select scale information and have poor flexibility. This paper proposes to aggregate multi-scale information into a new scale dimension and then combine it with subsequent space-time-scale fusion attention mechanism to enable the network to fully fuse different dimensions of information and re-weight features based on the principle of adaptively selecting important information at time-space-scale dimensions.

Let the input features be $X \in R^{C\times T\times V}$, and after passing through S different sizes of convolutional kernels, we get S equally sized features. We aggregate them in the new scale dimension into a feature tensor: $X_1 \in R^{C\times T\times V\times S}$.

3.3 Space-time-scale fusion attention

The output tensor of the multi-scale aggregation has four dimensions: space, time, scale, and feature channel. As shown in Figure 2, we then perform feature reduction along space, time and scale dimension respectively, the reduction operation named MC module consists of a mean pooling layer (M) and a 1×1 convolution block (C). The resulted feature tensors are: $F_1 \in R^{C\times T\times 1\times S}$, $F_2 \in R^{C\times 1\times V\times S}$, and $F_3 \in R^{C\times T\times V\times 1}$, which are then expanded to $C \times T \times V \times S$ respectively and added as $X_2 \in R^{C\times T\times V\times S}$. This process can be written as:

$$X_2 = R_V(F_1) + R_T(F_2) + R_S(F_3)$$

in which

$$F_1 = MC_V(X)$$
$$F_2 = MC_T(X)$$
$$F_3 = MC_S(X)$$

where $MC(.)$ the MC module, $R(.)$ is the repeat operation.

After reduction along a certain dimension, the information in the remaining dimensions can be fully fused without interference from the reduced dimension. The final addition operation will further merge the fusion results of each dimension. In the implementation, replication can be completed by the automatic expansion function of the addition operation (most deep learning frameworks such as PyTorch, Tensorflow, etc., support this function).

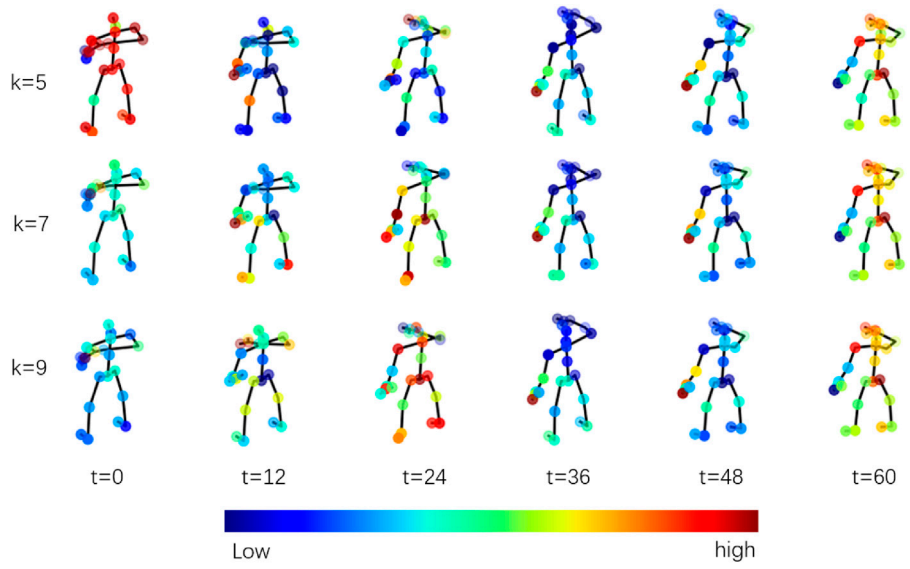

FIGURE 3
Visualization result of the learned attention by STSA.

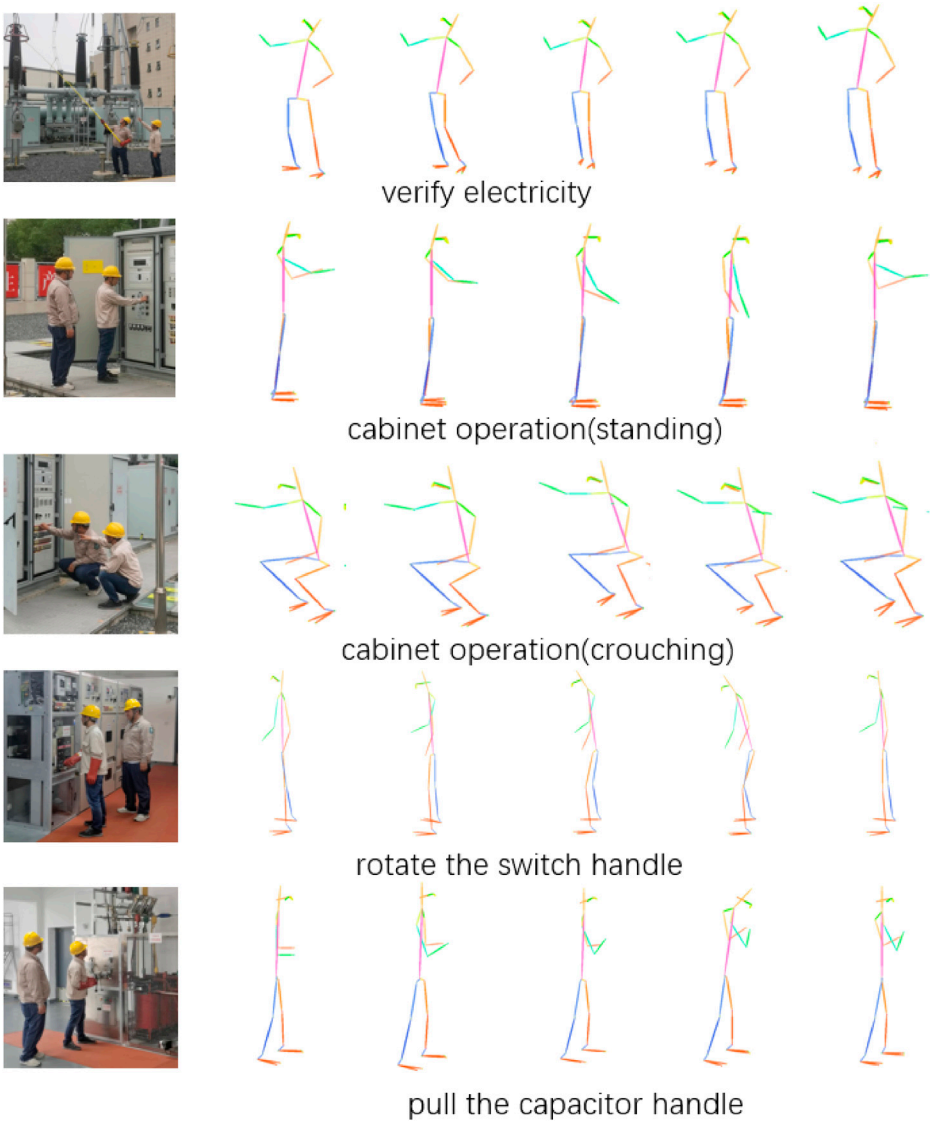

FIGURE 4
Five categories of substation operation actions.

TABLE 4 Number of samples in each action category.

Category	Num. Of samples
1. Verify electricity	86
2. Cabinet operation (standing)	92
3. Cabinet operation (crouching)	84
4. Rotate the switch handle	78
5. Pull the capacitor switch	81
Total	432

3.4 Adaptive GCN

The skeleton can be represented as a graph structure, with joint points as vertices and connections between joint points as edges. Let the set of joint feature vectors be denoted by $P = \{P_i\}_{i=1}^{V}$, where V is the number of joint points. The set of edges can be represented by an adjacency matrix A. By obtaining the adjacent points of each vertex, a neighborhood can be obtained for performing convolution operations similar to those used in image data:

$$p_i' = \sum_{p_j \in N(p_i)} p_j w_{ij}$$

Where $N(P_i)$ is the neighborhood of P_i. A linear approximation to the above convolution operator was proposed in (Kipf and Welling, 2016):

$$P' = \Lambda^{-\frac{1}{2}}(A + I)\Lambda^{-\frac{1}{2}} PW$$

Where P is the matrix of the combination of all the vertex features, and

$$\Lambda_{ij} = \sum_j \left(A_{ij} + I_{ij}\right)$$

TABLE 5 Action recognition results of the five action categories and overall results.

Category	Acc. (%) (proposed)	Acc. (%) (Chen et al., 2021a)	Acc. (%) (Yan et al., 2018)	Acc. (%) (Shi et al., 2019)
1. Verify electricity	100	100	98.1	96.2
2. Cabinet operation (standing)	97.3	94.6	92.4	89
3. Cabinet operation (crouching)	100	100	94	92
4. Rotate the switch handle	93.5	93.5	89.4	87.2
5. Pull the capacitor switch	100	94	91.8	89.8
Overall	98.3	96.5	92.9	90.9

In this paper, an adaptive topology structure similar to (Chen Y. et al., 2021) is used, where A is considered as a trainable parameter while the adjacency matrix serves as the initial values for A. This allows the network to go beyond the natural connections in topological structure and better describe the complex relationships between joint points.

4 Experiments

4.1 Evaluation on public datasets

The effectiveness of the proposed method was evaluated on two publicly available datasets: NTU-RGB + D (Shahroudy et al., 2016) and NTU-RGB + D 120 (Liu et al., 2019).

1) NTU-RGB + D: This dataset is a large-scale three-dimensional human skeleton action recognition dataset. It contains 56,880 skeleton motion clips. These actions were performed by 40 volunteers using three different perspectives of the Kinect v2 camera, categorized into 60 classes. Two common benchmarks used on this dataset are: 1) Cross-subject (cross-subject): training samples are from 20 volunteers, while testing samples are from the remaining 20 volunteers. 2) Cross-view (cross-view): training samples are from two camera perspectives, while testing data comes from a different perspective.
2) NTU RGB + D 120: This dataset is currently the largest three-dimensional human skeleton based action recognition dataset. It was created by adding an additional 57,367 skeleton motion clips to the NTU-RGB + D dataset, surpassing the number of categories to over 60. As a result, the dataset includes a total of 113,945 samples with more than 120 categories. Likewise, the newly added samples were also captured using three different perspectives of the Kinect v2 camera. Two common benchmarks used on this dataset are: 1) Cross-subject (cross-subject): training samples are from 53 volunteers, while testing samples come from the remaining 53 volunteers. 2) Cross-setup (cross-setup): training and testing samples are split based on the camera setup number.

The proposed method is implemented using the PyTorch deep learning framework, and training is completed on an RTX 3090 GPU. Stochastic gradient descent (SGD) algorithm with a learning rate of 0.1 and momentum of 0.9 is adopted as the optimizer. In all experiments, the number of training epochs is 65, with the first 5 rounds serving as warm-up to make training more stable.

As shown in Tables 1, 2, the proposed method is compared against existing methods on NTU RGB + D dataset and NTU RGB + D 120 dataset. These comparative methods are all of relatively high performance in recent years. As can be seen from Table 1, the proposed method achieved the best performance on the NTU RGB + D dataset in the Cross-sub benchmark. On the other benchmark: Cross-view, although performance is not best, it also had a small gap with the best performance. From Table 2, we can see that the proposed method achieved the best performance on two benchmarks of NTU RGB + D 120 (Cross-sub and Cross-set). These results demonstrate the effectiveness of proposed method. All the results are recognition top-1 accuracy, which is computed as the number of corrected predicted samples divided by the total number of samples.

In order to evaluate the impact of different combination of temporal convolution kernels, we conduct a series of experiments on cross-sub benchmark of NTU RGB + D 120, the evaluation results are shown in Table 3. The method with kernels of sizes 5, 7, 9 achieved the best performance. Adopting larger kernels or smaller kernels will not boost the performance. We also tried adding more convolutional kernels, but this did not lead to an improvement in performance.

In order to evaluate the role of the space-time-scale fusion attention (STSA) mechanism, we conducted an experiment with STSA removed. As shown in Table 3, the performance drops significantly, which demonstrate the effectiveness of the STSA. We also evaluate the role of different dimensions in STSA by removing one of the dimension branches. As shown in Table 3, we evaluate time-scale, space-time and space-scale fusion respectively. Among them, space-time fusion yields relatively better result, which is yet lower than space-time-scale fusion.

To visualize the content learned by our network, especially the STSA attention mechanism proposed in this paper, we present the results of the STSA attention mechanism in the first temporal-spatial processing unit in Figure 3. The example is a “drinking water” scenario. Red indicates high weights, and blue indicates low weights. The weights are normalized using the following equation:

$$w_{normalized} = \frac{w - \min}{\max - \min}$$

In terms of the scale dimension (kernel size k), we can see that at different scales, the network focuses on different contents, which means that the network has the ability to adaptively select the scale.

4.2 Application in power substation operation training

The proposed method was applied to operation training in power substation. We collected the operation videos of trainees during the training process and used body posture estimation algorithm Alphapose (Fang et al., 2022) to extract 2D skeleton data of human bodies for action recognition. The model was trained on Halpe dataset (Fang et al., 2022) which is able to extract 2D skeleton including 26 joints. In order to make the network's structure unchanged, the 2D data is treated the same way as 3D skeleton data. The action categories of trainees were divided into five types: 1) verify electricity; 2) cabinet operation (standing); 3) cabinet operation (crouching); 4) rotate the switch handle; 5) pull the capacitor switch. Examples of the five categories of actions are shown in Figure 4. The colors in Figure 4 represent different parts of human skeleton. We collected multiple videos from multiple perspectives of operators for each category. Similarly to NTU60, we resampled the skeleton data extracted from each video in time, and all the resampled skeleton data had the same dimension in time. We selected 60% of them as training samples and the remaining as testing samples. The number of samples in each action category is listed in Table 4.

The recognition system runs on a PC with Intel i9 CPU, 32 GB RAM and RTX3090 GPU. The system is able to achieve real-time recognition. For each frame, the computation time of posture estimation is 41 ms, and the computation time of action recognition is 12 ms, so the system runs at 18.9 FPS which is sufficient for most of the real-time applications.

In these five action categories, the first and third categories are relatively easy to identify, while the remaining three categories are more similar, with the main difference being hand movements. The proposed method is compared against (Yan et al., 2018; Shi et al., 2019; Chen Y. et al., 2021). The proposed method and (Chen Y. et al., 2021) achieved 100% accuracy in the first and third categories. And the other two methods (Yan et al., 2018; Shi et al., 2019) made wrong predictions in these two categories. The proposed method also achieved all correct classification results in the fifth category which outperforms other three methods. The overall recognition rate of the method in this paper exceeded 98% which outperformed (Chen Y. et al., 2021) by 1.8% (Yan et al., 2018), by 5.4% and (Shi et al., 2019) by 7.4%. See Table 5 for comparison results. From the results, we can learn that the action of "Rotate the switch handle" is most prone to misclassification. Though the proposed method achieved an accuracy of 93.5% ranking first alongside (Chen Y. et al., 2021), in our future work, we will conduct further research on this category of action.

5 Conclusion

In this paper, we propose a skeleton-based action recognition method that aggregates convolutional information of different scales in the time dimension and a space-time-scale attention module that enables effective communication and weight generation between dimensions. Our proposed method is validated on public datasets NTU60 and NTU120, with experimental results demonstrated its effectiveness. For substation operation training, we built a recognition system and collected hundreds of videos for evaluation, including 5 categories of actions, and achieved satisfactory recognition accuracy.

Data availability statement

Publicly available datasets were analyzed in this study. This data can be found here: https://rose1.ntu.edu.sg/dataset/actionRecognition/.

Ethics statement

Written informed consent was obtained from the individual(s) for the publication of any potentially identifiable images or data included in this article.

Author contributions

YW: Conceptualization, Visualization, Writing–original draft. GR: Data curation, Investigation, Methodology, Validation, Visualization, Writing–review and editing. BJ: Investigation, Validation, Writing–original draft. WD: Investigation, Methodology, Visualization, Writing–review and editing. NJ: Data curation, Formal Analysis, Investigation, Methodology, Validation, Writing–original draft. XC: Data curation, Formal Analysis, Methodology, Resources, Visualization, Writing–review and editing.

Funding

The author(s) declare financial support was received for the research, authorship, and/or publication of this article. This research is funded by the Science and Technology Project of State Grid Jiangsu Electric Power Company, grant number J2021215.

Acknowledgments

The authors would like to thank the editors and reviewers for improving this paper.

Conflict of interest

Authors YW, GR, NJ, and XC were employed by Technican Training Center of State Grid Jiangsu Electric Power Co., Ltd. Author WD was employed by State Grid Jiangsu Electric Power Co., Ltd.

The remaining author declares that the research was conducted in the absence of any commercial or financial relationships that could be construed as a potential conflict of interest.

The authors declare that this study received funding from State Grid Jiangsu Electric Power Company. The funder had the following involvement in the study: design, collection, analysis, interpretation of data, the writing of this article and the decision to submit it for publication.

Publisher's note

References

Allan, J. F., and Beaudry, J. (2014). "Robotic systems applied to power substations-a state-of-the-art survey," in Proceedings of the 2014 International Conference on Applied Robotics for the Power Industry (CARPI), Foz do Iguassu, Brazil, October 2014 (IEEE), 1–6. doi:10.1109/CARPI.2014.7030049

Chan, W. L., Leo, P. S. L., and Ma, C. F. (2004). "Computer vision applications in power substations," in Proceedings of the 2004 International Conference on Electric Utility Deregulation, Restructuring and Power Technologies (DRPT), Hong Kong, China, April 2004 (IEEE), 383–388. doi:10.1109/DRPT.2004.1338526

Chen, H., Sun, S., Wang, T., Zhao, X., and Tan, M. (2015). "Automatic busbar detection in substation: using directional Gaussian filter, gradient density, Hough transform and adaptive dynamic K-means clustering," in Proceedings of 2015 Chinese Control Conference (CCC), Qing Dao, China, July 2015 (IEEE), 4668–4672. doi:10.1109/ChiCC.2015.7260360

Chen, Y., Zhang, Z., Yuan, C., Li, B., Deng, Y., and Hu, W. (2021a). "Channel-wise topology refinement graph convolution for skeleton-based action recognition," in Proceedings of the 2021 international conference on computer vision (ICCV), Montreal, QC, Canada, October 2021 (IEEE), 13359–13368. doi:10.1109/iccv48922.2021.01311

Chen, Z., Li, S., Yang, B., Li, Q., and Liu, H. (2021b). Multi-scale spatial temporal graph convolutional network for skeleton-based action recognition. *Proc. 2021 Conf. Artif. Intell. (AAAI)* 35 (2), 1113–1122. doi:10.1609/aaai.v35i2.16197

Cheng, K., Zhang, Y., Cao, C., Shi, L., Cheng, J., and Lu, H. (2020). "Decoupling gcn with dropgraph module for skeleton-based action recognition," in Proceedings of the Computer Vision–ECCV 2020: 16th European Conference (ECCV), Berlin, Heidelberg, August 2020 (Springer), 536–553. doi:10.1007/978-3-030-58586-0_32

Dai, M., Sun, Z., Wang, T., Fen, J., and Jia, K. (2023). Global spatio-temporal synergistic topology learning for skeleton-based action recognition. *Pattern Recognit.* 140, 109540. doi:10.1016/j.patcog.2023.109540

Dong, L., Chen, N., Liang, J., Li, L., Yan, Z., and Zhang, B. (2023). "A review of indoor-orbital electrical inspection robots in substations. *Industrial Robot Int. J. robotics Res. Appl.* 50 (2), 337–352. doi:10.1108/IR-06-2022-0162

Du, Y., Wang, W., and Wang, L. (2015). "Hierarchical recurrent neural network for skeleton based action recognition," in Proceedings of the 2015 conference on computer vision and pattern recognition (CVPR), Boston, USA, June 2015 (IEEE), 1110–1118. doi:10.1109/cvpr.2015.7298714

Fang, H. S., Li, J., Tang, H., Xu, C., Zhu, H., Xiu, Y., et al. (2022). Alphapose: whole-body regional multi-person pose estimation and tracking in real-time. *IEEE Trans. Pattern Analysis Mach. Intell.* 2022, 7157–7173. doi:10.1109/tpami.2022.3222784

Kipf, T. N., and Welling, M. (2016). Semi-supervised classification with graph convolutional networks. Available at: https://arxiv.org/abs/1609.02907.

Li, J., Liu, H., Wang, T., Jiang, M., Li, K., and Zhao, X. (2017). "Safety helmet wearing detection based on image processing and machine learning," in Proceedings of the 2017 international conference on advanced computational intelligence (ICACI), Doha, Qatar, February 2017 (IEEE), 201–205. doi:10.1109/ICACI.2017.7974509

Li, M., Chen, S., Chen, X., Zhang, Y., Wang, Y., and Tian, Q. (2019). "Actional-structural graph convolutional networks for skeleton-based action recognition," in Proceedings of the 2019 conference on computer vision and pattern recognition (CVPR), Long Beach, USA, June 2019 (IEEE), 3595–3603. doi:10.1109/cvpr.2019.00371

Liu, J., Shahroudy, A., Perez, M., Wang, G., Duan, L., and Kot, A. C. (2019). Ntu RGB+ d 120: a large-scale benchmark for 3d human activity understanding. *IEEE Trans. pattern analysis Mach. Intell.* 42 (10), 2684–2701. doi:10.1109/tpami.2019.2916873

Liu, J., Shahroudy, A., Xu, D., and Wang, G. (2016). "Spatio-temporal lstm with trust gates for 3d human action recognition," in Proceedings of the Computer Vision–ECCV 2016: 14th European Conference (ECCV), Amsterdam, Netherlands, October 2016 (Springer), 816–833. doi:10.1007/978-3-319-46487-9_50

Lu, S., Zhang, Y., and Su, J. (2017). "Mobile robot for power substation inspection: a survey,", 830–847. doi:10.1109/JAS.2017.7510364*IEEE/CAA J. Automatica Sinica*44

Shahroudy, A., Liu, J., Ng, T. T., and Wang, G. (2016). "NTU RGB+D: a large scale dataset for 3D human activity analysis," in Proceedings of the 2016 conference on computer vision and pattern recognition (CVPR), Las Vegas, USA, June 2016 (IEEE), 1010–1019. doi:10.1109/cvpr.2016.115

Shi, L., Zhang, Y., Cheng, J., and Lu, H. (2019). "Two-stream adaptive graph convolutional networks for skeleton-based action recognition," in Proceedings of the 2019 conference on computer vision and pattern recognition (CVPR), Long Beach, USA, June 2019 (IEEE), 12026–12035. doi:10.1109/cvpr.2019.01230

Shi, L., Zhang, Y., Cheng, J., and Lu, H. (2020). Skeleton-based action recognition with multi-stream adaptive graph convolutional networks. *IEEE Trans. Image Process.* 29, 9532–9545. doi:10.1109/tip.2020.3028207

Song, Y. F., Zhang, Z., Shan, C., and Wang, L. (2022). Constructing stronger and faster baselines for skeleton-based action recognition. *IEEE Trans. pattern analysis Mach. Intell.* 45 (2), 1474–1488. doi:10.1109/tpami.2022.3157033

Vemulapalli, R., Arrate, F., and Chellappa, R. (2014). "Human action recognition by representing 3d skeletons as points in a lie group," in Proceedings of the 2014 conference on computer vision and pattern recognition (CVPR), Columbus, USA, June 2014 (IEEE), 588–595. doi:10.1109/cvpr.2014.82

Weng, J., Weng, C., and Yuan, J. (2017). "Spatio-temporal naive-bayes nearest-neighbor (st-nbnn) for skeleton-based action recognition," in Proceedings of the 2017 conference on computer vision and pattern recognition (CVPR), Hawaii, USA, July 2017 (IEEE), 4171–4180. doi:10.1109/cvpr.2017.55

Wu, Z., Pan, S., Chen, F., Long, G., Zhang, C., and Yu, P. S. (2020). A comprehensive survey on graph neural networks. *IEEE Trans. neural Netw. Learn. Syst.* 32 (1), 4–24. doi:10.1109/TNNLS.2020.2978386

Yan, S., Xiong, Y., and Lin, D. (2018). "Spatial temporal graph convolutional networks for skeleton-based action recognition," in Proceedings of the 2018 conference on artificial intelligence (AAAI), Louisiana, USA, February 2018, 7444–7452. doi:10.1609/aaai.v32i1.12328

Ye, F., Pu, S., Zhong, Q., Li, C., Xie, D., and Tang, H. (2020). "Dynamic GCN: context-enriched topology learning for skeleton-based action recognition," in Proceedings of the 2020 ACM international conference on multimedia, Seattle, USA, October 2020 (ACM), 55–63. doi:10.1145/3394171.3413941

Zhang, S., Liu, X., and Xiao, J. (2017). "On geometric features for skeleton-based action recognition using multilayer lstm networks," in Proceedings of the 2017 winter conference on applications of computer vision (WACV), California, USA, March 2017 (IEEE), 148–157. doi:10.1109/wacv.2017.24

frontiers | Frontiers in Energy Research

TYPE Original Research
PUBLISHED 29 December 2023
DOI 10.3389/fenrg.2023.1335184

OPEN ACCESS

EDITED BY
Rufeng Zhang,
Northeast Electric Power University, China

REVIEWED BY
Junjun Xu,
Nanjing University of Posts and Telecommunications, China
Peishuai Li,
Nanjing University of Science and Technology, China
Pudong Ge,
Imperial College London, United Kingdom

*CORRESPONDENCE
Xiaolong Xiao,
xiaoxiaolong@seu.edu.cn

RECEIVED 08 November 2023
ACCEPTED 13 December 2023
PUBLISHED 29 December 2023

CITATION
Xiao X, Guo J, Yang J, Fang X, Shi M, Liu Y, Guo M, Yang Z and Wu Z (2023), A novel switchgear state assessment framework based on improved fuzzy C-means clustering method with deep belief network.
Front. Energy Res. 11:1335184.
doi: 10.3389/fenrg.2023.1335184

A novel switchgear state assessment framework based on improved fuzzy C-means clustering method with deep belief network

Xiaolong Xiao[1,2]*, Jiahao Guo[1], Jinggang Yang[1,2], Xing Fang[1], Mingming Shi[1], Yang Liu[3], Maosen Guo[2], Zhencheng Yang[2] and Zaijun Wu[2]

[1]State Grid Jiangsu Electric Power Company Research Institute, Nanjing, China, [2]School of Electrical Engineering, Southeast University, Nanjing, China, [3]State Grid Jiangsu Electric Power Company, Nanjing, China

Due to the problems such as fuzzy state assessment grading boundaries, the recognition accuracy is low when using traditional fuzzy techniques to grade the switchgear state. To address this problem, this paper proposes a switchgear state assessment and grading method based on deep belief network (DBN) and improved fuzzy C-means clustering (IFCM). Firstly, the switchgear state information data are processed by normalization method; then the feature parameters are extracted from the switchgear state information data by using DBN, and finally the extracted feature parameters are categorised according to the condition of switchgear equipment through clustering using IFCM. The experimental results show that the accuracy of the method in assessing the switchgear state under small sample conditions reaches 94, which exceeds the accuracy of other switchgear state assessment grading methods currently in use.

KEYWORDS

deep belief networks, partial discharge, improved fuzzy c-means clustering, multisource data fusion, switchgear state assessment

1 Introduction

Switchgear is a critical component in power systems, playing a vital role in the control, protection, and other aspects of line operations. Safe and dependable operation of the power system is dependent on operational condition of switchgear. (Subramaniam et al., 2021; Montanari et al., 2022). The current periodic maintenance approach involves blind inspection and maintenance without knowing the operational status of the switchgear, often leading to the wastage of maintenance resources. Online monitoring and status evaluation of the switchgear are significant for ensuring its normal operation, reducing maintenance frequency, and further bolstering the dependability of the power grid. (Zhong et al., 2015; Wang et al., 2017).

At present, the status assessment of switchgear primarily relies on signals detected from partial discharges, temperature, humidity, voltage, current, etc. Among them, the analysis of partial discharge signals has become a crucial basis for switchgear status assessment (Yumbe et al., 2013; Janssen et al., 2014). Based on this, scholars from both China and abroad have

successively proposed classic switchgear status assessment methods such as the Key Gas Method (KGM) (Razi-Kazemi and Niayesh, 2021), IEC Ratio Method (IRM) (Zhou et al., 2023), and Duval Triangle Method (DTM) (Liang et al., 2009). However, these methods are based on knowledge accumulated over a long period and have inherent limitations, making it difficult to guarantee the accuracy of status assessment. As machine learning continues to advance, intelligent techniques such as the Support Vector Machine (SVM) (Zhong et al., 2018), Bayesian Networks (Ding et al., 2014), and Extreme Learning Machine (ELM) (Chang et al., 2013) have been widely applied to switchgear status assessment and have achieved certain diagnostic effects. However, they also have some shortcomings. SVM performs admirably when applied to problems involving small samples; however, its nature restricts it to binary classification, rendering it suboptimal when applied to complex problems involving multiple classes and data, such as switchgear status assessment. (Kim et al., 2019). Bayesian Networks require the satisfaction of many conditional attributes for use, which is not conducive to practical engineering applications (Chen et al., 2020). ELM has fast training speed, but its robustness is poor (Faiz and Soleimani, 2017; Fang et al., 2023), which cannot meet the requirements for long-term stable diagnosis. In addition, the multi-source data collected on-site often lack data labels, restricting the further development of the above methods in switchgear status assessment.

Given these issues, some unsupervised learning methods have been introduced into switchgear status assessment, such as Fuzzy C-means Clustering (FCM) (Dai et al., 2017; Qiu et al., 2022), which can effectively classify unlabeled samples and provide a good interpretation of DGA data (Dehghani et al., 2020). However, due to the presence of local minima in its membership function, the diagnostic accuracy of this method is affected. In order to tackle this issue, LI Enwen and others introduced a method for evaluating the status of switchgear that utilises Improved Fuzzy C-means Clustering (IFCM). (Wang et al., 2015; de Assis et al., 2019), which expand the conventional membership function by incorporating an exponential form. This method effectively solved the local minima problem present in the traditional membership function, resulting in further improvements in diagnostic accuracy compared to FCM. However, this method has difficulties in ensuring the proportion of low-level signals in the distance calculation, affecting the further improvement of diagnostic accuracy (Hinow and Mevissen, 2011). Additionally, both FCM and IFCM base their classifications on the similarity between fault data, without uncovering the differences between different fault types, making it difficult for their diagnostic results to fulfil the requirements of operational engineering applications.

To address the above issues, this paper proposes a switchgear status assessment method based on Deep Belief Network (DBN) and Improved Fuzzy C-means Clustering (DBN-IFCM). By leveraging the DBN's ability to extract abstract features from data, this method performs feature extraction on the original fault data. While ensuring the retention of important information from each feature, it avoids the loss of small signal features during direct distance calculation. Additionally, the features extracted are more representative of the essence of each fault than the original data. Using these feature data in place of the original data for clustering further improves the accuracy of switchgear status assessment. By establishing Cluster Validity Indicators (CVI) based on a weighted ensemble, which assess the validity of the clustering results, the proposed evaluation method is ultimately validated using actual detection data from a switchgear. By conducting a comparative analysis of the clustering outcomes produced by various algorithms, the evaluation method's superiority is confirmed.

2 Improved fuzzy c-means clustering based on DBN

2.1 Improved fuzzy clustering algorithm

The process of dividing a set of physical or abstract objects into multiple clusters comprised of similar objects is known as clustering. This process aims to discover the natural groupings of data samples, ensuring high similarity within each cluster while keeping the similarity between different clusters as low as possible. In contrast to the supervised learning process of classification, clustering operates without the need for pre-defined classes or labelled samples. In order to facilitate data comprehension and analysis, clustering assigns similar data points to the same segment according to predetermined criteria. In the sample space R containing various sample points, there is a data set $X = \{x_1, x_2, \ldots, x_n\}$ consisting of n data points, where $x_i \in R$. The data set X is then divided into several disjoint data sets C_m through a specific method, which can be represented as:

$$\begin{cases} X = C_1 \cup C_2 \cup \cdots \cup C_m \\ C_i \cap C_j = \varnothing \, (i \neq j) \end{cases} \tag{1}$$

The conventional Fuzzy C-means (FCM) algorithm integrates fuzzy and clustering theories, recognising that equipment states are not binary and that a fuzzy region of similarity exists between various defect states. Fuzzy comprehensive evaluation is a method used to make a reasonable comprehensive evaluation of things that are influenced by multiple attributes or factors. Through fuzzy comprehensive evaluation, a clear conclusion can be derived, reflecting the cat-egory of an object's attributes at a certain membership level, following the "maximum membership degree" principle. Based on the basic idea of fuzzy criteria, membership relations are used as the partitioning condition, and the maximum membership degree principle is applied to segment samples, transitioning from "non-membership" to "membership" and breaking the restrictions of absolute partitioning. After introducing membership functions, samples no longer belong directly to a specific category, but instead reflect their degree of membership through their membership degrees to each category. This not only allows for the classification of sample information but also provides a more intuitive reflection of the degree of membership of each sample.

The concept underlying the FCM clustering method is outlined in the algorithm. The clustering sample set $X = \{x_1, x_2, \ldots, x_n\}$ is partitioned into c classes, $2 < c < n$, in the sample space R; $x_1, x_2, \ldots, x_n$ denote the clustering samples; n is the number of samples; and the clustering centre matrix is denoted by $V=(v_1, v_2, \ldots, v_c)^{\mathrm{T}}$. The calculation of the objective function of FCM is represented by formula (2):

$$\min J(X, V, v_1, v_2, \cdots, v_k, \cdots, v_c) = \sum_{k=1}^{c}\sum_{i=1}^{n} u_{ki}^{m_0} d_{ki}^2 \quad (2)$$

$$s.t. 0 < u_{ki} < 1, \quad \sum_{k=1}^{c} u_{ki} = 1, \quad (3)$$

Where u_{ki} represents membership degree correlation among the points in the sample x_i (i = 1,2, . . . ,N) and the clustering center v_k, m_0 represents the fuzzy index, with the value range [1.5, 2.5], and d_{ki} signifies the Euclidean separation between the sample point and x_i and each clustering center v_k.

The Lagrange multiplier method is employed to minimise the objective function of the FCM algorithm, and defining it as a Lagrangian function with the constraint conditions, the iterative formulas for the membership degree matrix and clustering centers can be finally obtained.

The update formula for membership degree and clustering centre is as follows:

$$u_{ik} = \frac{1}{\sum_{k=1}^{f}\left(d_{ij}/d_{ik}\right)^2}, \quad (4)$$

$$v_k = \frac{\sum_{i=1}^{n} {u_{ik}}^2 \cdot x_i}{\sum_{i=1}^{n} {u_{ik}}^2}. \quad (5)$$

Where d_{ij} signifies the Euclidean separation between the sample point and x_i and each clustering center v_k. When the clustering objective function satisfies the convergence condition, or the algorithm iterates to the maximum number of times required, the clustering ends.

FCM is an effective clustering method; however, the selection of initial centroids has a substantial influence on the clustering results due to the local search-based updates of the clustering centres and membership functions during the iteration process. The utilisation of arbitrary initial centroids facilitates the objective function's descent into local optimal values, which substantially compromises the precision of state evaluation. FCM is additionally extremely susceptible to anomalies, noise data, and initialization conditions. The utilisation of the Euclidean distance as a distance metric introduces susceptibility to aberrant influence, thereby impeding the attainment of superior classification outcomes.

Therefore, firstly, the idea of point density is introduced. Starting from the perspective of information granularity, the clustering effectiveness function is constructed using the principle of granularity analysis. This function can evaluate the effectiveness of clustering results based on the cohesion and coupling of information granularity. In this function, the density of points around is used to reflect the density of sample distribution, and to determine the degree of influence of sample points on clustering. By using the effectiveness function to evaluate the clustering results, the best clustering results and the most appropriate number of clustering categories can be selected, thereby improving the deficiency of traditional FCM in randomly selecting initial clustering centers. The density function is defined as follows, with respect to each sample point x_i:

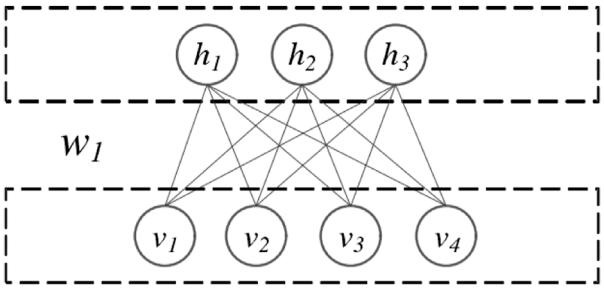

FIGURE 1
DBN network structure.

$$Z_i = \sum_{j=1, j\neq i}^{n} \frac{1}{d_{ij}}, \ d_{ij} \le e, \ 1 \le i \le n, \quad (6)$$

$$d_{ij} = \left\| x_i - x_j \right\|, \ 1 \le i \le n, \ 1 \le j \le n, \quad (7)$$

Where, e signifies the range limit value of the density, satisfying min (d_{ij})<e < max (d_{ij}). Based on empirical judgment, selecting the most dense area in d_{ij} yields better results. The larger Z_i is, the more sample points there are around sample point x_i.

The clustering results are immediately influenced by the centre selection in the conventional FCM algorithm, which requires each iteration update to initialise the clustering centre. It becomes challenging to ascertain the optimal number of clustering categories when the selected number fails to correspond with the characteristics of the data distribution. Calculating the utmost number of clustering categories for the sample set is the initial step in resolving this issue. Subsequently, the point density function is employed to determine the point density of each sample point. The initial clustering centres are determined by the function value size of the first points. The optimal number of clustering categories is then determined by comparing the effectiveness function values of clustering results across all clustering category numbers.

In clustering algorithms, the clustering standard of "highest similarity within classes, highest distinction between classes" has always been upheld. This can also be expressed as the distance within the same category being the smallest, and the distance between different categories being the largest. According to this clustering standard, the clustering centers between categories are merged successively, that is, merging the two categories with the smallest distance and closest to each other. Two clustering centres must be measured in order to determine the distance between two categories. By means of several consolidations, one can acquire an additional classification and a clustering hub. This constitutes the fusion procedure:

1) Determine the separation between any two clustering centres using the Euclidean distance formula.
2) Compare the values and merge the clustering centers that are closer than the set merge threshold;
3) Update the clustering center.

The range of clustering category is $c \in (5, \sqrt{n})$. The clustering iteration start from c = $\sqrt{n}$. Then, the process merge the center

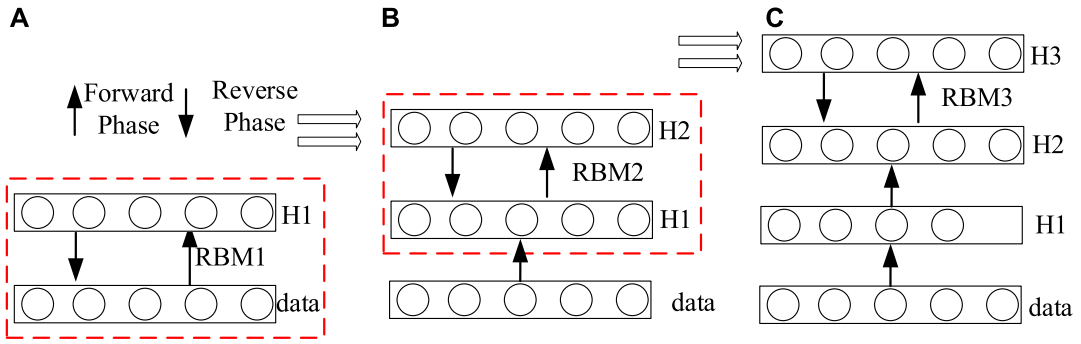

FIGURE 2
Training process of three RBMs in DBN model.

points with close distance. Also, the number of clustering centers continues to decrease, and finally loop decrement until the lower limit of the number of categories.

2.2 Deep belief network

The Deep Belief Network is constructed by layering multiple restricted Boltzmann machines (RBMs), upon which it is built. The Boltzmann machine consists of two entirely connected layers, each of which is a two-layer neural network comprising a visible and concealed layer. In Figure 1, the DBN network architecture is illustrated.

A complete connection exists between neurons in adjacent layers, but none between neurons in the same layer. This principle is adhered to by every individual neuron. An inherent property of neurons is that their activation conditions are independent of one another; the state of a single neuron will influence other neurons with a specific probability. hj denotes the *j*th neuron in the hidden layer, which was obtained via the weight matrix from the previous layer RBM. vi signifies the *i*th visible layer neuron and simultaneously functions as the input to the subsequent RBM. Denoted as follows is the RBM energy function:

$$\begin{aligned} E(v,h) &= -\sum_i a_i v_i - \sum_j b_j h_j - \sum_i \sum_j v_i \omega_{ij} h_{ij} \\ &= -\boldsymbol{a}^T \boldsymbol{v} - \boldsymbol{b}^T \boldsymbol{h} - \boldsymbol{v}^T \boldsymbol{W} \boldsymbol{h}, \end{aligned} \tag{8}$$

Where, a_i represents the bias amount of v_i in the visible layer, b_i represents the bias amount of h_i in the visible layer; ω_{ij} represents the weight coefficient between the neuron v_i in the visible layer and the neuron h_j in the hidden layer. And the joint probability distribution function is as follow:

$$\begin{aligned} p(v,h) &= \frac{1}{Z}\exp(-E(v,h)) \\ &= \frac{1}{Z}\exp\left(\boldsymbol{a}^T \boldsymbol{v}\right)\exp\left(\boldsymbol{b}^T \boldsymbol{h}\right)\exp\left(\boldsymbol{v}^T \boldsymbol{W} \boldsymbol{h}\right) \end{aligned} \tag{9}$$

Where, Z is the normalization factor. Consequently, it is possible to express the conditional probabilities of the visible and concealed layers of RBM as:

$$p(v_i = 1|h) = \sigma\left(a_i + \sum_j \omega_{ij} h_j\right) \tag{10}$$

$$p\left(h_j = 1|v\right) = \sigma\left(b_i + \sum_i \omega_{ij} h_i\right) \tag{11}$$

Where, $\sigma(x) = 1/1 + e^{-x}$ is the nonlinear Sigmoid function, giving the network non-linear mapping capabilities and enhancing the network's representation ability. The joint distribution of (v,h) corresponds to the likelihood function as follows:

$$\begin{cases} p(v) = \sum_h p(v,h) = \frac{1}{Z}\sum_h e^{-E(v,h)} \\ p(h) = \sum_v p(v,h) = \frac{1}{Z}\sum_v e^{-E(v,h)} \end{cases}. \tag{12}$$

Through network training, the model is fitted to the training dataset, so that the output distribution can represent the key features of the samples as much as possible. Therefore, given the training sample $X = \{x_1, x_2, \ldots, x_n\}$, the log likelihood function expression of the training dataset is as follows:

$$\mathcal{L}(D; W, a, b) = \frac{1}{N}\sum_{n=1}^{N} \log p\left(\hat{v}^{(n)}; W, a, b\right) \tag{13}$$

The process of network training is illustrated in Figure 2. Unsupervised layer-by-layer training is implemented initially as shown in Figure 2A. The forward propagation technique is employed to efficiently extract state features from the initial sample data in order to diagnose the switchgear equipment. The initial sample data is utilised as the input for the RBM in the first stratum as shown in Figure 2B. The output of each subsequent layer RBM is then utilised as the input for the subsequent layer RBM. By spatially mapping the samples across multiple RBM layers, additional feature information is preserved. The output of the final layer RBM is classified by the BP network, and the weight parameters in the network are subsequently modified via the backward propagation method in multiple iterations as shown in Figure 2C.

TABLE 1 State quantities and corresponding feature information.

State variable	Corresponding feature information
v_1	Partial discharge amplitude measured by TEV
v_2	Partial discharge pulse number measured by TEV
v_3	Partial discharge amplitude measured by Ultrasonic method
v_4	Equipment information score
v_5	Pre-test inspection score

3 Switchgear state assessment based on DBN-FCM

3.1 Selection of equipment evaluation state variable

Switchgears in different conditions will inevitably exhibit unique differences in certain characteristic parameters. Some features with significant variations can be directly assessed by humans through visual or auditory means for a preliminary evaluation of the equipment's health status. However, there is still a substantial amount of feature information in the equipment that cannot be perceived, and the health status judged based on intuitive information is not sufficient, making it difficult to accurately represent the equipment's condition. Therefore, when using multi-source data for assessment, the selection of characteristic parameters for evaluating the switchgear will greatly affect the results of the equipment state assessment. The state of the switchgear is influenced by multiple characteristic factors, which are interrelated yet diverse, exhibiting different health capabilities under different conditions. When selecting characteristic parameters, it is necessary to ensure that all necessary information is covered while avoiding redundancy and omission of information.

The parameters of the switchgear state mainly come from grid information, cabinet information, power outage test information, live detection information, and online monitoring information. Considering the practical field testing and modeling needs, this paper has selected five types of state quantities as the feature information of the samples based on the existing distribution network equipment state evaluation guidelines, as shown in Table 1.

3.2 Selection of equipment evaluation state variable

By utilising the existing distribution network equipment state evaluation guidelines and observing the equipment's health status, it is possible to classify the current health condition of the switchgear into one of five categories: severe, attention, good, or very good. The correspondence between the health status grades and the current operating status of the switchgear is shown in Table 2.

Based on the state results and operating status table, and referring to the measured key characteristic parameters of the equipment and routine equipment state analysis, the correspondence between the characteristic parameter values and the equipment state is determined, with reference to relevant technical specifications, as shown in Table 3.

Given the significant variations in the numerical ranges of different features, which may lead to the model being overly sensitive to certain features or ignoring others, there is a potential impact on the model's accuracy and stability. In this paper, the selected features undergo normalization based on their upper and lower limits, converting data of various scales or ranges into a unified standard range. This ensures that all feature values fall between [0, 1], eliminating dimensional differences between data and enabling a fairer comparison and balance of the impact of different features on the model.

TABLE 2 Switchgear operation state evaluation standards.

Evaluation result	Operation state
Very good	Switchgear operates in normal condition
Good	Switchgear operates in basically normal condition
Attention	There are hidden dangers of insulation in the switchgear, but it can still continue to operate
Abnormal	There are hidden dangers of accidents in the switchgear, which can run for a short time
Severe	There is a major accident hidden danger in the switch cabinet, and the operation should be stopped immediately

TABLE 3 State quantity evaluation standard range.

State variable	Very good	Good	Attention	Abnormal	Severe
v_1/dB	0–5	5–10	10–20	20–30	30–50
v_2	0–50	50–100	100–200	200–300	300–400
v_3/dB	−6~-3	−3~0	0–6	6–250	25–68
v_4	90–100	80–90	70–80	60–70	0–60
v_5	90–100	80–90	70–80	60–70	0–60

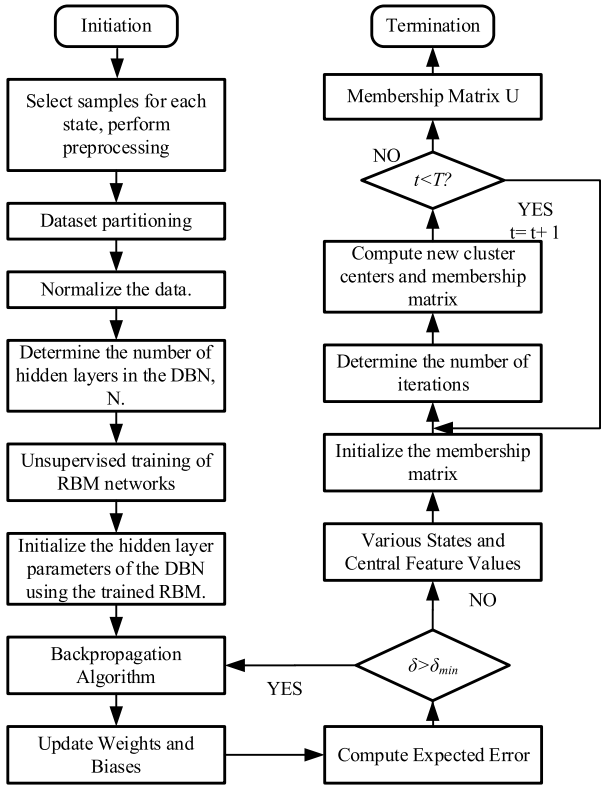

FIGURE 3
Switchgear state analysis process.

3.3 Switchgear state analysis process based on DBN and improved FCM

The switchgear state analysis process based on DBN feature extraction and improved FCM clustering method is illustrated in Figure 3, with specific steps as follows:

1) Data Preprocessing: Process the collected sample data for data anomalies, divide them into labeled and unlabeled training sets, as well as test sets, and normalize them based on Table 3.
2) DBN Network Training: Use the unlabeled training set for layer-by-layer unsupervised training of the entire DBN network until the number of RBMs equals the preset number of hidden layers. Then, use the labeled samples in conjunction with the BP algorithm to perform classification training on the model after unsupervised training, updating the network's weight parameters through the backpropagation algorithm.
3) DBN Feature Extracting: Following the completion of training, determine the quantity of nodes to be included in each concealed layer of the DBN and execute feature extraction in accordance with this quantity.
4) Improved FCM Clustering Analysing: Build a multi-source data state detection model, set initial values, and initialize the membership degree matrix; input the extracted features into the improved FCM clustering model; continuously iterate and solve based on the cluster centers and membership degree functions until convergence conditions are met.

FIGURE 4
Field experiment.

5) The belonging State Calculating:Calculate the belonging state of the sample points in the test set based on the above methods, compute the distance to the cluster centers, and determine the sample points' state of affiliation based on the principle of maximum membership degree.

4 Case study

4.1 Experimental preparation

To validate the feasibility of the method proposed in this research, we selected a dataset of 44 groups of switchgear live detection data from a 10 kV distribution room. The live detection operation was carried out on 6 May 2022, with an ambient temperature of 25°C and a relative humidity of 53%. The partial discharge detector used was the portable online partial discharge detector produced by Nanjing Zhongda Intelligent Technology Co., Ltd., with the model PDSwitch3.0 and a sampling rate set at 100MSa/s. Switchgear model is HXGN17-12, is a three-phase AC rated voltage 10 kV, rated frequency 50 Hz indoor box-type AC metal-enclosed switchgear. The field experiment is shown in Figure 4.

In addition to background noise data, environmental condition data, and operational years of the switchgear, the detection data for each switchgear comprises TEV and ultrasonic data from six detection points on the switchgear. Following the process of denoising and standardising the detection data of the switchgear, a dataset comprising the switchgear's multi-dimensional features was constructed.

Through data screening, this experiment determined to use 1000 groups of experimental data as the entire experiment's samples, with 700 training samples (including 200 unlabeled samples and 500 labeled samples) and 300 test samples (all labeled and arranged by different statuses). In these data, the

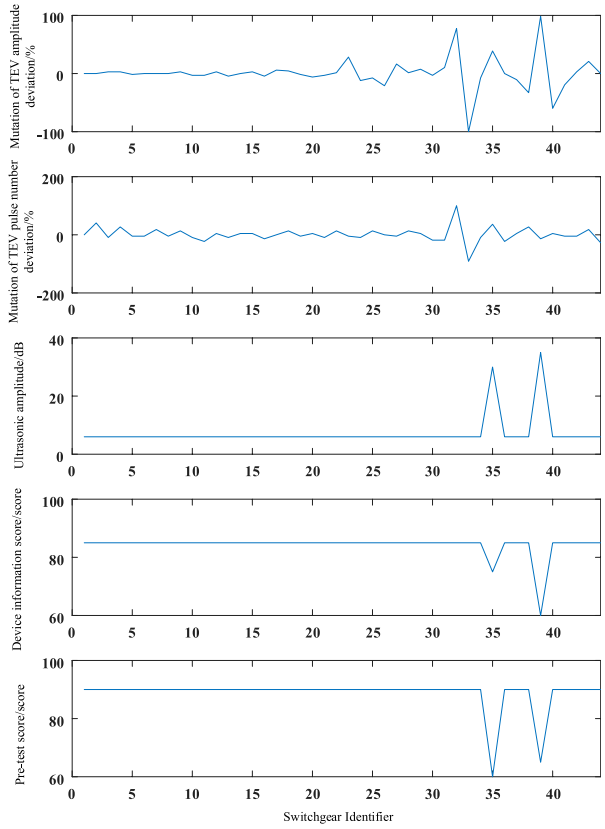

FIGURE 5
Detection data of various parameters for the switchgear in the distribution room.

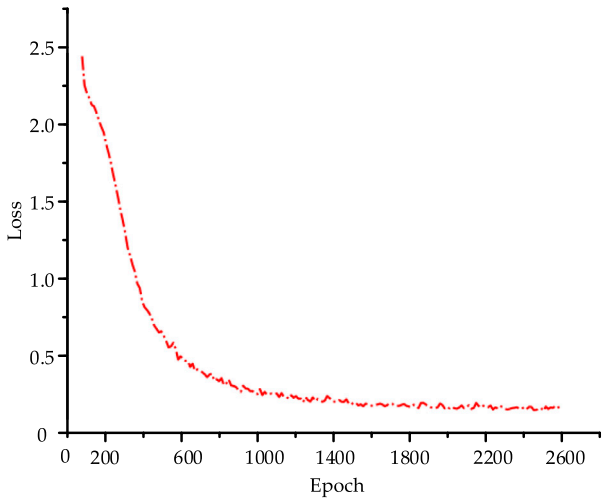

FIGURE 6
Training error curve.

data of TEV amplitude, TEV pulse number, ultrasonic amplitude, equipment information score, and pre-test inspection score obtained from the live test are displayed in Figure 5. To enhance the accuracy of the evaluation results and avoid significant discrepancies between the evaluation results and reality, when the values of different parts of the switchgear differ, the worst value of the important parts of the switchgear is taken as the measurement value of that feature.

4.2 Result analysis

The number of nodes in each layer of DBN is 5-6-9-10-5, the number of trainings in the unsupervised pre-training phase is 256 and the learning rate is 0.1, the number of trainings in the fine-tuning phase is 64 and the learning rate is 0.05. The specific error curve is shown in Figure 6.

The aggregate training error of the network decreases progressively as the number of training iterations increases, as illustrated in Figure 6. The error drops quickly at the beginning of training, and after the training error reaches 0.2, its rate of decrease gradually slows down. The error meets the requirements after 2000 training iterations. After the training of the DBN was completed, the well-trained DBN network was used to extract features from a test set of 300 samples. Some of the extracted features are shown in Figure 7.

The final features derived by the DBN from a luminance image are displayed in Figure 7. A brightness value that is less than one signifies a value of the matrix near zero, whereas a brightness value that is greater than one signifies a value near one. As shown in Figure 7, the distribution of the same fault across various dimensions is generally consistent, whereas the distributions of distinct faults vary across these dimensions. Different types of faults exhibit distinct distributions, which facilitates the differentiation of switchgear states.

In order to cluster the fault-free data attributes of the daily inspection dataset, the K-means algorithm was implemented. Unknown is the number of clusters utilised in K-means clustering. A subjective artificial setting for the number of clusters devoid of any theoretical foundation is incapable of producing effective clustering outcomes. In order to determine the optimal number of categories, we compute the sum of squared errors and determine the number of clusters in accordance with the actual circumstance. The loss function $J(c,u)$ for the current K value is obtained by summing the squared errors of all clusters:

$$J(c,u) = \sum_{i=1}^{n} \|x_i - u_{ci}\|^2, \tag{14}$$

Where, x_i denotes the *ith* sample, c_i signifies the cluster to which xi is assigned, u_{ci} signifies the cluster's centre point, and n signifies the total number of samples.

Commonly used clustering effectiveness analysis often adopts a single internal effectiveness index, which lacks an analysis and research on the characteristics of the switchgear dataset, resulting in certain one-sidedness. Internal effectiveness indexes are sensitive to background noise and are suitable for datasets with clear classifications, evaluating clustering results from aspects such as separability, compactness, and overlapping. However, the switchgear dataset has characteristics like strong adhe-siveness,

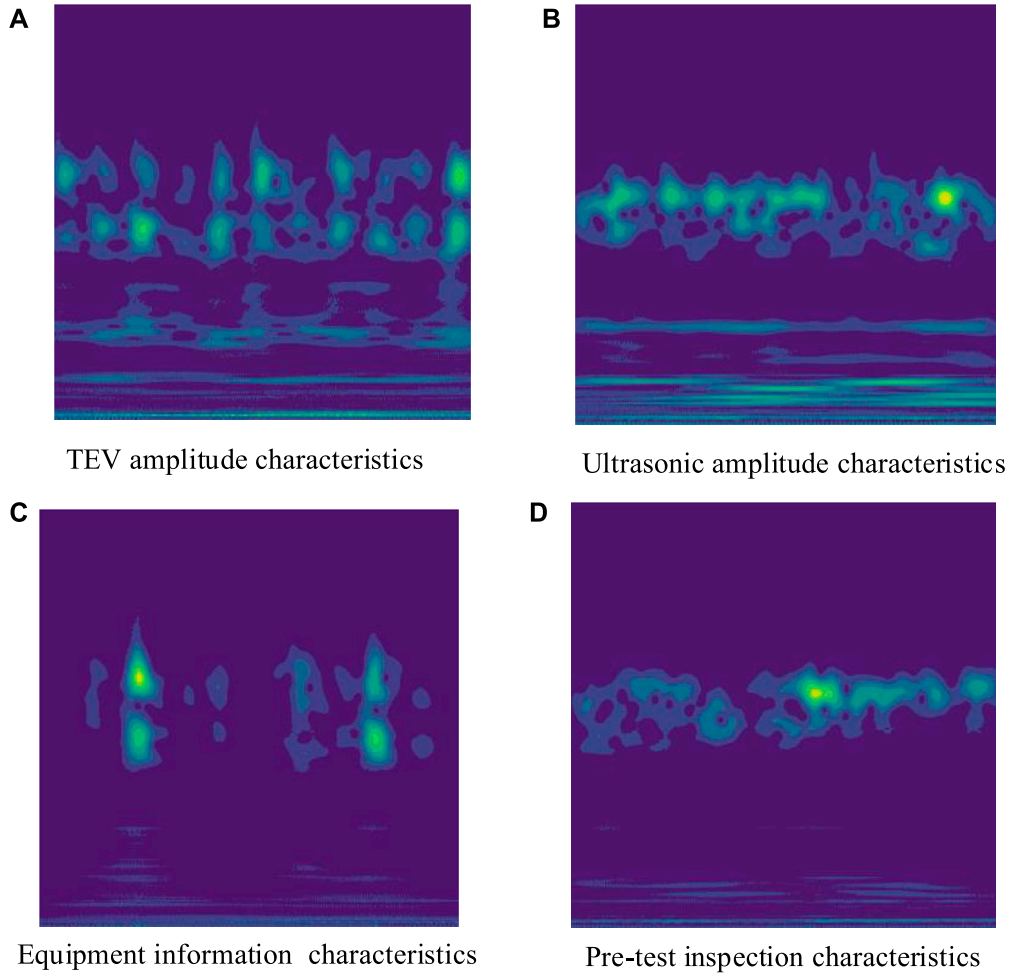

FIGURE 7
TEV, ultrasonic, equipment information and pre-test inspection features extracted by the DBN.

unclear geometric classification, and vague distribution properties. Using a single internal effectiveness index cannot fully reflect the effectiveness of clustering results. In order to assess the quality of clustering on an unidentified dataset with unknown structure and properties, this study develops the CVI index by weighted integration of four indexes: silhouette coefficient, Davies-Bouldin index, Calinski-Harabasz index, and silhouette coefficient. These indices reflect geometric structural features and take into account the inherent characteristics of the switchgear dataset. The criteria of CVI is defined as:

$$CVI = \sum_{i=1}^{4} \omega_i f_i(x) = \omega_1 f_1 + \omega_2 f_2 + \omega_3 f_3 + \omega_4 f_4 \qquad (15)$$

Where, ω_i is the weight of the ith effectiveness index, and f_i is the ith effectiveness index. f_1 is the silhouette coefficient, an index used to measure the density and dispersion of clustering categories. f_2 is the Calinski-Harabasz index, an index used to measure the tightness within categories. Its advantage lies in its simplicity, directness, and fast calculation speed, with a larger value indicating better clustering results. f_3 is the Davies-Bouldin Index (DBI), also known as the classification appropriateness index, used to measure the degree of rationality in classification. A smaller DBI value indicates better clustering results. f_4 is also the Davies-Bouldin Index.

The switchgear multidimensional feature dataset was classified using the K-means clustering algorithm; the CVI line relationship for various K values is depicted in Figure 8. As shown in Figure 8, the clustering structure effectiveness index indicates that when K = 5, i.e., when the switchgear states are divided into five categories, there is a significant clustering effect.

At the same time, the clustering results obtained for $K = 3$, $K = 4$, and $K = 5$ were visualized using the t-SNE dimensionality reduction algorithm, as shown in Figure 9. The effect of the clustering procedure proposed in this paper is favourable, as distinct boundaries exist between groupings. Comparing the t-SNE visualizations for $K = 3$ and $K = 4$, $K = 5$ is verified to be the optimal number of categories. When $K = 3$, it represents that the healthy operating states of the switchgear will be divided into three categories, lacking more detailed classification, making it difficult for maintenance personnel to make good decisions about the switchgear. When $K = 4$, the number of data labeled "good" is roughly equal to the "general" data, which does not conform to the evaluation results of daily live maintenance, indicating an over-partitioning phenomenon at this time.

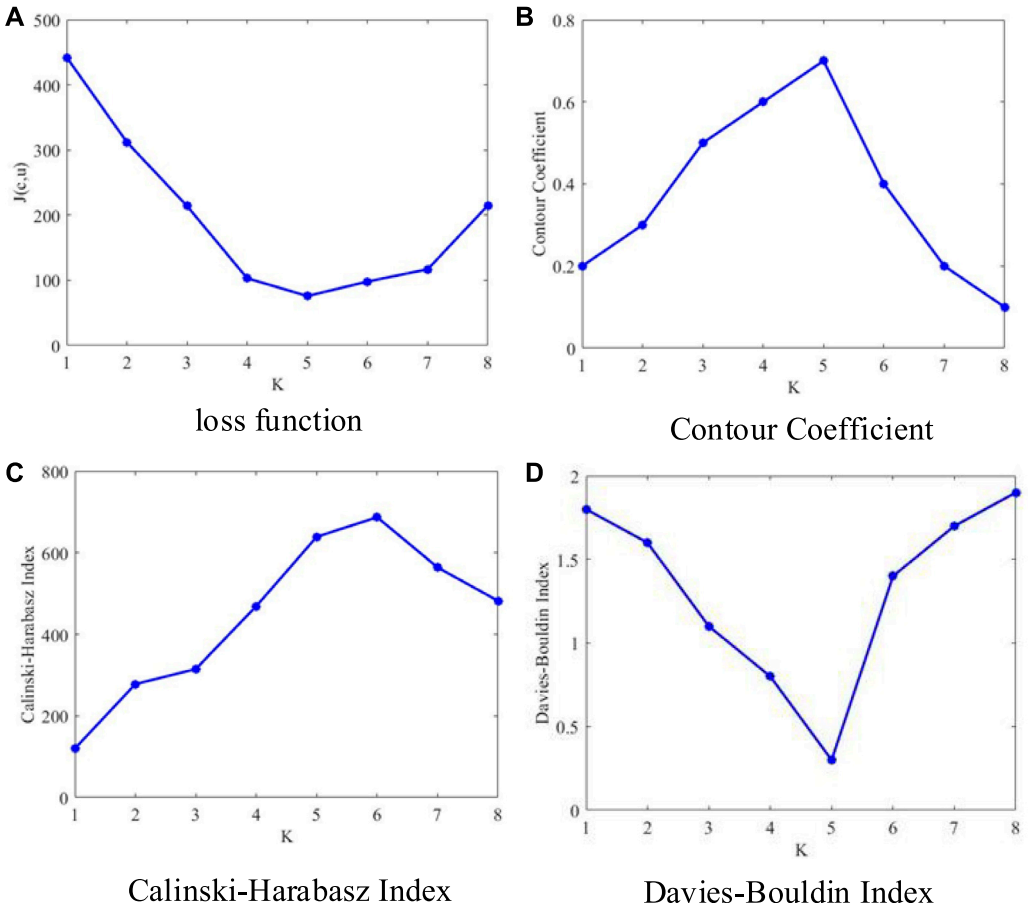

FIGURE 8
Loss function, contour coefficient, calinski-harabasz index and davies-bouldin index under different K values.

When $K = 5$, this scheme clearly and reasonably divides the health status of partial discharge in the live detection of switchgear. The number of switchgears that need immediate inspection and troubleshooting is small, followed by the switchgears that need more attention, while most of the data shows that the switchgears are still operating stably, conforming to the evaluation criteria of general on-site operation and maintenance.

Using the above fuzzy clustering method, the state of the switchgear in this distribution room was assessed, and the assessment outcomes are illustrated in Figure 10. The abnormality of the state assessment result for switchgear 32 is evident, switchgears 35 and 39 are marked as needing attention, and the assessment results of the other switchgears are all very good. Among them, the TEV amplitude of the live electrical test data of switchgears 35 and 39 was found to be excessively high. Also, the ultra-sonic amplitude of the live electrical test data of switchgear 32 was found to be excessively high. It is evident from the clustering outcomes that the approach suggested in this article aligns with the results of the state evaluation carried out in adherence to the protocols for assessing the condition of distribution network equipment. The health evaluation method suggested in this article has the capability to provide an unbiased reflection of the switchgear's operational condition. Maintenance strategies for the switchgear's future operation and upkeep can be devised using the results of the state assessment.

4.3 Comparison

Finally, the state of the switchgear was assessed using the above sample features, and the results were compared with other diagnostic methods, as shown in Table 4. Compared with traditional FCM and IFCM methods, this method has achieved a significant improvement in state assessment accuracy. Compared with traditional FCM and IFCM clustering methods, the accuracy has increased by 36% and 22%, respectively, using the proposed method. Compared with the switchgear state assessment methods of DBN-FCM, DBN-IFCM improves on the membership degree function of FCM, solving the problem of local minima in membership degrees and further enhancing diagnostic performance. Compared with deep learning methods based on DBN and ReLU-DBN, the classification effect of the proposed method is also significantly improved.

From Table 4, it can be seen that the switchgear state assessment method based on deep belief networks and fuzzy clustering proposed in this paper has a good state assessment effect and

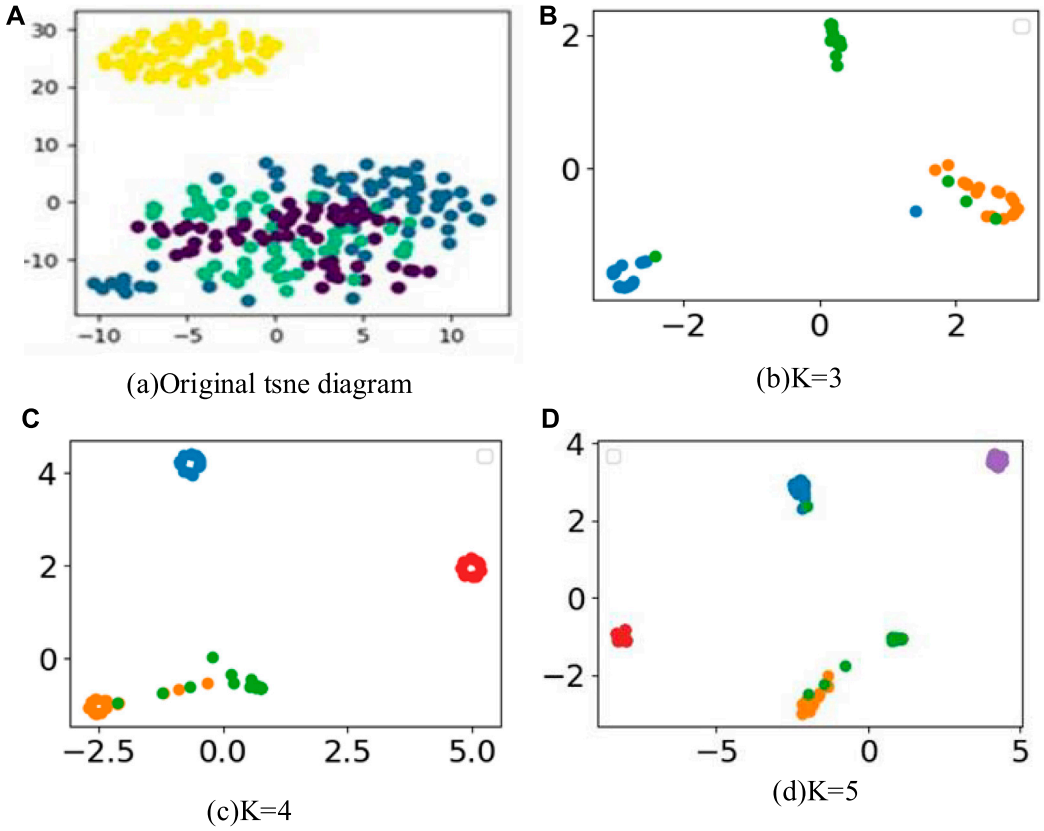

FIGURE 9
Visualization of clustering effect in unclustered as well as different clustering K values.

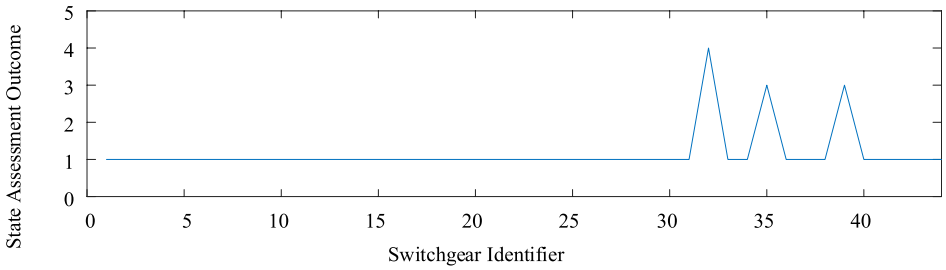

FIGURE 10
State evaluation results of switchgears in the distribution room.

high assessment accuracy. It solves the problem of lack of depth in feature extraction and insufficient assessment accuracy in traditional state assessment methods, providing a new method for switchgear state assessment and fault diagnosis.

The following discussion focuses on the impact of the signal-to-noise ratio (SNR) on the accuracy of switchgear state assessment. Keeping other parameters constant, we consider scenarios with SNRs of −10dB, -5dB, 0dB, 5dB, and 10 dB. We compare the diagnostic results of four different switchgear state assessment methods under various SNR conditions, as shown in Figure 11.

As shown in Figure 11, at lower SNRs (−10 dB), the diagnostic accuracy and robustness of the switchgear state assessment technique based on DBN are comparatively inferior to those of the other three methods. To address the issue of strong noise interference, this paper utilizes fuzzy clustering, which better interprets the scenarios where the physical boundaries between state gradations are not very clear. Under the condition of an SNR of −10dB, the diagnostic relative error is able to be maintained at 5.65%. The proposed method meets the accuracy requirements for switchgear state assessment under low SNR conditions.

TABLE 4 Assessment accuracy of switchgear with different methods.

Method	Fuzzy coefficient	Testing set	Misdivision	Accuracy/%
FCM	m = 2.1	300	124	58.67
IFCM	m = 2.2	300	83	66.33
DBN-FCM	m = 2.0	300	21	93.40
DBN-IFCM	m = 2.2	300	17	94.33
DBN	—	300	28	92.54
ReLU-DBN	—	300	25	93.37

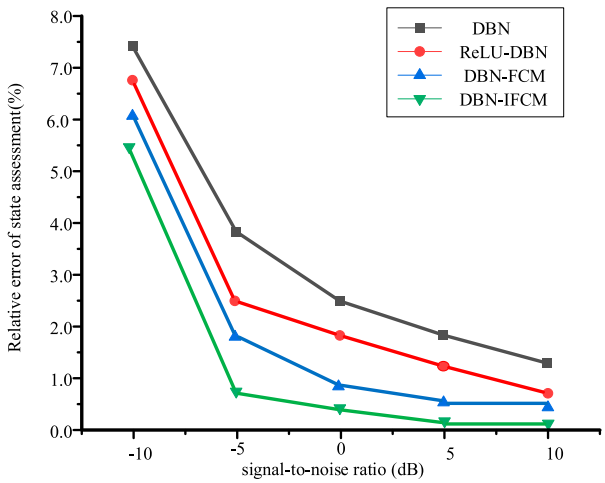

FIGURE 11
Comparison of relative errors in state assessment at different SNRs.

5 Conclusion

Aiming at the problems of fuzzy boundary delineation and low accuracy of state assessment grading in traditional fuzzy methods for state assessment, the paper proposes a switchgear state assessment framework based on DBN and IFCM (DBN-IFCM). The method uses DBN to extract feature parameters from normalized switchgear condition data, and adopts IFCM c to cluster the extracted feature parameters to appropriately assess switchgear condition. The main conclusions of this paper are as follows:

1) The DBN-IFCM-based switchgear state assessment method is able to accurately classify the state of the switchgear with satisfactory results, and the state assessment classification accuracy rate is up to 94%. Compared with traditional clustering methods such as FCM and IFCM, the accuracy of the proposed method is improved by 36% and 22%, respectively; compared with deep learning methods based on DBN-FCM, DBN and ReLU-DBN, the grading accuracy of the proposed method is improved by 0.9%, 1.8% and 1%, respectively.
2) The switchgear state assessment method based on DBN-IFCM is capable of learning the characteristics of various graded states from a large amount of state data, overcoming the disadvantage of traditional clustering methods that cannot learn autonomously.
3) Compared with other deep neural network switchgear state assessment methods, using fuzzy clustering better explains situations where the physical boundaries between state grades are not very clear. Additionally, this method provides a new perspective for addressing state grading issues when label samples are scarce or label information is difficult to obtain.

Data availability statement

The raw data supporting the conclusion of this article will be made available by the authors, without undue reservation.

Author contributions

XX: Conceptualization, Writing–original draft, Software. JG: Data curation, Formal Analysis, Writing–original draft. JY: Investigation, Writing–original draft. XF: Writing–review and editing. MS: Writing–review and editing. YL: Writing–review and editing, Resources. MG: Writing–review and editing. ZY: Writing–review and editing. ZW: Writing–review and editing.

Funding

The author(s) declare financial support was received for the research, authorship, and/or publication of this article. This research was funded by the Science and Technology Project of Jiangsu Electric Power Co. Ltd., Grant No. J2021056.

Conflict of interest

Authors XX, JG, JY, XF, and MS were employed by State Grid Jiangsu Electric Power Company Research Institute. Author YL was employed by State Grid Jiangsu Electric Power Company.

The remaining authors declare that the research was conducted in the absence of any commercial or financial relationships that could be construed as a potential conflict of interest.

The authors declare that this study received funding from the Science and Technology Project of Jiangsu Electric Power Co. Ltd. The funder had the following involvement in the study: The funder was involved in the collection, analysis and interpretation of data, the writing experimental part of the article, and the decision to submit it for publication.

Publisher's note

References

Chang, W., Li, C., Su, Q., and Ge, Z. (2013). Study on development of partial discharges at the defect caused by a needle damage to a cable joint. *Proc. Chin. Soc. Electr. Eng.* 33 (7), 192–201. doi:10.13334/j.0258-8013.pcsee.2013.07.026

Chen, P., Ma., T., Xiang, W., Fan, C., Li, C., and Hu, X. (2020). "The switch cabinet status evaluation model based on dynamic evidence theory," in 2020 2nd International Conference on Power Data Science (ICPDS), Kunming, China, December, 2020, 36–42. doi:10.1109/ICPDS51559.2020.9332519

Dai, J., Song, H., Sheng, G., and Jiang, X. (2017). Dissolved Gas analysis of insulating oil for power transformer fault diagnosis with deep belief network. *IEEE Trans. Dielectr. Electr. Insul.* 24 (5), 2828–2835. doi:10.1109/TDEI.2017.006727

de Assis, E. M., Costa Lima, G. A., Prestes, A., Marinho, F., and Nagasaki Costa, L. A. (2019). Q-weibull applied to Brazilian hydropower equipment. *IEEE Trans. Reliab.* 68 (1), 122–132. doi:10.1109/TR.2018.2864550

Dehghani, N. L., Darestani, Y. M., and Shafieezadeh, A. (2020). Optimal life-cycle resilience enhancement of aging power distribution systems: a MINLP-based preventive maintenance planning. *IEEE ACCESS* 8, 22324–22334. doi:10.1109/ACCESS.2020.2969997

Ding, De., Tang, C., Gao, W., Liu, W., Yao, S., and Zhao, Y. (2014). Frequency attributes and propagation properties of typical partial discharge in GIS. *High. Volt. Eng.* 40 (10), 3243–3251. doi:10.13336/j.1003-6520.hve.2014.10.042

Faiz, J., and Soleimani, M. (2017). Dissolved Gas analysis evaluation in electric power transformers using conventional methods a review. *IEEE Trans. Dielectr. Electr. Insul.* 24 (2), 1239–1248. doi:10.1109/TDEI.2017.005959

Fang, M., Huang, R., Lv, T., Liu, C., Ding, X., and Wang, P. (2023). "Research on state assessment method of key equipment in distribution network," in 2023 8th Asia Conference on Power and Electrical Engineering (ACPEE), Tianjin, China, April, 2023, 2614–2618. doi:10.1109/ACPEE56931.2023.10135928

Hinow, M., and Mevissen, M. (2011). Substation maintenance strategy adaptation for life-cycle cost reduction using genetic algorithm. *IEEE Trans. Power Deliv.* 26 (1), 197–204. doi:10.1109/TPWRD.2010.2065247

Janssen, A., Makareinis, D., and Solver, C.-E. (2014). International surveys on circuit-breaker reliability data for substation and system studies. *IEEE Trans. Power Deliv.* 29 (2), 808–814. doi:10.1109/TPWRD.2013.2274750

Kim, Y., Kweon, D., Park, T., Kim, S., and Lim, J. S. (2019). Classification of fault and failure types determined by dissolved Gas analysis for transformers. *J. Electr. Eng. Technol.* 14, 1665–1674. doi:10.1007/s42835-019-00175-0

Liang, J., Wang, Z., and Liu, X. (2009). State estimation for coupled uncertain stochastic networks with missing measurements and time-varying delays: the discrete-time case. *IEEE Trans. Neural Netw.* 20 (5), 781–793. doi:10.1109/TNN.2009.2013240

Montanari, G. C., Ghosh, R., Cirioni, L., Galvagno, G., and Mastroeni, S. (2022). Partial discharge monitoring of medium voltage switchgears: self-condition assessment using an embedded bushing sensor. *IEEE Trans. Power Deliv.* 37 (1), 85–92. doi:10.1109/TPWRD.2021.3053658

Qiu, J., Liang, Y., Cheng, X., Zhao, X., and Ma, L. (2022). "State assessment of key equipment of microgrid based on multi-source data fusion method," in 2022 10th Joint International Information Technology and Artificial Intelligence Conference (ITAIC), Chongqing, China, June, 2022, 710–714. doi:10.1109/ITAIC54216.2022.9836941

Razi-Kazemi, A. A., and Niayesh, K. (2021). Condition monitoring of high voltage circuit breakers: past to future. *IEEE Trans. Power Deliv.* 36 (2), 740–750. doi:10.1109/TPWRD.2020.2991234

Subramaniam, A., Sahoo, A., Manohar, S. S., Raman, S. J., and Panda, S. K. (2021). Switchgear condition assessment and lifecycle management: standards, failure statistics, condition assessment, partial discharge analysis, maintenance approaches, and future trends. *IEEE Electr. Insul. Mag.* 37 (3), 27–41. doi:10.1109/MEI.2021.9399911

Wang, C., Hou, Y., Qin, Z., Peng, C., and Zhou, H. (2015). Dynamic coordinated condition-based maintenance for multiple components with external conditions. *IEEE Trans. Power Deliv.* 30 (5), 2362–2370. doi:10.1109/TPWRD.2015.2442291

Wang, Y. B., Chang, D. G., Fan, Y. H., Zhang, G. J., Zhan, J. Y., Shao, X. J., et al. (2017). Acoustic localization of partial discharge sources in power transformers using a particle-swarm-optimization-route-searching algorithm. *IEEE Trans. Dielectr. Electr. Insul.* 24 (6), 3647–3656. doi:10.1109/TDEI.2017.006857

Yumbe, Y., Hasegawa, T., and Furukawa, N. (2013). Optimization method for inspection scheduling of power distribution facilities. *IEEE Trans. Power Deliv.* 28 (3), 1558–1565. doi:10.1109/TPWRD.2013.2253806

Zhong, J., Li, W., Billinton, R., and Yu, J. (2015). Incorporating a condition monitoring based aging failure model of a circuit breaker in substation reliability assessment. *IEEE Trans. Power Syst.* 30 (6), 3407–3415. doi:10.1109/TPWRS.2014.2387334

Zhong, J., Li, W., Wang, C., and Yu, J. (2018). A RankBoost-Based data-driven method to determine maintenance priority of circuit breakers. *IEEE Trans. Power Deliv.* 33 (3), 1044–1053. doi:10.1109/TPWRD.2017.2748146

Zhou, N., Xu, Y., Cho, S., and Wee, C. T. (2023). A systematic review for switchgear asset management in power grids: condition monitoring, health assessment, and maintenance strategy. *IEEE Trans. Power Deliv.* 38 (5), 3296–3311. doi:10.1109/TPWRD.2023.3272883

frontiers | Frontiers in Energy Research

TYPE Original Research
PUBLISHED 29 December 2023
DOI 10.3389/fenrg.2023.1326100

OPEN ACCESS

EDITED BY
Lu Zhang,
China Agricultural University, China

REVIEWED BY
Yunhao Zhao,
North China Electric Power University, China
Tianyang Zhao,
Royal Institute of Technology, Sweden
Peng Xia,
State Grid Energy Research Institute (SGCC), China

*CORRESPONDENCE
Wenting Zha,
wtzha@cumtb.edu.cn

RECEIVED 22 October 2023
ACCEPTED 28 November 2023
PUBLISHED 29 December 2023

CITATION
Zhou J, Tuo J, Wang L, Shi Y and Zha W (2023), Calculation of electricity sales based on multi-factor correlation analysis.
Front. Energy Res. 11:1326100.
doi: 10.3389/fenrg.2023.1326100

Calculation of electricity sales based on multi-factor correlation analysis

Jian Zhou[1], Jianjun Tuo[2], Lingbo Wang[1], Yaqi Shi[3] and Wenting Zha[4]*

[1]Tianshui Power Supply Company of State Grid, Tianshui, China, [2]State Grid Gansu Electric Power Company, Lanzhou, China, [3]School of Artificial Intelligence, China University of Mining and Technology-Beijing, Beijing, China, [4]School of Mechanical and Electrical Engineering, China University of Mining and Technology-Beijing, Beijing, China

Electricity sales is one of the important assessment indexes of a power grid company's operation. Since electricity sales is closely related to many factors, how to consider the influence of multiple factors and improve the accuracy of the calculation of electricity sales is a difficult problem that needs to be solved urgently. In this paper, we first analyze the six dimensions affecting electricity sales and select the key influencing factors that can be quantified statistically. Secondly, the key influencing factors are screened according to Pearson's correlation coefficient and then the calculation model of electricity sales is established based on the random forest algorithm. Finally, we validate the feasibility and validity of the proposed calculation method for electricity sales through a case study.

KEYWORDS

electricity sales, investors, correlation, random forest, calculation accuracy

1 Introduction

Electricity sales is an important efficiency assessment index for the operation and management of power grid companies. Calculation of electricity sales is one of the fundamental tasks in the operation of the electricity market. It helps utilities understand the quantity and amount of electricity they sell so that they can make accurate financial analyses and market forecasts. However, the amount of electricity sales in a region is affected by many complex factors. For example, grid investment has a profound impact on electricity sales. The current large-scale rough investment strategy is no longer applicable, the precise investment strategy has been applied in many countries, and how to accurately invest to enhance electricity sales has become the focus of the investment strategy of many power grid enterprises. In addition, the economic situation, technological development, and other factors also have a certain degree of impact on electricity sales. Under the current transmission and distribution tariff policy, the positive growth of electricity sales directly determines the economic efficiency of the grid company, which is an important basis for judging whether the value of grid assets is preserved or increased. Therefore, It is necessary to analyze and process the data of electricity sales at a deeper level and discover its inherent change rules at the same time. It can provide the basis for the operators of power grid enterprises to support their business decisions, and help them better understand the market development trend and make correct business decisions.

With the development of data technology, it is an effective way to construct the calculation model of electricity sales by mining the intrinsic relationship between the

historical data of multiple factors and electricity sales. At present, most of the relevant research results are focused on accurate forecasting of electricity sales, and the commonly used forecasting methods are the time series method (Billinton et al., 1996; Toyoda et al., 1970; Pektas and Cigizoglu, 2013), regression analysis method (Dudek, 2016; Sarduy et al., 2016), and grayscale forecasting method (EI-Fouly et al., 2006; Li et al., 2011). First of all, historical electricity sales data have time series characteristics, time series-based forecasting methods are widely used in the field of electricity sales forecasting (Madden, 2005). Kim M et al. (2023) applied a new model and scientific approach to power prediction in IoT and big data environments using traditional time series prediction methods. The work (Sarkodie et al., 2017) used an Autoregressive Integrated Moving Average (ARIMA) model to forecast the electricity consumption in Ghanaian regions up to 2030. This method requires high data accuracy and can only handle relatively smooth time series data. However, electricity sales are usually perturbed by stochastic factors such as temperature, precipitation, and season, which cannot be handled by this method. Secondly, the regression analysis method is similar to the time series-based electricity sales prediction method, which constructs a regression model for the prediction of electricity sales by mining the historical data of electricity sales. The difference is that this method considers different factors affecting electricity sales, which makes the model more stable by considering the factors of electricity sales from a higher dimension. The work (Lai et al., 2023) built the annual contribution electricity forecast model based on Logistic regression analysis. The work (Vu et al., 2015) analyzed the importance of climate for the prediction of electricity sales under different geographical conditions and established a multiple regression model for the prediction of monthly electricity demand by selecting appropriate variables. The predictive accuracy of the proposed model is also verified based on the data of New South Wales, Australia. Finally, the gray prediction method, proposed by Deng (Chan et al., 2010), is a multidisciplinary theory for analyzing gray systems. The method has been widely used in many fields such as agriculture, industry, and environmental systems research (Cai and Liao, 2021). As an important part of the gray system theory, the gray forecasting model has been widely used in time series forecasting due to its simplicity and ability to describe unknown systems with only four data points (Mohamed and Bodger, 2004a; Mohamed and Bodger, 2004b). Electricity demand forecasting can be regarded as a gray system problem because we know that some factors such as population, economic conditions, and weather have an impact, but we are not sure how they affect the electricity demand (H Morita et al., 1996; Zhou et al., 2005 proposed a simple triangular gray pre-method to forecast electricity demand. On this basis, it is combined with the idea of interval prediction in multiple regression, and the method's feasibility is proved through actual case analysis. However, the gray prediction also has some defects, when electricity sales are in a smooth change the method predicts poorly. Therefore, the methods in the above-mentioned literatures are only suitable for dealing with linear data, which does not work for electricity sales with non-linear and non-stationary characteristics.

In order to improve the accuracy of electricity sales calculations, this paper intends to establish a calculation model of electricity sales by analyzing and screening the factors based on correlation ranking and random forest algorithm. The use of big data technology to analyze and quantify the relationship between grid investment and electricity sales growth in different regions has a positive effect on grid companies to further improve the level of investment precision. The main contributions of this paper are as follows:

(1) The influencing factors on electricity sales are selected by analyzing different dimensions and the Pearson's correlation coefficient is utilized to filter out the key influencing factors.
(2) The artificial intelligence algorithm is introduced into the calculation method of electricity sales to improve the accuracy.

2 Materials and methods

2.1 Analysis of dimensions and key factors affecting electricity sales

According to the experts' selection and actual operation experience, it is known that the six dimensions of infrastructure, technological transformation, inherent loss, load development, power supply construction and power supply characteristics have a greater impact on power sales, which are analyzed as follows.

2.1.1 Infrastructure

Grid infrastructure is the hardware facilities to guarantee the power supply, such as transmission and distribution lines, substations, and auxiliary equipment. The infrastructure directly determines the maximum power supply capacity of the region, which in turn affects the amount of electricity sales. In this dimension, the total amount of grid infrastructure investment is chosen as one of the key influencing factors. The total investment in grid infrastructure should be compatible with the local load development level, and its calculation formula is as follows:

$$C_1^T = \sum_{i=1}^{I}\left(C_{ne,i}^T + C_{tr,i}^T + C_{au,i}^T\right) \tag{1}$$

Where T is the statistical period, C_1^T is the total investment in grid infrastructure under the statistical period, $C_{ne,i}^T, C_{tr,i}^T, C_{au,i}^T$ is the total investment in transmission line construction, distribution line construction, and transformer construction in the ith region under the statistical period, respectively. I is the total number of regions.

2.1.2 Technological transformation

Electricity technology renovation is the improvement of assets such as existing grid production equipment, facilities and related auxiliary facilities by utilizing advanced technologies, equipment, processes and materials. The total amount of investment in agricultural network upgrading and transformation is selected as one of the key influencing factors under this dimension, and its calculation formula is as follows:

$$C_2^T = \sum_{i=1}^{I}\left(C_{pe,i}^T + C_{pf,i}^T + C_{af,i}^T\right) \tag{2}$$

Where C_2^T is the total amount of investment in upgrading and transforming the agricultural network under the statistical cycle, and $C_{pe,i}^T, C_{pf,i}^T, C_{af,i}^T$ is the total amount of investment in assets such as equipment, facilities, and related auxiliary facilities for improving

the production of power grids in the *i*th region under the statistical cycle, respectively.

Reforming and upgrading rural distribution grids can improve the power supply capacity of agricultural grids, thus boosting the growth of electricity sales.

2.1.3 Intrinsic loss

When electricity is transmitted over long distances, it generates active losses in the lines and transformers, which directly affects the transmission efficiency. When the power generation remains unchanged and the loss is too high, the power transmitted to the customer side will decrease, which will inevitably cause a decrease in power sales. Under this dimension, the line loss rate is selected as one of the key influencing factors, and its calculation formula is as follows:

$$\Delta P\% = \frac{\sum_{i=1}^{8760} \Delta E_i}{E_{G\cdot\Sigma}} \tag{3}$$

Where $\Delta P\%$ is the annual average line loss rate, ΔE_i is the statistical line loss power per hour, and $E_{G\cdot\Sigma}$ is the total power generation for the year.

2.1.4 Load development

With the increasing electrification of industrial, agricultural, commercial, and residential loads, the load power demand is increasing, which is the intrinsic reason for the growth of electricity sales. Under this dimension, the maximum load power for the year is selected as one of the key influencing factors, the value of which is obtained from the yearly statistics and labeled as $P^{T}_{\max}$.

2.1.5 Power supply construction

In recent years, renewable energy has become an important part of the global new energy market. In this dimension, new energy installed capacity is chosen as one of the key influencing factors, and its calculation formula is as follows:

$$P^{T}_{\Sigma} = \sum_{i=1}^{I}\left(P^{T}_{wp,i} + P^{T}_{pi,i} + P^{T}_{ot,i}\right) \tag{4}$$

Where P^{T}_{Σ} is the total amount of new energy installed under the statistical cycle, and $P^{T}_{wp,i}, P^{T}_{pi,i}, P^{T}_{ot,i}$ is the installed capacity of wind power, photovoltaic, and other new energy in the *i*th region, respectively.

2.1.6 Power supply characteristics

While the proportion of installed new energy has increased significantly, the new energy has the characteristics of intermittent supply and high volatility, which poses a hidden danger to the safe and orderly operation of the power system, and inversely restricts its grid-connected capacity, leading to short-term power supply tightness in some areas, indirectly affecting electricity sales. Therefore, under this dimension, the maximum load utilization hours of new energy is chosen as one of the key influencing factors, and its calculation formula is as follows:

$$T_{\Sigma} = \sum_{i=1}^{8760} \frac{E_i}{C_i} \tag{5}$$

Where T_{Σ} is the maximum load utilization hours of new energy, E_i is the power generation on day *i*, and C_i is the maximum power generation on day *i*. This calculation method can solve the problem of capacity expansion.

Figure 1 shows the trend of seven types of data, including line loss rate, maximum load of electricity consumption, new energy installation and utilization hours, completion of grid infrastructure investment, completion of agricultural network upgrading and electricity sales in a region from 2015 to 2022. According to Figure 1, it can be seen that: line loss rate is approximately inversely correlated with electricity sales, installed capacity of new energy is positively correlated with electricity sales, and the rest have no consistent correlation characteristics. In this case, it is particularly important to screen key influencing factors, which may have a greater impact on electricity sales. Therefore, it is necessary to screen the key influencing factors to make the calculation of electricity sales more efficient.

2.2 Calculation method of electricity sales based on multi-factor correlation analysis

In this chapter, the Pearson correlation coefficient is first proposed to screen the key influencing factors, which provides the theoretical basis for the correlation simulation conducted in Chapter 4; Then, it introduces the calculation model of electricity sales based on the random forest algorithm, which puts forward a new idea for the computation of electricity sales under the influence of multiple factors.

2.2.1 Correlation analysis of key factors affecting electricity sales

Based on the above analysis, it is clear electricity sales are affected by a variety of factors, including, but not limited to, market demand, economic development, policy support, energy mix, etc. These factors may interact with each other and have varying degrees of influence on electricity sales. Therefore, if all the influencing factors are directly used in the calculation of electricity sales, the calculation accuracy and generalization ability of the model may be affected due to the excessive dimensions of the input data.

To solve this problem, correlation analysis is introduced to help filter key factors, which is a statistical method that measures the degree of association between variables. Through correlation analysis, the most relevant factors to electricity sales can be found and used in the calculation of electricity sales, thus reducing the dimensionality of the input data and improving the computational efficiency of the model.

In this paper, the Pearson correlation coefficient is introduced for key factor screening, whose calculation formula is as follows

$$P = \frac{\sum_{i=1}^{n}(X_i - \bar{X})(Y_i - \bar{Y})}{\sqrt{\sum_{i=1}^{n}(X_i - \bar{X})^2}\sqrt{\sum_{i=1}^{n}(Y_i - \bar{Y})^2}} \tag{6}$$

Where X is the quantitative value of the influencing factor, Y is the amount of electricity sold, $\bar{X}$ and $\bar{Y}$ represent the mean value of X and Y, respectively. The value of P is taken between −1 and 1. The larger the absolute value of P, the higher the correlation between the variables X and Y. The smaller the absolute value of P, the lower the

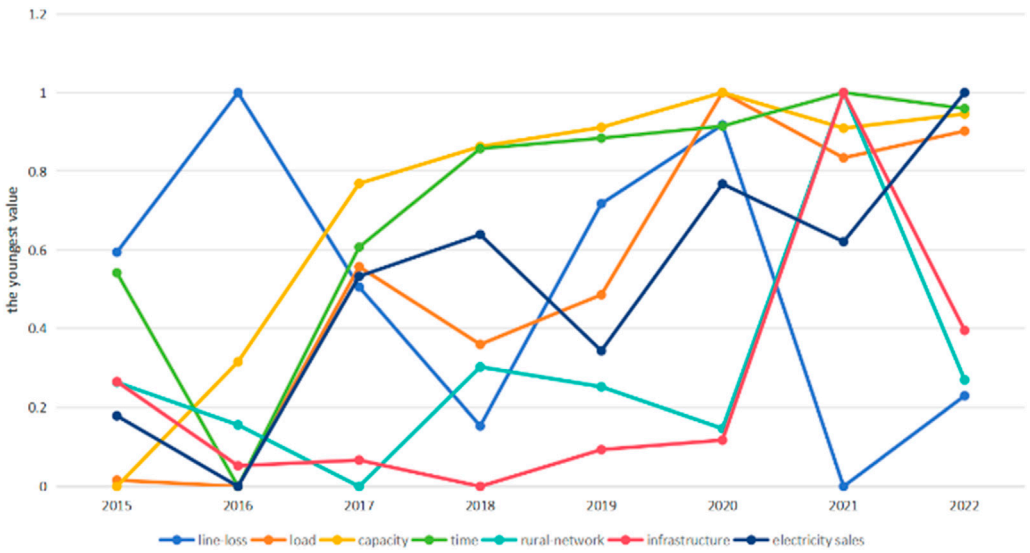

FIGURE 1
Schematic correlation between key influencing factors and electricity sales.

TABLE 1 The degree of relevance for the Pearson correlation coefficient.

Range of $\|P\|$	Degree of relevance
$0.0 \leq \|P\| \leq 0.2$	Very weakly correlated or uncorrelated
$0.2 \leq \|P\| \leq 0.4$	Weak correlation
$0.4 \leq \|P\| \leq 0.6$	Moderately relevant
$0.6 \leq \|P\| \leq 0.8$	Strong correlation
$0.8 \leq \|P\| \leq 1.0$	Highly relevant

correlation between the variable X and the variable Y. The criterion is shown in Table 1.

Therefore, according to the Eq. 6, the Pearson correlation coefficient between the sales of electricity and six types of data, such as line loss rate $\Delta P\%$, maximum load of electricity consumption $P^T_{\max}$, installed capacity of new energy P^T_{Σ}, utilization hours of new energy T_{Σ}, completion of upgrading and transformation of the agricultural network C^T_2, and completion of investment in grid infrastructure C^T_1. Then, $|P|$ greater than 0.4 were selected as key influencing factors to build the calculation model to achieve higher calculation accuracy with smaller data dimensions.

2.2.2 Computational models and methods based on random forests

This subsection establishes a mapping of the relationship between different influencing factors and electricity sales, achieving accurate linkage. In this paper, the random forest regression algorithm is selected. Random Forest Regression (RFR) algorithm as a machine learning algorithm, has been applied to several fields. Compared with regression algorithms such as SVM, the RFR algorithm does not require normalization of data and can perform feature selection through the algorithm itself, resulting in better robustness. The schematic diagram of the algorithm principle is shown in Figure 2:

The main decision tree algorithm used for random forest regression is the CART (classification and regression tree) algorithm. The decision tree algorithm alone often performs well on training data, but due to the drawbacks of overfitting, the model does not have universality and engineering application capabilities. To make up for the shortcomings of decision trees, the concept of random sampling is introduced into the RF algorithm. Its algorithmic formulation is based on the decision tree regression model, and the prediction function for each decision tree can be expressed as shown in Eq. 7:

$$f_k(x) = \sum_{j=1}^{J_k} c_{kj} I\left(x \in R_{kj}\right) \tag{7}$$

Where k denotes the kth decision tree, x denotes the input sample, J_k denotes the number of leaf nodes of the kth decision tree, c_{kj} denotes the predicted value of the jth leaf node of the kth decision tree, and R_{kj} denotes the set of samples of the jth leaf node of the kth decision tree.

The prediction function of a multiple decision tree can be expressed as:

$$f(x) = \frac{1}{K}\sum_{k=1}^{K} f_k(x) \tag{8}$$

With the number of decision trees k.

In this paper, the computational model based on random forest is calculated as follows:

Step 1: Data preparation: The dataset including the filtered influencing factors is divided into two parts, the training set Tr and the test set Te according to a certain proportion. The training set is used to train the model and the test set is used to evaluate the performance of the model.

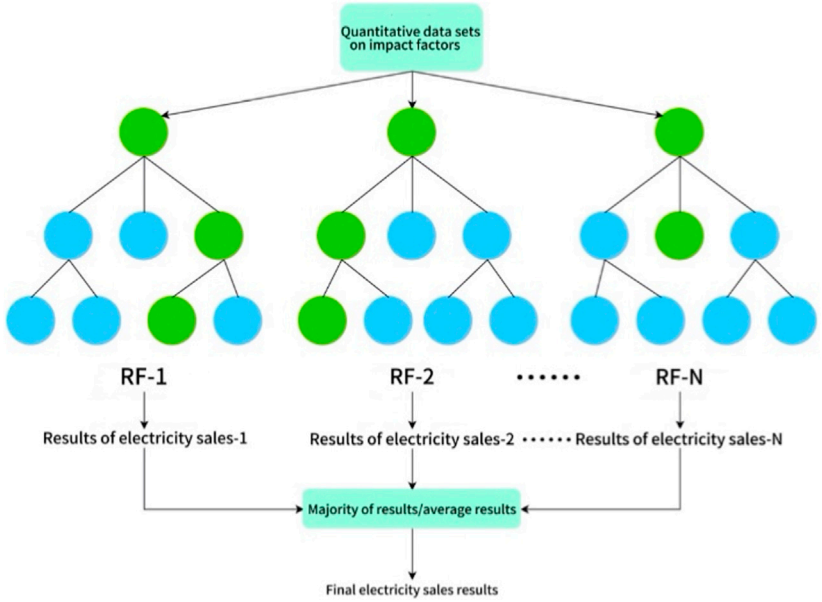

FIGURE 2
Random Forest algorithm schematic.

Step 2: Model construction and training: Initialize the model and set some model parameters to control the behavior of the random forest, such as the number of decision trees, the way of feature selection, the way of decision tree growth, and so on.

The model will construct multiple decision trees based on the samples in the training set and the values of the target variables, and perform feature selection and segmentation on each tree. This splitting continues until all the training samples at the node belong to the same class, and the optimal model for the calculation of electricity sales is obtained without pruning during the splitting process of the decision tree.

Step 3: Calculation results and evaluation: Based on the optimal random forest model, the sales electricity of the samples in the test set can be calculated. The model will average or weighted average the calculation results of each decision tree to get the final regression results. For model evaluation, the Relative Root Mean Square Error (RRMSE) is used to measure the deviation between the observed (true values) and calculated values. Its calculation formula is as follows:

$$RRMSE = \frac{\sqrt{\frac{1}{N}\sum_{t=1}^{N}\left(y_t - y_t^{'}\right)^2}}{\max(y)} \tag{9}$$

Where y_t is the true value of the electricity sales in the t th region, $y_t^{'}$ is the calculated value of electricity sales in the t th region, and $\max(y)$ is the maximum electricity sales in N regions.

3 Results

3.1 Calculation process of electricity sales

In this paper, the dataset of electricity sales of 13 cities in a region in recent years is used to conduct a case study, with a statistical period of years. These historical data come from historical data collected by power grid companies. The specific steps of electricity sales calculation are as follows:

First, the six key factor indicators of each city in each calendar year are calculated according to the six-dimensional formulas in Section 2. Among them, the data from 2015–2018 is regarded as the training set, totaling 52 sets of data, and the data in 2021 is used as the test set Te, totaling 13 sets of data Then, correlation analysis is performed on the training set Tr, and the Pearson correlation coefficients between the key factors and the electrical sales are shown in Figure 3.

Through analyzing and screening, three items with absolute values greater than 0.4, namely, line loss rate $\Delta P\%$, maximum load of electricity consumption $P_{\max}^{T}$, and completion of grid infrastructure investment C_1^T, are selected as the key factors to construct the new training set Tr' and test set Te'.

Finally, a random forest-based electricity sales calculation model is established. In the experiments, the iteration number is set to 30. Based on the training set Tr', the model is trained, and the optimal electricity sales model is obtained by continuously optimizing the loss function, and finally, the computational effect is evaluated by using the data in the test set Te' to verify the effectiveness of the model.

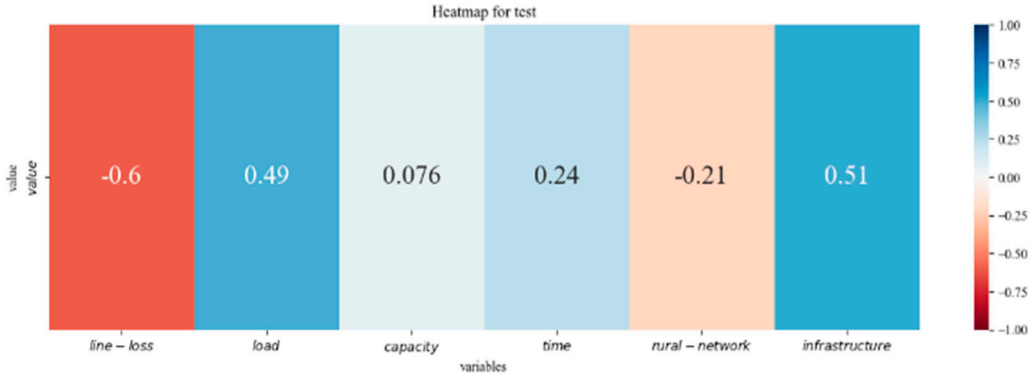

FIGURE 3
The results of the Pearson correlation analysis.

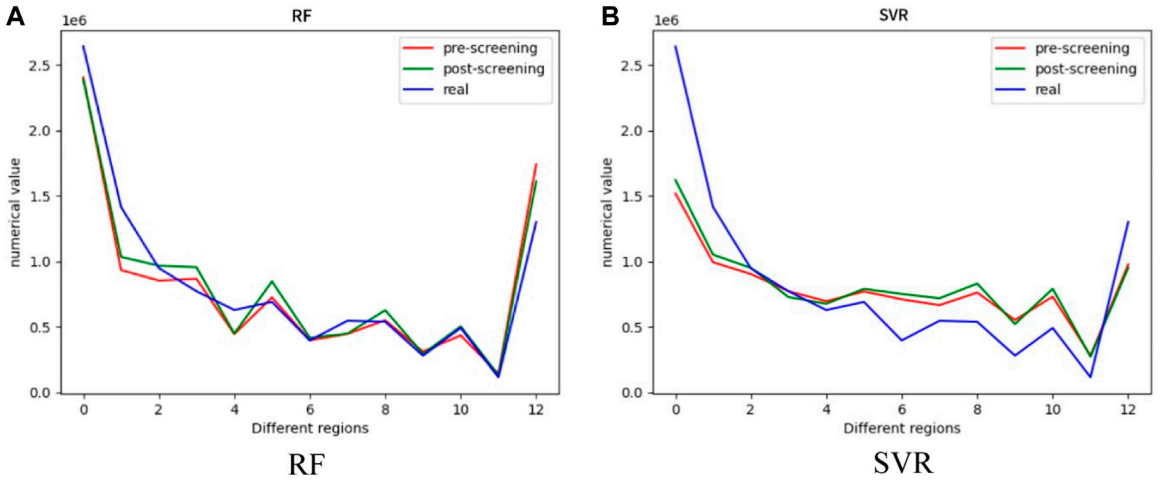

FIGURE 4
The plot of the calculation results of the two models. **(A)** RF. **(B)** SVR.

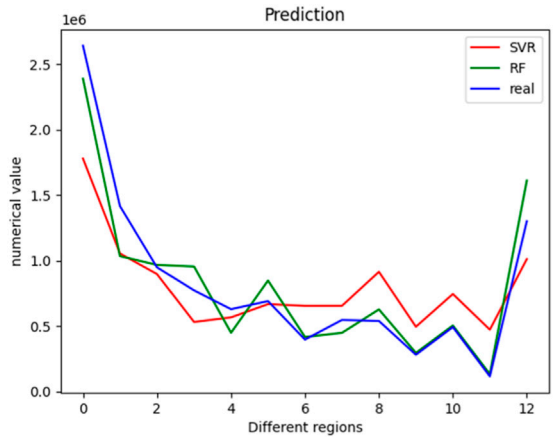

FIGURE 5
Graph of calculation results after screening of key factors.

TABLE 2 Relative error in the calculation results of electricity sales.

Model	RF (%)	SVR (%)
Pre-screening	7.79	14.39
Post-screening	6.75	13.77

3.2 Analysis of the results of electricity sales calculations

To validate the proposed method for calculating electricity sales based on correlation factor analysis and random forest, ablation experiments and comparative experiments are conducted in this section. To demonstrate the advancement of Random Forest, the SVR model is built as the control group. Moreover, the calculation models based on all influencing factors are constructed for SVR and RF in this section as a comparison, respectively.

In the calculation of electricity sales based on the SVR model, it is necessary to carry out the normalization of all the data to the same scale, which is conducive to improving the accuracy. In addition, a linear kernel function is adopted in the SVR model, which makes the calculation process simple and efficient.

The calculation results of these two models using different influencing factors on the test set are shown in Figure 4. The horizontal axis corresponds to the 13 different regions, and the vertical axis represents the values of electricity sales. The blue curve is the real value of electricity sales, while the red and green curves represent the calculation values of electricity sales before and after the screening of influencing factors, respectively. In Figure 4A, it can be seen that the trends of the calculation curves are consistent with the change of the actual values, and the calculation curve is closer to the actual one when only three key factors after screening are input. Similarly, corresponding conclusions can also be drawn in the calculation curves of electricity sales based on SVR in Figure 4B. Therefore, both models have shown better computational accuracy with only three key factors, indicating the importance of multi-factor screening.

To verify the progressiveness of the RF algorithm, Figure 5 shows the calculation curves of RF and SVR based on three key influencing factors. The blue curve in the figure shows the actual value of electricity sales, while the green and red colors represent the results of the RF model and SVR model calculations, respectively. From the figure, it can be seen that the green curve is closer to the blue curve than the red curve in the 6th to 11th regions, which means the RF model calculations have a smaller error from the true values. Compared with the RF model, although the calculation results of the SVR model generally follow the changes in actual values, there is a significant difference between them. It indicates that the electricity sales calculation method based on RF shows better performance in terms of trend capture and accuracy, while the performance of the SVR model may be affected by a variety of factors, such as data complexity, leading to a decrease in the reliability of the calculation results.

The *RRMSE* values of these two electricity sales calculation models on the whole test set are obtained according to Eq. 9, as shown in Table 2. From the indicators in the table, it can be found that the *RRMSE* of the calculation after screening the influencing factors is significantly smaller than before, and based on this, the *RRMSE* based on the RF model is lower. Therefore, the electricity sales calculation model based on random forest proposed in this paper can reflect the relationship between multi-factors and power sales and effectively improve the calculation precision.

4 Discussion

By analyzing the importance of calculating electricity sales for power grid investment, construction, and planning development, this article has proposed to explore the inherent relationship between multi-factors and electricity sales, which is an effective way to improve the calculation accuracy. The Pearson correlation coefficients have been calculated and three key factors have been screened out. Then, a calculation model of electricity sales is constructed based on the RF method. The comparative experimental results show that the proposed model has smaller computational errors and higher accuracy. It can better achieve accurate linkage between investment and electricity sales for power grid companies, improve the refinement of management, and enhance the economic benefits of enterprises.

In addition, due to the limited dataset, this work also has limitations in analyzing the dimensions that affect electricity sales. At the same time, there is a possibility of further optimization in the constructed RF regression calculation model. Further research will be conducted in the future to address these issues.

Data availability statement

The datasets analyzed during the current study are not publicly available because they involve the data security of the operating unit, but are available from the corresponding author on reasonable request.

Author contributions

JZ: Writing–review and editing. JT: Writing–review and editing. LW: Writing–review and editing. YS: Writing–original draft. WZ: Writing–original draft, Writing–review and editing.

Funding

The author(s) declare that no financial support was received for the research, authorship, and/or publication of this article.

Conflict of interest

Authors JZ and LW were employed by Tianshui Power Supply Company of State Grid. Author JT was employed by State Grid Gansu Electric Power Company.

The remaining authors declare that the research was conducted in the absence of any commercial or financial relationships that could be construed as a potential conflict of interest.

Publisher's note

References

Billinton, R., Chen, H., and Ghajar, R. (1996). Time-series models for reliability evaluation of power systems including wind energy. *Microelectron. Reliab.* 36 (9), 1253–1261. doi:10.1016/0026-2714(95)00154-9

Cai, X., and Liao, Y. (2021). Transformer order demand forecasting based on grey forecasting model. *IOP Conf. Ser. Earth Environ. Sci.* 831 (1), 012004. doi:10.1088/1755-1315/831/1/012004

Chan, B. L., FengSu, S., and Yen, T.H. (2010). High-precision forecast using grey models. *Int. J. Syst. Sci.* 32 (5), 609–619. doi:10.1080/00207720120323

Dudek, G. (2016). Pattern-based local linear regression models for short-term load forecasting. *Electr. Power Syst. Res.*, 130. doi:10.1016/j.epsr.2015.09.001

Ei-Fouly, T. H. M., Ei-Saadany, E. F., Salama, M. M. A., El-Fouly, T., and El-Saadany, E. (2006). Grey predictor for wind energy conversion systems output power prediction. *IEEE Trans. Power Syst.* 21 (3), 1450–1452. doi:10.1109/tpwrs.2006.879246

Kim, M., Lee, S., and Jeong, T. (2023). Time series prediction methodology and ensemble model using real-world data. *Electronics* 12 (13), 2811. doi:10.3390/electronics12132811

Lai, G. S., Wu, G. Y., Lan, Z. Q., Wu, X. F., and Xia, S. H. (2023). Annual contribution electricity forecasting model based on logistic regression analysis. *J. Phys. Conf. Ser.* (1), 2530. doi:10.1088/17426596/2530/1/012008

Li, G. D., Wang, C. H., Nagai, M., Masuda, S., et al. (2011). A research on short-term load forecasting problem applying improved grey dynamic model. *Int. J. Electr. Power & Energy Syst.* 33 (4), 809–816. doi:10.1016/j.ijepes.2010.11.005

Madden, C. (2005). Indicators for arts and cultural policy: a Global perspective. *Cult. Trends* 14 (3), 217–247. doi:10.1080/09548960500436824

Mohamed, Z., and Bodger, P. (2004a). Forecasting electricity consumption in New Zealand using economic and demographic variables. *Energy* 30 (10), 1833–1843. doi:10.1016/j.energy.2004.08.012

Mohamed, Z., and Bodger, P. (2004b). A comparison of Logistic and Harvey models for electricity consumption in New Zealand. *Technol. Forecast. Soc. Change* 72 (8), 1030–1043. doi:10.1016/j.techfore.2004.05.002

Morita, H., Kase, T., Tamura, Y., and Iwamoto, S. (1996). Interval prediction of annual maximum demand using grey dynamic model. *Int. J. Electr. Power Energy Syst.* 18 (7), 409–413. doi:10.1016/0142-0615(95)00019-4

Pektas, A. O., and Cigizoglu, H. K. (2013). ANN hybrid model versus ARIMA and ARIMAX models of runoff coefficient. *J. Hydrology* 50 (13).

Sarduy, J. R. G., Di Santo, K. G., and Saidel, M. A. (2016). Linear and non-linear methods for prediction of peak load at University of Sao Paulo. *Measurement*, 78. doi:10.1016/j.measurement.2015.09.053

Sarkodie, S. A. (2017). Estimating Ghana's electricity consumption by 2030:An ARIMA forecast. *Energy Sources Part B-economics Plan. Policy* 12 (10), 936–944. doi:10.1080/15567249.2017.1327993

Toyoda, J., Chen, M., and Inoue, Y. (1970). An application of state estimation to short-term forecasting. *IEEE Trans PAS* 89 (7). doi:10.1109/tpas.1970.292823

Vu, D. H., Muttaqi, K. M., and Agalgaonkar, A. P. (2015). A variance inflation factor and backward elimination-based robust regression model for forecasting monthly electricity demand using climatic variables. *Appl. Energy*, 140. doi:10.1016/j.apenergy.2014.12.011

Zhou, P., Ang, B. W., and Poh, K. L. (2005). A trigonometric grey prediction approach to forecasting electricity demand. *Energy* 31 (14), 2839–2847. doi:10.1016/j.energy.2005.12.002

frontiers | Frontiers in Energy Research

TYPE Original Research
PUBLISHED 03 January 2024
DOI 10.3389/fenrg.2023.1338195

OPEN ACCESS

EDITED BY
Rufeng Zhang,
Northeast Electric Power University, China

REVIEWED BY
Yunyang Zou,
Nanyang Technological University, Singapore
Han Wang,
Shanghai Jiao Tong University, China

*CORRESPONDENCE
Qipei Zhang,
zhangqipei@sgepri.sgcc.com.cn

RECEIVED 14 November 2023
ACCEPTED 13 December 2023
PUBLISHED 03 January 2024

CITATION
Zhang Q, Tang N, Lu J, Wang W, Wu L and Kuang W (2024), A hybrid RBF neural network based model for day-ahead prediction of photovoltaic plant power output.
Front. Energy Res. 11:1338195.
doi: 10.3389/fenrg.2023.1338195

A hybrid RBF neural network based model for day-ahead prediction of photovoltaic plant power output

Qipei Zhang*, Ningkai Tang, Jixiang Lu, Wei Wang, Lin Wu and Wenteng Kuang

NARI Research Institute, NARI Technology Co, Ltd, Nanjing, Jiangsu, China

Renewable energy resources like solar power contribute greatly to decreasing emissions of carbon dioxide and substituting generators fueled by fossil fuels. Due to the unpredictable and intermittent nature of solar power production as a result of solar radiance and other weather conditions, it is very difficult to integrate solar power into conventional power systems operation economically in a reliable manner, which would emphasize demand for accurate prediction techniques. The study proposes and applies a revised radial basis function neural network (RBFNN) scheme to predict the short-term power output of photovoltaic plant in a day-ahead prediction manner. In the proposed method, the linear as well as non-linear variables in the RBFNN scheme are efficiently trained using the whale optimization algorithm to speed the convergence of prediction results. A nonlinear benchmark function has also been used to validate the suggested scheme, which was also used in predicting the power output of solar energy for a well-designed experiment. A comparison study case generating different outcomes shows that the suggested approach could provide a higher level of prediction precision than other methods in similar scenarios, which suggests the proposed method can be used as a more suitable tool to deal such solar energy forecasting issues.

KEYWORDS

photovoltaic power plant, solar energy forecasting, radial basis function neural network, whale optimization algorithm, low carbon

1 Introduction

In addition to reducing fossil fuel use and assisting electric grid operators in meeting peak demand during peak hours, solar photovoltaic (PV) energy has become a rapidly expanding renewable energy source and major energy supply (Hong et al., 2019; Jaihuni et al., 2022). With the advent of this kind of renewable relevant technology, solar power production is being integrated more efficiently into the electrical grid with operation features (Wentz et al., 2022). Nevertheless, solar PV system operators face challenges when their output power varies due to climate patterns (such as cloudy, rainy, and sunny days; abrupt weather changes; winter weather; and so on). It is essential for the system to operate reliably and securely in these cases when solar PV power generated is forecasted accurately with good enough precision (Li et al., 2019; Succetti et al., 2020). Especially for the short-term forecasting that involves numerous uncertainty sources, which become extremely hard for conventional methods depends heavily on the time series modeling (Inman et al., 2013;

Tuohy et al., 2015). On the other hand, PV plant power output forecasting is the process of forecasting solar energy production at the intersection of different domain knowledge in different fields, such as the energy industry, meteorology, data science, and machine learning (Inman et al., 2013; Gutierrez-Corea et al., 2016; Reindl et al., 2017). By forecasting solar irradiance, grid operators, power traders or solar farms can plan and manage better electricity production and consumption. This is essential to ensure the stable operation of the power grid, reducing operating costs, and promote the widespread usage of renewable energy sources (Islam et al., 2008; Ellabban et al., 2014). There are a variety of methods for solar irradiance and energy prediction (Blaga et al., 2019; Han et al., 2022), including physical model-based methods, statistical methods and machine learning methods that are mostly dealing with short-term forecasting issue. Within these methods, physical model-based approaches depend a lot on modeling and simulation of physical factors such as solar radiation, clouds, and atmospheric conditions, which are even highly dynamic during any short time periods. In comparison, statistical methods, presented in most current works, build data-driven probabilistic models that can be based on historical data to predict short-term future solar energy production (Blaga et al., 2019; Snegirev et al., 2019; Han et al., 2022) either in long-term or short-term time period. Machine learning methods, especially deep learning techniques, are also playing an increasingly important role in solar energy prediction. These methods learn and automatically extract complex patterns in the solar power relevant data to provide more accurate predictions. However, due to the complexity and uncertainty of weather conditions, solar forecasting remains a challenging task (Zhang et al., 2013). In order to improve the accuracy of prediction, it is necessary to consider a variety of factors, such as geographical location, climatic conditions, seasonal changes, equipment performance and so on (Sangrody et al., 2017; Sobri et al., 2018). In addition, real-time data acquisition and processing, model selection and optimization, uncertainty estimation are also key issues in solar energy prediction.

In general, solar forecasting is a complex and important task that involves knowledge and technology from multiple fields. With the popularization of renewable energy and the advancement of intelligent grid, solar energy prediction will play an even more important role in the future (Vanderstar et al., 2018; Wentz et al., 2022). The work in (Hong et al., 2019) describes a number of solar power prediction methods that mostly deal with short-term forecasting issues. A significant research trend is that recent works have focused heavily on deep learning techniques that are purely data-driven with model-free design, especially for short-term small-scale forecasting problem. Ref (Jaihuni et al., 2022) demonstrates the effectiveness of deep Recurrent Neural Networks (RNNs) in estimating 1-week solar radiance using highly accurate Canadian solar data. Ref (Wentz et al., 2022) shows that the power prediction technique using a radiance metric and Long Short-Term Memory (LSTM) has a Mean Absolute Percentage Error (MAPE) of 6.95% that is highly below the average MAPE of conventional methods. Ref (Succetti et al., 2020) uses a multiple variable network with associated parameters such as temperature, wind speed, humidity, solar radiation, and PV power output, and achieves a Normalized Mean Absolute Error (NMAE) of 7.91%, which can be taken as good enough record in day-ahead short-term PV power output forecasting.

In addition to ANN and Fuzzy Logic, soft computing methods were applied to obtain accurate energy predictions. A Recurrent Neural Network method for estimating insolation was presented in ref (Li et al., 2019) A number of ANN methods were employed in ref (Obiora et al., 2021) for predicting solar irradiation, while both multivariate and univariate methods were employed for forecasting power. A weather-driven hybrid approach was used in ref (Akhter et al., 2022) for forecasting solar power output daily, and for decreasing adverse effects the following day. A climate-driven prediction model was used in Ref (Gao et al., 2019) for predicting solar plants for a day ahead, overcoming the effects of fluctuation. Further, ref (Sridharan, 2023) examined how multi-linear regression, polynomial regression, logarithmic regression, and artificial neural networks can be employed for predicting PV power using data from the prior year. Ref (Sangrody et al., 2017) applied Backpropagation Neural Network (BPNN) using Lavenberg - Marquardt algorithms to update weights.

A solar power prediction method based on echo state networks and principal component analysis was examined in ref (Ling et al., 2023). ANNs are not the only models used to forecast solar power; deep learning is likewise used. In ref (Zhang et al., 2019), deep recurrent neural networks using long short-term memory units (DRNN-LSTM) were used to forecast solar power and loads using day-ahead and weekly-ahead historical data. A radiance prediction algorithm based on LSTM deep neural networks was used in ref (Jaihuni et al., 2022) to analysis the radiance impact on solar energy. In neural network modeling, training non-linear variables requires considerable effort, despite the fact that many neural network schemes are available. In spite of their problems with complexities and formulations, meta-heuristic algorithms (MAs) serve as efficient optimization methods that can help improve the parameter-tuning. Therefore, numerous MAs are widely applied for optimizing neural network nonlinear variables, including grey wolf optimizations, monarch butterfly optimizations (MBOs), genetic algorithms (GA), biogeography-based optimizations (BBOs), particle swarm optimizations (PSO), glowworm swarm optimizations (GSOs), and whale optimization problems (WOAs), so on. Radical basis function neural networks are known for their simplicity and ability to approximate non-linear behavior. An artificial bee colony method was used in (Alzaeemi and Sathasivam, 2020) for training fuzzy RBFNNs using data granulation. In (Tsoulos and Charilogis, 2023), a combined PSO-GA approach was employed for optimizing the evolution of RBF neural network to predict rain.

The study proposes and implements a whale optimization-driven RBF neural network to solve the solar production problem. The study's main contributions are as follows, 1) the study uses Whale optimization-driven RBF scheme to train non-linear variables in RBF scheme for the first time. 2) Efficiency of suggested WOA-driven model training techniques was evaluated against conventional MA techniques on a number of nonlinear model problems.

Following are the sections in the study. Section 2 presents the general framework and preliminary methods for the PV plant power output forecasting scenarios, including the proposed WOA-driven RBF approach. Section 3 presents the simulations and case study

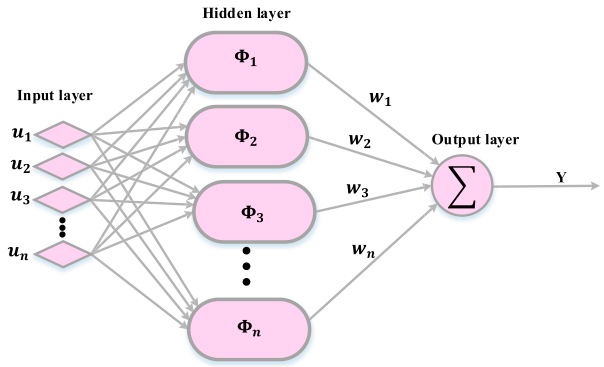

FIGURE 1
RBF network framework.

results to implement the test cases with demonstration of the numerical values for the performance validation. Section 4 concludes and discusses the major founding with suggestion of the future research work.

2 Preliminaries of the framework

The following part discusses preliminary techniques such as competitive swarm optimization and the canonical RBFNN, which provides good fundamental for the proposed PV plant power output forecasting framework.

2.1 RBFNN

Traditionally, RBF neural networks are multi-input and single-output (MISO) neural network structures, using Gaussian functions acting as the activation function. Figure 1 shows three layers of RBF neural networks, consisting of input layer, hidden layer, and output layer. The basic structure could be represented as the following Eq. 1:

$$y(t) = \sum_{i=1}^{n} w_i . \varnothing_i (X) \tag{1}$$

In which, $y(t)$ shows the neural network model output during t. w_i shows the linear output weight of the i^{th} node hidden layer. For input vector, the radial basis function φ_i can be determined as standard Gaussian function formulation in the following way of Eq. 2:

$$\varnothing_i (X) = \exp\left(-\frac{1}{2\sigma_i^2} \| X - c_i \|^2 \right), i = 1, 2, \ldots, n \tag{2}$$

Where, σ_i shows the Gaussian distributed width and c_i shows center of the i^{th} hidden node. n shows the number of hidden layers. Euclidean distance formulas and denominator contain non-linear function variables, requiring efficient optimization methods. The weighting parameters of RBF-based neural network can be efficiently computed via combination with any computationally tractable heuristic optimization method, which makes it easily for parameter tuning compared with other hyper-parameter sensitive methods.

2.2 Whale optimization algorithm (WOA)

WOA is an optimization algorithm derived from bubble-net hunt methods used in meta-heuristic algorithms (Mi et al., 2016). In this algorithm, it is described how humpback whales hunt. Humpback whales follow the usual bubbles when they encircle preys, creating a circle or '9-shaped path'. Basically, bubble-net hunting or feeding is explained by humpback whales diving 10–15 m in water and subsequently starting to generate bubbles encasing preys, followed by following the bubbles and moving up. According to the algorithm presented in (Mi et al., 2016), Whale Optimization algorithm (WOA) is modeled in the following ways.

2.2.1 An encircled prey formula

After encircling the target, the humpback whales update their location to reach the optimum solution over a series of iterations.

$$\vec{D} = \left| C.\vec{X}(t) - X(t) \right| \tag{3}$$

$$\vec{X}(t+1) = \vec{X}(t) - \vec{A}.\vec{D} \tag{4}$$

In which, $\vec{A}$, $\vec{D}$ show coefficient vectors. t shows present iteration. $\vec{X}^*(t)$ shows the position vector of optimal solution. $X(t)$ shows the position vector. $\vec{A}$, $\vec{D}$ can be described in the following way:

$$\vec{A} = 2\vec{a} * r - \vec{a} \tag{5}$$

$$\vec{A} = 2 * r \tag{6}$$

In which, $\vec{a}$ reduces linearly from two to zero over during iteration and r shows a randomly selected number between [0, 1]. In this way, Eqs 3–6 could control the optimal search direction and learning rate of the global optimality convergence.

2.2.2 Bubble-net attack approach

Humpback whale bubble-net behaviors can be mathematically described using 2 approaches:

A. **Method for shrinking encirclement:** In the method, $\vec{a}$ was linearly decreased from two to zero. Random value for vector in domain amongst $[-1, 1]$.
B. **Spiral updating position:** As a result of the helix-shaped motion of the humpback whales and target, the following formula can be derived as Eq. 7:

$$\vec{X}(t+1) = \vec{D}' * e^{bt} * \cos(2\pi l) + \vec{X}(t) \tag{7}$$

In which, l represents a randomly selected number between $[-1, 1]$. b shows fixed logarithmic shape. $\vec{D}' = |\vec{X}^*(t) - X(t)|$ shows the distance among i^{th} whale to the target mean optimal solution.

During optimization, whales are assumed to follow either a shrinking encirclement or logarithmic path 50%–60% of the time. The mathematical model is based on the following Eq. 8:

$$\vec{X}(t+1) = \begin{cases} \vec{X}(t) - \vec{A}\vec{D} & if \quad p < 0.5 \\ \vec{D}'.e^{N}.\cos(2\pi l) + \vec{X}(t) & p \geq 0.5 \end{cases} \tag{8}$$

In which, p is a randomly selected parameter in the value range of $[0, 1]$. $\vec{A}$, $\vec{D}$ still indicate the coefficient vectors to tune the learning rate of optimal solutions.

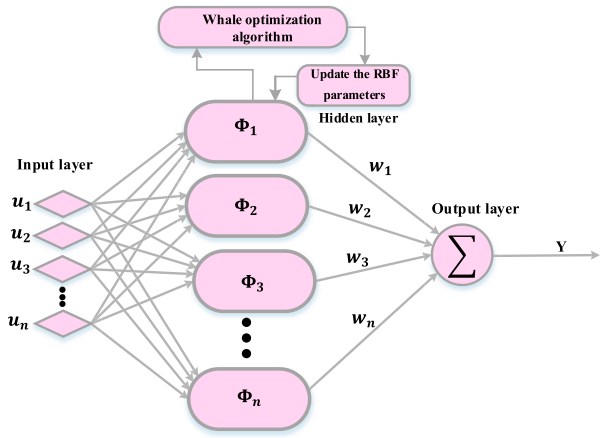

FIGURE 2
Process of WOA optimized RBF network.

TABLE 1 PV Power plant information.

Variables	Amount
Capacity	1 *MW*
MJB panels	02 Nos
Inverters	02 Nos
Entire number of SCB (String connection box)	24 Nos
Entire number of strings	200
Maximum string current	7.9 *A*

2.2.3 Searching for target

Exploration is done using $\vec{A}$ to find the target. Additionally, $\vec{A}$ accepts values above 1 or below −1. There are 2 requirements for exploration.

$$\vec{D} = \left|\vec{C}.\overrightarrow{X_{rand}} - \vec{X}\right| \tag{9}$$

$$\vec{X}(t+1) = \overrightarrow{X_{rand}} - \vec{A}\vec{D} \tag{10}$$

Lastly, the following should be followed (Zhang et al., 2013):

- $|\vec{A}| > 1$ would enforce exploration to WOA algorithm for determining global optimal avoid local optimal.
- $|\vec{A}| < 1$ should be chosen in order to update the location of present searching agent/optimal solution.

3 Suggested WOA optimized RBF neural network

An RBF neural network's architecture and variables must be defined, just like any other neural network scheme. A scheme training process can be divided into three main categories depending on the flexibility of its determination. The first one involves determining the model structure and non-linear variables via trial and error and subsequently obtaining linear

TABLE 2 PCC among the plant output power and various weather variables within 2022 data.

Factor	PCC
Wind direction	$6e-3$
Wind speed	$101e-3$
Module temperature	$802e-3$
Ambient temperature	$106e-3$
Solar irradiance	$992e-3$

weights using minimum squares or various approximations. The second one involves fixing the model structure including input and hidden node number and allowing the optimization approach for training the non-linear and linear variables. Lastly, the third one involves simultaneous training of the model structure and variables. As part of the Model Training Type 2 presented in the study, the WOA approach has been used to train the non-linear and linear variables based on an established neural network model framework. As a fitness function for optimizing RBF networks, the root mean square error (RMSE) has been used, as shown in Eqs 5, 6)

$$\min f = \sqrt{\frac{1}{N_m}.\sum_{i=1}^{N_m}(\hat{y} - y_m)^2} \tag{11}$$

In which, $\hat{y}$ shows the forecast value and y_m shows the measured information set. It is important to calculate each parameter in advance of computing $\hat{y}$, as expressed in Eq. (12):

$$\hat{y} = \sum_{i=1}^{n_h} w_i.\exp\left(-\frac{1}{2\sigma_i^2}\|X - c_i\|^2\right), i = 1, 2, \ldots, n \tag{12}$$

An RBF neural network training procedure can likewise be considered an unrestricted optimization problem along with the objective function. The decision parameters are expressed in the following manner, assuming i and j are the input node and hidden node in Eq. (13):

$$\text{particle}(i) = \left[c_{11}, c_{21}, \ldots, \sigma_1, w_1, c_{12}, c_{22}, \ldots, c_{j2}, \sigma_2, w_2, \ldots . c_{1k}, c_{2k}, \ldots, c_{jk}, \sigma_k, w_k\right] \tag{13}$$

There is full encoding of non-linear variables in all hidden nodes and their associated linear weighting factors. Figure 2 shows the in-depth process of this suggested WOA-driven RBF model approach:

1) Initialization:
   (a) Input information vectors are selected and adopted into the RBF neural networks; b) The number of hidden nodes for RBF neural networks is determined and pre-defined according to empirical analysis; c) The decision parameters based on the current framework are encoded according to the solar power predication factors; d) Decision parameter values of the entire population are initialized by random values;
2) Optimization procedure:
   (a) The mean value $X_k^{'}(t)$ of the entire population is calculated;
   b) The entire population is divided into two categories

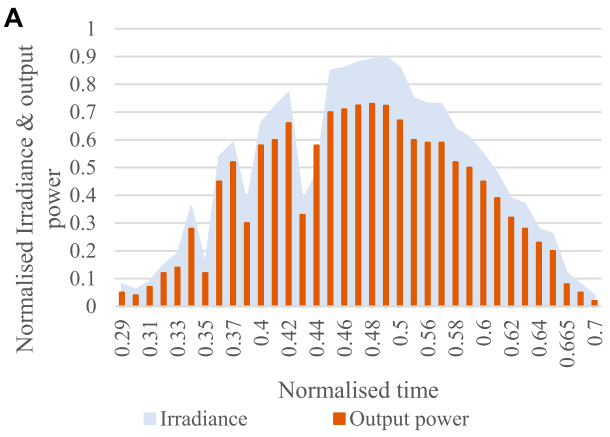

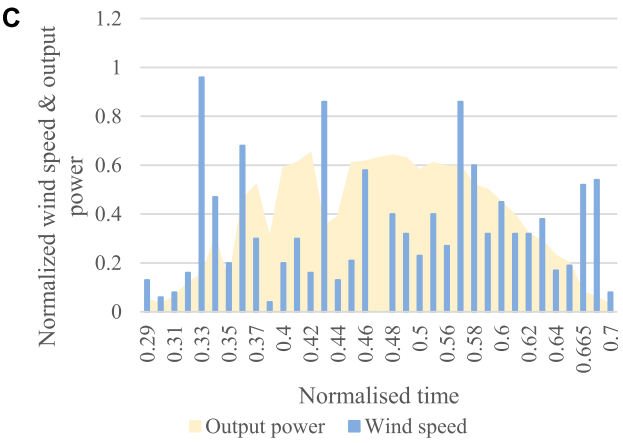

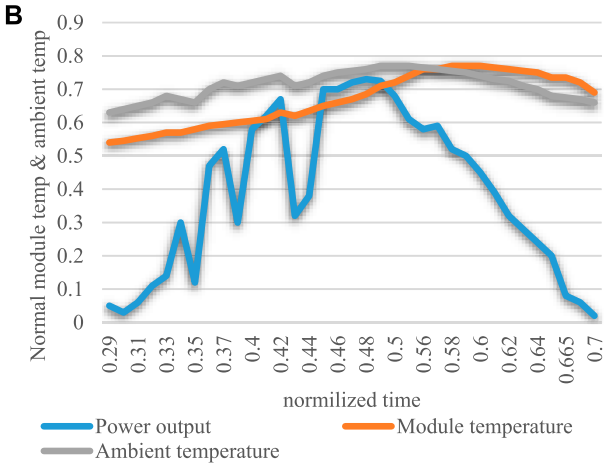

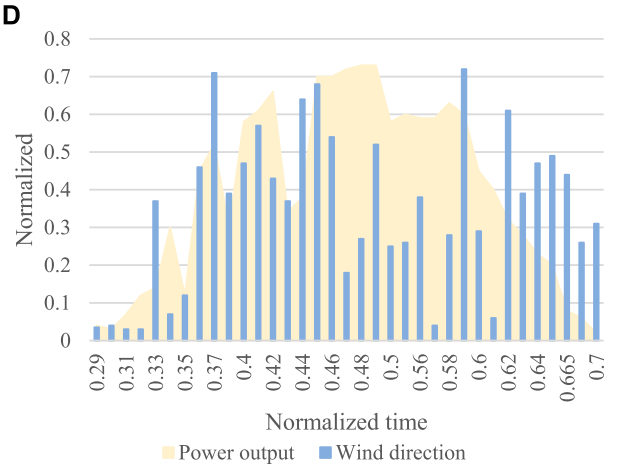

FIGURE 3
A representation of normalized weather variables and plant output power against normalized time for 8 January 2022 **(A)** Radiance **(B)** Ambient and Module temperatures **(C)** Wind speed and **(D)** Wind direction.

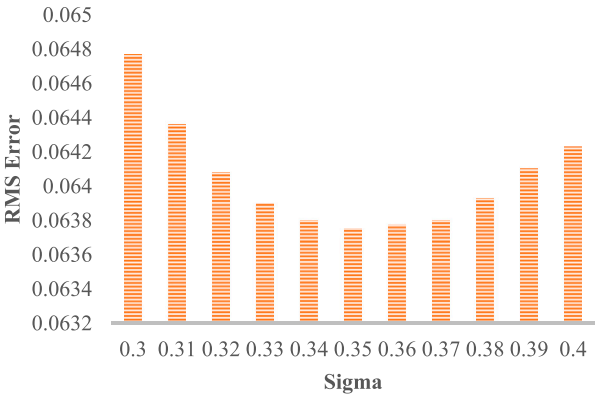

FIGURE 4
RMSE *versus* sigma for RBF.

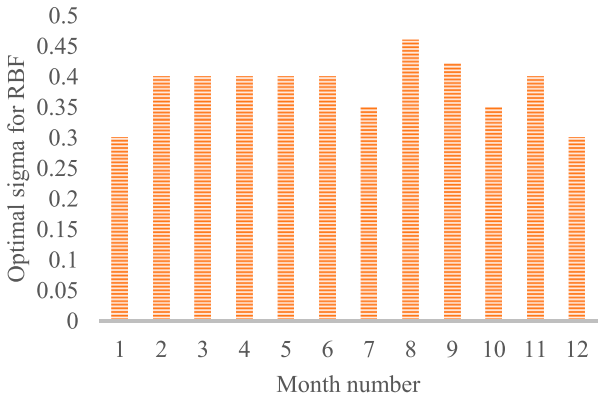

FIGURE 5
Optimum Sigma (σ_{opt}) for RBF training monthly.

containing the same number of particles; c) one population from every category is selected at the random group and the fitness function Eq. 11 for the two particles is calculated; d) The loser based on Eqs 9, 10 is updated; e) The new loser and the winner are added to the upcoming generation population; f) The step 2)-(c) to step 2)-(e) should be repeated until there are no whales left.

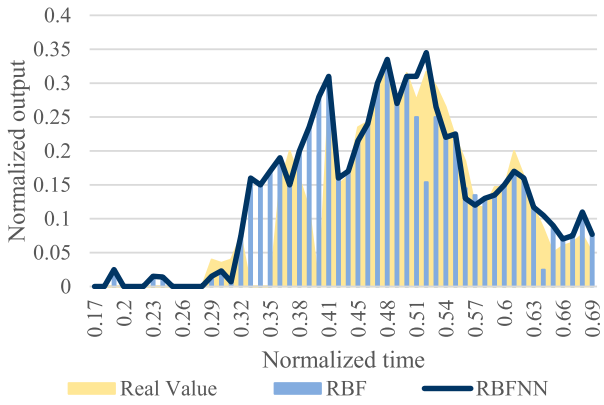

FIGURE 6
Comparing the output of RBF, FFNN, decision-driven algorithm and the real power production of the plant.

3) Finalization procedure:
   (a) The maximum number of iterations should be determined according pre-defined tolerance; b) The step 2)-(a) should be repeated until the max number of iterations has been reached; c) The procedure is terminated via iteration limitation or convergence tolerance with the optimal value generated.

4 Simulation and case study

Even though PV power output is mainly determined by radiance, other weather conditions and associated parameters (the temperature of the module, surrounding temperature, the direction and speed of the wind) are also important and have impact on the ultimate PV plant power output. For instance, the open circuit voltage of crystalline silicon PV modules reduces in response to increasing temperature, reaching a value of −0.45%/K, and short-circuit current ranges from 0.4%/K to 0.9%/K. Consequently, wind speed is usually used as a predicting variable to account for the cooling impact, heat dissipation, and PV panel cleaning. Those weather and environmental conditions could be coded as corresponding variables in the RBFNN as modified input data. The short-term forecasting for PV plant power output should include considerable determining factors to guarantee the accuracy and forecasting reliability.

4.1 Simulation setup

Table 1 shows the plant information. Information is captured by the SCADA system daily and is used to monitor and record weather conditions. A weather variable's output is correlated using Pearson Correlation Coefficient (PCC). The Pearson Correlation Coefficient is described by Eq. (14) in which x-axis shows the time series of output power, y-axis shows the time series for all climate dependent parameters.

$$PCC = \frac{n(\sum xy) - (\sum x)\left(\sqrt{y}\right)}{\sqrt{\left[n\sum x^2 - \left(\sqrt{x}\right)^2\right]\left[n\sum y^2 - \left(\sum y\right)^2\right]}} \quad (14)$$

TABLE 3 The minimal forecasting RMSE error for different weather conditions in different seasons.

Weather conditions	Clear-sky	Cloudy
Winter	0.0642	0.0724
Spring	0.0611	0.0695
Summer	0.0622	0.0718
Autumn	0.0628	0.0709

The PCC parameter setting for a weather variable is shown in Table. 2 to illustrate the association among the variable and the plant's power output. An example of a radiance and power output profile is shown in Figure 3A, in which a near-unity PCC value predicts that radiance and power output are heavily correlated. In contrast, variables such as module temperature, ambient temperature, and the direction and speed of the wind show less correlation with power output (see Figures 3B, C, D). Wind variables can be key to forecasting unplanned blackouts in coastal areas such as Odisha due to adverse climate conditions.

The networks are trained using information from 2012 to 2013. The information from 2022 to 2023 is either inaccurate (for example, incorrect SCADA reading) or indicates unusual circumstances (for example, blackouts). In the absence of power generation, the information is eliminated using a MATLAB program. MATLAB's 'nntool' function is used to train the network during July 2022 and 2023 datasets to produce forecasts in July 2024. A comparison of the trained ANN's output with the calculated 2024 information set helps to determine how effective the algorithm is.

4.2 Method performance

A neural network schema is trained for information gathered in July 2022 and July 2023 and evaluated for information gathered in July 2024. A comparison of the approach with the real output information of 18 July 2014 is shown in Figure 4. The optimum Sigma (σ_{opt}) of RBF training monthly is shown in Figure 5. In Figure 6, the proposed approach and others are simulated alongside the PV power generation of the plant measured on 18 July 2024.

As a result of the proposed approach's low RMSE, it produces an improved fit compared with other existing methods that usually range from 0.7–0.9 for RMSE. As well as a low RMSE, the algorithm has also produced an irregular envelope around the real output with limited upper bound and lower bound. In this way, WOA-RBF actually increases power output envelope by having greater RMSE than the proposed approach. Although the proposed approach has the lowest RMSE among others, simulated output power drops sharply around 0.5 during normalized time. There is a possibility that at the RBFEF training, one point of the dataset was anomalous near the input data point, which can cause unexpected drops in simulated output.

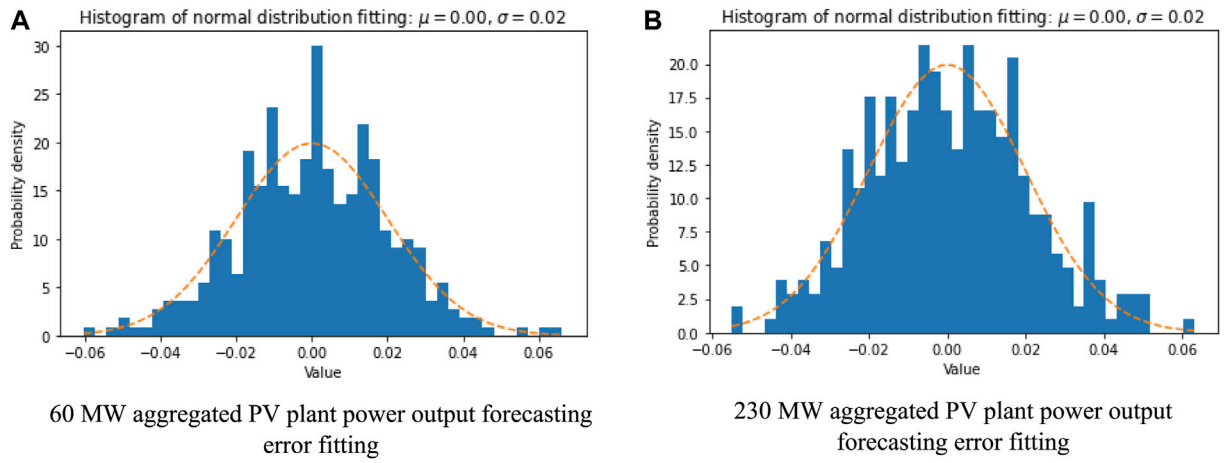

FIGURE 7
The forecasting error with normal distribution fitting for different large-scale aggregated PV plant. **(A)** 60 MW aggregated PV plant power output forecasting error fitting. **(B)** 230 MW aggregated PV plant power output forecasting error fitting.

4.3 Analysis in different application scenarios

With the consideration of different weather condition effect, the proposed method has also been tested in different application scenarios via RBFNN parameter tuning according to the clear-sky day forecasting or cloudy day forecasting applications in different seasons.

By tuning the optimal hyper-parameters of RBFNN, Table 3 shows the minimal forecasting RMSE error of PV plant power output for different weather conditions in different seasons. Compared with other forecasting methods, the proposed one could deal with more different scenarios since it depends little on any specific features that should be pre-defined. It is easily observed that generally speaking most short-term PV power output forecasting results are better in clear-sky day conditions than cloudy day conditions due to the uncertain shadowing effect of massive cloud impact on the sunny irradiance. It is worth mentioning that this phenomenon is also observed in other existing methods. The specific forecasting RMSE error also varies with the season change over the whole year, since the temperature or humidity condition will play a role as well in determining the specific energy generation level of PV plant power output.

In Figure 7, we also try the normal distribution fitting for the forecasting errors to observe the error reduction and error growth phenomenon in application scenarios of different aggregated PV plant power output capacity. It can be found that for smaller 60 MW PV plant power output forecasting, the fitting error has a more stochastic error distribution since the internal aggregation of PV cell units usually suffers less counteracting effect compared with larger 230 MW PV plant power output forecasting.

On the other hand, the operation of larger PV plant would provide larger resource capacity and better forecasting reliability margin to deal with the manual feature extraction issues. It is believed that with proper design of the hyper-parameter of RBFNN framework and gradient calculation of WOA optimization, the short-term PV plant power output forecasting could be self-adaptive to the changes of external environmental weather conditions and power dispatch scheduling of each PV generation unit.

5 Conclusion

The work proposes a whale optimization algorithm combined with RBFNN to forecast solar production. The suggested approach framework allows for simultaneous determination of linear and non-linear variables in RBFs. Several non-linear evaluations and a forecast task for solar production have confirmed its competitiveness. This paper also proposes the whale optimization algorithm using RBF to help forecast PV power plant output directly day-ahead in advance with acceptable forecasting errors. A comparison study case is experimented to generate different outcomes that shows the proposed approach could provide a higher level of prediction precision than other conventional methods in similar scenarios, especially for PV plant power output in various conditions. According to the specific application scenarios, this work suggests and concludes the proposed method can be used as a more suitable tool to deal with such solar energy and PV plant power output forecasting problems. In the future work, we will consider more sources of uncertainty and combine the current method with some auto-encoder framework to efficiently extract the significant features of the forecasting problem, which would further improve the short-term prediction accuracy for large-scale PV plant capacity. The proposed method can also be combined with the coupled operation framework to facilitate the end-to-end decision-making of forecasting-based power system operation.

Data availability statement

The original contributions presented in the study are included in the article/Supplementary Material, further inquiries can be directed to the corresponding author.

Author contributions

QZ: Conceptualization, Investigation, Software, Writing–original draft, Writing–review and editing. NT: Conceptualization, Data curation, Investigation, Methodology, Writing–review and editing. JL: Conceptualization, Data curation, Investigation, Methodology, Software, Supervision, Writing–review and editing. WW: Formal Analysis, Project administration, Validation, Writing–original draft, Writing–review and editing. LW: Formal Analysis, Funding acquisition, Resources, Visualization, Writing–review and editing. WK: Funding acquisition, Methodology, Resources, Supervision, Validation, Writing–review and editing.

Funding

The author(s) declare financial support was received for the research, authorship, and/or publication of this article. This work is supported by NARI Technology Co., Ltd. Technology Project under No. 524608220177. The funder was not involved in the study design, collection, analysis, interpretation of data, the writing of this article, or the decision to submit it for publication.

Conflict of interest

Authors QZ, NT, JL, WW, LW and WK were employed by NARI Research Institute, NARI Technology Co, Ltd.

Publisher's note

All claims expressed in this article are solely those of the authors and do not necessarily represent those of their affiliated organizations, or those of the publisher, the editors and the reviewers. Any product that may be evaluated in this article, or claim that may be made by its manufacturer, is not guaranteed or endorsed by the publisher.

References

Akhter, M. N., Mekhilef, S., Mokhlis, H., Ali, R., Usama, M., Muhammad, M. A., et al. (2022). A hybrid deep learning method for an hour ahead power output forecasting of three different photovoltaic systems. *Appl. Energy* 307, 118185. doi:10.1016/j.apenergy.2021.118185

Alzaeemi, S. A., and Sathasivam, S. (2020). Artificial immune system in doing 2-satisfiability based reverse analysis method via a radial basis function neural network. *Processes* 8 (10), 1295. doi:10.3390/pr8101295

Blaga, R., Sabadus, A., Stefu, N., Dughir, C., Paulescu, M., and Badescu, V. (2019). A current perspective on the accuracy of incoming solar energy forecasting. *Prog. energy Combust. Sci.* 70, 119–144. doi:10.1016/j.pecs.2018.10.003

Ellabban, O., Abu-Rub, H., and Blaabjerg, F. (2014). Renewable energy resources: current status, future prospects and their enabling technology. *Renew. Sustain. energy Rev.* 39, 748–764. doi:10.1016/j.rser.2014.07.113

Gao, M., Li, J., Hong, F., and Long, D. (2019). Day-ahead power forecasting in a large-scale photovoltaic plant based on weather classification using LSTM. *Energy* 187, 115838. doi:10.1016/j.energy.2019.07.168

Gutierrez-Corea, F. V., Manso-Callejo, M. A., Moreno-Regidor, M. P., and Manrique-Sancho, M. T. (2016). Forecasting short-term solar irradiance based on artificial neural networks and data from neighboring meteorological stations. *Sol. Energy* 134, 119–131. doi:10.1016/j.solener.2016.04.020

Han, R., Hu, Q., Cui, H., Chen, T., Quan, X., and Wu, Z. (2022). An optimal bidding and scheduling method for load service entities considering demand response uncertainty. *Appl. Energy* 328, 120167. doi:10.1016/j.apenergy.2022.120167

Hong, T., Xie, J., and Black, J. (2019). Global energy forecasting competition 2017: hierarchical probabilistic load forecasting. *Int. J. Forecast.* 35 (4), 1389–1399. doi:10.1016/j.ijforecast.2019.02.006

Inman, R. H., Pedro, H. T., and Coimbra, C. F. (2013). Solar forecasting methods for renewable energy integration. *Prog. energy Combust. Sci.* 39 (6), 535–576. doi:10.1016/j.pecs.2013.06.002

Islam, M. R., Islam, M. R., and Beg, M. R. (2008). Renewable energy resources and technologies practice in Bangladesh. *Renew. Sustain. Energy Rev.* 12 (2), 299–343. doi:10.1016/j.rser.2006.07.003

Jaihuni, M., Basak, J. K., Khan, F., Okyere, F. G., Sihalath, T., Bhujel, A., et al. (2022). A novel recurrent neural network approach in forecasting short term solar irradiance. *ISA Trans.* 121, 63–74. doi:10.1016/j.isatra.2021.03.043

Li, G., Wang, H., Zhang, S., Xin, J., and Liu, H. (2019). Recurrent neural networks based photovoltaic power forecasting approach. *Energies* 12 (13), 2538. doi:10.3390/en12132538

Ling, Y., Li, X., Li, C., and Chen, T. (2023). "An intelligent adversarial deep forecasting model for load demand using hybrid modified DA-GAN," in IEEE/IAS Industrial and Commercial Power System Asia (I&CPS Asia) (IEEE), 1340–1345.

Mirjalili, S., and Lewis, A. (2016). The whale optimization algorithm. *Adv. Eng. Softw.* 95, 51–67. doi:10.1016/j.advengsoft.2016.01.008

Obiora, C. N., Hasan, A. N., Ali, A., and Alajarmeh, N. (2021). Forecasting hourly solar radiation using artificial intelligence techniques. *IEEE Can. J. Electr. Comput. Eng.* 44 (4), 497–508. doi:10.1109/icjece.2021.3093369

Reindl, T., Walsh, W., Yanqin, Z., and Bieri, M. (2017). Energy meteorology for accurate forecasting of PV power output on different time horizons. *Energy Procedia* 130, 130–138. doi:10.1016/j.egypro.2017.09.415

Sangrody, H., Sarailoo, M., Zhou, N., Tran, N., Motalleb, M., and Foruzan, E. (2017). Weather forecasting error in solar energy forecasting. *IET Renew. Power Gener.* 11 (10), 1274–1280. doi:10.1049/iet-rpg.2016.1043

Snegirev, D. A., Eroshenko, S. A., Khalyasmaa, A. I., Dubailova, V. V., and Stepanova, A. I. (2019). "Day-ahead solar power plant forecasting accuracy improvement on the hourly basis," in In2019 IEEE Conference of Russian Young Researchers in Electrical and Electronic Engineering (EIConRus) (IEEE), 1088–1091.

Sobri, S., Koohi-Kamali, S., and Rahim, N. A. (2018). Solar photovoltaic generation forecasting methods: a review. *Energy Convers. Manag.* 156, 459–497. doi:10.1016/j.enconman.2017.11.019

Sridharan, M. (2023). Generalized regression neural network model based estimation of global solar energy using meteorological parameters. *Ann. Data Sci.* 10 (4), 1107–1125. doi:10.1007/s40745-020-00319-4

Succetti, F., Rosato, A., Araneo, R., and Panella, M. (2020). Deep neural networks for multivariate prediction of photovoltaic power time series. *IEEE Access* 8, 211490–211505. doi:10.1109/access.2020.3039733

Tsoulos, I. G., and Charilogis, V. (2023). Locating the parameters of RBF networks using a hybrid particle swarm optimization method. *Algorithms* 16 (2), 71. doi:10.3390/a16020071

Tuohy, A., Zack, J., Haupt, S. E., Sharp, J., Ahlstrom, M., Dise, S., et al. (2015). Solar forecasting: methods, challenges, and performance. *IEEE Power Energy Mag.* 13 (6), 50–59. doi:10.1109/mpe.2015.2461351

Vanderstar, G., Musilek, P., and Nassif, A. (2018). "Solar forecasting using remote solar monitoring stations and artificial neural networks," in In2018 IEEE Canadian conference on electrical & computer engineering (CCECE) (IEEE), 1–4.

Wentz, V. H., Maciel, J. N., Gimenez Ledesma, J. J., and Ando Junior, O. H. (2022). Solar irradiance forecasting to short-term PV power: accuracy comparison of ann and LSTM models. *Energies* 15 (7), 2457. doi:10.3390/en15072457

Zhang, J., Hodge, B. M., Florita, A., Lu, S., Hamann, H. F., and Banunarayanan, V. (2013). *Metrics for evaluating the accuracy of solar power forecasting*. Golden, CO (United States): National Renewable Energy Lab.NREL.

Zhang, X., Pipattanasomporn, M., Chen, T., and Rahman, S. (2019). An IoT-based thermal model learning framework for smart buildings. *IEEE Internet Things J.* 7 (1), 518–527. doi:10.1109/jiot.2019.2951106

Zhang, Y., Qian, W., Ye, Y., Li, Y., Tang, Y., Long, Y., et al. (2023). A novel non-intrusive load monitoring method based on ResNet-seq2seq networks for energy disaggregation of distributed energy resources integrated with residential houses. *Appl. Energy* 349, 121703. doi:10.1016/j.apenergy.2023.121703

frontiers | Frontiers in Energy Research

TYPE Original Research
PUBLISHED 08 January 2024
DOI 10.3389/fenrg.2023.1345840

OPEN ACCESS

EDITED BY
Rufeng Zhang,
Northeast Electric Power University, China

REVIEWED BY
Hongkun Wang,
Shihezi University, China
Qi Liu,
Shandong University of Science and Technology, China
Qianyu Zhao,
Tianjin University, China

*CORRESPONDENCE
He Lei,
xahlei@163.com

RECEIVED 28 November 2023
ACCEPTED 18 December 2023
PUBLISHED 08 January 2024

CITATION
Lei H, Rufeng L, Baofeng T, Kaifeng Z, Binyu J and Lin X (2024), Evaluating and forecasting methods for assessing the health status of cables under the load of large-scale electric vehicle charging. *Front. Energy Res.* 11:1345840. doi: 10.3389/fenrg.2023.1345840

Evaluating and forecasting methods for assessing the health status of cables under the load of large-scale electric vehicle charging

He Lei*, Li Rufeng, Tang Baofeng, Zhou Kaifeng, Jia Binyu and Xue Lin

State Grid XiongAn New Area Electric Power Supply Company, Xiong'an New Area, Hebei, China

The assessment of the health status and prediction of the lifespan of cable equipment are critical for ensuring the stability and efficiency of the power grid. This paper develops a temperature-current-capacity-life calculation model for cables, considering the fast and slow charging demands of electric vehicles (EVs). Analyses under scenarios of rapid and slow charging demands are conducted, introducing a cable health index and establishing a health status assessment framework based on this index. The framework accounts for various factors leading to cable faults, offering a comprehensive evaluation of the health status of cables with different fault rates. Building upon this, a prediction method using the Fire Hawk Optimization (FHO) Algorithm and Convolutional Neural Network (CNN) is proposed. This method enhances performance by optimizing the hyperparameters of Bidirectional Gated Recurrent Unit (BiGRU) through FHO, effectively searching and determining the optimal hyperparameter configuration. The impact of different scenarios and varying EV penetration rates on cable temperature is analyzed through case studies, facilitating the assessment and prediction of health status.

KEYWORDS

health status assessment, cable, electric vehicle, deep learning, health index

1 Introduction

As modern society's reliance on electricity intensifies, cables, being an indispensable component of the power grid, play a pivotal role in ensuring the safety and reliability of the entire electrical system (Rajendran et al., 2021). The escalating demand for electric vehicle (EV) charging, especially the high current requirements of direct current fast charging, raises challenges for cable equipment, leading to increased cable temperatures (Gupta et al., 2021). This not only impacts their performance and lifespan but also poses potential safety hazards. Moreover, cable equipment is subject to various internal and external factors such as aging, climate change, and operational stress, leading to potential performance deterioration over time (Hossain et al., 2021). Therefore, the health assessment and prediction of cable equipment's status are of paramount importance.

Cables are designed with a lifespan of approximately 40 years, predominantly affected by thermal aging and electrical aging (Li et al., 2007). Thermal aging suggests that a cable's lifespan is mainly influenced by load rate, insulation material properties, and ambient

temperature, whereas electrical aging posits that a cable's expected lifespan is inversely proportional to insulation field strength, as proven in relevant studies. Research documented in (Nemati et al., 2019) utilizes the Weibull parametric proportional hazard model to estimate the failure rate of each cable based on its years of usage and a set of explanatory factors (Dinmohammadi et al., 2019). proposes a lifespan prediction model for submarine cables under specific seabed conditions and tidal flows, predicting the expected lifespan of cables affected by erosion and wear. Further (Montanari et al., 2019), assesses the insulation condition of electrical equipment as a function of operating time, evaluating the feasibility and scope of maintenance measures and life extension plans based on aging and life models (Wang et al., 2019). examines the impact of EV charging loads on the temperature and thermal life of distribution network cables, focusing on the harmonic characteristics of 3.3 kW and 6.6 kW AC slow charging under peak and off-peak scenarios. However, in the context of dual carbon goals, the continuous increase in EV ownership, reaching 18.21 million in China by September 2023, and the establishment of DC fast charging and even Chaoji fast charging standards, allowing charging powers up to an astonishing 900 kW, impose higher current loads on cables (Yu et al., 2022). Excessive current loads can lead to overheating and material degradation, reducing the efficiency and reliability of cables (Li and Li, 2017). Research in this specific area is not yet comprehensive, and the lifespan prediction of operational cables needs to consider stochastic characteristics, including faults due to defects, external damage, and environmental factors.

In the realm of cable equipment health monitoring and lifespan prediction, numerous domestic and international researchers have pioneered a variety of innovative methods, broadly categorized into model-based predictions and data-based predictions (Liao and Kottig, 2014). Model-based predictions focus on in-depth analysis of cable equipment's structure and material properties, often involving complex fault mechanism mathematical models (Ahmad et al., 2022). However, due to their high complexity, the practical application of these methods is somewhat limited. On the other hand, data-based prediction methods do not require an in-depth understanding of mechanisms; instead, they assess the health and predict the lifespan of equipment by analyzing data and measurement parameters collected by sensors. These methods are further divided into statistical methods and machine learning methods (Carvalho et al., 2019). Traditional machine learning methods, such as Support Vector Machine (SVM) (Yan et al., 2020) and Random Forest (RF) (Gan et al., 2022), are favored for their flexibility and efficiency in extracting shallow features for health assessment and lifespan prediction. The latest research trend is employing deep learning technologies, particularly CNN and Recurrent Neural Networks (RNN) (Han et al., 2021), to process cable data, aiming to enhance prediction accuracy and robustness. The application of deep learning in cable equipment's lifespan prediction and health status assessment mainly encompasses Deep Belief Networks (DBN) (Peng et al., 2019), Long Short-Term Memory networks (LSTM) (Zhang et al., 2018), Gated Recurrent Units (GRU) (Luo et al., 2020), CNN, Graph Neural Networks (GNN) (Kong et al., 2022), and Transfer Learning (TL) (Zhang et al., 2021). These cutting-edge studies are continually advancing the monitoring and lifespan prediction technologies for cable equipment.

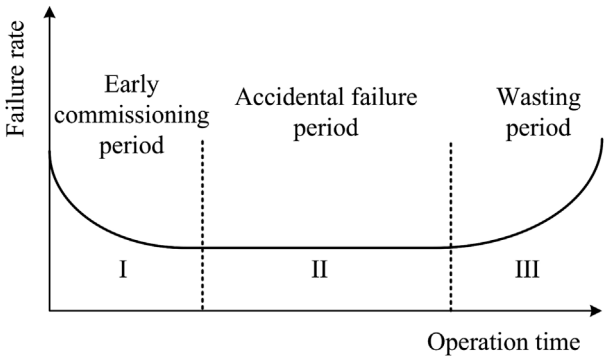

FIGURE 1
Bathtub curve of failure rates.

This paper introduces an innovative approach for assessing and predicting the health status of cables in the context of large-scale electric vehicle (EV) charging loads. The key contributions of this study are summarized as follows:

(1) Development of a cable temperature-current-capacity-life calculation model. This model conducts a comprehensive analysis of both rapid and slow charging scenarios and explores through case studies the impact of different charging scenarios and EV penetration rates on cable temperature. This offers new perspectives and solutions for cable management in EV charging facilities.
(2) Introduction of the concept of a Cable Health Index and the construction of a cable health status assessment framework based on this index. Taking into account various factors that could lead to cable faults, this framework allows for a comprehensive health assessment of cables with different fault rates, significantly enhancing the safety and efficiency of cable usage.
(3) Proposal of a predictive method that combines the FHO Algorithm with a CNN. This method uses the FHO algorithm to optimize the hyperparameters of the BiGRU, enhancing predictive performance. It effectively searches and determines the optimal hyperparameter configuration, enabling precise assessment and prediction of cable health status.

The remainder of the paper is organized as follows: Section 2 constructs the cable model considering EV charging demands and analyzes rapid and slow charging requirements. Section 3 presents a deep learning-based method for predicting the health status of cable equipment. Section 4 offers simulation results and discusses the outcomes of the tests. Finally, Section 5 concludes the study.

2 Cable model considering EV charging demand

The historical data of cables include operational years and routine inspections. As operational years increase, the condition of the cables deteriorates. The lifecycle of a cable follows a "bathtub curve," which can be divided into three phases: the early debugging

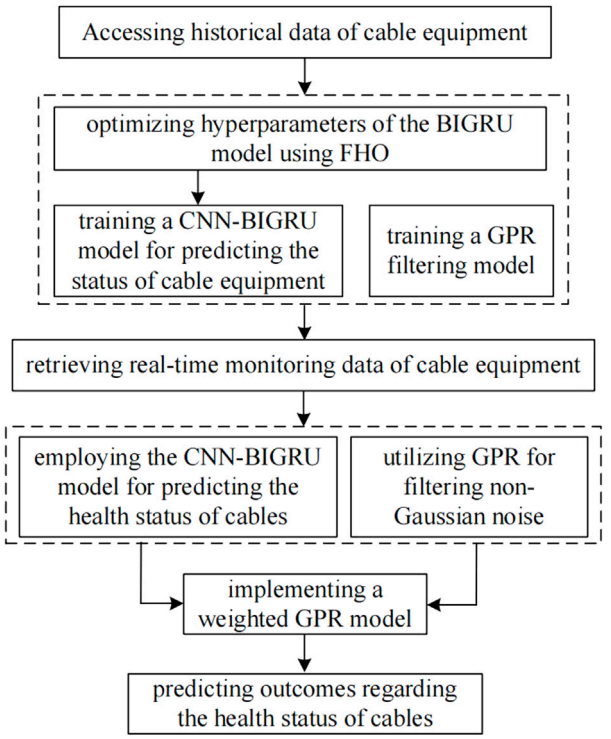

FIGURE 2
Flowchart for predicting cable health status.

period, the random failure period, and the wear-out period, as illustrated in Figure 1.

To quantify the impact of EV charging loads on cables, this paper constructs a cable equipment temperature-current-capacity-life calculation model, considering both rapid and slow EV charging demands.

2.1 Slow charging demand

Considering that the charging mode allows EVs to charge without exceeding the battery capacity and that the constant current process in a complete slow charging cycle is very short, the entire slow charging process is approximated as constant voltage charging. Assuming that the charging current for slow charging is 0.1C (C refers to battery capacity), the charging power Pc of a typical EV falls within the range of 2–3 kW and follows a uniform distribution, with its probability distribution function as (Eq. 1)

$$f_{P_c}(x) = \begin{cases} 1 & x \in [2,3] \\ 0 & \text{otherwise} \end{cases} \tag{1}$$

The time required for each EV's slow charging is calculated as (Eq. 2)

$$T_c = \frac{SW_{100}}{100P_c} \tag{2}$$

Considering two types of slow charging modes: dispersed and centralized, this study focuses on dispersed slow charging for both pure electric and hybrid vehicles. Assuming that all slow-charging EVs finish their last daily trip and return to their parking spots at the time which marks the beginning of charging. Based on a survey of American household vehicles, the start time of charging is also approximated as a normal distribution, with the specific probability density function as (Eq. 3):

$$f_s(x) = \begin{cases} \frac{1}{\sigma_s\sqrt{2\pi}} \exp\left[-\frac{(x-\mu_s)^2}{2\sigma_s^2}\right] & (\mu_s - 12) < x \le 24 \\ \frac{1}{\sigma_s\sqrt{2\pi}} \exp\left[-\frac{(x+24-\mu_s)^2}{2\sigma_s^2}\right] & 0 < x \le (\mu_s - 12) \end{cases} \tag{3}$$

With the initial scale of EVs in the region, combining the EV driving mileage and charging start time, the remaining battery charge of each vehicle can be calculated.

2.2 Rapid charging demand

In rapid charging mode, the initial phase of EV charging generally involves constant current charging, following an exponential distribution. When the battery is charged to 80% of its rated capacity, the process is as (Eq. 4):

$$P_{fc}(t) = P_N e^{-\frac{P_N}{(0.9-SOC_0)C}t} \tag{4}$$

For instance, P_N = 100 kW, for a battery capacity of 60 kW and a remaining charge of 40%, an EV would require approximately 0.67 h to charge.

The extent of EV charging and battery swapping demand is primarily influenced by user behavior, battery capacity, and the technical level of charging equipment. At a certain stage of development, constrained by the level of technology, battery capacity and the power rating of charging equipment are generally fixed, hence EV charging and swapping demand mainly depends on daily driving mileage.

To obtain the daily load curve of EV charging and swapping, it is first necessary to know the daily driving mileage S of EV users and the electric energy W_{100} consumed per 100 km by the EV. The product of these two factors gives the daily power consumption of the EV. Based on relevant statistical survey data, the daily mileage is approximated to fit a log-normal distribution, with the corresponding probability density function as (Eq. 5):

$$f(d) = \frac{1}{d\sigma_{D,i}\sqrt{2\pi}} \exp\left[-\frac{(\ln d - \mu_{D,i})^2}{2\sigma_{D,i}^2}\right], i = 1, 2, ..., 7 \tag{5}$$

Compared to the dispersed slow charging mode, the rapid charging mode sees a higher degree of charging demand, mainly affected by the power consumption during various time periods. This paper assumes that the distribution of start times for rapid charging is consistent with the swapping time distribution in the swapping mode. It is also assumed that when pure electric and hybrid EVs undergo rapid charging, the remaining battery charge follows a normal distribution of (0.4, 0.133), leading to a specific probability density function for the remaining battery capacity (Eq. 6).

$$f_K(x) = \frac{1}{\sigma_K\sqrt{2\pi}} \exp\left[-\frac{(x-\mu_K)^2}{2\sigma_K^2}\right] \tag{6}$$

2.3 Cable temperature calculation model

The introduction of nonlinear loads by AC charging of EVs leads to the generation of harmonics. These harmonic signals affect both voltage and current, encompassing harmonic voltage and current. According to the definition by IEC 61000, these are represented as (Eq. 7) and (Eq. 8):

$$\sigma_{\mathrm{THD}u} = \frac{\sqrt{\sum_{2}^{n} U_n^2}}{U_1} \tag{7}$$

$$\sigma_{\mathrm{THD}i} = \frac{\sqrt{\sum_{2}^{n} I_n^2}}{I_1} \tag{8}$$

As per the IEC 60287 standard, the core temperature θ of a 10 kV three-core cable can be expressed as $\theta = \theta_c + \theta_0$, the values of related parameters can be found in Wang et al. (2019) θ_c can be calculated by (Eq. 9).

$$\theta_c = \sum_{i=1}^{n} I_i^2 R_{\mathrm{AC}}(i)\left(T_1 + c_i T_2 + c_i\left(1 + \lambda_2(i)\right)\left(T_3 + T_4\right)\right) \tag{9}$$

2.4 Cable current carrying capacity calculation model

The harmonic currents generated during the charging process of EVs can cause the total current carrying capacity of the cable to exceed its design value, potentially leading to overload and safety issues. The current carrying capacity of 10 kV three-core cable can be calculated using (Eq. 10)

$$I_{h,\mathrm{rated}} = \sqrt{\Delta\theta_c \Big/ \sum_{i=1}^{n} \frac{I_i^2}{I_1^2} R_{AC}(i)\left(T_1 + (1 + \lambda_1(i))T_2 + (1 + \lambda_1(i) + \lambda_2(i))(T_3 + T_4)\right)} \tag{10}$$

2.5 Cable life calculation model

The harmonic currents produced during the EV charging process cause additional heating in the cable, affecting its thermal life. The cable's life per hour is given by (Eq. 11):

$$L_h(t) = 8760 \cdot L_0 \mathrm{e}^{-\frac{\Delta w}{k_B T(t)}} \tag{11}$$

The daily life degradation of the cable is expressed as (Eq. 12):

$$L_d = \sum_{t=1}^{24} \frac{1}{L_h(t)} \tag{12}$$

2.6 Failure rate model

Cable fault sample data follow a Weibull distribution with the sought parameters. Such a function can simulate various fault factors by selecting appropriate parameters and can also assess the systemic reliability when the cable fault rate dynamically changes. The mathematical model for cable fault rate is shown as (Eq. 13):

$$\lambda(t) = \frac{\beta}{\eta}\left(\frac{t}{\eta}\right)^{\beta-1} \tag{13}$$

To account for the difference in cable fault rates before and after maintenance, this paper introduces an age regression factor α, representing the actual change in cable fault rate. The actual service age of the cable is then given by (Eq. 14):

$$T_{\mathrm{real}} = T - \alpha T = (1 - \alpha)T \tag{14}$$

This allows for the determination of the fault rate after the k-th maintenance. As shown in (Eq. 15).

$$\lambda_k(t) = \lambda[t + (1 - \alpha)kT] = \frac{\beta}{\eta}\left[\frac{t + (1 - \alpha)kT}{\eta}\right]^{\beta-1} \tag{15}$$

3 Deep learning-based method for predicting the health status of cable equipment

To avoid the issues of cable current carrying capacity overload and temperature rise caused by concentrated EV charging, this study proposes a data-driven and weighted Gaussian regression method for predicting the operational state of cable equipment. This approach utilizes CNN and LSTM networks to predict parameters of cable equipment, thereby enhancing the performance of Gaussian Process Regression (GPR), aiming to improve the accuracy of predicting parameters like cable temperature and current carrying capacity.

The proposed FHO-CNN-BIGRU method for predicting the operational state of cable equipment employs the CNN algorithm to mine data relationships and mitigate noise interference. The extracted features are then fed into a BiGRU model optimized by the FHO Algorithm for time series prediction, enhancing the stability of the forecasts. Additionally, this method incorporates a GPR filtering model to smooth the data using Gaussian process regression, thus improving data accuracy and reliability. The cable health status prediction flow chart is shown in Figure 2.

3.1 FHO optimization of BiGRU hyperparameters

The FHO algorithm is a meta-heuristic algorithm that simulates the foraging behavior of fire hawks, considering processes like setting fires, spreading, and capturing prey. Initially, several candidate solutions are determined as the location vectors of the fire hawks and prey, using a random initialization process as per the given formula to identify these vectors' initial positions in the search space. As shown in (Eq. 16) and (Eq. 17).

$$\mathrm{X} = \begin{bmatrix} \mathrm{X}_1 \\ \vdots \\ \mathrm{X}_i \end{bmatrix} = \begin{bmatrix} \mathrm{x}_1^1 \mathrm{x}_1^2 \cdots \mathrm{x}_1^j \\ \vdots \\ \mathrm{x}_i^1 \mathrm{x}_i^2 \cdots \mathrm{x}_i^j \end{bmatrix}, \begin{cases} i = 1, 2, \ldots, N \\ j = 1, 2, \ldots, D \end{cases} \tag{16}$$

$$x_i^j(0) = x_{i,\min}^j + rand \cdot \left(x_{i,\max}^j - x_{i,\min}^j\right) \quad (17)$$

The distance between a fire hawk m and prey n is calculated to determine the nearest prey around each fire hawk and define their territories. As shown in (Eq. 18).

$$D_n^m = \sqrt{(x_n - x_m)^2 + (y_n - y_m)^2} \quad (18)$$

Then, positions are updated: fire hawk m collects burning sticks from the main fire and throws them into a specific area to force the prey to flee. The detailed process of updating positions can be referred to in the cited literature (Azizi et al., 2023).

Based on the solution process of the aforementioned FHO optimization algorithm, the steps to optimize the BiGRU model hyperparameters are as follows:

Step 1: Define the Hyperparameter Search Space. Identify the hyperparameters of the BiGRU model to be optimized and establish a range or a set of possible values for each hyperparameter.

Step 2: Initialize Solution Candidates. Generate initial solution candidates of hyperparameter combinations randomly, in accordance with the defined search space.

Step 3: Evaluate Initial Solution Candidates. Employ cross-validation or other suitable methods to train the model and assess the performance of the initial solution candidates, calculating their fitness values (such as accuracy, loss function values, etc.).

Step 4: Set the Global Optimum. Designate the best solution among the initial candidates as the global optimum.

Step 5: Iterative Optimization. Continuously update the hyperparameter combinations by generating falcons and prey. The distance between falcons and prey is computed, and territories of the falcons are determined. Falcons update their hyperparameter combinations based on their positions, and prey both within and outside the territories also update their combinations. By evaluating the fitness values of the updated hyperparameter combinations and updating the global optimum to the current best solution, the FHO algorithm progressively searches for improved hyperparameter combinations, thereby enhancing the BiGRU model's performance through iterative optimization.

Step 6: Return the Global Optimum. Upon completion of the iterations, the global optimum is returned as the optimized set of hyperparameters for the BiGRU model.

3.2 FHO-CNN-BiGRU prediction model

Step 1: Data Preprocessing. Undertake preparatory processing of the monitoring data for cable equipment, involving data cleansing and normalization among other procedures, to ready the input data.

Step 2: Feature Extraction. Utilize a CNN to extract salient features from the cable equipment monitoring data, capturing key temporal sequence characteristics.

Step 3: Sequence Modeling. Employ a BiGRU to model the extracted time series features, considering both historical and prospective state information.

Step 4: Predictive Output. Utilize the terminal temporal step's BiGRU hidden state as the vector representation of the equipment's health status, and input this into a fully connected layer for the prediction of the health state.

Step 5: Model Optimization. Apply the FHO algorithm to refine hyperparameters such as the convolutional kernel size, GRU's hidden unit count, learning rate, and other factors pertinent to model performance, thereby enhancing the accuracy of health status prediction.

Step 6: Model Evaluation. Assess the model's performance using appropriate metrics (like accuracy, recall, F1 score, etc.), comparing it against the actual health states of the equipment.

Step 7: Health Status Prediction. Utilize the optimized FHO-CNN-BiGRU model to predict the health status of cable equipment based on new monitoring data, thus obtaining prognostications regarding the health state of the cable apparatus.

3.3 Construction of gaussian process regression model

Combining the FHO-CNN-BiGRU prediction model, the GPR model is utilized for its superiority in handling nonlinear problems to obtain nonlinear mappings between measurements and state quantities. The integration of FHO-CNN-BiGRU and GPR algorithms allows for weighting the predicted values from FHO-CNN-BiGRU and the state estimates from GPR, leading to more accurate predictions of the cable equipment's state.

The Gaussian Regression model maps input features to a high-dimensional space through a set of basis functions, denoted as $\psi(\cdot)$, thereby facilitating the discovery of linear relationships among data in this elevated dimensional space. By representing the measured quantities Z, with these basis functions $\psi(\cdot)$, one can derive the probability associated with new data.

The GPR uses confidence judgment to estimate results, which can mitigate noise interference, thereby improving the accuracy of the estimates. Offline training is first conducted based on the nonlinear relationship between historical measurement and state data of cable equipment, followed by state prediction using the trained model based on new measurement data.

3.4 Method for assessing the health status of cable equipment

Aging and deterioration are phenomena that span the entire lifecycle of equipment. Cables, especially those operating in

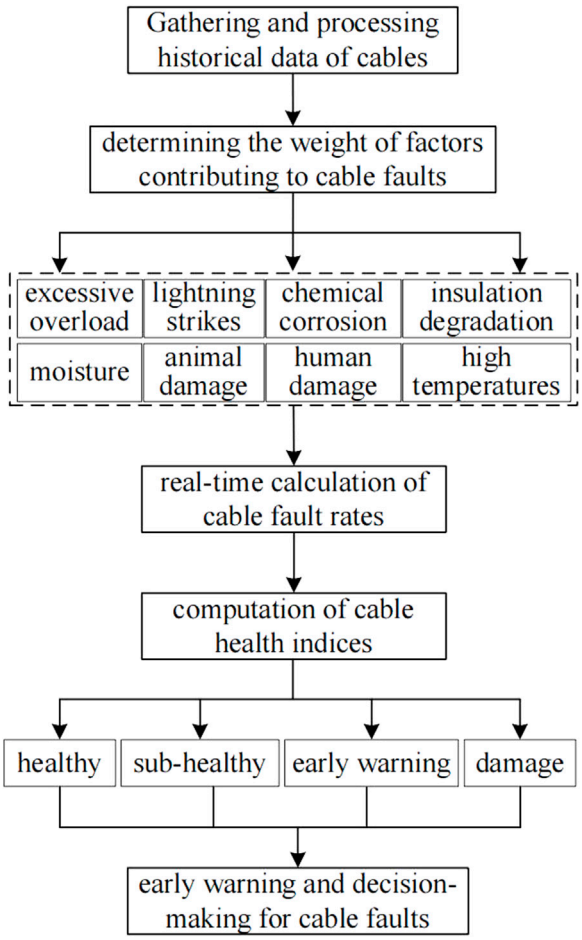

FIGURE 3
Cable fault early warning and decision-making process.

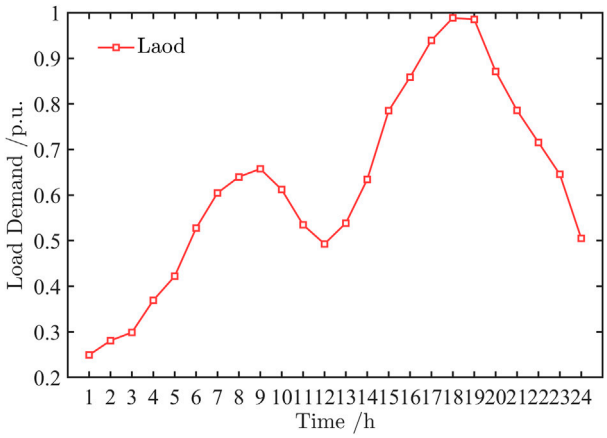

FIGURE 4
Daily residential electricity load profile.

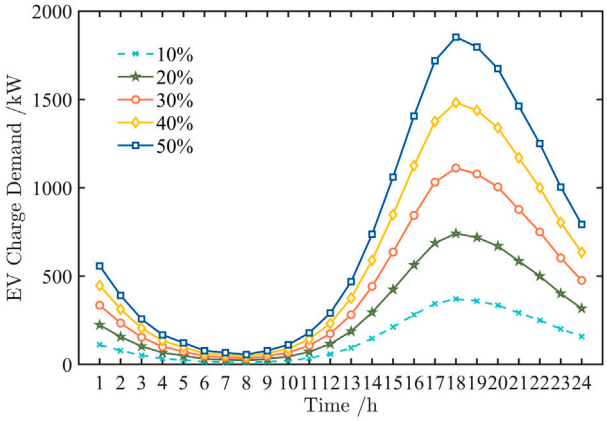

FIGURE 5
Charging demand at different EV penetration rates.

humid environments for extended periods, are prone to water tree aging. The operational state of the cable, maintenance strategies, construction quality, and operating environment significantly impact cable deterioration. Maintenance can enhance the performance of components and extend the equipment's life to a certain extent, but it cannot restore the equipment to its original healthy state, as the rate of deterioration remains unchanged. Assessing the health status is an effective way to monitor the condition of cable equipment. Based on the cable status prediction results, this paper introduces the concept of a Cable Health Index and constructs a cable health status assessment framework based on this index. The cable health status assessment process, as illustrated in Figure 3, involves the following detailed steps:

Step 1: Data Collection and Processing. Utilize distributed fiber optic sensors to collect relevant data of the cable, including its lifespan, insulation thermal resistance, and other parameters. Combine these with predicted parameters like current carrying capacity, temperature, and lifespan to construct a health status assessment dataset. Analyze and process the collected data, employing methods like Principal Component Analysis to remove redundant features and repair missing data.

Step 2: Determination of Cable Fault Factor Weights. Considering the operational conditions of the cable, use the Analytic Hierarchy Process to calculate the weights of factors that could potentially cause cable faults, obtaining the weight w_i for the ith type of fault factor. Factors include heavy overload, lightning strikes, high temperatures, humidity, chemical corrosion, human-induced damage, animal damage, and insulation aging.

Step 3: Calculation of Cable Fault Rate. Calculate the cable fault rate $\lambda(t)$ and the fault rate λ_k after kth maintenance using the designated (Eq. 19). Modify the fault rate based on the cable's service age using the appropriate (Eq. 20) to obtain the real-time fault rate.

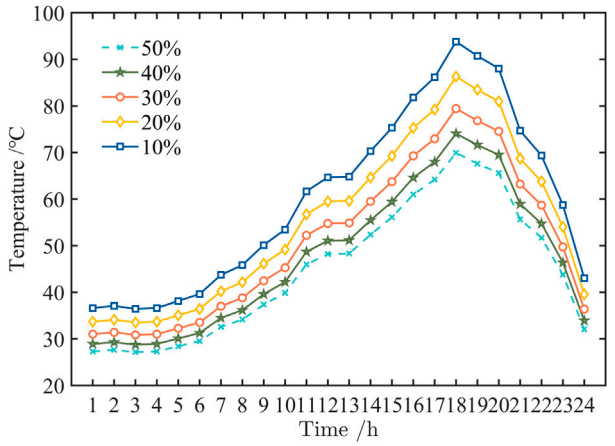

FIGURE 6
Cable temperature variations under different EV penetration rates.

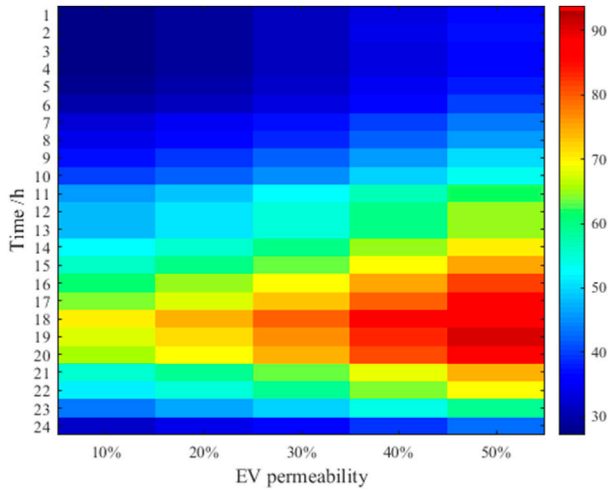

FIGURE 7
Temperature impacts in slow charging scenarios at different EV penetration rates.

$$\lambda(t) = \begin{cases} 0.0198 & t \le 20 \\ \dfrac{6.849}{35.536} \times \left(\dfrac{t}{35.536}\right)^{5.849} & t > 20 \end{cases} \tag{19}$$

$$\lambda^{\star} = w_i \cdot \lambda_k \tag{20}$$

Step 4: Calculation of Cable Health Index. Utilize the real-time fault rate to calculate the cable's real-time health index $H^{\star}$. As shown in (Eq. 21).

$$H^{\star} = \frac{1}{\xi}\ln\left(\frac{\lambda^{\star}}{K}\right) \tag{21}$$

Step 5: Assessment of Cable Health Status. Based on the calculated real-time health index, assess the health status of the cable. Categorize the cable into different health statuses, including healthy, sub-healthy, early warning, and damaged, according to predefined standards and thresholds.

Step 6: Early Warning and Decision-Making. Set warning thresholds based on the real-time fault rate and health index. When the fault rate exceeds the threshold or the health index declines, the system can issue an alert, prompting maintenance personnel to take appropriate actions such as repair, replacement, or upgrade of the cable.

4 Case analysis

This paper focuses on a case study of a community with 2000 private EVs. For simplicity in the simulation, it is assumed that EVs charge at a constant power, with a battery capacity of 70 kWh. The study considers AC slow charging and DC fast charging, setting the ratio of fast to slow charging at 3:7. According to the standard charging modes defined in IEC61851-1, a 6.6 kW AC charging station for electric cars has a current of 32A, and a 35 kW DC charging station has a current of 160A. The temperature limit of XLPE cables is set at 90°C. Due to higher losses in AC cables under the same load conditions compared to DC cables, the temperature changes caused by fast charging are not considered initially. Figure 4 shows the typical daily load curve without considering EV charging, and Figure 5 presents the charging demand curves at different EV penetration rates.

TABLE 1 Maximum cable temperatures at different EV penetration rates in various scenarios.

EV penetration rate	Temperature (°C)		
	Considering harmonics	Disregarding harmonics	Disregarding fast charging
0	63.56	63.56	63.56
10%	67.96	64.85	69.92
20%	71.23	67.55	74.05
30%	76.80	71.61	79.43
40%	83.58	79.56	86.30
50%	91.67	90.03	93.82

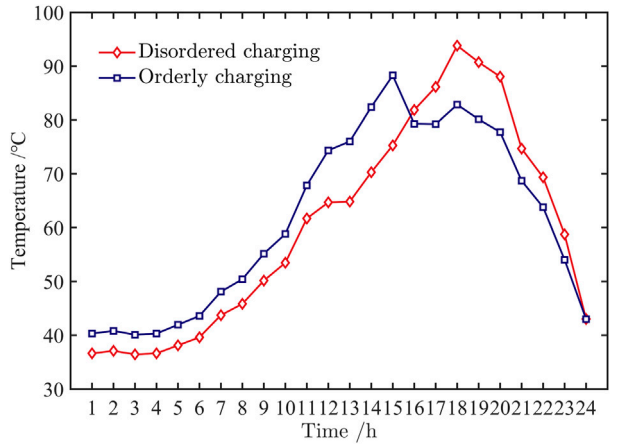

FIGURE 8
Effects of ordered and unordered charging on temperature.

4.1 Impact of EV charging demand on cables

To assess the impact of different scales of EV integration on cable temperature rise, we analyzed cable temperatures under various charging demands, setting EV penetration rates at 0%, 10%, 20%, 30%, 40%, and 50%. The simulation tested the cable temperature variations in each scenario, as shown in Figure 6; Table 1.

From Figure 6, it is evident that with the increase in the number of EVs, the rising charging demand leads to a continuous increase in cable temperature. Especially when the EV penetration rate reaches half of the total number of private cars in the community, the cable temperature exceeds the permissible limit. At peak demand times, the cable temperature reaches 91.67°C, exceeding the 90°C limit even without considering the impact of harmonics. Therefore, reducing harmonics and improving cable thermal management are crucial for the reliable operation of cables and the entire distribution system. Implementing rational orderly charging strategies or incentivizing users to charge during off-peak hours through time-of-use tariffs could mitigate the risk of cable current exceeding limits due to the cumulative demand of charging and base electrical loads.

4.2 Impact of EV charging strategies on cables

To verify the impact of different charging strategies on cable life, the temperature variations under slow charging demands at different EV penetration rates are shown in Figure 7. Additionally, considering the peak and off-peak periods as defined in (Sun et al., 2019), Figure 8 shows the temperature variation curves for two scenarios at a 50% penetration rate under time-of-use charging.

From the figures, it is seen that in uncoordinated charging, all EV users start charging immediately upon returning home, with charging concentrated between 6 p.m. and 2 a.m. the next day. At 6 p.m., the cable temperature reaches 91.67°C due to the peak in total electricity demand from both charging and base loads. Under the influence of time-of-use tariffs, EV users tend to choose lower-priced periods for charging, mostly during the peak hours of solar power generation. Although the surge in charging demand increases the cable temperature, it effectively avoids the temperature rise caused by "peak upon peak" by occurring during the low-demand period of the grid. The cable temperature remains at 88.28°C, not exceeding its maximum tolerance, thereby reducing the fluctuation range of cable temperature. This strategy not only avoids impact on the cable but also enhances the utilization of solar power in the grid.

TABLE 2 Health grade classification.

Health index	Health level	Health status
100 ≥ H ≥ 75	S1	Health
75 ≥ H ≥ 50	S2	Sub-health
50 ≥ H ≥ 20	S3	Early warning
20 ≥ H ≥ 0	S4	Damage

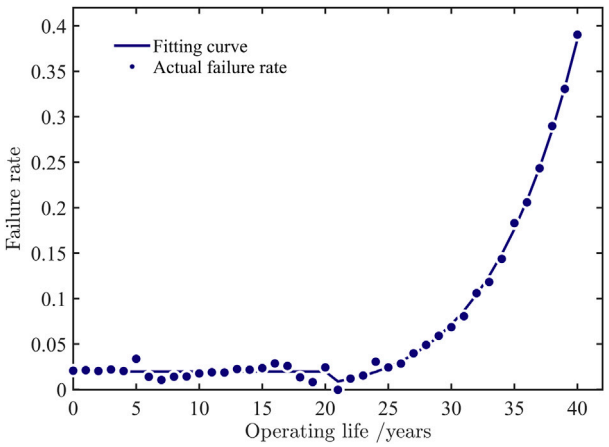

FIGURE 9
Fitted curve of cable failure rates.

4.3 Cable health status assessment and prediction

An analysis is conducted on the operational status of cables under the two charging scenarios mentioned above, and a health status assessment is performed using the health index. The criteria for classifying health levels are shown in Table 2, and the future health status of the cables is predicted using the model proposed in this paper.

As indicated in Table 2, S1 represents equipment that meets all performance standards, with good foundational conditions, intact technical performance, and stable operational conditions, capable of withstanding external environmental risks. S2 denotes equipment with intact functionality and performance, though slightly below the healthy state, still meeting standard operational requirements. S3 indicates equipment in basically good condition, capable of performing specified functions, but with some performance degradation, having a minor overall impact and needing maintenance. S4 signifies equipment with severe technical performance deficiencies, unable to meet operational standards, and posing a threat to system safety and stability, urgently requiring replacement.

TABLE 3 Weighting of fault factors.

Failure factors	Overload	Heavy rain	Lightning strike	High temperature	Others
Weight	0.212	0.356	0.093	0.098	0.241

TABLE 4 Cable failure rates and health information.

Cable	Failure rate	HI	HS	Future HI	Future HS
1	0.020	74.150	S2	67.094	S2
2	0.010	80.090	S1	72.468	S2
3	0.008	81.816	S1	74.030	S2
4	0.004	87.738	S1	79.388	S1
5	0.007	83.380	S1	75.445	S1
6	0.019	74.740	S2	67.628	S2
7	0.004	87.738	S1	79.388	S1
8	0.017	75.309	S2	68.142	S2
9	0.013	77.623	S2	70.236	S2
10	0.007	83.380	S1	75.445	S1

TABLE 5 Comparison of prediction methods.

Method	Accuracy rate (%)			
	S1	S2	S34	Comprehensive
BPNN	76.1	85.7	73.6	79.4
SVM	84.1	87.2	83.8	85.3
Proposed method	92.5	93.6	90.3	92.5

Figure 9 shows an increase in the fault rate of cables over time. Considering the climate environment of the Xiong'an New Area, 100 cables are selected, and the weights of various fault factors are calculated using the Analytic Hierarchy Process, as shown in Table 3.

The cable fault rate and health index are calculated based on the weights of the fault factors and used as initial parameters to predict future changes in the cable's health status. Table 4 presents the fault rates and health information of 10 selected cables and predicts their future health status.

4.4 Comparison of prediction method efficacy

To validate the superiority of the method proposed in this study, its prediction results were compared with those of the Back Propagation Neural Network (BPNN) and Support Vector Machine (SVM) models, as shown in Table 5. S1 and S2 respectively correlate to the health grades outlined in Table 2. The amalgamation of S3 and S4, denoted as S34, indicates that the cable is in a state of malfunction or pre-alert.

The analysis of the provided data in Table 5 reveals a clear superiority of the proposed method in accuracy rates across all categories. It surpasses both BPNN and SVM, achieving 92.5% in S1, 93.6% in S2, and 90.3% in the combined S34 category, with a comprehensive accuracy of 92.5%. This consistently higher performance across all metrics establishes the "Proposed Method" as the most effective and accurate among the methods evaluated.

5 Conclusion

In this paper, we proposed a method for assessing and predicting the health status of cables under the load of large-scale EV charging. Through detailed case analysis, the following conclusions were drawn:

(1) The increase in EV charging demand poses a risk of exceeding cable temperature limits, particularly under the influence of harmonics in AC slow charging scenarios. Addressing this involves both reducing harmonic interference and enhancing cable thermal management, which are essential for ensuring the reliability of the cable system and the overall distribution network.
(2) Cables experience more severe operational challenges and increased risk, especially with prolonged use of AC slow charging by EVs. Implementing time-of-use tariffs to encourage orderly charging can mitigate issues like cable current overload from cumulative charging and base load demands. Additionally, at a 50% EV penetration rate, uncoordinated charging can lead to cable overloading, while time-of-use tariffs can help regulate charging demand distribution, thus reducing peak-to-valley differences and lowering cable temperatures during high grid load periods.
(3) The method proposed in this paper for assessing and predicting cable health status effectively evaluates the operational state of cables and issues timely warnings. It accurately predicts future changes in cable health, providing essential support for grid dispatchers to arrange maintenance and operation plans, thereby enhancing the reliability of the distribution system.

Future research will aim to enhance predictive models and thermal management, facilitating efficient integration of EVs into the electrical grid.

Data availability statement

The original contributions presented in the study are included in the article/supplementary material, further inquiries can be directed to the corresponding author.

Author contributions

HL: Conceptualization, Writing–original draft. LR: Data curation, Writing–review and editing. TB: Software, Writing–review and editing.

ZK: Methodology, Writing–review and editing. JB: Validation, Writing–review and editing. XL: Resources, Writing–review and editing.

Funding

The author(s) declare financial support was received for the research, authorship, and/or publication of this article. This research was funded by the Science and Technology Project of Hebei Electric Power Company of State Grid (SGHEXA00GDJS2250285).

Conflict of interest

Authors HL, LR, TB, ZK, JB, XL were employed by State Grid XiongAn New Area Electric Power Supply Company.

The authors declare that this study received funding from Hebei Electric Power Company of State Grid. The funder had the following involvement in the study: design, collection, analysis, interpretation of data, the writing of this article and the decision to submit it for publication.

Publisher's note

References

Ahmad, T., Madonski, R., Zhang, D., Huang, C., and Mujeeb, A. (2022). Data-driven probabilistic machine learning in sustainable smart energy/smart energy systems: key developments, challenges, and future research opportunities in the context of smart grid paradigm. *Renew. Sustain. Energy Rev.* 160, 112128. doi:10.1016/j.rser.2022.112128

Azizi, M., Talatahari, S., and Gandomi, A. H. (2023). Fire Hawk Optimizer: a novel metaheuristic algorithm. *Artif. Intell. Rev.* 56, 287–363. doi:10.1007/s10462-022-10173-w

Carvalho, T. P., Soares, F. A. A. M. N., Vita, R., Francisco, R. da P., Basto, J. P., and Alcalá, S. G. S. (2019). A systematic literature review of machine learning methods applied to predictive maintenance. *Comput. Ind. Eng.* 137, 106024. doi:10.1016/j.cie.2019.106024

Dinmohammadi, F., Flynn, D., Bailey, C., Pecht, M., Yin, C., Rajaguru, P., et al. (2019). Predicting damage and life expectancy of subsea power cables in offshore renewable energy applications. *IEEE Access* 7, 54658–54669. doi:10.1109/ACCESS.2019.2911260

Gan, L., Wu, H., and Zhong, Z. (2022). Fatigue life prediction considering mean stress effect based on random forests and kernel extreme learning machine. *Int. J. Fatigue* 158, 106761. doi:10.1016/j.ijfatigue.2022.106761

Gupta, R. S., Tyagi, A., and Anand, S. (2021). Optimal allocation of electric vehicles charging infrastructure, policies and future trends. *J. Energy Storage* 43, 103291. doi:10.1016/j.est.2021.103291

Han, T., Pang, J., and Tan, A. C. C. (2021). Remaining useful life prediction of bearing based on stacked autoencoder and recurrent neural network. *J. Manuf. Syst.* 61, 576–591. doi:10.1016/j.jmsy.2021.10.011

Hossain, E., Roy, S., Mohammad, N., Nawar, N., and Dipta, D. R. (2021). Metrics and enhancement strategies for grid resilience and reliability during natural disasters. *Appl. Energy* 290, 116709. doi:10.1016/j.apenergy.2021.116709

Kong, Z., Jin, X., Xu, Z., and Zhang, B. (2022). Spatio-temporal fusion attention: a novel approach for remaining useful life prediction based on Graph neural network. *IEEE Trans. Instrum. Meas.* 71, 1–12. doi:10.1109/TIM.2022.3184352

Li, S., and Li, J. (2017). Condition monitoring and diagnosis of power equipment: review and prospective. *High. Volt.* 2, 82–91. doi:10.1049/hve.2017.0026

Li, S., Li, J., Zhang, X., Gockenbach, E., Wasserberg, V., and Borsi, H. (2007). Estimation of the lifetime of the electrical components in distribution networks. *IEEE Trans. Power Del* 22, 515–522. doi:10.1109/TPWRD.2006.876661

Liao, L., and Kottig, F. (2014). Review of hybrid prognostics approaches for remaining useful life prediction of engineered systems, and an application to battery life prediction. *IEEE Trans. Rel.* 63, 191–207. doi:10.1109/TR.2014.2299152

Luo, Q., Chang, Y., Chen, J., Jing, H., Lv, H., and Pan, T. (2020). Multiple degradation mode analysis via gated recurrent unit mode recognizer and life predictors for complex equipment. *Comput. Ind.* 123, 103332. doi:10.1016/j.compind.2020.103332

Montanari, G. C., Hebner, R., Morshuis, P., and Seri, P. (2019). An approach to insulation condition monitoring and life assessment in emerging electrical environments. *IEEE Trans. Power Del.* 34, 1357–1364. doi:10.1109/TPWRD.2019.2897905

Nemati, M., Sant'Anna, A., Nowaczyk, S., Jürgensen, J. H., and Hilber, P. (2019). Reliability evaluation of power cables considering the restoration characteristic. *Int. J. Electr. Power Energy Syst.* 105, 622–631. doi:10.1016/j.ijepes.2018.08.047

Peng, K., Jiao, R., Dong, J., and Pi, Y. (2019). A deep belief network based health indicator construction and remaining useful life prediction using improved particle filter. *Neurocomputing* 361, 19–28. doi:10.1016/j.neucom.2019.07.075

Rajendran, G., Vaithilingam, C. A., Misron, N., Naidu, K., and Ahmed, M. R. (2021). A comprehensive review on system architecture and international standards for electric vehicle charging stations. *J. Energy Storage* 42, 103099. doi:10.1016/j.est.2021.103099

Sun, Y., Yue, H., Zhang, J., and Booth, C. (2019). Minimization of residential energy cost considering energy storage system and EV with driving usage probabilities. *IEEE Trans. Sustain. Energy* 10, 1752–1763. doi:10.1109/TSTE.2018.2870561

Wang, H., Zhou, W., Qian, K., and Meng, S. (2019). Modelling of ampacity and temperature of MV cables in presence of harmonic currents due to EVs charging in electrical distribution networks. *Int. J. Electr. Power Energy Syst.* 112, 127–136. doi:10.1016/j.ijepes.2019.04.027

Yan, M., Wang, X., Wang, B., Chang, M., and Muhammad, I. (2020). Bearing remaining useful life prediction using support vector machine and hybrid degradation tracking model. *ISA Trans.* 98, 471–482. doi:10.1016/j.isatra.2019.08.058

Yu, H., Niu, S., Shang, Y., Shao, Z., Jia, Y., and Jian, L. (2022). Electric vehicles integration and vehicle-to-grid operation in active distribution grids: a comprehensive review on power architectures, grid connection standards and typical applications. *Renew. Sustain. Energy Rev.* 168, 112812. doi:10.1016/j.rser.2022.112812

Zhang, J., Wang, P., Yan, R., and Gao, R. X. (2018). Long short-term memory for machine remaining life prediction. *J. Manuf. Syst.* 48, 78–86. doi:10.1016/j.jmsy.2018.05.011

Zhang, W., Li, X., Ma, H., Luo, Z., and Li, X. (2021). Transfer learning using deep representation regularization in remaining useful life prediction across operating conditions. *Reliab. Eng. Syst. Saf.* 211, 107556. doi:10.1016/j.ress.2021.107556

Nomenclature

Parameters

T_c	Charging duration
S	Daily driving mileage of the EV
W_{100}	Power consumption per 100 km, in kWh/(100 km)
μ_s, σ_s	Mean and variance
C	Rated battery capacity
SOC_0	Initial state of charge
R_{AC}	AC resistance
T_1	Thermal resistance of the insulation layer
T_2	Thermal resistance from the shielding layer to the armor layer
T_3	Thermal resistance of the armor layer and the outer sheath
T_4	External thermal resistance
c_i	Number of cable cores
θ_0	Ambient temperature
k_B	Boltzmann constant
L_0	Designed lifespan of the cable
Δw	Activation energy
β	Shape parameter
η	Scale parameter
$\mathbf{x}^j_{i,\max}$	Upper bound
$\mathbf{x}^j_{i,\min}$	Lower bound
$\mathbf{D}$	Dimension
ξ	Curvature coefficients
$\mathbf{K}$	Proportionality coefficients

Variables

P_N	Rapid charging power
I_1, I_n	Effective values of the fundamental and nth harmonic currents, respectively
U_1, U_n	Effective values of the fundamental and nth harmonic voltages, respectively
h	Order of the higher harmonics
λ_1	Ratio of the shield layer loss to the conductor loss
λ_2	Proportion of loss attributed to the armor layer
θ_c	Temperature rise of the cable
$L_h(t)$	Cable's life at time t
$T(t)$	Cable's temperature at time t hours
$\mathbf{X}_i$	ith candidate solution
$\mathbf{N}$	Total number of candidate solutions
$\mathbf{x}^j_i$	jth decision variable representing the ith candidate solution
H^*	Cable's real-time health index
$\lambda(t)$	Cable fault rate
λ_k	Fault rate after kth maintenance
$\psi(\cdot)$	Basis functions
$\mathbf{Z}$	Measured quantities

frontiers | Frontiers in Energy Research

TYPE Original Research
PUBLISHED 08 January 2024
DOI 10.3389/fenrg.2023.1296037

OPEN ACCESS

EDITED BY
Lu Zhang,
China Agricultural University, China

REVIEWED BY
Xiangjun Zeng,
China Three Gorges University, China
Xuran Zhang,
State Grid Smart Grid Research Institute Co., LTD, China
Zongshuai Jin,
Shandong University, China

*CORRESPONDENCE
Zhengzhong Gao,
skdgzz@163.com

RECEIVED 18 September 2023
ACCEPTED 16 October 2023
PUBLISHED 08 January 2024

CITATION
Yin X, Gao Z, Cheng Y, Hao Y and You Z (2024), An ultra-short-term forecasting method for multivariate loads of user-level integrated energy systems in a microscopic perspective: based on multi-energy spatio-temporal coupling and dual-attention mechanism. *Front. Energy Res.* 11:1296037. doi: 10.3389/fenrg.2023.1296037

An ultra-short-term forecasting method for multivariate loads of user-level integrated energy systems in a microscopic perspective: based on multi-energy spatio-temporal coupling and dual-attention mechanism

Xiucheng Yin[1], Zhengzhong Gao[1]*, Yumeng Cheng[1], Yican Hao[1] and Zhenhuan You[2]

[1]Institute of Automation, Shandong University of Science and Technology, Qingdao, China, [2]China Huangdao Customs, Qingdao, China

An ultra-short-term multivariate load forecasting method under a microscopic perspective is proposed to address the characteristics of user-level integrated energy systems (UIES), which are small in scale and have large load fluctuations. Firstly, the spatio-temporal correlation of users' energy use behavior within the UIES is analyzed, and a multivariate load input feature set in the form of a class image is constructed based on the various types of load units. Secondly, in order to maintain the feature independence and temporal integrity of each load during the feature extraction process, a deep neural network architecture with spatio-temporal coupling characteristics is designed. Among them, the multi-channel parallel convolutional neural network (MCNN) performs independent spatial feature extraction of the 2D load component pixel images at each moment in time, and feature fusion of various types of load features in high dimensional space. A bidirectional long short-term memory network (BiLSTM) is used as a feature sharing layer to perform temporal feature extraction on the fused load sequences. In addition, a spatial attention layer and a temporal attention layer are designed in this paper for the original input load pixel images and the fused load sequences, respectively, so that the model can better capture the important information. Finally, a multi-task learning approach based on the hard sharing mechanism achieves joint prediction of each load. The measured load data of a UIES is analyzed as an example to verify the superiority of the method proposed in this paper.

KEYWORDS

load pixel image, spatio-temporal coupling, attention mechanism, multi-task learning, MCNN

1 Introduction

Due to the swift economic and social growth, global warming, shortage of fossil energy and environmental pollution problems are becoming more and more prominent (Ji et al., 2018). Promoting the transformation of the traditional energy system, to improve the efficiency of energy utilisation and to reduce carbon emissions is currently a major issue facing the global energy industry (Cheng et al., 2019a). The traditional energy system is limited to the independent planning, design and operation of energy systems such as electricity, gas, heat and cold, which artificially severs the coupling relationship between different types of energy sources, and is unable to give full play to the complementary advantages between energy sources (Wang et al., 2019). Energy utilisation efficiency, renewable energy consumption, energy conservation and emission reduction have all encountered bottlenecks (Cheng et al, 2019b). In response to the above problems, the concepts of energy internet (EI) and integrated energy system (IES) have been put forward and highly valued by many countries, which emphasise the development mode of changing from the production and supply of each energy source to the operation of joint scheduling of multiple energy sources (Li et al., 2018; Li and Xu, 2018; Zhu et al., 2021). Among them, IES, as an important physical carrier of EI, is an important energy utilisation method in the process of energy transition, as well as an effective method to promote renewable energy consumption and improve energy efficiency (Wu et al., 2016). User-side multivariate load ultra-short-term prediction as the IES optimal scheduling, the primary premise of energy management, is no longer limited to the independent prediction of a single energy consumption, it must take into account multiple energy systems at the same time (Li et al., 2022), which puts forward higher requirements for the accuracy and reliability of the IES multivariate load prediction, and it has become one of the research hotspots in the energy field at the present time.

Theoretically, traditional load forecasting has developed into a more developed system that focuses mostly on single loads like electricity, natural gas, cooling, and heating. Data-driven artificial intelligence techniques have been extensively employed in the research of load forecasting applications since the emergence of a new generation of artificial intelligence technology. On a technological level, there are two general groups of AI-based load prediction techniques: deep learning techniques and conventional machine learning techniques.

To accurately anticipate daily peak demand for the next month, Gao et al. (2022a) used a hybrid of extreme gradient boosting (XGBoost) and multiple linear regression (MLR). Short-term load forecasting in the literature (Singh et al., 2017) was accomplished with the help of a three-layer feedforward artificial neural network (ANN). For predicting the following day's electrical usage over a period of 24 h, a support vector regression machine (SVM) based technique was presented in the literature (Sousa et al., 2014). Short-term electric demand forecasting using a hybrid model based on feature filtering convolutional neural network (CNN) with long and short-term memory was developed by Lu et al. (2019). Short-term cold load prediction in buildings using deep learning algorithms was achieved by Fan et al. (2017). It was suggested by Gao et al. (2022b) to forecast the cold load of big commercial buildings using a hybrid prediction model based on random forest (RF) and extreme learning machine (ELM), and the benefits of this model were validated in terms of time complexity and its own superior generalisation ability. Xue et al. (2019) proposed a heat load prediction framework based on multiple machine learning algorithms, such as SVM, deep neural network (DNN), and XGBoost, and then implemented a multi-step ahead heating load prediction in a district heating system to verify the superiority of the recursive strategy. A novel empirical wavelet transform (EWT) technique has been developed in the literature (Al-Musaylh et al., 2021) for revealing the intrinsic patterns in daily natural gas consumption demand data. For short-term gas load forecasting, Xu and Zhu, 2021 created a neural network that combines a time-domain convolutional network (TCN) with a bi-directional gated recurrent unit (BiGRU).

The foundation of conventional machine learning techniques is feature engineering, which is labor-intensive, sensitive to noise and outliers, and inefficient when dealing with high-dimensional data. Contrarily, the multi-layer mapping of deep learning allows for the effective extraction of the data's deep characteristics, greatly enhancing the model's capacity to represent the pattern of sample distribution. As a result, it demonstrates improved load forecasting prediction accuracy.

In fact, traditional energy system studies focus on a single type of energy, while IES considers diverse energy demands and focuses on high-quality multi-class energy studies (Hu et al., 2019). If the traditional single-load prediction method is still used, it is difficult to capture the correlation characteristics between different loads, and the prediction accuracy cannot be guaranteed. Therefore, how to properly dispose of the coupling relationship between multiple loads, set a more complete input feature set, effectively learn multiple energy coupling information, and achieve accurate IES multiple load forecasting based on this information is the focus of current research. The main mainstream techniques to deal with the coupling are multivariate phase space reconstruction (MPSR) (Zhao et al., 2016), multi-task learning (MTL) (Shi et al., 2018), and convolutional neural networks (CNN) (Li et al., 2022). In addition, Bai et al. (2022) utilized the minimum redundancy maximum relevance (MRMR) to screen feature sequences and the Seq2Seq model based on the dual attention mechanism to learn the spatio-temporal properties of urban energy load sequences. The above literature verifies that considering the coupling characteristics among loads helps to improve the forecasting accuracy, and also verifies the role of the attention mechanism.

Previously, IES load prediction models have focused on single-load independent prediction, while single-task load prediction methods consider every prediction task simply, mutually independent subproblem, which ignores the coupling relationships within multiple source loads in IES (Zhu et al., 2019). Multi-task learning improves model generalization by using a shared mechanism to train multiple tasks in parallel to obtain information implicit in multiple related tasks. In recent years, multi-task learning has been gradually applied to IES multivariate load prediction. Niu et al. (2022) constructed a new multi-task loss function weight optimisation method to search for optimal multi-task weights for balanced multi-task learning (MTL), which improves the prediction of IES multivariate loads.

Currently, the vast majority of studies on IES multivariate load forecasting are limited to macroscopic class load forecasting

methods, focusing only on mining the correlation between each load's own sequence and sequences of other external macro-factors. However, in some cases, the load variation patterns of different load nodes (e.g., substations, parks, and customers) within the same region may be potentially correlated in space and time due to the same external factors (e.g., weather and electricity prices). In order to improve the IES multiple load forecasting method, it is necessary to consider the spatial and temporal correlation of each load node in the IES. At this stage, the research on IES multiple load forecasting based on microscopic class load forecasting methods is still in its infancy. Compared with the previous studies, the contributions of this paper are as follows.

(1) The spatio-temporal correlation of the energy-using behavior of each load unit in the UIES is comprehensively analyzed, and each load unit is defined as a load pixel point. Based on the strong correlation of adjacent pixel points in static images and with reference to the storage method of color images, an IES multivariate load input feature set in the form of image-like based on the microscopic class load prediction method is proposed, which is a novel method for constructing the IES input feature set.
(2) A deep spatio-temporal feature extraction network (MCNN-BiLSTM) for multivariate load prediction is proposed. Among them, MCNN is used to perform independent spatial feature extraction for each load component pixel image, and BiLSTM is used to realize temporal feature extraction for fused load features at each time step. To realize end-to-end training from space to time and collaborative mining of spatio-temporal information.
(3) A multi-head attention mechanism is introduced in the spatial and temporal dimensions, respectively. This attention mechanism is a plug-and-play module that is placed before MCNN and before BiLSTM to enable the model to pay differential attention to the information in the original input load pixel image and the fused load sequence during the learning process.
(4) Using BiLSTM as the feature sharing layer, a multi-task learning approach under the hard sharing mechanism is adopted to further learn the inherent coupling information among electricity, heat, and cold loads. In order to adapt to the characteristics of the fluctuation of the three load profiles, as well as to explore the correlation of each load with meteorological factors and calendar rules, three fully connected neural networks with different structures are designed as feature interpretation modules.

2 User-level IES load characterization

2.1 User-level IES energy coupling mechanism

A user-level IES is an integrated energy system constructed at the distribution and usage levels to meet the diversified energy needs of multiple types of users, such as industrial parks, commercial centres, residential buildings and educational institutions. A typical interactive structure of a user-level IES is shown in Figure 1, which can be roughly divided into the IES side and the end-user side. On the IES side, the IES service provider conducts accurate multiple load forecasting based on the metered data of users' energy consumption of electricity, heat, cooling, etc. collected in real time through intelligent terminals, so as to coordinate the transformation, storage, and distribution of energy sources within the IES to satisfy the diversified energy demand of users.

In IES operation, external energy inputs come from the grid and the natural gas network, internal energy generation comes from rooftop photovoltaic systems and micro-gas turbines, various energy conversion equipment couples the different energy systems in a flow of energy, and energy storage equipment is used to increase the economy and flexibility of the system operation. The IES provider's ability to provide electricity, heat, and cooling to its customers for a variety of energy needs is significantly affected by meteorological conditions, day-type information and building characteristics. In terms of meteorological conditions, the demand for heating and cooling loads varies seasonally with the gradual change in temperature. In terms of day-type information, the difference in human production activities between weekdays and holidays results in differences in energy demand. In terms of building characteristics, different system functions are important reasons for influencing the characteristics of energy use. Industrial areas tend to consume large amounts of electrical loads, and the cooling and heating loads play an auxiliary role to jointly serve the production schedule. The fluctuation of cooling and heating loads in commercial and living areas is closely related to human activities and shows some correlation. Figure 2 shows the variation of the total electric, thermal and cooling loads of the user-level IES studied in this paper under four seasons of the year, and the temperature variation under the corresponding moments.

As can be seen from Figure 2, the fluctuation of various types of loads in this UIES is accompanied by obvious seasonal changes. And the degree of coupling between the loads under different time periods has a certain degree of variability. Among them, the demand size of each load in summer and winter seasons has a large difference, which is especially obvious in the hot and cold loads. The spring and autumn seasons show a clear transition, with the change of temperature, the fluctuation of the hot and cold loads show a diametrically opposite trend, and the cold loads show a high degree of consistency between the overall external morphology and the temperature change. In addition, the overall trend of electric load and cold load is consistent in different periods, which indicates that the change in demand for cold load also affects the level of electric energy consumption.

2.2 Spatial correlation analysis of load units

In this paper, buildings and activity places with load collection equipment are defined as load units in the UIES, and the macro load sequence of the UIES is aggregated from the corresponding micro load sequence of each load unit. In UIES, the energy consumption behavior of users is a dual reflection of the energy demand of load units at both macro and micro levels, which depends on macro-level factors such as energy price fluctuations, climate seasons, day-type information, etc., as well as micro-level factors such as regional planning layout and building design characteristics. At the macro

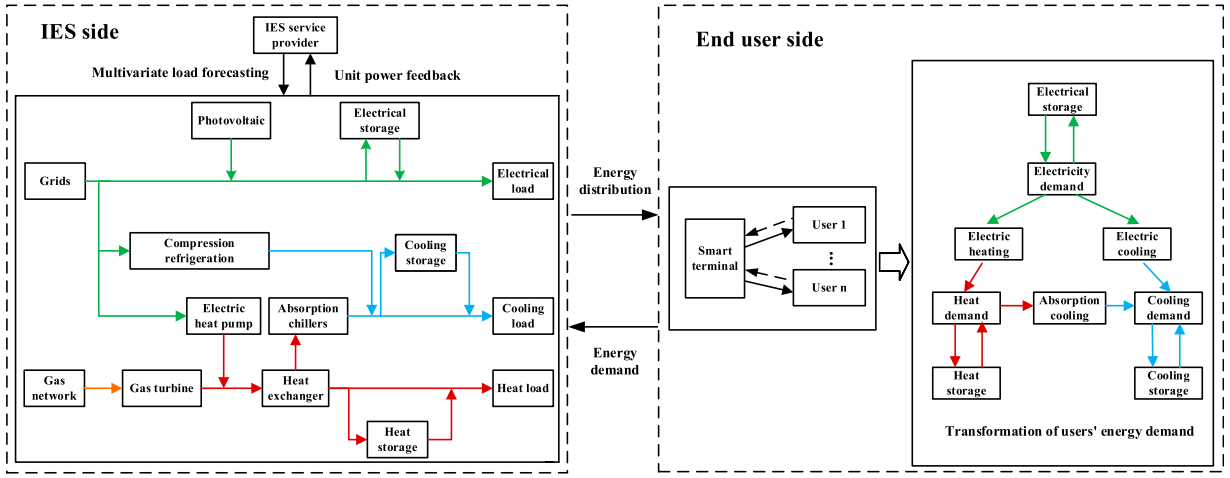

FIGURE 1
Simplified model of the UIES interaction structure.

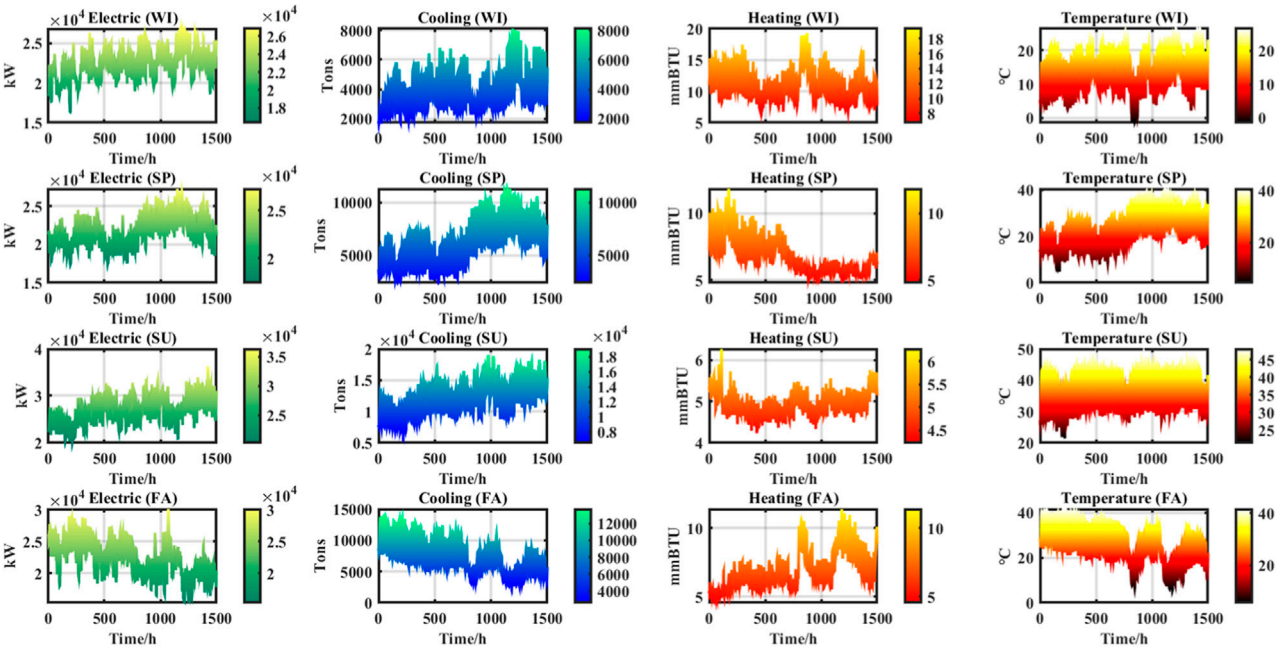

FIGURE 2
Multi-energy load correlation analysis of UIES.

level, UIES is confined to smaller spatial scales, load units are influenced by the same microclimatic conditions in the same local area, and the energy use behavior of users maintains a certain degree of consistency. At the micro level, load units with similar geospatial locations or with the same functional attributes tend to have similar energy use habits. However, the types of load units with different functional attributes and their building sizes are often different, which directly leads to some differences in users' energy use habits, energy end-uses (cooling, heating, lighting, etc.) and the proportion of each energy consumption. In addition, users' energy use behavior can be simultaneously affected by equipment accidents and maintenance, extreme weather, major events and other emergencies, resulting in sudden changes in loads. Figure 3 shows the electrical, thermal and cooling load change curves for the nine load units in the UIES over a 240-h period.

As can be seen in Figure 3, the three types of loads in each load unit exhibit a high degree of variability in their external patterns. Among them, the electrical load is significantly affected by the variation of day types. In addition to User1, the load change patterns of User2 to User9 have some correlation, which is manifested as having continuous fixed large peaks on weekdays and certain small peaks on double holidays. The fluctuation of the cold load has no obvious weekday or double holiday pattern, showing a gradual increase in progressive change. For the heat

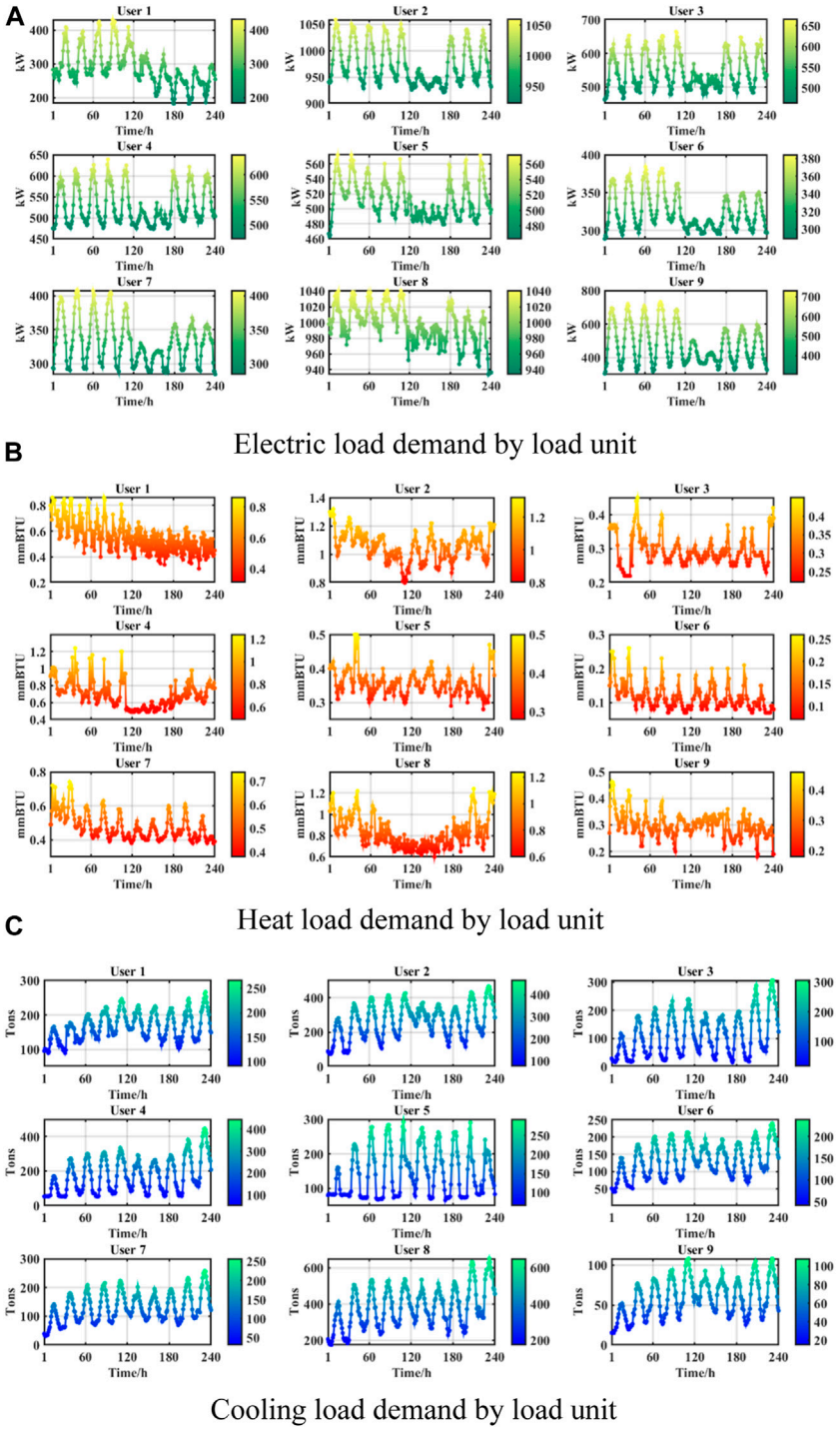

FIGURE 3
Demand for various types of energy of load units. **(A)** Electric load demand by load unit. **(B)** Heat load demand by load unit. **(C)** Cooling 199 load demand by load unit.

load, affected by the climate characteristics, its demand scale is much smaller than the electricity, cold load, the user heat behavior is more random. In addition to User3, User6 and User7 heat load changes have a certain correlation, the rest of the heat load fluctuation of the load unit has a strong randomness and time-varying changes, the cyclical law of change is not traceable.

After the above analysis, it can be seen that the non-independence of load change of load unit is not only related to its own building functional characteristics, scale size, location and other factors, but also has a close connection with local climate characteristics and calendar rules. Various types of load units are complex aggregates with broad spatial correlation. Therefore, the load change of each load unit is the deeper "implied information" in

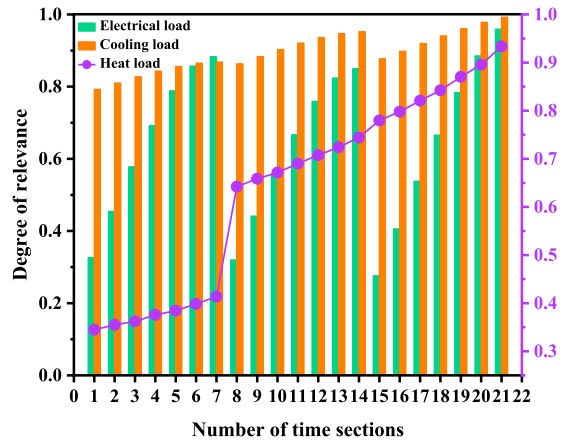

FIGURE 4
Time correlation analysis.

the change rule of the total load of UIES, and it is the "underlying logic" that reveals the characteristics of the total load's external form, which contains a wealth of information to be mined.

2.3 Temporal correlation analysis of load units

Time correlation analysis is an essential and important part of load forecasting work. Referring to time correlation can select reasonable historical load variation intervals as input features in the subsequent actual load forecasting work, which is helpful to improve the model learning efficiency and reduce the computational overhead of the model. Therefore, in this paper, a certain number of load units are randomly selected for time correlation analysis based on Pearson correlation coefficients, which are shown in Figure 4.

In Figure 4, the time sections of historical data selected in this paper are the first seven historical moments (numbered 15–21) from the current moment $(t + 1)$, the $t + 1$ moment and the first six moments a day ago (numbered 8–14), and the $t + 1$ moment and the first six moments a week ago (numbered 1–7). According to the results of the time correlation analysis, the fluctuation of electric and cold loads has an obvious cyclical law of change, and the load at the current moment is not only affected by the load at the neighbouring historical moment but also has a strong correlation with the load at the same moment a day and a week ago. Among them, the fluctuation change of the cold load is the most stable and has strong predictability. While the temporal correlation of heat load gradually decreases with the increase in time interval, This is because changes in heat load demand are easily influenced by external factors. When the time span is large, the external factors change a lot, resulting in the heat load fluctuation no longer having a clear regularity.

3 Integrated load pixel image construction and spatio-temporal feature extraction

3.1 Integrated load pixel image construction

Compared with the inter-regional level IES and regional level IES, the UIES is smaller in size, its lack of random error elimination due to load aggregation effect, and greater load volatility. It is sometimes difficult to generalize the internal change pattern of each total load in the UIES if the macroscopic class load forecasting method is adopted. From the analysis in Subsections 2.2 and 2.3, it can be seen that the load data of each load unit in the UIES contains a large amount of spatio-temporal data, which is the most intuitive characteristic information for portraying the change patterns of each type of total load in the UIES.

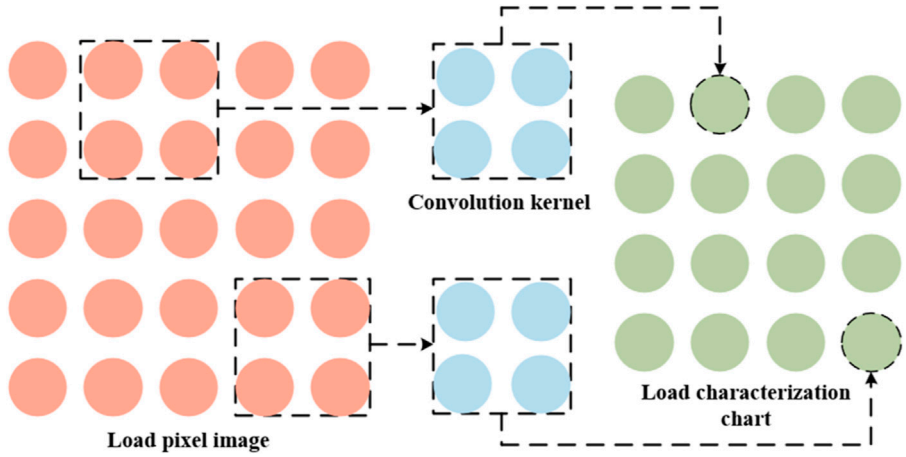

FIGURE 5
CNN-based feature extraction for load pixel images.

This paper is based on a microscopic class load forecasting method, which focuses on the energy demand of each load unit in the UIES region, and ultimately produces the overall consumption forecast results for each type of energy in the UIES. Compared with the macroscopic class load forecasting method, this type of method explores the energy consumption characteristics of users from within the region, and its modeling is more detailed and thorough, so that more accurate forecast results can be obtained.

Usually, there is a strong correlation between a pixel point of a static image and its relative neighbouring pixel points, so in the field of image recognition, convolutional neural networks are often able to capture the local features of an image through a small receptive field so as to form a feature quantity with certain regularity and correlation in the high-dimensional space. Based on the analysis in subsection 2.2, it can be seen that there is also a certain correlation between the load units of UIES, and the correlation is more significant for load units with the same functional attributes and closer geospatial locations, which is similar to the pixel law of still images. Analogous to the application of CNN in the field of image recognition, as shown in Figure 5. In this paper, each load unit in the studied UIES is regarded as a load pixel point, and the local feature extraction capability of CNN is used to mine the hidden information among load units from local to global perspectives so as to realize ultra-short-term prediction of various types of total loads in the UIES.

For a colour image, each pixel contains the three colour components of RGB, which can be regarded as a superposition of three layers of two-dimensional arrays, each layer representing a color channel. In the context of this paper, each load unit in UIES has different levels of demand for electricity, heat and cold, so load unit contains the characteristic information of three kinds of loads. Following the storage form of color images, each load pixel follows a certain arrangement to form a comprehensive load pixel image, which consists of three load component images of electricity, heat and cold. In this paper, from the functional characteristics of the load units contained in the studied UIES, the load units are divided into several categories according to their functional attributes, and the load units with close spatial locations in each category are arranged closely. For example, the UIES under study contains N load units, which constitute a composite load pixel image of length and width $\lceil\sqrt{N}\rceil$. The load units of each attribute category are filled with load pixel points of each row along the image column direction in turn, and finally the blank load pixel points are processed by complementary 0.

Based on the analyses in subsection 2.3, the integrated load pixel images with different time delays from the predicted moment are constructed separately, as shown in Figure 6. In this paper, the integrated load pixel image at each moment is regarded as a frame of $(\lceil\sqrt{N}\rceil\times\lceil\sqrt{N}\rceil)$, and the load demand fluctuation of each load unit in the time period $(t-h+1,t)$ can be reflected by stacking h frames. In this way, the input feature is a three-dimensional matrix with spatio-temporal information and covering the three load coupling features at the same time, while the output feature is the total electric, thermal and cooling loads at the moment $t+1$ to be predicted.

3.2 Spatial feature extraction based on parallel multichannel convolutional neural network

When CNN performs feature extraction on colour images, it uses the multi-channel mechanism to access the three colour channels of the colour image. Although the load pixel image constructed in this paper has similarities with the colour image, the three load components of the load pixel are more independent and have different meanings compared to the RGB components of the pixel points. Therefore, two aspects should be taken into account when using CNN for the spatial feature extraction of load pixels. One is that the feature independence of each load itself should be preserved in the feature extraction process. Second, the input features in this paper are loading pixel images at different moments, which need to be formed into a standard time-step format before subsequent time-dependent capturing. If the multi-channel mechanism of CNN is directly used to extract features from the load pixel images at different moments, the feature information of the three loads at different moments will be fused at the same time in the first convolution process, and the independence and temporal integrity of the loads embedded in the input sequences will not be preserved. Therefore, in this paper, a multi-channel parallel CNN structure is designed for the research context. Figure 7 shows its network architecture.

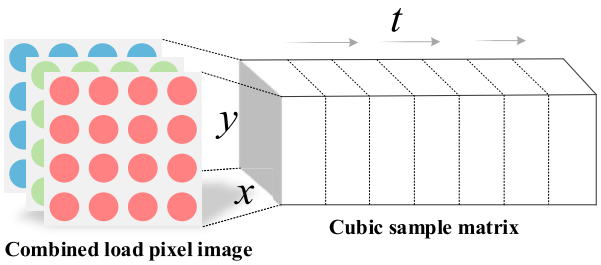

FIGURE 6
Integrated load pixel images at different moments.

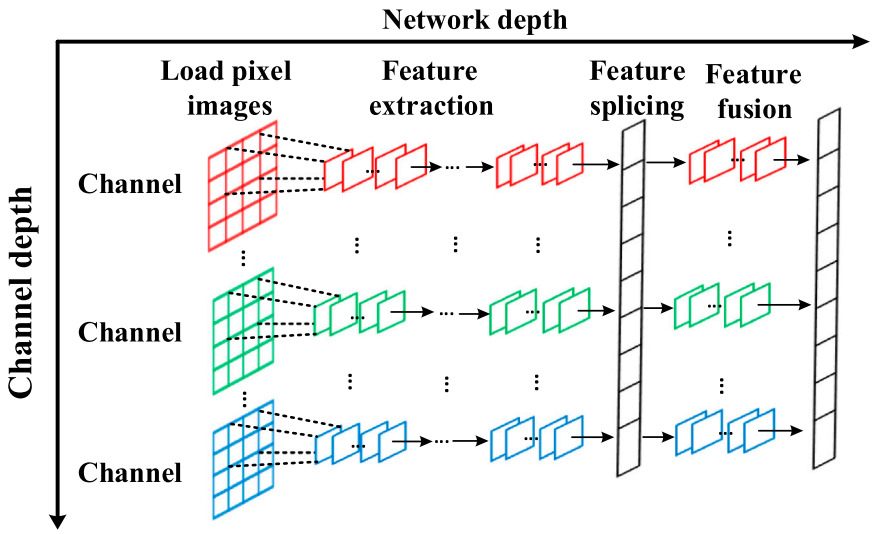

FIGURE 7
Multi-channel feature extraction CNN network structure.

In Figure 7, the multichannel convolutional neural network (MCNN) constructed in this paper has the dual characteristics of channel depth and network depth. In the channel depth direction, no information is exchanged between each feature extraction channel until feature fusion, and the own features of each load component image under each time section are extracted separately and independently. The spatial characteristics of the load pixels are extracted in a sub-category, time-segmented manner. Therefore, the number of channels of MCNN is always kept as $T_{se} \times N_{lo}$ during feature extraction, where T_{se} is the number of time sections and N_{lo} is the number of load types in the studied IES. In the direction of network depth, considering that increasing the pooling layer will accelerate the convergence speed of the network but also cause certain information loss phenomenon, so this paper only uses the convolutional layer for feature extraction. For a certain channel, the feature extraction process is shown below.

$$\boldsymbol{C}_{i,j}^{(k)} = f\left(\sum_{S=1}^{M} \boldsymbol{C}_{S,j-1}^{(k)} \otimes \boldsymbol{W}_{i,j}^{(k)} + \boldsymbol{b}_{i,j}^{(k)}\right) \boldsymbol{C}_{0,0}^{(k)} \in \boldsymbol{G} \tag{1}$$

In the formula: $\boldsymbol{C}_{S,j-1}^{(k)}$ is the S-th feature map in the $j-1$-th convolution layer of the k-th channel; $\boldsymbol{W}_{i,j}^{(k)}$ is the weight matrix of the i-th convolution kernel in the j-th convolution layer of the k-th channel; $\boldsymbol{b}_{i,j}^{(k)}$ is the bias matrix; $\boldsymbol{C}_{i,j}^{(k)}$ is a feature map output from the j-th convolution layer; $\otimes$ is the convolution operation; f is the activation function; M is the number of feature maps; $\boldsymbol{G}$ is the original set of each load pixel image; $\boldsymbol{C}_{0,0}^{(k)}$ is a load component image under a certain time section of the input to the k-th channel.

On the basis of MCNN fully extracting each load component image under each time section, the final number of feature maps output by all channels is $T_{se} \times N_{lo} \times M_{nu}$, where M_{nu} is the number of convolution kernels in the last convolution layer of each channel. It can be seen that the spatial features of each type of load output by MCNN not only maintain the feature independence of each load itself, but also retain the information of the time dimension of each load feature, which can be expressed as:

$$\boldsymbol{C}^{e,h,c} = \left[\boldsymbol{C}_{t-h+1}^{e}, \boldsymbol{C}_{t-h+1}^{h}, \boldsymbol{C}_{t-h+1}^{c}, \ldots, \boldsymbol{C}_{t}^{e}, \boldsymbol{C}_{t}^{h}, \boldsymbol{C}_{t}^{c}\right] \tag{2}$$

In the formula: $\boldsymbol{C}^{e,h,c}$ is the set of feature maps for the output of each channel of the MCNN; $\boldsymbol{C}^{e}$, $\boldsymbol{C}^{h}$, $\boldsymbol{C}^{c}$ are the set of spatial characteristic maps of electrical, thermal and cooling loads at a given moment in time, respectively.

Before proceeding with the subsequent temporal feature extraction, the spatial features of various types of loads at the same moment in time need to be fused again using the multi-channel mechanism. At this time, the number of channels of MCNN is T_{se}, and the input features of each channel are under the same moment $\boldsymbol{C}^{e}$, $\boldsymbol{C}^{h}$, $\boldsymbol{C}^{c}$. Finally, the output fused load feature maps of each channel are flattened and the features are spliced in chronological order in order to form a fused load feature sequence with a standard time step, as shown in the following equation:

$$\boldsymbol{R} = \left[\boldsymbol{F}_{t-h+1}, \boldsymbol{F}_{t-h+2}, \ldots, \boldsymbol{F}_{t}\right] \tag{3}$$

In the formula: $\boldsymbol{R}$ is the fused load feature sequence; $\boldsymbol{F}$ is the fused load feature vector at a certain time section.

3.3 Time-dependent capture based on bidirectional long and short-term memory networks

LSTM is a variant of the traditional recurrent neural network (RNN), which is improved by introducing input gates, forgetting gates, and output gates, thus solving the long-term dependence problem of RNN in the training process and avoiding the gradient explosion and gradient dispersion phenomenon. The rules for calculating each variable in LSTM are shown below.

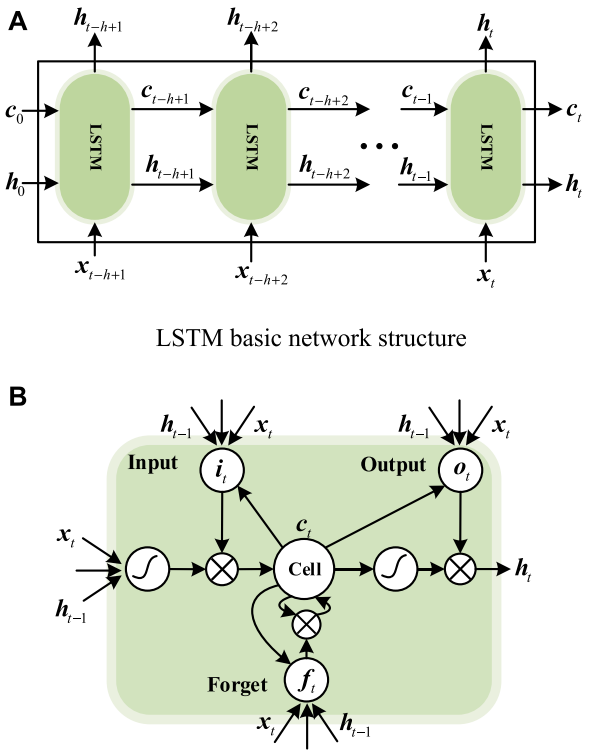

FIGURE 8
LSTM network architecture.

$$\begin{cases} \boldsymbol{u}_t = \sigma(\boldsymbol{W}_{xu}\boldsymbol{x}_t + \boldsymbol{W}_{hu}\boldsymbol{h}_{t-1} + \boldsymbol{b}_u) \\ \boldsymbol{f}_t = \sigma\left(\boldsymbol{W}_{xf}\boldsymbol{x}_t + \boldsymbol{W}_{hf}\boldsymbol{h}_{t-1} + \boldsymbol{b}_f\right) \\ \boldsymbol{o}_t = \sigma(\boldsymbol{W}_{xo}\boldsymbol{x}_t + \boldsymbol{W}_{ho}\boldsymbol{h}_{t-1} + \boldsymbol{b}_o) \\ \boldsymbol{g}_t = tanh\left(\boldsymbol{W}_{xg}\boldsymbol{x}_t + \boldsymbol{W}_{hg}\boldsymbol{h}_{t-1} + \boldsymbol{b}_g\right) \\ \boldsymbol{c}_t = \boldsymbol{c}_{t-1} \odot \boldsymbol{f}_t + \boldsymbol{g}_t \odot \boldsymbol{u}_t \\ \boldsymbol{h}_t = tanh(\boldsymbol{c}_t) \odot \boldsymbol{o}_t \end{cases} \tag{4}$$

In the formula: $\boldsymbol{u}_t$, $\boldsymbol{f}_t$, $\boldsymbol{o}_t$ denote the input gate, forgetting gate and output gate at time t; $\boldsymbol{W}_{xu}$, $\boldsymbol{W}_{xf}$, $\boldsymbol{W}_{xo}$, $\boldsymbol{W}_{xg}$ are the weight coefficients corresponding to $\boldsymbol{x}_t$; $\boldsymbol{W}_{hu}$, $\boldsymbol{W}_{hf}$, $\boldsymbol{W}_{ho}$, $\boldsymbol{W}_{hg}$ are the weight coefficients corresponding to $\boldsymbol{h}_{t-1}$; $\boldsymbol{b}_u$, $\boldsymbol{b}_f$, $\boldsymbol{b}_o$, $\boldsymbol{b}_g$ are the bias vectors; $\boldsymbol{x}_t$ is the input at time t ; $\boldsymbol{h}_t$ is the hidden state at moment t; $\boldsymbol{c}_t$ is the intermediate state value; $\boldsymbol{\sigma}$ is the sigmoid activation function; $\odot$ denotes the element-by-element product. The basic network structure and internal structure of the LSTM are shown in Figure 8.

In the traditional one-way LSTM, the update of internal variables follows a strict one-way transfer rule, which leads to a one-way temporal dependence of the hidden states of the LSTM at each moment from the history to the future. As shown in Figure 8, the final state $\boldsymbol{h}_t$ of the network is intrinsically related to $(\boldsymbol{x}_1, \boldsymbol{x}_2, \cdots, \boldsymbol{x}_t)$ at all previous moments, while the hidden state $\boldsymbol{h}_{t-1}$ at the previous moment cannot be linked to $\boldsymbol{x}_t$. Therefore, in the one-way LSTM, only the final hidden state can utilize all the input information, while the hidden state of the previous moment cannot be influenced by the subsequent input information. For the load sequence, there is a close relationship between the historical moment's load and the future moment's load. The one-way LSTM is only capable of capturing the time dependence of the load sequence from the past to the future, and is unable to derive feature information in the reverse direction. This paper uses BiLSTM for temporal feature extraction of load sequences in order to resolve the inherent defects of one-way LSTM. Figure 9 depicts the structure of BiLSTM, which consists of both forward- and backward-facing one-way LSTMs. BiLSTM can be trained forward and backward. BiLSTM can fully utilize the input information and perform temporal feature extraction more comprehensively than one-way LSTM.

As can be seen in Figure 9, the hidden state $\boldsymbol{h}$ of the BiLSTM is determined by the forward LSTM and the inverse LSTM together as follows:

$$\boldsymbol{h} = \left[\vec{\boldsymbol{h}} \oplus \overleftarrow{\boldsymbol{h}}\right] \tag{5}$$

To summarize the previous analysis, it uses BiLSTM to capture the temporal dependencies of the fused load feature sequence $\boldsymbol{R}$ obtained in subsection 3.2. The number of time steps of BiLSTM is h.

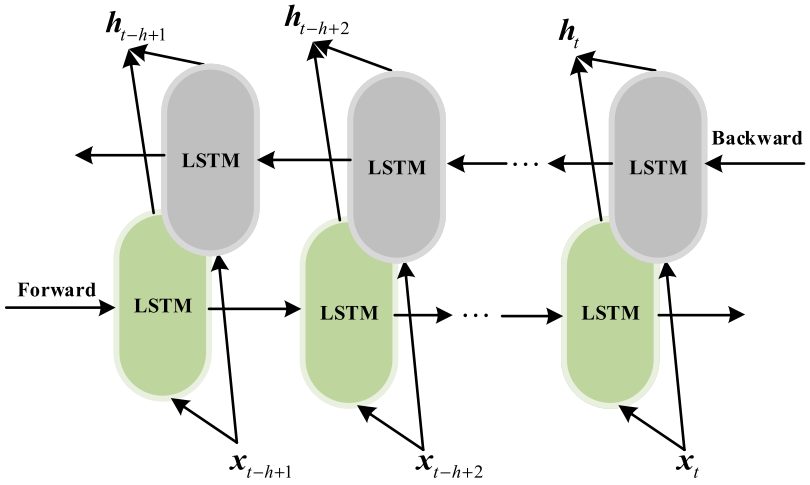

FIGURE 9
Bidirectional LSTM network structure.

The hidden state vector output from the last hidden layer of BiLSTM is shown as follows:

$$\boldsymbol{h}_t = [h_t^1, h_t^2, \ldots, h_t^n] \tag{6}$$

In the formula: $\boldsymbol{h}_t$ is the vector of hidden states output by BiLSTM; h_t is a hidden state at time t; n is the number of hidden states, which depends on the number of neurons in the top hidden layer of BiLSTM.

4 Attentional mechanisms and multitask learning

4.1 Multi-head attention mechanism

The attention mechanism can be viewed as a means of resource allocation in the model learning process, with the weight parameter of each feature serving as the resource of interest for the attention mechanism in deep neural networks. The attention mechanism focuses the model on important information by adaptively assigning weights to input variables. This paper proposes a multi-head attention mechanism model, as shown in Figure 10.

Taking a set of input features $\boldsymbol{X} = [x_1, x_2, \cdots, x_M]$ of dimension M as an example, a shared linear layer is used to obtain a preliminary weight vector $\boldsymbol{Y}$, as shown below:

$$\boldsymbol{Y} = \boldsymbol{\sigma}(\boldsymbol{W}\boldsymbol{X} + \boldsymbol{b}) \tag{7}$$

Where, $\boldsymbol{Y} = [y_1, y_2, \ldots, y_M]$ denotes the initial weight coefficients of each input feature; $\boldsymbol{W}$ is the weight matrix; $\boldsymbol{b}$ is the bias matrix; $\boldsymbol{\sigma}$ is the linear activation function.

On this basis, because this paper adopts the multi-head attention mechanism, a total of N linear transformations are performed, and the preliminary weight vector obtained by the N-th linear transformation is $\boldsymbol{Y}^{(N)} = [y_1^{(N)}, y_2^{(N)}, \ldots, y_M^{(N)}]$, and then the N preliminary weight vectors obtained are averaged to obtain the preliminary mean weight vector $\bar{\boldsymbol{Y}}$ is:

$$\bar{\boldsymbol{Y}} = \frac{1}{N}\sum_{S=1}^{N} Y^{(S)} \tag{8}$$

The relu activation function is used to restrict the initial mean weight vector $\bar{\boldsymbol{Y}} = [\bar{y}_1, \bar{y}_2, \ldots, \bar{y}_M]$ to a non-negative interval, and then normalize the weight coefficients by the Sigmoid function to obtain the final attention weight coefficients $\boldsymbol{\alpha} = [\alpha_1, \alpha_2, \ldots, \alpha_M]$, as shown below:

$$\boldsymbol{\alpha} = sigmoid\left(relu\left(\left[\bar{y}_1, \bar{y}_2, \ldots, \bar{y}_M\right]\right)\right) \tag{9}$$

In this paper, the initial mean weight vector $\bar{\boldsymbol{Y}}$ is first one-sidedly suppressed to the positive interval by the Relu function, and then normalized using Sigmoid. Finally, the final obtained feature attention weight vector is multiplied with the original input feature vector by elemental correspondence to obtain the weighted input feature vector, as shown below:

$$\boldsymbol{X}' = \boldsymbol{\alpha} \odot \boldsymbol{X} = [\alpha_1 x_1, \alpha_2 x_2, \ldots, \alpha_M x_M] \tag{10}$$

In the formula: $\boldsymbol{X}'$ is the weighted eigenvector; $\odot$ is the Hadamard product.

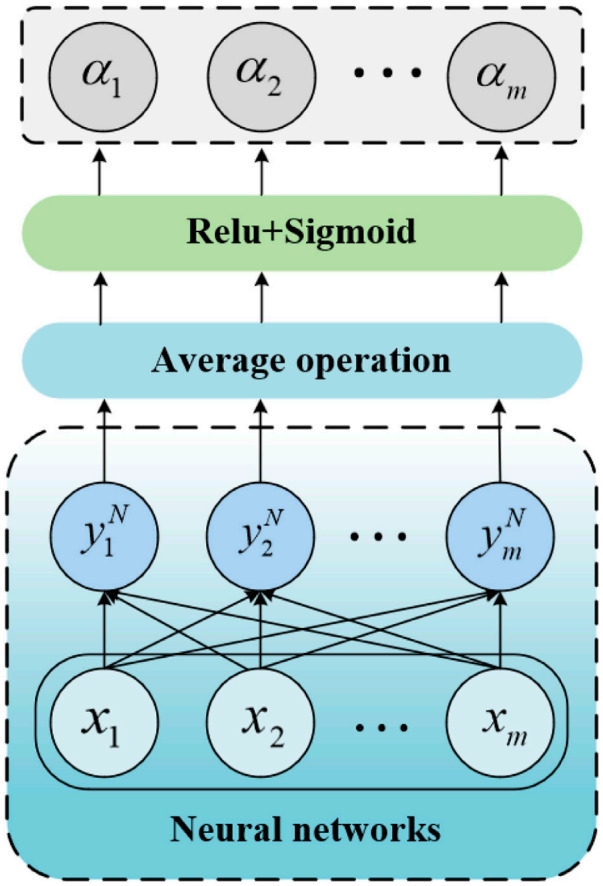

FIGURE 10
Multi-head attention mechanism.

4.1.1 Spatial attention

The most direct input feature of this paper is the load demand of each load unit at different moments in time, where the proportion of consumption of the three energy sources varies among load units and where a portion of the load units consume only one or two types of energy. Load pixel points that are irrelevant to a certain total load demand are not only unhelpful to the prediction result but even cause information interference in the model prediction. In this paper, the weights assigned to different load pixels can be calculated dynamically by introducing the spatial attention mechanism. The basic structure of the spatial attention mechanism model is shown in Figure 10, in which the input of the multi-head attention mechanism model is the pixel image of each load component constructed in subsection 3.1, and the output is the load pixel image after weighting each load pixel point. Due to the introduction of the spatial attention mechanism, the spatial attention weights can be used to express the contribution of different load pixels to each type of total load, so that the prediction model can focus on "important" load pixels in the learning process.

4.1.2 Temporal attention

Load forecasting is a typical time series forecasting problem, which is reflected in the extremely high dependence on historical information. In this paper, the temporal attention mechanism is introduced into the model to deeply mine the time series information. The basic structure of the temporal attention

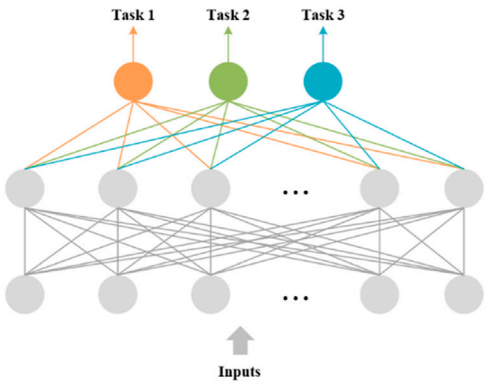

FIGURE 11
Multi-task learning network structure based on hard sharing mechanism.

mechanism is shown in Figure 10, in which the input to the model of the multi-head attention mechanism is the fused load sequence at the standard time step in subsection 3.2. Attention weights are assigned to the fusion features under each time step by the temporal attention mechanism to increase the model's attention to the important time point information during the training process.

4.2 Multitask learning mechanism

The data recorded by UIES contains a large amount of shared information about energy conversion. Multi-task learning can utilize this shared information to learn and acquire knowledge among multiple load prediction tasks and train the shared hidden layer on all tasks in parallel, thus improving the prediction accuracy of each load. In addition, the parameter sharing strategies for multi-task learning can be broadly categorized into hard and soft sharing (Niu et al., 2022). Considering the strong coupling of each load in UIES, this paper chooses the hard sharing mechanism that is suitable for dealing with more strongly correlated tasks. The structure of the hard sharing mechanism for multi-task learning is shown in Figure 11.

For a multi-task learning under a hard sharing mechanism, which contains multiple learning tasks $\boldsymbol{y}^m\,(m \in M)$ and data sets $\{\boldsymbol{x}_i, y_i^1, y_i^2, \ldots, y_i^M\}$, $(i = 1, 2, \ldots, N)$, where M is the number of tasks, N is the number of data samples, and y_i^m is the m-th task label of the i-th data point. $f^m(\boldsymbol{x}; \boldsymbol{\theta}^{sh}, \boldsymbol{\theta}^{ea})$, $\boldsymbol{x} \rightarrow \boldsymbol{y}^m$ is the prediction function, where $\boldsymbol{\theta}^{sh}$ is the shared parameter of each task in the shared layer, and $\boldsymbol{\theta}^{ea}$ is the independent correlation parameter of each task itself. Under multi-task learning, the overall objective optimization loss function is defined as:

$$\begin{cases} L(\boldsymbol{\theta}) = min\sum_{m=1}^{M}\lambda^m \hat{L}^m\left(\boldsymbol{\theta}^{sh}, \boldsymbol{\theta}^{ea}\right) \\ \hat{L}^m\left(\boldsymbol{\theta}^{sh}, \boldsymbol{\theta}^{ea}\right) = \frac{1}{N}\sum_{i=1}^{N}\hat{L}^m\left(f^m\left(\boldsymbol{x}_i; \boldsymbol{\theta}^{sh}, \boldsymbol{\theta}^{ea}\right), y_i^m\right) \end{cases} \tag{11}$$

In the formula: λ^m is the weight coefficient of each task; $\hat{L}^m(\boldsymbol{\theta}^{sh}, \boldsymbol{\theta}^{ea})$ is the loss function; $L(\boldsymbol{\theta})$ is the overall objective optimization loss function.

5 IES multiple load prediction framework based on spatio-temporal coupling and multi-headed attention

The forecasting workflow in this paper is divided into the following six stages:

Step 1: Load pixel image construction

Based on the load pixel image construction method in subsection 3.1, a comprehensive load pixel image containing three load components of electricity, heat, and cold is constructed at a certain moment, as shown below.

$$\boldsymbol{P} = \left[\begin{bmatrix} p_{1,1}^e & \cdots & p_{1,n}^e \\ \vdots & \ddots & \vdots \\ p_{n,1}^e & \cdots & p_{n,n}^e \end{bmatrix}, \begin{bmatrix} p_{1,1}^h & \cdots & p_{1,n}^h \\ \vdots & \ddots & \vdots \\ p_{n,1}^h & \cdots & p_{n,n}^h \end{bmatrix}, \begin{bmatrix} p_{1,1}^c & \cdots & p_{1,n}^c \\ \vdots & \ddots & \vdots \\ p_{n,1}^c & \cdots & p_{n,n}^c \end{bmatrix}\right] \tag{12}$$

In the formula: $\boldsymbol{P}$ is the integrated load pixel image at a certain time section; p^e, p^h, and p^c represent the electric load, hot load, and cooling load pixel points respectively; $n \times n$ is the size of the load pixel image, which can also be regarded as the resolution size.

Based on this, the integrated load pixel images at different historical moments from the prediction target moment $(t+1)$ need to be constructed separately. Further, the time-varying nature of the load is demonstrated by a frame by frame load pixel image, and the pixel values at any specific location will be continuously updated according to a certain temporal resolution, as shown in equation 13. The dimension size of the input features is thus $n \times n \times 3h$, where n is the spatial dimension, h is the channel dimension, which is the length of the historical time period.

$$\boldsymbol{G} = \left[\boldsymbol{P}_{t-h+1}, \boldsymbol{P}_{t-h+2}, \ldots, \boldsymbol{P}_t\right] \tag{13}$$

Step 2: Spatial attention weighting

Before inputting each load component pixel image into MCNN for spatial feature extraction, the spatial attention layer is constructed using the multi-head attention mechanism proposed in subsection 4.1 of this paper. The input features' spatial dimension is first reduced to their channel dimension, and the input feature dimension becomes $1 \times 1 \times 3nnh$, which is then input to multiple shared linear layers. The dynamic assignment of spatial attention weights during model learning is realized according to equation 7 to equation 10, and each load pixel point is assigned its own spatial attention weight coefficient. Finally, the attention weight vector is dimensionally recovered as $n \times n \times 3h$, and multiply it with the corresponding load pixel points of the original load pixel image to obtain a weighted load pixel image $\boldsymbol{G}'$.

$$\boldsymbol{G}' = \left[\boldsymbol{\alpha}_{t-h+1}\boldsymbol{P}_{t-h+1}, \boldsymbol{\alpha}_{t-h+2}\boldsymbol{P}_{t-h+2}, \ldots, \boldsymbol{\alpha}_t\boldsymbol{P}_t\right] \tag{14}$$

$$\boldsymbol{\alpha P} = \begin{bmatrix} \alpha_{1,1}p_{1,1}^e & \cdots & \alpha_{1,n}p_{1,1}^e \\ \vdots & \ddots & \vdots \\ \alpha_{n,1}p_{n,1}^e & \cdots & \alpha_{n,n}p_{n,n}^e \end{bmatrix} \tag{15}$$

In the formula: $\boldsymbol{\alpha}$ is the attention weight vector of the integrated load pixel image at a certain moment; α is the attention weight coefficient of a load pixel point.

Step 3: Spatial feature extraction and fusion

On the basis of step 2, this paper inputs the weighted pixel images of each load component into the MCNN neural network architecture constructed in subsection 3.2 for spatial feature extraction and fusion.

Step 4: Temporal attention weighting

Before inputting the fused load time series obtained from step 3 into the BiLSTM shared layer, the temporal attention layer is constructed using the multi-head attention mechanism proposed in subsection 4.1. First, the fusion load feature vectors under each time step are sequentially input into multiple shared linear layers, and the feature vectors under each time step are dynamically assigned with temporal attention weight coefficients based on equations 7 to 10. Finally, the weighted fusion load time series is obtained by multiplying the temporal attention weight vector with the feature vectors under each time step by element. This is shown in the following equation:

$$\boldsymbol{R} = [\boldsymbol{\beta}_{t-h+1}\boldsymbol{F}_{t-h+1}, \boldsymbol{\beta}_{t-h+2}\boldsymbol{F}_{t-h+2}, \ldots, \boldsymbol{\beta}_t\boldsymbol{F}_t] \tag{16}$$

In the formula: $\boldsymbol{\beta}$ is the temporal attention weight vector at a certain moment.

Step 5: Time-dependent relationship capture

The weighted fused load time series obtained from step4 is input to BiLSTM feature sharing layer for bidirectional temporal information mining to extract temporal feature information.

Step 6: Multi-task learning joint prediction

In this paper, a multi-task learning approach based on a hard-sharing mechanism is used for joint forecasting of electricity, heat, and cold loads. In this, the parameters of BiLSTM as the bottom layer are uniformly shared, and the parameters of each fully connected layer as the top layer are independent of each other. Due to different physical dynamics and different energy demand characteristics, the various types of loads have different fluctuation frequencies. In the UIES studied in this paper, the electric and thermal load profiles have large local fluctuations with rich details, while the cooling load profile is relatively smooth. The same feature interpretation network (the same top layer structure) cannot simultaneously portray the fluctuation characteristics of each load curve, and it is difficult to make the three kinds of loads achieve a better fitting state at the same time. Therefore, it is necessary to construct independent, fully connected neural network (FCNN) for the three loads as the feature interpretation network.

According to the analyses in subsections 2.1 and 2.2, it can be seen that the actual load changes have obvious correlations with meteorological factors and calendar rules. In the calendar rule, hourly, day-type information as well as holiday information are incorporated. The meteorological factors are selected as temperature, dew point, irradiance, and humidity. The calendar rules and meteorological factors as external input features are extracted through three fully connected layers and spliced with the output features of BiLSTM, which are input to the top inputs of electric, heat, and cold loads, respectively, to fully explore the dependence of each load on the calendar and meteorological information.

$$\boldsymbol{h}_t^{'} = [h_t^1, h_t^2, \ldots, h_t^n, \boldsymbol{c}_t, \boldsymbol{d}_{t+1}] \tag{17}$$

In the formula: $\boldsymbol{h}_t^{'}$ is the extended feature vector; $\boldsymbol{c}_t$ is the vector of meteorological information under the historical moment preceding the moment to be predicted; $\boldsymbol{d}_{t+1}$ is a vector of calendar information under the moment to be predicted.

As shown in Figure 12, the user-level IES multivariate load prediction framework based on multi-energy spatio-temporal coupling and spatio-temporal attention mechanism, which is a neural network framework with deep spatio-temporal correlation, has been fully completed.

6 Experiment setup and result analysis

6.1 Introduction to data sources

The data source for this paper is the user-level IES at Arizona State University's Tempe campus, which is located in a tropical desert climate with high demand for cooling and electrical loads and

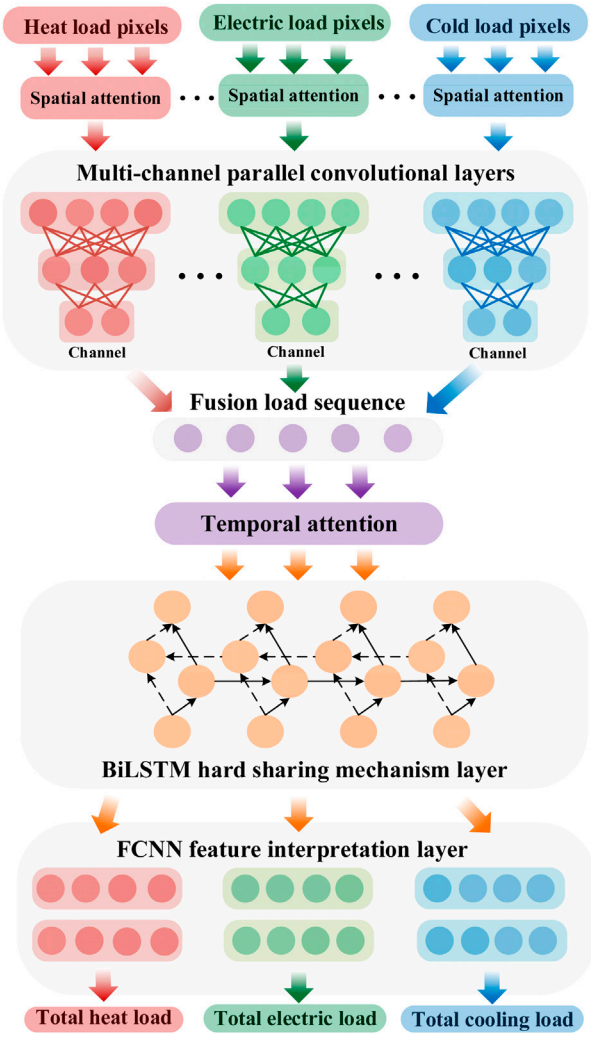

FIGURE 12
UIES multivariate load forecasting framework.

low demand for heat loads, and a large portion of the cooling loads come from electric cooling equipment in the IES system. Electricity, heat, and cooling load data (including all types of load data for 115 load units and all types of total load data) recorded by the university's Campus Metabolism project web platform from January 2019 to March 2020 were used, with a time resolution of 1 h. Based on the forecasting framework in Figure 12, the total electrical, thermal, and cooling loads for the next 1 h for this IES system are forecasted. Before constructing the input feature set, considering that there are some missing and anomalous mutations in the data stored in this UIES, this paper firstly replaces and supplements the anomalies and vacancies, and normalizes the original data to the interval [0,1] according to the following formula for model training.

$$x_\omega = \frac{x_\varphi - x_{min}}{x_{max} - x_{min}} \tag{18}$$

In the formula: x_ω is the normalized value of a load in a basic energy consumption unit; x_φ is the actual value with a dimension; x_{min} and x_{max} are the minimum and maximum values.

In this paper, each load unit is classified according to its functional attributes, of which 24 are teaching venues, 15 are scientific research venues, 13 are administrative venues, 4 are art venues, 11 are sports venues, 29 are residential venues, 11 are public activity venues, and 8 are other auxiliary venues. On this basis, the load component pixel images under different moments of size 11×11 are constructed according to subsection 3.1.

The determination of the length of the historical time period h is considered to take into account two aspects, which are the difficulty of model training and the completeness of the knowledge embedded in the input features. If h is too small, there will be insufficient knowledge in the historical sequence for the model to learn, thus limiting the prediction accuracy and generalization ability of the model. Conversely, if h is too large by considering only the completeness of knowledge information in the historical sequence, it will increase the complexity of model training and thus affect the optimization of model parameters. Therefore, the value of h needs to balance the above two aspects. Combined with the analysis in subsection 2.3 and through a large number of experimental comparisons, the length of h is finally determined to be 9. The historical data of $t+1$ moments a week ago and a day ago, as well as the historical data of the first seven historical moments ($t-6$ to t) near the forecast target moment, are taken as the reference for the current load forecast at $t+1$ moments. As a result, the dimension size of the input features of the prediction model constructed in this paper is $11 \times 11 \times 27$.

A pixel image of the electrical load at 3 consecutive moments is shown as an example, as shown in Figure 13 (load is normalized value). Since the temporal resolution is 1 h, the variation of the electrical load can be represented as a frame by frame picture at 1 h intervals.

6.2 Basic evaluation indicators

In this paper, the mean absolute percentage error (MAPE) and root mean square error (RMSE) metrics are selected to evaluate the forecasting effectiveness of each load, and the expressions are:

$$RMSE = \sqrt{\sum_{\theta=1}^{M} \frac{\left(Y(\theta) - \hat{Y}(\theta)\right)^2}{M}} \tag{19}$$

$$MAPE = \frac{1}{M}\sum_{\theta=1}^{M}\left|\frac{Y(\theta) - \hat{Y}(\theta)}{Y(\theta)}\right| \times 100\% \tag{20}$$

In the formula: $\hat{Y}(\theta)$ is the predicted value of load at the θ -th sampling point; $Y(\theta)$ is the actual value of load at the θ -th sampling point; M is the number of test samples.

In addition, in order to evaluate the performance of the multivariate load forecasting model as a whole, this paper considers the importance of different loads in the system, assigns different importance weights to different loads, and evaluates the overall forecasting effect of the model by using the mean absolute percentage error of multiple weights (WMAPE). Since the proportion of cold and electric loads in UIES is high and the proportion of heat loads is low, the weights of cold loads, heat loads and electric loads are set to 0.4, 0.2 and 0.4, respectively. The expressions of specific evaluation indexes are as follows.

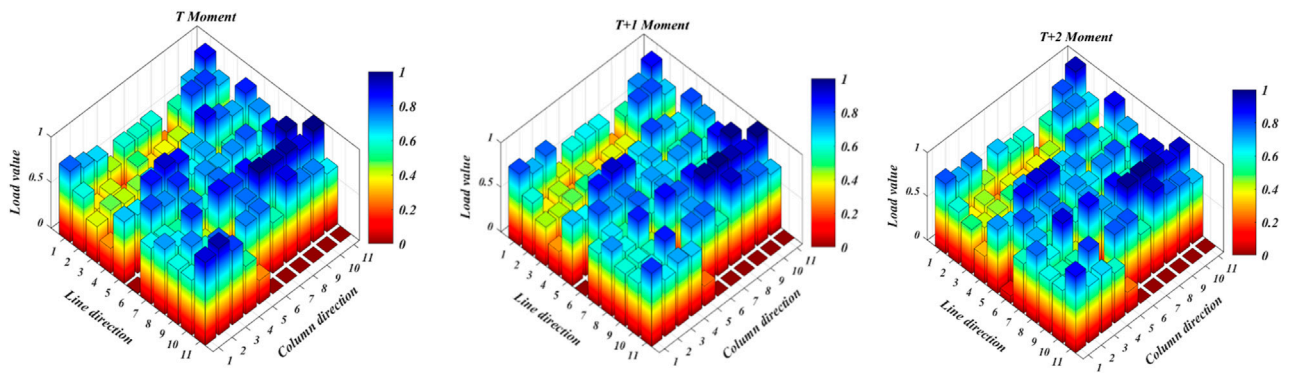

FIGURE 13
Pixel images of the electrical load at different moments.

$$\begin{cases} WMAPE = \sum_{k=1}^{N} R_k MAPE(k) \\ \sum_{k=1}^{N} R_k = 1 \end{cases} \tag{21}$$

In the formula: $WMAPE$ is the mean absolute percentage error of the integrated load; R_k is the importance weight of the k -th type of load; N is the number of load types.

6.3 Model hyperparameter settings

For the MCNN network proposed in this paper, it is known from subsection 6.1 that its input feature set is an electrical, thermal, and cold load pixel image of size 11×11 at 9 moments, so the dimensional size of the MCNN input features is $11 \times 11 \times 27$. Based on the analysis in subsection 3.2, the number of channels of MCNN is determined to be 27, and each channel has a 4-layer independent structure with only convolutional layer and no pooling layer, and the convolutional kernel sliding step is 1, and no Padding operation is performed. First, the first convolution layer of each channel consists of eight convolution kernels of size 5×5, thus covering a larger number of loaded pixel points in the spatial association domain, so that each pixel point in the generated feature map can obtain a large perceptual field. Second, the size of the convolutional kernels in the second to fourth layers is 3×3 and the number of convolutional kernels increases in the order of 16, 32, and 64. Finally, the size of each feature map output by MCNN is 1×1, and its perceptual field size in theory is the original input load pixel image, which contains global information, and the number of feature maps is 27×64. Based on this, we again use the multi-channel idea to set up 9 channels, each with a convolutional kernel size of 1×1 and a number of 64. After one convolution operation, the spatial features of electric, thermal and cooling loads under the same time section are fused to form a time series of fused load features at standard time steps.

The number of neurons and hidden layers are the two critical hyperparameters for BiLSTM. In the study findings of recurrent neural networks represented by LSTM used to load prediction, the majority of them are empirically compared and eventually set the number of hidden layers in the network from 1 to 5, with the number of neurons in each hidden layer often not exceeding 200. BiLSTM has been observed to frequently experience overfitting, which lowers prediction accuracy when the number of hidden layers or the number of neurons in the hidden layers is excessive. In this study, we carried out a number of tests and discovered that BiLSTM functions best when there are two hidden layers and an increase in the number of neurons in each layer on the order of 64,128.

For the three different structures of feature interpretation modules, the fully connected layer for cold loads is designed as one layer with 16 neurons. The fully connected layer for electrical loads is designed as two layers with 32 and 16 neurons per layer, respectively. The fully connected layer for thermal load is designed as 3 layers with 64, 32, and 16 neurons per layer, respectively.

The Adam algorithm is chosen to train the network with a learning rate of 0.01 within this paper, a batch size of 256, and an iteration number of 100. To prevent overfitting, a droup-out operation is added to the training process, and the probability parameter is kept at 0.9. The model is developed in the Keras deep learning framework. The hyperparameter configuration of the model is shown in Table 1.

6.4 Comparative analysis of prediction results

In order to fully validate the effectiveness of the IES multivariate load prediction framework (Case 7) proposed in this paper, six contrasting models are set up in this section. Among them, Case1 to Case3 are predicted by multi-task learning, and Case4 to Case6 are predicted by single-task learning. Among them, the multi-task learning models all consider the coupling characteristics of each load, while the single-task learning models do not consider the coupling characteristics of each load.

Case 1: Based on Case 7, the spatial features are extracted using MCNN without considering the feature independence of each load, and only the temporal integrity is preserved. The number of

TABLE 1 Network hyperparameter settings.

Number	Layer Name	Number of neurons/Convolutional kernels	Convolution kernel size	Number of channels/Attention heads
1	Attention layer	$11 \times 11 \times 27 = 3267$	—	4
2	MCNN layer 1	8	5×5	27
3	MCNN layer 2	16	3×3	27
4	MCNN layer 3	32	3×3	27
5	MCNN layer 4	64	3×3	27
6	MCNN layer 5	64	1×1	9
7	Attention layer	$64 \times 9 = 576$	—	4
8	BiLSTM layer	64	—	—
9	BiLSTM layer	128	—	—

channels of MCNN is 9, and the input feature of each channel is the integrated load pixel image at the corresponding moment. The hyperparameters of MCNN, BiLSTM and spatio-temporal attention layer are the same as Case 7 except that there is no feature fusion operation based on MCNN. Multi-task learning is used to simultaneously predict the total electric, cooling and heating loads at the next moment.

Case 2: The input and output feature sets, model structure and hyperparameters are the same as Case7, except that the attention mechanism is not used, and Case2 considers feature independence and temporal integrity of each load during feature extraction.

Case 3: The historical values of the total electrical, thermal and cooling loads are used as input features and then BiLSTM is used as a feature sharing layer for joint prediction of each of the total loads by multi-task learning. The hyperparameters of BiLSTM are the same as those of Case7's BiLSTM.

Case 4: Based on Case7, the coupling characteristics of each load are not considered. The number of input channels of MCNN is 9, and the input feature of each channel is the pixel image of a certain type of load component at the corresponding moment. The hyperparameters of MCNN, BiLSTM and spatio-temporal attention layer are the same as Case7 except that there is no feature fusion operation based on MCNN. The total load of each category at the next moment is predicted independently using single-task learning.

Case 5: Same as Case4, but without the spatio-temporal attention layer based on the multiple attention mechanism.

Case 6: Based on Case 3, the total electrical, thermal, and cooling loads are predicted separately and independently using single-task learning without using multi-task learning. The input features are the historical values of a particular total load itself, and the hyperparameter configuration is the same as in Case3.

Considering that the energy consumption patterns of this UIES in summer and winter are quite different, the external morphological characteristics presented by each load show a large change. Therefore, in this paper, the comparison experiments are designed by selecting the data for each load for a week in winter and summer, respectively. Figure 14; Figure 15 show the prediction results of electric, thermal, and cooling loads for 1 week in different seasons, and Table 2, Table 3 show the prediction errors for each case in the test set.

6.4.1 Analysis of the effect of cold load prediction

The results of the cold load forecasts under the summer and winter time periods are shown in Figure 14A and Figure 15A, respectively. It is easy to see that the cold load demand size under the two seasons has a large change. In the summer season, the daily cold load change has obvious regularity, and the forecast models can track the load change trend better. In winter, the cooling load curves shown in the 96th to 120th hour change significantly compared with the other hours, and it can be seen that the prediction error in this hour is much larger than the other hours.

(1) Analysis of the effectiveness of multitask learning models for cold load prediction

In the summer, as shown in Table 2, the prediction accuracies of Case 1, Case 2, and Case 7 are higher than those of Case 3, which indicates that, compared with BiLSTM based on macroscopic class load prediction methods, the microscopic class load prediction method can learn the intrinsic law of change of the loads better, which is attributed to the rich information embedded in its input features. Compared with Case 1, the RMSE of Case 2 is reduced by 6.18%, and the MAPE is reduced by 2.23%. This indicates that even with the introduction of the attention mechanism in Case 1, better prediction results can still be achieved by taking into account the independent characteristics of the loads themselves in the feature extraction process. Compared with Case 2, the RMSE of Case 7 is reduced by 15.18%, and the MAPE is reduced by 15.84%.

As shown in Table 3, the prediction accuracy of the models on cooling loads during the winter time period is ranked as Case7>Case2>Case1>Case3. The RMSE of Case 1 is reduced by 6.77 percent, and the MAPE is reduced by 3.31 percent as compared to Case 3. Case 2 had a 1.32% lower RMSE and 10.26% lower MAPE compared to Case 1. RMSE was reduced by 19.26% and MAPE was reduced by 20.13% for Case 7 compared to Case 2.

(2) Analysis of the effectiveness of single-task learning models for cold load prediction

The prediction accuracies of the models for the two seasons with respect to the cooling loads were ranked as Case 4 > Case 5 > Case 6. The RMSE and MAPE of Case4 were 17.23% and 10.67% lower in the summer time period, respectively, as compared to Case5. Under the winter time period, Case 4 had 11.74% lower RMSE and 17.22% lower MAPE than Case 5. This indicates that the introduction of the attention mechanism can strengthen the significant features of the loaded pixel images and fused load sequences so as to obtain more important feature information in the feature extraction process and improve the prediction accuracy of the model.

(3) Multi-task learning model VS. Single-task learning model

During the summer time period, Case 2 had the best prediction performance among the multi-task models except Case 7. Among the single-task models, the highest prediction accuracy is achieved by Case 4. Compared to Case 2, Case 4 has a 2.08% lower RMSE and a 3.72% lower MAPE. This is because the summer cold load fluctuation is more regular, and only relying on its own load pixels is enough for the model to learn its own intrinsic pattern of change, while the attention mechanism introduced in Case 4 further improves the model performance.

In the winter time period, the prediction accuracy of Case2 is slightly higher than that of Case4, and its RMSE is reduced by 0.66% and MAPE is reduced by 1.36% compared with Case4. This is because the cold load's volatility is strengthened at this time, and relying only on its own load pixel does not allow the model to learn the intrinsic correlation between the cold load and other loads, which weakens the model's ability to perceive the fluctuation pattern of the cold load itself. In addition, the introduction of the attention

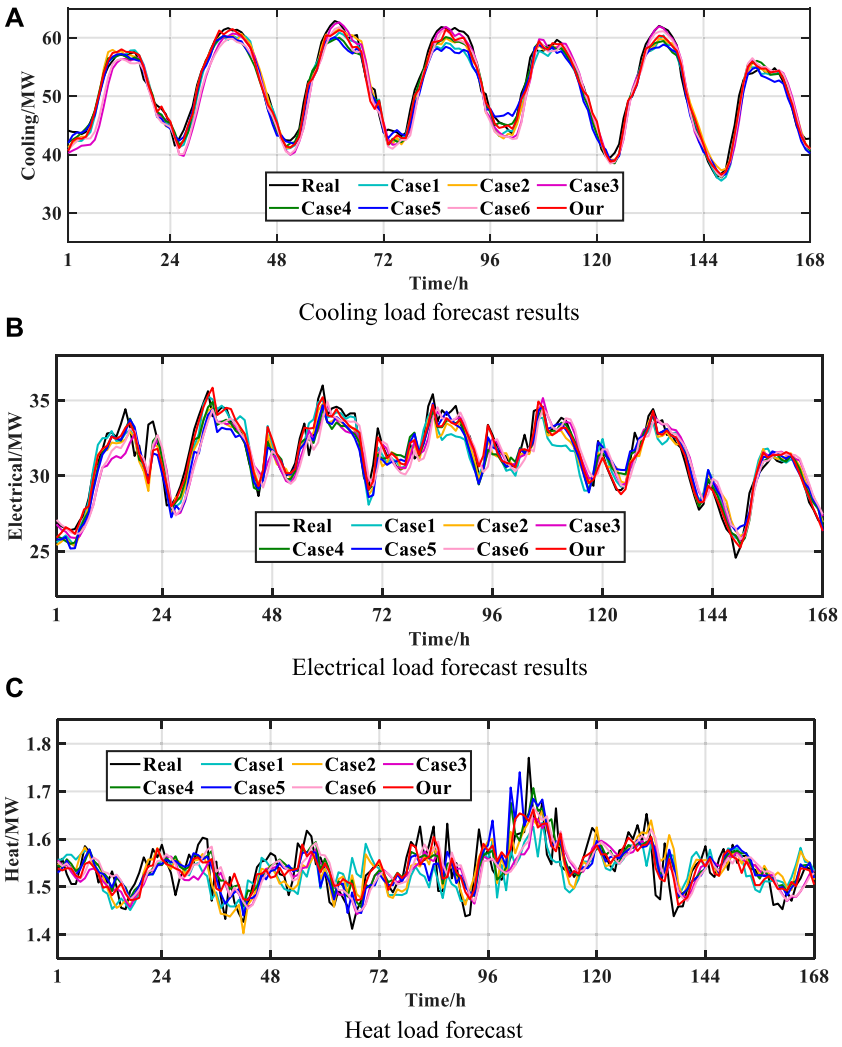

FIGURE 14
Results of each load forecast in summer. **(A)** Cooling load forecast results. **(B)** Electrical load forecast results. **(C)** Heat load forecast.

mechanism in Case 4 compensates for the defect of limited information expressed by input features to a certain extent.

6.4.2 Analysis of the effect of electrical load prediction

The predicted electric loads for the summer and winter periods are shown in Figure 14B and Figure 15B, respectively. Combining Figure 14A and Figure 15A, it can be seen that the electric load fluctuates more than the cold load, which is especially obvious in the winter, and the prediction curves of Case1 deviate more from the actual curves in some time periods, while the prediction curves of Case7 follow the actual load curves in the best way. Compared with the cold load forecasting task, the models show more obvious performance differences in electrical load forecasting.

(1) Analysis of the effectiveness of multitask learning models for electrical load prediction

As shown in Table 2, the RMSE of Case 1 decreased by 17.02% and the MAPE decreased by 17.10% compared to Case 3. The reason for the difference in the performance of the two models is that the input features of Case 3 only include the historical data of each total load, which covers limited information and does not allow the model to fully learn the fluctuation pattern of each load. Compared with Case 1, the RMSE of Case 2 decreased by 2.78% and the MAPE decreased by 4.08%. This again shows that it is important to maintain the independence of each load in the feature extraction process. In addition, the RMSE of Case 7 decreased by 21.78% and the MAPE decreased by 29.28% compared to Case 2. This again demonstrates that the attention mechanism improves the model learning performance.

As can be seen from Table 3, Case 3 had the lowest prediction accuracy. The RMSE and MAPE of Case1 were reduced by 10.15% and 3.30%, respectively, compared to Case3. The RMSE and MAPE of Case 2 were reduced by 18.03% and 20.65%, respectively, compared to Case 3. The RMSE and MAPE of Case 2 were 8.77% and 17.94% lower than Case 1, respectively. The more drastic load fluctuations in the winter compared to the summer lead to a further increase in the

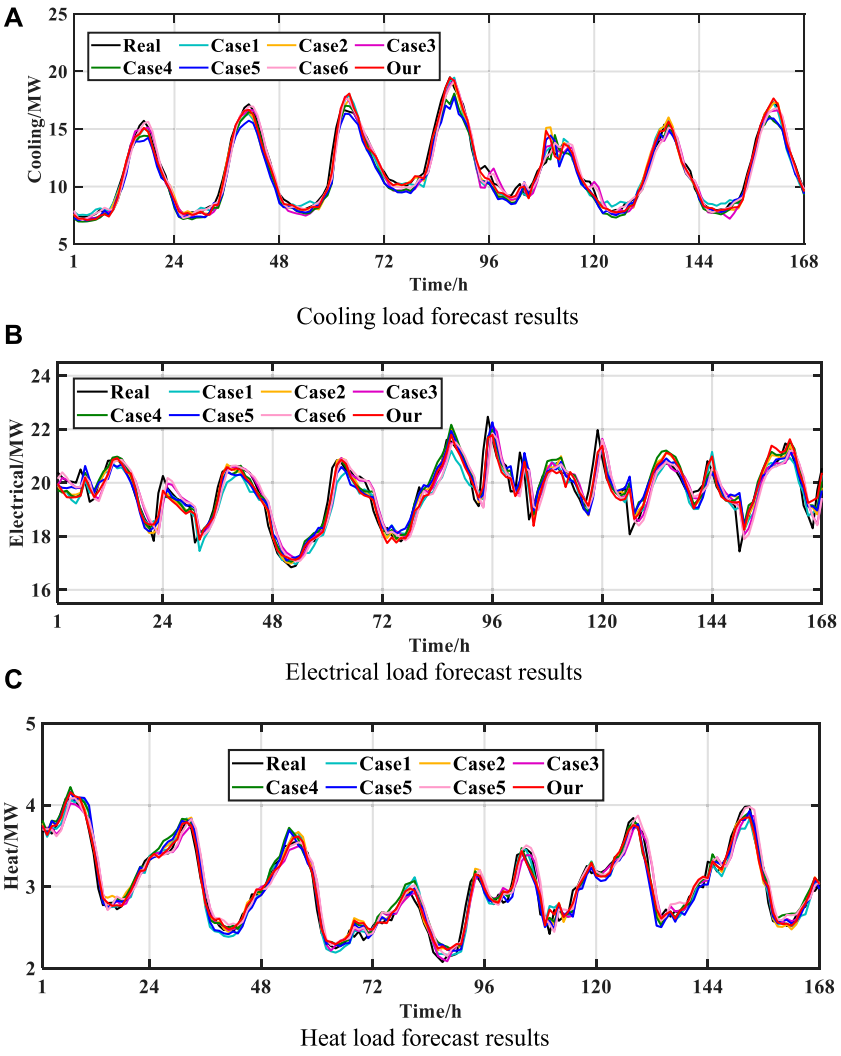

FIGURE 15
Results of each load forecast in winter. . **(A)** Cooling load forecast results. **(B)** Electrical load forecast results. **(C)** Heat load forecast.

TABLE 2 Evaluation index of prediction effect of each model in summer.

Model	RMSE/MW			MAPE/%			WMAPE/%
	Electrical	Heat	Cooling	Electrical	Heat	Cooling	Combined
Case1	0.897	0.047	1.537	2.225	2.384	2.415	2.332
Case2	0.872	0.040	1.442	2.134	2.017	2.361	2.201
Case3	1.081	0.044	1.988	2.684	2.259	3.127	2.776
Case4	0.832	0.039	1.412	2.087	1.997	2.273	2.143
Case5	0.923	0.041	1.706	2.326	2.058	2.643	2.399
Case6	1.166	0.044	1.914	2.941	2.312	3.107	2.881
Case7	**0.682**	**0.038**	**1.223**	**1.509**	**1.916**	**1.987**	**1.585**

performance difference between Case1 and Case2 on the load forecasting task. The RMSE and MAPE of Case 7 are only 5.34% and 1.12% lower than those of Case 2, respectively. This is due to the high volatility of electrical loads in winter, resulting in the introduction of an attentional mechanism that does not have a significant improvement effect.

TABLE 3 Evaluation index of prediction effect of each model in winter.

Model	RMSE/MW			MAPE/%			WMAPE/%
	Electrical	Heat	Cooling	Electrical	Heat	Cooling	Combined
Case1	0.513	0.104	0.605	1.962	2.728	4.178	3.001
Case2	0.468	0.096	0.597	1.610	2.610	3.749	2.665
Case3	0.571	0.122	0.649	2.029	3.073	4.321	3.224
Case4	0.482	0.107	0.601	1.759	3.012	3.801	2.826
Case5	0.512	0.111	0.681	1.768	3.021	4.592	3.145
Case6	0.595	0.130	0.731	2.167	3.370	5.301	3.661
Case7	**0.443**	**0.091**	**0.482**	**1.591**	**2.446**	**2.994**	**2.339**

(2) Analysis of the effectiveness of single-task learning models for electrical load prediction

The ranking of the accuracy of the models on the task of electrical load forecasting under two seasons is Case4>Case5>Case6. In the summer time period, RMSE for Case 4 was 9.85% lower than Case 5, and MAPE was 10.27% lower than Case 5. In the winter, the RMSE and MAPE of Case 4 were only 5.85% and 0.51% lower than those of Case 5, respectively.

(3) Multi-task learning model VS. Single-task learning model

The RMSE and MAPE of Case4 are 4.58% and 2.20% lower than those of Case2 on the electric load forecasting task in the summer time period, respectively. This indicates that the introduction of the attention mechanism focusing on the electric load's own load pixels is better than mining the potential correlations among loads based on various types of load pixels. In contrast, under the winter time period, the RMSE for Case 2 is 2.90% lower than Case 4, and the MAPE is 8.47% lower than Case 4. The reason for analysing the above results is the same as that of the cold load forecasting task, which is because the cold loads in this UIES are mainly from electric loads, and the trend of electric load changes is largely consistent with the cold loads.

6.4.3 Analysis of the effect of heat load prediction

The heat load prediction results under the summer and winter time periods are shown in Figure 14C and Figure 15C, respectively. Among them, winter is a typical heat-consuming season for thermal systems, and the heat load demand decreases abruptly during the day and increases at night with obvious regularity. Each model can track the actual fluctuation changes of heat load better. For summer, the user heat demand is small and the heat behavior is random, which directly leads to the heat load fluctuation being extremely violent, the rule of change is not traceable. The prediction results of each model can't fit the actual curve of heat load well, and some of the prediction results of Case 1 and Case 5 have a big deviation from the actual value.

(1) Analysis of the effectiveness of multitask learning models for heat load prediction

The prediction accuracies of the models on the task of heat load prediction in summer are Case7>Case2>Case3>Case1. Compared to Case 1, Case 3 has a 6.38% lower RMSE and a 5.24% lower MAPE. Due to the extremely random variation of heat load, its correlation with electricity and cooling load is small. Meanwhile, Case 1 does not consider the independent characteristics of each load in feature extraction, which increases the difficulty of the model learning the fluctuation law of heat load, resulting in poor heat load feature extraction. This point also illustrates the effectiveness and reasonableness of Case7 and Case2 in constructing feature extraction channels independently for each load component pixel image. Case 3 predicts the heat load based on its own historical data and achieves better prediction results than Case 1.

The prediction accuracies of the models on the heat load prediction task in winter time are Case7>Case2>Case1>Case3, and the RMSE and MAPE of Case2 are only 7.69% and 4.32% lower than those of Case1 and Case2, respectively. This is because the correlation between the heat load and the electricity and cooling loads is stronger at this time, and the simultaneous feature extraction of the pixel images of each load component at the same moment in time does not have much effect on the learning effect of the model. Compared with Case 2, the RMSE and MAPE of Case 7 are only reduced by 5.21% and 6.28%, respectively. This is because the heat load fluctuation pattern is obvious, and the model can extract the heat load feature information better, resulting in the improvement effect of the attention mechanism that is not obvious.

(2) Analysis of the effectiveness of single-task learning models for heat load prediction

The prediction accuracies of the models on the heat load prediction task in the two seasons are ranked as Case 4 > Case 5 > Case6. In the summer, the RMSE of Case4 and Case5 are reduced by 11.36% and 6.81%, respectively, and the MAPE is reduced by 13.62% and 10.98%, respectively, compared with Case6. Case4 and Case5 extract features from the heat load pixels, which can learn the complex fluctuation patterns within the heat load in a more detailed way and are more advantageous than mining feature information directly from the heat load's own historical data. In winter time, compared with Case6, the RMSE of Case4 and Case5 are reduced by

TABLE 4 Comparative analysis of the proposed model Case7 with other models in terms of forecasting accuracy of each load in summer season.

Model	RMSE/MW			MAPE/%			WMAPE/%
	Electrical (%)	Heat (%)	Cooling (%)	Electrical (%)	Heat (%)	Cooling (%)	Combined (%)
vs. Case1	23.96	19.14	20.42	32.17	19.63	17.72	32.03
vs. Case2	21.78	5.01	15.18	29.28	5.03	15.84	27.98
vs. Case3	36.91	13.63	38.48	43.77	15.18	36.45	42.90
vs. Case4	18.02	2.56	13.38	27.69	4.05	12.58	26.03
vs. Case5	26.11	7.31	28.31	35.12	6.89	24.82	33.93
vs. Case6	41.51	13.63	36.10	48.69	17.12	36.04	44.98

TABLE 5 Comparative analysis of the proposed model Case7 with other models in terms of forecasting accuracy of each load in winter season.

Model	RMSE/%			MAPE/%			WMAPE/%
	Electrical (%)	Heat (%)	Cooling (%)	Electrical (%)	Heat (%)	Cooling (%)	Combined (%)
vs. Case1	13.64	12.50	20.33	18.39	10.33	28.33	22.05
vs. Case2	5.34	5.21	19.26left	1.12	6.28	20.13	12.23
vs. Case3	22.41	25.41	25.73	21.58	20.40	30.71	27.45
vs. Case4	8.09	14.95	19.80	9.55	18.79	21.23	17.23
vs. Case5	13.47	18.01	29.22	10.01	19.03	34.79	25.62
vs. Case6	25.54	30.00	34.06	26.58	27.41	43.52	36.11

17.69% and 14.61%, respectively, and the MAPE is reduced by 10.62% and 10.35%.

(3) Multi-task learning model VS. Single-task learning model

During the summer, the RMSE and MAPE of Case 4 were only 2.50% and 0.99% lower than Case 2, respectively. And the RMSE and MAPE of Case 7 were only 2.56% and 4.05% lower than Case 4, respectively. This shows that there is no valid information associated with the change of heat load in the pixel images of electric and cold loads, and also verifies that the idea of independent feature extraction for each load component pixel image in the front-end and fusion of each load feature at the same moment in the back-end proposed in this paper is correct. During the winter season, RMSE decreased by 10.28% and MAPE decreased by 13.34% in Case 2 compared to Case 4, and RMSE decreased by 5.21% and MAPE decreased by 6.28% in Case 7 compared to Case 2. This indicates that at this time there are signals in the electrical and cold load pixel images that are related to changes in the heat load, which helps to improve the feature extraction of the heat load.

6.4.4 The strengths analysis of the model

The data shown in Tables 4 and 5 indicate that Case 7 exhibits the best level of prediction accuracy for each load when compared to the other models. This is due to the fact that the proposed method in this paper is able to predict the multivariate loads of the UIES in a refined and three-dimensional way by load types and spatial and temporal characteristics. Case7 performs independent feature extraction on the pixel images of each load component at different moments and fuses the spatial features of the loads in the high-dimensional space, which takes into full consideration the independence of the features of the loads. The end-to-end information flow delivery of spatial feature extraction and time-dependent relationship capture is also realized. In addition, a multi-head attention mechanism is introduced to assign weight coefficients to load pixels and fused load features, respectively, which realizes the model's differentiated attention among different features. Finally, multi-task learning is utilised for joint prediction of each load, which further exploits the coupling characteristics among loads. Through the close cooperation of the above three links, the advantages of each module are fully utilised, and more accurate prediction results are achieved.

7 Conclusion

In this paper, a MCNN-BiLSTM load prediction method considering multi-energy spatio-temporal correlation is proposed for small-scale UIES, which realizes the stereoscopic feature extraction of UIES multivariate load spatio-temporal information. The following conclusions are obtained:

(1) The load units covered by the user-level IES hide the multidimensional information of various types of total loads, for which the input feature set in the form of an image is built, and with the powerful feature extraction capability of CNN, the prediction error caused by load uncertainty can be significantly reduced.

(2) There are many types of user-level IES loads with high volatility and complex correlations among loads. When feature extraction is performed for each load, the independence of each load needs to be fully considered, which could lead to more accurate results.
(3) Through the experimental comparative analysis, the introduction of the attention mechanism layer can assist the model in better mining the intrinsic law of change of each load, which improves the load prediction accuracy to a certain extent.

Along with the rise of digital twin technology, the energy system will develop in the direction of intelligence and digitalization. In the future, data-driven load forecasting methods will be widely used in integrated energy systems at all levels. How to combine macroscopic class load forecasting methods with microscopic class load forecasting methods, give full play to their respective advantages, and apply them to IES load forecasting is our next work plan.

Data availability statement

Publicly available datasets were analyzed in this study. This data can be found here: http://cm.asu.edu.

Author contributions

XY: Conceptualization, Data curation, Formal Analysis, Investigation, Methodology, Visualization, Writing–original draft, Writing–review and editing. ZG: Funding acquisition, Resources, Software, Supervision, Writing–original draft. YC: Conceptualization, Data curation, Visualization, Writing–review and editing. YH: Data curation, Writing–original draft. ZY: Funding acquisition, Resources, Writing–original draft.

Funding

The author(s) declare financial support was received for the research, authorship, and/or publication of this article. This work was supported by the National Natural Science Foundation of China (62273215) and the Natural Science Foundation of Shandong Province (ZR2020MF071).

Conflict of interest

The authors declare that the research was conducted in the absence of any commercial or financial relationships that could be construed as a potential conflict of interest.

Publisher's note

References

Al-Musaylh, M. S., Al-Daffaie, K., and Prasad, R. (2021). Gas consumption demand forecasting with empirical wavelet transform based machine learning model: a case study. *Int. J. Energy Res.* 45 (10), 15124–15138. doi:10.1002/er.6788

Bai, B. Q., Liu, J. T., Wang, X., et al. (2022). Short-term forecasting of urban energy multiple loads based on MRMR and dual attention mechanism. *Power Syst. Autom.* 46 (17), 44–55.

Cheng, H. Z., Hu, X., Wang, Li., et al. (2019b). A review of research on regional integrated energy system planning. *Power Syst. Autom.* 43 (07), 2–13.

Cheng, Y. H., Zhang, N., Lu, Z. X., and Kang, C. (2019a). Planning multiple energy systems toward low-carbon society: a decentralized approach. *IEEE Trans. Smart Grid* 10 (5), 4859–4869. doi:10.1109/TSG.2018.2870323

Fan, C., Xiao, F., and Zhao, Y. (2017). A short-term building cooling load prediction method using deep learning algorithms. *Appl. energy* 195, 222–233. doi:10.1016/j.apenergy.2017.03.064

Gao, Z. K., Yu, J. Q., Zhao, A. J., Hu, Q., and Yang, S. (2022b). A hybrid method of cooling load forecasting for large commercial building based on extreme learning machine. *Energy* 238, 122073. doi:10.1016/j.energy.2021.122073

Gao, Z. Z., Yin, X. C., Zhao, F. Z., Meng, H., Hao, Y., and Yu, M. (2022a). A two-layer SSA-XGBoost-MLR continuous multi-day peak load forecasting method based on hybrid aggregated two-phase decomposition. *Energy Rep.* 8, 12426–12441. doi:10.1016/j.egyr.2022.09.008

Hu, X., Shang, C., Chen, D. W., et al. (2019). Multi-objective planning method for regional integrated energy systems considering energy quality. *Automation Electr. Power Syst.* 43 (19), 22–31.

Ji, L., Zhang, B. B., Huang, G. H., Xie, Y. L., and Niu, D. X. (2018). GHG-mitigation oriented and coal-consumption constrained inexact robust model for regional energy structure adjustment -A case study for jiangsu province China. *Renew. Energy* 123, 549–562. doi:10.1016/j.renene.2018.02.059

Li, C., Li, G., Wang, K. Y., and Han, B. (2022). A multi-energy load forecasting method based on parallel architecture CNN-GRU and transfer learning for data deficient integrated energy systems. *Energy* 259, 124967. doi:10.1016/j.energy.2022.124967

Li, Y., Tian, X. M., Liu, T. L., and Tao, D. C. (2018). On better exploring and exploiting task relationships in multitask learning: joint model and feature learning. *IEEE Trans. Neural Netw. Learn. Syst.* 29 (5), 1975–1985. doi:10.1109/TNNLS.2017.2690683

Li, Z. M., and Xu, Y. (2018). Optimal coordinated energy dispatch of a multi-energy microgrid in grid-connected and islanded modes. *Appl. Energy* 210 (1), 974–986. doi:10.1016/j.apenergy.2017.08.197

Li, Z. M., and Xu, Y. (2019). Temporally-coordinated optimal operation of a multi-energy microgrid under diverse uncertainties. *Appl. Energy* 240 (1), 719–729. doi:10.1016/j.apenergy.2019.02.085

Lu, J. X., Zhang, P. Q., Yang, Z. H., et al. (2019). A short-term load forecasting method based on CNN-LSTM hybrid neural network model. *Power Syst. Autom.* 43 (08), 131–137.

Niu, D. X., Yu, M., Sun, L. J., Gao, T., and Wang, K. K. (2022). Short-term multi-energy load forecasting for integrated energy systems based on CNN-BiGRU optimized by attention mechanism. *Appl. Energy* 313, 118801. doi:10.1016/j.apenergy.2022.118801

Shi, J. Q., Tan, T., Guo, J., et al. (2018). Multivariate load forecasting for campus based integrated energy systems based on deep structured multitask learning. *Power Grid Technol.* 42 (03), 698–707. doi:10.13335/j.1000-3673.pst.2017.2368

Singh, S., Hussain, S., and Bazaz, M. A. (2017). Short term load forecasting using artificial neural network. Proceedings of the 2017 Fourth International Conference on Image Information Processing (ICIIP), Shimla, India, December 2017, 1–5. doi:10.1109/ICIIP.2017.8313703

Sousa, J. C., Jorge, H. M., and Neves, L. P. (2014). Short-term load forecasting based on support vector regression and load profiling. *Int. J. Energy Res.* 38 (3), 350–362. doi:10.1002/er.3048

Wang, Y. L., Wang, Y. D., Huang, Y. J., Li, F., Zeng, M., et al. (2019). Planning and operation method of the regional integrated energy system considering

economy and environment. *Energy* 171, 731–750. doi:10.1016/j.energy.2019.01.036

Wu, J. Z., Yan, J. Y., Jia, H. J., Hatziargyriou, N., Djilali, N., and Sun, H. (2016). Integrated energy systems. *Appl. Energy* 67, 155–157. doi:10.1016/j.apenergy.2016.02.075

Xu, D., and Zhu, D. (2021). "Short-term gas load forecast based on TCN-BiGRU," in Proceedings of the 2021 China Automation Congress (CAC), Beijing, China, October 2021, 7978–7983. doi:10.1109/CAC53003.2021.9727821

Xue, P. N., Jiang, Y., Zhou, Z. G., Chen, X., Fang, X., and Liu, J. (2019). Multi-step ahead forecasting of heat load in district heating systems using machine learning algorithms. *Energy* 188, 116085. doi:10.1016/j.energy.2019.116085

Zhao, F., Sun, B., and Zhang, C. H. (2016). Cooling, heating and electrical load forecasting method for CCHP system based on multivariate phase space reconstruction and kalman filter. *Proc. CSEE* 36 (2), 399–406. doi:10.13334/j.0258-8013.pcsee.2016.02.010

Zhu, J. Z., Dong, H. J., Li, S. L., et al. (2021). A review of data-driven load forecasting for integrated energy systems. *Proc. CSEE* 41 (23), 7905–7924. doi:10.13334/j.0258-8013.pcsee.202337

Zhu, R. J., Guo, W. L., and Gong, X. J. (2019). Short-term load forecasting for CCHP systems considering the correlation between heating, gas and electrical loads based on deep learning. *Energies* 12 (17), 3308. doi:10.3390/en12173308

frontiers | Frontiers in Energy Research

TYPE Original Research
PUBLISHED 18 January 2024
DOI 10.3389/fenrg.2023.1349887

OPEN ACCESS

EDITED BY
Shuai Yao,
Cardiff University, United Kingdom

REVIEWED BY
Xiangmin Xie,
Qingdao University, China
Dong Wang,
Qingdao University of Science and Technology, China

*CORRESPONDENCE
Xiaobo Hao,
37496900@qq.com

RECEIVED 05 December 2023
ACCEPTED 31 December 2023
PUBLISHED 18 January 2024

CITATION
Hao X, Liu P, Deng Y and Meng X (2024), A MIC-LSTM based parameter extraction method for single-diode PV model.
Front. Energy Res. 11:1349887.
doi: 10.3389/fenrg.2023.1349887

A MIC-LSTM based parameter extraction method for single-diode PV model

Xiaobo Hao[1]*, Pengcheng Liu[1], Yanhui Deng[1] and Xiangjian Meng[2]

[1]Ningxia Hongdunzi Coal Ind., Yinchuan, Ningxia, China, [2]Shandong University of Science and Technology, Qingdao, Shandong, China

In recent years, the installed capacity of renewable energy systems has seen rapid growth, particularly in photovoltaic (PV) power. Photovoltaic modules, being the fundamental elements of the PV system, play a crucial role in determining system performance. However, the challenge arises from the inconsistent decay rates of PV modules, which significantly impact the accuracy of PV system modeling. To address this issue, this paper introduces a novel MIC-LSTM based parameter extraction method for the single-diode PV model. This method focuses on accurately deriving PV module model parameters under various decay rates. By establishing a mapping relationship between the current-voltage (I-V) curve characteristics and the five unknown parameters in the photovoltaic module model, the proposed method demonstrates high precision in parameter extraction. Simulation and experimental verifications are carried out to validate the proposed method, where the extraction accuracy is 99.3%, 98.39%, 98.85%, 97.91%, and 98.36% for the five unknown model parameters.

KEYWORDS

maximal information coefficient, LSTM, parameter extraction, single-diode PV model, feature value

1 Introduction

Modeling photovoltaic (PV) modules is a key technology for evaluating the economic benefits of PV generation systems in complex operating conditions. Accurate PV module models could depict the output characteristics of PV module under different conditions. The physical PV models can be categorized into single diode and double diode models based on the number of diodes. The single diode model can be further divided based on the number of parameters in the equivalent circuit, including the ideal model (Pavan et al., 2014), four-parameter model (Walker, 2001; Xiao et al., 2004; Chenni et al., 2007), and five-parameter model (Appelbaum and Peled, 2014; Kumar and Shiva, 2019; Muttillo et al., 2020). The ideal model regards the entire PV cell as a basic P-N junction. The four-parameter model assumes an infinite parallel resistance, thereby neglecting the leakage current of the P-N junction. Compared with ideal model, four-parameter model is more accurate with a small leakage current in the P-N junction. However, high temperatures or low irradiance can reduce model accuracy. Researchers have proposed a more complex double diode model (Cotfas et al., 2013; Babu and Gurjar, 2014) to better accurately depict the current losses in the PV module model as well as to better describe the output characteristics under low irradiance conditions. Although the double-diode model can more accurately

describe the output characteristics of PV modules under certain conditions, the additional diode could increase the number of parameters in the equivalent circuit of PV module, which will lead to the increased difficulty in parameter extraction due to complex coupling relationships between parameters. Unlike the four-parameter model, the five-parameter model achieves higher modeling accuracy by introducing a parallel resistance to simulate the leakage current of the P-N junction. Therefore, the five parameter PV model could effectively balance model accuracy and difficulty in extracting model parameters, which has widely implemented.

In recent years, researchers have conducted extensive analyses on the working mechanisms and output characteristics of PV modules. Existing methods can be categorized into analytical and numerical methods. Analytical methods aim to simplify and equivalize the equivalent circuit of PV module to different extents and then analyze the output data from key points on the elementary functions and the I-V curve of PV module to obtain the unknown model parameters. Xiao et al. (2006) established a polynomial relationship between the output current and voltage of a PV module at various load under standard test conditions (STC). Although this analytical method exhibits high accuracy under standard test conditions, the model accuracy is low when weather changes rapidly. Additionally, this method requires collecting a large amount of I-V curve data to achieve a high fitting accuracy, making the data collection process over complicated. Ishaque et al. (2011); Elbaset et al. (2014); Villalva et al. (2009), and other researchers implemented standard product data sheets of PV module to extract model parameters such as open-circuit voltage, short-circuit current, maximum power point voltage, and maximum power point current. Based on open-circuit voltage, short-circuit current, maximum power point voltage, maximum power point current, voltage temperature coefficient, and current temperature coefficient, these methods established a system of equations to solve for unknown model parameters, including the series resistance (R_s) and expressing the photocurrent (I_{ph}), diode reverse saturation current (I_D), and shunt resistance (R_{sh}). However, these kinds of methods cannot take the decay of PV modules into considerations. The models established using this approach can only describe the output characteristics of the modules at the time of manufacturing and do not meet the requirements of practical applications.

Compared to analytical methods, numerical methods require analyzing the entire I-V curve of PV modules. Due to the multimodal nature of the fitness function in parameter extraction problems, intelligent optimization algorithms are widely applied, including Particle Swarm Optimization (PSO) (Soon and Low, 2012), Artificial Bee Swarm Optimization (ABSO) (Askarzadeh and Rezazadeh, 2013; Oliva et al., 2014; Garoudja et al., 2015), Cuckoo Search (CS) (Chakrabarti et al., 2016), Bacterial Foraging Algorithm (BFA) (Asif and Li, 2008; Krishnakumar et al., 2013; Rajasekar et al., 2013; Subudhi and Pradhan, 2018), Genetic Algorithm (GA) (Harrag and Messalti, 2015; Kumar and Shiva, 2019), Differential Evolution (DE) (Ishaque and Salam, 2011; Jiang et al., 2013), and Flower Pollination Algorithm (FPA) (Benkercha et al., 2018; Khursheed et al., 2021). In Ref (Soon and Low, 2012), the particle swarm optimization algorithm was employed, and the concept of inverse barrier constraints was introduced to restrict the parameter search space and thereby enhance the accuracy of parameter identification. Ref (Askarzadeh and Rezazadeh, 2013) proposed an ABSO-based technique for identifying parameters in both single and double diode models. The comparisons between the ABSO-based algorithms and the other algorithms for the single diode model parameter identification indicates that ABSO-based algorithms could achieve a higher parameter extraction accuracy. Ref (Subudhi and Pradhan, 2018) presented a novel approach to extract parameters for PV modules using the Bacterial Foraging Optimization (BFO) technique for optimal determination of parameters (R_s, R_{sh} and n) at both variable temperatures and irradiance level, which is applicable for extracting parameters of various types of PV modules. Ref (Jiang et al., 2013) presented an improved adaptive Differential Evolution (IADE)-based optimization technique to achieve parameter extraction of PV module. By using a simple structure based on the feedback of fitness value in the evolutionary process, it achieves a better extraction accuracy than other popular optimization methods such as particle swarm optimization, genetic algorithm, conventional DE, and simulated annealing (SA). In Khursheed et al. (2021), the improved Firefly Particle Algorithm (Modified FPA) is employed, introducing dynamic switch probability and step size function to enhance the accuracy of parameter estimation for photovoltaic (PV) models. This method utilizes the improved Firefly Particle Algorithm, dynamically adjusting switch probability and step size function to more effectively explore the parameter space, thereby optimizing the parameter estimation of PV models. In summary, the intelligent optimization algorithms can achieve high accuracy in parameter extraction. However, the computational cost is significantly increased due to the updating of particle positions and velocities at each step, leading to slow convergence rates. Some researchers have proposed PV module parameter extraction methods based on artificial intelligence algorithms (Gastli et al., 2015). However, the accuracy of parameter extraction in this algorithm is relatively low. In summary, existing methods for extracting parameters in photovoltaic module models still struggle to balance convergence speed and modeling accuracy.

Since the decay of photovoltaic module has a time-dependent nature, this paper introduces a MIC-LSTM based method for extracting parameters in the single-diode five-parameter PV model. This method enables parameter extraction using experimentally measured current-voltage (I-V) curves of PV modules, which could achieve the parameter extractions under any practical condition. Initially, a dataset with numerous I-V characteristic curves is created by assigning random values to the five parameters of the photovoltaic module model and extracting feature values from the I-V curves. Using these feature values as known input parameters and the five unknown parameters of the photovoltaic module model as output parameters, an LSTM training set is constructed to establish the mapping relationship between I-V curve feature values and the five unknown parameters. To enhance the prediction accuracy and reduce computational complexity, the Maximal Information Coefficient (MIC) is calculated for each of the five parameters with the I-V curve features. Feature values exhibiting

high correlation with unknown parameters will be selected as input parameters for the LSTM model, facilitating the precise extraction of the five parameters in the photovoltaic module model.

2 Principle of LSTM-based parameter extraction method for single-diode PV model

2.1 Analysis of photovoltaic model output characteristics based on Newton-Raphson method

Figure 1 shows the one-diode model of a PV module. Due to its effective balance between modeling accuracy and the difficulty of parameter extraction, the single-diode five-parameter model has gained broader application. Its output characteristics are derived based on solid-state physics principles, Ohm's Law, and the equivalent circuit of the physical model of PV modules. Its I-V characteristic equation can be expressed as:

$$I = I_{ph} - I_D\left(\exp\left(\frac{q}{nkT_c}(V + IR_s)\right) - 1\right) - \frac{V + IR_s}{R_{sh}} \quad (1)$$

Where I_{ph} represents the photocurrent of the photovoltaic module, I_D is the reverse saturation current of the diode, Rs is the series resistance, R_{sh} is the parallel resistance, n is the ideality factor of the diode, q is the elementary charge constant (1.602×10^{-19} C), k is the Boltzmann constant (1.3807×10^{-23} J/K), T_c is the temperature of the photovoltaic cell, I is the output current of the photovoltaic module, and V is the output voltage of the photovoltaic module.

In Eq. 1, the photocurrent (I_{ph}), reverse saturation current (I_D), series resistance (R_s), parallel resistance (R_{sh}), and ideality factor of the Shockley diode (n) are five parameters determining the output characteristics of the PV module model. These parameters establish an effective correlation between the output voltage (V) and output current (I) of the PV module and the working temperature, irradiance, device structure, and material characteristics. This correlation provides each component in the equivalent circuit with a clear physical meaning, enabling an intuitive description of the impact of various environmental factors on the output characteristics of the PV module.

In Eq. 1, the complex nonlinearity of the I-V characteristics of the PV module makes it difficult to be solved using traditional algorithms. The Newton-Raphson method, also known as Newton's method, emerges as a crucial approach for finding roots of complex equations. Its fundamental concept involves using the first-order Taylor series expansion of the function to estimate the root iteratively, refining this estimate to converge accurately to the function's root. The computational steps are outlined as follows:

Firstly, expand the function $f(x)$ at the point x_0 using a first-order Taylor series which is expressed by Eq. 2:

$$f(x) = f(x_0) + f'(x_0)(x - x_0) \quad (2)$$

The root of the equation $f(x)$ can be expressed as:

$$f(x_0) + f'(x_0)(x - x_0) = 0 \quad (3)$$

Transforming Eq. 3:

$$x = x_0 - \frac{f(x_0)}{f'(x_0)} \quad (4)$$

Since only a first-order expansion of the function $f(x)$ has been performed, the current value of x is an approximate value of the equation's root. To enhance the accuracy of the solution, further iterative steps are required:

$$x_{n+1} = x_n - \frac{f(x_n)}{f'(x_n)} \quad (5)$$

When solving Eq. 1, it is necessary to construct the function for the photovoltaic cell model. By taking the output voltage of the photovoltaic model as a known quantity and the output current as an unknown which is expressed by Eq. 6:

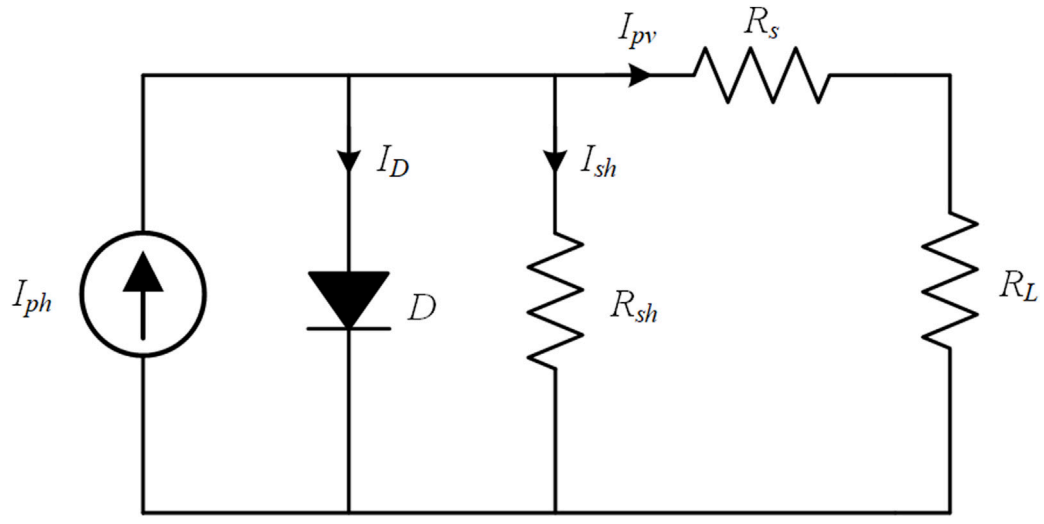

FIGURE 1
Equivalent circuit of single-diode model of PV cell.

$$f(I) = I - I_{ph} - I_D\left(\exp\left(\frac{q}{nkT_c}(V + IR_s)\right) - 1\right) - \frac{V + IR_s}{R_{sh}} \quad (6)$$

Taking the derivative of the equation $f(I)$ Eq. 7 can be obtained:

$$f'(I) = 1 + \frac{qIR_s}{nkT_c}\exp\left(\frac{q}{nkT_c}(V + IR_s)\right) + \frac{R_s}{R_{sh}} \quad (7)$$

Based on Eqs 4, 5, the current value for the (N+1)-th iteration can be expressed by Eq. 8:

$$I_{n+1} = I_n - \frac{f(I_n)}{f'(I_n)} \quad (8)$$

Where I_{n+1} represents the output current value of the photovoltaic cell model at a specific output voltage. The entire I-V curve of the photovoltaic cell model can be obtained by slowly increasing the voltage from zero to the open-circuit voltage.

2.2 Data processing

Due to the extensive numerical variation in the parameters of photovoltaic components, it is essential to normalize these parameters initially to enhance the training accuracy and convergence speed of LSTM. Common normalization methods include min-max normalization, Z-Score normalization. Due to the widespread utilization of the min-max normalization method in neural network systems, this paper applies it to linearly transform the model parameters of PV modules to the range of (0, 1) which is shown in Eq. 9:

$$x = \frac{x - x_{min}}{x_{max}} \quad (9)$$

Where x representing the normalized model parameters for photovoltaic module, x_{max} representing the maximum value within the dataset, and x_{min} indicating the minimum value within the dataset. By randomly assigning values to the five unknown parameters to the PV model and collecting multiple sets of I-V curves for photovoltaic modules, the feature values of each I-V curve can be captured. Then the data set containing various I-V curves under different decay rate can be constructed.

Sorting the data from numerous I-V curves of PV modules in the dataset based on the magnitude of I_{ph} allows for the characterization of decay RATE, which could arrange the dataset into a time series and be further processed by LSTM. Due to the large number of elements in dataset, the whole dataset is segmented into multiple subsets, where the data segmentation process is shown in Figure 2. For each subset, it contains n I-V curves with similar decay level. The blocks of each I-V curves represent the feature value drawn from each I-V curve. From subset 1 to subset n, the degree of decay increases progressively. Doing so, the degree of decay in each subset will be gradually increased, which can be easier processed by LSTM.

2.3 Data dimensionality reduction based on maximal information coefficient

The I-V curve of a PV module is shown in Figure 3. The short-circuit current and open-circuit voltage are critical characteristics that describe the module's output performance. These parameters are instrumental in deriving unknown values within the PV module. Furthermore, the voltage and current at the maximum power point, along with the slopes of the I-V curve at the short-circuit current, maximum power point and open-circuit voltage, are highly correlated with the module's output characteristics. As a result, they can also be utilized to deduce unknown parameters of the PV module. In summary, each I-V curve encompasses seven feature values, considered as known quantities. Therefore, this paper employs the derivation and computation of five unknown parameters based on seven feature values extracted from experimentally measured I-V curves to achieve precise modeling of photovoltaic modules.

Due to the substantial number of feature values and unknown parameters, along with their interdependence, this paper employs the Maximal Information Coefficient (MIC) to analyze correlations among

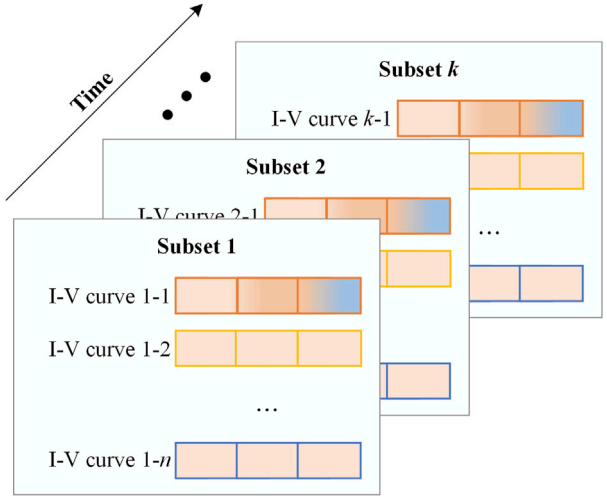

FIGURE 2
Decay-based data segmentation.

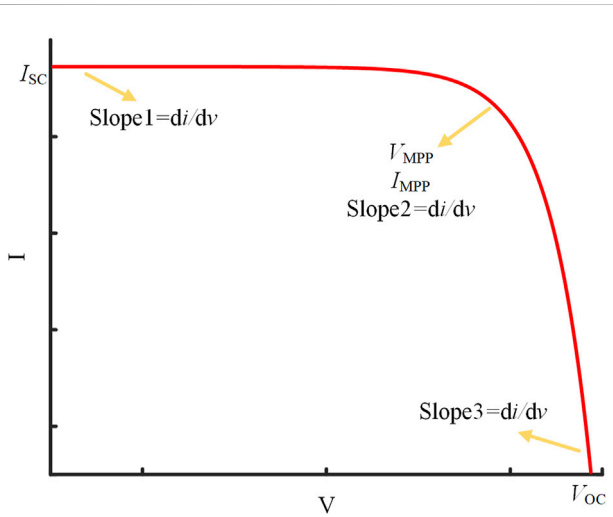

FIGURE 3
I-V characteristic curve of PV module.

10.3389/fenrg.2023.1349887

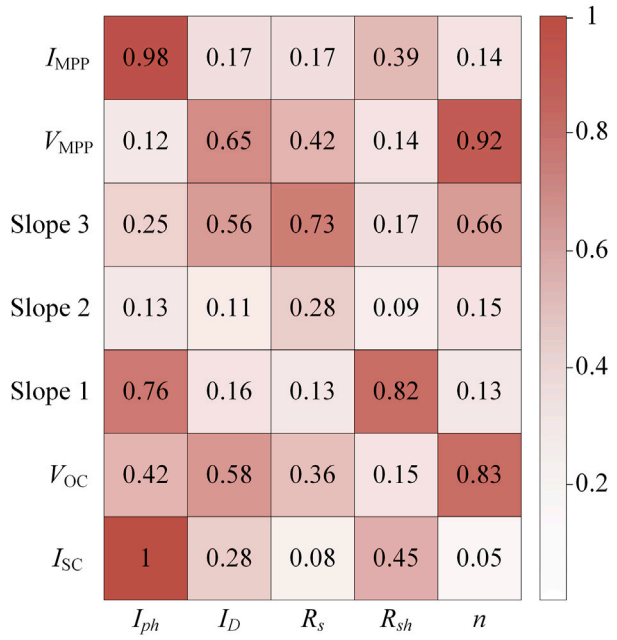

FIGURE 4
MIC analysis results between PV model parameters and feature values.

these parameters. MIC is a statistical measure utilized in data analysis to capture nonlinear dependencies between variables, with the goal of identifying and quantifying associations that may not be adequately described by traditional linear correlation measures. Given the highly nonlinear nature of the five unknown parameters among seven feature values, MIC is particularly suitable for evaluating the correlation level. Only those feature values exhibiting a high correlation with the unknown parameters will be selected as input parameters for the LSTM, facilitating data dimensionality reduction.

The procedure for computing MIC values involves the following steps:

1. Compute mutual information: Apply a specified grid scale to grid the scatter plot formed by two variables. Tally the points within each grid, calculate the joint probability of the two variables, and determine the mutual information (MI) for each grid. Select the maximum mutual information value as the MIC value for the given grid scale.
2. Standardize MIC values: Ensure a consistent range between 0 and 1 by normalizing the MIC values obtained in step 1.
3. Compute the MIC value: Adjust the grid scale from step 1 and repeat the above two steps, the largest MIC value will be the result.

The MI mentioned in step 1 can be expressed by Eq. 10:

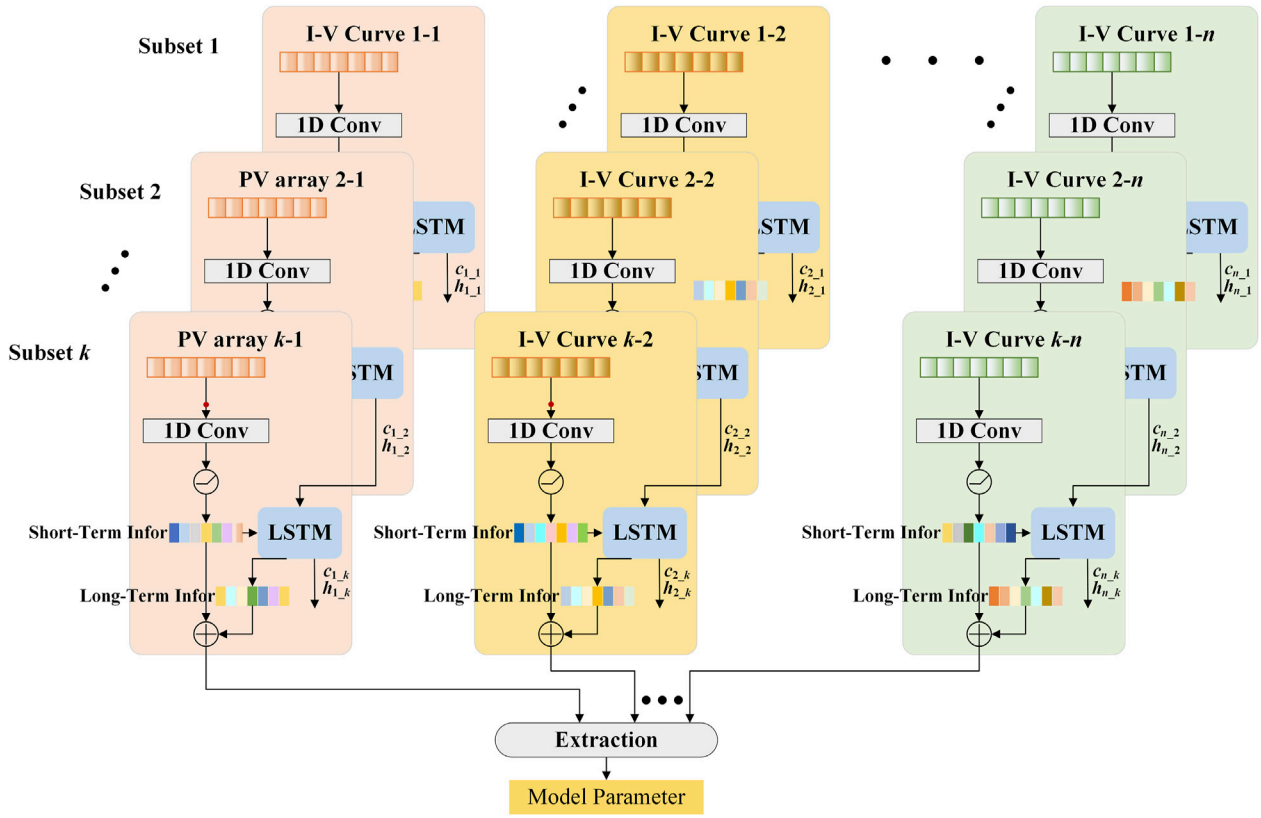

FIGURE 5
LSTM model training.

TABLE 1 MAPE of model parameter extraction by MIC-LSTM, LSTM, and ANN.

Algorithm	I_{ph} (%)	I_D (%)	R_s (%)	R_{sh} (%)	n (%)
MIC-LSTM	0.07	1.61	1.15	2.09	1.64
LSTM	0.17	2.68	1.54	3.80	3.13
ANN	0.15	1.73	1.28	3.97	3.72

$$I(x.y) = \int p(x,y)\log_2\frac{p(x,y)}{p(x)p(y)}dxdy \tag{10}$$

Where x and y represent two variables, p (x, y) represents the joint probability density distribution function of variable x and y, $p(x)$ and $p(y)$ represent the marginal probability density functions of x and y, respectively. The value of MIC can be expressed by Eq. 11:

$$\mathbf{MIC}(x,y) = \max_{a*b<B} \frac{I(x,y)}{\log_2 \min(a,b)} \tag{11}$$

where a and b represent the number of grid divisions in the x and y directions, respectively. B represents a constant, which is normally set to be 0.6 times of the dataset size. The MIC value ranges from 0 to 1. When MIC = 0, it indicates that the two variables are independent of each other. When MIC = 1, it indicates that the two variables are highly dependent of each other. Therefore, the feature values with higher MIC should be chosen as input parameters during LSTM training process.

2.4 Long-short term memory

Long-short term memory (LSTM) networks is a subtype of recurrent neural networks (RNNs). It has become widely recognized for their adeptness in capturing extensive dependencies within sequential data. The basic structure of LSTM is composed by:

Input gate which can be expressed by Eq. 12:

$$i_t = \sigma(W_{ii}x_t + b_{ii} + W_{hi}h_{t-1} + b_{hi}) \tag{12}$$

This equation calculates the input gate activation, where x_t is the input at time t, h_{t-1} is the hidden state from the previous time step, W_{ii} and W_{hi} are input and hidden weight matrices, and b_{ii} and b_{hi} are the corresponding biases. σ represents the sigmoid activation function.

Forget Gate (f_t) which can be expressed by Eq. 13:

$$f_t = \sigma(W_{if}x_t + b_{if} + W_{hf}h_{t-1} + b_{hf}) \tag{13}$$

The forget gate activation is computed to determine what information from the previous cell state should be discarded.

Cell State Update (C_t) which can be expressed by Eq. 14:

$$\tilde{C}_t = \tanh(W_{ig}x_t + b_{ig} + W_{hg}h_{t-1} + b_{hg}) \tag{14}$$

The cell state is updated by combining the previous cell state (C_{t-1}) and the candidate cell state (C_t), with the forget and input gates serving as control mechanisms.

Output Gate (O_t) which can be expressed by Eq. 15:

$$o_t = \sigma(W_{io}x_t + b_{io} + W_{ho}h_{t-1} + b_{ho}) \tag{15}$$

The output gate activation is computed to determine what part of the cell state should be output as the hidden state.

Hidden State (h_t) which can be expressed by Eq. 16:

$$h_t = o_t \odot tanh(C_t) \tag{16}$$

The final hidden state is generated by applying the output gate to the cell state.

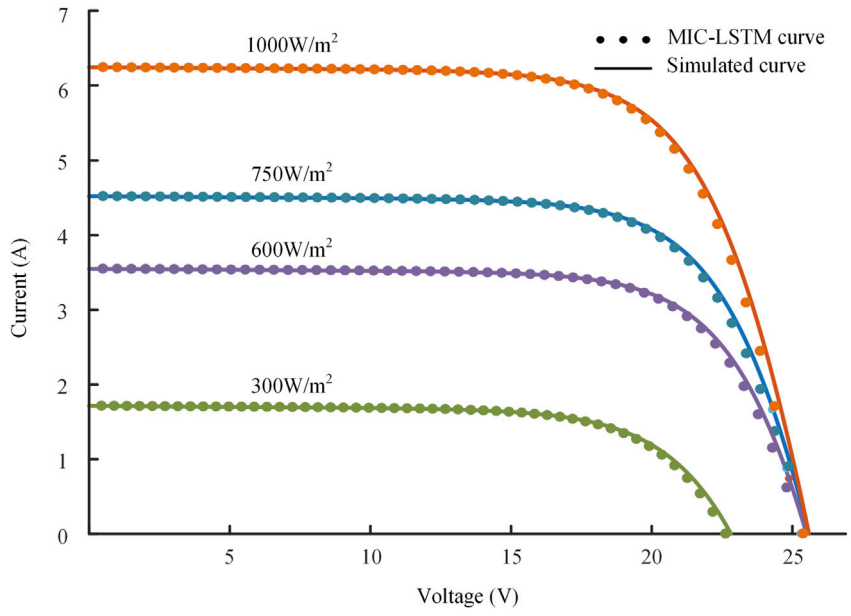

FIGURE 6
IV characteristic curve using MIC-LSTM under different irradiance.

TABLE 2 MAPE of model parameter extraction by MIC-LSTM, LSTM, and ANN.

Parameter	Value
P_{max}	100 W
V_{OC}	21.5 V
I_{SC}	6.27 A
V_{MPP}	18 V
I_{MPP}	5.55 A

The above equations regulate the information flow within an LSTM unit, which enables the network to selectively retain or discard information across multiple time steps and rendering it highly effective in managing sequential data characterized by long-range dependencies.

3 Simulation verifications

3.1 Dataset preprocessing

In this section, a dataset consisting of 10,000 I-V curves has been created. Each subset comprises 5 I-V curves, resulting in a total of 2,000 subsets. Among these, 1,800 subsets serve as the training set, while the remaining 200 subsets are designated as the validation set. Before carrying out LSTM model training, MIC is applied to achieve data dimensionality reduction. Figure 4 illustrates MIC analysis results.

As shown in Figure 4, the ideality factor n is highly correlated with V_{OC}, Slope 3 and V_{MPP} while the MIC value between n and I_{SC}, Slope 1, Slope 2 and I_{MPP} is low. In this paper, the threshold of MIC value is set to be 0.3. Therefore, the input parameters for extracting n should be V_{OC}, Slope 3 and V_{MPP}, which could effectively reduce the data dimensionality.

3.2 LSTM model training

As shown in Figure 4, the ideality factor n is highly correlated with V_{OC}, Slope 3 and V_{MPP} while the MIC value between n and I_{SC}, Slope 1, Slope 2 and I_{MPP} is low. In this paper, the threshold of MIC value is set to be 0.3. Therefore, the input parameters for extracting n should be V_{OC}, Slope 3 and V_{MPP}, which could effectively reduce the data dimensionality.

Figure 5 illustrates the training process of LSTM. Five LSTM models are constructed, where each LSTM model is applied to extract one unknown model parameter. The input data for each LSTM is those feature values whose MIC are larger than 0.3. The I-V Curve feature values in the subsets are extracted using 1-dimensional convolution (1D Conv). The dataset is segmented during data preprocessing, and each segment represents the output characteristics of PV modules for a specific decay level. Consequently, these feature values are classified as Short-term Information. To mitigate the risk of extracting inaccurate model parameter values due to poor data quality, the information from adjacent segments is incorporated as supplementary data. This helps ensure the accuracy and reliability of the extracted model parameters.

The entire dataset is divided into smaller subsets, and the data in adjacent subsets capture the characteristics of the continuous decay of PV modules. To extract the decay characteristics of adjacent data, The long-short term memory (LSTM) algorithm is employed, which is a typical recurrent neural network. LSTM could selectively remember the characteristics of the current moment and transmit them to the next moment through two transmission states: the hidden state (h) and the cell state (c). Consequently, the feature values obtained through LSTM can reflect the characteristics of a more extended period in the past, termed Long-term Information.

In order to verify the parameter extraction accuracy of the proposed algorithm, the parameter extraction accuracy of

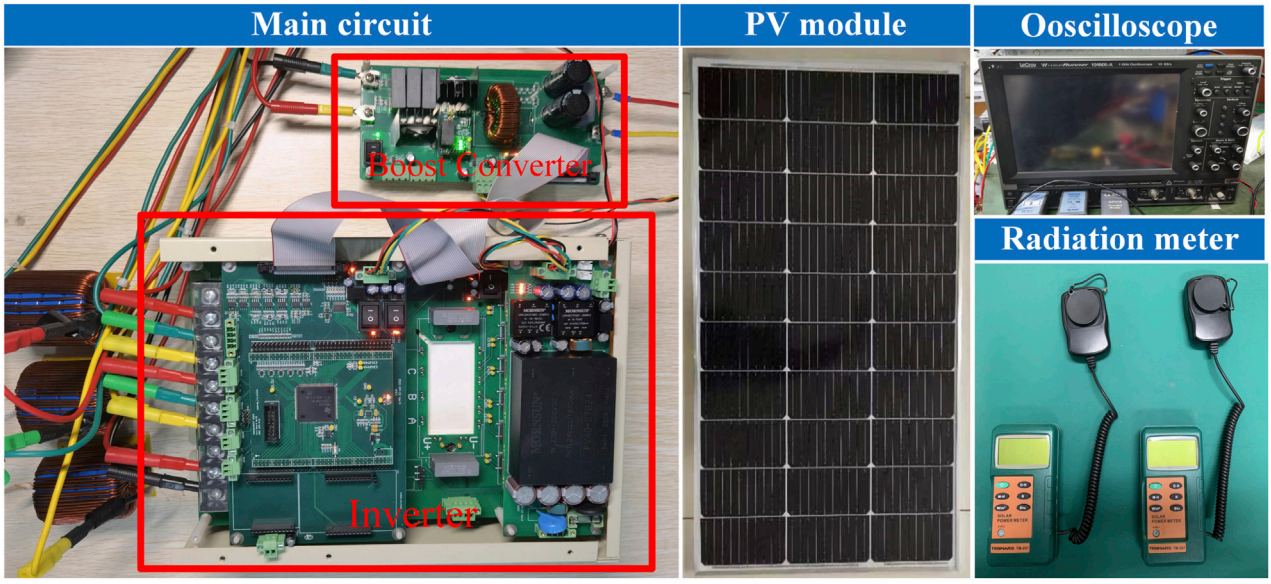

FIGURE 7
Experimental testbed.

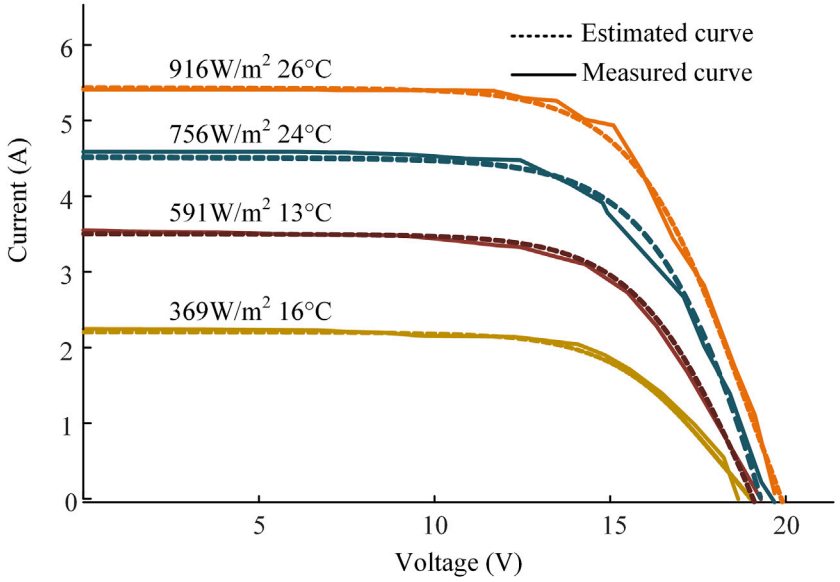

FIGURE 8
Measured and estimated I-V curve of PV module.

traditional LSTM and ANN is also evaluated, which is shown in Table 1. The comparisons indicates that the proposed could achieve a higher model parameter extraction accuracy than other algorithms. The obtained I-V curve based on extracted model parameters under different irradiance is shown in Figure 6.

4 Experimental verifications

For experimental verification of the proposed MIC-LSTM algorithm, the PV module ZY-6M-100 is applied, whose parameters is shown in Table 2.

The experimental testbed is illustrated in Figure 7. The main circuit includes boost converter and inverter, which aims to better simulate the real grid-connected conditions of photovoltaic modules. Two radiation meters are applied to measure the irradiance of PV, module. Firstly, by adjusting the duty ratio of boost converter, the I-V curve of PV, module can be obtained. The feature values of I-V curves, including V_{OC}, I_{SC}, V_{MPP}, I_{MPP}, and di/dt at OC, SC, and MPP., by continuously collecting output data from photovoltaic modules, the feature values at various irradiance levels can be obtained.

Figure 8 shows measured and estimated I-V curve of PV module ZY-6M-100 by applying the proposed MIC-LSTM algorithm under different working conditions. It can be verified that output characteristics of PV model by implementing the proposed MIC-LSTM algorithm could accurately describe the actual I-V characteristics of the PV module under various conditions.

5 Conclusion

In this paper, a novel MIC-LSTM based parameter extraction method for single-diode PV model. With the application of MIC, the dimensionality of the input parameter is reduced, which could effectively exclude the impact of low-correlation inputs on parameter extraction accuracy. With the proposed MIC-LSTM algorithm, the model parameters of PV module can be extracted based on the feature value of its I-V curves, which achieves to construct the accurate PV model at any decay level without large amount of computation. Simulations and experimental verifications were carried out, which validated the feasibility and correctness of proposed MIC-LSTM algorithm.

Data availability statement

The original contributions presented in the study are included in the article/Supplementary Material, further inquiries can be directed to the corresponding author.

Author contributions

XH: Data curation, Supervision, Writing–original draft, Writing–review and editing, Conceptualization, Software, Validation, Visualization. PL: Conceptualization, Data curation, Writing–original draft. YD: Methodology, Writing–review and editing. XM: Validation, Writing–review and editing.

Funding

The author(s) declare that no financial support was received for the research, authorship, and/or publication of this article.

Conflict of interest

Authors XH, PL, and YD were employed by Ningxia Hongdunzi Coal Ind.

The remaining author declares that the research was conducted in the absence of any commercial or financial relationships that could be construed as a potential conflict of interest.

Publisher's note

References

Appelbaum, J., and Peled, A. (2014). Parameters extraction of solar cells-A comparative examination of three methods. *Sol. Energy Mater. Sol. Cells* 122, 164–173. doi:10.1016/j.solmat.2013.11.011

Asif, S., and Li, Y. (2008). Solar cell modeling and parameter optimization using simulated annealing. *J. Propuls. Power* 24 (5), 1018–1022. doi:10.2514/1.35037

Askarzadeh, A., and Rezazadeh, A. (2013). Artificial bee swarm optimization algorithm for parameters identification of solar cell models. *Appl. Energy* 102, 943–949. doi:10.1016/j.apenergy.2012.09.052

Babu, B., and Gurjar, S. (2014). A novel simplified two-diode model of photovoltaic (PV) module. *IEEE J. Photovoltaics* 4 (4), 1156–1161. doi:10.1109/jphotov.2014.2316371

Benkercha, R., Moulahoum, S., and Taghezouit, B. (2018). "Parameters extraction of single and double diode model using the flower algorithm," in 2018 International Conference on Photovoltaic Science and Technologies (PVCon), Ankara, Turkey, 4-6 July 2018.

Chakrabarti, T., Sharma, U., and Chakrabarti, T. (2016). "Extraction of efficient electrical parameters of solar cell using firefly and cuckoo search algorithm," in 2016 7th India International Conference on Power Electronics (IICPE), Patiala, India, 17-19 November 2016.

Chenni, R., Makhlouf, M., Kerbache, T., and Bouzid, A. (2007). A detailed modeling method for photovoltaic cells. *Energy* 32 (9), 1724–1730. doi:10.1016/j.energy.2006.12.006

Cotfas, D., Cotfas, P., and Kaplanis, S. (2013). Methods to determine the dc parameters of solar cells: a critical review. *Renew. Sustain. Energy Rev.* 28, 588–596. doi:10.1016/j.rser.2013.08.017

Elbaset, A., Ali, H., and Abd-El, M. (2014). Novel seven-parameter model for photovoltaic modules. *Sol. Energy Mater. Sol. Cells* 130, 442–455. doi:10.1016/j.solmat.2014.07.016

Garoudja, E., Kara, K., and Chouder, A. (2015). "Parameters extraction of PV module for long-term prediction using artificial bee colony optimization," in 2015 3rd International Conference on Control, Engineering & Information Technology (CEIT), Tlemcen, Algeria, 25-27 May 2015.

Gastli, A., Ben-Brahim, L., and Rhouma, M. (2015). "ANN-based extraction approach of PV cell equivalent circuit parameters," in 2015 17th European Conference on Power Electronics and Applications (EPE'15 ECCE-Europe), Geneva, 8-10 September 2015.

Harrag, A., and Messalti, S. (2015). "Extraction of solar cell parameters using genetic algorithm," in 2015 4th International Conference on Electrical Engineering (ICEE), Boumerdes, Algeria, 13-15 December 2015.

Ishaque, K., and Salam, Z. (2011). An improved modeling method to determine the model parameters of photovoltaic (PV) modules using differential evolution (DE). *Sol. Energy* 85 (9), 2349–2359. doi:10.1016/j.solener.2011.06.025

Ishaque, K., Salam, Z., and Taheri, H. (2011). Simple, fast and accurate two-diode model for photovoltaic modules. *Sol. Energy Mater. Sol. Cells* 95 (2), 586–594. doi:10.1016/j.solmat.2010.09.023

Jiang, L., Maskell, D., and Patra, J. (2013). Parameter estimation of solar cells and modules using an improved adaptive differential evolution algorithm. *Appl. Energy* 112, 185–193. doi:10.1016/j.apenergy.2013.06.004

Khursheed, M., Alghamdi, M., Khan, M., Khan, A. K., and Ahmed, A. (2021). PV model parameter estimation using modified FPA with dynamic switch probability and step size function. *IEEE Access* 9, 42027–42044. doi:10.1109/access.2021.3064757

Krishnakumar, N., Venugopalan, R., and Rajasekar, N. (2013). "Bacterial foraging algorithm based parameter estimation of solar PV model," in 2013 Annual International Conference on Emerging Research Areas and 2013 International Conference on Microelectronics, Communications and Renewable Energy, Kanjirapally, India, 4-6 June 2013.

Kumar, M., and Shiva, D. (2019). "Modelling and parameter estimation of solar cell using genetic algorithm," in 2019 International Conference on Intelligent Computing and Control Systems (ICCS), Madurai, India, May 15-17, 2019.

Muttillo, M., Muttillo, V., and de Rubeis, T. (2020). "Towards the design of microcontroller based embedded sensory systems with a five-parameter single diode estimation method for photovoltaic panels," in 2020 IEEE International Workshop on Metrology for Industry 4.0 & IoT, Roma, Italy, 3–5 June 2020.

Oliva, D., Cuevas, E., and Pajares, G. (2014). Parameter identification of solar cells using artificial bee colony optimization. *Energy* 72, 93–102. doi:10.1016/j.energy.2014.05.011

Pavan, A., Mellit, A., and Lughi, V. (2014). Explicit empirical model for general photovoltaic devices: experimental validation at maximum power point. *Sol. Energy* 101, 105–116. doi:10.1016/j.solener.2013.12.024

Rajasekar, N., Krishna Kumar, N., and Venugopalan, R. (2013). Bacterial Foraging Algorithm based solar PV parameter estimation. *Sol. Energy* 97, 255–265. doi:10.1016/j.solener.2013.08.019

Soon, J., and Low, K. (2012). Photovoltaic model identification using particle swarm optimization with inverse barrier constraint. *IEEE Trans. Power Electron.* 27 (9), 3975–3983. doi:10.1109/tpel.2012.2188818

Subudhi, B., and Pradhan, R. (2018). Bacterial foraging optimization approach to parameter extraction of a photovoltaic module. *IEEE Trans. Sustain. Energy* 9 (1), 381–389. doi:10.1109/tste.2017.2736060

Villalva, J., Gazoli, J., and Filho, E. (2009). Comprehensive approach to modeling and simulation of photovoltaic arrays. *IEEE Trans. Power Electron.* 24 (5), 1198–1208. doi:10.1109/tpel.2009.2013862

Walker, G. (2001). Evaluating MPPT converter topologies using a MATLAB PV model. *J. Electr. Electron. Eng. Aust.* 21 (1), 49–56. doi:10.3316/informit.537020271845747

Xiao, W., Dunford, W., and Capel, A. (2004). "A novel modeling method for photovoltaic cells," in 2004 IEEE 35th Annual Power Electronics Specialists Conference, Aachen, Germany, 20-25 June 2004.

Xiao, X., Lind, M., Dunford, W., and Capel, A. (2006). Real-time identification of optimal operating points in photovoltaic power systems. *IEEE Trans. Industrial Electron.* 53 (4), 1017–1026. doi:10.1109/tie.2006.878355

frontiers | Frontiers in Energy Research

TYPE Original Research
PUBLISHED 19 January 2024
DOI 10.3389/fenrg.2023.1331076

OPEN ACCESS

EDITED BY
Rufeng Zhang,
Northeast Electric Power University, China

REVIEWED BY
Linfei Yin,
Guangxi University, China
Ghulam Hafeez,
University of Engineering and Technology, Pakistan

*CORRESPONDENCE
Minghu Wang,
wangminghu@xauat.edu.cn

RECEIVED 31 October 2023
ACCEPTED 29 December 2023
PUBLISHED 19 January 2024

CITATION
Wang M, Xia Y and Zhang X (2024), Research on renewable energy power demand forecasting method based on IWOA-SA-BILSTM modeling. *Front. Energy Res.* 11:1331076.
doi: 10.3389/fenrg.2023.1331076

Research on renewable energy power demand forecasting method based on IWOA-SA-BILSTM modeling

Minghu Wang*, Yushuo Xia and Xinsheng Zhang

School of Management, Xi'an University of Architecture and Technology, Xi'an, China

This paper introduces a novel coupling method to enhance the precision of short- and medium-term renewable energy power load demand forecasting. Firstly, the Tent chaotic mapping incorporates the standard WOA and modifies its internal convergence factor to a nonlinear convergence mode, resulting in an improved IWOA. It is used for the weight optimization part of BILSTM. Then, the SA is introduced to optimize the learning rate, the number of nodes in hidden layers 1 and 2, and the number of iterations of BILSTM, constructing an IWOA-SA-BILSTM prediction model. Finally, through case analysis, the prediction model proposed in this paper has the highest improvement of 76.7%, 74.5%, and 45.9% in terms of Mean Absolute Error, Root Mean Square Error, and R2, respectively, compared to other optimal benchmark models, proving the effectiveness of the model.

KEYWORDS

bi-directional long and short-term memory neural networks, whale optimization algorithm, multidimensional feature analysis, simulated annealing algorithm, load demand forecasting

1 Introduction

In order to accelerate the transformation of the industrial structure of the power system, China has vigorously promoted the development of renewable energy power, and in recent years more and more renewable energy power has been incorporated into the power grid system. With the increase in installed capacity of renewable energy power generation, the planning and deployment of power has gradually become the focus of the grid work system. The power sector's production deployment and optimal planning depends on the accuracy of power demand forecasting, therefore, improve the accuracy of renewable energy power demand forecasting is the focus of the current power workers research.

The process of forecasting electricity can be divided into three stages: ultra-short-term forecasting, short-term forecasting, and medium-and long-term forecasting. Ultra-short-term forecasting is to forecast the future power load demand in terms of hours; short-term forecasting is to forecast the power load demand in the future period in terms of days, weeks, and quarters; and medium- and long-term forecasting is to forecast the power load demand in the future time in terms of years. Currently, short-term forecasting has become the focus of renewable energy power demand research.

Researchers worldwide are conducting studies to enhance the accuracy of forecasting electricity demand. Forecasting methods are primarily divided into three categories: statistical, artificial intelligence, and hybrid. Statistical methods mainly include time series forecasting models (Dong, 2019; Ma et al., 2022; Gao, 2023) and exponential

smoothing models (Trull et al., 2021). For example, Shang Fangyi et al. (Shang et al., 2015) utilized the gray Verhulst model to enhance the precision of electricity demand analysis and forecasting; Zhang Tao et al. (Zhang and Gu, 2018) introduced Markov chains into the study of renewable energy load forecasting, and achieved effective results; Luo Yi-wang (Luo, 2018) applied the ARMR model to the study of electricity demand forecasting methods, and claimed that the forecasting errors were less than 1% in all of their studies; Zhang Yunfei et al. (Zhang Yunfei et al., 2021) developed a grid peaking demand forecasting model using ridge regression, demonstrating its effectiveness through a case study; Wu et al. (He et al., 2021) combined the Seasonal Exponential Adjustment Method (SEAM) with the time series regression method for the study of load demand forecasting and confirmed the superiority of the model. Artificial intelligence forecasting methods include Extreme Learning Machine (ELM) (He et al., 2021), Support Vector Machine (SVM) (Shi et al., 2019; MuSAA et al., 2021), and various neural network forecasting models (Machado et al., 2021; Rajbhandari et al., 2021; Hu et al., 2023). For example, Shi et al. (Shi et al., 2012) utilized SVM to forecast the amount of photovoltaic (PV) load generation and claimed that the results were good; Zare-Noghabi et al. (Zare-Noghabi et al., 2019) demonstrated the effectiveness of Support Vector Regression (SVR) in forecasting power system load demand using actual data; Guo et al. (Guo et al., 2021) developed a load forecasting model using LSTM, considering demand response, and demonstrated its practicality through experiments; Wen et al. (Wen et al., 2022) proposed a short-term load demand forecasting model based on Bi-directional Long Short-Term Memory(BILSTM) considering the uncertainty of short-term load demand and claimed that the model was superior to the traditional forecasting methods; Su Chang et al. (Su et al., 2023) utilized LSTM and combined it with multi-feature fusion coding to forecast the power load demand, which improved the accuracy of the power load forecasting; Zhang Suning et al. (Zhang et al., 2022) proposed a cross-region power demand forecasting model based on XGBoost for different forms of power demand in multiple regions and claimed that the method can provide fast and accurate forecasting of power demand; Shu Zhang et al. (Zhang Shu et al., 2021) proposed a neural network forecasting model based on feature analysis of the LSTM, which improves the prediction accuracy of short-term power demand. Hybrid forecasting methods (Qinghe et al., 2022; He et al., 2023; Sekhar and Dahiya, 2023) combine various effective forecasting methods to enhance the accuracy of electricity demand forecasting. For example, Moalem et al. (Moalem et al., 2022) successfully combined the ELATLBO method with LSTM neural network for power demand forecasting through experiments; Hu et al. (Hu et al., 2019) proposed a decomposition-based combined forecasting model, which will have the advantage of being able to dynamically combine various models based on data.

At present, more and more scholars have started using ensemble models to improve the accuracy and effectiveness of renewable energy demand prediction research. Various optimization algorithms have also been used by many scholars to optimize the parameters of basic prediction models, thereby further improving the prediction performance of the models. Simulated Annealing Algorithm (SAA) and Whale Optimization Algorithm (WOA) are two optimization algorithms with good performance. SAA has the following advantages: 1. The algorithm boasts a superior global optimization ability, enabling it to find the global optimal solution, thereby avoiding local optimal solutions; 2. SAA is suitable for dealing with large-scale complex problems; 3. Compared with other algorithms, SAA has simpler description, more flexible use, higher operating efficiency, and is less affected by initial conditions; 4. SA does not depend on the specific form and attributes of the problem, only needs to define the objective function and neighbor structure. WOA has the following advantages: 1. Simulating natural behavior makes it have stronger optimization ability; 2. The three population update mechanisms of WOA are independent of each other, and the global search and local development processes can be separately run and controlled, which is beneficial to find the optimal solution; 3. WOA does not require manual setting of various parameters, reducing the difficulty of use and improving the operation efficiency; 4. WOA has shown good optimization performance in solving many numerical optimization and engineering problems. Therefore, this article chooses two optimization algorithms to enhance the prediction accuracy and effectiveness of the basic algorithm.

Therefore, this article adopts a bidirectional long short-term memory network (BILSTM) as the benchmark prediction model. Firstly, the benchmark whale optimization algorithm (WOA) has been improved by incorporating Tent chaos mapping and nonlinear convergence factor to create an evolutionary whale optimization algorithm (IWOA); then the weight matrix of BILSTM is optimized using the evolutionary whale optimization algorithm (IWOA); at the same time, the simulated annealing algorithm (SA) is utilized simultaneously to optimize crucial parameters of BILSTM. Finally, the effectiveness and feasibility of the proposed model are verified using real-world data from a region in China.

The contributions of this article can be summarized as follows: 1. A new coupling algorithm is proposed to predict the demand for renewable energy power, which enhances the accuracy and efficiency of prediction. 2. The standard WOA algorithm has been enhanced to improve its global search and local optimization capabilities, potentially paving the way for future research. 3. The BILSTM model's prediction performance is enhanced by introducing a heuristic algorithm to optimize its weights and key parameters.

2 Factor analysis and data processing

2.1 Renewable electricity demand analysis

There are many factors that affect the demand for renewable electricity, which can be categorized into significant and non-significant factors. Significant factors, i.e., factors that can cause large fluctuations in the demand for renewable electricity within a short period of time, are mainly meteorological factors, such as temperature, humidity, atmospheric pressure, and so on. Secondly, the power generation of fossil energy will also have an impact on the demand for renewable electricity, because if fossil energy cannot support the general demand for electricity by residents within a short period of time, then the social electricity consumption needs to be supported by renewable electricity, so the power generation of fossil energy is taken as a significance factor. Fossil power generation

is also considered as a significant factor, as the fluctuation in electricity demand during legal holidays can also be caused by short periods of time. Non-significant factors, i.e., factors that require a long period of sustained influence to cause fluctuations in renewable energy power demand, generally include economic factors, policy factors, etc. As this paper aims to improve the accuracy of short-term demand forecasting of renewable electricity, the non-significant factors are considered to be stable in this study, and the significant factors are emphasized for in-depth study.

2.2 Factor data analysis

Meteorological data includes three types of factors, namely, temperature, relative humidity and atmospheric pressure, with the temperature factor divided into maximum, minimum and average temperatures. According to the existing data statistics, when the daily relative humidity is higher than 80%, the demand for electricity will rise, while when the daily relative humidity is lower than 51%, the demand for electricity will be relatively low, so this paper takes the relative humidity as one of the influencing factors. Secondly, according to the existing data, holidays and legal holidays also cause large fluctuations in peak electricity consumption, so holidays are also an influential factor that cannot be ignored in the study of renewable electricity demand. In this study, the sum of the number of days of holidays and legal holidays is used as the value of the holiday indicator.

Since the scope of this paper is the renewable energy power demand within the province, the temperature indicator takes the average temperature as the temperature state of the province. The provincial average temperature is weighted and averaged with the temperature values of the municipalities in the province to obtain the final provincial average temperature. Let the average temperature of the province as T_a, its expression is as follows:

$$T_a = \frac{\sum_{i=1}^{n} T_i}{n} \tag{1}$$

Among them, $T_i\,(i = 1, 2, \ldots, n)$ is the temperature value of each prefecture-level city, and the total number of prefecture-level cities within a province is denoted by n.

This paper uses Pearson correlation coefficient to verify the correlation between temperature data and renewable energy power load demand data in historical data to enhance experimental data validity and scientificity:

$$R_s = \frac{\sum_{i=1}^{n}(X_i - \bar{X})(Y_i - \bar{Y})}{\sqrt{\sum_{i=1}^{n}(X_i - \bar{X})^2}\sqrt{\sum_{i=1}^{n}(Y_i - \bar{Y})^2}} \tag{2}$$

R_s is the correlation coefficient between X and Y, X_i is the value of the independent variable, $\bar{X}$ is the average value of the independent variable, Y_i is the value of the dependent variable, $\bar{Y}$ is the average value of the dependent variable, R_s is in the range of 0–1, and the closer the value is to 1, the stronger the correlation is, and when R_s is < 0.3, it means that the two indicators are weakly correlated.

The test results are shown in Table 1, the correlation coefficients between all three types of temperature indicators and renewable energy power load demand are greater than 0.3, indicating that all three types of temperature indicators have a non-negligible impact on renewable energy power load demand, and therefore all three types of temperatures will be used as research factors.

In addition, there may be linear correlation between various types of factors, which leads to the emergence of multicollinearity problem and affects the prediction accuracy of the model. Therefore, this paper does the covariance test using variance inflation factor (VIF) on the collected data, and eliminates the covariance between the influencing factors through LASSO regression, and finally utilizes the filtered data for renewable energy power load demand prediction. The formula for variance inflation factor (VIF) is as follows:

$$VIF_i = \frac{1}{1 - R^2} \tag{3}$$

Where R^2 indicates the correlation between a variable in the independent variables and the rest of the variables; the larger the VIF, the more serious the covariance the independent variables with other variables; in this paper, when we take $0 < VIF < 10$, there is no multicollinearity, $10 \le VIF \le 100$, there is a strong multicollinearity, and $VIF \ge 100$, there is a serious multicollinearity.

3 Multidimensional feature analysis and prediction model based on IWOA-SAA-BILSTM

This part constructs the IWOA-SAA-BILSTM prediction model. There are three steps in the construction process: 1. Building and improving the standard Whale Optimization Algorithm (WOA), introducing the Tent chaotic mapping algorithm to enhance WOA's global solution-seeking ability in the solution process and avoid it easily falling into local optimal solutions. At the same time, the convergence factor in WOA is improved to be nonlinear, which can better simulate the predation mechanism of whale populations and improve the algorithm's global search ability. 2. The BILSTM model's prediction effect is enhanced by optimizing the weights using the improved Whale Optimization Algorithm (IWOA). 3. Introducing simulated annealing algorithm (SAA) to optimize four hyperparameters of BILSTM's hidden layer 1 and hidden layer 2, including the number of neurons, iteration rate, and learning rate. After the above three steps, the IWOA-SAA-BILSTM prediction model is constructed.

3.1 Whale optimization algorithm and its improvement

3.1.1 Whale optimization algorithm

The Whale optimization algorithm, introduced by Australian scholars Mirjalili et al., in 2016, is an intelligent optimization method. The idea of this algorithm originates from the hunting behavior of humpback whales, which have two main hunting behaviors, the first one is encircling hunting and the other one is bubble net hunting. In this algorithm, the position of each individual whale during the hunting process is considered as a potential solution to the problem to be optimized (Yin et al., 2023). The algorithm uses a random search agent and a spiral structure to

TABLE 1 Pearson's coefficients for renewable energy load demand and various types of temperatures.

	Renewable electricity demand (billion kWh)	Maximum temperature	Minimum temperature	Average temperatures
Renewable electricity demand (billion kWh)	1	0.621	0.521	0.601

simulate the humpback whale bubble net attack mechanism, offering a simple optimization search mechanism and local optimum jump capability.

3.1.1.1 Surrounding the prey

The WOA algorithm is a method used to optimize the global solution space of a problem when a group of whales hunt for prey. The target prey is considered the optimal solution, and the current location searched by a whale is considered the best candidate solution. When the best candidate solution is defined, other whales flock to it, and Equation 4 represents the distance between other whales and the best candidate solution:

$$\vec{D} = \left|\vec{C}\cdot\overrightarrow{X^*}(t) - \vec{X}(t)\right| \tag{4}$$

where $\vec{D}$ represents the distance between other whale individuals and the best candidate solution; $\vec{C}$ is the oscillation factor with the expression $\vec{C} = 2\cdot rand$, *rand* denotes a random number with the value range of [0,1]; $\overrightarrow{X^*}(t)$ is the position of the best whale individual during the tth update iteration; $\vec{X}(t)$ the position of the whale individual during the tth update iteration.

Equation 5 is the formula for updating the position of an individual whale during the t+first search:

$$\vec{X}(t+1) = \overrightarrow{X^*}(t) - \vec{A}\cdot\vec{D} \tag{5}$$

Where $\vec{A}$ is the distance adjustment factor, the expression is $\vec{A} = 2a\cdot rand - a$, *rand* denotes a random number with the value range of [0,1], and *a* is the convergence factor, whose value is linearly decreasing from 2 to 0 following the increase of the number of iterations; the meanings of the remaining variables are the same as that of Equation 4.

3.1.1.2 Bubble net hunting

Humpback whales use contraction encirclement and spiral renewal predation methods in bubble nets, choosing based on the probability of the mechanism, p, within the [0,1] range. When $p < 0.5$, humpback whales choose the contraction encirclement method; when $p \geq 0.5$, humpback whales use the spiral renewal mechanism.

When contraction envelopment is used, the distance between individual whales is reduced by a convergence factor *a*. When 当 $|A| < 1$ 时, the position of individual whales after updating will be close to the target prey, thus realizing contraction envelopment.

When the spiral update mechanism is used, the position update between it and the target prey uses the spiral update mechanism with the following expression:

$$\vec{X}(t+1) = \overrightarrow{D^b}\cdot e^{bl}\cdot\cos(2\pi l) + \overrightarrow{X^*}(t) \tag{6}$$

$$\overrightarrow{D^b} = \left|\overrightarrow{X^*}(t) - \vec{X}(t)\right| \tag{7}$$

Style:

$\overrightarrow{D^b}$ denotes the distance of the current individual whale from the optimal solution;

b A constant representing the shape of a logarithmic spiral;

l denotes a random number whose value range is [-1,1]

3.1.1.3 Random search for prey

When $|A| \geq 1$, the individual whale no longer updates its position according to the position of the best individual whale in the population, but randomly selects an individual whale and approaches it with the following position update formula:

$$\vec{D} = \left|\vec{C}\cdot\vec{X}_{rand}(t) - \vec{X}(t)\right| \tag{8}$$

$$\vec{X}(t+1) = \vec{X}_{rand}(t) - \vec{A}\cdot\vec{D} \tag{9}$$

Style:

$\vec{X}_{rand}(t)$ denotes the position of a randomly selected individual whale, and the rest of the variables have the same meaning as in the above equation.

3.1.2 Improved whale optimization algorithm

The optimization ability of a swarm intelligence algorithm is influenced by the diversity and uniformity of its initialization population. The traditional whale optimization algorithm adopts random number to generate the initial population, which leads to the uneven distribution of the initial population and too much simplicity. In the process of population optimization, it cannot optimize in the whole solution space, which leads to some solution sets cannot be found, and ultimately leads to the algorithm falling into the local optimal state. At the same time, it will also affect the convergence speed of the algorithm. Tent chaotic mapping can generate chaotic sequences with strong randomness, universality and uniformity, which can improve the problem that WOA falls into local optimal in the process of population iteration. At the same time, the standard WOA algorithm's convergence factor decreases linearly with population iterations until it reaches 0, adjusting global search and local development abilities of the population. However, the article introduces a nonlinear convergence factor to the standard WOA algorithm, which enhances its capacity to simulate population predation and optimize population optimization, as the linear decrease of convergence factor a cannot effectively adjust global search ability and local development ability.

3.1.2.1 Tent chaos mapping initialization population

Tent chaotic mapping maps the optimization variables to the value intervals of the entire solution space through the chaotic mapping rules, so as to make use of the universality, uniformity and regularity of the chaotic variables for optimization, and ultimately transform the optimization solution set into the optimization space. Tent chaotic mapping is characterized by a uniform distribution of

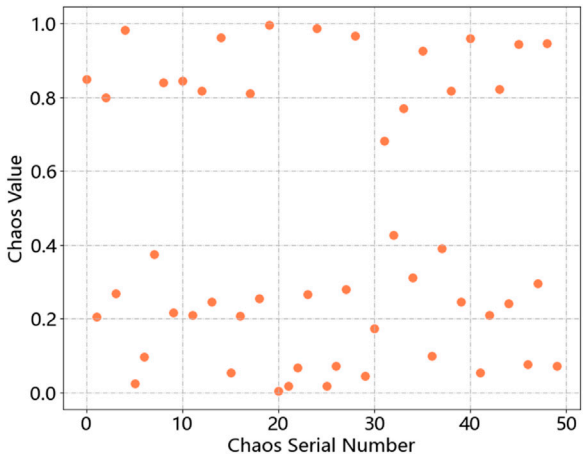

FIGURE 1
Population distribution after adding Tent chaotic mapping.

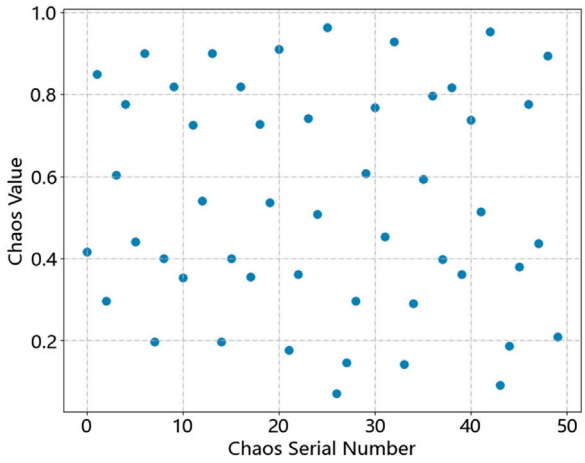

FIGURE 2
Population distribution before adding Tent chaotic mapping.

the functions and good correlation between the functions, and its expression is as follows:

$$H_{i+1} = \begin{cases} \dfrac{H_i}{\alpha}, & H_i \in (0, \alpha] \\ \dfrac{(1 - H_i)}{(1 - \alpha)}, & H_i \in (\alpha, 1) \end{cases} \tag{10}$$

where H_i is the chaotic mapping value at the ith moment; α is the chaotic mapping coefficient.

The WOA after adding chaotic mapping is able to produce a uniformly distributed initial population during the process of population initialization, thus avoiding the defect of the algorithm falling into local optimum. Figures 1, 2 show the distribution of the initial population before and after the addition of the Tent chaotic mapping.

3.1.2.2 Nonlinear convergence factor

The improved convergence factor is used to vary the factor size in a nonlinear way with the following update formula:

$$a = \left(a_{initial} - a_{final}\right) - \sin\left(\frac{t}{T_{max}}\right)^{*} \cos(\lambda)\mu \tag{11}$$

where $a_{initial}$ is the starting value of the convergence factor and a_{final} is the final value; The maximum number of iterations of the algorithm is denoted by T_{max}, while the current number of iterations is represented by t; λ and μ are the coefficient numbers.

The flowchart of the improved whale optimization algorithm is shown in Figure 3.

The specific steps are:

1. Introduce Tent chaotic mapping, use Tent chaotic mapping to initialize the population, set the maximum number of iterations of the population t_{Max};
2. Calculate the fitness of individual whales in the population, confirm the optimal whale individual in the current population and keep its position information;
3. Add a nonlinear convergence factor a, calculate the probability of predation mechanism p, distance adjustment vector $\vec{A}$ and $\vec{D}$. Judge p. If p < 0.5, further judge the value of $|\vec{A}|$; otherwise, use the spiral update mechanism to update the position;
4. Make a judgment on the mode $|\vec{A}|$ of the distance adjustment vector, if $|\vec{A}| < 1$, then adopt the way of encircling the prey, and use Eq. 5 to carry out the position updating; otherwise, adopt the way of random search, and use Eq. 8 to carry out the position updating;
5. After the position update of the population, calculate the fitness of each whale individual in the population again, compare it with the fitness of the previous optimal whale individual, and if it is better than that, replace the previous optimal whale individual with the current whale individual;
6. Determine whether the population reaches the maximum number of iterations, if so, output the optimal solution, otherwise return to step 3 for the next iteration.

3.2 Simulated annealing algorithm

The Simulated Annealing Algorithm (SAA) is a stochastic optimization technique developed in the early 1980s, employing the Monte Carlo iterative solution strategy. The algorithm simulates the physical process in thermodynamics in which an object gradually cools down from some higher temperature and is called annealing. The advantage of the simulated annealing algorithm is its ability to select the worse of the solutions in the current solution neighborhood with a certain probability, which avoids the problem of local optimality and thus achieves the advantage of finding the optimal solution globally.

The main step of the Simulated Annealing Algorithm consists of two inner and outer loops. The outer loop defines the algorithm loop's termination condition, while the inner loop focuses on finding a new optimal solution within the current hyperparameters of the bi-directional neural network. When the loop ends, the algorithm converges to the optimal solution. The specific steps are as follows:

1. Initialization parameters, set the cooling table temperature T_0, the end of iteration temperature T_{end}, the temperature decay

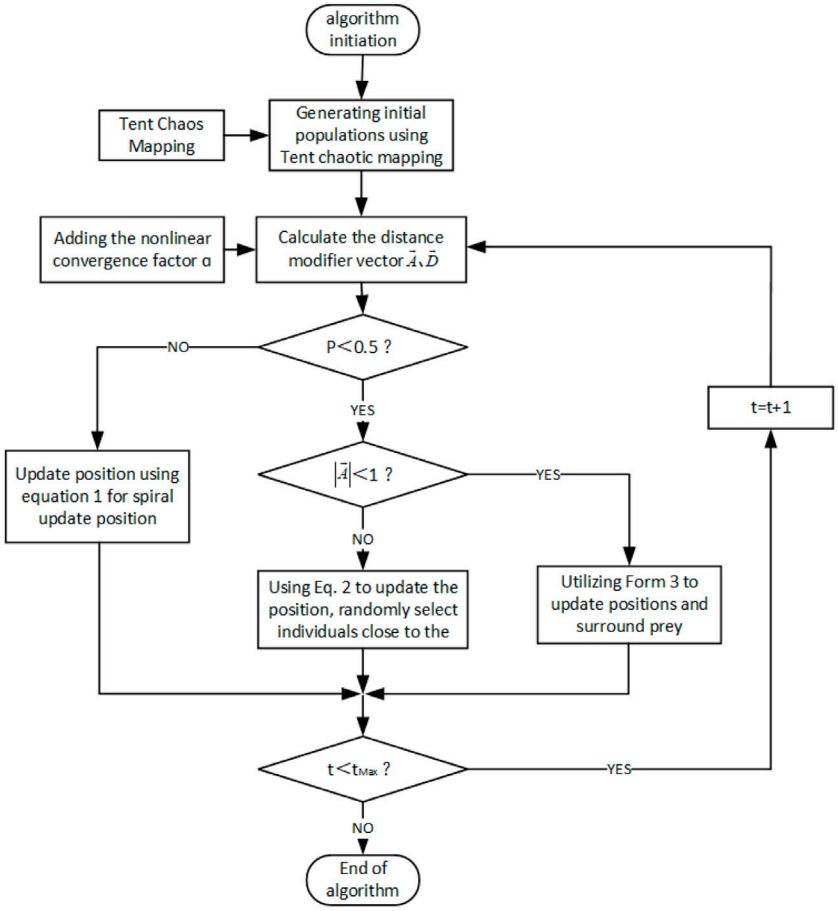

FIGURE 3
Flowchart of IWOA algorithm.

frequency q, the number of inner loop iterations K, the number of outer loop iterations W, the initial solution x_0;

2. Start the kth iteration at the current temperature, k = 1,2, . . . , K;
3. Randomly generate a new solution x_1;
4. Compute the function $E(x) = E(x_1) - E(x_0)$ to obtain ΔE;
5. Determine the excellence of the solution. If $\Delta E \leq 0$, the new solution x_1 can be used as the current optimal solution, in this case, let $x_0 = x_1$; if $\Delta E > 0$, calculate the probability that the new solution x_1 is accepted, P, $P = \exp(\frac{-\Delta E}{T})$, and T is the current temperature; if x_1 is accepted, then $x_0 = x_1$;
6. Slowly cool down the temperature, so that $T = T^*q$, when $T < T_{end}$, output the optimal solution, the algorithm ends. Otherwise repeat steps (3) (4) (5).

3.3 Bidirectional long and short-term memory networks

The creation of BILSTM goes back to RNNs (Recurrent Neural Networks). RNNs are commonly utilized in time series prediction, but they often face issues like gradient vanishing or explosion when dealing with long time series, which leads to the algorithms failing to capture the long term dependencies. To solve this problem, researchers proposed LSTM (Long Short-Term Memory Neural Network). When the data is input to the LSTM, it selects the input value by adjusting the input gate parameter; the role of the forgetting gate when the extracted invalid information is eliminated, and at the same time, the extracted valid information will be input to the next mitigation, and finally, its structure is shown in Figure 4.

However, with the widespread application of LSTM, researchers have found that LSTM has a problem of unidirectional prediction, which can only predict based on the forward information input to the neural network. To solve the unidirectional prediction problem of LSTM, BILSTM was born. BILSTM is composed of a forward LSTM and a backward LSTM under the same time series. Its gate unit is the same as that of standard LSTM, and its advantage is that it can combine forward and backward information to process input data bi-directionally, thus mining hidden features in the data sequence and improving the prediction effect. Its structure is shown in Figure 5.

3.4 IWOA-SAA-BILSTM

In this paper, in order to improve the prediction effect of the benchmark BILSTM, the standard BILSTM algorithm is improved,

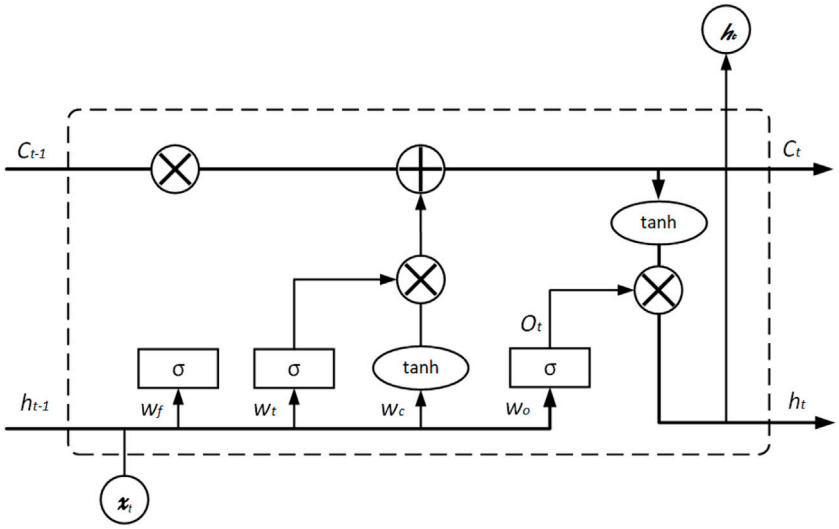

FIGURE 4
Structure of LSTM neural network.

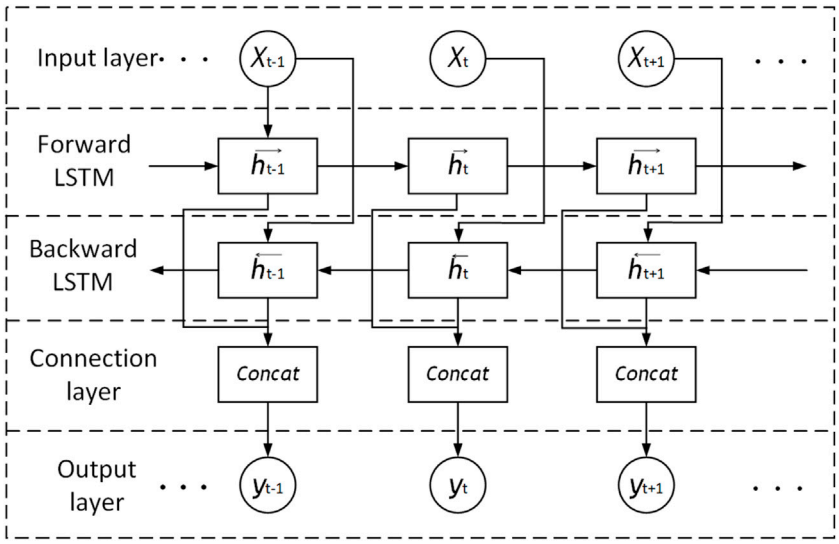

FIGURE 5
Structure of BILSTM neural network.

which is mainly optimized for the weights and hyperparameters. Specifically, the improved whale optimization algorithm (IWOA) and simulated annealing algorithm (SAA) are introduced to optimize the weights and hyperparameters of BILSTM, respectively. The specific improvement ideas of the model are as follows: Firstly, tent chaos mapping is introduced as a new feature in the standard whale optimization algorithm (WOA)., so that the WOA can produce uniformly distributed populations to avoid falling into local optimum; then, the WOA's convergence factor is modified to a nonlinear factor during iteration to enhance the optimality-seeking capacity of whale populations, and the improved IWOA is obtained; and the weights and hyperparameters of the standard BILSTM are optimized by using the IWOA. weights for optimization. At the SAA me time, the simulated annealing algorithm (SAA) is introduced to optimize the hyperparameters of the standard BILSTM, specifically including the number of nodes in the hidden layer 1, the number of nodes in the hidden layer 2, the number of neural network iterations, and the neural network learning rate. Finally, the IWOA-SAA-BILSTM prediction model is obtained. The flowchart of the algorithm is shown in Figure 6.

The specific steps of IWOA-SAA-BILSTM include:

1. Input data. Test the data for missing values and outliers and normalize the data. Divide the data, divide the training set and test set according to 4:1.

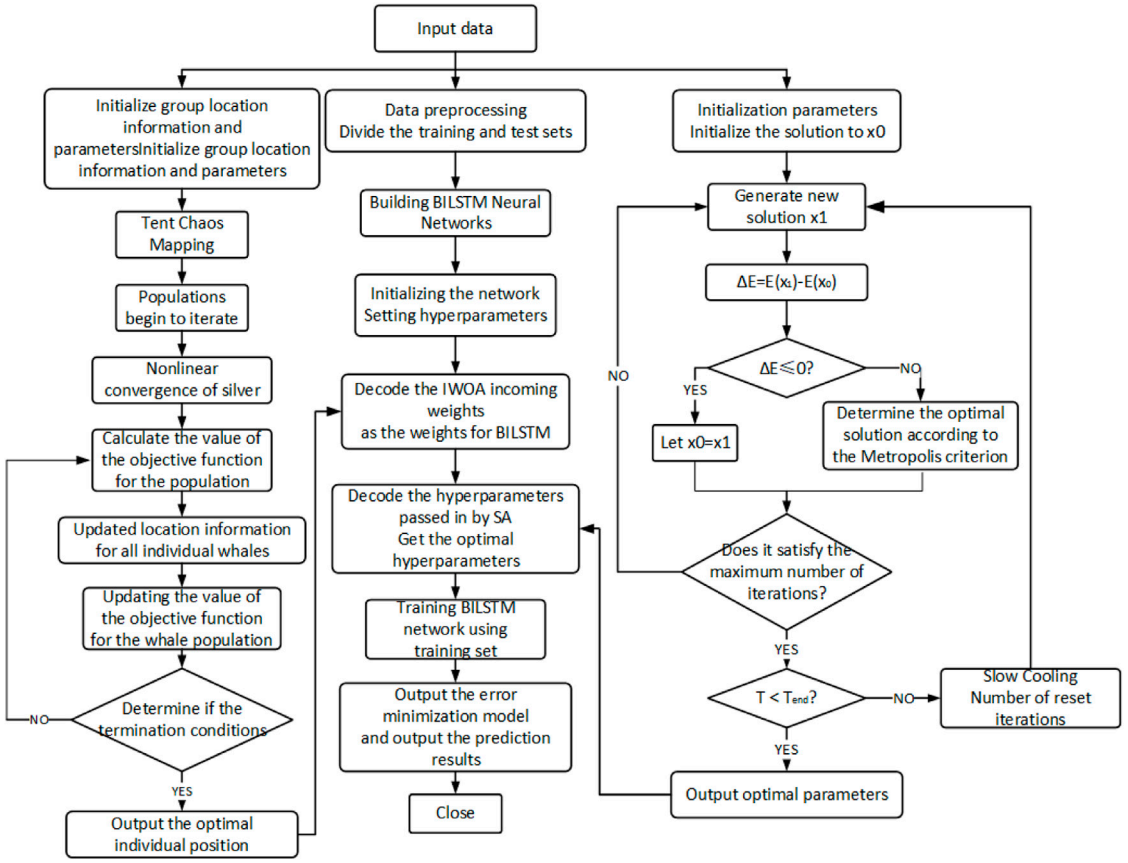

FIGURE 6
Flowchart of IWOA-SAA-BILSTM algorithm.

2. Construct the BILSTM network, initialize the parameters, set the number of hidden layer 1, the number of hidden layer 2, the learning rate, and the number of iterations.
3. Build the IWOA weight optimization model. Set the important parameters such as whale population size, number of population iterations, and spatial dimension; meanwhile, introduce Tent chaotic mapping to generate the initial whale population, and the other population converges and iterates according to the nonlinear way, and the objective function is to determine the value of the population. The optimal whale population position information is mapped into the weights of BILSTM.
4. Build the SAA optimization algorithm. Initialize the SAA parameters, set the cooling table temperature T_0, the iteration end temperature T_{end}, the temperature decay frequency q, the number of inner loop iterations K, the number of outer loop iterations W, and set the initial temperature. The input variables of the algorithm are set as important parameters of BILSTM, and the parameters optimized in this paper are the number of nodes in hidden layer 1, the number of nodes in hidden layer 2, the number of iterations in a neural network and its learning rate are crucial factors to consider. Perform the algorithm iteration and take the prediction error as the return value of the objective function.
5. Run the algorithm and judge whether IWOA and SAA reach the maximum number of iterations and whether it meets the termination conditions, respectively; if the weak algorithm meets the termination conditions, the optimal parameters are encoded and outputted to the BILSTM network, otherwise, repeat step 3.
6. After many iterations, the objective function with the minimum error as well as the optimal parameters and weights can finally be obtained, and finally the IWOA-SAA-BILSTM prediction model is obtained.

This article presents a model with several advantages:

a. The IWOA-SAA-BILSTM model improves the initial population distribution of the standard WOA by making it more uniform, the goal is to enhance the diversity of the population and enhance their global search ability. The introduction of a dynamic step factor enhances the optimization performance of the whale algorithm by regulating its local development and global search abilities.
b. The BILSTM network in the IWOA-SAA-BILSTM model has its own dual memory units and gating mechanism, which can effectively capture and store long-term dependencies in bidirectional sequences, and learn models and features from the data, which enables the model to better predict. In addition, the

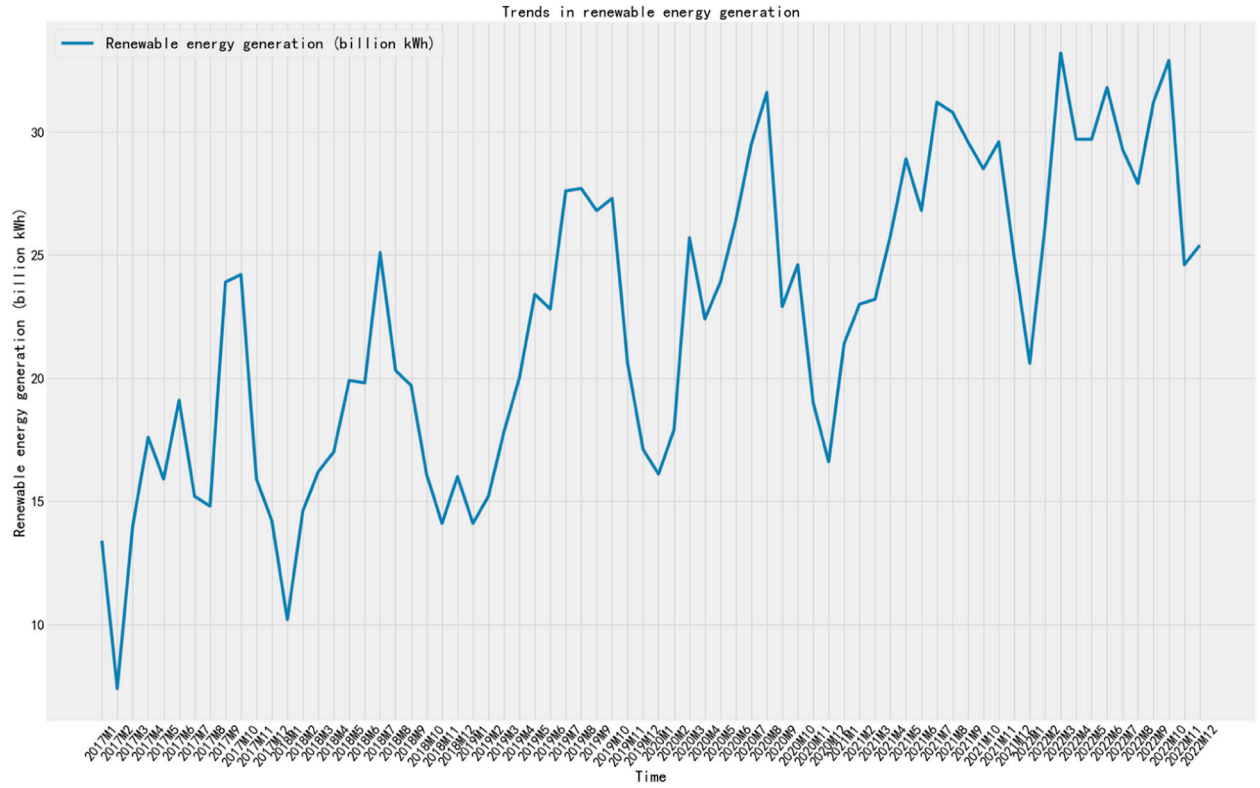

FIGURE 7
Renewable electricity load demand, January 2017 to December 2022.

TABLE 2 Optimal parameter combination of BILSTM model.

Parameters	R^2
Learning rate	0.0045
The number of neurons in hidden layer 1	49
The number of neurons in hidden layer 2	52
Number of iterations	200
Time step	5

IWOA-SAA-BILSTM model optimizes the weights and important parameters of the BILSTM model to better leverage the predictive performance of BILSTM and improve prediction efficiency.

3.5 Pseudo code of main functions of the algorithm

```
1.Improve the whale optimization algorithm
def tent_map(x):
    return 1–2 * abs(x)
    #dynamic step factor
def dynamic_step_size(iter_num, max_iter, step_size)
    return step_size/(iter_num/max_iter)
    # Initialize whale optimization algorithm
whale_optimizer = initialize_whale_optimizer()
2.Simulated annealing algorithm initialization
simulated_annealing = initialize_simulated_annealing()
3.Initialize BILSTM neural network
bilstm_model = initialize_bilstm_model()
4.Constructing IWOA-SA-BILSTM
for iter_num in range(max_iter):
    # Improving whale optimization algorithm using Tent chaotic mapping
    whale_optimizer.improve(tent_map(whale_
    optimizer.position))
    # Optimizing BILSTM weights using an improved whale optimization algorithm
    bilstm_model.optimize(whale_optimizer.position)
    # Optimizing BILSTM hyperparameters using simulated annealing algorithm
    simulated_annealing.optimize(bilstm_model.hyperparameters)
    # Dynamically adjust the step factor
    whale_optimizer.step_size = dynamic_step_size(iter_num, max_iter, whale_optimizer.step_size)
```

4 Arithmetic analysis

4.1 Description of the arithmetic example

In this part, the renewable energy power load demand forecasting model IWOA-SAA-BILSTM proposed in this paper is used, for example, prediction to verify its reliability and superiority in

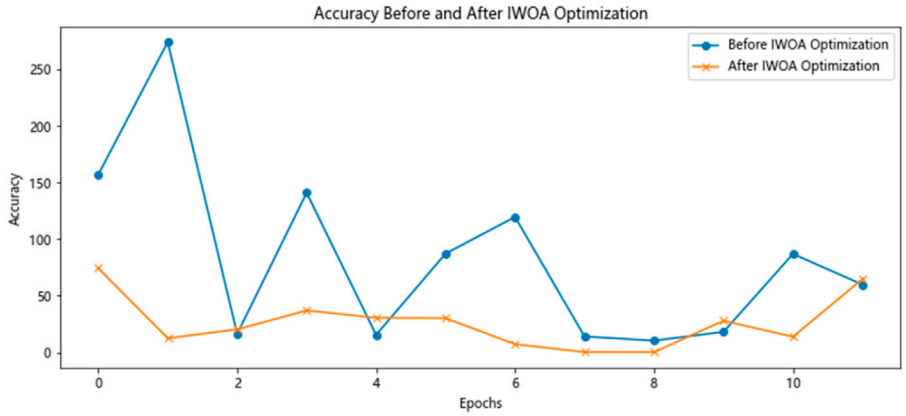

FIGURE 8
Model stability before and after IWOA optimization.

practical application. The experimental data are taken from the official website of the National Bureau of Statistics of China, the China Price Information Network, and the Xihe Energy Big Data Platform, and the preliminary data are firstly extracted, and then the data are precisely analyzed according to the data processing method in the second part of this paper, and the data are collated to obtain a total of 72 monthly renewable energy power load demand and various types of data in Shaanxi Province of China, including the data of the renewable energy power load demand for the period from January 2017 to December 2022, including thermal power generation and the data of the renewable energy power load demand in China. The data reveals six influencing factors, including thermal power generation, maximum temperature, minimum temperature, average temperature, relative humidity, and the number of legal holidays, the dependent variable is the renewable energy power load demand, Figure 7 shows the change curve graph of load demand between January 2017 and December 2022.

4.2 Experimental environment and parameter settings

This article conducted experiments in a virtual Python3.9 environment on Anaconda2.0.3, using a Windows11 system laptop with an Intel Core i7-9750H CPU, NVIDIA GTX 1660ti GPU, and 16G RAM.

In existing research, it is known that among the hyperparameters of BILSTM neural networks, The number of hidden layer neurons (m) and learning rate (l) significantly influence the prediction performance of neural networks. The number of hidden layer neurons m in neural networks is usually determined by empirical formulas, as shown in formula (12). Using this formula, an approximate range of values for the number of hidden layer neurons in a neural network can be obtained. Within this range, specific parameter settings can be obtained through repeated experiments.

$$m = \sqrt{\alpha + \beta} + n \tag{12}$$

The formula involves α representing the number of output layer nodes, β representing the number of input layer nodes, and n being a constant.

The study employs the Adam optimizer with an initial learning rate of [0.0001, 0.01], a maximum of 500 iterations, and an initial population generated by Tent chaos; SA's initial temperature is set to 100°C, and temperature decay frequency is set to 0.95; both IWOA and SAA optimization algorithms aim to achieve a target error of 0. BILSTM neural network's initial input layer node range is [1, 50], hidden layer node range is [1, 100], and time step is set to 5; forget gate and input gate activation functions choose Sigmoid function, and output gate activation function chooses tanh function. In the iterative process, after each iteration, validation is performed, and the model parameters with the smallest error obtained in the latest iteration are used to replace the previous optimal parameters for the next loop. Finally, the model with the smallest error throughout the entire iterative process is retained as the final prediction model. The experiment employs the Mean Squared Error (MSE Loss) loss function, which is expressed as follows:

$$MSE = \frac{1}{n}\sum_{i=1}^{n}(y_i - \overline{y_i})^2 \tag{13}$$

After multiple iterations of the IWOA and SA algorithms, the optimal parameters of the BiLSTM model were finally output, resulting in the optimal parameter combination shown in Table 2.

4.3 Evaluation indicators

The model's prediction accuracy is tested using three indicators: Root Mean Square Error (RMSE), Mean Absolute Error (MAE), and R_squared. The formulas for the three indicators are respectively:

$$RMSE = \sqrt{\frac{1}{n}\sum_{i=1}^{n}(\hat{y}_i - y_i)^2} \tag{14}$$

$$MAE = \frac{1}{n}\sum_{i=1}^{n}\left|\hat{y}_i - y_i\right| \tag{15}$$

$$R^2 = 1 - \frac{\sum_{i=1}^{n}\frac{(y_i - \hat{y}_i)^2}{n}}{\sum_{i=1}^{n}\frac{(y_i - \overline{y_i})^2}{n}} \tag{16}$$

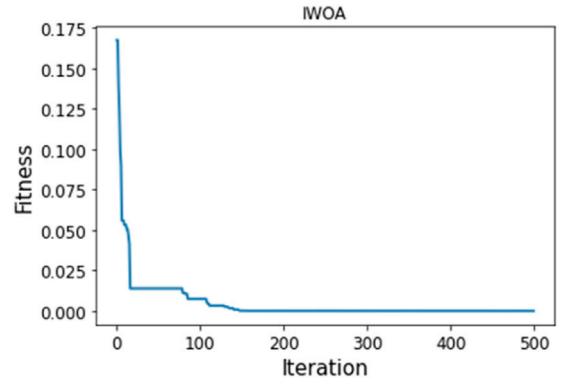

FIGURE 9
IWOA adaptation curve.

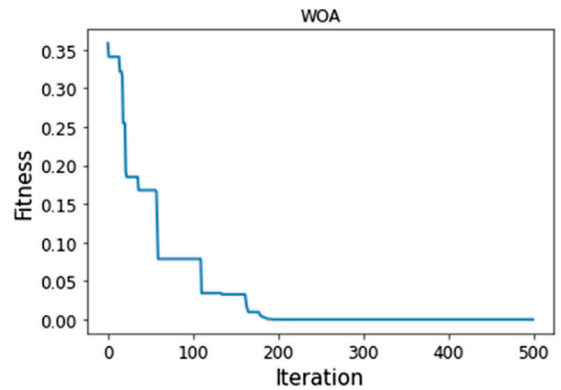

FIGURE 10
WOA adaptation curve.

FIGURE 11
Plot of IWOA-SAA-BILSTM predicted values vs actual values.

TABLE 3 Evaluation index values for BILSTM, IWOA-BILSTM, IWOA-SAA-BILSTM.

Model	MAE(BKWh)	RMSE(BKWh)	R^2
BILSTM	2.75	3.47	0.62
IWOA-BILSTM	1.98	2.27	0.75
IWOA-SAA-BILSTM	**1.39**	**1.67**	**0.89**

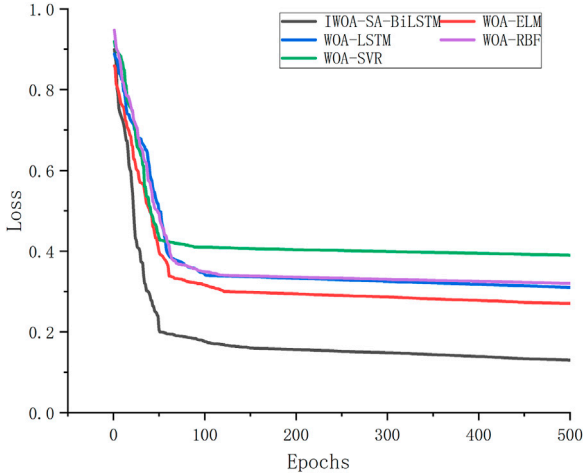

FIGURE 12
Loss function change curve diagram of five groups of models.

4.4 Ablation experiments

This paper uses a mode of ablation experiment to assess the effectiveness of model improvement. Specifically, the example prediction is carried out with BILSTM, IWOA-BILSTM and the proposed model IWOA-SAA-BILSTM in this paper, respectively. In order to make the prediction results more scientific and reliable, the initial parameters of the BILSTM part of the three groups of models are kept consistent with part 7.1 during the experiment. In addition, the IWOA parameter settings of the IWOA-BILSTM model and the IWOA-SAA-BILSTM model were kept consistent. The model parameters were set, and the data was divided into training and test sets in an 8:2 ratio. After testing, the model stability before and after adding the IWOA optimization model is shown in Figure 8, and the IWOA model adaptation curve is shown in Figure 9:

The model's accuracy improved by IWOA has remained stable, with 90% of points now better than before, indicating a significant impact of IWOA on model prediction accuracy. Figure 9 and Figure 10 reveal that IWOA has a significantly faster convergence speed than WOA. IWOA has approached the optimal solution around the 140th iteration, while WOA needs to iterate 200 times to reach the optimal solution. The paper demonstrates the effectiveness of the proposed optimization method by highlighting the significant improvement in prediction efficiency and accuracy through the enhancement of WOA.

TABLE 4 Evaluation index value of each prediction model.

Model	MAE(BKWh)	Increase in percentage	RMSE(BKWh)	Increase in percentage	R^2	Increase in percentage
WOA-SVR	5.97	76.7%	6.54	74.5%	0.61	45.9%
WOA-RBF	5.63	75.3%	6.31	73.5%	0.65	36.9%
WOA-LSTM	4.93	71.8%	5.85	71.5%	0.69	29%
WOA-ELM	3.36	58.6%	4.53	63.1%	0.76	17.1%
IWOA-SAA-BILSTM	**1.39**	——	**1.67**	——	**0.89**	——

Figure 11 displays the predicted and actual values of the IWOA-SAA-BILSTM model after three different model runs. By doing the ablation experiment with the other two groups of models, all the evaluation indexes of the models proposed in this paper are better than the other two groups of models. The ablation experiment demonstrates that the proposed model improvement can enhance the performance of the original model, thereby improving prediction efficiency and accuracy. Table 3 displays the evaluation indexes of the prediction results of the three model groups:

4.5 Comparative experiments

In addition to ablation experiments on the proposed model, this article also built several other commonly used models in existing research to demonstrate that the proposed model is not only superior to the pre-improved basic model, but also superior to common models in current research. This article selected four models with good performance in existing research, including WOA-SVM, WOA-LSTM, WOA-RBF, and WOA-ELM, as comparison models. The parameters of the IWOA-SAA-BILSTM model in this part of the experiment were kept consistent with the ablation experiment.

First, five groups of models were used to train the set, and the test set was used for fitting. The learning ability and fitting of the five groups of models for the data variation rule were compared. After the experiment, the loss function changes of the five groups of models are shown in the following figure.

Figure 12 provides a clear representation of the situation, the loss function of IWOA-SA-BILSTM is the smallest at the later stage of the iterative process, indicating that the model fitting effect of IWOA-SAA-BILSTM is superior to other models; and the loss function variation curve of IWOA-SAA-BILSTM decreases continuously with the increase of fitting times, until it reaches a stable state in the final stage of fitting, indicating that the IWOA-SAA-BILSTM model can correctly capture the data variation rules in the training data, has strong learning ability, and thus performs better prediction.

At the same time, using actual data for testing, we used evaluation indicators to measure the prediction accuracy and prediction accuracy of the five models. Table 4 displays the rating indicators of the four comparative models and the proposed model based on comparative experiments.

From the table, it can be seen that the prediction effects of IWOA-SAA-BILSTM are all better than the other four comparison models, with the optimal MAE value of 1.39 BKWh and the optimal RMSE value of 1.67 BKWh, this paper presents results that

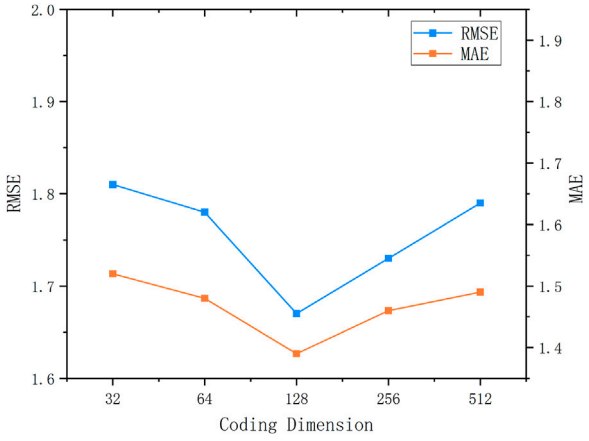

FIGURE 13
The influence of encoding dimensions on model performance.

demonstrate the effectiveness of enhancing the standard whale optimization algorithm. And the R2 value shows that the effect of IWO-SAA-BILSTM prediction model is more stable. Therefore, the model proposed in this paper can be used as a favorable tool for renewable energy power load demand forecasting research.

4.6 Parameter sensitivity analysis

The model's encoding dimension directly impacts the number of parameters and prediction performance. Therefore, analyzing the encoding dimension on the prediction performance of the model can help to find the optimal encoding dimension position, the model's prediction performance has been enhanced.

Set the encoding dimensions to {32, 64, 128, 256, 512} and perform model operations separately. Use RMSE and MAE as evaluation metrics for model performance. The experimental results are shown in Figure 13.

As can be seen from the figure, when the model encoding dimension is 32 dimensions, the model is too simple and cannot learn enough effective data, resulting in poor model performance. Therefore, the model's predictive performance can be enhanced by increasing its embedding dimension. When the encoding dimension is 128 dimensions, as can be seen from the figure, the prediction performance of the model is the best. This is because a higher model dimension can store more data information, allowing the model to better learn and simulate the regularities and changing characteristics

of the data. However, an excessive encoding dimension is also not conducive to improving model performance. For example, when set to 256 dimensions and 512 dimensions, the prediction performance of the model decreases, which is due to the learning of excessive data noise and redundant information during data learning and feature simulation, affecting the prediction performance of the model.

Therefore, when the encoding dimension of the model is set to 128 dimensions, the IWOA-SAA-BILSTM model achieves the best prediction performance.

5 Conclusion

The objective is to enhance the precision of medium and short-term renewable energy power load demand forecasting, this article proposes an IWOA-SAA-BILSTM prediction model based on multi-dimensional feature analysis. Firstly, the factors that affect the renewable energy power load demand are screened, the study identifies the significant factors that significantly influence medium and short-term load demand. Then, the benchmark Whale Optimization Algorithm (WOA) is improved by adding Tent chaos mapping, and its internal convergence method is improved to be nonlinear, the improved Whale Optimization Algorithm (IWOA) has been obtained. Then, IWOA is used to optimize the weights of BILSTM, and Simulated Annealing Algorithm (SAA) is introduced to optimize the learning rate of BILSTM, the number of nodes in hidden layers 1 and 2 and the number of iterations are crucial factors to consider. The IWOA-SAA-BILSTM prediction model is obtained. At the end of the article, through case analysis, the prediction accuracy indicators of the model proposed in this article are: MAE is 1.39, RMSE is 1.67, and R_squared index is 0.89, which are all better than other comparison models. It shows that the prediction results of this model are reliable, and can provide corresponding theoretical basis for the research on renewable energy power load demand forecasting, as well as more theoretical guidance for power planning departments.

Data availability statement

The original contributions presented in the study are included in the article/Supplementary Material, further inquiries can be directed to the corresponding author.

Author contributions

MW: Writing–original draft. YX: Writing–original draft, Writing–review and editing. XZ: Writing–review and editing.

Funding

The author(s) declare financial support was received for the research, authorship, and/or publication of this article. This work was supported by the (Key Industry Innovation Chain Project of Shaanxi Provincial Department of Science and Technology), (Grant Number 22ZDLGY06); the (Shaanxi Provincial Philosophy and Social Science Research Specialized Key Issues), (2023HZ1659); the (Key Project of Philosophy and Social Sciences of Shaanxi Provincial Department of Education), (21JZ035); and the (Natural Science Foundation of Xi'an University of Architecture and Technology), (004/1603720032).

Conflict of interest

The authors declare that the research was conducted in the absence of any commercial or financial relationships that could be construed as a potential conflict of interest.

Publisher's note

Supplementary material

The Supplementary Material for this article can be found online at: https://www.frontiersin.org/articles/10.3389/fenrg.2023.1331076/full#supplementary-material

References

Dong, J. (2019). Demand response baseline load forecasting based on the combination of time series and kalman filter. *Am. J. Electr. Power Energy Syst.* 8 (3), 71. doi:10.11648/j.epes.20190803.11

Gao, G. (2023). *Risk assessment due to load demand and electricity Price forecast uncertainty*. Doctoral thesis (Glasgow, Scotland: University of Strathclyde).

Guo, X., Zhao, Q., Wang, S., Shan, D., and Gong, W. (2021). A short-term load forecasting model of LSTM neural network considering demand response. *Q. Sun. Complex.* 2021, 1–7. doi:10.1155/2021/5571539

He, M., Li, Y., and Zou, W. (2021). Application of ALO-ELM in load forecasting based on Big data. https://www.preprints.org/manuscript/202110.0302/v1.

He, Z., Lin, R., Wu, B., Zhao, X., and Zou, H. (2023). Pre-attention mechanism and convolutional neural network based multivariate load prediction for demand response. *Energies Multidiscip. Digit. Publ. Inst.* 16 (8), 3446. doi:10.3390/en16083446

Hu, S., Tang, H., Lu, K., et al. (2023). Deep belief network short-term load forecasting method considering generalized demand-side resources. *Control theory Appl.* 40 (3), 493–501. doi:10.7641/CTA.2021.10209

Hu, Z., Ma, J., Yang, L., Li, X., and Pang, M. (2019). Decomposition-based dynamic adaptive combination forecasting for monthly electricity demand. *Sustainability* 11 (5), 1272. doi:10.3390/su11051272

Luo, Y. (2018). Research on electricity demand forecasting based on structured data. *Electron. Meas. Technol.* 41 (12), 21–26. doi:10.19651/j.cnki.emt.1701420

Ma, T., Barajas-Solano, D. A., Huang, R., and Tartakovsky, A. M. (2022). Electric load and power forecasting using ensemble Gaussian process regression. *J. Mach. Learn. Model. Comput.* 3 (2), 87–110. doi:10.1615/jmachlearnmodelcomput.2022041871

Machado, E., Pinto, T., Guedes, V., and Morais, H. (2021). Electrical load demand forecasting using feed-forward neural networks. *Energies* 14 (22), 7644. doi:10.3390/en14227644

Moalem, S., Ahari, R. M., Shahgholian, G., Moazzami, M., and Kazemi, S. M. (2022). Long-term electricity demand forecasting in the steel complex micro-grid electricity supply chain—a coupled approach. *Energies Multidiscip. Digit. Publ. Inst.* 15 (21), 7972. doi:10.3390/en15217972

MuSAA, B., Yimen, N., Abba, S. I., Adun, H. H., and Dagbasi, M. (2021). Multi-state load demand forecasting using hybridized support vector regression integrated with optimal design of off-grid energy systems—a metaheuristic approach. *Processes* 9 (7), 1166. doi:10.3390/pr9071166

Qinghe, Z., Wen, X., Boyan, H., Jong, W., and Junlong, F. (2022). Optimised extreme gradient boosting model for short term electric load demand forecasting of regional grid system. *Sci. Rep.* 12 (1), 19282. doi:10.1038/s41598-022-22024-3

Rajbhandari, Y., Marahatta, A., Ghimire, B., Shrestha, A., Gachhadar, A., Thapa, A., et al. (2021). Impact study of temperature on the time series electricity demand of urban Nepal for short-term load forecasting. *Appl. Syst. Innov.* 4 (3), 43. doi:10.3390/asi4030043

Sekhar, C., and Dahiya, R. (2023). Robust framework based on hybrid deep learning approach for short term load forecasting of building electricity demand. *Energy* 268, 126660. doi:10.1016/j.energy.2023.126660

Shang, F., Yang, Z., Cheng, H., et al. (2015). Application of improved Verhulst model in saturated load forecasting. *J. Power Syst. Automation* 27 (1), 64–68. doi:10.3969/j.issn.1003-8930.2015.01.012

Shi, J., Lee, W.-J., Liu, Y., Yang, Y., and Wang, P. (2012). Forecasting power output of photovoltaic systems based on weather classification and support vector machines. *IEEE TranSAActions Industry Appl.* 48 (3), 1064–1069. doi:10.1109/tia.2012.2190816

Shi, J., Xie, L., and Wang, Z. (2019). Research on short-term load forecasting of industrial parks under construction based on the combination of discriminant analysis and support vector machine. *Technol. innovation Appl.* (10), 61–62. doi:10.3969/j.issn.2095-2945.2019.10.023

Su, C., Jin, C., Bian, S., et al. (2023). Power demand load forecasting method based on multi-feature fusion coding. *Small Microcomput. Syst.*, 1–9.

Trull, O., García-Díaz, J. C., and Troncoso, A. (2021). One-day-ahead electricity demand forecasting in holidays using discrete-interval moving seasonalities. *Energy* 231, 120966. doi:10.1016/j.energy.2021.120966

Wen, J., Xian, Z., Chen, K., and Luo, W. (2022). A novel forward operator-based Bayesian recurrent neural network-based short-term net load demand forecasting considering demand-side renewable energy. *Front. Energy Res.* 10, 963657. doi:10.3389/fenrg.2022.963657

Yin, M., Ke, P., and Zhang, C. (2023). An improved whale optimization algorithm integrating multiple strategies. *J. Wuhan Univ. Sci. Technol.* 46 (2), 145–152. doi:10.3969/j.issn.1674-3644.2023.02.009

Zare-Noghabi, A., Shabanzadeh, M., and Saangrody, H. (2019). "Medium-term load forecasting using support vector regression, feature selection, and symbiotic organism search optimization," in 2019 IEEE Power & Energy Society General Meeting (PESGM), Atlanta, GA, USA, August, 2019.

Zhang, S., Liao, X., and Cheng, Y. (2021b). Research on short-term power demand forecasting method of LSTM neural network based on characteristic analysis. *Electr. Power Big Data* 24 (5), 9–17. doi:10.19317/j.cnki.1008-083x.2021.05.002

Zhang, S., Wang, F., Zhu, Y., et al. (2022). Multi-regional power demand forecasting based on extreme gradient boosting. *Comput. Mod.* (3), 18–22+29. doi:10.3969/j.issn.1006-2475.2022.03.004

Zhang, T., and Gu, J. (2018). Markov short-term load forecasting method for high-proportion renewable energy power system. *Grid Technol.* 42 (4), 1071–1078. doi:10.13335/j.1000-3673.pst.2017.2479

Zhang, Y., Min, Li, Tian, K., et al. (2021a). Research on power grid peak regulation demand forecasting based on ridge regression. *Hydropower pumped storage* 7 (6), 74–76. doi:10.3969/j.issn.2096-093X.2021.06.020

frontiers | Frontiers in Energy Research

TYPE Original Research
PUBLISHED 02 February 2024
DOI 10.3389/fenrg.2024.1351324

OPEN ACCESS

EDITED BY
Rufeng Zhang,
Northeast Electric Power University, China

REVIEWED BY
Xiaoxue Wang,
Hebei University of Technology, China
Guoqiang Zu,
State Grid Tianjin Electric Power Research Institute, China
Lv Chaoxian,
China University of Mining and Technology, China

*CORRESPONDENCE
Zhang Kun,
kunzhang1998@tju.edu.cn

RECEIVED 06 December 2023
ACCEPTED 15 January 2024
PUBLISHED 02 February 2024

CITATION
Feng L, Jianfu N, Zhuofei Y, Kun Z, Qianyu Z and Shouxiang W (2024), Fixed and mobile energy storage coordination optimization method for enhancing photovoltaic integration capacity considering voltage offset.
Front. Energy Res. 12:1351324.
doi: 10.3389/fenrg.2024.1351324

Fixed and mobile energy storage coordination optimization method for enhancing photovoltaic integration capacity considering voltage offset

Liang Feng[1], Ni Jianfu[1], Yu Zhuofei[1], Zhang Kun[2,3]*, Zhao Qianyu[2,3] and Wang Shouxiang[2,3]

[1]Grid Electric Power Research Institute Corporation, Nari Group Corporation State, Nanjing, Jiangsu, China, [2]Tianjin Key Laboratory of Power System Simulation Control, Tianjin, China, [3]Key Laboratory of Smart Grid of Ministry of Education (Tianjin University), Tianjin, China

Mobile energy storage has the characteristics of strong flexibility, wide application, *etc.*, with fixed energy storage can effectively deal with the future large-scale photovoltaic as well as electric vehicles and other fluctuating load access to the grid resulting in the imbalance of supply and demand. To this end, this paper proposes a coordinated two-layer optimization strategy for fixed and mobile energy storage that takes into account voltage offsets, in the context of improving the demand for local PV consumption. Among them, the upper layer optimization model takes into account the minimum operating cost of fixed and mobile energy storage, and the lower layer optimization model minimizes the voltage offset through the 24-h optimal scheduling of fixed and mobile energy storage in order to improve the *in-situ* PV consumption capacity. In addition, considering the multidimensional nonlinear characteristics of the model, the interaction force of particles in the Universe is introduced, and the hybrid particle swarm-gravitational search algorithm (PSO-GSA) is proposed to solve the model, which is a combination of the individual optimization of the particle swarm algorithm and the local search capability of the gravitational search algorithm, which improves the algorithm's optimization accuracy. Finally, the feasibility and effectiveness of the proposed model and method are verified by simulation analysis with IEEE 33 nodes.

KEYWORDS

distribution grids, photovoltaic local consumption, fixed energy storage systems, mobile energy storage systems, energy storage scheduling strategies, hybrid particle swarmgravitational search algorithms

1 Introduction

With the large-scale integration and increasing penetration rate of distributed energy sources, the stochastic, intermittent, and fluctuating nature of their outputs constrains the absorptive capacity of the distribution network. Energy storage systems, leveraging their flexible energy management capabilities and rapid power regulation capabilities, can address issues such as wind and solar power curtailment, voltage violations, and insufficient peak shaving capacity in the distribution network. Properly configuring

energy storage systems is of paramount importance for the efficient operation of the distribution network (Wang et al., 2014; Wang et al., 2021).

In recent years, scholars both domestically and internationally have conducted research on grid energy storage optimization strategies to facilitate the integration of renewable energy. In the realm of fixed energy storage systems, Fixed Energy Storage Systems (FESS), literature (Shi et al., 2021) establishes a joint configuration model for solar and storage with the objective of optimizing photovoltaic integration and system economy. Literature (Zhou et al., 2016), considering the impact of solar and storage as well as demand response, develops a microgrid investment profit model with the goals of optimizing photovoltaic utilization and operational economy. Literature (Pasetti et al., 2021) indicates that as the capacity and quantity of energy storage systems increase, they become susceptible to network attacks. Application of Man-in-the-Middle (MitM) attacks on BESS can decrease the lifespan of storage, lead to economic losses, and affect the security and stability of the power grid. Collaboration with Distribution System Operators (DSOs) through increased cross-checks is proposed as a preventive measure. Literature (Morstyn et al., 2018) reviews the progress of microgrid energy storage coordination control strategies and proposes a distributed intelligent microgrid control framework based on intelligent agent networks. The framework aims to provide a universally applicable control strategy for the development of intelligent decentralized power grids, offering insights into the future development of distribution networks. Literature (Lu et al., 2023) presents a dual-layer optimization model for the rapid recovery of EMS distribution systems. The upper layer minimizes system load shedding rate from a scheduling perspective, while the lower layer addresses post-disaster economic dispatch issues through Karush-Kuhn-Tucker (KKT) simplification into a single-layer mixed-integer linear programming problem. Focusing on flexible switchgear in AC/DC distribution networks, literature (Ma et al., 2023) considers equipment constraints, peak shaving, and voltage deviation constraints to build a real and reactive power dispatch model with the minimum operating cost as the primary objective. Through the construction of a two-stage stochastic-distributionally robust optimization model, solar output variability is simulated. Literature (Wei et al., 2023) proposes a flexible interconnection distribution network optimization and control strategy considering transformer and SOP loss characteristics. A dual-layer model is established with the upper layer aiming for the lowest annual comprehensive cost and the lower layer seeking the lowest comprehensive loss. Considering intelligent topology changes, literature (Pan et al., 2023) introduces a consistency algorithm and establishes a SOP cluster control model for distribution networks. Through an SOP cluster strategy based on the consistency algorithm, global SOP collaborative optimization is achieved, enhancing the balance of distribution network feeders. Literature (Liu et al., 2023) presents a dual-layer planning method for distributed power sources and generalized energy storage. The upper layer addresses location and capacity decisions considering system planning costs and response incentives, while the lower layer uses an adaptive parameter particle swarm optimization algorithm to solve the optimization problem based on the continuity and reliability of the distribution network. Literature (Yang et al., 2022) introduces a multi-objective dual-layer structure for energy storage systems. The inner layer aims to maximize operational revenue using the peafowl optimization algorithm, while the outer layer targets minimum operation and maintenance costs, minimum voltage fluctuation, and minimum load fluctuation using the multi-objective peafowl optimization algorithm. Literature (Mao et al., 2019) introduces a dual-layer optimization for generalized energy storage configuration, with the upper layer utilizing a genetic algorithm for energy storage configuration and the lower layer obtaining optimal energy storage operation using dynamic programming. In the aforementioned studies, joint planning of energy storage primarily focuses on the reliability and economic viability on the grid side, yet there is a lack of research on the impact of the uncertainty of distributed energy source outputs on energy storage planning and the optimization of distribution network operation.

Mobile Energy Storage Systems (MESS) are primarily composed of energy storage devices and mobile equipment. Compared to fixed energy storage, MESS can flexibly select access points and capacities based on load characteristics, reducing daily maintenance costs, peak shaving, and enhancing the flexibility of the distribution network. Literature (Astero et al., 2017) indirectly controls photovoltaic integration through electricity prices for electric vehicles. Literature (Kwon et al., 2020) establishes two-stage mobile energy storage optimization models. Literature (Abdeltawab and Mohamed, 2017) considers the fuel costs of mobile energy storage vehicles and the full lifecycle of energy storage. Literature (Yao et al., 2020) utilizes mobile energy storage as a backup power source for natural disasters or emergency situations. In summary, MESS possesses both mobility and energy storage functions, allowing flexible selection of access points and capacities based on grid operating conditions. This capability can effectively avoid redundant waste, reduce daily maintenance costs, and significantly improve the economic viability of peak shaving. However, its drawback lies in its smaller capacity. MESS can complement fixed energy storage, jointly participating in grid regulation. Through real-time monitoring of power system operations, rational control of both BESS and MESS is crucial for improving load characteristics (Chen et al., 2016).

This paper integrates FESS and MESS collaborative optimization methods, proposing energy storage configuration and operation strategies to enhance photovoltaic absorption capacity in extreme scenarios. Both upper and lower layers adopt an improved Particle Swarm Optimization-Gravitational Search Algorithm (PSO-GSA) method, combining the individual optimization capability of the particle swarm algorithm with the local search capability of the gravitational search algorithm to enhance global search capability. In the upper layer, decision variables include fixed energy storage site selection, capacity, and mobile energy storage access nodes and capacity, comprehensively considering the economic operation of FESS and MESS. The lower layer dynamically optimizes energy storage charging and discharging strategies with the objective of minimizing grid voltage deviation. In extreme photovoltaic scenarios, the goal is to enhance on-site photovoltaic absorption capacity and improve grid operation conditions.

2 Distribution network component model

2.1 Photovoltaic penetration rate definition

Photovoltaic penetration rate is defined as the ratio of the maximum photovoltaic output power to the maximum load output power:

$$D_{PV} = \frac{F_{MAX}}{F_{L,MAX}} \times 100\% \tag{1}$$

In the formula 1: D_{PV} represents the photovoltaic penetration rate; F_{MAX} represents the maximum photovoltaic output power; $F_{L,MAX}$ represents the maximum load output power.

People have different criteria for judging the level of photovoltaic penetration. Generally, when it is below 20%, it is considered a low-penetration stage, where the scale of photovoltaic integration into the grid is small, and its impact on the power grid is minimal. As the penetration of photovoltaics increases, when the photovoltaic penetration rate reaches 20%–80%, it becomes necessary to address the issue of enhancing the carrying capacity of photovoltaics in concentrated areas. At this stage, the significant integration of photovoltaics may lead to power reverse flow in the power system. When the photovoltaic penetration rate exceeds 100%, it can be considered a high-penetration stage. At this point, there is a substantial reverse flow of photovoltaic power into the power system, and the role of photovoltaic energy shifts to the supply side. The difficulty of on-site absorption of photovoltaics increases, requiring interventions such as energy storage to enhance the capacity for photovoltaic integration.

2.2 Photovoltaic on-site absorption rate definition

The on-site absorption of photovoltaic power is primarily influenced by the load and energy storage. In this paper, we define the on-site absorption rate of photovoltaic power as:

$$\varphi = \sum_{t=6}^{19}\left(\frac{P_{PV,fact,t} - P_{LOAD,t} - P_{ESS,t}}{P_{PV,fact,t}}\right) \times 100\% \tag{2}$$

In the formula 2: Where φ represents the on-site absorption rate of photovoltaic power; $P_{PV,fact,t}$ represents the actual generation of photovoltaics at time t. $P_{LOAD,T}$ represents the distribution network load during the photovoltaic generation period at time t, and $P_{ESS,t}$ represents the load for energy storage charging during the photovoltaic generation period at time t.

2.3 Distributed power generation model

2.3.1 Photovoltaic output model

The photovoltaic generation intensity is controlled by the regional solar irradiance. Solar irradiance is commonly considered to follow a Beta distribution, where the Beta probability density function is given by:

$$\mathbf{f}(r) = \frac{\Gamma(\alpha+\beta)}{\Gamma(\alpha)\Gamma(\beta)}\left(\frac{r}{r_{\max}}\right)^{\alpha-1}\left(1-\frac{r}{r_{\max}}\right)^{\beta-1} \tag{3}$$

In the formula 3: Where α and β are the shape parameters of the Beta distribution; r is the actual solar irradiance during a specific time period, and $r_{\max}$ is the maximum solar irradiance during that time period. Research indicates that the output power of photovoltaic generation is influenced by solar irradiance, photovoltaic panel area, and photovoltaic conversion efficiency. Therefore, the relationship between the output power of photovoltaic generation and solar irradiance is given by:

$$P_s = rMA\eta \tag{4}$$

$$\mathbf{f}(r) = \frac{\Gamma(\alpha+\beta)}{\Gamma(\alpha)\Gamma(\beta)}\left(\frac{P_S}{r_{\max}A\eta}\right)^{\alpha-1}\left(1-\frac{P_S}{r_{\max}A\eta}\right)^{\beta-1} \tag{5}$$

In the formulas 4, 5: Where P_s represents the photovoltaic output power; A is the photovoltaic panel area; η is the photovoltaic conversion efficiency.

2.3.2 Fixed energy storage model

The charging and discharging model for fixed energy storage is as follows:

$$\begin{cases} P_{ES,j}(t) \le 0, ES_j(t) = ES_j(t-1)(1-\delta) + P_{ES,j}(t)\eta_c\Delta t \\ P_{ES,j}(t) > 0, ES_j(t) = ES_j(t-1)(1-\delta) - \dfrac{P_{ES,j}(t)\Delta t}{\eta_d} \\ \sum_{t=1}^{T}\left[P_{ES,j}(t)a_1\eta_c + P_{ES,j}(t)\dfrac{a_2}{\eta_d}\right]\Delta t = 0 \end{cases} \tag{6}$$

In the formula 6: Where $P_{ES,j}(t) \le 0$ represents energy storage charging, η_c represents the charging efficiency of energy storage, and in this case $a_1 = 1, a_2 = 0$; $P_{ES,j}(t) > 0$ represents energy storage discharging, η_d represents the discharging efficiency of energy storage, and in this case $a_1 = 0, a_2 = 1$.

2.3.3 Mobile energy storage model

The charging and discharging model for mobile energy storage is as follows:

$$-P_N \le P_{i,t}^{MES} \le P_N \tag{7}$$

$$E_{t+1}^{MES} = E_t^{MES} - P_{i,t}^{MES}\Delta t \tag{8}$$

$$E_{\min}^{MES} \le E_t^{MES} \le E_{\max}^{MES} \tag{9}$$

$$E_0^{MES} = E_T^{MES} \tag{10}$$

In the formulas 7–10: Where P_N represents the rated power of mobile energy storage; $P_{i,t}^{MES}$ represents the injected power at node i by mobile energy storage at time t; E_t^{MES} represents the state of charge of mobile energy storage at time t; $E_{\min}^{MES}$ and $E_{\max}^{MES}$ are the maximum and minimum values of the state of charge of mobile energy storage, respectively; E_0^{MES} and E_T^{MES} are the state of charge of mobile energy storage at the beginning and end of the operating cycle, respectively.

2.4 Electric vehicle charging model

Monte Carlo sampling is used to analyze the electric vehicle charging model.

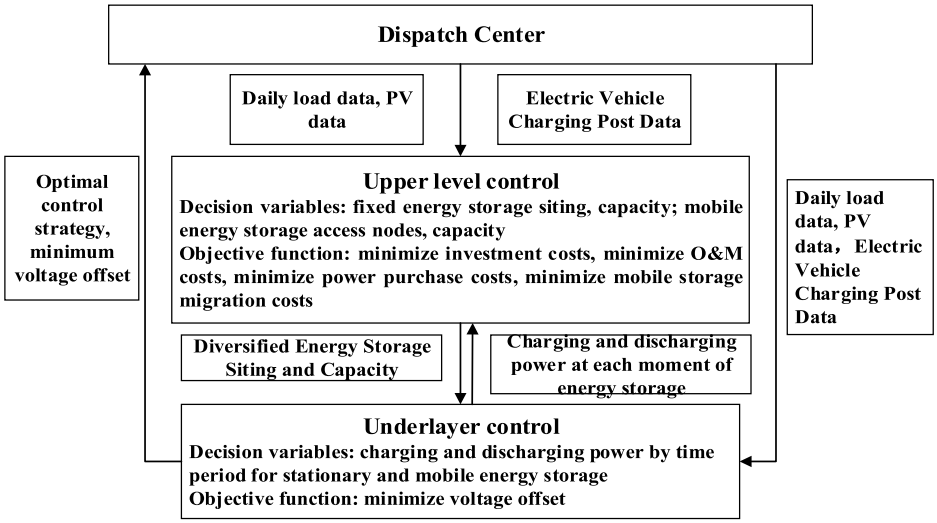

FIGURE 1
Dual layer optimization model.

(1)Probability Distribution of Daily Driving Distance

Processing behavioral data on electric vehicle usage, it is determined that the daily driving distance follows a log-normal distribution, i.e.,:

$$f_s(x) = \frac{1}{x}\frac{1}{\sqrt{2\pi}}\exp\left(-\frac{(\ln x - \mu_s)^2}{2\sigma_s^2}\right) \tag{11}$$

In the formula 11: Where μ_s taking the mean as 3.2 and σ_s the variance as 0.88.

(2)Probability Distribution of Initial Charging Time

The charging time of electric vehicles $f_t(x)$ follows a normal distribution, i.e.,:

$$f_t(x) = \begin{cases} \frac{1}{\sigma_s}\frac{1}{\sqrt{2\pi}}\exp\left(-\frac{(x-\mu_s)^2}{2\sigma_s^2}\right), & (\mu_s - 12 < x < 24) \\ \frac{1}{\sigma_s}\frac{1}{\sqrt{2\pi}}\exp\left(-\frac{(x+24-\mu_s)^2}{2\sigma_s^2}\right), & (0 < x < \mu_s - 12) \end{cases} \tag{12}$$

In the formula 12: Where μ_s taking the mean as 17.6 and σ_s the variance as 3.4.

3 Construction of dual-layer optimization model in electrical engineering terminology

The dual-layer optimization model as shown in Figure 1.

The upper-layer optimization model has decision variables for fixed energy storage location, capacity, and mobile energy storage access nodes and capacity. The optimization objectives include minimizing investment costs, operating costs, power purchase costs, and mobile energy storage migration costs. The constraints involve energy storage output constraints and grid power purchase constraints.

The lower-layer optimization model has decision variables for the charging and discharging power of fixed and mobile energy storage during different time periods. The optimization objective is to minimize voltage offset. Constraints include voltage amplitude constraints, distributed renewable energy output constraints, and power balance constraints.

The dispatch center inputs photovoltaic data, daily load data, and electric vehicle charging station data. The upper layer solves the model to minimize operating costs, and the location and capacity of energy storage are passed as parameters to the lower layer. The lower layer controls the charging and discharging power of energy storage at each moment to minimize voltage offset. Iterations are performed until the optimal control strategy is obtained.

3.1 Upper-layer objective function

The upper layer involves multi-energy storage optimization configuration, with the objective function being the minimization of equipment investment costs, equipment operating costs, and grid power purchase costs.

$$f_{up} = w_1 \times f_1 + w_2 \times f_2 + w_3 \times f_3 + w_4 \times f_4 \tag{13}$$

In the formula 13: Where f_1 represents equipment investment costs; f_2 represents equipment operating costs; f_3 is the grid power purchase cost; f_4 represents the cost of mobile energy storage migration; w_1、w_2、w_3、w_4 is a random number between 0 and 1, and $w_1 + w_2 + w_3 + w_4 = 1$.

(1) Minimize equipment investment costs

The equipment investment cost includes one-time investment costs for both energy storage devices and photovoltaic equipment.

$$\begin{cases} f_1 = Q\sum_{z=1}^{Z} N_z C_z \\ Q = \dfrac{q(1+q)^y}{(1+q)^y - 1} \end{cases} \tag{14}$$

In the formula 14: Q represents the capital recovery factor; q represents the annual interest rate; Z represents equipment type; C_z represents the investment cost of equipment type Z; N_z represents the number of equipment type Z.

(2) Minimize equipment operating costs

The operating cost of equipment refers to the costs associated with regular maintenance and repair of equipment damage.

$$f_2 = \sum_{t=1}^{T}\sum_{z=1}^{Z} C_z^{loss} t + A \tag{15}$$

In the formula 15: C_z^{loss} represents the daily operational maintenance cost of equipment z; A represents the cost of repairing equipment damage, where t is the operating time.

(3) Minimize grid power purchase costs

$$f_3 = \sum_{t=1}^{24} P_t^{line} w_t^{line} \tag{16}$$

In the formula 16: P_t^{line} represents the power purchased from the grid at time t, and w_t^{line} represents the electricity price at time t.

(4) Minimize the cost of relocating mobile energy storage

$$f_4 = \sum_{t=1}^{24} C_{FUEL} O_{DISTANCE} \tag{17}$$

In the formula 17: Where f_4 represents the cost of relocating mobile energy storage; C_{FUEL} represents the unit distance cost, and $O_{DISTANCE}$ represents the distance traveled by the energy storage vehicle.

3.2 Upper-layer objective constraints

(1) Energy Storage Output Constraint.

$$\begin{cases} P_{ES,j}^{\min} \le P_{ES,j}(t) \le P_{ES,j}^{\max} \\ 0.2 \le SOC_j(t) \le 0.9 \\ SOC_j(0) = 0.5 \end{cases} \tag{18}$$

In the formula 18: Where $P_{ES,j}^{\min}$ represents the lower limit of the charging or discharging power for the jth energy storage unit, $P_{ES,j}(t)$ represents the charging or discharging power of the jth energy storage unit at time t, $P_{ES,j}^{\max}$ represents the upper limit of the charging or discharging power for the jth energy storage unit, and $SOC_j(t)$ represents the state of charge of the energy storage at time t, with a range from 0.2 to 0.9. When t is zero, the initial state of charge $SOC_j(0)$ is set to 0.5.

(2) Electricity Purchasing Power Constraint

$$P_{t,buy} \ge 0 \tag{19}$$

In the formula 19: Where $P_{t,buy}$ represents the electricity purchasing power.

3.3 Lower-level objective function

The lower level involves 24-h economic dispatch of the distribution network, with the minimization of voltage deviation as the objective function.

In power systems, voltage difference reflects the operational safety of the distribution network, as excessive voltage deviation can impact the operation of electrical equipment and the quality of electrical energy.

$$f_{low} = \sum_{t=1}^{24}\left(\sum_{i=1}^{N}\left(\frac{\Delta U_{i,t}}{U_{i,\max} - U_{i,\min}}\right)^2\right) \tag{20}$$

$$\Delta U_{i,t} = \begin{cases} U_{i,\min} - U_{i,t}, U_{i,t} < U_{i,\min} \\ 0, U_{i,\min} \le U_{i,t} \le U_{i,\max} \\ U_{i,t} - U_{i,\max}, U_{i,t} \ge U_{i,\max} \end{cases} \tag{21}$$

In the formulas 20, 21: Where $\Delta U_{i,t}$ represents the voltage deviation at time t, $U_{i,t}$ represents the voltage at node i at time t, and $U_{i,\min}$, $U_{i,\max}$ represent the upper and lower limits of node i, respectively. In medium and low voltage distribution networks, the permissible range for voltage deviation is −5% to +5%.

3.4 Lower-level objective constraints

(1) Voltage magnitude constraints

$$U_{i,\min} \le U_{i,t} \le U_{i,\max} \tag{22}$$

In the formula 22: Where $U_{i,\min}$ represents the voltage lower limit at node i, U_i represents the voltage at node i, and $U_{i,\max}$ represents the voltage upper limit at node i.

(2) Distributed New Energy Output Constraint

$$P_{pv,\min} \le P_{pv}^t \le P_{pv,\max} \tag{23}$$

In the formula 23: Where $P_{pv,\min}$ represents the minimum output of photovoltaic power, P_{pv}^t represents the photovoltaic power output at time t, and $P_{pv,\max}$ represents the maximum output of photovoltaic or wind power.

(3) Power Balance Constraint

$$\begin{cases} P_{s,i} - P_{L,i} = U_i\sum_{j=1}^{n} U_j\left(G_{ij}\cos\theta_{ij} + B_{ij}\sin\theta_{ij}\right) \\ Q_{s,i} - Q_{L,i} = U_i\sum_{j=1}^{n} U_j\left(G_{ij}\sin\theta_{ij} - B_{ij}\cos\theta_{ij}\right) \end{cases} \tag{24}$$

In the equation 24: $P_{s,i}$ represents the active power output at node i due to the power source; $P_{L,i}$ represents the active power output of the load at node i; U_i represents the voltage at node i; U_j represents the voltage at node j; $Q_{s,i}$ represents the reactive power output at node i due to the power source; $Q_{L,i}$ represents the reactive power output of the load at node i.

4 Optimization solving algorithm based on PSO-GSA

The ultimate goal of heuristic algorithms is global optimization. To achieve this goal, the exploratory and exploitative capabilities of heuristic algorithms are particularly crucial.

4.1 Particle swarm algorithm

The particle swarm algorithm (Anantathanavit and Munlin, 2013) models each particle considering the current velocity, current position, and a distance-modifying function to pbest and gbest as follows.

$$v_i^{t+1} = wv_i^t + c_1 \times rand \times \left(pbest_i^t - x_i^t\right) + c_2 \times rand \times \left(gbest - x_i^t\right) \tag{25}$$

In the equation 25: w represents the weighted function; v_i^t represents the velocity of the i th particle at generation t; c_1 represents the weighting factor; $rand$ is a random number between 0 and 1; $pbest_i^t$ represents the best position of the particle at generation t; x_i^t represents the position of the particle at generation t; c_2 represents the weighting factor; $gbest$ represents the best solution. wv_i^t represents the exploration ability of the particle; $c_1 \times rand \times (pbest_i^t - x_i^t)$ represents the personal ability of the particle; $c_2 \times rand \times (gbest - x_i^t)$ represents the cooperative ability of the particle

$$x_i^{t+1} = x_i^t + v_i^{t+1} \tag{26}$$

In the formula 26: Where x_i^{t+1} represents the position of particle i at generation t+1.

4.2 Gravity search algorithm

GSA (Doraghinejad et al., 2012) originates from Newton's fundamental theory: the interaction force among particles in the Universe, a force proportional to the particle mass and inversely proportional to the distance between them, is modeled as follows.

$$F_{ij}^d(t) = G(t)\frac{M_{pi}(t) \times M_{aj}(t)}{R_{ij}(t) + \xi}\left(x_j^d(t) - x_i^d(t)\right) \tag{27}$$

In the formula 27: Where $F_{ij}^d(t)$ represents the gravitational force of particle i on particle j in the d-dimensional space at the tth iteration; $G(t)$ represents the value of universal gravitational force at the tth iteration; $M_{pi}(t)$ is the active gravitational mass; $M_{aj}(t)$ is the passive gravitational mass; $R_{ij}(t)$ represents the Euclidean distance between i and j; ξ is a constant; $x_j^d(t)$ represents the position of particle j in the d-dimensional space at the tth generation; $x_i^d(t)$ represents the position of particle i in the d-dimensional space at the tth generation.

$$G(t) = G_0 \times e^{\frac{-\partial \times iter}{\max iter}} \tag{28}$$

In the formula 28: Where ∂ represents the descent coefficient; G_0 represents the initial value; $iter$ is the current iteration number; max $iter$ is the maximum iteration number.

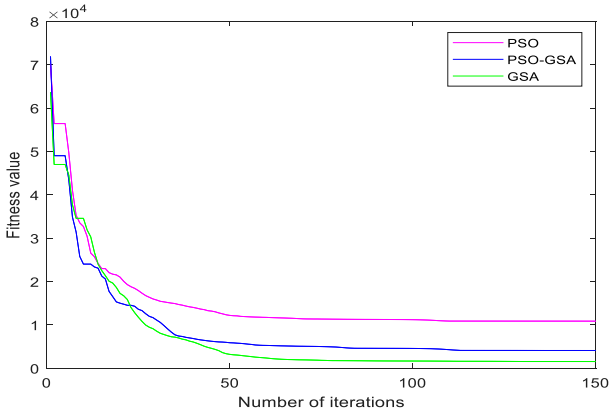

FIGURE 2
Comparison of convergence speed of different functions.

$$F_i^d(t) = \sum_{j \neq i, j \in kbest}^{N} rand_j F_{ij}^d(t) \tag{29}$$

In the formula 29: Where $F_i^d(t)$ represents the total force experienced by individual i in the d-dimensional space at the tth iteration.

$$a_i^d(t) = \frac{F_i^d(t)}{M_i(t)} \tag{30}$$

In the formula 30: Where represents $a_i^d(t)$ the equation for the acceleration of individual i in the d-dimensional space; $M_i(t)$ represents the mass of individual i at generation t.

$$v_i^d(t+1) = rand \times v_i^d(t) + a_i^d(t) \tag{31}$$

In the formula 31: Where $v_i^d(t+1)$ represents the velocity of particle i in the d-dimensional space at generation t+1.

$$x_i^d(t+1) = x_i^d(t) + v_i^d(t+1) \tag{32}$$

In the formula 32: Where $x_i^d(t+1)$ represents the position of particle i in the d-dimensional space at generation t+1.

4.3 PSO-GSA hybrid algorithm

The PSO-GSA hybrid algorithm combines the individual optimization capability of PSO with the local search ability of GSA such as the formulas 33, 34. The improved convergence of PSO-GSA surpasses that of standalone PSO and GSA.

$$v_i^{t+1} = wv_i^t + c_1 \times rand \times a_i^t + c_2 \times rand \times \left(gbest - x_i^t\right) \tag{33}$$

$$x_i^{t+1} = x_i^t + v_i^{t+1} \tag{34}$$

Initially, each particle is considered to have a candidate solution. After initialization, the gravitational force, gravitational constant, and resultant force between particles are calculated. During the iteration process, the algorithm updates to the current best solution, computes the velocity of

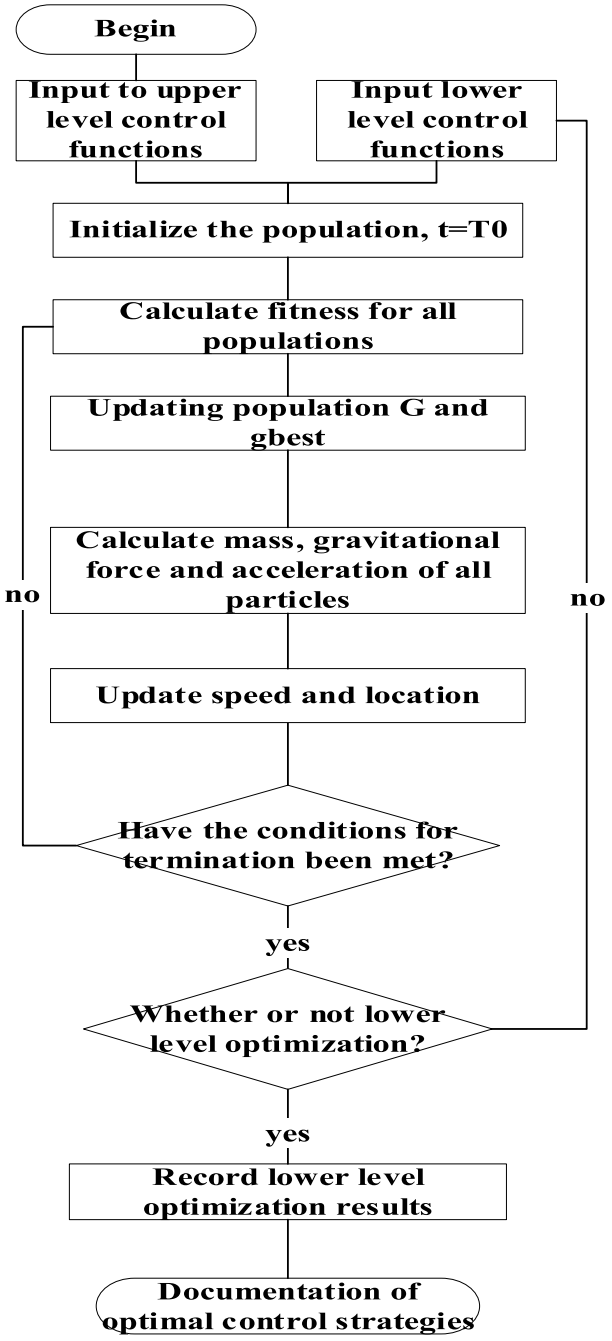

FIGURE 3
Algorithm flowchart.

particles for the (n+1)-th generation, and finally updates the positions of the particles.

The improved convergence of PSO-GSA is superior to that of PSO and GSA, as shown in Figure 2.

4.4 The Flowchart of the PSO-GSA Algorithm.

The flow chart of the PSO-GSA algorithm is shown in Figure 3.

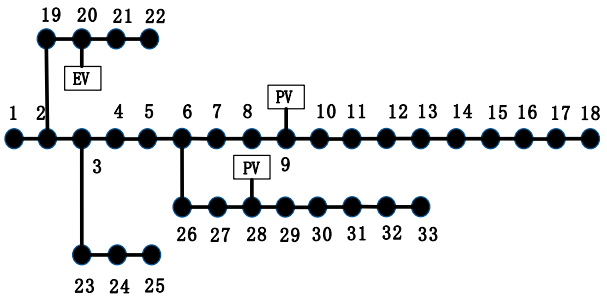

FIGURE 4
IEEE 33 node distribution network.

5 Case analysis

5.1 Case parameters

Simulations were conducted on the IEEE 33-node distribution network using Matlab 2021a software. The system's base voltage is 12.66 kV, and the maximum load is 3.715 MW. To provide reserve capacity for photovoltaic integration at system nodes, the upper limit of node voltage is set to 1.05, and the lower limit is set to 0.95. Photovoltaic panels are integrated at nodes 9 and 28, while an electric vehicle charging station is added at node 20, as illustrated in Figure 4.

Monte Carlo simulations were employed to model the starting density and charging power of electric vehicles, with a total of 2000 vehicles. The simulation results are presented in Appendix Figure A1 and Figure A2.

This study focuses primarily on the impact of the fixed and mobile energy storage access points and capacities on the integration of photovoltaics. The basic information for both fixed and mobile energy storage is as follows: the energy storage maintenance coefficient is 0.02; the unit capacity investment cost is 1000 CNY/KW; the discount rate is 0.08; the service life is 20 years. For mobile energy storage, the cost per kilometer varies based on the distance traveled each time, and here it is calculated at a monthly cost of 3,000 Yuan. The energy storage electricity prices are 0.31 CNY/kWh from 0:00 to 8:00, 0.84 CNY/kWh from 9:00 to 11:00, 0.31 CNY/kWh from 12:00 to 13:00, 0.84 CNY/kWh from 14:00 to 21:00, and 0.31 CNY/kWh from 22:00 to 24:00.

To achieve coordinated optimization of fixed and mobile energy storage for enhancing the distribution network's consumption capacity, a PSO-GSA hybrid algorithm is applied to both the upper-layer multi-energy storage optimization configuration and the lower-layer energy storage optimization scheduling. The fixed energy storage locations range from node 2 to 33, with capacities from 0.5 MW to 1 MW. The access nodes for mobile energy storage range from node 2 to 33 (assuming node 1 is the reference node), with capacities from 0.4 MW to 0.9 MW. Fixed energy storage charges during off-peak hours or when photovoltaic energy cannot be accommodated and discharges during peak electricity demand. In contrast, mobile energy storage offers more flexible charge and discharge regulation, responding dynamically to real-time situations in case of emergencies or when fixed energy storage cannot effectively regulate. The PSO-GSA hybrid algorithm is applied to both upper and lower layers with 50 particles each, 50 iterations, an individual learning factor of 0.5, and a global learning factor of 1.5.

TABLE 1 Energy storage parameters.

Scenes	Fixed energy storage, mobile energy storage access location	Fixed energy storage, mobile energy storage access capacity/MW	Total cost of energy storage operation/ten thousand yuan	Voltage offset	Photovoltaic local consumption rate (%)
Scene 1	-	-	0	0.0082	64.39
	-	-			
Scene 2	27	0.9849	317.07	0.0072	67.40
	-	-			
Scene 3	29	0.7339	421.94	0.0064	70.16
	22	0.6096			
Scene 4	27	0.7070	419.76	0.0033	71.39
	31	0.6265			

5.2 Optimization result analysis

Firstly, without the addition of any energy storage, gradually increasing photovoltaics until the voltage exceeds the limit at nodes 9 or 28, marks the maximum photovoltaic capacity that the distribution network can bear. The maximum capacity is determined to be 2.9 MW.

Considering the future large-scale integration of photovoltaics and the transition of photovoltaic energy from the demand side to the supply side, there may be reverse power flows. In such scenarios, energy storage can be flexibly adjusted to enhance photovoltaic energy integration, reduce the risk of voltage exceeding limits, and improve the stability of the power system. When there is a sudden increase in photovoltaics and fixed energy storage devices cannot regulate effectively, flexible adjustments can be made using mobile energy storage. The following case considers an extreme photovoltaic output scenario of 2.9 MW and a charging station output of 0.6 MW.

To validate the effectiveness of the proposed model and method, a comparison is made across four different scenarios. Scenario One: integration of photovoltaics without energy storage; Scenario Two: integration of photovoltaics with optimized configuration of fixed energy storage; Scenario Three: integration of photovoltaics with coordinated optimization of fixed and mobile energy storage; Scenario Four: integration of photovoltaics, electric vehicle charging station, and coordinated optimization of fixed and mobile energy storage. The analysis includes voltage offset, multi-energy storage operating costs, and on-site photovoltaic integration rate, as shown in Table 4-1.

According to Table 1, compared to Scenario One, Scenario Two, which adds fixed energy storage, reduces the voltage offset by 0.0010 and increases the on-site photovoltaic integration rate by 3.01%. Scenario Three, with the addition of both fixed and mobile energy storage, reduces the voltage offset by 0.0018 and increases the on-site photovoltaic integration rate by 5.77% compared to Scenario One. In Scenario Four, with the addition of an electric vehicle charging station load, the voltage offset is 0.0033, the on-site photovoltaic integration rate is 71.39%. Compared to Scenario One, the voltage offset increases by 0.1638, and the curtailment rate decreases by 0.8081%. These results indicate that fixed energy storage adjustment has limitations, and through coordinated optimization of fixed and mobile energy storage, the on-site photovoltaic integration can be increased, and voltage offset can be reduced.

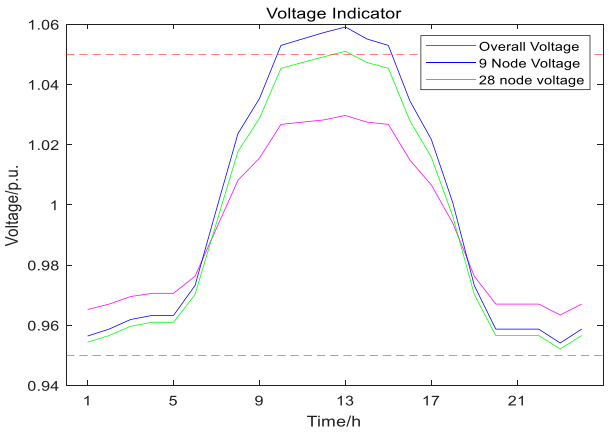

FIGURE 5
Scene 1 target node voltage.

To further illustrate the improvement in power grid stability through the coordinated optimization of fixed and mobile energy storage, a comparative analysis is conducted among Scenario One, Scenario Two, and Scenario Three.

As shown in Figure 5, Figure 6, and Figure 7, in extreme photovoltaic Scenario One, voltage exceeds the limit at nodes 9 and 28 when photovoltaics are added. From the node voltage diagram in Scenario Two, it is evident that by adding fixed energy storage, only node 9 experiences a voltage limit exceedance, and the degree of voltage offset is smaller compared to Scenario One. The node voltage diagram in Scenario Three indicates that through the coordinated action of fixed and mobile energy storage, all nodes are within the range of 0.95 p. u. to 1.05 p. u., demonstrating the efficient synergy between fixed and mobile energy storage. This synergy can significantly enhance the capacity for photovoltaic integration.

As shown in Figure 8, for the charge and discharge strategy of fixed energy storage, during 3:00–7:00 when the grid load is relatively low, the energy storage system remains in the charging state. During 10:00–14:00 when the load is high and there is sufficient photovoltaic output, fixed energy storage discharges at a lower power. From 19:00 to 22:00, when the load is high, fixed energy storage discharges, and

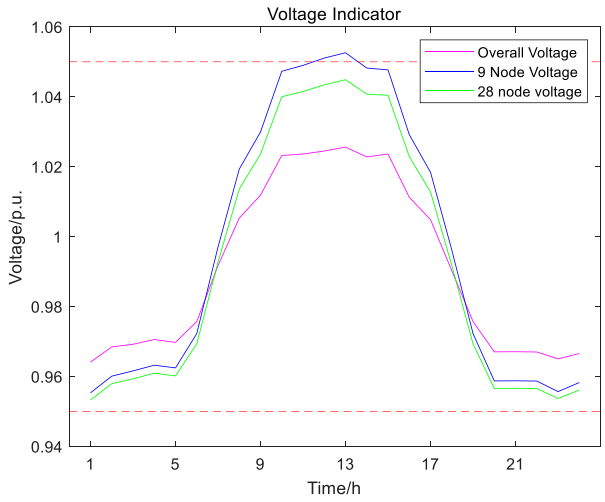

FIGURE 6
Scene 2 target node voltage.

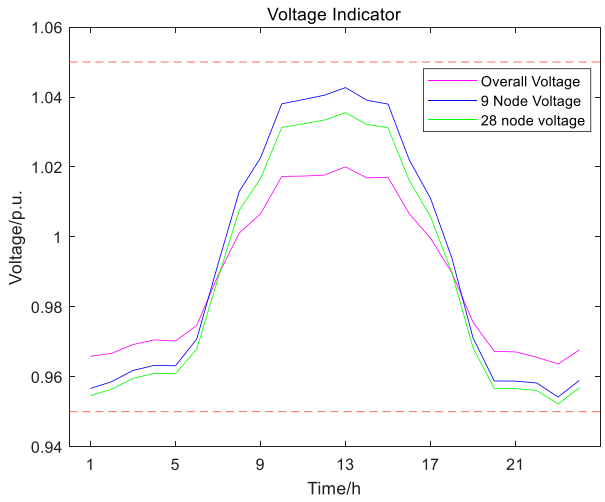

FIGURE 7
Scene 3 target node voltage.

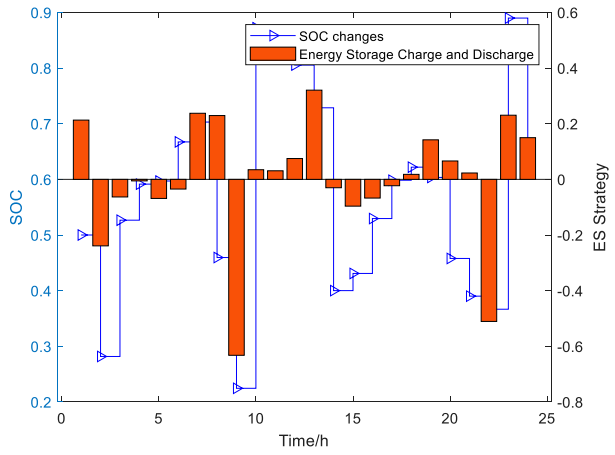

FIGURE 8
Charging and discharging strategy for stationary energy storage in Scenario 3.

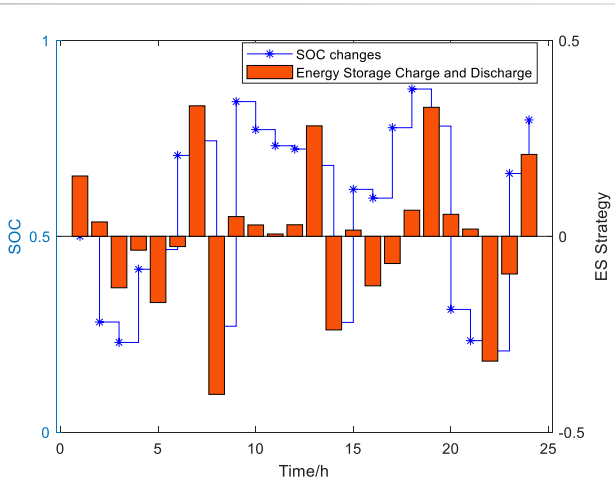

FIGURE 9
Mobile energy storage charging and discharging strategy in scenario 3.

when fixed energy storage cannot meet the load requirements, coordinated operation with mobile energy storage is employed to jointly provide power support to the grid.

As illustrated in Figure 9, due to the uncertainty of photovoltaic output, there are two charging methods for the charge and discharge strategy of mobile energy storage: one is during 3:00–7:00 when the electricity price is lower, mobile energy storage utilizes grid electricity for charging; the other is during 14:00–16:00 when the load is low and photovoltaics cannot fully integrate, mobile energy storage is charged at the access node. During peak electricity demand periods at 10:00–14:00 and 19:00–22:00, if fixed energy storage cannot effectively regulate the grid voltage, coordinated discharge of mobile and fixed energy storage is implemented to maintain the stable operation of the power system.

6 Conclusion

Energy storage, due to its flexible output and dynamic adjustment characteristics, can provide rich elastic support for the grid, facilitating the efficient integration of large-scale distributed new energy sources and ensuring the stable operation of the grid. This paper proposes a multi-energy storage coordinated optimization strategy that takes into account voltage offset. Initially, a two-layer model is established around the optimal operation cost of Mobile Energy Storage System and Fixed Energy Storage System, as well as minimizing the grid voltage offset. The model is solved and validated using the PSO-GSA algorithm in the IEEE 33-node distribution system, leading to the following conclusions.

(1) In extreme photovoltaic scenarios, based on predicted load data, using the objectives of minimizing operating costs and

minimizing voltage offset, BESS and FESS are optimized in terms of configuration and dispatch. Suitable parameters for energy storage are selected, and mobile energy storage is dispatched to different nodes to provide charging and discharging services. By comparing fixed energy storage with the coordinated operation of fixed and mobile energy storage, and optimizing the configuration and operational strategies of energy storage, the results show that coordinated operation of fixed and mobile energy storage can improve on-site photovoltaic integration while reducing grid voltage offset.

(2) Guiding energy storage systems to participate in the optimal operation of distribution networks through time-of-use electricity prices and time-of-use loads. The strategy involves charging during low demand and discharging during high demand, balancing the demands of both the grid side and the load side. This approach reduces curtailment, minimizes the impact of distributed energy source output instability on the grid, and equips the distribution network with sufficient flexibility to adapt to peak-valley differences, fluctuations, and the growing normality of daily loads.

(3) The mathematical model presented in this paper exhibits multi-dimensional non-linear characteristics. The PSO-GSA hybrid algorithm is employed for model solving, combining the individual optimization of particle swarm algorithm with the local search ability of gravitational search algorithm. This hybrid approach offers better convergence for solving multi-dimensional non-linear problems.

The optimization strategies mentioned in this paper do not consider the impact of different seasons on photovoltaic output, the influence of mobile energy storage routes, and traffic congestion. In future work, these factors, along with the consideration of the impact of different seasons on photovoltaic output, traffic congestion, and the use of smart switches, could be incorporated into the analysis.

Data availability statement

The raw data supporting the conclusion of this article will be made available by the authors, without undue reservation.

Author contributions

LF: Writing–original draft, Writing–review and editing, Conceptualization, Funding acquisition, Supervision. NJ: Writing–original draft, Writing–review and editing, Funding acquisition, Investigation. YZ: Writing–original draft, Writing–review and editing, Funding acquisition, Methodology. ZK: Writing–original draft, Writing–review and editing, Conceptualization, Software. ZQ: Conceptualization, Data curation, Formal Analysis, Funding acquisition, Methodology, Supervision, Validation, Writing–original draft, Writing–review and editing. WS: Writing–original draft, Writing–review and editing, Funding acquisition, Investigation, Methodology.

Funding

The author(s) declare financial support was received for the research, authorship, and/or publication of this article. This research was funded by NR Group Science and Technology Project 'Research on Functional Structure, System Architecture, Evaluation Index and Method of Distribution Network with High Proportion of New Energy' (524608210241).

Conflict of interest

Authors LF, NJ, and YZ were employed by Nari Group Corporation State.

The remaining authors declare that the research was conducted in the absence of any commercial or financial relationships that could be construed as a potential conflict of interest.

Publisher's note

References

Abdeltawab, H. H., and Mohamed, Y. A.-R. I. (2017). Mobile energy storage scheduling and operation in active distribution systems. *IEEE Trans. Ind. Electron.* 64, 6828–6840. doi:10.1109/TIE.2017.2682779

Anantathanavit, M., and Munlin, M.-A. (2013). "Radius particle swarm optimization," in 2013 International Computer Science and Engineering Conference (ICSEC), Nakorn Pathom, Thailand, September 4-6, 2013 (IEEE), 126–130. doi:10.1109/ICSEC.2013.6694765

Astero, P., Choi, B. J., and Liang, H. (2017). Multi-agent transactive energy management system considering high levels of renewable energy source and electric vehicles. *IET Generation, Transm. Distribution* 11, 3713–3721. doi:10.1049/IET-GTD.2016.1916

Chen, Y., Zheng, Y., Luo, F., Wen, J., and Xu, Z. (2016). Reliability evaluation of distribution systems with mobile energy storage systems. *IET Renew. Power Gener.* 10, 1562–1569. doi:10.1049/iet-rpg.2015.0608

Doraghinejad, M., Nezamabadi-pour, H., Hashempour Sadeghian, A., and Maghfoori, M. (2012). "A hybrid algorithm based on gravitational search algorithm for unimodal optimization," in 2012 2nd International eConference on Computer and Knowledge Engineering (ICCKE), Mashhad, 18-19 October 2012, 129–132. doi:10.1109/ICCKE.2012.6395365

Kwon, S.-Y., Park, J.-Y., and Kim, Y.-J. (2020). Optimal V2G and route scheduling of mobile energy storage devices using a linear transit model to reduce electricity and transportation energy losses. *IEEE Trans. Ind. Appl.* 56, 34–47. doi:10.1109/TIA.2019.2954072

Liu, Z., Yu, P., and Li, J. (2023). Planning of distributed generation and generalized energy storage in distribution network considering operation characteristics. *Dianli Zidonghua Shebei/Electric Power Autom. Equip.* 43, 72–79. doi:10.16081/j.epae.202208029

Lu, Q., Jiang, L., Bie, Z., Zheng, J., Yang, Y., Yu, Z., et al. (2023). Post-disaster fault restoration strategy for distribution network considering optimal scheduling of user-side energy. *Automation Electr. Power Syst.* 47, 44–54. doi:10.7500/AEPS20220226001

Ma, Z., Wei, Z., Chen, S., Zheng, Y., and Wu, T. (2023). Active-reactive power optimal dispatch of AC/DC distribution network based on soft open point. *Automation Electr. Power Syst.* 47, 48–58. doi:10.7500/AEPS20220702002

Mao, M., Liu, Y., Zhang, L., and Zhang, J. (2019). Optimal configuration of generalized energy storage in distribution network with high-penetration renewable energy. *Dianli Xit. Zidonghua/Automation Electr. Power Syst.* 43, 77–85. doi:10.7500/AEPS20180615002

Morstyn, T., Hredzak, B., and Agelidis, V. G. (2018). Control strategies for microgrids with distributed energy storage systems: an overview. *IEEE Trans. Smart Grid* 9, 3652–3666. doi:10.1109/TSG.2016.2637958

Pan, Y., Geng, G., and Jiang, Q. (2023). Consistency algorithm based control strategy for soft open point cluster. *Dianli Xit. Zidonghua/Automation Electr. Power Syst.* 47, 101–109. doi:10.7500/AEPS20211017004

Pasetti, M., Ferrari, P., Bellagente, P., Sisinni, E., de Sá, A. O., Prado, C. B. do, et al. (2021). Artificial neural network-based stealth attack on battery energy storage systems. *IEEE Trans. Smart Grid* 12, 5310–5321. doi:10.1109/TSG.2021.3102833

Shi, M., Xu, K., Wang, J., Yin, R., and Zhang, P. (2021). Short-term photovoltaic power forecast based on grey relational analysis and GeoMAN model. *Trans. China Electrotech. Soc.* 36, 2298–2305. doi:10.19595/j.cnki.1000-6753.tces.200538

Wang, C., Wu, Z., and Li, P. (2014). The prospects and challenges of distributed electricity storage technology. *Automation Electr. Power Syst.* 38, 1–73. doi:10.7500/AEPS20140108002

Wang, S., Liu, Q., Zhao, Q., and Wang, H. (2021). Connotation analysis and prospect of distribution network elasticity. *Automation Electr. Power Syst.* 45, 1–9. doi:10.7500/AEPS20200112006

Wei, C., Li, J., Tu, C., Wang, X., Guo, Q., and Xiao, F. (2023). Optimal regulation and control strategy for flexible interconnected distribution network considering loss characteristics of transformers and soft open points. *Dianli Xit. Zidonghua/Automation Electr. Power Syst.* 47, 69–78. doi:10.7500/AEPS20220915007

Yang, B., Wang, J., Yu, L., Cao, P., Shu, H., and Yu, T. (2022). Peafowl optimization algorithm based Bi-level multi-objective optimal allocation of energy storage systems in distribution network. *Shanghai Jiaot. Daxue Xuebao/Journal Shanghai Jiaot. Univ.* 56, 1294–1307. doi:10.16183/j.cnki.jsjtu.2021.371

Yao, S., Wang, P., Liu, X., Zhang, H., and Zhao, T. (2020). Rolling optimization of mobile energy storage fleets for resilient service restoration. *IEEE Trans. Smart Grid* 11, 1030–1043. doi:10.1109/TSG.2019.2930012

Zhou, N., Fan, W., Liu, N., Lin, X., Zhang, J., and Lei, J. (2016). Battery storage multi-objective optimization for capacity configuration of PV-based microgrid considering demand response. *Dianwang Jishu/Power Syst. Technol.* 40, 1709–1716. doi:10.13335/j.1000-3673.pst.2016.06.015

Nomenclature

Indices

N_I	Equipment type I
C_I	Investment cost of equipment type I
C_I^{loss}	Daily operational maintenance cost of equipment I
G_0	Initial value
P_t^{line}	Power purchased from the grid at time t
w_t^{line}	Electricity price at time t
C_{FUEL}	Unit distance cost

Parameters

D_{PV}	Photovoltaic penetration rate
F_{MAX}	Maximum photovoltaic output power
$F_{L,MAX}$	Maximum load output power
$P_{PV,fact,t}$	Actual generation of photovoltaics at time t
$P_{LOAD,T}$	Distribution network load during the photovoltaic generation period at time t
$P_{ESS,t}$	Load for energy storage charging during the photovoltaic generation period at time t
$P_{i,t}^{MES}$	Injected power at node i by mobile energy storage at time t
E_t^{MES}	State of charge of mobile energy storage at time t
E_{min}^{MES}, E_{max}^{MES}	Maximum and minimum values of the state of charge of mobile energy storage
E_0^{MES}, E_T^{MES}	State of charge of mobile energy storage
f_1	Equipment investment costs
f_2	Equipment operating costs
f_3	Grid power purchase cost
f_4	Cost of mobile energy storage migration
P_s	Photovoltaic output power
P_N	Rated power of mobile energy storage
$Q_{s,i}$	Reactive power output at node i due to the power source
$Q_{L,i}$	Reactive power output of the load at node i
C_{first}	Equipment investment cost
Q	Capital recovery factor

Variables

φ	On-site absorption rate of photovoltaic power
α, β	Shape parameters of the Beta distribution
r	Actual solar irradiance during a specific time period
r_{max}	Maximum solar irradiance during that time period
A	Photovoltaic panel area
η	Photovoltaic conversion efficiency
η_c	Charging efficiency of energy storage
η_d	Discharging efficiency of energy storage
w_1、w_2、w_3、w_4	Random number between 0 and 1
q	Annual interest rate
Z	Cost of repairing equipment damage
$O_{DISTANCE}$	Distance traveled by the energy storage vehicle
$P_{ES,j}^{min}$	Lower limit of the charging or discharging power for the *j*th energy storage unit
$P_{ES,j}(t)$	Charging or discharging power of the *j*th energy storage unit at time t
$P_{ES,j}^{max}$	Upper limit of the charging or discharging power for the *j*th energy storage unit
$SOC_j(t)$	State of charge of the energy storage at time t
$P_{t,buy}$	Electricity purchasing power
$\Delta U_{i,t}$	Voltage deviation at time t
$U_{i,t}$	Voltage at node i at time t
$U_{i,min}$, $U_{i,max}$	Upper and lower limits of node i
$P_{pv,min}$	Minimum output of photovoltaic power
P_{pv}^t	Photovoltaic power output at time t
$P_{pv,max}$	Maximum output of photovoltaic or wind power
$P_{s,i}$	Active power output at node i due to the power source
$P_{L,i}$	Active power output of the load at node i
U_i	Voltage at node *i*
U_j	Voltage at node *j*
v_i^t	Velocity of the ***i*** th particle at generation t
$pbest_i^t$	The best position of the particle at generation t
x_i^t	The position of the particle at generation t
$gbest$	The best solution
w	Weighted function
c_1	Weighting factor
c_2	Weighting factor
ξ	A constant
∂	Descent coefficient
wv_i^t	Exploration ability of the particle
x_i^{t+1}	Position of particle i at generation t+1
$F_{ij}^d(t)$	Gravitational force of particle i on particle j in the d-dimensional space at the *t*th iteration
$G(t)$	Value of universal gravitational force at the *t*th iteration
$M_{pi}(t)$	Active gravitational mass
$M_{aj}(t)$	Passive gravitational mass
$R_{ij}(t)$	Euclidean distance between i and j
$x_j^d(t)$	Position of particle j in the d-dimensional space at the *t*th generation
$x_i^d(t)$	Position of particle i in the d-dimensional space at the *t*th generation

$F_i^d(t)$	Total force experienced by individual i in the d-dimensional space at the *t*th iteration
$a_i^d(t)$	Equation for the acceleration of individual i in the d-dimensional space
$M_i(t)$	Mass of individual i at generation t
$v_i^d(t+1)$	Velocity of particle i in the d-dimensional space at generation t+1
$x_i^d(t+1)$	Position of particle i in the d-dimensional space at generation t+1

frontiers | Frontiers in Energy Research

TYPE Original Research
PUBLISHED 07 February 2024
DOI 10.3389/fenrg.2024.1349995

OPEN ACCESS

EDITED BY
Hao Wang,
Monash University, Australia

REVIEWED BY
Lv Chaoxian,
China University of Mining and Technology, China
Yang Lei,
Anhui University, China
Yongliang Liang,
Shandong University, China

*CORRESPONDENCE
Mengdi Wei,
wmd18054369586@tju.edu.cn

RECEIVED 05 December 2023
ACCEPTED 17 January 2024
PUBLISHED 07 February 2024

CITATION
Chen B, Liu R, Wei M, Wang X, Sun Y and Sun D (2024), PV output estimation method of power distribution station area based on federated learning framework and improved transformer neural network.
Front. Energy Res. 12:1349995.
doi: 10.3389/fenrg.2024.1349995

PV output estimation method of power distribution station area based on federated learning framework and improved transformer neural network

Bo Chen[1], Rui Liu[1], Mengdi Wei[2]*, Xian Wang[1], Yi Sun[1] and Donglei Sun[1]

[1]Economic and Technological Research Institute, State Grid Shandong Electric Power Company, Jinan, China, [2]School of Electrical Automation and Information Engineering of Tianjin University, Tianjin, China

In contemporary distribution networks (DNs), characterized by extensive integration of distributed energy, the photovoltaic (PV) power output data from the distribution station areas become crucial for system planning and operational optimization. Since many PVs are installed behind-the-meter (BTM), it is difficult to directly obtain PV power data through measurement devices. Therefore, it is important to estimate the BTM PV power from the aggregating data that can be directly obtained. However, the existing estimation methods usually require centralized large-scale data training, which brings certain privacy leakage risks. In order to solve these problems, we propose a federated learning-based improved Transformer Neural Network strategy to estimate BTM PV generation at the community level with data privacy protection. Initially, enhanced Transformer neural networks, employing a fused-attention mechanism, are deployed to precisely delineate the solar power generation pattern. Subsequently, federated learning principles facilitate the sharing of specific parameters among multiple edge endpoints and a central server. This model bifurcates into two layers: an individual layer, where parameters are retained locally, and an exchange layer, where parameters are collectively shared and conveyed through momentum aggregation. This dual-layer structure effectively synchronizes the capture of both unique and common characteristics. The test on the Australian residential load dataset verifies the effectiveness of the proposed method.

KEYWORDS

PV Estimation, BTM, improved Transformer, federated Learning, momentum aggregation

1 Introduction

As the energy landscape evolves, the adoption of distributed photovoltaics, particularly on residential and commercial building rooftops, has surged. By the end of 2020, approximately 2.66 million Australian homes were equipped with rooftop solar systems (Australian Government, 2020). However, due to budgetary limitations, most of these installations lack dedicated metering devices, making direct power measurement challenging. The growing prevalence of such unmonitored distributed PV systems poses

significant risks to the economic and safe operation of distribution station areas. These include issues like voltage instability (Rosado and Khadem, 2019), inaccurate load forecasting (Wang et al., 2017), and suboptimal fault recovery (Chen et al., 2018). Consequently, accurately estimating behind-the-meter (BTM) PV power generation using robust methodologies has become increasingly crucial.

The methodological core of estimating BTM PV is to establish a link between other data available and unknown PV data. It can be divided into two main categories: physical model-based and data-driven methods.

The physical model-based approaches employ PV array performance models to represent physical PV arrays. In (Chen and Irwin, 2017), PV arrays are integrated with a clear-sky model to estimate customer-level solar power generation. Reference (Wang et al., 2017) employs a virtual equivalent PV plant model to represent the collective power generation of regional behind-the-meter (BTM) PV systems. Reference (Cheung et al., 2018) introduces an unsupervised consumer mixture model for PV estimation. In (Kabir et al., 2019; Kabir et al., 2023), physical PV models and statistical models are respectively utilized to estimate BTM solar power generation and local demand. A major drawback of these physical model-based approaches is the need for detailed PV array parameters or accurate meteorological data. However, in practice, these parameters are usually not available to the utility. In addition, obtaining meteorological data may impose additional costs on utilities. In (Li et al., 2019a), the net demand under heterogeneous weather conditions is used to estimate the BTM PV capacity, which is multiplied with the standard solar power time series to infer the BTM PV generation. Reference (Sossan et al., 2018) proposed an estimation method on transformer level PV generation based on the variation difference of load and solar power.

Data-driven methodologies predominantly utilize artificial intelligence techniques for deep learning model training. As detailed in reference (Lin et al., 2022), a method for real-time energy decomposition is proposed, enabling the segregation of behind-the-meter (BTM) solar energy from a substation's total energy consumption, employing partially labeled aggregated data for model training. Reference (Shaker et al., 2016) introduces a data-driven strategy for estimating BTM solar power generation, encompassing data dimensionality reduction and mapping functions, and involves selecting a limited number of representative sites for model training. Since support vector machine has the ability to learn the complex hidden relationships in the energy decomposition problem, reference (Li et al., 2019b) proposed a supervised machine learning model based on multiple Support Vector Regression (SVR) to regression the solar power generation on the extracted feature input. However, these methods fail to make full use of historical data to comprehensively reflect the features of different resources and mine the intrinsic relationship of historical data. At the same time, many time-series regression models with excellent performance are not considered.

In addition, traditional data-driven methods are centralized, and their performance largely depends on the quality and quantity of training data. However, this centralized approach may raise a series of concerns about data privacy, especially in a competitive electricity market (Li et al., 2023). Reference (Yang et al., 2023) solves the potential privacy problem by introducing the framework of federated learning. In literature (Lin et al., 2022), the problem of privacy protection and the uncertainty of various types of data are considered, and the Bayesian neural network is used for PV estimation.

Building on the aforementioned analysis, this study introduces an enhanced Transformer neural network approach, underpinned by federated learning, designed to estimate community-level BTM PV generation. Federated learning mechanism can share training parameters and private training data, which can not only improve data quality but also protect user privacy. Considering the successful application of the self-attention mechanism in the electric power field in recent years (Azam and Younis, 2021; Wang et al., 2023; Zhou et al., 2023), a decentralized improved Transformer model is designed, and the model is further divided into two parts: individual and center, so as to adapt to the specific needs of each community (Tzeng et al., 2014; Chen et al., 2020). Furthermore, the study implements a hierarchical parameter strategy for model updating. Experimental evaluations demonstrate the efficacy of this method on real-world datasets.

In summary, this paper makes the following contributions.

1. The refined Transformer model, applied to BTM PV estimation, incorporates a fused attention mechanism to thoroughly extract PV-related information from net load data.
2. The federated learning mechanism is used to realize parameter sharing between different communities while considering privacy protection, so the receptive field and generalization ability of the model are improved.
3. A novel hierarchical parameter update mechanism is introduced in the enhanced Transformer model, consisting of an exchange layer and an individual layer. This configuration facilitates the sharing of exchange layer parameters through momentum aggregation while retaining individual layer parameters, thereby augmenting the model's capacity to address both individual and common feature challenges.

The remaining structure of the paper is as follows: Section II introduces the main models involved in this paper; Section III introduces the data set used and the numerical example verification. Section IV provides a summary and outlook.

2 Main models

2.1 Community PV estimation model

Since most of the user-level distributed PVs are deployed behind the meters, only the net load data can be directly observed for most user. A small number of users can directly obtain the photovoltaic output information. The net load power value is equal to the difference between the load and the PV power, as shown in the following equation:

$$P_{Ni,t} = P_{Li,t} - P_{Gi,t} \tag{1}$$

Where $P_{Ni,t}$ is the observed net load of the corresponding user of the ith community at time t; $P_{Li,t}$, $P_{Gi,t}$ is the corresponding actual

load value and the BTM PV power generation value. Since there is no illumination intensity at night, 7–17 h are selected as the reference in this paper.

Through the above analysis, the data-driven based BTM PV estimation strategy can be abstracted and modeled as:

$$P_G = h(q, P_N, S) \tag{2}$$

Where P_G is the PV estimated value, h is the transfer function of the network, q is the network parameter, P_N is the available net load data, S is relevant weather information.

2.2 Federated learning framework

Data-driven BTM PV decomposition strategies rely on large amounts of data for model training. It is difficult for a community to collect a large amount of labeled data. On the one hand, only a small number of users can measure the PV behind the meter. On the other hand, collecting data from neighboring communities has the risk of privacy leakage. Centralized data collection and optimization models are not advantageous in dealing with the BTM PV estimation problem.

This paper addresses the challenge by employing a federated learning framework. Federated learning offers a mechanism enabling multiple entities to collaboratively train and refine a model, without the need for direct raw data sharing. This approach not only safeguards data privacy and security but also facilitates the distributed training of the BTM solar power generation estimation model across multiple data sources, thereby enhancing the model's generalization capability. A supervised model for photovoltaic estimation is constructed under the federated learning framework, in the form of Formula 3:

$$\begin{aligned}[P_{G,1}, P_{G,2}, \ldots, P_{G,n}] = H\left(q_1^p\left(P_{N,1}, S_1\right), q_2^p\left(P_{N,2}, S_2\right), \ldots,\right. \\ \left. q_n^p\left(P_{N,n}, S_n\right)\right)\end{aligned} \tag{3}$$

Where i is the index of the community, $P_{G,i}$ is the estimated PV output, H is the global shared parameters, q_i^p is the individual parameter, $P_{N,i}$ is the net load data as input, and S_i is the meteorological information.

It is worth noting that there are differences in the relationship between net load and solar power generation in different local communities due to geographical location and weather conditions. In order to capture this difference, refer to the idea of reference (Azam and Younis, 2021), the model layer is divided into individual layer and exchange layer, where:

$$q_i = [q_i^p; q_i^c] \tag{4}$$

Where q_i is the learnable parameters of the ith community, q_i^p is the individual parameter, q_i^c is the exchange parameter.

In the implementation of the federated learning framework, a momentum aggregation strategy is selectively employed, particularly suitable for the complex nonlinear dynamics and potential non-convex optimization challenges inherent in photovoltaic (PV) estimation. This strategy expedites model convergence towards an optimal solution by integrating gradient information from preceding iterations, a critical factor in handling large-scale, intricate datasets. Additionally, when processing data from diverse buildings and regions, the model often faces oscillatory challenges. Momentum aggregation addresses this by smoothing the model's update process, thereby enhancing the stability and reliability of the training procedure. The parameter update process based on momentum aggregation is formulated as follows:

$$H^{t+1} = \beta H^t + (1-\beta)\left(\frac{1}{N}\sum_{i=1}^{N} q_i^{c,t+1}\right) \tag{5}$$

Where t is the number of iterations index, β is the parameter of momentum, N is the number of communities.

The specific structure of BTM PV estimation based on the federated learning framework is shown in Figure 1.

2.3 Improved transformer network

Transformer is a network architecture based on self-attention mechanism, which inherits the advantages of self-attention mechanism in dealing with long distance sequences with volatility. At the same time, it integrates residual network and other structures to solve the problems of gradient disappearance caused by depth deepening, so that the model has higher plasticity. All these advantages enable it to achieve better results in dealing with long-distance serial regression problems.

The complexity of PV power data, characterized by its time-series attributes, poses challenges for traditional attention mechanisms, especially in capturing short-term (e.g., intraday) and long-term (e.g., seasonal) variations. The integration of local and global attention mechanisms offers a solution. The local mechanism concentrates on accurately predicting critical periods, while the global mechanism discerns long-term trends and impacts, thereby enriching the overall comprehension of factors influencing PV output. This dual approach not only bolsters the model's capacity to navigate data nonlinearity and variability, thereby enhancing prediction accuracy and robustness, but also augments model interpretability by delineating distinct temporal dependencies. Crucially, this method also elevates computational efficiency, a vital aspect for processing large-scale PV data. The expression is as follows:

$$\begin{aligned}Ac(Q, K, V) = \lambda \cdot M\left(soft\max\left(\frac{QK}{\sqrt{d_k}}\right)V\right) \\ + \gamma \cdot soft\max\left(\frac{QK}{\sqrt{d_k}}\right)V\end{aligned} \tag{6}$$

Where AC is the output of fused self-attention, M is the window selection function, λ, γ is the weight parameters, respectively. Q, K and V is the query, key and value, respectively. d_k is the dimension of K.

When training the model, the inputs of the encoder and decoder are timing data and training labels respectively. Both are mapped to the high-dimensional space through a linear network, and the high-dimensional data are endowed with location characteristics by the location coding function. Then, the input data passes through N cyclic units composed of multi-head fusion attention structure and feedforward neural network respectively, and the output is finally obtained.

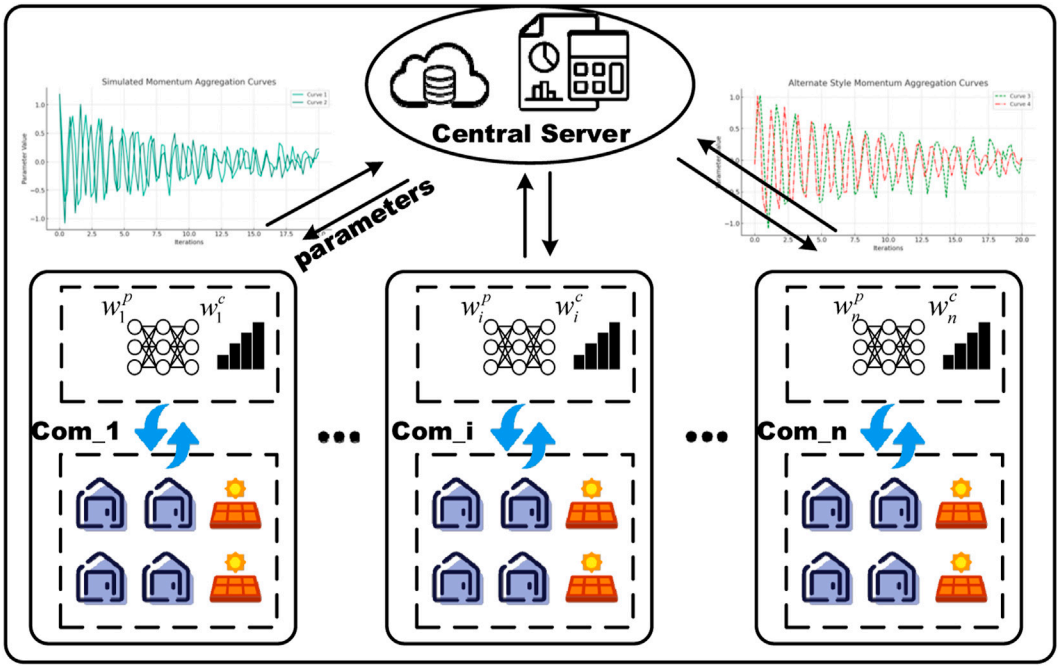

FIGURE 1
Federal learning framework for BMT PV estimation.

The feedforward neural network is composed of fully connected layers with the transfer function as follows:

$$FFN(x) = \max(0, xW_1 + b_1)W_2 + b_2 \tag{7}$$

Where, $FFN(x)$ is the output of the fully connected layer, W_1,b_1 and W_2, b_2 are the parameters of the two fully connected layers, and non-linear transformation is performed by retaining non-negative data to improve the network expression ability.

Due to the existence of the residual network structure, the actual output of each layer in the network is the sum of the theoretical output and the residual:

$$O_i = Norm(in_i + o_{idea}) \tag{8}$$

Where in_i is the input of the ith layer structure in the model; o_{idea} is the theoretical output of this layer. $Norm$ is the layer normalization operation. o_i is the actual output of layer i.

The attention mechanism, by applying attention operations uniformly across all data, results in an output matrix devoid of original positional information. This leads to the model's inability to learn the data's order information, necessitating the infusion of positional features into the input sequence.

The sine and cosine functions with different frequencies are used to encode the position, so as to give the absolute and relative position information to the time series data. The position-encoding function is as follows:

$$P_{x,2i} = \sin\left(\frac{x}{10000^{2i/dm}}\right) \tag{9}$$

$$P_{x,2i+1} = \cos\left(\frac{x}{10000^{2i/dm}}\right) \tag{10}$$

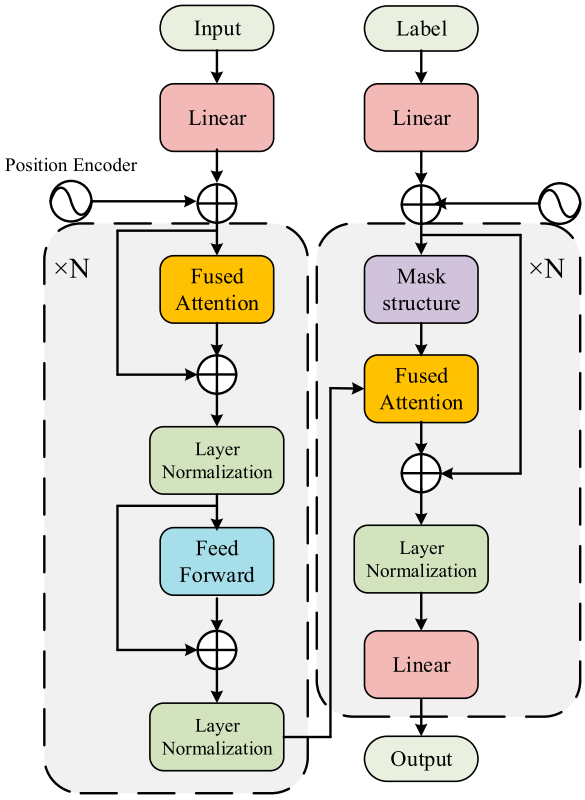

FIGURE 2
Improved transformer structure.

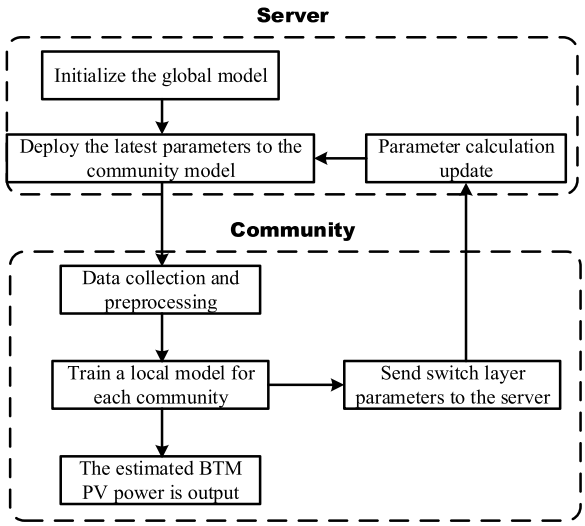

FIGURE 3
PV estimation process.

Where d_m is the dimension of time series data, i is the dimension index, x is the absolute position, P_x is the position encoding.

In the decoder structure, the initial output reaches the same dimension as the training label through a normalization layer and a linear layer, and the final output is the estimated result.

The improved Transformer structure is shown in Figure 2:

The enhanced Transformer network serves as both the sub-network and global network for each community. It undergoes hierarchical processing and parameter updates in the individual and exchange layers, aligned with the federated learning architecture. This culminates in the creation of a cloud-edge collaborative supervised regression model, where a central server facilitates interaction, and multiple communities function as distinct training units. The overall process is shown in Figure 3.

3 Results analysis

3.1 Introduction of the dataset and description of the experimental platform

The performance of the proposed model is evaluated using the Ausgrid Solar Home Electric (ASHE) dataset (Ratnam et al., 2017). Comprising actual smart meter data from households in and around Sydney, Australia, this publicly accessible dataset encompasses controlled load consumption for each household, general consumption over the entire period, and solar power generation data at 30-min intervals.

After data preprocessing, the data of 300 users in 4 communities from 1 July 2010 to 30 June 2011 were selected for analysis. The actual load of a user can be directly determined by the sum of controlled and general consumption. The corresponding net demand is calculated by subtracting the solar generation from the actual load. Subsequently, by aggregating the measurements from the consumer communities, we can obtain the net load and BTM solar generation at the community level.

TABLE 1 Hyperparameter setting.

Hyperparameter description	Value
Number of parameter exchanges	20
Number of sub-model training rounds	100
Learning rate	1*e*-3

Experimental platform setup: Intel i5-13600k and NVIDIA GeForce RTX 3070 are used as the core processors, Python 3.7 is used as the programming language for the algorithm model, and the network model is built based on the open source machine learning framework Pytorch.

The hyperparameter Settings of the proposed model are shown in Table 1.

3.2 Evaluation function

Root Mean Square Error (RMSE), Standardized Root Mean Square Error (NRMSE), Mean Absolute Error (MAE) and Mean Absolute Percentage Error (MAPE) are used as indicators to measure the prediction results of the model, and the expressions are as follows:

$$RMSE = \sqrt{\frac{1}{n}\sum_{i=1}^{n}\left(y_{i\_tru} - y_i\right)^2} \tag{11}$$

$$NRMSE = \frac{RMSE}{y_{i\_tru\_\max} - y_{i\_tru\_\min}} \tag{12}$$

$$MAE = \frac{1}{n}\sum_{i=1}^{n}\left|y_{i\_tru} - y_i\right| \tag{13}$$

$$MAPE = \frac{1}{n}\sum_{i=1}^{n}\left|\frac{y_{i\_tru} - y_i}{y_{i\_tru}}\right| \tag{14}$$

Where, y_{i_tru} is the real value of photovoltaic power generation at time i; y_i is the predicted value of photovoltaic power generation at time i; n is the total number of sampled data.

3.3 Error comparison

To assess the decomposition performance of the proposed model, it is compared with different learning frameworks and state-of-the-art methods. These include Local Learning (LL), where communities independently train and evaluate the model without interaction; Centralized Learning (CL), which involves aggregating data from all communities for unified model training by a central server; and Federated Learning (FL), where each community trains the model individually, exchanges layer parameters with a central server for updating global model parameters, and then conducts gradient descent training. We call the attention-integrated Transformer model FTransformer.

Specifically, FL-FTransformer, FL-BNN, FL-LSTM, FL-Transformer, LL-FTransformer, and CL-FTransformer are compared.

The historical net load data of the current moment and the same time of the previous week and the corresponding meteorological

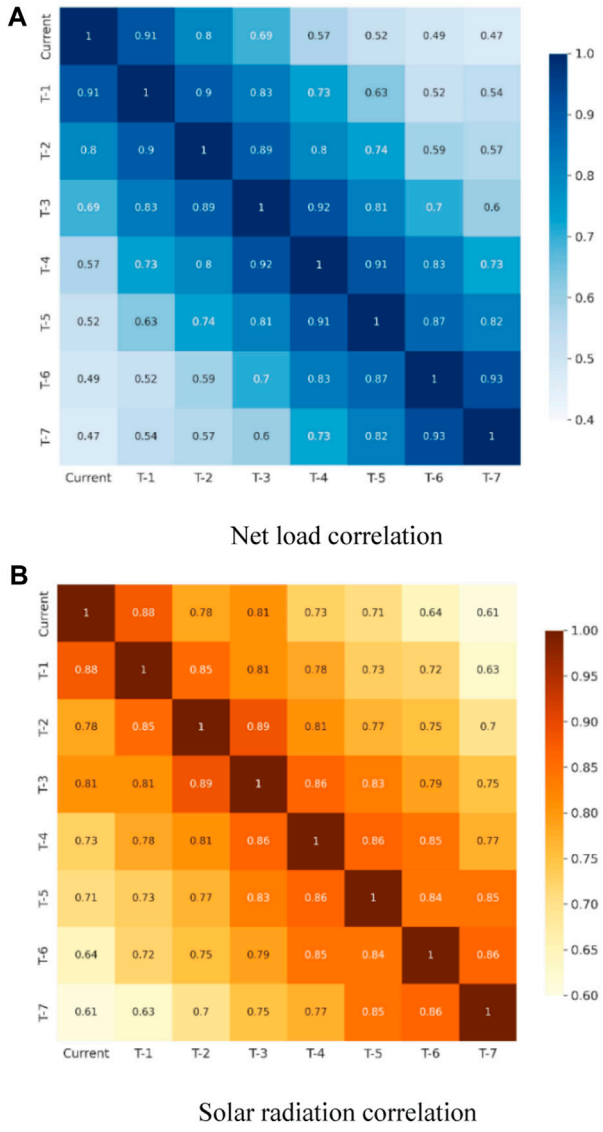

FIGURE 4
Feature correlation heat map.

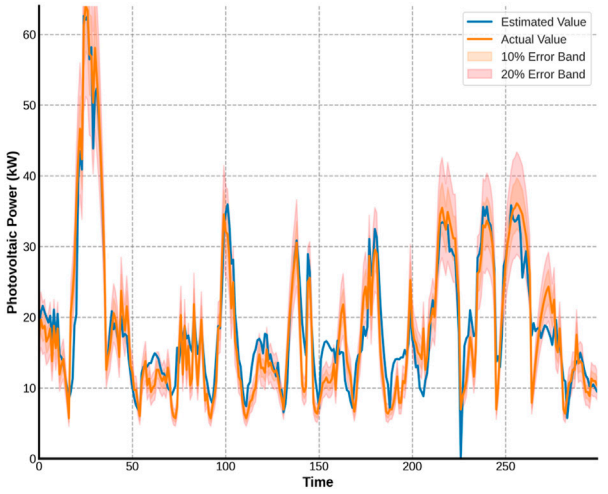

FIGURE 5
FL-FTransformer output comparison.

TABLE 2 Error comparison of different models.

	RMSE (kW)	NRMSE (%)	MAE (kW)	MAPE (%)
FL-FTrans	1.52	2.43	4.56	11.72
FL-BNN	2.39	3.37	5.22	13.47
FL-LSTM	2.15	2.88	4.93	12.58
FL-Trans	2.21	2.75	5.04	12.43
LL- FTrans	3.62	5.47	6.52	15.88
CL- FTrans	1.79	2.74	4.88	12.14

data are selected as the input features of the model. Figure 4 illustrates the correlation between the net load value and solar radiation at the historical time and the PV power at the current time.

According to the heat map, it can be found that the closer to the current time, both the net load data and the solar radiation intensity have a greater impact on the PV power at the current time, which proves the effectiveness of feature selection.

Figure 5 selects part of community 1 to visually compare the estimated PV power output of FL-FTransformer network with the real value. It can be found that even in the case of large data fluctuations, the proposed model can still achieve accurate estimation of PV power. Since the visual difference between many models in the comparison diagram is not large, and it is easy to stack together, it is impossible to intuitively compare the used model with the real value. Therefore, the power curve of other models is not added in the comparison diagram, and the effectiveness of the proposed model is proved through the comparison of error indicators.

Table 2 shows the error index situation of the proposed FL-FTransformer model and the comparison model. Under the same FL framework, the improved FTransformer improves RMSE and MAPE respectively compared with BNN, LSTM and Transformer 0.87kW, 0.63kW, 0.69kW, 1.65%, 0.86%, and 0.71%. Under the same improved FTransformer network, FL, compared with LL and CL, improves 2.1kW, 0.27kW, 4.16% and 0.42%.

In a horizontal analysis, the augmented FTransformer model, integrated within the federated learning (FL) framework, outperforms across four key metrics. This superiority is attributed to its combined attention and parallel processing capabilities, which provide robust and versatile model for temporal regression tasks like BTM PV estimation. In a vertical comparison, the FL architecture, also employing the enhanced FTransformer as its core network, demonstrates superior performance. This is due to FL's ability to expand data scope and enhance model generalization compared to local learning. Additionally, unlike centralized learning, FL's two-layer training mechanism not only emphasizes the unique characteristics of each community but also safeguards user data privacy while broadening the data pool.

Table 3 compares the performance of different models in different seasons, and the FL-FTransformer model achieves the

TABLE 3 Error comparison of different seasons.

	Spring	Summer	Autumn	Winter
FL-FTrans	1.55	1.61	1.58	1.65
FL-BNN	2.37	2.44	2.35	2.40
FL-LSTM	2.13	2.32	2.21	2.18
FL-Trans	2.25	2.28	2.64	2.21
LL- FTrans	3.60	3.85	3.69	3.71
CL- FTrans	1.82	1.85	1.71	1.77

TABLE 4 Error Comparison of Different communities.

	com1	com2	com3	com4
Estimated value (kW·h)	62.55	70.42	65.84	72.49
True value (kW·h)	65.72	67.49	71.34	70.06
Deviation (kW·h)	3.17	2.93	5.50	2.43
Proportion of deviation (%)	4.82	4.34	7.71	3.47

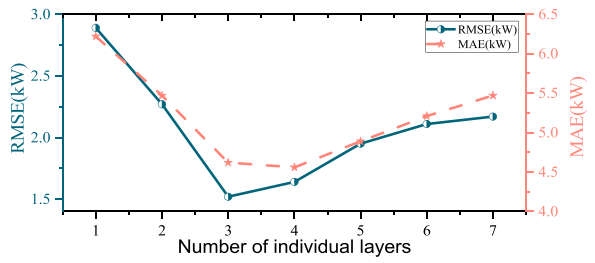

FIGURE 6
Error comparison of different individual layers.

best performance in different seasons. Due to the fluctuation difference of illumination radiation in different seasons, the specific error indicators are also different. The incorporation of the fused attention mechanism enables the enhanced FTransformer network to adeptly manage varying degrees of PV fluctuations across different seasons.

The estimated value of PV generation in each community is compared with the true value from 12:00 to 13:00 when the solar radiation is sufficient. Since the PV power does not fluctuate much in the time scale of 1 hour, the PV power at 12:30 is selected as the average power in this period for the calculation of power generation, and the summary results are shown in Table 4.

As can be seen from Table 4, the error of PV generation of each community in the selected period is about 5%, which has a high accuracy, indicating that the proposed model has the ability to accurately estimate the regional PV power generation.

Figure 6 illustrates the error comparison for different number of individual layers. In summary, when the number of individual layers is 3, the model evaluation effect is the best, and it is used as the final output model. It shows that the model has a compromise between focusing on community characteristics and global commonality.

4 Conclusion

This study addresses regional photovoltaic (PV) power estimation by proposing a deep learning model that leverages an improved Transformer within a federated learning framework. The model's efficacy is validated through experiments, yielding notable findings:

1) The FL-Transformer model effectively utilizes community-level data in a distributed manner for behind-the-meter (BTM) PV estimation, enhancing the model's generalizability, estimation accuracy, and user privacy protection.
2) The proposed two-layer training mechanism not only pays attention to the characteristics of a single community data, but also pays attention to the commonality between multiple communities, which significantly improves the performance of the model. The method of updating global parameters by momentum aggregation improves the robustness and solution efficiency of the model.
3) Enhancements to the traditional Transformer model, incorporating both global and local attention mechanisms, markedly improve the model's capacity to discern long and short cycle features, thereby refining decomposition accuracy.

Data availability statement

The original contributions presented in the study are included in the article/Supplementary material, further inquiries can be directed to the corresponding author.

Author contributions

BC: Conceptualization, Writing–review and editing. RL: Investigation, Writing–review and editing. MW: Methodology, Writing–original draft. XW: Data curation, Writing–review and editing. YS: Supervision, Writing–review and editing. DS: Formal Analysis, Writing–review and editing.

Funding

The author(s) declare financial support was received for the research, authorship, and/or publication of this article. This research is funded by the Science and Technology Project of Economic and Technological Research Institute, State Grid Shandong Electric Power Company (52062522000N). This research was funded by the Spatial and Temporal Layout of Shandong New Energy Power Project considering development potential and system constraints.

Conflict of interest

Authors BC, RL, XW, YS, and DS were employed by the State Grid Shandong Electric Power Company.

The remaining author declares that the research was conducted in the absence of any commercial or financial relationships that could be construed as a potential conflict of interest.

Publisher's note

References

Australian Government (2020). Solar PV installation information in Australia. [Online].Available: https://www.energy.gov.au/households/solar-pv-and-batteries.

Azam, M. F., and Younis, M. S. (2021). Multi-horizon electricity load and price forecasting using an interpretable multi-head self-attention and EEMD-based framework. *IEEE Access* 9, 85918–85932. doi:10.1109/access.2021.3086039

Chen, B., Chen, C., Wang, J., and Butler-Purry, K. L. (2018). Sequential service restoration for unbalanced distribution systems and microgrids. *IEEE Trans. Power Syst.* 33 (2), 1507–1520. doi:10.1109/tpwrs.2017.2720122

Chen, D., and Irwin, D. (2017). "SunDance: black-box behind-the-meter solar disaggregation," in Proc. 8th Int. Conf. Future Energy Syst, Shatin Hong Kong, May, 2017, 16–19.

Chen, Y., Sun, X., and Jin, Y. (2020). Communication-efficient federated deep learning with layerwise asynchronous model update and temporally weighted aggregation. *IEEE Trans. Neural Netw. Learn. Syst.* 31 (10), 4229–4238. doi:10.1109/tnnls.2019.2953131

Cheung, C. M., Zhong, W., Xiong, C., Srivastava, A., Kannan, R., and Prasanna, V. K. (2018). "Behind-the-meter solar generation disaggregation using consumer mixture models," in Proc. IEEE Int. Conf. Commun., Control, Comput. Technol. Smart Grids, Aalborg, Denmark, October, 2018, 1–6.

Kabir, F., Yu, N., Yao, W., Yang, R., and Zhang, Y. (2019). "Estimation of behind-the-meter solar generation by integrating physical with statistical models," in IEEE Int. Conf. Commun. Control Comput. Technol. Smart Grids, Beijing, China, October, 2019, 1–6.

Kabir, F., Yu, N., Yao, W., Yang, R., and Zhang, Y. (2023). Joint estimation of behind-the-meter solar generation in a community. *IEEE Trans. Sustain. Energy* 12 (1), 682–694. doi:10.1109/tste.2020.3016896

Li, D., Guo, Q., and Feng, J. (2023). Private settlement model of distributed power transactions based on blockchains. *Power Syst. Technol.*, 1–19.

Li, K., Wang, F., Mi, Z., Fotuhi-Firuzabad, M., Duić, N., and Wang, T. (2019a). Capacity and output power estimation approach of individual behind-the-meter distributed photovoltaic system for demand response baseline estimation. *Appl. Energy* 253, 113595. doi:10.1016/j.apenergy.2019.113595

Li, K., Wang, F., Mi, Z., Fotuhi-Firuzabad, M., Duić, N., and Wang, T. (2019b). Capacity and output power estimation approach of individual behind-the-meter distributed photovoltaic system for demand response baseline estimation. *Appl. Energy* 253, 113595. doi:10.1016/j.apenergy.2019.113595

Lin, J., Ma, J., and Zhu, J. (2022). A privacy-preserving federated learning method for probabilistic community-level behind-the-meter solar generation disaggregation. *IEEE Trans. Smart Grid* 13 (1), 268–279. doi:10.1109/tsg.2021.3115904

Ratnam, E. L., Weller, S. R., Kellett, C. M., and Murray, A. T. (2017). Residential load and rooftop PV generation: an Australian distribution network dataset. *Int. J. Sustain. Energy* 36 (8), 787–806. doi:10.1080/14786451.2015.1100196

Rosado, S. P., and Khadem, S. K. (2019). Development of community grid: review of technical issues and challenges. *IEEE Trans. Industry Appl.* 55 (2), 1171–1179. doi:10.1109/tia.2018.2883010

Shaker, H., Zareipour, H., and Wood, D. (2016). A data-driven approach for estimating the power generation of invisible solar sites. *IEEE Trans. Smart Grid* 7 (5), 2466–2476. doi:10.1109/tsg.2015.2502140

Sossan, F., Nespoli, L., Medici, V., and Paolone, M. (2018). Unsupervised disaggregation of photovoltaic production from composite power flow measurements of heterogeneous prosumers. *IEEE Trans. Industrial Inf.* 14 (9), 3904–3913. doi:10.1109/tii.2018.2791932

Tzeng, E., Hoffman, J., Zhang, N., Saenko, K., and Darrell, T. (2014). Deep domain confusion: maximizing for domain invariance. [Online]. Available: https://arxiv.org/abs/1412.3474.

Wang, W., Feng, B., Huang, G., Liu, Z., and Ji, W. (2023). Short-term net load forecasting based on self-attention encoder and deep neural network. *Proc. CSEE*, 1–13.

Wang, Y., Zhang, N., Chen, Q., Kirschen, D. S., Li, P., and Xia, Q. (2017). Data-driven probabilistic net load forecasting with high penetration of behind-the-meter PV. *IEEE Trans. Power Syst.* 33 (3), 3255–3264. doi:10.1109/tpwrs.2017.2762599

Yang, T., Qin, X., Xiangwei, F., and Xu, Z. (2023). Federated learning electric vehicle short-term charging load prediction accounting for user charging behavior and privacy protection. *High. Volt. Eng.*, 1–8.

Zhou, S., Li, Y., Guo, Y., Qiao, X., and Liu, Y. (2023). Ultra-short-term load forecasting based on temporal convolutional network considering temporal feature extraction and dual attention fusion. *Automation Electr. Power Syst.*, 1–21.

frontiers | Frontiers in Energy Research

TYPE Original Research
PUBLISHED 20 February 2024
DOI 10.3389/fenrg.2024.1344837

OPEN ACCESS

EDITED BY
Rufeng Zhang,
Northeast Electric Power University, China

REVIEWED BY
Weiqi Wang,
Shandong University of Science and Technology, China
Zhan Ma,
RWTH Aachen University, Germany
Tao Xu,
Shandong University, China

*CORRESPONDENCE
Xiaobo Hao,
37496900@qq.com

RECEIVED 26 November 2023
ACCEPTED 18 January 2024
PUBLISHED 20 February 2024

CITATION
Hao X, Liu P and Deng Y (2024), Joint optimization of operational cost and carbon emission in multiple data center micro-grids. *Front. Energy Res.* 12:1344837. doi: 10.3389/fenrg.2024.1344837

Joint optimization of operational cost and carbon emission in multiple data center micro-grids

Xiaobo Hao*, Pengcheng Liu and Yanhui Deng

Ningxia Hongdunzi Coal Ind, Ningxia, China

As the internet data centers are mushrooming, the energy consumption and carbon emission of data centers are increasing rapidly. To cut down the electricity cost and carbon emission of the data centers, we proposed an optimization method to reduce the electricity cost and carbon emission in geo-distributed multiple data centers. In the proposed method, the carbon tax is considered in the overall operation cost to optimize the carbon emission. The spatial and temporal flexibility of computational workload is fully utilized by considering the difference in renewable energy power output, local electricity and carbon emission of multiple geo-distributed data centers to achieve a better performance. Furthermore, the nonlinear characteristics of the power loss of uninterruptible power supply (UPS) are considered in the optimization. To verify the proposed optimization method, simulation of six cases is carried out with realistic data, and results have proved the proposed method can reduce the operational costs by 4.93%–12.7% and decrease carbon emissions by up to 10%.

KEYWORDS

data center, multiple micro-grids, optimal scheduling, carbon emission, demand response

1 Introduction

Carbon emissions, being an important cause of phenomena such as global warming, have garnered escalating attention worldwide (Carbon Tax Center, 2021). In response, an increasing number of countries have implemented carbon taxes to incentivize factories and enterprises to reduce their carbon emission. (World Bank Group, 2020). As a significant consumer of electricity, energy consumption and carbon emission of data centers have become increasingly prominent as the number of data centers increases, which pose a serious carbon emissions issue. As reported by the NRDC, U.S. data centers are forecasted to consume 140 billion kW hours of power by 2020, resulting in an electricity cost of nearly 13 billion dollars and emission of carbon dioxide 150 million tons (Delforge, 2014). The energy consumption and carbon emission have led to negative impacts on the environment, as well as great operational cost under the carbon tax policy (Liu et al., 2020). Therefore, reducing the electricity cost and carbon emission can meet the expectations of government and data center operators alike, which have drawn increasing attention from both academia and industry all over the world (Ni and Bai, 2017).

Most existing research on the aforementioned issue focuses on reducing the power consumption rather than carbon emission of data centers (Yu et al., 2014), which tried three main ways to reduce the energy consumption in the data centers. The first is to boost the power conversion efficiency of data center power supply system by improving the efficiency of power converters, such as power supply unit (PSU) or uninterruptible power supply

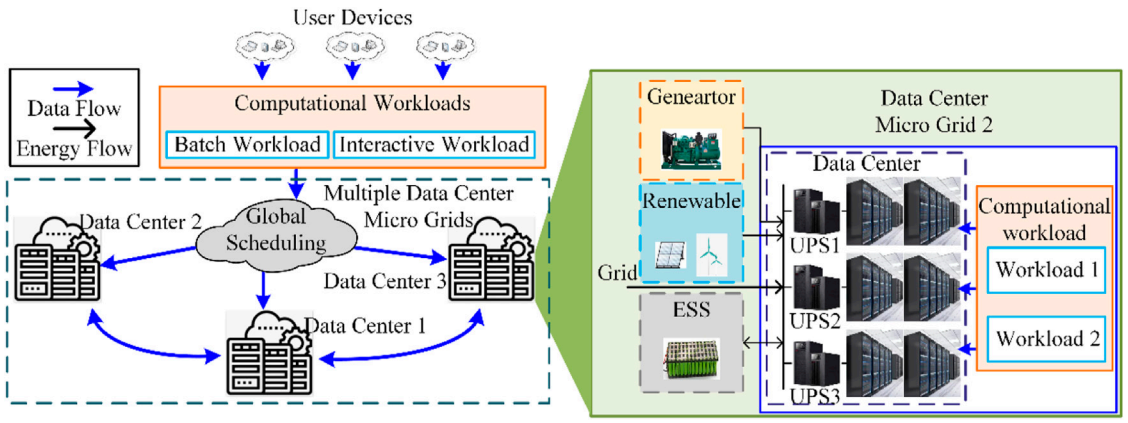

FIGURE 1
Multiple data center micro grid system.

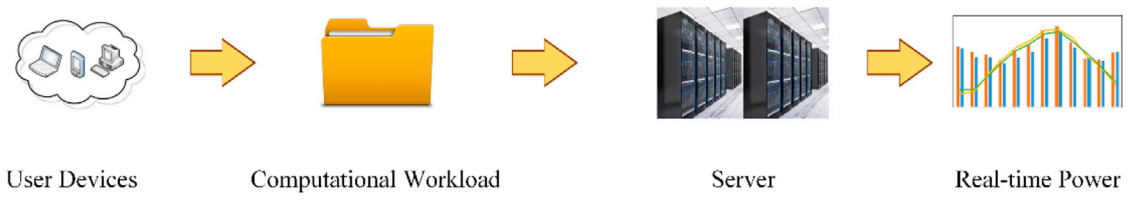

FIGURE 2
Relationship between computational workload and data center real-time power.

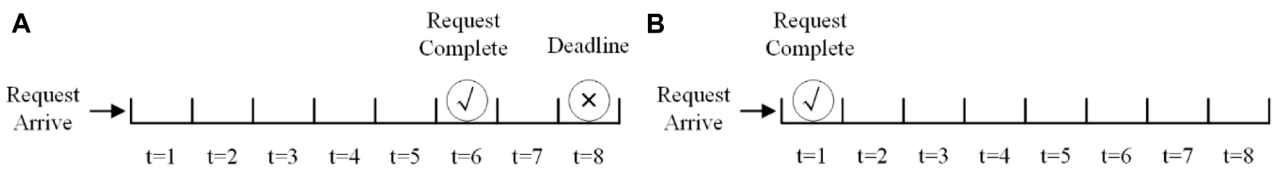

FIGURE 3
Computational workload; **(A)** Batch workload, **(B)** interactive workload.

(UPS) (Ahmed et al., 2017; Zhao et al., 2019). The second is to jointly optimize the computational workload scheduling with the micro grid operations in data centers, or optimize the planning of data center micro grid (Li et al., 2018). The third method is to optimize the workload distribution in multiple distributed data centers in different city and cut down operational cost by utilizing the local electricity cost and renewable energy output (Liu et al., 2012; Qi et al., 2019). Microsoft and Equinix have also introduced micro grid into data center (Peter, 2017). Yang et al. have built the prototype of waste heat recovery system, which has also been verified by commercial application (Luo et al., 2019). And the related data center testbed has been built at RISE ICE Datacenter in northern Sweden in order to perform experiments on load balancing, micro-grid interactions and the use of renewable energy sources (Brannvall, 2020). The aforementioned methods can effectively reduce energy consumption while simultaneously decreasing the accompanying carbon emissions. However, according to literature (Li et al., 2011; Na et al., 2022), there is a certain deviation between the optimal points of energy consumption and carbon emissions, therefore the research focused on energy consumption cannot guarantee the optimization of carbon emissions. Hence, in the optimization process, it is necessary to consider reducing carbon emissions as an optimization objective concurrently.

The reduction of carbon emissions in data centers can be achieved through two main methods: cutting down energy consumption in data centers and maximizing the utilization of renewable energy. Li *et. al.* proposed a data center micro grid planning method, which introduces the renewable energy devices

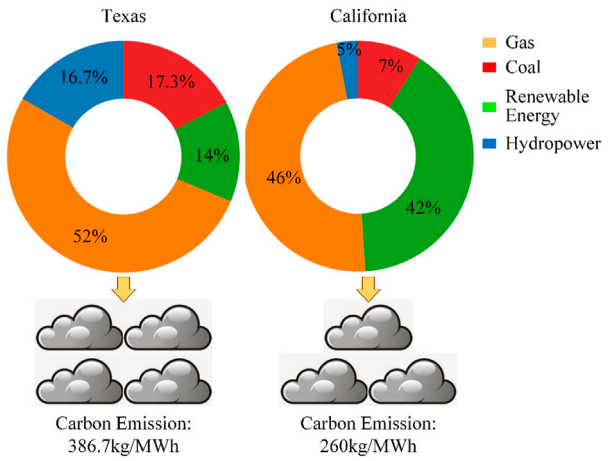

FIGURE 4
Relationship between computational workload and data center real-time power.

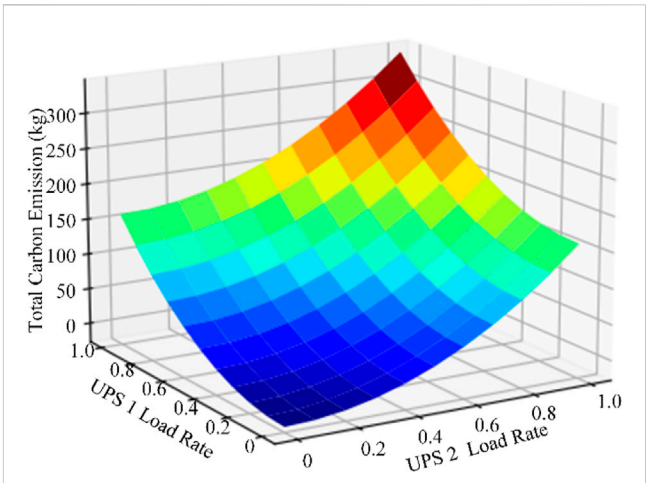

FIGURE 6
UPS load rate and carbon emission.

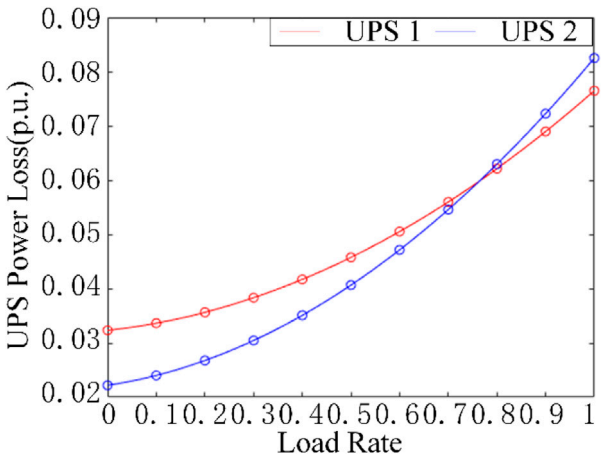

FIGURE 5
UPS power loss curve.

into data center (Cui et al., 2016). However, carbon emission is not considered in the planning method. Ding proposed a multi objective method to reduce the carbon emission and electricity consumption, but research did not considered the scheduling of computational workload in multiple data centers, and the nonlinear characteristics of the power supply system inside of the data center (Ding et al., 2018). Ting et al. proposed a carbon reduction method in four data centers in different city, but the electricity consumption is not taken into account (Ting et al., 2022). Zhou et al. proposed an electricity consumption reducing method in geo-distributed data center micro grids with renewable energy, but the carbon emission are not directly taken into consideration (Zhou et al., 2016; Liu and Xu, 2023; Zhang et al., 2023 proposed several optimal planning methods of data centers considering carbon emission, however it achieves the optimal planning of single data center and ignores the spatial scheduling flexibility of workloads in data centers; Wu et al., 2023; Yang et al., 2023 proposed carbon emission aware scheduling method in multiple data center, while the UPS characteristics are ignored. Furthermore; Misaghian et al., 2023 proposed a carbon aware flexibility assessment method to estimate the operational flexibility of data centers, however it has not proposed the relevant scheduling method. In brief, the characteristics of power supply devices, such as uninterruptible power supply (UPS) are not considered in the exiting methods, which may lead to extra energy consumption and carbon emission.

In view of this, we proposed a hybrid operation optimization method to reduce the electricity cost and carbon emission in geo-distributed data center by jointly considering computational workload scheduling, carbon emission, micro grid operation and characteristics of UPSs. The proposed method reduced the operational cost and carbon emission by utilizing the degree of freedom in computational workload scheduling to limit the nonlinear growth of UPS power losses. To balance the electricity reduction and carbon emission reduction, the carbon tax is introduced as a parameter in the optimization object, which describes the carbon emission of both micro grid devices and the marginal carbon emission caused by electricity purchasing from the utility grid. Six cases are simulated on the Gurobi platform, and results have verified the effectiveness of the proposed method.

2 The influence of workload scheduling and UPS power on optimization objectives

The system architecture of a typical geo-distributed data centers is given in Figure 1. The proposed method can reduce the energy consumption and carbon emission simultaneously by jointly considering the scheduling flexibility of the computational workloads the data centers and the nonlinear characteristics of UPS power losses. Therefore, the relationship between workload

scheduling and carbon emission is firstly analyzed, and then the relation between UPS characteristics and carbon emission is given. Furthermore, the necessity of incorporating both carbon emissions and operating costs as optimization objectives is discussed below:

2.1 The influence of computational workload scheduling on carbon emission

As shown in Figure 2, the real-time power of data center is decided by computational workload, which can be scheduled through the internet. Therefore, the most prominent feature of a data center micro grid, as opposed to a traditional micro grid, is its exceptional scheduling flexibility. On the one hand, computational workloads exhibit a high degree of flexibility, as they can be scheduled in both time and space dimensions, which can coordinate with renewable energy sources and electricity prices to minimize carbon emissions resulting from data center energy consumption. On the other hand, the devices within a data center micro grid, such as energy storage systems and conventional generator units, possess flexible regulation characteristics. The operation of these devices also affects the carbon emissions of the data center micro grid. In the following sections, we will analyze the flexibility of load scheduling and the data center carbon emissions separately.

2.1.1 Scheduling flexibility of computational workload

The computational workload can be briefly divided into batch workload and interactive workload (Cao et al., 2019). The interactive workload, such as online shopping and game service, should be dealt in a short time delay, which is usually no more than minutes or seconds, as shown in Figure 3A. The service delay of this kind of workload will lead to high economic losses. So the interactive workload cannot be scheduled through different time period. Since the computational workloads are mainly data blocks, it can be scheduled between data centers in different cities with a small delay through the data network.

The batch workload, such as processing of scientific research data and training of neural network, can endure an hourly responds delay, as shown in Figure 3B. Therefore, the batch workload can be scheduled spatially and temporally, which means the potentiality of participating in optimizing scheduling or demand response. Furthermore, the batch workload can also be scheduled through long distance with a small delay, which is negligible in the hourly scheduling, and the scheduling delay is mainly decided by network bandwidth.

Therefore, the computational workloads can be scheduled spatially and temporally in coordinated with renewable energy and conventional generators, whose output power can influence the carbon emission.

2.1.2 Composition and influencing factors of carbon emission

The carbon emissions resulting from the operation of a data center micro grid consist of two aspects: the carbon emissions caused by the operation of the conventional generators in the micro grid and the carbon emissions resulting from the electricity provided by the utility grid, which is generated by thermal power plants. In this paper, both aspects are considered and optimized.

The carbon emissions caused by the operation of the conventional generators in the data center micro grid are primarily determined by the fuel type and real-time power output (Ye and Gao, 2022), and the operation of coal-based generator units and oil-based generator units cause different levels of carbon emissions per unit of electricity produced.

The carbon emissions resulting from the electricity provided by the grid are mainly determined by the proportion of electricity generated by thermal power plants. As shown in Figure 4, the proportion of electricity generated by thermal power plants and renewable energy varies at different times within a day, resulting in difference of carbon emissions in each unit of the consumed electricity. Additionally, the differences in energy structure among different cities also lead to differences in carbon emissions when the same unit of electricity is consumed.

2.2 The influence of UPS power losses on carbon emission

In the exiting researches, few work is focused on the influence of the energy consumption characteristics of data center power supply equipment, such as UPS, in the data center scheduling optimization. However, the efficiency and power losses of UPSs do influence the energy consumption and carbon emission of data center micro grids. In implementation, the energy consumption of UPS varies depending on the model and load rate. On the one hand, the power supply efficiency and losses of different UPS equipment vary, which may lead to differences in power supply efficiency among different data centers. On the other hand, UPS energy consumption increases non-linearly with load rate, resulting in corresponding increases in power supply energy consumption and carbon emissions. To further optimize the data center consumption, the characteristics of UPS power losses and its influence on carbon emission are considered in the optimization and illustrated below.

2.2.1 Characteristics of UPS power losses

Uninterruptible Power Supplies (UPSs) play a critical role in ensuring the reliability of data center power supply. Essentially, UPSs consist of multi-stage converters. According to current research, UPS power losses contribute to around 5%–10% of total data center electricity consumption.

UPS power losses exhibit variability based on the load rate, as illustrated in Figure 4, featuring nonlinear curves. In practice, UPS power losses encompass three distinct components (Pratt et al., 2007):

Power losses independent of output power, such as those attributed to generating housekeeping power. These losses predominate during light loads.

Power losses linearly proportional to output power, including switching losses of power semiconductors, gate driver losses, and core losses in magnetics.

Power losses varying with the square of output power, arising from circuit resistance, encompassing conduction losses of power semiconductors and winding losses in magnetics. These losses are prominent under heavy loads.

2.2.2 Relationship between UPS power losses with data center carbon emission

The impact of uninterruptible power supply (UPS) on carbon emissions in data centers is mainly due to increased energy consumption. As illustrated in Figure 5, the efficiency of different UPS devices varies, resulting in differences in the additional energy consumption generated during the power supply process, and UPS energy consumption changes non-linearly with the load rate. Therefore, the distribution of loads on different UPS devices will affect the energy consumption generated by UPS devices, as shown in Figure 6, which thereby causes extra carbon emissions.

However, it should be noted that energy consumption is not the sole factor affecting carbon emissions in data centers. Due to the existence of new energy generation, energy storage, generator equipment, and real-time electricity purchase in micro grids, the optimization of carbon emissions should comprehensively consider factors such as micro grid operation and local energy structure.

3 System model and mathematical formulation

This section presents the system and mathematical models for the optimization problem. The depicted typical system architecture of geo-distributed data centers is outlined in Figure 1, wherein each data center operates within a micro-grid featuring renewable power sources, conventional generator units, and energy storage devices. Within each data center, multiple UPS nodes are deployed, corresponding to sets of UPS devices and a substantial number of servers. The system is discretely modeled in time, with equal-length time slots, each spanning 1 h.

The system is delineated into the power demand side and power supply side. On the power demand side, we construct models for workloads and UPS, elucidating the relationship between computational workloads and data center power consumption. On the power supply side, models for energy storage and conventional generator units are formulated, with power balance considerations. Ultimately, the optimization problem is formulated in this section, with the objective of minimizing operational costs and electricity bills across the entire system.

3.1 Power demand side

The energy consumption of power supply equipment is primarily composed of the energy consumption of servers and UPS devices. The energy consumption of servers is linearly determined by the computational load rate, which can be expressed as follows:

$$\boldsymbol{\lambda}_{i,j,t} = \boldsymbol{\zeta}^{inter}_{i,j,t} + \sum_{a}^{A} \boldsymbol{\mu}^{batch}_{a,i,j,t} \left(\forall \boldsymbol{i,j,t}\right) \tag{1}$$

$$\mathbf{0} \le \boldsymbol{\lambda}_{i,j,t} \le Cap_{i,j} \left(\forall \boldsymbol{i,j,t}\right) \tag{2}$$

$$\sum_{t_a^{batch}}^{D_a^{batch}} \boldsymbol{\mu}^{batch}_{a,i,j,t} = \sum_{a}^{A} \boldsymbol{\mu}^{batch}_{total,a} \left(\forall \boldsymbol{a} \in \boldsymbol{A}\right) \tag{3}$$

$$\boldsymbol{P}^{servers}_{i,j,t} \le \boldsymbol{P}^{UPS}_{rated,i,j} \left(\forall \boldsymbol{i,j,t}\right) \tag{4}$$

Furthermore, for each time slot i, the aggregate real-time power of node j in the data center is:

$$\boldsymbol{P}^{servers}_{i,j,t} = M_{ij} \times \left(\boldsymbol{\varphi}^{server}_{i,j} \times \boldsymbol{\lambda}_{i,j,t} + \boldsymbol{P}^{idle}_{i,j}\right) \left(\forall \boldsymbol{i,j,t}\right) \tag{5}$$

where $\boldsymbol{\varphi}^{server}_{i,j} = \boldsymbol{P}^{peak}_{i,j} - \boldsymbol{P}^{idle}_{i,j}$ (6)

The power losses of UPS exhibit non-linear variations contingent upon the load rate, which is decided by server power and can be expressed as follows:

$$\boldsymbol{P}^{Loss\_UPS}_{i,j,t} = \boldsymbol{P}^{Loss\_UPS}_{rated,i,j} \times \left[\boldsymbol{a}_0 + \boldsymbol{a}_1 \times \frac{\boldsymbol{P}^{servers}_{i,j,t}}{\boldsymbol{P}^{Loss\_UPS}_{rated,i,j}} + \boldsymbol{a}_2 \times \left(\frac{\boldsymbol{P}^{servers}_{i,j,t}}{\boldsymbol{P}^{Loss\_UPS}_{rated,i,j}}\right)^2\right] \left(\forall \boldsymbol{i,j,t}\right) \tag{7}$$

where $\boldsymbol{a}_0$, $\boldsymbol{a}_1$ and $\boldsymbol{a}_2$ are constants decided by UPS type.

So the UPS input power is as follows:

$$\boldsymbol{P}^{UPS}_{i,j,t} = \boldsymbol{P}^{Loss\_UPS}_{rated,i,j} + \boldsymbol{P}^{servers}_{i,j,t} \left(\forall \boldsymbol{i,j,t}\right) \tag{8}$$

3.2 Power supply side

In each micro grid, servers and UPS units derive power from a mix of solar and wind energy, conventional generators, and the utility grid. Energy storage devices are deployed to stabilize renewable energy variability and leverage daily electricity price fluctuations, reducing overall costs.

Conventional generator unit commitment decision model can be described as follows (Wang et al., 2012):

$$\boldsymbol{P}^{unit}_{min,i,l} \cdot \boldsymbol{o}^{unit}_{i,l,t} \le \boldsymbol{P}^{unit}_{i,l,t} \le \boldsymbol{P}^{unit}_{max,i,l} \cdot \boldsymbol{o}^{unit}_{i,l,t} \left(\forall \boldsymbol{i,j,t}\right) \tag{9}$$

$$-\boldsymbol{o}^{unit}_{i,l,t-1} + \boldsymbol{o}^{unit}_{i,l,t} - \boldsymbol{o}^{unit}_{i,l,k} \le \mathbf{0}$$

$$2 \le k - (t-1) \le \boldsymbol{MU}^{unit}_{i,l} \quad \left(\forall \boldsymbol{i,j,t}\right) \tag{10}$$

$$\boldsymbol{o}^{unit}_{i,l,t-1} - \boldsymbol{o}^{unit}_{i,l,t} + \boldsymbol{o}^{unit}_{i,l,k} \le \mathbf{1}$$

$$2 \le k - (t-1) \le \boldsymbol{MD}^{unit}_{i,l} \quad \left(\forall \boldsymbol{i,j,t}\right) \tag{11}$$

$$-\boldsymbol{o}^{unit}_{i,l,t-1} + \boldsymbol{o}^{unit}_{i,l,t} + \boldsymbol{u}^{unit}_{i,l,t} \le \mathbf{0} \left(\forall \boldsymbol{i,j,t}\right) \tag{12}$$

$$\boldsymbol{o}^{unit}_{i,l,t-1} - \boldsymbol{o}^{unit}_{i,l,t} + \boldsymbol{v}^{unit}_{i,l,t} \le \mathbf{0} \left(\forall \boldsymbol{i,j,t}\right) \tag{13}$$

$$\boldsymbol{P}^{unit}_{i,l,t} - \boldsymbol{P}^{unit}_{i,l,t-1} \le \left(2 - \boldsymbol{o}^{unit}_{i,l,t-1} - \boldsymbol{o}^{unit}_{i,l,t}\right) \cdot \boldsymbol{P}^{unit}_{min,i,l} + \left(1 + \boldsymbol{o}^{unit}_{i,l,t-1} - \boldsymbol{o}^{unit}_{i,l,t}\right) \cdot \boldsymbol{UR}^{unit}_{i,l} \quad \left(\forall \boldsymbol{i,j,t}\right) \tag{14}$$

$$\boldsymbol{P}^{unit}_{i,l,t-1} - \boldsymbol{P}^{unit}_{i,l,t} \le \left(2 - \boldsymbol{o}^{unit}_{i,l,t-1} - \boldsymbol{o}^{unit}_{i,l,t}\right) \cdot \boldsymbol{P}^{unit}_{min,i,l} + \left(1 - \boldsymbol{o}^{unit}_{i,l,t-1} + \boldsymbol{o}^{unit}_{i,l,t}\right) \cdot \boldsymbol{DR}^{unit}_{i,l} \quad \left(\forall \boldsymbol{i,j,t}\right) \tag{15}$$

$$\boldsymbol{o}^{unit}_{i,l,t}, \boldsymbol{v}^{unit}_{i,l,t}, \boldsymbol{u}^{unit}_{i,l,t} \in \{\mathbf{0}, \mathbf{1}\} \left(\forall \boldsymbol{i,j,t}\right) \tag{16}$$

In the aforementioned equations, Eq. 9 outlines the generator capacity constraint, Eqs 10 and 11 outlines the unit minimum-up/down time constraints, Eqs 12 and 13 delineate the unit start-up and shut-down constraints, while (14)–(15) specify unit ramping up/down.

The ESS can be described by the following equations:

$$ES_{i,t+1} = ES_{i,t} + \eta_i^{char} \cdot P_{i,t}^{char} - \eta_i^{dischar} \cdot P_{i,t}^{dischar} \ (\forall i, t) \quad (17)$$

$$ES_{min,i} \le ES_{i,t} \le ES_{max,t} \ (\forall i, t) \quad (18)$$

$$Z_{i,t}^{char}, Z_{i,t}^{dischar} \in \{0, 1\} \ (\forall i, t) \quad (19)$$

$$Z_{i,t}^{char} + Z_{i,t}^{dischar} \le 1 \ (\forall i, t) \quad (20)$$

$$0 \le P_{i,t}^{char} \le P_{max,i}^{char} \cdot Z_{i,t}^{char} \ (\forall i, t) \quad (21)$$

$$0 \le P_{i,t}^{dischar} \le P_{max,i}^{dischar} \cdot Z_{i,t}^{dischar} \ (\forall i, t) \quad (22)$$

In the given equations, Eq. 17 characterizes the energy storage condition for each time slot, determined by the charging and discharging operations. Considering the conversion loss during power charging and discharging, energy conversion efficiency is incorporated in (17). Furthermore, the state of charge must fall within the specified maximum and minimum energy storage bounds, ensuring satisfaction of Eq. 18. Eqs 19 and 20 articulate the charge/discharge constraints, while (21)–(22) describe the constraints on maximum charging/discharging power.

Integrating the supply side and demand side, the power balance constraints can be derived as follows:

$$P_{i,t}^{grid} = \sum_j^J P_{i,j,t}^{UPS} + \eta_i^{char} \cdot P_{i,t}^{char} - \eta_i^{dischar} \cdot P_{i,t}^{dischar} - \sum_l^L P_{i,l,t}^{unit} - P_{i,t}^{PV} - P_{i,t}^{wind} \ (\forall i, t) \quad (23)$$

Given the spatial and temporal variability of electricity, the electricity bill within each micro grid can be formulated as:

$$C_{i,t}^{grid} = P_{i,t}^{grid} \cdot \pi_{i,t}^{grid} \ (\forall i, t) \quad (24)$$

The operational cost of conventional units is delineated in Eq. 25. As depicted in the equation, the operational cost of conventional units comprises no-load cost, marginal cost, as well as start-up and shut-down costs.

$$C_{i,t}^{unit} = \sum_j^J \left(CU_{i,l}^{unit} \cdot u_{i,l,t}^{unit} + CD_{i,l}^{unit} \cdot v_{i,l,t}^{unit} + CO_{i,l}^{unit} \cdot o_{i,l,t}^{unit} + CM_{i,l}^{unit} \cdot P_{i,l,t}^{unit} \right) (\forall i, t) \quad (25)$$

Also, since the proportion of renewable energy and thermal power is different in different geographical location, the carbon emission rate per kilo W hours is different. Furthermore, the operation of conventional generators in each data center micro grid also generate carbon dioxide. Therefore, the carbon emission in each micro grid can be expressed by:

$$EM_{i,t}^{grid} = P_{i,t}^{grid} \cdot e_{i,t}^{grid} \ (\forall i, t) \quad (26)$$

$$EM_{i,t}^{unit} = P_{i,t}^{unit} \cdot e_{i,t}^{unit} \ (\forall i, t) \quad (27)$$

$$C_{i,t}^{carbon} = \left(EM_{i,t}^{grid} + \sum_l^L EM_{i,l,t}^{unit} \right) \cdot \rho_{i,t} \ (\forall i, t) \quad (28)$$

In the above equations, (26) describes the carbon emission brought about by the electricity bought from the utility grid, (27) describe the carbon of conventional generator, and (28) describe the overall carbon tax in each data center micro grid.

3.3 Optimization problem

In order to address both the economic and environmental impact of energy consumption in data centers, we consider the operational cost and carbon emissions as optimization objectives and use a carbon tax as a proportionality factor to transform the bi-objective optimization problem into a single-objective optimization problem. Hence, the optimization problem can be formulated as follows:

$$min \sum_{i=1}^I \sum_{t=1}^T \left(C_{i,t}^{grid} + C_{i,t}^{unit} + C_{i,t}^{carbon} \right) \quad (29)$$

$$s.t.$$

$$\lambda_{i,j,t} = \zeta_{i,j,t}^{inter} + \sum_a^A \mu_{a,i,j,t}^{batch} \ (\forall i, j, t) \quad (30)$$

$$0 \le \lambda_{i,j,t} \le Cap_{i,j} \ (\forall i, j, t) \quad (31)$$

$$\sum_{t_a^{batch}}^{D_a^{batch}} \mu_{a,i,j,t}^{batch} = \sum_a^A \mu_{total,a}^{batch} \ (\forall a \in A) \quad (32)$$

$$P_{i,j,t}^{servers} \le P_{rated,i,j}^{UPS} \ (\forall i, j, t) \quad (33)$$

$$P_{i,j,t}^{servers} = M_{ij} \times \left(\varphi_{i,j}^{server} \times \lambda_{i,j,t} + P_{i,j}^{idle} \right) (\forall i, j, t) \quad (34)$$

$$\varphi_{i,j}^{server} = P_{i,j}^{peak} - P_{i,j}^{idle} \ (\forall i, j) \quad (35)$$

$$P_{i,j,t}^{Loss\_UPS} = P_{rated,i,j}^{Loss\_UPS} \times \left[a_0 + a_1 \times \frac{P_{i,j,t}^{servers}}{P_{rated,i,j}^{Loss\_UPS}} + a_2 \times \left(\frac{P_{i,j,t}^{servers}}{P_{rated,i,j}^{Loss\_UPS}} \right)^2 \right] (\forall i, j, t) \quad (36)$$

$$P_{i,j,t}^{UPS} = P_{rated,i,j}^{Loss\_UPS} + P_{i,j,t}^{servers} \ (\forall i, j, t) \quad (37)$$

$$P_{min,i,l}^{unit} \cdot o_{i,l,t}^{unit} \le P_{i,l,t}^{unit} \le P_{max,i,l}^{unit} \cdot o_{i,l,t}^{unit} \ (\forall i, j, t) \quad (38)$$

$$-o_{i,l,t-1}^{unit} + o_{i,l,t}^{unit} - o_{i,l,k}^{unit} \le 0, 2 \le k - (t-1) \le MU_{i,l}^{unit} \quad (\forall i, j, t) \quad (39)$$

$$o_{i,l,t-1}^{unit} - o_{i,l,t}^{unit} + o_{i,l,k}^{unit} \le 1, 2 \le k - (t-1) \le MD_{i,l}^{unit} \quad (\forall i, j, t) \quad (40)$$

$$-o_{i,l,t-1}^{unit} + o_{i,l,t}^{unit} + u_{i,l,t}^{unit} \le 0 \ (\forall i, j, t) \quad (41)$$

$$o_{i,l,t-1}^{unit} - o_{i,l,t}^{unit} + v_{i,l,t}^{unit} \le 0 \ (\forall i, j, t) \quad (42)$$

$$P_{i,l,t}^{unit} - P_{i,l,t-1}^{unit} \le \left(2 - o_{i,l,t-1}^{unit} - o_{i,l,t}^{unit} \right) \cdot P_{min,i,l}^{unit} + \left(1 + o_{i,l,t-1}^{unit} - o_{i,l,t}^{unit} \right) \cdot UR_{i,l}^{unit} \ (\forall i, j, t) \quad (43)$$

$$P_{i,l,t-1}^{unit} - P_{i,l,t}^{unit} \le \left(2 - o_{i,l,t-1}^{unit} - o_{i,l,t}^{unit} \right) \cdot P_{min,i,l}^{unit} + \left(1 + o_{i,l,t-1}^{unit} - o_{i,l,t}^{unit} \right) \cdot DR_{i,l}^{unit} \ (\forall i, j, t) \quad (44)$$

$$o_{i,l,t}^{unit}, v_{i,l,t}^{unit}, u_{i,l,t}^{unit} \in \{0, 1\} \ (\forall i, j, t) \quad (45)$$

$$ES_{i,t+1} = ES_{i,t} + \eta_i^{char} \cdot P_{i,t}^{char} - \eta_i^{dischar} \cdot P_{i,t}^{dischar} \ (\forall i, t) \quad (46)$$

$$ES_{min,i} \le ES_{i,t} \le ES_{max,t} \ (\forall i, t) \quad (47)$$

$$Z_{i,t}^{char}, Z_{i,t}^{dischar} \in \{0, 1\} \ (\forall i, t) \quad (48)$$

$$Z_{i,t}^{char} + Z_{i,t}^{dischar} \le 1 \ (\forall i, t) \quad (49)$$

$$0 \le P_{i,t}^{char} \le P_{max,i}^{char} \cdot Z_{i,t}^{char} \ (\forall i, t) \quad (50)$$

$$0 \le P_{i,t}^{dischar} \le P_{max,i}^{dischar} \cdot Z_{i,t}^{dischar} \ (\forall i, t) \quad (51)$$

$$P_{i,t}^{grid} = \sum_j^J P_{i,j,t}^{UPS} + \eta_i^{char} \cdot P_{i,t}^{char} - \eta_i^{dischar} \cdot P_{i,t}^{dischar} - \sum_l^L P_{i,l,t}^{unit} - P_{i,t}^{PV} - P_{i,t}^{wind} \ (\forall i, t) \quad (52)$$

$$C_{i,t}^{grid} = P_{i,t}^{grid} \cdot \pi_{i,t}^{grid} \ (\forall i, t) \quad (53)$$

$$C_{i,t}^{unit} = \sum_j^J \left(CU_{i,l}^{unit} \cdot u_{i,l,t}^{unit} + CD_{i,l}^{unit} \cdot v_{i,l,t}^{unit} + CO_{i,l}^{unit} \cdot o_{i,l,t}^{unit} + CM_{i,l}^{unit} \cdot P_{i,l,t}^{unit} \right) (\forall i, t) \tag{54}$$

$$EM_{i,t}^{grid} = P_{i,t}^{grid} \cdot e_{i,t}^{grid} \ (\forall i, t) \tag{55}$$

$$EM_{i,t}^{unit} = P_{i,t}^{unit} \cdot e_{i,t}^{unit} \ (\forall i, t) \tag{56}$$

$$C_{i,t}^{carbon} = \left(EM_{i,t}^{grid} + \sum_l^L EM_{i,l,t}^{unit} \right) \cdot \rho_{i,t} \ (\forall i, t) \tag{57}$$

As indicated above, the optimization objective is to minimize the system's operational cost, comprising electricity costs, operational costs of conventional units, and carbon taxes. Constraints (30)–(37) pertain to the power demand side, while constraints (38)–(52) ensure the functionality of the power supply side. Eqs 53–57 detail the operational cost and carbon emissions. The decision variables for the optimization problem encompass the allocation of interactive and batch workloads, as well as the operational schedule of energy storage systems (ESS) and conventional generator units. The proposed resource planning model is formulated as a mixed-integer linear programming (MILP) problem.

4 Case study

In this section, a geo-distributed data center micro grid system sample is created to assess the proposed methodology outlined in this paper. All system modeling and solving algorithms are implemented in the Gurobi platform (CPLEX, 2009), a widely employed tool for solving binary programming or mixed-integer programming problems. The simulations are executed on a desktop computer equipped with an Intel Core i5-8400 CPU @ 2.80GHz and 8 GB memory.

4.1 Simulation setup

To separately verify the impact of UPS characteristics and multiple data center scheduling on the optimization objectives, this study sets up two simulation scenarios: one with a single data center to verify the effect of UPS characteristics, and the other with multiple data centers to verify the effectiveness of multiple data center scheduling and the proposed approach. Within each micro grid, two conventional generators (one coal-based and another gas-based), along with distributed solar and wind generation units, are employed. Additionally, an energy storage system is integrated. These micro grids are interconnected with the utility grid, and each micro grid serves as the power source for a designated data center. In each data center, three UPS nodes supply power to servers. The simulation encompasses three types of UPSs, and to maintain simplicity, the deployment of these UPS types is identical across the data centers, meaning each data center features one of each UPS type. For ease of representation, the type and number of servers powered by the UPS nodes are also uniform. The system parameters are detailed in Tables 1–4. In the experiment, the time horizon T is set to be 24 h, which is the maximum time to get a relatively accurate electricity price and load status.

The attributes of conventional generation units and the energy storage system are calibrated using data from ERCOT scheduling data (Cao et al., 2019). Workload data is derived from Hu's (Hu et al., 2021) and Guo's (Guo et al., 2019) research papers. For the simulation scenario, it is assumed that the three data centers are located in Texas, New York, and California. Real-time electricity price data, solar and wind power output data are sourced from ERCOT (ERCOT, 2023), CAISO (CAISO, 2023), and NYISO (NYISO, 2023), respectively. Furthermore, the proportion of coal and gas in local electricity generation is collected from the website of U.S. energy and information administration and listed in Table 5 (EIA, 2023).

4.2 Case study in single data center

To avoid potential interaction effects between the two proposed improvements, we adopt the single-variable principle and conduct simulations separately. Specifically, we first set up a simulation with a single data center to verify the effectiveness of considering UPS characteristics in the process of reducing the operational cost and carbon emission. The simulation settings are as follows:

Case I. In a single data center, there are three groups of UPS with different supply efficiency and energy consumption characteristics. However, in the process of objective function calculating and scheduling optimization, the impact of UPS characteristics is not taken into account, and the computational workload is evenly distributed among the three UPS.

Case II. In a single data center, there are three groups of UPS with different supply efficiency and energy consumption characteristics. In the process of objective function calculating and scheduling optimization, the impact of UPS characteristics is taken into account, and the computational workload is optimally distributed among the three UPS.

4.3 Case study of multiple data center

To validate the effectiveness of the improvement that extending the optimization from single data center to multiple data center and takes the carbon tax and operational cost as dual-objective, we conducted simulation of three data centers system and established four scenarios as follows:

TABLE 1 Parameters of data centers.

UPS node	Maximum capacity (MW)	Number of servers	UPS type
Node 1	15	$6*10^4$	1
Node 2	15	$6*10^4$	2
Node 3	15	$6*10^4$	3

TABLE 2 UPS paramenters.

UPS Types	Power loss equation parameters		
	a_0	a_1	a_2
1	0.0086	0.0241	−0.0027
2	0.0241	0.0353	0.0617
3	0.0518	0.1787	0.0947

TABLE 3 Paramenters of conventional generator units.

Unit	Fuel type	High/Low sustainable limit (MW)	Ramp Up/ Down rate (MW/h)	Minimum Up/Down time (h)	Initial state	Initial power (MW)	Start-up/ Shut-down Cost ($)	No load Cost ($)	Marginal Cost ($/MWh)
Unit 1	Gas	15/5	4/4	4/4	On	10	50	40	18
Unit 2	Coal	20/9	6/6	3/3	On	14	40	30	16

TABLE 4 Paramenters of energy storage system.

Maximum/Minimum state (MWh)	Initial/Final state (MWh)	Maximum charge/Discharge rate (MW/h)	**Charge/Discharge efficiency**
30/5	5	5	0.8

TABLE 5 Energy structure and carbon emission rate.

City	**Proportion of coal (%)**	Proportion of gas (%)	Carbon emission Rate(kg/MWh)
Texas	16.75	52.05	381.55
New York	0.11	40.92	170.09
California	0.15	47.67	198.34

Case III. Three data centers are simulated, and the computational workload is evenly distributed among them, and the optimization objective is set to be the dual-objective of reducing the carbon tax and operational cost. Furthermore, the UPS characteristics are not considered in the process of objective function calculating and scheduling optimization.

Case IV. Three data centers are simulated, and the computational workload distribution among them is optimized, and the optimization objective is set to be the single-objective of reducing the carbon tax. Furthermore, the UPS characteristics are not considered in the process of objective function calculating and scheduling optimization.

Case V. Three data centers are simulated, and the computational workload distribution among them is optimized, and the optimization objective is set to be the dual-objective of reducing the carbon tax and operational cost. Furthermore, the UPS characteristics are not considered in the process of objective function calculating and scheduling optimization.

Case VI. Three data centers are simulated, and the computational workload distribution among them is optimized, and the optimization objective is set to be the dual-objective of reducing the carbon tax and operational cost. Furthermore, the UPS characteristics are considered in the optimization.

By comparing Case III and Case V, it can be shown that multiple data center scheduling has advantages over single IDC scheduling in terms of energy saving and carbon emission reduction. By comparing Case IV and Case V, it can be demonstrated that multi-objective optimization is superior to its counterpart which takes the carbon emission as the single optimization objective. By comparing Case V and Case VI, it can be shown that the combination of the proposed optimization methods can further improve the optimization results.

4.4 Result analysis

4.4.1 Result in single data center

The simulation results of Case I and Case II has been listed in Table 6. As can be seen in the table, the total operational cost has been reduced by 3.11%, and the carbon emission has been reduced by 3.48%. The total cost which includes the operational cost and carbon tax has been reduced by 3.24%.

To further demonstrate the impact of computation and UPS characteristics on optimization results, we compared the distribution of computing loads on UPS nodes between Case I and Case II, which has been plotted in Figure 7. It can be observed that in Case I, the computing load is evenly distributed, while in Case II, the computing load is mostly distributed on UPS1 and UPS2, which have higher power

10.3389/fenrg.2024.1344837

TABLE 6 Comparision of simulation results in three data centers.

Case III			Case IV			Case V			Case VI		
Operational Cost ($)	Carbon emission (kg)	Total cost ($)	Operational cost ($)	Carbon emission (kg)	Total cost ($)	Operational cost ($)	Carbon emission (kg)	Total cost ($)	Operational cost ($)	Carbon emission (kg)	Total cost ($)
15441	381500	23071	15691	308200	21855	13480	341470	20309	12815	342560	19665

supply efficiency and lower operating energy consumption. This confirms that computation and UPS characteristics have an effect on computing load distribution.

In order to further compare the carbon emissions, the hourly carbon emissions of Case I and Case II were plotted in Figure 8. It can be seen that after optimization (Case II), carbon emissions are significantly reduced.

4.4.2 Result in multiple data center

The simulation results of Case III to Case VI has been listed in Table. 7.

By comparing Case III and Case V, it can be shown that the operational cost, carbon emission and total cost in Case V decreased by approximately 12.7%, 10.5%, and 11.9% respectively, which has proved that the workload scheduling among multiple data center micro grids can bring about significant improvement in energy consumption and carbon emission reduction compared to single data center scheduling.

By comparing Case IV and Case V, it can be shown that the carbon emission has decreased by 10.76% compared to Case V, while the operational cost and total cost in increase 16.38% and 7.61% respectively, which has illustrated that the multi-objective optimization can perform better than the single-objective optimization.

Furthermore, by comparing Case V and Case VI, it can be concluded that Case VI resulted in a decrease of approximately 4.93%, 0.32%, and 3.17% for the operational cost, carbon emission, and total cost, respectively, compared to Case V. This has proved that considering UPS characteristics in the multiple data center scheduling can still reduce the total costs and carbon emission, and the Case VI which has adopted the proposed method performs better than any other cases.

4.4.3 Application and shortcomings

The proposed method can be easily implemented in the existing infrastructure without the need to add new hardware or change the platform since the self-contained network devices can sufficiently support the application of the proposed scheduling method.

Another difficulty that may hinder the application of our method is the control of the micro grid devices and the cooperative operation with data centers. However, the development of communication technology and automatic controllers makes such interaction conveniently (Cui, 2016). Therefore, this difficulty can be easily overcome in implementation.

The servers in this paper are modeled to be of the same type. However, in implementation, there are also data centers where the servers are heterogeneous. This method may not be applicable to heterogeneous data centers. The joint workload scheduling in heterogeneous data centers can be further explored in the future research.

5 Conclusion

This article proposes a dual-objective optimization method for the operational cost and carbon emission of a multi-data center micro grid that considers the characteristics of Uninterruptible Power Supplies

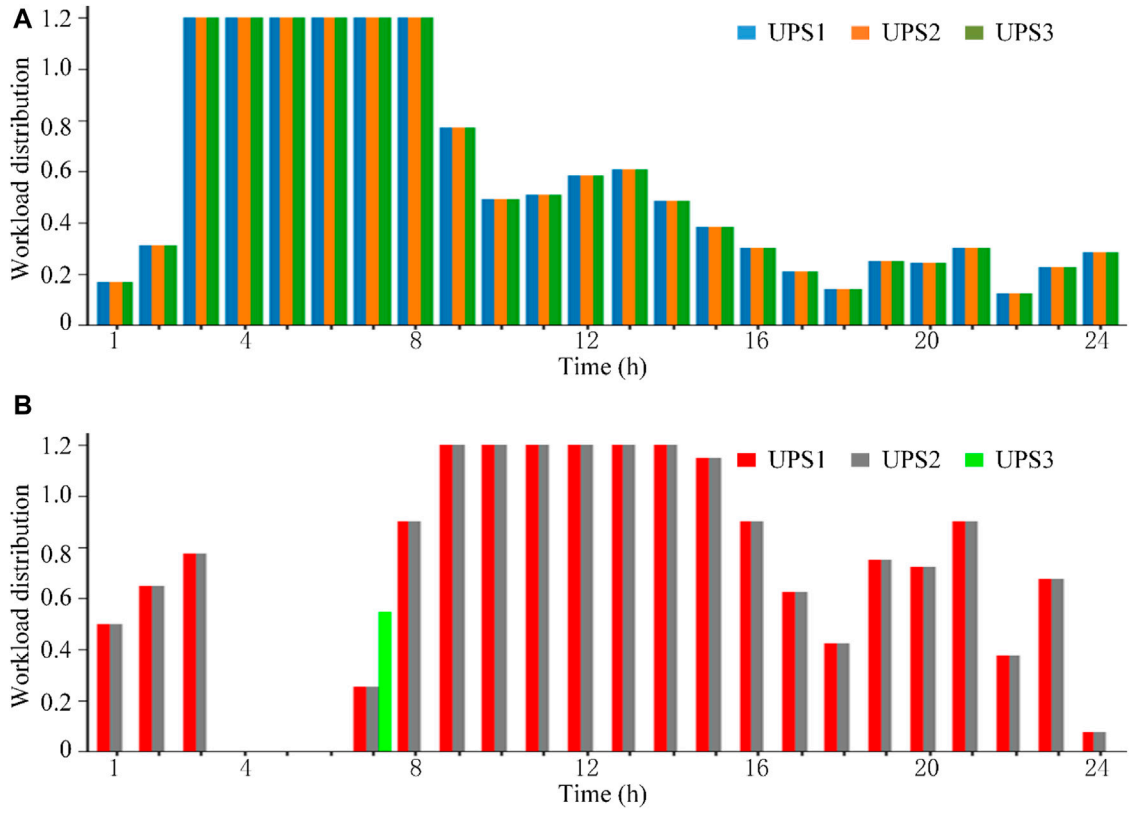

FIGURE 7
Computational workload distribution in **(A)** Case I, **(B)** Case II.

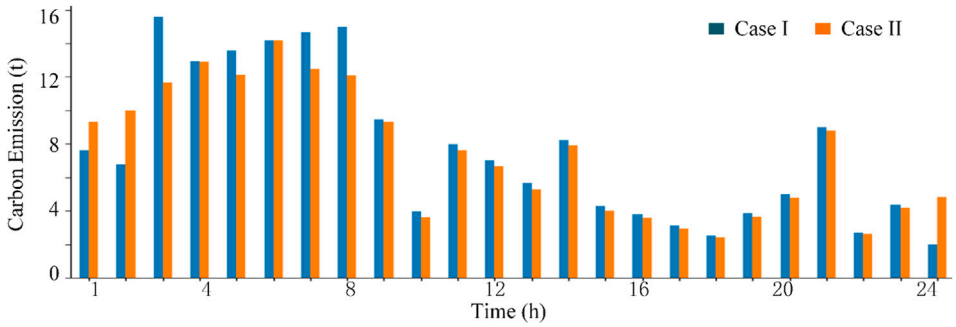

FIGURE 8
Hourly carbon emission in Case I and Case II.

TABLE 7 Comparision of simulation results in single data center.

Case I			Case II		
Operational Cost ($)	Carbon Emission (kg)	Total Cost ($)	Operational Cost ($)	Carbon Emission (kg)	Total Cost ($)
6150.4	183300	9816.4	5959.8	176930	9498.53

(UPS) and load flexibility. The article improves the energy consumption model of UPS and fully utilizes the scheduling flexibility of computing loads in time and space dimensions. Carbon tax is used as a balancing criterion to compromise the optimization objectives of carbon emission and operational cost, achieving further optimization of both cost and carbon emission. Simulation results indicate that the proposed method effectively reduces operational costs by 4.93%–12.7%, decrease carbon emissions by up to 10%, and lower total costs by 3.17%–11.9%.

Data availability statement

The original contributions presented in the study are included in the article/Supplementary material, further inquiries can be directed to the corresponding author.

Author contributions

XH: Conceptualization, Methodology, Software, Writing–original draft. PL: Formal Analysis, Methodology, Software, Writing–original draft. YD: Conceptualization, Resources, Supervision, Visualization, Writing–review and editing.

Funding

The author(s) declare that no financial support was received for the research, authorship, and/or publication of this article.

Conflict of interest

Author H-GG was employed by Ningxia Hongdunzi Coal Ind.

The remaining authors declare that the research was conducted in the absence of any commercial or financial relationships that could be construed as a potential conflict of interest.

Publisher's note

References

Ahmed, M. H., Fei, C., Lee, F. C., and Li, Q. (2017). 48-V voltage regulator module with PCB winding matrix transformer for future data centers. *IEEE Trans. Industrial Electron.* 64 (12), 9302–9310. doi:10.1109/tie.2017.2711519

Brannvall, R. "EDGE: microgrid data center with mixed energy storage," in Proceedings of the Eleventh ACM International Conference on Future Energy Systems, Sydney, Australia, June 2020, 466–473.

CAISO (2023). CAISO. http://www.caiso.com.

Cao, F., Wang, Y., Zhu, F., Cao, Y., and Ding, Z. (2019). UPS node-based workload management for data centers considering flexible service requirements. *IEEE Trans. Industry Appl.* 55 (6), 5533–5542. doi:10.1109/tia.2019.2933791

Carbon Tax Center, (2021). Where carbon is taxed. Available: http://www.carbontax.org/where-carbon-is-taxed/.

Cplex, I. B. M. ILOG (2009). 'V12.1: user's manual for CPLEX. *Int. Bus. Mach. Corp.* 46 (53), 157.

Cui, X., Wang, X., and Zhang, Y. (2016). Residential Appliances Direct load control in real-time using cooperative game. *IEEE Trans. Power Syst.* 31 (1), 226–233. doi:10.1109/tpwrs.2015.2391774

Delforge, P. (2014). *Americas data centers consuming and wasting growing amounts of energy*. New York, NY, USA: Natural Resource Defense Council.

Ding, Z., Xie, L., Lu, Y., Wang, P., and Xia, S. (2018). Emission-aware stochastic resource planning Scheme for data center microgrid considering batch workload scheduling and Risk management. *IEEE Trans. Industry Appl.* 54 (6), 5599–5608. doi:10.1109/tia.2018.2851516

EIA (2023). Available: https://www.eia.gov/.

ERCOT (2023). Available: http://www.ercot.com.

Guo, J. "Who limits the resource efficiency of my datacenter: an analysis of alibaba datacenter traces,' IWQoS '19," in Proceedings of the International Symposium on Quality of Service, Phoenix, Arizona, June 2019, 39.

Hu, B., Cao, Z., and Zhou, M. (2021). Energy-minimized scheduling of real-time parallel workflows on heterogeneous distributed computing systems. *IEEE Trans. Serv. Comput.* 15 (5), 2766–2779. doi:10.1109/tsc.2021.3054754

Li, C., Liu, Y., Cao, Y., Tan, Y., and Tang, S., (2011). Consistency evaluation of low-carbon generation dispatching and energy-saving generation dispatching. *Proc. CSEE* 31 (31), 1–8.

Li, J., and Qi, W. (2018). Toward optimal operation of internet data center microgrid. *IEEE Trans. Smart Grid* 9 (2), 971–979. doi:10.1109/tsg.2016.2572402

Liu, J., Xu, Z., Wu, J., Liu, K., Sun, X., and Guan, X. (2023). Optimal planning of internet data centers decarbonized by hydrogen-water-based energy systems. *IEEE Trans. Automation Sci. Eng.* 20 (3), 1577–1590. doi:10.1109/TASE.2022.3213672

Liu, X., Xie, L., and Liu, W., (2012). Coordinated energy cost management of distributed internet data centers in smart grid. *IEEE Trans. Smart Grid* 3 (1), 50–58. doi:10.1109/tsg.2011.2170100

Liu, Y., Wei, X., Xiao, J., Liu, Z., Xu, Y., and Tian, Y. (2020). Energy consumption and emission mitigation prediction based on data center traffic and PUE for global data centers. *Glob. Energy Interconnect.* 3 (3), 272–282. doi:10.1016/j.gloei.2020.07.008

Luo, Y., Andresen, J., Clarke, H., Rajendra, M., and Maroto-Valer, M. (2019). A decision support system for waste heat recovery and energy efficiency improvement in data centres. *Appl. Energy* 250 (1), 1217–1224. doi:10.1016/j.apenergy.2019.05.029

Misaghian, M. S., Tardioli, G., Cabrera, A. G., Salerno, I., Flynn, D., and Kerrigan, R. (2023). Assessment of carbon-aware flexibility Measures from data centres using machine learning. *IEEE Trans. Industry Appl.* 59 (1), 70–80. doi:10.1109/TIA.2022.3213637

Na, H., Sun, J., Qiu, Z., Yuan, Y., and Du, T. (2022). Optimization of energy efficiency, energy consumption and CO2 emission in typical iron and steel manufacturing process. *Energy* 257, 124822. doi:10.1016/j.energy.2022.124822

Ni, J., and Bai, X. (2017). A review of air conditioning energy performance in data centers. *Renew. Sustain. Energy Rev.* 67, 625–640. doi:10.1016/j.rser.2016.09.050

Nyiso, (2023). Available: http://www.nyiso.com.

Peter, A. (2017). *Data centers and advanced microgrids*. Rueil-Malmaison, France: Schneider Electric.

Pratt, A., Kumar, P., and Aldridge, T., "Evaluation of 400V DC distribution in Telco and data centers to improveenergy efficiency," in Proceedings of the 29th International Telecommunications Energy Conference, Rome, Italy, 32–39.

Qi, W., Li, J., Liu, Y., and Liu, C. (2019). Planning of distributed internet data center microgrids. *IEEE Trans. Smart Grid* 10 (1), 762–771. doi:10.1109/tsg.2017.2751756

Ting, Y., Jiang, H., Hou, Y., and Geng, Y., (2022). Study on carbon neutrality regulation method of interconnected multi-datacenter based on spatio-temporal dual-dimensional computing load migration. *Proc. CSEE* 42 (01), 164–177.

Wang, Q., Guan, Y., and Wang, J. (2012). A chance-constrained two-stage stochastic program for unit commitment with uncertain wind power output. *IEEE Trans. Power Syst.* 27 (1), 206–215. doi:10.1109/tpwrs.2011.2159522

World Bank Group (2020). State and trends of carbon pricing 2020. Available: https://openknowledge.worldbank.org/handle/10986/33809.

Wu, Z., Chen, L., Wang, J., Zhou, M., Li, G., and Xia, Q. (2023). Incentivizing the spatiotemporal flexibility of data centers toward power system coordination. *IEEE Trans. Netw. Sci. Eng.* 10 (3), 1766–1778. doi:10.1109/TNSE.2023.3234445

Yang, T., Jiang, H., Hou, Y., and Geng, Y. (2023). Carbon management of multi-datacenter based on spatio-temporal Task migration. *IEEE Trans. Cloud Comput.* 11 (1), 1078–1090. doi:10.1109/TCC.2021.3130644

Ye, G., and Gao, F., (2022). Coordinated optimization scheduling of data center and electricity retailer based on cooperative game theory. *CPSS Trans. Power Electron. Appl.* 7 (3), 273–282. doi:10.24295/cpsstpea.2022.00025

Yu, L., Jiang, T., Cao, Y., and Qi, Q. (2014). Carbon-aware energy cost minimization for distributed internet data centers in smart microgrids. *IEEE Internet Things J.* 1 (3), 255–264. doi:10.1109/jiot.2014.2322606

Zhang, Y., Zhang, B., Zhou, Y., Xu, H., and Liu, W., (2023). Research on interactive integration planning of data centers and distribution network driven by carbon emission reduction. *Trans. China Electrotechnical Soc.* 38 (23), 6433–6450.

Zhao, S., Khan, N., Nagarajan, S., and Trescases, O. (2019). Lithium-ion-capacitor-based distributed UPS architecture for reactive power mitigation and phase balancing in datacenters. *IEEE Trans. Power Electron.* 34 (8), 7381–7396. doi:10.1109/tpel.2018.2878682

Zhou, Z., Liu, F., Zou, R., Liu, J., Xu, H., and Jin, H. (2016). Carbon-aware online control of geo-distributed Cloud services. *IEEE Trans. Parallel Distributed Syst.* 27 (9), 2506–2519. doi:10.1109/tpds.2015.2504978

frontiers | Frontiers in Energy Research

TYPE Original Research
PUBLISHED 14 March 2024
DOI 10.3389/fenrg.2024.1345839

OPEN ACCESS

EDITED BY
Lu Zhang,
China Agricultural University, China

REVIEWED BY
Haiwen Chen,
Hebei University of Technology, China
Na Zhang,
Inner Mongolia University of Technology, China
Shouxiang Wang,
Tianjin University, China
Ghaeth Fandi,
Czech Technical University in Prague, Czechia

*CORRESPONDENCE
Tang Baofeng,
bftang2023@163.com

RECEIVED 28 November 2023
ACCEPTED 27 February 2024
PUBLISHED 14 March 2024

CITATION
Baofeng T, Lei H, Lidong Z, Hongtao Z, Kang W and Pengliang Z (2024), Robust fault recovery strategy for multi-source flexibly interconnected distribution networks in extreme disaster scenarios.
Front. Energy Res. 12:1345839.
doi: 10.3389/fenrg.2024.1345839

Robust fault recovery strategy for multi-source flexibly interconnected distribution networks in extreme disaster scenarios

Tang Baofeng*, He Lei, Zhou Lidong, Zhao Hongtao, Wang Kang and Zhang Pengliang

State Grid XiongAn New Area Electric Power Supply Company, Xiong'an New Area, Hebei, China

To enhance the resilience of power distribution networks against extreme natural disasters, this article introduces a robust fault recovery strategy for multi-source, flexible interconnected power distribution networks, particularly under scenarios of extreme disasters. Initially, the comprehensive risk of system failure due to ice load on distribution lines and poles is fully considered, and a model for the overall failure rate of lines is constructed. This model addresses the diverse failure scenarios triggered by various meteorological conditions. Through the use of information entropy, typical extreme disaster failure scenarios are identified, and lines with high failure rates under these scenarios are determined. Subsequently, a box-type interval model is developed to represent the uncertainty in the output of distributed generation (DG), and on this basis, a robust fault recovery model for multi-source power distribution networks interconnected through soft open points (SOPs) is established, and use the Column and Constraint Generation (C&CG) algorithm to solve the problem. Finally, the fault recovery model and strategy proposed are validated through an illustrative example based on a modified IEEE 33-node interconnected system.

KEYWORDS

extreme disasters, fault recovery, robust, soft open point, Column and constraint generation

1 Introduction

In recent years, the frequency and intensity of extreme weather events, such as severe ice and snow storms, hurricanes, and floods, have significantly increased (Nasri et al., 2022). The complexity of their operating environments and the vulnerability of numerous components to external conditions make distribution networks particularly susceptible to these extreme weather phenomena, often resulting in widespread power outages (Jufri et al., 2019). While existing research on power distribution network fault recovery has predominantly focused on the electrical characteristics of the networks, it has largely overlooked the comprehensive impact of meteorological conditions and natural disasters. This includes a notable gap in integrating collected weather data with early warning systems for accidents, which is crucial for enhancing response strategies and reducing the vulnerability of these networks to such catastrophic events.

To mitigate the impacts of extreme natural disasters on distribution networks, scholars from around the world have developed specific disturbance event models tailored to extreme weather conditions (Dehghani et al., 2021). For example, Ref. (Zhou et al., 2018). explored the influence of typhoon conditions on the fault rates of distribution network lines, establishing a model that correlates typhoon wind speed and direction with line fault rates. Similarly, other research has formulated models to assess the fault rates of distribution networks during severe ice, snow, and earthquake conditions (Yang et al., 2020; Yan et al., 2021). In an effort to bolster the resilience of distribution networks, researchers have proposed a variety of response strategies, focusing on network planning and operational scheduling. These strategies encompass both preventive measures before disasters strike and recovery actions post-disaster (Gazijahani et al., 2022). However, existing research mainly focuses on post-disaster recovery measures aimed at prioritizing the restoration of power supply to users. Although traditional distribution networks can restore power supply to outaged areas through network reconfiguration, their capabilities are limited in cases of main network disconnection or multiple faults caused by extreme disasters. According to the IEEE 1547-2003 standard (Standards Coordinating Committee, 2003), improving the reliability of power supply requires users to implement local DG islanding operation under technical compliance, to maximize the recovery of lost loads. Within this framework, researchers are delving into post-disaster fault recovery strategies for active distribution networks through various innovative approaches. These include heuristic algorithms (Gao et al., 2016), multi-agent systems (Li et al., 2020b), artificial intelligence algorithms (Wang et al., 2018), and mathematical programming methods (Li et al., 2019).

Regarding recovery strategies, Ref. (Yin et al., 2023). introduced a novel approach for fault recovery in active distribution networks, focusing on networks with reducible loads. Ref. (Liu et al., 2020). developed a two-step fault recovery methodology that initially reconfigures the main network before segmenting the remaining unrecovered sections into isolated islands. Ref. (Li et al., 2020b). further integrated the concepts of island partitioning and network reconfiguration, presenting a comprehensive fault recovery strategy for active distribution networks. Due to the uncertainty of DG output that can affect the effectiveness of fault recovery, it is necessary to consider this uncertainty in the active distribution network fault recovery model. Common methods to handle this uncertainty include interval optimization (Wang et al., 2020), stochastic optimization (Lu et al., 2020), and robust optimization (Chen et al., 2016). Robust optimization has been widely applied due to its ability to operate without describing probability distributions, with main solution methods including the Benders decomposition method (Han Gao and Zhengshuo Li, 2021) and the C&CG algorithm (Chuan He et al., 2017). Considering the uncertainty of load and DG output, a two-stage robust fault recovery strategy was proposed in (Zhao et al., 2020). Another study considered the uncertainty of wind and photovoltaic unit output and proposed a robust island recovery strategy for distribution networks using electric vehicles as emergency dispatch resources (Chen et al., 2018).

However, the above fault recovery strategies have not effectively modeled the fault rate of distribution networks under extreme natural disasters, and thus cannot fully address the impact of extreme natural disasters on distribution networks (Li et al., 2023). Particularly, as a flexible power electronic device, the SOP can provide necessary voltage support in the event of a fault, effectively expanding the possibilities for fault recovery and significantly enhancing the self-healing capability of the distribution network (Ali Arefifar et al., 2023). This role was verified in a study where the SOP was shown to play a key role in the recovery of distribution system faults, significantly enhancing the supply range and overall resilience of the system (Li et al., 2020a). In light of this, the primary objective of this study is to bolster the resilience of power distribution networks against extreme natural disasters and to expedite the restoration of power to areas impacted by outages. This research endeavors to investigate fault recovery strategies for distribution networks under extreme weather conditions. Through the lens of case study analysis, the efficacy of the proposed model and strategies in quickly reinstating critical loads within distribution networks under severe disaster scenarios has been corroborated. The principal contributions of this paper are delineated as follows:

(1) A model to predict fault rates in lines and poles under severe weather conditions has been developed, employing the information entropy method to pinpoint scenarios with an increased likelihood of failure. This method effectively tackles the myriad of fault scenarios arising in complex meteorological conditions, thereby enhancing the reliability of the distribution network.
(2) A comprehensive fault recovery model for a multi-sourced distribution network, interconnected through the use of SOPs, has been established. Tailored recovery strategies for lines prone to frequent faults were devised, aiming for swift restoration of service following power outages by implementing pre-designed recovery plans in the event of actual faults.
(3) A box-type interval model has been formulated to encapsulate the uncertainty inherent in DG outputs. The advanced robust fault recovery strategy, which prepares for the most adverse DG output scenarios, outperforms traditional deterministic approaches by offering enhanced recovery effectiveness and greater resilience to the unpredictability in DG outputs.

The remainder of the paper is organized as follows: Section 2 involves the construction of a fault model and the filtration of fault scenarios. Section 3 develops a robust fault recovery model for a multi-sourced distribution network interconnected with SOPs. Section 4 provides a detailed description of the solution methodology. Section 5 conducts a case study analysis, and Section 6 concludes the paper with a summary of its findings.

2 Fault model construction and scenario filtering

2.1 Fault rate model

During extreme natural disasters, the ice load on power lines is considered to gradually increase over time. When the ice layer becomes overloaded, significant bending occurs in the line.

Excessive bending deformation can lead to line breakage. The ice overload or breakage of lines results in an increase in unbalanced loads on the poles. If the acting load exceeds the pole's maximum load-bearing capacity, the crossarms may be damaged, leading to bending and twisting of the pole itself, eventually causing breakage and collapse.

2.1.1 Ice load on distribution lines

Many factors influence the ice load on distribution lines, including the intensity and duration of the disaster, as well as the distance from the center of the storm. By establishing a mathematical model using a coordinate system with the root node of the distribution feeder as the origin, the variation in ice thickness over time for a particular segment of the line j can be deduced and represented as Eqs 1, 2:

$$L_{ice}\left(x_j, y_j, t\right) = \int_0^t A_{rate} \exp\left(-\frac{1}{2}\left(\left(\frac{x_j - \mu_x(t)}{\sigma_x}\right)^2 + \left(\frac{y_j - \mu_y(t)}{\sigma_y}\right)^2\right)\right)dt \tag{1}$$

$$\begin{aligned} \mu_x(t) &= \mu_x(0) + V_{ice}\cos(\theta)t \\ \mu_y(t) &= \mu_y(0) + V_{ice}\sin(\theta)t \end{aligned} \tag{2}$$

where A_{rate} indicates the ice growth rate on the line, i.e., the change in ice coverage per unit length of line per unit time, expressed as Eq. 3:

$$A_{\text{rate}} = \frac{-0.0277D_{\text{line}} + \sqrt{(0.0277D_{\text{line}})^2 + 1.088a_{\text{rate}}}}{0.0554} \tag{3}$$

where a_{rate} is the ice growth rate factor, affected by disaster factors such as temperature, wind speed, and precipitation rate, expressed as Eq. 4:

$$a_{\text{rate}} = a_0 + a_1 T_{\text{temp}} + a_2 V_{\text{wind}} + a_3 P_{\text{preci}} \tag{4}$$

2.1.2 Ice load on tower

When considering the ice load on poles, several factors need to be taken into account: the impact of wind on ice accumulation on poles, the effect of the swaying of power lines hung on the poles, and the calibration of more straightforward design equations. In the ice-loading model for the tower-line system, the ice loads on insulator strings and poles are relatively minor compared to their own structural loads and can be neglected. Therefore, the focus is on calculating the ice loads on the conductors and ground wires. The unit ice load on power lines is as Eq. 5:

$$G_{ice}(t) = 0.0277L_{ice}(t) \times \left(L_{ice}(t) + D_{line}\right) \tag{5}$$

The ice load exerted on the poles by the power lines hanging at both ends primarily arises from the tension in the lines. In the case of uniform, windless conditions, it's necessary to calculate the vertical load borne by the pole, as Eq. 6:

$$G_{pole}(t) = G_{ice}(t)\left(\frac{l_1 + l_2}{2} + \left(\frac{F_{l1}h_1}{G_{ice}(t)l_1} + \frac{F_{l2}h_2}{G_{ice}(t)l_2}\right)\right) \tag{6}$$

where F_{l1} and F_{l2} represent the horizontal tension in the lines on either side of the pole. l_1 and l_2 are the span lengths on both sides of the pole. h_1 and h_2 denote the difference in height between the suspension points on either side of the pole, with a positive value indicating the neighboring pole is higher, and negative if it is lower.

2.1.3 Overall line fault rate

The aim of the component damage assessment method is to evaluate how weather conditions affect various components of the distribution network. The damage probability to the distribution network from extreme natural disasters is represented by fault rate curves, with the existing fault probability of distribution support structures approximated as an exponential function using historical data. The ice load ratio, described as the ratio of ice load to the design load of the distribution network, is used in conjunction with the relationships between line ice thickness, pole load, and line fault rate to establish a mathematical model for line fault rate, as Eq. 7:

$$\begin{cases} P_{ice}^{line}(t) = a_{line}e^{\frac{\eta_{line}(t)}{b_{line}}} \\ P_{ice}^{pole}(t) = a_{pole}e^{\frac{\eta_{pole}(t)}{b_{pole}}} \end{cases} \tag{7}$$

In severe weather conditions like ice and snow, multiple faults can occur along most lines, and the fault rate of a distribution line can be considered as the sum of the fault rates of each line and pole along that line. To facilitate the simulation of multiple faults along a line under extreme weather conditions, the lines can be divided into multiple segments based on span length and then connected in series. The overall fault rate of the line is given as Eq. 8:

$$P_{fault.j}(t) = 1 - \prod_m \left(1 - P_{ice.j.m}^{pole}(t)\right)\prod_n \left(1 - P_{ice.j.n}^{line}(t)\right) \tag{8}$$

2.2 Selection of typical fault scenarios

The primary impact of extreme weather on distribution networks is manifested in the significant increase in line fault rates and the occurrence of multiple line faults. Given the multitude of distribution network lines and the vast number of fault scenarios corresponding to different meteorological conditions, each with varying line fault rates, it is feasible to select typical fault scenarios based on their randomness. These scenarios can then provide the line fault rates necessary for research on distribution network fault recovery. Information entropy is a method used to quantify the disorder in a system (Shannon, 1948). The selection of typical fault scenarios based on the fault rates of distribution network lines involves choosing scenarios with a high probability of occurrence. The information entropy is represented as Eq. 9:

$$W = \sum_{i\in\Omega_l}\left(-\log_2 P_{j,t}^{\text{fault}}\right)\tau_{j,t}\ t \in T_{ice} \tag{9}$$

Each fault scenario corresponds to an $\tau_{j,t}$ vector, representing the entropy value of the system under that scenario. The occurrence probability of a typical fault scenario is relatively high, so its information entropy W should not be too large or too small and must satisfy the Eq. 10:

$$\begin{cases} W_{\min} \le \sum_{j\in\Omega_l}\left(-\log_2 P_{j,t}^{\text{fault}}\right)\tau_{j,t} \le W_{\max} \\ \sum_t \tau_{j,t} \le 1 \end{cases} \quad t \in T_{ice} \tag{10}$$

By calculating the entropy values of the distribution network under different scenarios and selecting typical fault scenarios based

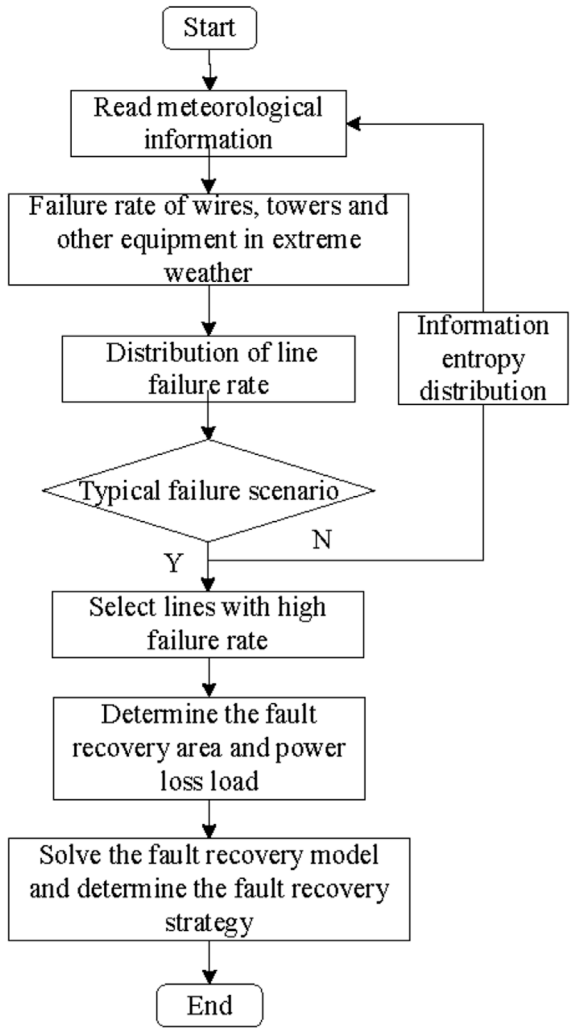

FIGURE 1
Fault recovery process of distribution network under extreme weather scenarios.

on reasonable entropy value limits, the fault lines corresponding to these entropy values can be identified. These identified fault lines are then used for the next step in the study of distribution network fault recovery measures.

2.3 Fault recovery process for distribution networks under extreme weather scenarios

The fault recovery process for distribution networks under extreme weather scenarios is illustrated in Figure 1.

Step 1: Input meteorological parameters for the extreme weather scenario and relevant data about the distribution network structure.

Step 2: Calculate the distribution of fault rates for each line under the current meteorological parameters using the ice load-based line fault rate model.

Step 3: Generate multiple fault scenarios by changing meteorological parameters, and calculate the corresponding entropy values using the information entropy formula.

Step 4: Determine whether the selected scenario is a typical fault scenario. If it is, select the high fault rate lines in that scenario and formulate a fault recovery strategy for them. if not, return to Step 2.

3 Robust fault recovery strategy for multi-source distribution networks interconnected with SOPs

3.1 Objective function

The objective is to minimize the sum of the load shedding amount, network loss cost, and DG operating cost, which is represented as:

$$f = \min_{\mathbf{x}} \max_{\mathbf{u}\in\mathbf{U}} \min_{\mathbf{h}} \left[\lambda_1 \sum_{i\in\Omega_n} (1-y_i) w_l P_{i,\text{load}} + \lambda_2 \left(\sum_{ij\in\Omega_b} I_{ij}^{sqr} R_{ij} + \sum_{i\in\Omega_n} \left(aP_{i,\text{DG}}{}^2 + bP_{i,\text{DG}} + c \right) \right) \right] \tag{11}$$

Analyzing Eq. 11, it's evident that the objective function of the proposed robust fault recovery strategy is a min-max-min problem: The first layer min problem uses **x** as the decision variable, aiming to generate a network topology with the least load shedding. The second layer max problem uses **u** as the decision variable to find the worst-case fluctuation scenario for DG injection power within the given uncertainty set **U**. The third layer min problem uses **h** as the decision variable.

3.2 Constraints

The constraints of the robust fault recovery strategy include power flow equations, system operational safety constraints, SOP operation constraints, and radial network configuration constraints. This paper constructs the distribution network branch power flow equations based on the second-order cone programming model proposed in literature (Farivar and Low, 2013), which include node injected power balance Eq. 12 and branch voltage drop Eq. 13. The specific forms are as follows:

(1) Node Injected Power Balance Equation

$$\begin{cases} \sum_{ij\in\Omega_b} P_{ij} - \sum_{ki\in\Omega_b} \left(P_{ki} - R_{ki} I_{ki}^{sqr} \right) = P_i \\ \sum_{ij\in\Omega_b} Q_{ij} - \sum_{ki\in\Omega_b} \left(Q_{ki} - X_{ki} I_{ki}^{sqr} \right) = Q_i \\ P_i = \tilde{P}_{i,\text{DG}} + P_{i,\text{SOP}} - y_i P_{i,\text{load}} \\ Q_i = \tilde{Q}_{i,\text{DG}} + Q_{i,\text{SOP}} - y_i Q_{i,\text{load}} \\ \tilde{P}_{i,\text{DG}} = P_{i,\text{DG}}^{\text{ref}} + \Delta P_{i,\text{DG}} \varepsilon_i, \varepsilon_i \in [-1,+1] \\ \tilde{Q}_{i,\text{DG}} = \tilde{P}_{i,\text{DG}} \tan\theta \end{cases} \quad \forall i \in \Omega_n \tag{12}$$

(2) Branch Voltage Drop Equation

$$\begin{cases} U_i^{sqr} - U_j^{sqr} = 2\left(P_{ij} R_{ij} + Q_{ij} X_{ij} \right) - \left(R_{ij}^2 + X_{ij}^2 \right) I_{ij}^{sqr}, \forall ij \in \Omega_b \\ I_{ij}^{sqr} U_i^{sqr} \geq P_{ij}^2 + Q_{ij}^2, \forall ij \in \Omega_b \end{cases} \tag{13}$$

During the fault recovery process, changes in the distribution network topology necessitate the relaxation of the branch flow voltage equation using the big-M method. When a branch ij is open, i.e., $x_{ij} = 0$,

the branch flow voltage equation need not be satisfied. Conversely, when a branch ij is closed, i.e., $x_{ij} = 1$, the branch voltage drop equation must be strictly adhered to. The revised Eq. 13 is as follows:

$$\begin{cases} U_i^{sqr} - U_j^{sqr} \le M\left(1 - x_{ij}\right) + 2\left(P_{ij}R_{ij} + Q_{ij}X_{ij}\right) - \left(R_{ij}^2 + X_{ij}^2\right)I_{ij}^{sqr}, \forall ij \in \Omega_b \\ U_i^{sqr} - U_j^{sqr} \ge -M\left(1 - x_{ij}\right) + 2\left(P_{ij}R_{ij} + Q_{ij}X_{ij}\right) - \left(R_{ij}^2 + X_{ij}^2\right)I_{ij}^{sqr}, \forall ij \in \Omega_b \\ I_{ij}^{sqr}U_i^{sqr} \ge P_{ij}^2 + Q_{ij}^2, \forall ij \in \Omega_b \end{cases} \tag{14}$$

(3) System Operational Safety Constraints

System operational safety constraints include node voltage Eq. 15 and branch capacity Eq. 16. Node voltage constraints ensure that the voltage at each node remains within a safe operating range during the fault recovery period. The constraint is represented as Eq. 15:

$$y_i\left(U_i^{\min}\right)^2 \le U_i^{sqr} \le y_i\left(U_i^{\max}\right)^2 \tag{15}$$

Branch capacity constraints ensure that the power in each branch does not exceed limits. The constraint is represented as Eq. 16:

$$\begin{cases} -\bar{P}_{ij}x_{ij} \le P_{ij} \le \bar{P}_{ij}x_{ij} \forall ij \in \Omega_b \\ -\bar{Q}_{ij}x_{ij} \le Q_{ij} \le \bar{Q}_{ij}x_{ij} \forall ij \in \Omega_b \\ I_{ij}^{sqr} \le x_{ij}\bar{I}_{ij}^{sqr} \end{cases} \tag{16}$$

(4) SOP Operating Constraints

$$P_{i,\mathrm{SOP}} + P_{j,\mathrm{SOP}} + P_{i,\mathrm{SOP}}^{\mathrm{L}} + P_{j,\mathrm{SOP}}^{\mathrm{L}} = 0 \tag{17}$$

$$\sqrt{\left(P_{i,\mathrm{SOP}}\right)^2 + \left(Q_{i,\mathrm{SOP}}\right)^2} \le S_{i,\mathrm{SOP}} \tag{18}$$

$$\sqrt{\left(P_{j,\mathrm{SOP}}\right)^2 + \left(Q_{j,\mathrm{SOP}}\right)^2} \le S_{j,\mathrm{SOP}} \tag{19}$$

$$P_{i,\mathrm{SOP}}^{\mathrm{L}} = A_{i,\mathrm{SOP}}\sqrt{\left(P_{i,\mathrm{SOP}}\right)^2 + \left(Q_{i,\mathrm{SOP}}\right)^2} \tag{20}$$

$$P_{j,\mathrm{SOP}}^{\mathrm{L}} = A_{j,\mathrm{SOP}}\sqrt{\left(P_{j,\mathrm{SOP}}\right)^2 + \left(Q_{j,\mathrm{SOP}}\right)^2} \tag{21}$$

(5) Description of DG Output Uncertainty

Instead of representing DG output with a single deterministic forecast value, a box-type interval model is constructed as Eq. 22:

$$U = \begin{cases} P_{i,\mathrm{DG}} \in \left[P_{i,\mathrm{DG}}^{\mathrm{ref}} - \Delta P_{i,\mathrm{DG}}, P_{i,\mathrm{DG}}^{\mathrm{ref}} + \Delta P_{i,\mathrm{DG}}\right] \\ \sum\limits_{i\in\Omega_n} \dfrac{\left|P_{i,\mathrm{DG}} - P_{i,\mathrm{DG}}^{\mathrm{ref}}\right|}{\Delta P_{i,\mathrm{DG}}} \le \Gamma^{\mathrm{DG}} \end{cases} \tag{22}$$

where Γ^{DG} is the "uncertainty parameter" for the possible values of the uncertain quantity, which can be chosen from the set {0, −1, 1}.

To contrast with the robust fault recovery model proposed in this paper, a deterministic fault recovery model is established as follows. The objective function of the deterministic model is to minimize the load shedding amount, network loss, and DG operating costs, specifically formulated as Eq. 23:

$$f = \min\left[\lambda_1 \sum_{i\in\Omega_n}(1 - y_i)w_{\mathrm{load}}P_{i,\mathrm{load}} + \lambda_2\left(\sum_{ij\in\Omega_b} I_{ij}^{sqr}R_{ij} + \sum_{i\in\Omega_n}\left(aP_{i,\mathrm{DG}}{}^2 + bP_{i,\mathrm{DG}} + c\right)\right)\right] \tag{23}$$

The constraint conditions, aside from the node injected power balance constraint, are the same as those in the robust fault recovery model. In the deterministic recovery model, the uncertainty of DG output is not considered, and the node injected power balance Eq. 12 is modified to Eq. 24:

$$\begin{cases} \sum\limits_{ij\in\Omega_b} P_{ij} - \sum\limits_{ki\in\Omega_b}\left(P_{ki} - R_{ki}I_{ki}^{sqr}\right) = P_i \\ \sum\limits_{ij\in\Omega_b} Q_{ij} - \sum\limits_{ki\in\Omega_b}\left(Q_{ki} - X_{ki}I_{ki}^{sqr}\right) = Q_i, \forall i \in \Omega_n \\ P_i = P_{i,\mathrm{SOP}} + P_{i,\mathrm{DG}} - y_iP_{i,\mathrm{load}} \\ Q_i = Q_{i,\mathrm{SOP}} + Q_{i,\mathrm{DG}} - y_iQ_{i,\mathrm{load}} \end{cases} \tag{24}$$

In summary, the objective function of the robust fault recovery model proposed in this paper is represented by Formula 11, with constraints including node injected power balance Eq. 12, branch voltage drop Eq. 14, node voltage Eq. 15, branch capacity Eq. 16, SOP operating Eqs 17–21, and DG uncertainty set (22). This model is a two-stage robust optimization form of a min-max-min problem with certain constraints and belongs to a large-scale combinatorial optimization problem, which is challenging to solve directly. The robust fault recovery model Eqs 11–22 and the deterministic model Eqs 13–21, 23, 24 provide a comprehensive framework for addressing fault recovery in power distribution networks under uncertain conditions.

4 Model transformation and solution

4.1 Compact form of the model

To better illustrate the algorithm's process, the two-stage robust optimization model Eqs 11–22 are integrated into the following compact form:

$$\min_{\boldsymbol{x}}\max_{\boldsymbol{u}\in\mathbf{U}}\min_{\boldsymbol{h}\in\boldsymbol{F}(\boldsymbol{x},\boldsymbol{u})} \boldsymbol{b}^{\mathrm{T}}\boldsymbol{h} \tag{25}$$

$$s.t.\ \boldsymbol{A}\boldsymbol{x} \le \mathbf{b} \tag{26}$$

$$\boldsymbol{B}\boldsymbol{x} = \boldsymbol{d} \tag{27}$$

$$\boldsymbol{F}(\boldsymbol{x},\boldsymbol{u}) = \begin{cases} \boldsymbol{h} \in \boldsymbol{S}_h\colon \boldsymbol{C}\boldsymbol{h} \ge \boldsymbol{E}\boldsymbol{x}, \boldsymbol{D}\boldsymbol{h} = \boldsymbol{u} \\ \|\boldsymbol{G}_l\boldsymbol{h}\| \le \boldsymbol{g}_l^{\mathrm{T}}\boldsymbol{h}, \forall l = 1, \ldots, m \end{cases} \tag{28}$$

Model Eqs 25–28 present a two-stage optimization problem that is challenging to solve directly. To address this, the C&CG algorithm is employed to decompose the two-stage robust optimization model into a master problem and sub-problems, which are then solved iteratively.

4.2 Master problem

The master problem decides the network topology under the condition that the output power of each DG unit, $\boldsymbol{u}_l^*$, is already determined. The expression for the master problem is:

$$\mathrm{MP}:\ \min_{\mathbf{x},\eta}\ \eta \tag{29}$$

$$\text{s.t. } \boldsymbol{A}\boldsymbol{x} \le \boldsymbol{b} \tag{30}$$

$$\eta \ge \boldsymbol{b}^{\mathrm{T}}\boldsymbol{h}^l, \forall l \le k \tag{31}$$

$$\boldsymbol{Ex} \le \boldsymbol{C}^l, \forall l \le k \tag{32}$$

$$\boldsymbol{Dy}^l = \boldsymbol{u}_l^*, \forall l \le k \tag{33}$$

$$\boldsymbol{G}_i \boldsymbol{h}^l \le \boldsymbol{g}_i^{\mathrm{T}} \boldsymbol{h}^l, i = 1, \ldots, m, \forall l \le k \tag{34}$$

A real variable η is introduced to replace the max-min problem in Eq. 25, and Eq. 31 is added to obtain a relaxed problem as shown in Eqs 29–34.

4.3 Subproblem

The subproblem, solved after determining the network topology in the first phase, finds the worst-case fluctuation scenario of distributed generation $\boldsymbol{u}_l^*$. The subproblem is described as Eqs 35–37:

$$\text{SP: } Q(\boldsymbol{x}^*) = \max_{\boldsymbol{u} \in \boldsymbol{U}} \min_{\boldsymbol{h} \in \boldsymbol{F}(\boldsymbol{x}^*, \boldsymbol{u})} \boldsymbol{b}^{\mathrm{T}} \boldsymbol{h} \tag{35}$$

$$\text{s.t.} \boldsymbol{Ch} \ge \boldsymbol{Ex}^* \tag{36}$$

$$\boldsymbol{Dh} = \boldsymbol{u} \tag{37}$$

$$\|\boldsymbol{G}_l \boldsymbol{x}\| \le \boldsymbol{g}_i^{\mathrm{T}} \boldsymbol{x}, \forall i = 1, \ldots, m \tag{38}$$

The subproblem is a max-min, two-layer optimization problem, which is difficult to solve directly. To address this, dual theory is applied to transform the inner min problem into its corresponding max problem, which is then combined with the outer max problem to form a single-layer max problem. The transformed subproblem expression is:

$$Q(\boldsymbol{x}^*) = \max_{\boldsymbol{u}, \boldsymbol{\pi}_1, \boldsymbol{\pi}_2, \boldsymbol{w}_i, \lambda_i} (\boldsymbol{Ex}^*)^{\mathrm{T}} \boldsymbol{\pi}_1 + \boldsymbol{u}^{\mathrm{T}} \boldsymbol{\pi}_2 \tag{39}$$

$$\text{s.t.} \boldsymbol{C}^{\mathrm{T}} \boldsymbol{\pi}_1 + \boldsymbol{D}^{\mathrm{T}} \boldsymbol{\pi}_2 + \sum_i (\boldsymbol{G}_i w_i + \boldsymbol{g}_i \lambda_i) = \boldsymbol{b} \tag{40}$$

$$\|\boldsymbol{w}_i\|_2 \le \lambda_i, i = 1, \ldots, n \tag{41}$$

where $\boldsymbol{\pi}_1, \boldsymbol{\pi}_2$ are the dual variables for Eqs 36, 37. $(\boldsymbol{w}_i, \lambda_i)$ is the dual variable for Eq. 38.

The objective function of the subproblem (39) contains the nonlinear, bilinear term $\boldsymbol{u}^{\mathrm{T}} \boldsymbol{\pi}_2$, which needs to be processed for easier solving of the model. The big-M method can be used to linearize $\boldsymbol{u}^{\mathrm{T}} \boldsymbol{\pi}_2$ as follows:

$$\begin{cases} \boldsymbol{u}^{\mathrm{T}} \boldsymbol{\pi}_2 = \sum_s u_s \pi_{2,s} = \sum_s g_s \\ g_s \le \pi_{2,s} \\ g_s \le M u_s \\ g_s \ge \pi_{2,s} - (1 - u_s) M \\ g_s \ge 0 \\ u_s \in \{0, 1\} \end{cases} \tag{42}$$

where g_s is a new variable introduced, which represents the dot product of the corresponding elements of the variables $\boldsymbol{u}$ and $\boldsymbol{\pi}_2$.

4.4 C&CG algorithm

The basic principle of robust optimization is to transform the original robust optimization model into a two-stage optimization problem, which is then solved using the C&CG algorithm. The algorithm iteratively solves the master and subproblems, adding the columns generated by the subproblem to the constraints of the master problem. The optimal result is output when both the upper and lower bounds meet the convergence precision. The model-solving process of the C&CG algorithm is illustrated in Figure 2.

The specific iterative process is as follows:

Step 1: Initialize data, set the upper and lower bounds of the objective, let $LB = -\infty, UB = +\infty, k = 0$, and set O as an empty set.

Step 2: Solve the master problem Eqs 29–34, obtaining the optimal solution $(\boldsymbol{x}_{k+1}^*, \boldsymbol{\eta}_{k+1}^*, \boldsymbol{h}^{1^*}, \ldots, \boldsymbol{h}^{k^*})$, and update the lower bound $LB = \boldsymbol{\eta}_{k+1}^*$ of the original problem.

Step 3: Substitute the given $\boldsymbol{x} = \boldsymbol{x}_{k+1}^*$ from the master problem into the subproblem Eqs 39–42, solve the worst-case scenario u_{k+1}^* and the optimal objective function value $\boldsymbol{Q}(\boldsymbol{x}_{k+1}^*)$, and update the upper bound $UB = \min\{UB, \boldsymbol{Q}(\boldsymbol{x}_{k+1}^*)\}$ of the original problem.

Step 4: Check if the convergence condition $\mathrm{UB} - \mathrm{LB} \le \varepsilon$ is met. If yes, the iteration is complete, and the current optimal solution is output. If not, proceed as follows:

(1) If $\boldsymbol{Q}(\boldsymbol{x}_{k+1}^*) < +\infty$, create a new decision variable $\boldsymbol{h}^{k+1}$, add the Eq. 43 to the master problem Eqs 29–34:

$$\begin{aligned} &\eta \ge \boldsymbol{b}\boldsymbol{h}^{k+1} \\ &\boldsymbol{Ex} \ge \boldsymbol{C}\boldsymbol{h}^{k+1} \\ &\boldsymbol{D}\boldsymbol{h}^{k+1} = \boldsymbol{u}_{k+1}^* \\ &\left\|\boldsymbol{G}_i \boldsymbol{h}^{k+1}\right\| \le \boldsymbol{g}_i^{\mathrm{T}} \boldsymbol{h}^{k+1} \end{aligned} \tag{43}$$

where $\boldsymbol{u}_{k+1}^*$ is the optimal value from Step 4). Set $k = k + 1$, $\mathbf{O} = \mathbf{O} \cup \{k + 1\}$, and return to Step 2.

(2) If $\boldsymbol{Q}(\boldsymbol{x}_{k+1}^*) = +\infty$, create a new decision variable $\boldsymbol{y}^{k+1}$, add the Eq. 44 to the master problem:

$$\begin{aligned} &\boldsymbol{Ex} \ge \boldsymbol{C}\boldsymbol{h}^{k+1} \\ &\boldsymbol{D}\boldsymbol{h}^{k+1} = \boldsymbol{u}_{k+1}^* \\ &\left\|\boldsymbol{G}_i \boldsymbol{h}^{k+1}\right\| \le \boldsymbol{g}_i^{\mathrm{T}} \boldsymbol{h}^{k+1} \end{aligned} \tag{44}$$

Update the constraint set accordingly. Set $k = k + 1$ and return to Step 2.

5 Case analysis

To analyze the fault recovery of distribution networks under extreme weather scenarios, a test was conducted using an interconnected distribution system based on SOPs. This system consists of three IEEE 33-node systems interconnected with SOPs (Yuduo Zhao et al., 2022). The initial topology, as shown in Figure 3, illustrates that the tie switches, represented by dashed lines, are initially open. A coordinate system is established with node 1 of Distribution Network A as the origin. The load data and line impedance for each IEEE 33-node system are referenced from (Shaheen et al., 2021).

Following the method proposed in (Lu Zhang et al., 2018), the positions for integrating DG and SOPs were determined. Four DG units were integrated into Distribution Network 1 at nodes 9, 14, 17, and 27, each with a predicted active power output of 150 kW and a power factor set at 0.9 (Zhu et al., 2017). The loads were classified according to their importance levels, with each load level and its corresponding weight settings presented in Table 1. SOP1 was connected between nodes a12 and a22 of Distribution Network 1, SOP2 between node a18 of Distribution Network 1 and node b18 of

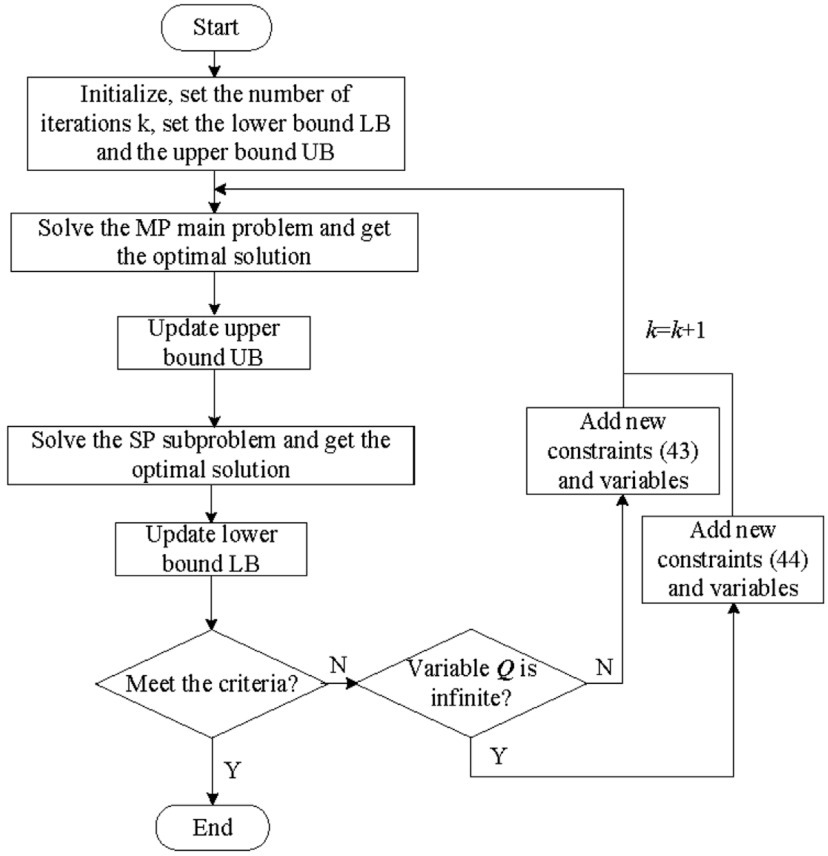

FIGURE 2
Model solving process of C&CG algorithm.

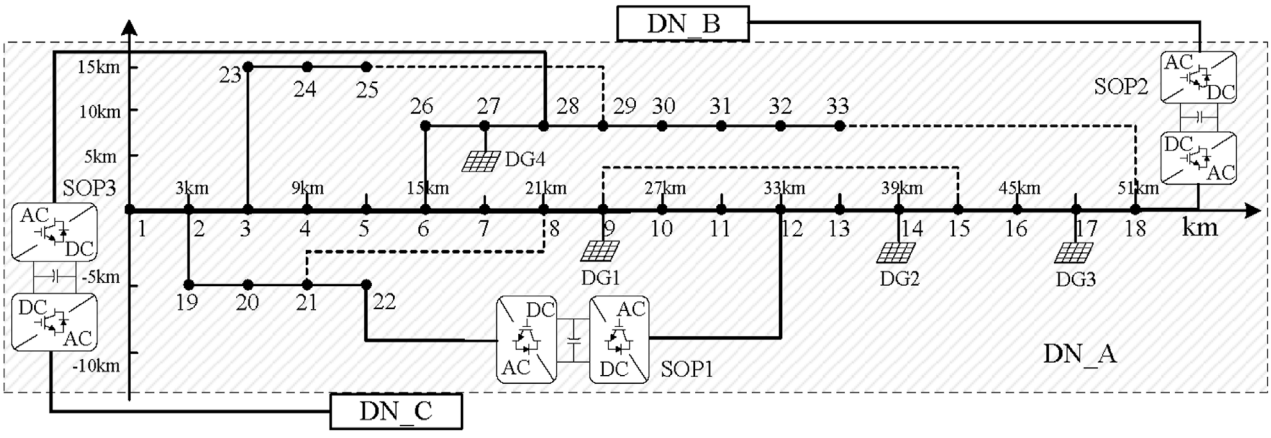

FIGURE 3
Modified IEEE 33-node distribution system based on SOP interconnection.

Distribution Network 2, and SOP3 between node a28 of Distribution Network 1 and node c28 of Distribution Network 3. All SOPs were set with a capacity of 200 kVA and a loss coefficient of 0.02. The permissible voltage fluctuation range at the nodes was set between 0.95 and 1.05 p.u. In the objective function, λ_1 and λ_2 were set to 100 and 1, respectively.

The effectiveness of fault recovery was assessed using the load recovery rate, defined as the ratio of the restored load to the total load lost before restoration. The recovery rates for primary, secondary, and tertiary loads were denoted as σ_1, σ_2, σ_3 with the total load recovery rate also represented by σ_s. This case study aims to evaluate the performance of the proposed fault recovery strategies

TABLE 1 Grade and weight of load.

Load level	Node number	Total load/kW	Load weight
Primary load	1–3, 9–11, 14, 32, 33	745	100
Secondary load	4, 5, 12, 15, 18–21, 25, 26, 29	1260	10
Tertiary load	6–8, 13, 16, 17, 22–24, 27, 28, 30, 31	1710	1

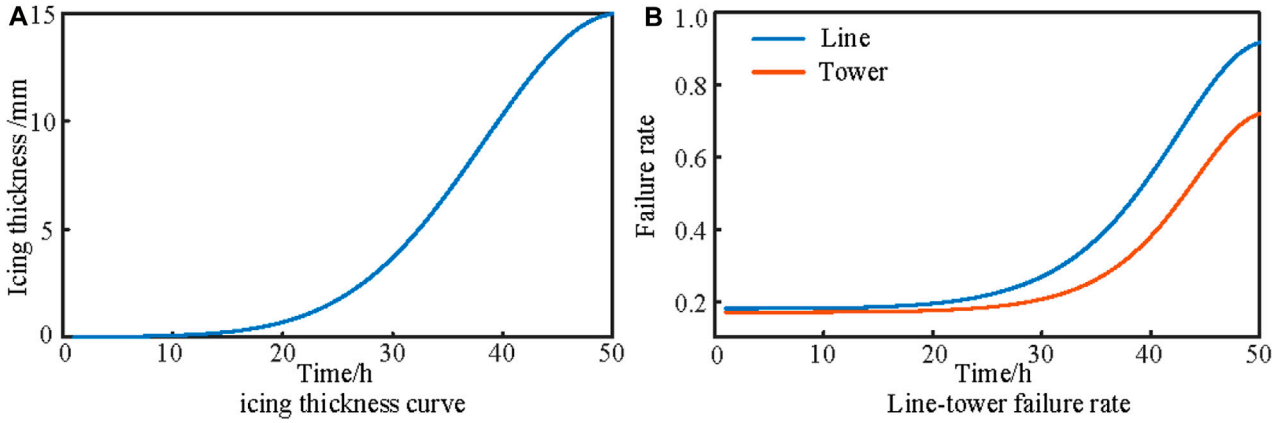

FIGURE 4
Icing thickness curve and line-tower failure rate. **(A)** Icing thickness curve; **(B)** Line-tower failure rate.

in restoring different levels of loads in the interconnected distribution network under adverse weather conditions.

5.1 Line fault rate analysis in typical fault scenarios

In the simulated scenario, the distribution network is under snowstorm conditions with an ambient temperature of −5°C, wind speed of 10 km/h, and precipitation rate of 40 mm/h. The center of the snowstorm, located at coordinates (−150 km, −150 km), moves towards the distribution network at a speed of 4.2 km/h in the 45° direction along the *x*-axis. The climate impact radius R is set at 130 km, with R values of 0.4 for line ice coverage fault rate, 0.18 for line fault rate, and 0.1 for pole ice coverage fault rate, increasing to 0.46 and 0.43, respectively, as conditions worsen. Over time, both the ice thickness and the line-pole fault rates change. Figure 4 illustrates the ice thickness and line-pole fault rates for this fault scenario.

Figure 4A shows that as the snowstorm center moves closer to the distribution network, the ice layer thickness on the lines rapidly increases. Figure 4B indicates that with the increase in ice layer thickness, the fault rates of lines and poles first experience a slow growth, then the line fault rate exhibits an exponential increase after 20 h, and the pole fault rate rises rapidly after 30 h. Line breakage may occur if the ice thickness exceeds the line's load-bearing capacity.

By varying environmental temperature, precipitation rate, snowstorm center location, and movement speed, various extreme ice and snow disaster scenarios can be simulated. The entropy value corresponding to each scenario can be calculated using Eq. 9, with the probability distribution of the system's information entropy shown in Figure 5. The higher the probability of occurrence of an entropy value, the more likely the scenario is considered a typical fault scenario.

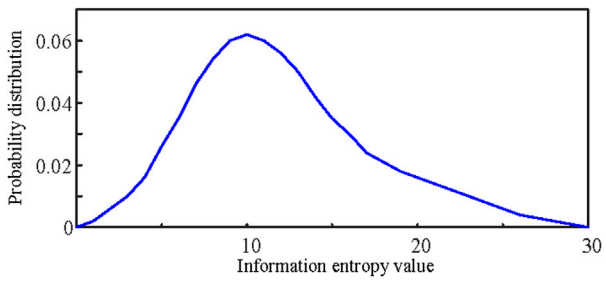

FIGURE 5
Entropy probability distribution.

For this simulation, the fault rates of each line in Distribution Network 1 are shown in Figure 6. The entropy value calculated for this scenario using Eq. 9 is 14.71. According to Figure 5, this entropy value has a high probability of occurrence, marking it as a typical extreme ice and snow fault scenario. Figure 6 reveals that Lines 1 (a1-a2) and 18 (a2-a19) in Distribution Network 1 have higher fault rates than other lines, indicating that these lines are relatively vulnerable within the system and more prone to faults due to ice and snow disasters. Consequently, the fault recovery strategies proposed in this paper will be applied specifically to these two high-fault-rate lines to formulate fault recovery plans.

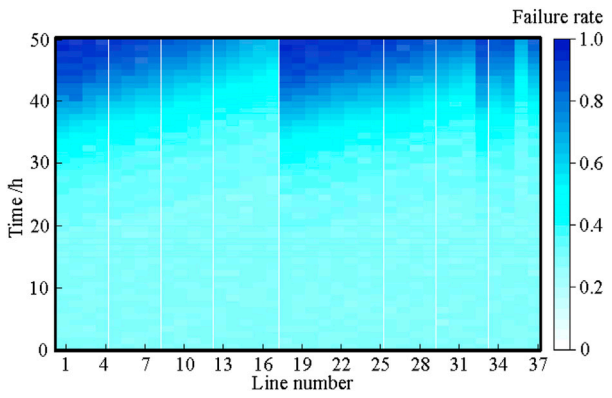

FIGURE 6
Failure rate of each line.

5.2 Impact of SOP integration on fault recovery effectiveness

For Distribution Network 1, Lines 1 and 18 were selected as fault lines, leading to the cessation of all loads from nodes a2 to a33, resulting in a substantial active power loss of up to 3715 kW. To analyze the impact of SOP integration on fault recovery, three SOP integration scenarios were tested:

Scenario 1: Fault recovery through internal SOP1 and network reconfiguration in Distribution Network 1. Scenario 2: Based on Scenario 1, connecting Distribution Network 2 through SOP2. Scenario 3: Based on Scenario 1, connecting Distribution Networks 2 and 3 through SOP2 and SOP3, respectively.

The fault recovery effects for these three scenarios are shown in Table 2.

Table 2 reveals that Scenario 1 has the lowest total load recovery rate at 31.89%. This is due to the disconnection of Distribution Network 1 from the main power source, with the required active power for loads being supplied only by internal DG and transmitted through internal SOP1, which also provides reactive power compensation. The fault recovery capacity in this scenario is limited. Comparing Scenarios 1 and 2, the total load recovery rate in Scenario 2 increases to 45.09%, indicating that connecting Distribution Network 1 with Network 2 through SOP2 allows flexible power transmission control, restoring more lost loads. Scenario 3 has the highest total load recovery rate at 55.31%, as the faulted distribution network is interconnected with Networks B and C through two SOPs, allowing two power sources to support power restoration in the outage area. However, not all loads are restored under this SOP capacity, as the capacity of SOP influences its power flow transfer ability and consequently affects the fault recovery outcome.

To analyze the impact of SOP capacity, Scenario 3 was tested under four different SOP capacities: 200, 400, 600, and 800 kVA, and the fault recovery conditions and SOP output powers were assessed. The influence of SOP capacity on fault recovery effectiveness is shown in Table 3.

As indicated in Table 3, as the integrated SOP capacity in the system increases, the fault recovery capability of the distribution network continuously strengthens. With a single SOP capacity of 200 kVA, the total load recovery rate is relatively low at 55.31%, with a primary load recovery rate of only 63.75%, indicating poor recovery effectiveness. At 400 kVA, the total load recovery rate improves to 72.01%, with primary loads fully restored, and a slight increase in the tertiary load recovery rate. At 600 kVA, nodes a7 and a25 are restored, with a high total load recovery rate of 88.69%, including 100% recovery for primary and secondary critical loads. With 800 kVA, the total SOP capacity accounts for 64.60% of the load power, with strong power flow transfer capability, resulting in the restoration of all lost loads.

The active power outputs of SOPs under four different capacities are shown in Figure 7.

Figure 7 shows that for all four SOP capacities, the active power of VSC a12 in Distribution Network 1 is negative, while VSC a22's is positive, indicating that the active power flow on the SOP is from node a12 to node a22. After Distribution Network 1 is disconnected from the main power source, VSC a12 obtains electrical energy from nearby DGs at nodes a9 and a14. VSC a22, lacking nearby DG resources, receives active power transmitted through SOP1 from node a12 to restore the lost loads 19–22. For SOP2 connecting Distribution Networks 1 and 2, the active power of VSC a18 is positive, and that of VSC b18 is negative, indicating active power flow from Network 2's node b18 to Network 1's node a18. Similarly, SOP3 injects active power from Distribution Network 3 into Network A's node a28 to provide electricity for the lost loads.

5.3 Impact of DG injection power on fault recovery effectiveness

Considering that the integration of DG changes the system's power flow distribution and affects the fault recovery outcome, this section analyzes the impact of DG integration on fault recovery. Based on the integration of three 200 kVA SOPs, a comparative analysis was conducted with different levels of DG injection power.

TABLE 2 Fault recovery effect of distribution network under three schemes.

Scheme	Loss of electric power node	Load shedding/kW	σ_1/%	σ_2/%	σ_3/%	σ_s/%
Before recovery	2–33	3715	0	0	0	0
1	2–4, 7, 8, 14, 19, 23–25,29–32	2530	30.20	40.47	26.31	31.89
2	7, 8, 14, 24, 25, 29–32	2040	55.70	57.14	31.58	45.09
3	7, 8, 24, 25, 31–33	1660	63.75	66.67	43.27	55.31

TABLE 3 Effect of SOP capacity on fault recovery.

SOP capacity/kVA	Loss of electric power node	Load shedding/kW	σ_1/%	σ_2/%	σ_3/%	σ_s/%
200	7, 8, 24, 25, 31–33	1660	63.75	66.67	43.27	55.31
400	7, 24, 25	1040	100	66.67	63.74	72.01
600	24	420	100	100	75.44	88.69
800	--	0	100	100	100	100

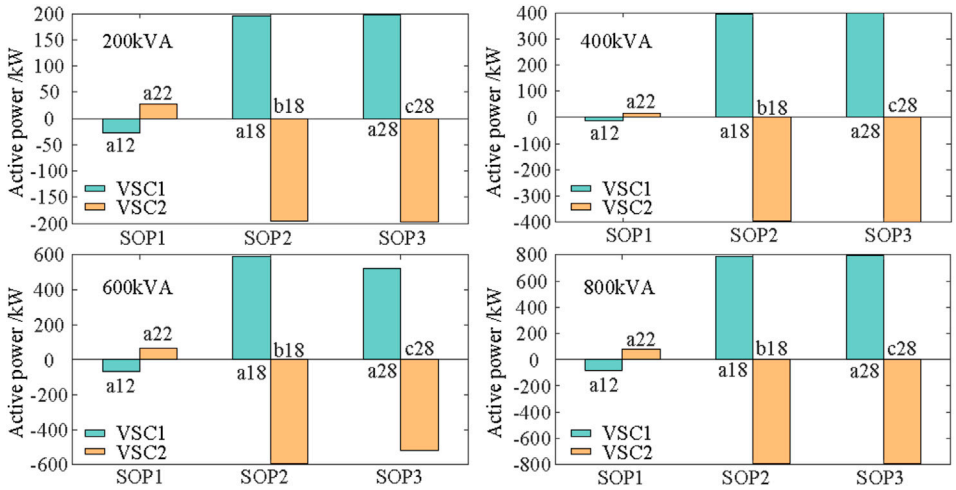

FIGURE 7
Active power output of SOP.

TABLE 4 Fault recovery effect under different DG injection Power.

Injected power of DG/kW	Loss of electric power node	Load shedding/kW	σ_1/%	σ_2/%	σ_3/%	σ_s/%
150	7, 8, 24, 25, 31–33	1660	63.75	66.67	43.27	55.31
225	7, 8, 20–22, 24	1090	100	85.71	46.78	70.66
300	7, 8, 16	460	100	100	73.10	87.62
375	--	0	100	100	100	100

The fault recovery effects under varying DG injection power levels are presented in Table 4.

Table 4 shows that with the increase in DG injection power, the total load recovery rate correspondingly rises from 55.31% to 100.0%. When the DG injection power is 150 kW, only 63.75% of primary load can be restored, indicating low power supply reliability. At a DG injection power of 225 kW, the recovery rate of primary load increases from 63.75% to 100%, and the recovery rates of secondary and tertiary loads also rise. With 300 kW of DG injection power, primary and secondary critical loads are fully restored, and the tertiary load recovery rate increases to 73.10%. At 375 kW, DG within the Distribution Network 1 accounts for 40.38% of the total load power, enabling the recovery of all loads. Thus, it is evident that DG injection power plays a positive role in fault recovery. DG injection power can locally meet the demands of nearby loads, enabling more loads to be restored.

5.4 Comparison of recovery effects between two fault recovery strategies

To demonstrate the effectiveness of the robust fault recovery strategy for distribution networks proposed in this paper, a comparison of fault recovery effects between deterministic and robust strategies was conducted. In the deterministic recovery strategy, DG power remains at the forecasted value, while in the robust strategy, DG output fluctuates within the range of an uncertainty set. With a single SOP capacity of 200 kVA and the same parameter settings, the fault recovery effects of the two strategies are shown in Table 5.

As evident from Table 5, the recovery effect of the robust strategy is superior to that of the deterministic strategy. The deterministic strategy, which bases the network topology on the predicted values of DG, has weaker adaptability to uncertainties, resulting in a lower total load recovery rate of only 55.31%. In contrast, the robust strategy, considering the worst-case DG output samples, achieves an improved

TABLE 5 Fault recovery effect of two fault recovery strategies.

Strategy	Loss of electric power node	Load shedding/kW	σ_1/%	σ_2/%	σ_3/%	σ_s/%
Deterministic strategy	7, 8, 24, 25, 31–33	1660	63.75	66.67	43.27	55.31
Robust strategy	7, 8, 21, 22, 24, 25	1420	100	59.52	46.78	61.78

TABLE 6 Fault recovery effect of two fault recovery strategies.

Strategy	Loss of electric power node	Load shedding/kW	σ_1/%	σ_2/%	σ_3/%	σ_s/%
Deterministic strategy	34, 35, 53, 57, 58, 69, 70, 76	1850.6	91.33	53.69	91.17	76.08
Robust strategy	34, 35, 50, 53, 57, 58	1440.4	100	59.96	91.17	81.38

total load recovery rate of 61.78%. Furthermore, it ensures 100% recovery of primary loads, though the recovery rate of secondary loads is slightly reduced. It is apparent that the proposed robust strategy yields better recovery results than the deterministic strategy and possesses a superior ability to adapt to the uncertainties in DG output.

To verify the scalability of the proposed method in large-scale actual systems, an analysis was conducted using a 234-node system interconnected by SOPs. This system consists of three 78-node systems interconnected through SOPs (Ji et al., 2023). In Distribution Network A, 7 DGs were connected at nodes 5, 24, 29, 47, 52, 60, and 78, with each having a forecasted active power of 150 kW and a power factor set to 0.9. SOP1 connects to Distribution Network A at nodes a22 and a59, SOP2 connects Distribution Network A at node a18 and Distribution Network B at node b18, and SOP3 connects Distribution Network A at node a28 and Distribution Network C at node c28, with each having a capacity set to 1000kVA and a loss coefficient of 0.02. Two fault recovery strategies, deterministic recovery strategy and robust recovery strategy, were compared. Table 6 presents the recovery effects of the two fault recovery strategies under the same fault location and parameter settings.

From Table 6, it is evident that the robust strategy still outperforms the deterministic strategy in terms of load recovery effectiveness. The deterministic strategy exhibits a weaker adaptability to the uncertainty of DGs, with a total load recovery rate of 76.08%. In contrast, the robust strategy achieves an improved total load recovery rate of 81.38%, with critical loads being fully restored to 100%. Thus, in large-scale actual systems, the proposed robust strategy can achieve better recovery outcomes than the deterministic strategy.

6 Conclusion

To enhance the distribution network's capability to cope with extreme ice and snow disasters, this paper proposes a robust fault recovery strategy for multi-source distribution networks under extreme weather conditions. Simulation analyses were conducted on systems with modified IEEE 33-node interconnected by SOPs, leading to the following conclusions:

(1) For lines with a high fault rate under typical extreme ice and snow disaster scenarios, pre-established fault recovery strategies enable the rapid restoration of lost loads after actual faults occur, thus improving the distribution network's ability to handle extreme ice and snow disasters.
(2) The proposed fault recovery strategy makes full use of the flow control capabilities of SOPs and the power support of DGs. The coordination of SOPs with network reconstruction effectively restores power supply to lost loads, enhancing the fault recovery capability of the distribution network.
(3) The proposed strategy accounts for the uncertainty of DG output, demonstrating superior adaptability to the uncertainties of DG output compared to deterministic strategies.

Future research focuses only on fault scenarios related to ice and snow weather disasters. It will be more practically significant to consider a wider range of fault scenarios in future studies.

Data availability statement

The original contributions presented in the study are included in the article/Supplementary material, further inquiries can be directed to the corresponding author.

Author contributions

TB: Methodology, Writing–original draft. HL: Conceptualization, Writing–review and editing. ZL: Validation, Writing–review and editing. ZH: Resources, Writing–review and editing. WK: Validation, Writing–review and editing.

Funding

The author(s) declare that financial support was received for the research, authorship, and/or publication of this article. This research was funded by the Science and Technology Project of Hebei Electric Power Company of State Grid (SGHEXA00GDJS2250285).

Conflict of interest

Authors TB, HL, ZL, ZH, WK, and ZP were employed by the State Grid Xiongan New Area Electric Power Supply Company.

The authors declare that this study received funding from the Science and Technology Project of Hebei Electric Power Company of State Grid. The funder had the following involvement in the study: study design, data collection and analysis, decision to publish, or preparation of the manuscript.

Publisher's note

References

Ali Arefifar, S., Shahin Alam, M., and Hamadi, A. (2023). A review on self-healing in modern power distribution systems. *J. Mod. Power Syst. Clean. Energy* 11, 1719–1733. doi:10.35833/MPCE.2022.000032

Chen, W., Zhou, X., Li, Y., and Guo, C. (2018). A robust islanding restoration policy for active distribution network considering optimal allocation of emergency electric vehicles. *Proc. CSEE* 38, 58–67. doi:10.13334/j.0258-8013.pcsee.180968

Chen, X., Wu, W., and Zhang, B. (2016). Robust restoration method for active distribution networks. *IEEE Trans. Power Syst.* 31, 4005–4015. doi:10.1109/TPWRS.2015.2503426

Dehghani, N. L., Jeddi, A. B., and Shafieezadeh, A. (2021). Intelligent hurricane resilience enhancement of power distribution systems via deep reinforcement learning. *Appl. Energy* 285, 116355. doi:10.1016/j.apenergy.2020.116355

Farivar, M., and Low, S. H. (2013). Branch flow model: relaxations and convexification—Part I. *IEEE Trans. Power Syst.* 28, 2554–2564. doi:10.1109/TPWRS.2013.2255317

Gao, H., Chen, Y., Xu, Y., and Liu, C.-C. (2016). Resilience-Oriented critical load restoration using microgrids in distribution systems. *IEEE Trans. Smart Grid* 7, 2837–2848. doi:10.1109/TSG.2016.2550625

Gao, H., and Li, Z. (2021). A Benders decomposition based algorithm for steady-state dispatch problem in an integrated electricity-gas system. *IEEE Trans. Power Syst.* 36, 3817–3820. doi:10.1109/TPWRS.2021.3067203

Gazijahani, F. S., Salehi, J., and Shafie-khah, M. (2022). Benefiting from energy-hub flexibilities to reinforce distribution system resilience: a pre- and post-disaster management model. *IEEE Syst. J.* 16, 3381–3390. doi:10.1109/JSYST.2022.3147075

He, C., Wu, L., Liu, T., and Shahidehpour, M. (2017). Robust Co-optimization scheduling of electricity and natural gas systems via ADMM. *IEEE Trans. Sustain. Energy* 8, 658–670. doi:10.1109/TSTE.2016.2615104

Ji, X., Zhang, X., Ye, P., Zhang, Y., Li, G., and Gong, Z. (2023). Dynamic reconfiguration of three-phase imbalanced distribution networks considering soft open points. *Energy Convers. Econ.* 4, 364–377. doi:10.1049/enc2.12099

Jufri, F. H., Widiputra, V., and Jung, J. (2019). State-of-the-art review on power grid resilience to extreme weather events: definitions, frameworks, quantitative assessment methodologies, and enhancement strategies. *Appl. Energy* 239, 1049–1065. doi:10.1016/j.apenergy.2019.02.017

Li, P., Ji, J., Ji, H., Song, G., Wang, C., and Wu, J. (2020a). Self-healing oriented supply restoration method based on the coordination of multiple SOPs in active distribution networks. *Energy* 195, 116968. doi:10.1016/j.energy.2020.116968

Li, W., Li, Y., Chen, C., Tan, Y., Cao, Y., Zhang, M., et al. (2020b). A full decentralized multi-agent service restoration for distribution network with DGs. *IEEE Trans. Smart Grid* 11, 1100–1111. doi:10.1109/TSG.2019.2932009

Li, Y., Xiao, J., Chen, C., Tan, Y., and Cao, Y. (2019). Service restoration model with mixed-integer second-order cone programming for distribution network with distributed generations. *IEEE Trans. Smart Grid* 10, 4138–4150. doi:10.1109/TSG.2018.2850358

Li, Z., Xu, Y., Wang, P., and Xiao, G. (2023). Coordinated preparation and recovery of a post-disaster Multi-energy distribution system considering thermal inertia and diverse uncertainties. *Appl. Energy* 336, 120736. doi:10.1016/j.apenergy.2023.120736

Liu, J., Qin, C., and Yu, Y. (2020). Enhancing distribution system resilience with proactive islanding and RCS-based fast fault isolation and service restoration. *IEEE Trans. Smart Grid* 11, 2381–2395. doi:10.1109/TSG.2019.2953716

Lu, R., Ding, T., Qin, B., Ma, J., Fang, X., and Dong, Z. (2020). Multi-stage stochastic programming to joint economic dispatch for energy and reserve with uncertain renewable energy. *IEEE Trans. Sustain. Energy* 11, 1140–1151. doi:10.1109/TSTE.2019.2918269

Nasri, A., Abdollahi, A., and Rashidinejad, M. (2022). Multi-stage and resilience-based distribution network expansion planning against hurricanes based on vulnerability and resiliency metrics. *Int. J. Electr. Power and Energy Syst.* 136, 107640. doi:10.1016/j.ijepes.2021.107640

Shaheen, A. M., El-Sehiemy, R. A., Kamel, S., Elattar, E. E., and Elsayed, A. M. (2021). Improving distribution networks' consistency by optimal distribution system reconfiguration and distributed generations. *IEEE Access* 9, 67186–67200. doi:10.1109/ACCESS.2021.3076670

Shannon, C. E. (1948). A mathematical theory of communication. *Bell Syst. Tech. J.* 27, 379–423. doi:10.1002/j.1538-7305.1948.tb01338.x

Standards Coordinating Committee (2003). IEEE standard for interconnecting distributed resources with electric power systems. *IEEE Std 1547-2003*, 1–28. doi:10.1109/IEEESTD.2003.94285

Wang, B., Zhang, C., and Dong, Z. Y. (2020). Interval optimization based coordination of demand response and battery energy storage system considering SOC management in a microgrid. *IEEE Trans. Sustain. Energy* 11, 2922–2931. doi:10.1109/TSTE.2020.2982205

Wang, H., Zhou, W., Qian, K., Meng, S., Chai, C., Wong, Y. D., et al. (2018). Tri-level optimal hardening plan for a resilient distribution system considering reconfiguration and DG islanding. *Appl. Energy* 210, 1266–1279. doi:10.1016/j.apenergy.2017.06.059

Yan, M., Shahidehpour, M., Paaso, A., Zhang, L., Alabdulwahab, A., and Abusorrah, A. (2021). Distribution system resilience in ice storms by optimal routing of mobile devices on congested roads. *IEEE Trans. Smart Grid* 12, 1314–1328. doi:10.1109/TSG.2020.3036634

Yang, Z., Dehghanian, P., and Nazemi, M. (2020). Seismic-Resilient electric power distribution systems: harnessing the mobility of power sources. *IEEE Trans. Ind. Appl.* 56, 2304–2313. doi:10.1109/TIA.2020.2972854

Yin, H., Wang, Z., Liu, Y., Qudaih, Y., Tang, D., Liu, J., et al. (2023). Operational reliability assessment of distribution network with energy storage systems. *IEEE Syst. J.* 17, 629–639. doi:10.1109/JSYST.2021.3137979

Zhang, Lu, Shen, C., Chen, Y., Huang, S., and Tang, W. (2018). Coordinated allocation of distributed generation, capacitor banks and soft open points in active distribution networks considering dispatching results. *Appl. Energy* 231, 1122–1131. doi:10.1016/j.apenergy.2018.09.095

Zhao, H., Lu, Z., He, L., Guo, X., Li, X., and Xiao, H. (2020). Two-stage multi-fault emergency rush repair and restoration robust strategy in distribution networks. *Electr. Power Syst. Res.* 184, 106335. doi:10.1016/j.epsr.2020.106335

Zhao, Y., Xiong, W., Yuan, X., and Zou, X. (2022). A fault recovery strategy of flexible interconnected distribution network with SOP flexible closed-loop operation. *Int. J. Electr. Power and Energy Syst.* 142, 108360. doi:10.1016/j.ijepes.2022.108360

Zhou, X., Ge, S., Li, T., and Liu, H. (2018). Assessing and boosting resilience of distribution system under extreme weather. *Proc. CSEE* 38, 505–513. doi:10.13334/j.0258-8013.pcsee.162547

Zhu, J., Gu, W., Lou, G., Wang, L., Xu, B., Wu, M., et al. (2017). Learning automata-based methodology for optimal allocation of renewable distributed generation considering network reconfiguration. *IEEE Access* 5, 14275–14288. doi:10.1109/ACCESS.2017.2730850

Nomenclature

Indices

Ω_l	Set of distribution network lines
Ω_n	Set of all load nodes
Ω_b	Set of all branches
U	Set of uncertainties for dg output
k	Number of iterations

Parameters

$L_{ice}(x_j, y_j, t)$	Ice load on the line j
(x_j, y_j)	Coordinate of line j
V_{ice}	Movement speed of the snowy weather
A_{rate}	Ice growth rate on the line
D_{line}	Outer diameter of the line
a_{rate}	Ice growth rate factor
T_{temp}	Ambient temperature
V_{wind}	Wind speed
P_{preci}	Precipitation rate
a_0, a_1, a_2, a_3	Constant
$L_{ice}(t)$	Thickness of ice covering the line
D_{line}	Outer diameter of the line
M_{line}	Design ice load of the line
a_{line}, b_{line}	Constants used to calibrate the line ice fault rate and ice load ratio
w_l	Weight coefficient of loads to distinguish between primary, secondary, and tertiary loads
$P_{i,load}$	Active load demand at node i
R_{ij}	Resistance of branch ij
a, b, c	Cost coefficients of DG operation
R_{ki}, X_{ki}	Resistance and reactance of branch ki
R_{ij}, X_{ij}	Resistance and reactance of branch ij
$\bar{P}_{ij}$	Maximum active power limit of branch ij
$\bar{Q}_{ij}$	Maximum reactive power limit of branch ij
$\bar{I}_{ij}^{sqr}$	Square of the maximum allowable current in branch ij
λ_1, λ_2	Weighting coefficients of the objective function

Variables

$(\mu_x(t), \mu_y(t))$	Coordinates of the blizzard center changing over time t
σ_x, σ_y	Load parameters corresponding to the x and y axes of the line, respectively
$P_{ice}^{line}(t)$	Line ice fault rate
$\eta_{line}(t)$	Line ice load ratio
$P_{fault,j}(t)$	Fault rate of line j
$P_{ice,j.m}^{pole}(t)$	Fault rate of the m-th pole of line j
$P_{ice,j.n}^{line}(t)$	Fault rate of the n-th span of line j
W	Information entropy
T_{ice}	Time taken for the disaster to pass through the distribution network area
$P_{j,t}^{fault}$	Fault rate of line j at moment t
$\tau_{j,t}$	Whether a fault occurs on line j at moment t, with 1 for a fault and 0 otherwise
x	Binary variables
x_{ij}	On-off status of branch ij and y_i indicating the load status of node i
u	Uncertain variable of DG output
h	A vector of continuous variables related to distribution network flow optimization
I_{ij}^{sqr}	Square of the current magnitude in branch ij
$P_{i,DG}$	Active output of DG at node i
P_{ij}, Q_{ij}	Active and reactive power flowing through branch ij, respectively
P_{ki}, Q_{ki}	Active and reactive power flowing through branch ki, respectively
I_{ki}^{sqr}	Square of the current magnitude in branch ki
P_i, Q_i	Active and reactive power injections at node i
$\tilde{P}_{i,DG}, \tilde{Q}_{i,DG}$	Actual active and reactive power outputs of the DG at node i
$P_{i,SOP}, Q_{i,SOP}$	Active and reactive power outputs of the SOP at node i
$P_i^{DG,ref}$	Predicted DG output
$\Delta P_{i,DG}$	Variation in output due to uncertainties
$\tan\theta$	Tangent of the power factor angle
U_i^{sqr}	Square of the voltage magnitude at node i
U_j^{sqr}	Square of the voltage magnitude at node j
$P_{i,SOP}^{L}, P_{j,SOP}^{L}$	Active power losses at nodes i and j for the SOP.
$P_{i,DG}, Q_{i,DG}$	Active and reactive power outputs of the DG at node i
x	First-layer optimization variables
u	Second-layer optimization variables
h	Third-layer optimization variables
η	Auxiliary variable of the C&CG algorithm

frontiers | Frontiers in Energy Research

TYPE Opinion
PUBLISHED 15 March 2024
DOI 10.3389/fenrg.2024.1378325

OPEN ACCESS

EDITED BY
Shuai Yao,
Cardiff University, United Kingdom

REVIEWED BY
Cao Yingping,
Hong Kong Polytechnic University, Hong Kong SAR, China
Xi Lu,
Southeast University, China

*CORRESPONDENCE
Xiaorui Liang,
xrliang@mail.tsinghua.edu.cn

RECEIVED 29 January 2024
ACCEPTED 04 March 2024
PUBLISHED 15 March 2024

CITATION
Liang X, Zhang H, Liu Z, Wang Q and Xie H (2024), A survey on resilient operations of active distribution networks with diversified flexibility resources.
Front. Energy Res. 12:1378325.
doi: 10.3389/fenrg.2024.1378325

A survey on resilient operations of active distribution networks with diversified flexibility resources

Xiaorui Liang*, Huaying Zhang, Zijun Liu, Qing Wang and Hong Xie

New Smart City High-Quality Power Supply Joint Laboratory of China Southern Power Grid, Shenzhen Power Supply Co., Ltd., Shenzhen, China

KEYWORDS

active distribution networks, cellular architecture, distributed algorithm, flexibility resources, resilience enhancement

1 Introduction

With the widespread utilization of distributed renewable energy and flexible power electronics devices in power distribution networks, the paradigm and characteristics of active distribution networks (ADNs) have undergone profound changes as the traditional radial electricity network will be transformed into multi-layer, multi-ring, AC-DC hybrid networks (Wang et al., 2019). Meanwhile, the unpredictable and intermittent nature of distributed wind and photovoltaic generation poses formidable challenges, hindering the efficient utilization of distributed energy resources (DERs). Furthermore, the renewable-dominated ADNs are usually vulnerable to extreme climate events, such as rainstorm, floods, blizzards and forest fires (Shi et al., 2022; Hua et al., 2023; Cao et al., 2024). Such events generally cause sustained faults of distribution system and renewable energy components, and various renewable energy units with power electronic converters will increase fault currents of distribution networks, resulting in voltage drop, network isolation, or even electricity outages (Khodayar et al., 2014; Ma et al., 2018; Yang et al., 2022). With the increasing penetration level of distributed energy storage (Fang et al., 2023) and electric vehicles (Khatami et al., 2020), the support capability of these flexibility resources can be used for improving the power supply quality and system resilience of active distribution networks. Hence, this investigation aims to offer insightful perspectives and discussions on the resilient operations of ADNs with diversified flexibility resources under extreme events.

The main contributions of this work can be twofold as listed: (1) A cellular architecture of ADNs is presented for renewable energy accommodation and interactive emergency support to enhance multi-microgrid resilience with diversified flexibility resources, and a two-stage resilient model including pre-event preparation and post-disaster restoration is formulated to decrease the load curtailment cost; (2) A multi-level distributed control strategy based on alternating direction method of multipliers (ADMM) is presented to solve the proposed two-stage model of cellular ADNs, thereby autonomous resilient operations and privacy preservation of multi-microgrids can be achieved.

2 Cellular architecture of active distribution networks with high renewables

With the growing grid-integration of distributed renewable energies and plug-and-play loads in traditional distribution networks, a series of operational issued are emerged, such as unbalanced three-phase power, voltage sag, transformer overload (Awad et al., 2021; Vijay

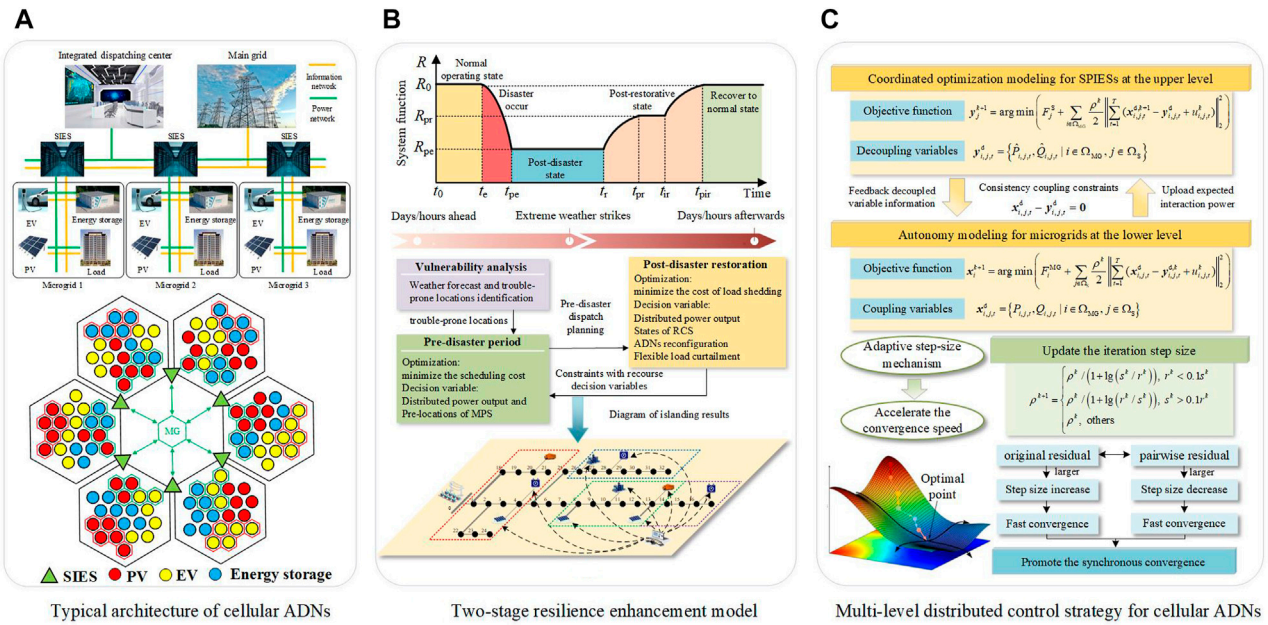

FIGURE 1
The proposed architecture, model and distributed control strategy for cellular ADNs. **(A)** Typical architecture of cellular ADNs **(B)** Two-stage resilience enhancement model **(C)** Multi-level distributed control strategy for cellular ADNs.

et al., 2021). The morphology of "cellular architecture" would be an efficient way to solve these electrical issues of future distribution networks. Cellular architecture of active distribution networks is a set of adjustable hexagonal feeder grids for fine-grained point-to-point power transport control of the ADN system with soft open points (SOPs), and then the economy and reliability of ADN operation can be improved. The unit in the cellular architecture of ADNs is actually an autonomous microgrid system, with high reliability of power supply and integration of flexible renewable energy (Wang et al., 2022).

In the cellular architecture of ADNs, heterogeneous microgrids are interconnected with each other with SOPs and smart information exchange stations (SIESs) (Zhou B. et al., 2021a) to improve the operational flexibility and efficient accommodation of DERs, as shown in Figure 1A. In each microgrid, DERs can be converted and regulated by various converters (Xiao et al., 2023) and storages to mitigate fluctuating renewable generations. The microgrid with surplus renewable energy can directly share with other microgrids, while the microgrid can be injected with energy support from others. Besides, communication techniques among microgrids can be performed by SIESs through the advanced measuring instruments and optical fiber deployed at the engaged sites (Cao et al., 2021). SIESs are designed as interfaces to coordinate the operation of multiple autonomous microgrids with DERs in cellular ADNs, and only informs the dispatch center on the total amount of surplus/deficit energy (Zhou B. et al., 2021a). Though the decentralized structure and coordinated operation, the intermittency and volatility of DERs within cellular ADNs can then be accommodated by diversified flexibility resources such as distributed energy storages and electric vehicles, and then power transmission losses and renewable energy curtailments can be alleviated.

The resilience of ADNs is generally used to assess the system capability for withstanding and recovering from significant energy outages under extreme weather events (Chen et al., 2017a). The resilient operation of cellular ADNs can rapidly disconnect microgrids from the main grid so as to protect power components from upstream disturbances, or to shield voltage sensitive loads from sudden voltage drops (Shi et al., 2022). Under the coordinated control of SIES, SOPs have the potential to island the microgrid from interferences such as failures or power quality incidents. After islanding, the reconnection of microgrids can be performed autonomously during fault recovery phase (Llaria et al., 2011). If the microgrid is partly damaged after a major outage, the SIES will restore energy supply services to emergency and nonemergency loads sequentially using dispatchable DERs such as mobile power sources (MPS) (Li C. et al., 2022a) and energy storages. Cellular ADNs can also be resynchronized with the main grid and shift from island mode to grid-connected mode after extreme events. Therefore, the cellular ADN structure can offer an effective and efficient way to utilize diversified flexibility resources to accommodate renewable energy and enhance system resilience.

3 Autonomous resilient operations of distribution networks under extreme climates

Generally, cellular ADNs are vulnerable to extreme climates and then lead to serious power outages and huge economic losses. A conceptual resilience curve related to an extreme weather is shown in Figure 1B to represent pre-disturbance, post-disaster degraded and post-disaster restorative stages for distribution networks (Shi

et al., 2022). In this paper, a two-stage resilience dispatch model is proposed to facilitate the pre-disaster prevention and post-disaster recovery of cellular ADNs. In the first stage, MPSs, SIES and SOPs are optimally scheduled to decrease the risk of damage to fault-prone power devices. In the second stage, optimal dispatch of network reconfiguration and flexibility resources is implemented to maintain sufficient and reliable power supplies to critical loads, as shown in Figure 1B.

In the pre-disaster prevention stage, the proposed model aims to dispatch various flexibility resources, including DERs, energy storage systems, MPSs, etc., for minimizing the scheduling cost of diversified flexibility resources and the interaction cost with the main grid. The fault-prone sites are identified based on the fragility model, and MPSs should be proactively pre-located to optimum sites with high potential of failures for survivability enhancement (Wang et al., 2021). DERs should also keep sufficient reserved capacity to cope with voltage fluctuations in the event of power imbalance (Wu et al., 2023). The objective function of pre-disaster preparation model is formulated as Eq. 1 follows,

$$F_1 = \min \sum_{t\in T_1}\Bigg[\sum_{i\in\Omega_{\mathrm{DG}}}\left(C^{\mathrm{DG}}P_{i,t}^{\mathrm{DG}}\right)+\sum_{i\in\Omega_{\mathrm{ESS}}}C_{\mathrm{ESS}}\left(\frac{P_{i,t}^{\mathrm{dc}}}{\eta_i^{\mathrm{dc}}}+\eta_i^{\mathrm{c}}P_{i,t}^{\mathrm{c}}\right) + \sum_{i\in\Omega_{\mathrm{MPS}}}\left(C^{\mathrm{M}}\eta^{\mathrm{M}}P_{i,t}^{\mathrm{M}}\right)+C^{\mathrm{buy}}P_t^{\mathrm{buy}}-C^{\mathrm{sell}}P_t^{\mathrm{sell}}\Bigg]\Delta t_1 \tag{1}$$

where T_1 refers to the set of pre-disaster scheduling periods; Δt_1 is the duration of each pre-disaster scheduling period; C^{DG}, C^{ESS}, C^{M} represents the cost coefficient of distributed power generation, energy storage operation and MPSs, respectively; C^{buy} denotes the electricity purchasing cost coefficient of the main grid; C^{sell} denotes the revenue coefficient from the sale of electricity; η_i^{c}, η_i^{dc} is the charging and discharging efficiency of energy storage system, respectively; η^{M} denotes the conversion efficiency between fuel consumption and power output of MPSs; $P_{i,t}^{\mathrm{DG}}$ represents the active power output of distributed energy resources at time period t; $P_{i,t}^{\mathrm{c}}$, $P_{i,t}^{\mathrm{dc}}$ denotes the charging and discharging power of energy storage system at time period t, respectively; $P_{i,t}^{\mathrm{M}}$ denotes the active power output of fuel-based generator; P_t^{buy}, P_t^{sell} refers to the purchased active power from the main grid and the sold active power to the main grid at time period t, respectively.

In the post-disaster restoration stage, the proposed model is to coordinate network reconfiguration, DERs and repair crew for minimizing the cost of load shedding. The network topology is reconstructed for critical load restoration by dynamically controlling status of sectionalizing and tie switches (Chen et al., 2017b; Shi et al., 2021). Diversified DERs are served as reserved generators to support the power supply within islands for reducing load curtailment (Chen et al., 2023). Moreover, the route and sequence of repair crew is optimized to facilitate the recovery of fault power devices (Arif et al., 2020). The objective function of post-disaster restoration model is presented as Eq. 2,

$$F_2 = \min \sum_{s\in S}\rho_s\left[\sum_{t\in T_2}\left(\sum_{l\in\Omega_{\mathrm{L}}}\left(C^{\mathrm{loss}}w_l P_{l.t.s}^{\mathrm{loss}}\right)\right)\Delta t_2\right] \tag{2}$$

where T_2 refers to the set of post-disaster scheduling periods; Δt_2 is the duration of each post-disaster scheduling period; ρ_s denotes the occurring probability of for scenario s; C^{loss} denotes the penalty coefficient of load shedding and the concrete value is determined on how critical the load is; w_l represents the weight of different loads; $P_{l.t.s}^{\mathrm{loss}}$ denotes the amount of load curtailment at time period t.

In order to verify the resilient operation capability of cellular ADNs with the two-stage model, the comparison of per unit of average voltage is shown in Figure 2A. It can be found that per unit of average voltage in cellular ADNs is more stable compared to conventional ADNs.

4 Multi-level distributed control strategy for diversified flexibility resources

Considering the individual autonomy and privacy preservation requirements of multi-microgrids in the cellular ADNs, a multi-level distributed control strategy is proposed for solving the two-stage resilient operation model to minimize overall load curtailment cost. At the upper level, SIESs serve as decision-makers to coordinate the energy exchange among multi-microgrids for maintaining power balance. At the lower level, each microgrid achieves autonomous operation through the coordinated scheduling of diversified flexibility resources (Wang et al., 2022). The proposed distributed control problem can be solved by ADMM algorithm, which combines the advantage of decomposability of dual ascent and excellent convergence properties of multiplier method (Rui et al., 2020; Liu et al., 2018). Taking the pre-event preparation model as an example, the resilient optimization problem of cellular ADNs can be decomposed into subproblems for microgrids and SIESs as Eq. 3. The respective optimization objectives are as Eqs 4, 5,

$$\min F_1 = \sum_{i\in\Omega_{\mathrm{S}}}F_i^{\mathrm{S}}+\sum_{i\in\Omega_{\mathrm{MG}}}F_i^{\mathrm{MG}} \tag{3}$$

$$F_i^{\mathrm{S}} = \sum_{t=1}^{T_1}\left(C^{\mathrm{buy}}P_{i,t}^{\mathrm{buy}}-C^{\mathrm{sell}}P_{i,t}^{\mathrm{sell}}\right)\Delta t_1 \tag{4}$$

$$F_i^{\mathrm{MG}} = \sum_{t=1}^{T_1}\left(C^{\mathrm{DG}}P_{i,t}^{\mathrm{DG}}+C_{\mathrm{ESS}}\left(\frac{P_{i,t}^{\mathrm{dc}}}{\eta_i^{\mathrm{dc}}}+\eta_i^{\mathrm{c}}P_{i,t}^{\mathrm{c}}\right)+C^{\mathrm{MPS}}\eta^{\mathrm{M}}P_{i,t}^{\mathrm{M}}\right)\Delta t_1 \tag{5}$$

where Ω_{MG}, Ω_{S} denotes the set of microgrids and SIESs; F_i^{S} and F_i^{MG} denotes the optimization objective for microgrids and SIESs, respectively.

The optimization variables of hierarchical distributed scheduling strategy for cellular ADNs include diversified flexibility resources regulation power comprised of distributed generation, energy storage and MPSs for microgrids, and the power purchased from or sold to the main grid for SIESs. In addition, the power interaction between interconnected microgrids and SIESs needs to be optimized as coupling variables. Hence, the expected interaction power for microgrid i and SIES j are proposed as coupling variables $\boldsymbol{x}_{i,j,t}^{\mathrm{d}}$ and decoupling variables $\boldsymbol{y}_{i,j,t}^{\mathrm{d}}$, respectively, to establish the consistency coupling constraints as Eq. 6 (Zhou X. et al., 2021b).

$$\begin{cases}\boldsymbol{x}_{i,j,t}^{\mathrm{d}} = \left\{P_{i,j,t},Q_{i,j,t}\middle|i\in\Omega_{\mathrm{MG}},j\in\Omega_{\mathrm{S}}\right\}\\ \boldsymbol{y}_{i,j,t}^{\mathrm{d}} = \left\{\hat{P}_{i,j,t},\hat{Q}_{i,j,t}\middle|i\in\Omega_{\mathrm{MG}},j\in\Omega_{\mathrm{S}}\right\}\\ \boldsymbol{x}_{i,j,t}^{\mathrm{d}}-\boldsymbol{y}_{i,j,t}^{\mathrm{d}} = \boldsymbol{0}\end{cases} \tag{6}$$

A Lagrange penalty function is added to the objective functions for microgrids and SIESs, as follows,

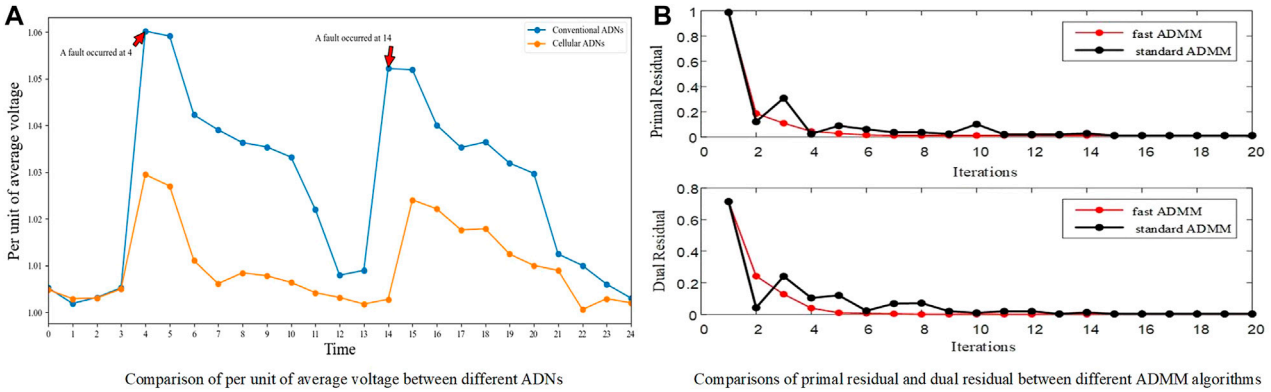

Comparison of per unit of average voltage between different ADNs

Comparisons of primal residual and dual residual between different ADMM algorithms

FIGURE 2
Comparison between different ADNs and comparisons different ADMM algorithms. **(A)** Comparison of per unit of average voltage between different ADNs **(B)** Comparisons of primal residual and dual residual between different ADMM algorithms.

$$\boldsymbol{x}_i^{k+1} = \operatorname{argmin}\left(F_i^{\mathrm{MG}} + \sum_{j\in\Omega_{\mathrm{S}}} \frac{\rho^k}{2}\left\| \sum_{t=1}^{T}\left(\boldsymbol{x}_{i,j,t}^{\mathrm{d}} - \boldsymbol{y}_{i,j,t}^{\mathrm{d},k} + \boldsymbol{u}_{i,j,t}^{k} \right) \right\|_2^2 \right) \tag{7}$$

$$\boldsymbol{y}_j^{k+1} = \operatorname{argmin}\left(F_j^{\mathrm{S}} + \sum_{i\in\Omega_{\mathrm{MG}}} \frac{\rho^k}{2}\left\| \sum_{t=1}^{T}\left(\boldsymbol{x}_{i,j,t}^{\mathrm{d},k+1} - \boldsymbol{y}_{i,j,t}^{\mathrm{d}} + \boldsymbol{u}_{i,j,t}^{k} \right) \right\|_2^2 \right) \tag{8}$$

where ρ^k is the iteration step size; $u_{i,j,t}^k$ is Lagrange multiplier; k is the number of iterations. The original optimization model is solved iteratively by the above two equations. On the one hand, each microgrid develops a scheduling plan independently with information of internal controllable flexibility resources and uploads the data of expected interaction power $\boldsymbol{x}_i^{k+1}$ to SIESs. On the other hand, each SIES determines the data of $\boldsymbol{y}_j^{k+1}$ and sends it to interconnected microgrids taking into account the needs of power balance and energy interaction. After each iteration, the primal residual r_k and dual residual s^k are calculated as convergence criterion according to Eqs 9, 10.

$$r_k = \sum_{i\in\Omega_{\mathrm{MG}}} \sum_{j\in\Omega_{\mathrm{S}}} \left\| \sum_{t=1}^{T}\left(\boldsymbol{x}_{i,j,t}^{\mathrm{d},k} - \boldsymbol{y}_{i,j,t}^{\mathrm{d},k} \right) \right\|_2 \le \varepsilon_r \tag{9}$$

$$s^k = \sum_{i\in\Omega_{\mathrm{MG}}} \rho \left\| \sum_{t=1}^{T}\left(\boldsymbol{x}_{i,t}^{\mathrm{d},k} - \boldsymbol{x}_{i,t}^{\mathrm{d},k-1} \right) \right\|_2 \le \varepsilon_{\mathrm{s}} \tag{10}$$

where ε_r, ε_{s} denotes the convergence threshold for primal residual and dual residual, respectively. If the convergence condition is not satisfied, Lagrange multipliers will be updated according to Eq. 11 and then a next iteration will be proceeded. Otherwise, the iteration is completed to obtain the final scheduling determination of diversified flexibility resources for cellular ADNs, as follows,

$$\boldsymbol{u}_{i,j,t}^{k+1} = \boldsymbol{u}_{i,j,t}^{k} + \boldsymbol{x}_{i,j,t}^{\mathrm{d},k+1} - \boldsymbol{y}_{i,j,t}^{\mathrm{d},k+1} \tag{11}$$

It can be shown from Eqs 7, 8 that both the Lagrange multipliers and iteration step have a dominated influence on convergence properties of the algorithm. The existing conventional method always keeps the iteration step size as a fixed parameter, which restricts the convergence properties owing to the imbalance of primal and dual residuals (Li Z. et al., 2022b; Mhanna et al., 2019). In order to accelerate the convergence speed, an adaptive step-size mechanism can be used to update the iteration step and promote the synchronous convergence of primal and dual residuals as shown in Eq. 12 (Gao et al., 2020; Ghadimi et al., 2015),

$$\rho^{k+1} = \begin{cases} \rho^k / \left(1 + \lg\left(s^k / r^k\right)\right), r^k < 0.1 s^k \\ \rho^k / \left(1 + \lg\left(r^k / s^k\right)\right), s^k > 0.1 r^k \\ \rho^k, \text{others} \end{cases} \tag{12}$$

when s^k is larger, the iteration step size ρ^{k+1} increases, accelerating the convergence of s^k. Contrarily, when r^k is larger, ρ^{k+1} decreases, preventing the oscillation of objective function and further promoting the local convergence of r^k.

The iterative process and acceleration principle of multi-level distributed control strategy for cellular ADNs based on adaptive ADMM algorithm are shown in Figure 1C. Comparisons of primal residuals and dual residuals between different ADMM algorithms are shown in Figure 2B. It can be found that the model convergence speed can be enhanced by 18.7% compared to conventional ADMM algorithms through the adaptive correction of step sizes.

5 Discussion and conclusion

A survey on resilient operations of cellular ADNs with flexibility resources under extreme events is presented in this paper. The following are the key findings of this study: 1) The proposed two-stage model utilizes the cellular ADN architecture and diversified flexibility resources to alleviate the damage caused by extreme climate events. 2) A multi-level distributed control strategy based on adaptive ADMM is proposed to solve the two-stage resilient model for the purpose of reducing overall load curtailment cost, and the convergence speed can enhance by 18.7% with the adaptive step-size mechanism. 3) The further

research will focus on diversified flexibility resources integration into active distribution networks.

Author contributions

XL: Conceptualization, Writing–original draft. HZ: Data curation, Formal Analysis, Writing–review and editing. ZL: Visualization, Writing–review and editing. QW: Writing–original draft. HX: Writing–original draft.

Funding

The author(s) declare financial support was received for the research, authorship, and/or publication of this article. This work is supported by the Science and Technology Project of China Southern Power Grid (090000KK52222143/SZKJXM20222116).

Conflict of interest

Authors XL, HZ, ZL, QW, and HX were employed by Shenzhen Power Supply Co., Ltd.

The authors declare that this study received funding from the Science and Technology Project of China Southern Power Grid. The funder had the following involvement in the study: conceptualization, data curation and formal analysis, visualization, writing the original draft and editing.

Publisher's note

References

Arif, A., Wang, Z., Chen, C., and Wang, J. (2020). Repair and resource scheduling in unbalanced distribution systems using neighborhood search. *IEEE Trans. Smart Grid* 11, 673–685. doi:10.1109/TSG.2019.2927739

Awad, A. S. A., Turcotte, D., and El-Fouly, T. H. M. (2021). Impact assessment and mitigation techniques for high penetration levels of renewable energy sources in distribution networks: voltage-control perspective. *J. Mod. Power Syst. Clean Energy* 10, 450. doi:10.35833/MPCE.2020.000177

Cao, Y., Zhou, B., Chung, C. Y., Wu, T., Zheng, L., and Shuai, Z. (2024). A coordinated emergency response scheme for electricity and watershed networks considering spatio-temporal heterogeneity and volatility of rainstorm disasters. *IEEE Trans. Smart Grid*, 1. doi:10.1109/TSG.2024.3362344

Cao, Y., Zhou, B., Or, S., Chan, K., Liu, N., and Zhang, K. (2021). An interactive tri-level multi-energy management strategy for heterogeneous multi-microgrids. *J. Clean. Prod.* 319, 128716. doi:10.1016/j.jclepro.2021.128716

Chen, C., Guo, C., Huang, G., Qi, J., and Wang, J. (2017b). Integration of preventive and emergency responses for power grid resilience enhancement. *IEEE Trans. Power Syst.* 32, 4451–4463. doi:10.1109/TPWRS.2017.2685640

Chen, C., Guo, C., Huang, G., Zhu, B., and Wang, J. (2017a). System resilience enhancement: smart grid and beyond. *Front. Eng. Manag.* 4, 271. doi:10.15302/J-FEM-2017030

Chen, H., Wang, J., Zhu, J., Xiong, X., Wang, W., and Yang, H. (2023). A two-stage stochastic mixed-integer programming model for resilience enhancement of active distribution networks. *J. Mod. Power Syst. Clean Energy* 11, 94–106. doi:10.35833/MPCE.2022.000467

Fang, R., Wang, H., Qin, B., Wu, D., and Zhu, Y. (2023). Underground energy storage system supported resilience enhancement for power system in high penetration of renewable energy. *Front. Energy Res.* 11. doi:10.3389/fenrg.2023.1138318

Gao, H., Wang, J., Liu, Y., Wang, L., and Liu, J. (2020). An improved ADMM-based distributed optimal operation model of AC/DC hybrid distribution network considering wind power uncertainties. *IEEE Syst. J.* 15, 2201–2211. doi:10.1109/JSYST.2020.2994336

Ghadimi, E., Teixeira, A., Shames, I., and Johansson, M. (2015). Optimal parameter selection for the alternating direction method of multipliers (ADMM): quadratic problems. *IEEE Trans. Automatic Control* 60, 644–658. doi:10.1109/TAC.2014.2354892

Hua, Z., Zhou, B., Or, S., Zhang, J., Li, C., and Wei, J. (2023). Robust emergency preparedness planning for resilience enhancement of energy-transportation nexus against extreme rainfalls. *IEEE Trans. Industry Appl.* 60, 1196–1207. doi:10.1109/TIA.2023.3274615

Khatami, R., Parvania, M., and Oikonomou, K. (2020). Deliverable energy flexibility scheduling for active distribution networks. *IEEE Trans. Smart Grid* 11, 655–664. doi:10.1109/TSG.2019.2927604

Khodayar, M., Che, L., and Shahidehpour, M. (2014). Adaptive protection system for microgrids: protection practices of a functional microgrid system. *IEEE Electrification Mag.* 2, 66–80. doi:10.1109/MELE.2013.2297031

Li, C., Xi, Y., Lu, Y., Liu, N., Chen, L., Ju, L., et al. (2022a). Resilient outage recovery of a distribution system: co-optimizing mobile power sources with network structure. *Prot. Control Mod. Power Syst.* 7, 32. doi:10.1186/s41601-022-00256-9

Li, Z., Li, P., Yuan, Z., Xia, J., and Tian, D. (2022b). Optimized utilization of distributed renewable energies for island microgrid clusters considering solar-wind correlation. *Electr. Power Syst. Res.* 206, 107822. doi:10.1016/j.epsr.2022.107822

Liu, H., Shi, W., and Zhu, H. (2018). Distributed voltage control in distribution networks: online and robust implementations. *IEEE Trans. Smart Grid* 9, 6106–6117. doi:10.1109/TSG.2017.2703642

Llaria, A., Curea, O., Jiméne, J., and Camblong, H. (2011). Survey on microgrids: unplanned islanding and related inverter control techniques. *Renew. energy* 36, 2052–2061. doi:10.1016/j.renene.2011.01.010

Ma, S., Wang, Z., and Chen, B. (2018). Resilience enhancement strategy for distribution systems under extreme weather events. *IEEE Trans. Smart Grid* 9, 1442–1451. doi:10.1109/TSG.2016.2591885

Mhanna, S., Verbic, G., and Chapman, A. (2019). Adaptive ADMM for distributed AC optimal power flow. *IEEE Trans. Power Syst.* 34, 2025–2035. doi:10.1109/TPWRS.2018.2886344

Rui, P., Ricardo, J., Jean, S., and Manuel, A. (2020). Distributed multi-period three-phase optimal power flow using temporal neighbors. *Electr. Power Syst. Res.* 182, 106228. doi:10.1016/j.epsr.2020.106228

Shi, Q., Li, F., Olama, M., Dong, J., Xue, Y., Starke, M., et al. (2021). Network reconfiguration and distributed energy resource scheduling for improved distribution system resilience. *Int. J. Electr. Power & Energy Syst.* 124, 106355. doi:10.1016/j.ijepes.2020.106355

Shi, Q., Zeng, B., Hui, H., Li, F., and Liu, W. (2022). Enhancing distribution system resilience against extreme weather events: concept review, algorithm summary, and future vision. *Int. J. Electr. Power & Energy Syst.* 138, 107860. doi:10.1016/j.ijepes.2021.107860

Vijay, A., Doolla, S., and Chandorkar, M. (2021). Varying negative sequence virtual impedance adaptively for enhanced unbalanced power sharing among DGs in islanded AC microgrids. *IEEE Trans. Energy Convers.* 36, 3271–3281. doi:10.1109/TEC.2021.3073150

Wang, D., Zhang, N., Lei, Y., Wang, C., and Zhang, Z. (2019). Prospects for key technologies of new-type urban integrated energy system. *Glob. Energy Interconnect.* 2, 402–412. doi:10.1016/j.gloei.2019.11.015

Wang, L., Zu, G., Xu, W., Zhu, W., and Luo, F. (2022). Honeycomb distribution networks: concept and central features. 2022 5th International Conference on Energy,

Electrical and Power Engineering (CEEPE), April 2022, Chongqing, China. IEEE. doi:10.1109/CEEPE55110.2022.9783369

Wang, Z., Ma, S., Arif, A., and Zhang, Q. (2021). Stochastic pre-event preparation for enhancing resilience of distribution systems. *Renew. Sustain. Energy Rev.* 152, 111636. doi:10.1016/j.rser.2021.111636

Wu, J., Gu, J., Jin, Z., and Liu, S. (2023). Strategies for improving resilience of regional integrated energy systems in the prevention–resistance phase of integration. *Prot. Control Mod. Power Syst.* 8, 29. doi:10.1186/s41601-023-00299-6

Xiao, H., He, H., Zhang, L., and Liu, T. (2023). Adaptive grid synchronization based grid-forming control for voltage source converters. *IEEE Trans. Power Syst.* 39, 4763–4766. doi:10.1109/TPWRS.2023.3338967

Yang, X., Zhou, Z., Zhang, Y., Liu, J., Wen, J., Wu, Q., et al. (2022). Resilience-oriented co-deployment of remote-controlled switches and soft open points in distribution networks. *IEEE Trans. Power Syst.* 38, 1350–1365. doi:10.1109/TPWRS.2022.3176024

Zhou, B., Zou, J., Chung, C. Y., Wang, H., Liu, N., Voropai, N., et al. (2021a). Multi-microgrid energy management systems: architecture, communication, and scheduling strategies. *J. Mod. Power Syst. Clean Energy* 9, 463–476. doi:10.35833/MPCE.2019.000237

Zhou, X., Zou, S., Wang, P., and Ma, Z. (2021b). ADMM-based coordination of electric vehicles in constrained distribution networks considering fast charging and degradation. *IEEE Trans. Intelligent Transp. Syst.* 22, 565–578. doi:10.1109/TITS.2020.3015122

frontiers | Frontiers in Energy Research

TYPE Original Research
PUBLISHED 15 March 2024
DOI 10.3389/fenrg.2024.1374986

OPEN ACCESS

EDITED BY
Yumin Zhang,
Shandong University of Science and Technology, China

REVIEWED BY
Nishant Kumar,
Indian Institute of Technology Jodhpur, India
Yang Lei,
Anhui University, China
Qi Liu,
Shandong University of Science and Technology, China

*CORRESPONDENCE
Li Quanjun,
sailor0227@163.com

RECEIVED 23 January 2024
ACCEPTED 04 March 2024
PUBLISHED 15 March 2024

CITATION
Quanjun L, Huazhong S, Mingming L, Jinbao L, Wenyu J and Kai W (2024), Complex affine arithmetic based uncertain sensitivity analysis of voltage fluctuations in active distribution networks.
Front. Energy Res. 12:1374986.
doi: 10.3389/fenrg.2024.1374986

Complex affine arithmetic based uncertain sensitivity analysis of voltage fluctuations in active distribution networks

Li Quanjun[1]*, Sun Huazhong[1], Liu Mingming[1], Li Jinbao[1], Ji Wenyu[1] and Wang Kai[2]

[1]State Grid Weifang Electric Power Company, Weifang, Shandong, China, [2]School of Electrical Automation and Information Engineering of Tianjin University, Tianjin, China

The uncertainties of distribution generations (DGs) and loads lead to severe voltage fluctuations in active distribution networks (ADNs). Meanwhile, energy storage systems (ESSs) and static var compensators (SVCs) can mitigate the uncertainties of power injections by regulating the active and reactive power. Considering the variations of multiple uncertain factors, this paper proposes a complex affine arithmetic (CAA) based uncertain sensitivity analysis method of voltage fluctuations in ADNs. First, affine models of active and reactive power injections are established. The correlations of noisy symbols are used to reflect the mitigation effects of ESSs and SVCs on the uncertainties introduced by DGs and loads. Next, sensitivity indicators of voltage fluctuations are defined based on the transitivity of noisy symbols. Then, a calculation method for sensitivity indicators based on the micro-increments of coefficients is proposed. Combined with the obtained indicators, a fast sensitivity method for calculating interval values of voltages is further proposed. The modified IEEE 33-bus system is tested to validate the accuracy and efficiency of the proposed method by comparison with the continuous utilization of power flow method. Moreover, the 292-bus system is tested to validate its applicability in a large distribution system. Facts have proved that this method improves the efficiency and reliability of calculations, and in different scenarios, it can achieve fast calculation of nodes and online analysis of the voltage fluctuation range in uncertain environments, provides an effective tool for voltage quality management in active distribution networks.

KEYWORDS

active distribution network, complex affine arithmetic, sensitivity analysis, uncertainty, voltage fluctuation

1 Introduction

The stochastic and intermittent characteristics of renewable energy resources cause the uncertainties of distributed generations (DGs) in active distribution networks (ADNs) (Alonso-Travesset et al., 2022). Meanwhile, the fluctuations of load demands have increased the uncertainties to some extent (Zhang et al., 2023). The uncertainties will induce severe voltage fluctuations in ADNs. The integration of energy storage systems (ESSs) and static var compensators (SVCs) can mitigate the uncertainties of power injections by regulating the active and reactive power, which will reduce the levels of voltage fluctuations. Considering the

variations of multiple uncertain factors, an uncertain sensitivity analysis method can help to control critical nodes and uncertain factors in such an uncertain environment.

The sensitivity analysis method generally uses the differential relationship of variables to indicate the sensitivity of output variables to the variations of input variables (Shang et al., 2021). According to different physical interpretations of variables, multiple sensitivity indicators are defined (Chang et al., 2022). For instance, the indicators dU_i/dP_j and dU_i/dQ_j represent the sensitivity of the voltage at node i to the variations of active and reactive power injections at node j. Voltage sensitivity indicators have been widely used in many research fields, including voltage stability analysis, voltage control, and DG allocation. In (Li et al., 2018), a fast sensitivity based preventive control selection method was proposed for online voltage stability assessment. Reference (Su et al., 2019) proposed a measurement based voltage control method for distribution networks combined with the sensitivity estimation. In (Gupta and Kumar, 2022), the optimal location and sizing of each DG were obtained by sensitivity based techniques.

Traditionally, there are three typical methods for calculating sensitivity indicators of voltages.

The first type is the Jacobian matrix method. In the process of Calculating the power flow of the Newtonian method, the Jacobian matrix J contains the partial derivatives of the node's net injection of active and reactive power with respect to the voltage. Through the inversion operation of the matrix, the sensitivity of the voltage to the change of the node's net injection of active and reactive power can be obtained. Indicators (Alzaareer et al., 2020; Song et al., 2020; Munikoti et al., 2021). When the Newtonian power flow calculation reaches the convergence state, the obtained Jacobian matrix and inversion operation can be used to obtain the voltage sensitivity index. Literature (Mlilo et al., 2021) considers the random output characteristics of wind power, uses the Jacobian matrix method to calculate the voltage sensitivity index, and combines the K-means clustering method and joint sensitivity to establish a voltage sensitivity analysis scenario.

The second type is the incremental method. The incremental method can also be called the perturb-and-observe approach. By giving a small change in the input variable, the change in the output variable is observed to calculate the voltage sensitivity index (Shuai et al., 2021; Gupta and Paolone, 2023). The incremental method is simple and easy to implement, and obtains high-precision voltage sensitivity indicators by making the changes in the net injected active and reactive power of the node tend to zero. From a simulation perspective, the incremental method is easy to implement. Literature (Alvarado-Barrios et al., 2020) developed a voltage sensitivity analysis software for the distribution network based on the incremental method, and set the increment of the node's net injected power to 0.5% of the average load level. To 2%, a high-precision voltage sensitivity index that meets the requirements is obtained. The incremental method has high adaptability to various functions or power flow algorithms, but when the input variables change, it is necessary to calculate and observe the changes in the output variables, which increases the overall calculation amount.

The third category is topological analysis method. The topological analysis method is based on the network topology, applies Tellegen's theorem, and combines the adjoint network theory to calculate the voltage sensitivity index (Bandler and El-Kady, 1980; Bai et al., 2020). Literature (Wang et al., 2018) elaborates on the adjoint network theory and the sensitivity calculation method based on the generalized Tellegen theorem, and applies the voltage sensitivity index to the vulnerability assessment of the power grid. Literature (Ye et al., 2021) proposed a new calculation method for voltage sensitivity index based on changes in the net injected active and reactive power of nodes in a three-phase unbalanced distribution network. This method calculates ABCD parameters based on network topology and realizes fast online calculation of voltage sensitivity indicators. The topological analysis method usually requires a power flow solution of a reference state in order to establish a specific adjoint network, and then use the network topology parameters to obtain the voltage sensitivity index.

The method based on the Jacobian matrix provides accurate results and is suitable for stability analysis, but requires recalculation when system conditions change, which is computationally intensive. The perturbation and observation method is easy to operate and suitable for rapid sensitivity assessment, but may not be as accurate as the Jacobian method. The method based on circuit theory has a solid theoretical foundation and is suitable for education and in-depth research, but the preparation work is more complicated.

However, considering voltage fluctuations caused by the uncertainties in ADNs, voltages become uncertain values with the lower and upper bounds, instead of deterministic point values. Each change in node voltage covers all point values in the range of change. But in previous sensitivity analysis, the variation only reflects the deviation between point values. Thus, new methods need to be studied to handle uncertain variables in the sensitivity analysis of voltage fluctuations.

Faced with the uncertainty problem, affine arithmetic (AA) can effectively deal with uncertain variables with the lower and upper bounds (Ruiz-Rodriguez et al., 2020). Compared with interval arithmetic, AA performs better in terms of more compact solution region and lower conservativeness. Further, AA is extended into the complex plane and complex affine arithmetic (CAA) is developed (Manson, 2005; Wang et al., 2019). Since AA and CAA have been used to handle the uncertainty problem in power systems, existing researches mainly focus on the uncertain power flow calculation (Guerrero et al., 2020; Meinecke et al., 2020; Tang et al., 2020; Zeynali et al., 2020; Wang et al., 2021). In addition, reference (Zhang et al., 2022) proposed a reactive power optimization method while using AA to handle interval uncertainties. CAA can keep track of correlations among uncertain variables, which helps to carry out sensitivity analysis in uncertain environments.

Therefore, a CAA based uncertain sensitivity analysis method of voltage fluctuations in ADNs is proposed. The main contributions are highlighted as follows.

1) CAA is used to quantify the uncertainties introduced by DGs and loads, as well as the mitigation effects of ESSs and SVCs. Affine models of active and reactive power injections are established based on the correlations of noisy symbols. Further, considering the variations of multiple factors, sensitivity indicators of voltage fluctuations are defined based on the transitivity of noisy symbols.
2) A calculation method for sensitivity indicators based on the micro-increments of coefficients is proposed. In the calculation process, an improved forward-backward sweep power flow based on CAA is used to calculate the voltages in affine form. The obtained indicators can quantitatively reflect the sensitivity of voltage fluctuations to the variations of uncertain factors.

3) A fast sensitivity method for calculating interval values of voltages is proposed. The proposed method avoids the continuous utilization of power flow algorithm while guaranteeing the accuracy and efficiency of calculation.

The rest of the paper is organized as follows. Section 2 describes the complex affine arithmetic. Section 3 establishes the affine models of active and reactive power injections considering correlations. Section 4 proposes a CAA based uncertain sensitivity analysis method of voltage fluctuations in ADNs. Section 5 conducts the case study and discusses the results. Finally, Section 6 draws the main conclusions.

2 Complex affine arithmetic

2.1 Mathematical theory

The complex affine variable is represented by a linear combination of the center value and a series of noise terms [19]. A complex affine variable is defined as in (1).

$$\hat{x} = x_0 + x_1\varepsilon_1 + \cdots + x_n\varepsilon_n = x_0 + \sum_{i=1}^{n} x_i\varepsilon_i \tag{1}$$

Each noisy symbol represents an uncertain factor and the corresponding coefficient reflects the magnitude of fluctuation around the center value.

Given two complex affine variables $\hat{x}$ and $\hat{y}$, operations can be expressed as follows:

$$\hat{x} \pm \hat{y} = (x_0 \pm y_0) + \sum_{i=1}^{n} (x_i \pm y_i)\varepsilon_i \tag{2}$$

$$\begin{aligned} \hat{x} \cdot \hat{y} &= \left(x_0 + \sum_{i=1}^{n} x_i\varepsilon_i\right) \times \left(y_0 + \sum_{i=1}^{n} y_i\varepsilon_i\right) \\ &= x_0 y_0 + \sum_{i=1}^{n} (x_0 y_i + y_0 x_i)\varepsilon_i + \sum_{i=1}^{n} x_i\varepsilon_i \times \sum_{i=1}^{n} y_i\varepsilon_i \end{aligned} \tag{3}$$

$$\hat{x} \Big/ \hat{y} = \hat{x} \cdot \frac{1}{\hat{y}} = \left(x_0 + \sum_{i=1}^{n} x_i\varepsilon_i\right) \Big/ \left(y_0 + \sum_{i=1}^{n} y_i\varepsilon_i\right) \tag{4}$$

In the above formula (2) and formula (3), $\boldsymbol{x}_0$ is a complex number, representing the central value; ε_i is the noise element, takes a value within $[-1, 1]$, representing the uncertainty factor; $\boldsymbol{x}_i$ is the noise coefficient, both are complex numbers, representing the offset relative to the central value, that is, the noise element causes uncertainty The size of the influence; n is the number of noise elements.

The main challenge is to find the optimal approximation for non-affine terms as in (Shang et al., 2021)-(4). The derivation and proof of basic operations can be referred to [20]. In the calculation process, the number of error terms will increase with the existence of non-affine terms.

2.2 Correlation and transitivity properties of noisy symbols

In this paper, uncertain sensitivity analysis of voltage fluctuations mainly relies on the correlation and transitivity properties of noisy symbols. In CAA, correlations among complex affine variables can be reflected by coexisting noisy symbols. Meanwhile, the coefficients of noisy symbols can reflect the uncertainty level of each complex affine variable.

For a multivariate function f with n input variables in affine form, the transitivity of noisy symbols is shown as in (5–7).

$$\hat{y} = f(\hat{x}_1, \hat{x}_2, \cdots, \hat{x}_n) \tag{5}$$

$$\hat{x}_i = x_{i0} + x_i\varepsilon_i \ (i = 1, 2, \cdots, n) \tag{6}$$

$$\begin{aligned} \hat{y} &= f(x_{10} + x_1\varepsilon_1, x_{20} + x_2\varepsilon_2, \cdots, x_{n0} + x_n\varepsilon_n) \\ &= y_0 + y_1\varepsilon_1 + \cdots + y_n\varepsilon_n + y_{k1}\varepsilon_{k1} + \cdots + y_{km}\varepsilon_{km} \end{aligned} \tag{7}$$

In the formula, $\hat{\boldsymbol{x}}_1, \hat{\boldsymbol{x}}_2, \cdots, \hat{\boldsymbol{x}}_n$ represents n uncertain input variables, all of which are complex affine variables; $\boldsymbol{x}_{10}, \boldsymbol{x}_{20}, \cdots, \boldsymbol{x}_{n0}$ is the central value of n complex affine variables, all of which are complex numbers; $\varepsilon_1, \varepsilon_2, \cdots, \varepsilon_n$ represents the main noise element introduced by the uncertainty input variables; $\boldsymbol{x}_1, \boldsymbol{x}_2, \cdots, \boldsymbol{x}_n$ is the main noise Coefficients are all complex numbers; $\hat{\boldsymbol{y}}$ is complex affine output variables.

Assuming that there are m non-affine operations in the function, noise terms of $\hat{y}$ can be divided into two parts, including $\{y_1\varepsilon_1, y_2\varepsilon_2, \cdots, y_n\varepsilon_n\}$ and $\{y_{k1}\varepsilon_{k1}, y_{k2}\varepsilon_{k2}, \cdots, y_{km}\varepsilon_{km}\}$. We call the first part the main noise terms, which contain the main noisy symbol set $\{\varepsilon_1, \varepsilon_2, \cdots, \varepsilon_n\}$ and the corresponding coefficient set $\{y_1, y_2, \cdots, y_n\}$. Meanwhile, we call the second part the error noise terms, which contain the error noisy symbol set $\{\varepsilon_{k1}, \varepsilon_{k2}, \cdots, \varepsilon_{km}\}$ and the corresponding coefficient set $\{y_{k1}, y_{k2}, \cdots, y_{km}\}$. The main noisy symbols are transmitted from input variables with uncertainties. The error noisy symbols are derived from the approximation for non-affine operations

For each uncertain variable $\hat{x}_i$, the variation of the uncertainty level is quantitatively represented by the variation of the corresponding coefficient x_i. In the complex plane, this variation reflects the change in the area of fluctuation around the central value.

When the uncertainty levels of input variables changes, the new complex affine variables are denoted as:

$$\begin{cases} \hat{x}'_i = \hat{x}_i + \Delta\hat{x}_i = x_{i0} + (x_i + \Delta x_i)\varepsilon_i \\ \Delta\hat{x}_i = \Delta x_i\varepsilon_i \end{cases} (i = 1, 2, \cdots, n) \tag{8}$$

In the formula (8), $\Delta\boldsymbol{x}_i$ is the change amount of the main noise coefficient, which is a complex number, quantitatively expressing the change in the uncertainty level of the input variable $\hat{\boldsymbol{x}}_i$; $\Delta\hat{\boldsymbol{x}}_i$ is the complex affine change amount.

Then, the output variable is updated by (9).

$$\begin{aligned} \hat{y}' &= f(\hat{x}_1 + \Delta\hat{x}_1, \hat{x}_2 + \Delta\hat{x}_2, \cdots, \hat{x}_n + \Delta\hat{x}_n) \\ &= y'_0 + y'_1\varepsilon_1 + \cdots + y'_n\varepsilon_n + y'_{k1}\varepsilon'_{k1} + \cdots + y'_{km}\varepsilon'_{km} \end{aligned} \tag{9}$$

The main effects of the variations on the output variable can be quantified by the corresponding coefficients of noisy symbols $(\varepsilon_1, \varepsilon_2, \cdots \varepsilon_n)$, which are transmitted from input variables. This property contributes to uncertain sensitivity analysis of voltage fluctuations in ADNs.

3 Affine models of active and reactive power injections considering correlations

Considering the uncertainties of DGs and loads, as well as the mitigation effects of ESSs and SVCs, affine models of active and reactive power injections are built. The correlations of noisy symbols

are used to reflect the mitigation effects of ESSs and SVCs on uncertainties introduced by DGs and loads.

3.1 Affine model of active power injection

The affine model of active power injection of phase φ at node i is shown as in (10).

$$\hat{P}^{\varphi}_{inj,i} = \alpha_i \hat{P}^{\varphi}_{L,i} - \beta_i \hat{P}^{\varphi}_{DG,i} - \gamma_i \hat{P}^{\varphi}_{ESS,i} \tag{10}$$

The model considers the active power of loads, DGs, and ESSs. The load power is regarded as the positive direction, and the positive value of $\hat{P}^{\varphi}_{ESS,i}$ indicates that the ESS is being discharged. The values of symbols are shown as in (11).

$$\alpha_i, \beta_i, \gamma_i = 0 \text{ or } 1 \tag{11}$$

Then, the affine model of each part in (10) is built, separately. Firstly, considering the uncertainties of loads, the interval model of load active power is shown as in (12), in which $\underline{P}^{\varphi}_{L,i}$ and $\bar{P}^{\varphi}_{L,i}$ are the lower and upper bounds. The affine model is obtained by the conversion operation as shown in (13).

$$\tilde{P}^{\varphi}_{L,i} = \left[\underline{P}^{\varphi}_{L,i}, \bar{P}^{\varphi}_{L,i}\right] \tag{12}$$

$$\hat{P}^{\varphi}_{L,i} = \left(\bar{P}^{\varphi}_{L,i} + \underline{P}^{\varphi}_{L,i}\right)/2 + \left(\bar{P}^{\varphi}_{L,i} - \underline{P}^{\varphi}_{L,i}\right) \cdot \varepsilon^{+}_{L,i}/2 \tag{13}$$

Secondly, considering the uncertainties of DGs, affine models of wind turbine generator and photovoltaic system are built based on meteorological conditions and power equations (23). The interval model of DG active power is shown as in (14), in which $\underline{P}^{\varphi}_{DG,i}$ and $\bar{P}^{\varphi}_{DG,i}$ are the lower and upper bounds. The affine model is further obtained by (15).

$$\tilde{P}^{\varphi}_{DG,i} = \left[\underline{P}^{\varphi}_{DG,i}, \bar{P}^{\varphi}_{DG,i}\right] \tag{14}$$

$$\hat{P}^{\varphi}_{DG,i} = \left(\bar{P}^{\varphi}_{DG,i} + \underline{P}^{\varphi}_{DG,i}\right)/2 + \left(\bar{P}^{\varphi}_{DG,i} - \underline{P}^{\varphi}_{DG,i}\right) \cdot \varepsilon^{+}_{DG,i}/2 \tag{15}$$

Thirdly, for the ESS connected at node i, the interval model of active power is shown as in (16), in which $\underline{P}^{\varphi}_{ESS,i}$ and $\bar{P}^{\varphi}_{ESS,i}$ are the lower and upper bounds. Then, the affine model is obtained by (17).

$$\tilde{P}^{\varphi}_{ESS,i} = \left[\underline{P}^{\varphi}_{ESS,i}, \bar{P}^{\varphi}_{ESS,i}\right] \tag{16}$$

$$\hat{P}^{\varphi}_{ESS,i} = \left(\bar{P}^{\varphi}_{ESS,i} + \underline{P}^{\varphi}_{ESS,i}\right)/2 + \left(\bar{P}^{\varphi}_{ESS,i} - \underline{P}^{\varphi}_{ESS,i}\right) \cdot \varepsilon^{-}_{ESS,i}/2 \tag{17}$$

On the one hand, noisy symbols of DGs and loads are marked with "+", which reflects the uncertainty sources. On the other hand, noisy symbols of ESSs are marked with "-", which reflects the mitigation effects on uncertainties. Since the coefficients of $\hat{P}^{\varphi}_{DG,i}$ and $\hat{P}^{\varphi}_{ESS,i}$ in (10) have the same sign, Eq. 18 shows the correlation of noisy symbols. Collocated with the DG at node i, the ESS can mitigate the uncertain fluctuations of active power injection.

$$\varepsilon^{+}_{DG,i} = -\varepsilon^{-}_{ESS,i} \tag{18}$$

3.2 Affine model of reactive power injection

Considering the reactive power of loads, DGs, and SVCs, the affine model of reactive power injection of phase φ at node i is shown as in (19). The value of δ_i is 0 or 1.

$$\hat{Q}^{\varphi}_{inj,i} = \alpha_i \hat{Q}^{\varphi}_{L,i} - \beta_i \hat{Q}^{\varphi}_{DG,i} - \delta_i \hat{Q}^{\varphi}_{SVC,i} \tag{19}$$

The affine model of each part in (19) is built, separately. Firstly, Eq. 20 shows the interval model of load reactive power with the lower and upper bounds. Then, the affine model is obtained by (21).

$$\tilde{Q}^{\varphi}_{L,i} = \left[\underline{Q}^{\varphi}_{L,i}, \bar{Q}^{\varphi}_{L,i}\right] \tag{20}$$

$$\hat{Q}^{\varphi}_{L,i} = \left(\bar{Q}^{\varphi}_{L,i} + \underline{Q}^{\varphi}_{L,i}\right)/2 + \left(\bar{Q}^{\varphi}_{L,i} - \underline{Q}^{\varphi}_{L,i}\right) \cdot \varepsilon^{+}_{L,i}/2 \tag{21}$$

Secondly, assuming that DGs are operating at a constant power factor, the affine model of DG reactive power is obtained by (22).

$$\hat{Q}^{\varphi}_{DG,i} = \hat{P}^{\varphi}_{DG,i} \cdot \tan\theta_{DG,i} \tag{22}$$

Thirdly, the interval model of SVC reactive power is shown as in (23), in which $\underline{Q}^{\varphi}_{SVC,i}$ and $\bar{Q}^{\varphi}_{SVC,i}$ are the lower and upper bounds. Then, the affine model is obtained by (24).

$$\tilde{Q}^{\varphi}_{SVC,i} = \left[\underline{Q}^{\varphi}_{SVC,i}, \bar{Q}^{\varphi}_{SVC,i}\right] \tag{23}$$

$$\hat{Q}^{\varphi}_{SVC,i} = \left(\bar{Q}^{\varphi}_{SVC,i} + \underline{Q}^{\varphi}_{SVC,i}\right)/2 + \left(\bar{Q}^{\varphi}_{SVC,i} - \underline{Q}^{\varphi}_{SVC,i}\right) \cdot \varepsilon^{-}_{SVC,i}/2 \tag{24}$$

Noisy symbols of SVCs are marked with "-", which reflects the mitigation effects on uncertainties. SVCs can provide reactive power for loads and mitigate the uncertainties introduced by loads. Since the coefficients of $\hat{Q}^{\varphi}_{L,i}$ and $\hat{Q}^{\varphi}_{SVC,i}$ in (19) have the opposite sign, Eq. 25 shows the correlation of noisy symbols of the load and SVC at node i.

$$\varepsilon^{+}_{L,i} = \varepsilon^{-}_{SVC,i} \tag{25}$$

4 Uncertain sensitivity analysis of voltage fluctuations based on CAA

4.1 Sensitivity indicators of voltage fluctuations to active and reactive power injections

Based on the transitivity of noisy symbols, sensitivity equations of voltage fluctuations with complex affine variables are established. The equations take into account not only the variations of uncertainty levels of DGs and loads, but also the variations of mitigation levels of ESSs and SVCs.

Assuming that there are q noise symbols introduced by the uncertainties of power injections, the calculation process from power injections to voltages is shown as in (26). The number of buses is n. Considering the variations of multiple factors, affine valued voltages at the initial and current states are obtained.

$$\begin{cases} \hat{U}^{\varphi}_{i} = g\left(\hat{P}^{\varphi}_{inj,1} + \mathrm{j}\cdot\hat{Q}^{\varphi}_{inj,1}, \cdots, \hat{P}^{\varphi}_{inj,n} + \mathrm{j}\cdot\hat{Q}^{\varphi}_{inj,n}\right) \\ \quad = U^{\varphi}_{i,0} + U^{\varphi}_{i,1}\varepsilon_1 + \cdots + U^{\varphi}_{i,q}\varepsilon_q + U^{\varphi}_{i,r}\varepsilon^{U}_{i,r} + \mathrm{j}\cdot U^{\varphi}_{i,im}\varepsilon^{U}_{i,im} \\ \hat{U}'^{\varphi}_{i} = g\left[\left(\hat{P}^{\varphi}_{inj,1} + \Delta\hat{P}^{\varphi}_{inj,1}\right) + \mathrm{j}\cdot\left(\hat{Q}^{\varphi}_{inj,1} + \Delta\hat{Q}^{\varphi}_{inj,1}\right), \cdots, \right. \\ \qquad \left.\left(\hat{P}^{\varphi}_{inj,n} + \Delta\hat{P}^{\varphi}_{inj,n}\right) + \mathrm{j}\cdot\left(\hat{Q}^{\varphi}_{inj,n} + \Delta\hat{Q}^{\varphi}_{inj,n}\right)\right] \\ \quad = U'^{\varphi}_{i,0} + U'^{\varphi}_{i,1}\varepsilon_1 + \cdots + U'^{\varphi}_{i,q}\varepsilon_q + U'^{\varphi}_{i,r}\varepsilon^{U}_{i,r} + \mathrm{j}\cdot U'^{\varphi}_{i,im}\varepsilon^{U}_{i,im} \end{cases} \tag{26}$$

In the formula, φ is the A, B or C phase; $\hat{P}^{\varphi}_{inj,1}, \hat{P}^{\varphi}_{inj,2}, \cdots, \hat{P}^{\varphi}_{inj,n}$ and $\hat{Q}^{\varphi}_{inj,1}, \hat{Q}^{\varphi}_{inj,2}, \cdots, \hat{Q}^{\varphi}_{inj,n}$ are the affine values of the net injected active and reactive power of the node in the starting state respectively; $\varepsilon_1, \varepsilon_2, \cdots, \varepsilon_q$

are the main noise elements introduced by the uncertainty of the input variables; $\boldsymbol{U}_{i,0}^{\varphi}$ and $\boldsymbol{U}_{i,1}^{\varphi}, \boldsymbol{U}_{i,2}^{\varphi}, \cdots, \boldsymbol{U}_{i,q}^{\varphi}$ are the starting The central value and the main noise coefficient of $\hat{\boldsymbol{U}}_{i}^{\varphi}$ in the state; $U_{i,r}^{\varphi}\varepsilon_{i,r}^{U}$ and $\mathrm{j}\cdot U_{i,im}^{\varphi}\varepsilon_{i,im}^{U}$ are the error noise terms of $\hat{\boldsymbol{U}}_{i}^{\varphi}$ in the starting state; $\Delta\hat{P}_{inj,1}^{\varphi}, \Delta\hat{P}_{inj,2}^{\varphi}, \cdots, \hat{P}_{inj,n}^{\varphi}$ and $\Delta\hat{Q}_{inj,1}^{\varphi}, \Delta\hat{Q}_{inj,2}^{\varphi}, \cdots, \Delta\hat{Q}_{inj,n}^{\varphi}$ are the affine values of the changes in the net injected active and reactive power of the node, respectively, indicating the changes in the uncertainty level of the input variables; $\boldsymbol{U}_{i,0}^{\prime\varphi}$ and $\boldsymbol{U}_{i,1}^{\prime\varphi}, \boldsymbol{U}_{i,2}^{\prime\varphi}, \cdots, \boldsymbol{U}_{i,q}^{\prime\varphi}$ are the central value and main noise coefficient of $\hat{\boldsymbol{U}}_{i}^{\prime\varphi}$ after the change; $U_{i,r}^{\prime\varphi}\varepsilon_{i,r}^{U}$ and $\mathrm{j}\cdot U_{i,im}^{\prime\varphi}\varepsilon_{i,im}^{U}$ are the error noise terms of $\hat{\boldsymbol{U}}_{i}^{\prime\varphi}$ after the change.

Specifically, the variations of active and reactive power injections are obtained by (27).

$$\begin{cases} \Delta\hat{P}_{inj,i}^{\varphi} = \alpha_i\Delta\hat{P}_{L,i}^{\varphi} - \beta_i\Delta\hat{P}_{DG,i}^{\varphi} - \gamma_i\Delta\hat{P}_{ESS,i}^{\varphi} \\ \Delta\hat{Q}_{inj,i}^{\varphi} = \alpha_i\Delta\hat{Q}_{L,i}^{\varphi} - \beta_i\Delta\hat{Q}_{DG,i}^{\varphi} - \delta_i\Delta\hat{Q}_{SVC,i}^{\varphi} \\ \Delta\hat{P}_{L,i}^{\varphi} = \Delta P_{L,i}^{\varphi}\varepsilon_{L,i}^{+}; \quad \Delta\hat{Q}_{L,i}^{\varphi} = \Delta Q_{L,i}^{\varphi}\varepsilon_{L,i}^{+} \\ \Delta\hat{P}_{DG,i}^{\varphi} = \Delta P_{DG,i}^{\varphi}\varepsilon_{DG,i}^{+}; \quad \Delta\hat{Q}_{DG,i}^{\varphi} = \Delta Q_{DG,i}^{\varphi}\varepsilon_{DG,i}^{+} \\ \Delta\hat{P}_{ESS,i}^{\varphi} = \Delta P_{ESS,i}^{\varphi}\varepsilon_{ESS,i}^{-} \\ \Delta\hat{Q}_{SVC,i}^{\varphi} = \Delta Q_{SVC,i}^{\varphi}\varepsilon_{SVC,i}^{-} \end{cases} \tag{27}$$

In the formula, α_i、 β_i、 γ_i and δ_i are respectively the flags of whether there is load, DG, ESS and SVC at node i, taking 0 or 1; $\varepsilon_{L,i}^{+}$, $\varepsilon_{DG,i}^{+}$, $\varepsilon_{ESS,i}^{-}$ and $\varepsilon_{SVC,i}^{-}$ are respectively the main noise elements of load, DG, ESS and SVC at node i.

The main noise terms of $\hat{U}_{i}^{\varphi}$ and $\hat{U}^{\prime\varphi}{}_{i}$ in (26) represent the voltage fluctuations derived from uncertainties of power injections. Since the coefficients of error noisy symbols are extremely smaller than those of main noisy symbols, the levels of voltage fluctuations are mainly determined by main noisy terms. The main noise terms are denoted as $\hat{U}_{i,main}^{\varphi}$ and $\hat{U}^{\prime\varphi}{}_{i,main}$, which are shown as in (28).

$$\begin{cases} \hat{U}_{i,main}^{\varphi} = U_{i,1}^{\varphi}\varepsilon_1 + \cdots + U_{i,q}^{\varphi}\varepsilon_q \\ \hat{U}^{\prime\varphi}{}_{i,main} = U_{i,1}^{\prime\varphi}\varepsilon_1 + \cdots + U_{i,q}^{\prime\varphi}\varepsilon_q \end{cases} \tag{28}$$

Further, the formula is represented by the real and imaginary parts. For instance, the expression of $\hat{U}_{i,main}^{\varphi}$ is shown as in (29).

$$\begin{pmatrix} \hat{U}_{i,main,real}^{\varphi} \\ \hat{U}_{i,main,imag}^{\varphi} \end{pmatrix} = \begin{pmatrix} U_{i,1,real}^{\varphi} & U_{i,2,real}^{\varphi} \cdots U_{i,q,real}^{\varphi} \\ U_{i,1,imag}^{\varphi} & U_{i,2,imag}^{\varphi} \cdots U_{i,q,imag}^{\varphi} \end{pmatrix} \begin{pmatrix} \varepsilon_1 \\ \varepsilon_2 \\ \cdots \\ \varepsilon_q \end{pmatrix} \tag{29}$$

The level of voltage fluctuation at node i is denoted as $\lambda(\,)$, which is obtained by summing the absolute values of coefficients of the main noisy symbols. The calculation of $\lambda(\,)$ is shown as in (30).

$$\begin{cases} \lambda\left(\hat{U}_{i,main,real}^{\varphi}\right) = \sum_{k=1}^{q}\left|U_{i,k,real}^{\varphi}\right| \\ \lambda\left(\hat{U}_{i,main,imag}^{\varphi}\right) = \sum_{k=1}^{q}\left|U_{i,k,imag}^{\varphi}\right| \end{cases} \tag{30}$$

Then, indicators are defined for evaluating the sensitivity of voltage fluctuations to the above variations in power injections.

4.1.1 Sensitivity indicator towards individual variation

The voltage fluctuation at node i is affected by the variations of multiple factors in power injections as shown in (27). Considering the variations of uncertainty levels of DGs and loads, as well as mitigation levels of ESSs and SVCs, the variations of corresponding coefficients can be expressed as $\left\{\Delta P_{L,i}^{\varphi}, \Delta Q_{L,i}^{\varphi}, \Delta P_{DG,i}^{\varphi}, \Delta Q_{DG,i}^{\varphi}, \Delta P_{ESS,i}^{\varphi}, \Delta Q_{SVC,i}^{\varphi}\right\}$. The general form ΔS_m^{φ} is used to represent the variation of the mth coefficient.

The effect of individual variation on the voltage fluctuation at node i can be evaluated by the transitivity of corresponding noisy symbol. Assuming that ΔS_m^{φ} corresponds to the kth noisy symbol, the variation of the level of voltage fluctuation at node i is represented by the variation of the absolute value of corresponding coefficient, which is shown as in (31).

$$\begin{cases} \Delta\left|U_{i,k,real}^{\varphi}\right| = \left|U_{i,k,real}^{\prime\varphi}\right| - \left|U_{i,k,real}^{\varphi}\right| \\ \Delta\left|U_{i,k,imag}^{\varphi}\right| = \left|U_{i,k,imag}^{\prime\varphi}\right| - \left|U_{i,k,imag}^{\varphi}\right| \end{cases} (k = 1, 2, \cdots, q) \tag{31}$$

Then, sensitivity indicator of the voltage fluctuation at node i to individual variation is defined as in (32).

$$\begin{cases} K_{i,k,m,real}^{\varphi} = \dfrac{\partial\left|U_{i,k,real}^{\varphi}\right|}{\partial S_m^{\varphi}} = \left.\dfrac{\Delta\left|U_{i,k,real}^{\varphi}\right|}{\Delta S_m^{\varphi}}\right|_{\Delta S_m^{\varphi}\to 0} \\ K_{i,k,m,imag}^{\varphi} = \dfrac{\partial\left|U_{i,k,imag}^{\varphi}\right|}{\partial S_m^{\varphi}} = \left.\dfrac{\Delta\left|U_{i,k,imag}^{\varphi}\right|}{\Delta S_m^{\varphi}}\right|_{\Delta S_m^{\varphi}\to 0} \end{cases} \tag{32}$$

In the formula, $K_{i,k,m,real}^{\varphi}$ and $K_{i,k,m,imag}^{\varphi}$ are respectively the single-factor uncertainty sensitivity index of the fluctuation range of the real and imaginary parts of the voltage of node i; the closer ΔS_m^{φ} to 0, the more accurate the single-factor sensitivity index value obtained.

4.1.2 Sensitivity indicator towards total variations

Considering total variations of multiple factors, the variation of the level of voltage fluctuation at node i is calculated by (33).

$$\begin{cases} \Delta\lambda\left(\hat{U}_{i,main,real}^{\varphi}\right) = \sum_{k=1}^{q}\left(\left|U_{i,k,real}^{\prime\varphi}\right| - \left|U_{i,k,real}^{\varphi}\right|\right) \\ \Delta\lambda\left(\hat{U}_{i,main,imag}^{\varphi}\right) = \sum_{k=1}^{q}\left(\left|U_{i,k,imag}^{\prime\varphi}\right| - \left|U_{i,k,imag}^{\varphi}\right|\right) \end{cases} \tag{33}$$

Then, sensitivity indicator of the voltage fluctuation at node i to total variations is defined as in (34).

$$\begin{cases} K_{i,real}^{\varphi} = \left.\dfrac{\Delta\lambda\left(\hat{U}_{i,main,real}^{\varphi}\right)}{\sum_{m\in M}\Delta S_m^{\varphi}}\right|_{\Delta S_m^{\varphi}\to 0} \\ K_{i,imag}^{\varphi} = \left.\dfrac{\Delta\lambda\left(\hat{U}_{i,main,real}^{\varphi}\right)}{\sum_{m\in M}\Delta S_m^{\varphi}}\right|_{\Delta S_m^{\varphi}\to 0} \end{cases} \tag{34}$$

In the formula, $K_{i,real}^{\varphi}$ and $K_{i,imag}^{\varphi}$ are the multi-factor uncertainty sensitivity indicators of the voltage real part and imaginary part fluctuation intervals respectively; M is the set of uncertainty factors in the net injected active and reactive power; the closer ΔS_m^{φ} to 0, the obtained multi-factor The sensitivity index value is more accurate.

4.2 Calculation method for sensitivity indicators based on the micro-increments of coefficients

4.2.1 Micro-increments of coefficients of noisy symbols

Eqs 32, 34 use the general form ΔS_m^{φ} to represent the variation of the mth coefficient, which quantitatively reflects the variation of

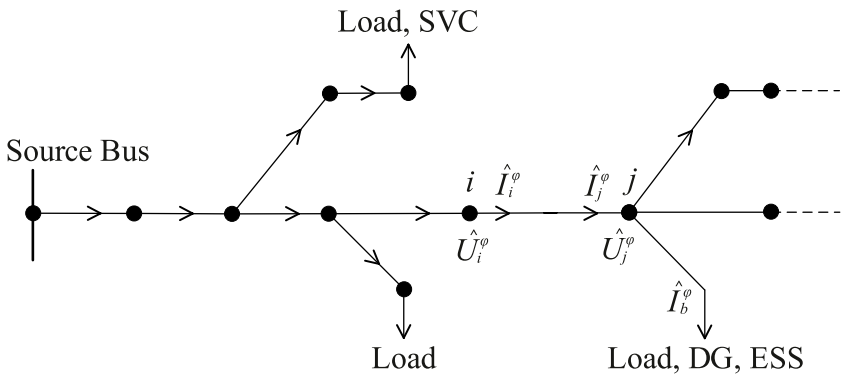

FIGURE 1
Topology of an ADN with DGs, loads, ESSs, and SVC.

uncertainty level or mitigation level of corresponding factor. When ΔS_m^{φ} is closer to 0, sensitivity indicators become more accurate. Thus, a calculation method for sensitivity indicators based on the micro-increments of coefficients is proposed.

In [12], the sensitivity analysis of voltages with point values is studied and a sensible strategy is to set each micro-increment as a percentage of load power. It is demonstrated that when each micro-increment is set as 0.5%–2% of load power, the obtained results have high accuracy. In this paper, the micro-increment is set as 1% of the uncertainty level or mitigation level of each factor. That is, each micro-increment is 1% of the coefficient of corresponding noisy symbol in the affine model of each factor.

4.2.2 CAA-based improved forward-backward sweep power flow

In the calculation process of sensitivity indicators, an improved forward-backward sweep power flow based on CAA is used to calculate voltages in affine form. Sensitivity indicators are further calculated based on the obtained coefficients of noisy symbols.

In previous CAA based forward-backward sweep power flow [23], a brand new noisy symbol is generated after approximation for each non-affine operation. Meanwhile, voltages and currents are updated repeatedly in the iterative process. As a result, numerous error noise terms are continually generated. The redundancy of error noise terms affects the clarity of sensitivity-related coefficients.

Therefore, a cutting method for error noise terms of voltages and currents is proposed. The coefficients of error noisy symbols are merged by summing the absolute values of their real and imaginary parts, respectively. Since the coefficients of error noisy symbols are extremely smaller than those of main noisy symbols, it guarantees the completeness of true solutions and has little effect on the conservativeness.

In the process of forward and backward sweep, the improvement mainly lies in de-redundancy of error noise terms of voltages and currents. Figure 1 shows the topology of an ADN with DGs, loads, ESSs, and SVCs.

For instance, in the process of forward sweep, the downstream voltage $\hat{U}_j^{\varphi}$ is calculated by (35), in which [c] and [d] are matrices determined by the topology of a distribution network (Kersting, 2001). Eqs (36, 37) show the process of cutting error noise terms of the voltage $\hat{U}_j^{\varphi}$.

$$\begin{bmatrix} \hat{U}_j^A \\ \hat{U}_j^B \\ \hat{U}_j^C \end{bmatrix} = [c] \begin{bmatrix} \hat{U}_i^A \\ \hat{U}_i^B \\ \hat{U}_i^C \end{bmatrix} - [d] \begin{bmatrix} \hat{I}_i^A \\ \hat{I}_i^B \\ \hat{I}_i^C \end{bmatrix} = \begin{bmatrix} U_{j,0}^A + U_{j,1}^A \varepsilon_1 + \cdots + U_{j,q}^A \varepsilon_q + U_{j,r}^A \varepsilon_{j,r}^U + \mathrm{j} \cdot U_{j,im}^A \varepsilon_{j,im}^U \\ U_{j,0}^B + U_{j,1}^B \varepsilon_1 + \cdots + U_{j,q}^B \varepsilon_q + U_{j,r}^B \varepsilon_{j,r}^U + \mathrm{j} \cdot U_{j,im}^B \varepsilon_{j,im}^U \\ U_{j,0}^C + U_{j,1}^C \varepsilon_1 + \cdots + U_{j,q}^C \varepsilon_q + U_{j,r}^C \varepsilon_{j,r}^U + \mathrm{j} \cdot U_{j,im}^C \varepsilon_{j,im}^U \end{bmatrix} \quad (35)$$

$$U_{j,r}^{\varphi} = \sum_{k \in K_{error}} \left| \mathrm{Re}\left(U_{j,k}^{\varphi} \right) \right| \quad (36)$$

$$U_{j,im}^{\varphi} = \sum_{k \in K_{error}} \left| \mathrm{Im}\left(U_{j,k}^{\varphi} \right) \right| \quad (37)$$

4.2.3 Calculation process of sensitivity indicators

Combined with the improved forward-backward sweep power flow based on CAA, sensitivity indicators are calculated based on the micro-increments of coefficients of noisy symbols. The detailed process of calculation is as follows:

i) Initialize the network parameters such as node number and line impedance. Based on the affine models of DGs, loads, ESSs, and SVCs, active and reactive power injections at the initial state are obtained by (Song et al., 2020) and (19). Then, the initial voltages in affine form are calculated by the improved forward-backward sweep power flow based on CAA.
ii) For the variations of factors in active power injections, the micro-increments of coefficients of corresponding noisy symbols are set. Combined with the improved forward-backward sweep power flow based on CAA, sensitivity indicator of the voltage fluctuation at node i to individual variation in active power injections is calculated by (32).
iii) Similarly, for the variations of factors in reactive power injections, sensitivity indicator of the voltage fluctuation at node i to individual variation in reactive power injections is calculated by (32).
iv) Considering total variations of factors in power injections, the micro-increments of coefficients of corresponding noisy symbols are set. Then, combined with the improved forward-backward sweep power flow based on CAA, sensitivity indicator of the voltage fluctuation at node i to total variations is calculated by (34).

4.3 A fast sensitivity method for calculating voltage intervals

Based on the obtained sensitivity indicators, a fast sensitivity method for calculating interval values of voltages is further proposed. The proposed method takes into account actual variations of uncertainty levels of DGs and loads, as well as mitigation levels of ESSs and SVCs. According to sensitivity indicators and actual variations of factors, the variations of voltage fluctuations are obtained by a linear calculation model. The proposed method avoids the continuous utilization of the power flow algorithm to calculate interval values of voltages.

Considering actual variations of multiple factors in power injections, the variation of the absolute value of the kth coefficient of the voltage at node i is calculated by (38).

$$\begin{cases} \Delta\left|U^{\varphi}_{i,k,real}\right| = \sum\limits_{m\in M} \dfrac{\partial\left|U^{\varphi}_{i,k,real}\right|}{\partial S^{\varphi}_{m}} \cdot \Delta S^{\varphi}_{m} = \sum\limits_{m\in M} K^{\varphi}_{i,k,m,real} \cdot \Delta S^{\varphi}_{m} \\ \Delta\left|U^{\varphi}_{i,k,imag}\right| = \sum\limits_{m\in M} \dfrac{\partial\left|U^{\varphi}_{i,k,imag}\right|}{\partial S^{\varphi}_{m}} \cdot \Delta S^{\varphi}_{m} = \sum\limits_{m\in M} K^{\varphi}_{i,k,m,imag} \cdot \Delta S^{\varphi}_{m} \end{cases} \tag{38}$$

Then, the variation of the level of voltage fluctuation at node i is calculating by summing the variations of the absolute values of all coefficients, which is shown as in (39). Combined with the initial voltages in affine form, the voltages at current state are further obtained.

$$\begin{cases} \Delta\lambda\left(\hat{U}^{\varphi}_{i,main,real}\right) = \sum\limits_{k\in Q}\sum\limits_{m\in M} K^{\varphi}_{i,k,m,real} \cdot \Delta S^{\varphi}_{m} \\ \Delta\lambda\left(\hat{U}^{\varphi}_{i,main,imag}\right) = \sum\limits_{k\in Q}\sum\limits_{m\in M} K^{\varphi}_{i,k,m,imag} \cdot \Delta S^{\varphi}_{m} \end{cases} \tag{39}$$

5 Case study

5.1 System parameters and initial state

Considering the uncertainties of DGs and loads, as well as the mitigation effects of ESSs and SVCs, the proposed method is verified by the modified IEEE 33-bus distribution system. Figure 2 shows the topology of the system with DGs, loads, ESSs, and SVCs.

At the initial state, uncertainty levels of DGs and loads, as well as mitigation levels of ESSs and SVCs are set as follows:

1) DG1 and DG2 are integrated to buses 5 and 15, respectively. The interval of DG active power is [200,300] kW and the power factor is $\cos\theta = 0.95$.
2) L1 and L2 are the fluctuating loads at buses 20 and 30. The uncertainty level is ± 10%.
3) Bus 15 is connected with an ESS and the interval of ESS active power is [-60,-20] kW.
4) Bus 30 is connected with a SVC and the interval of SVC reactive power is [45,50] kvar.

Then, based on affine models of active and reactive power injections, the affine valued power of each DG, load, ESS, and SVC can be obtained as shown in Table 1.

5.2 Discussion of the results of uncertain sensitivity analysis

5.2.1 Sensitivity indicators of voltage fluctuations to DGs/loads

Firstly, considering the variation of uncertainty level of individual DG or load, sensitivity indicator of the voltage fluctuation at each bus is calculated. As for the real parts of voltages of phase A, Figure 3 shows sensitivity indicators of voltage fluctuations to active power of DG1 and L1. Secondly, considering total variations of DGs and loads, sensitivity indicator of the voltage fluctuation at each bus is calculated. Figure 4 shows sensitivity indicators of voltage fluctuations to all DGs and loads.

It can be seen from Figures 3, 4 that the obtained indicators can quantitatively reflect the sensitivity of voltage fluctuations to the variations of uncertainty levels of DGs and loads. The results show that buses close to the locations of DGs and loads have larger values of sensitivity indicators, which means that these buses are more sensitive to the variations of uncertain factors. Meanwhile, buses located at the end of the branch are more sensitive than those close to the source bus.

Taking into account the changes in uncertainty fluctuation levels of DG1, DG2, L1 and L2, the multi-factor uncertainty sensitivity index shown in Figure 4 represents the overall sensitivity of the voltage fluctuation range of each node to changes in all uncertainty fluctuation factors. For all uncertainty fluctuation factors in the distribution network shown in Figure 2, that is, DG1 and DG2 at nodes 5 and 15 and L1 and L2 at nodes 20 and 30, the results show that the uncertainty fluctuation factors are close to the location where the uncertainty fluctuation factors are connected and located on the branch. Nodes at the end of the road have larger multi-factor sensitivity index values and are more sensitive to changes in uncertainty fluctuation factors in the network; nodes far away from the access location of uncertainty fluctuation factors and close to the source node have smaller multi-factor sensitivity index values. The overall sensitivity to changes in uncertainty fluctuation factors in the network is low.

5.2.2 Sensitivity indicators of voltage fluctuations to ESSs/SVCs

The integration of ESSs and SVCs can mitigate the uncertainties of power injections. Considering the variation of the mitigation level of individual ESS or SVC, sensitivity indicator of the voltage fluctuation at each bus is calculated. Figure 5 shows sensitivity indicators of voltage fluctuations to individual ESS and SVC. Then, considering total variations of ESSs and SVCs, sensitivity indicator of the voltage fluctuation at each bus is calculated. Figure 6 shows sensitivity indicators of voltage fluctuations to all ESSs and SVCs.

As for the variations of mitigation levels of ESSs and SVCs, the values of sensitivity indicators are negative. As the mitigation levels increase, the levels of voltage fluctuations decrease. The results show that buses close to the locations of ESSs and SVCs have larger absolute values of sensitivity indicators. Similarly, buses located at the end of the branch are more sensitive than those close to the source bus.

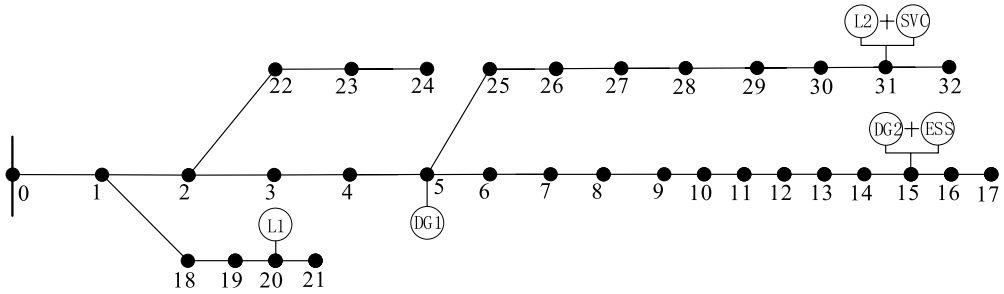

FIGURE 2
Topology of the modified IEEE 33-bus distribution system.

TABLE 1 Power of DGs, loads, ESSs and SVCs in The Initial State.

No.	Bus	Power in affine form
DG1	5	$\hat{P}_{DG,5} = 250 + 50 \cdot \varepsilon^{+}_{DG,5}$, $\hat{Q}_{DG,5} = \hat{P}_{DG,5} \cdot \tan\theta_{DG}$
DG2	15	$\hat{P}_{DG,15} = 250 + 50 \cdot \varepsilon^{+}_{DG,15}$, $\hat{Q}_{DG,15} = \hat{P}_{DG,15} \cdot \tan\theta_{DG}$
L1	20	$\hat{S}_{20} = (90 + j \cdot 40) + (90 + j \cdot 40) \times 10\% \cdot \varepsilon^{+}_{L,20}$
L2	30	$\hat{S}_{30} = (150 + j \cdot 70) + (150 + j \cdot 70) \times 10\% \cdot \varepsilon^{+}_{L,30}$
ESS	15	$\hat{P}_{ESS,15} = -40 + 20 \cdot \varepsilon^{-}_{ESS,15}$
SVC	30	$\hat{Q}_{SVC,30} = 47.5 + 2.5 \cdot \varepsilon^{-}_{SVC,30}$

The multi-factor uncertainty sensitivity index shown in Figure 6 represents the overall sensitivity of the voltage fluctuation range of each node to changes in all uncertainty reduction factors. For all uncertainty reduction factors in the distribution network shown in Figure 2, the results further show that nodes close to the access location of the uncertainty reduction factors and located at the end of the branch have a larger absolute value of the sensitivity index, which has a greater impact on the uncertainty in the network. Changes in reduction factors are more sensitive; nodes that are far away from the access location of uncertainty reduction factors and close to the source node have a smaller absolute value of the sensitivity index and are less affected by changes in uncertainty reduction factors in the network.

5.2.3 Comparative analysis

Based on the initial state, 6 scenarios are set considering actual variations of uncertainty levels of DGs and loads, as well as mitigation levels of ESSs and SVCs. The interval values of voltages are calculated and the results are compared between the proposed sensitivity method (Method 1) and the continuous utilization of the power flow method (Method 2).

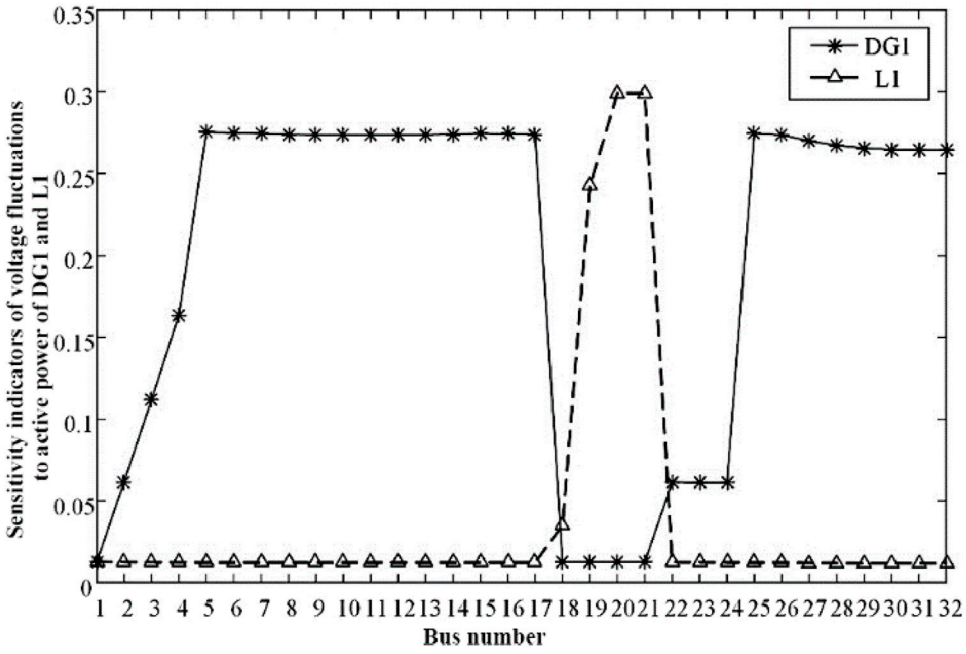

FIGURE 3
Sensitivity indicators of voltage fluctuations to active power of DG1/L1.

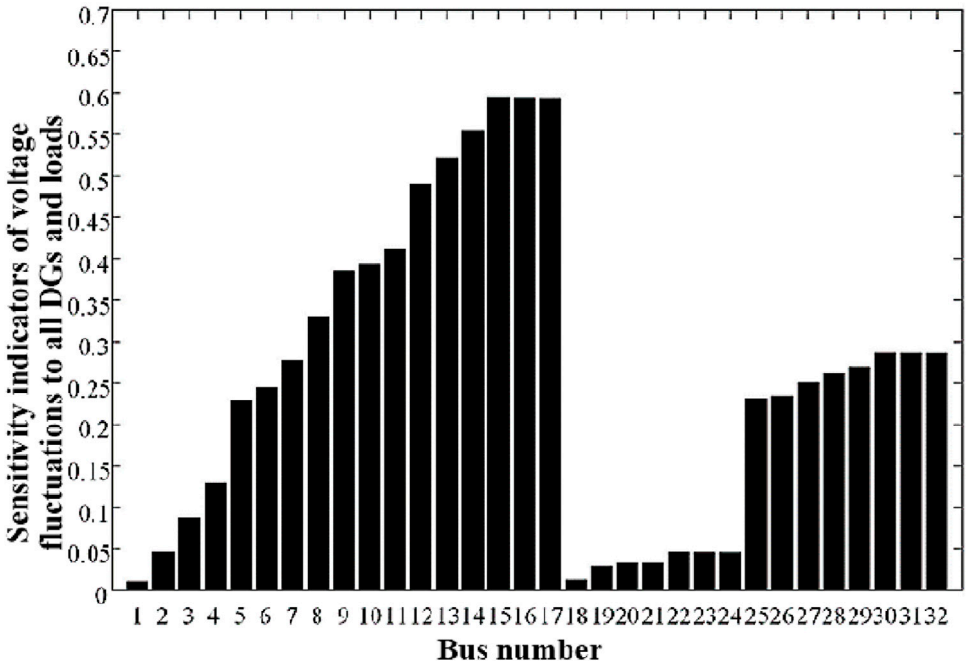

FIGURE 4
Sensitivity indicators of voltage fluctuations to all DGs and loads.

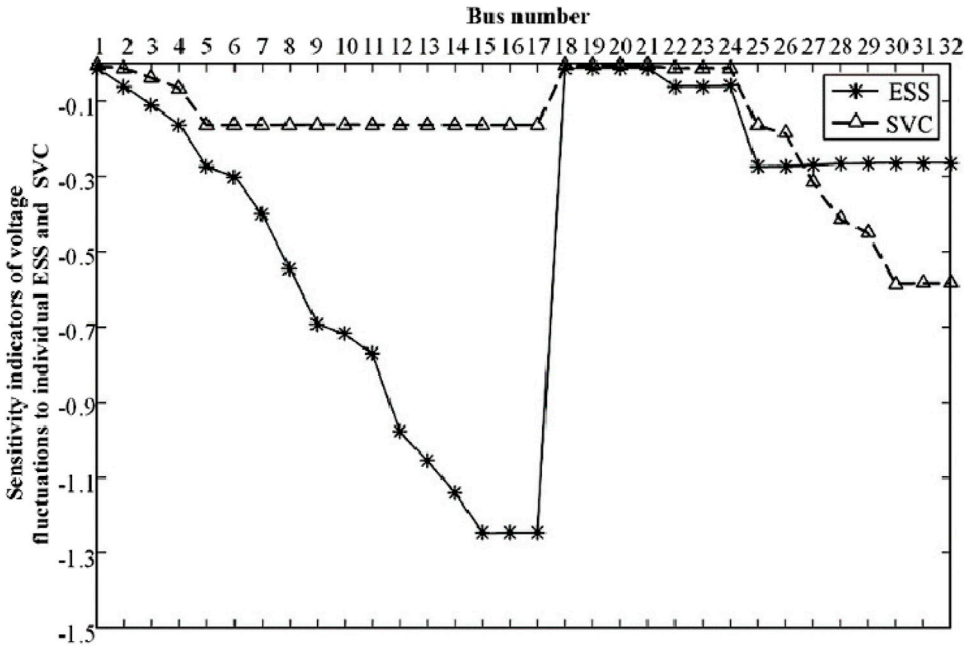

FIGURE 5
Sensitivity indicators of voltage fluctuations to individual ESS/SVC.

In scenarios 1-3, uncertainty levels of DG1, DG2, L1, and L2 gradually increase based on the initial state. Specifically, the fluctuation levels around central values increased by 2%, 4%, and 6%, respectively. In scenarios 4-6, uncertainty levels of DGs and loads are the same as in scenario 3. The intervals of ESS active power are [-65,-15] kW [-70,-10] kW, and [-75,-5] kW, respectively. The intervals of SVC reactive power are [43,52] kvar [41,54] kvar, and [39,56] kvar, respectively.

Considering the variations of multiple factors, the variation of the level of voltage fluctuation at node i can be quantified by (33). As for the real parts of voltages of phase A, Figure 7 shows the variations

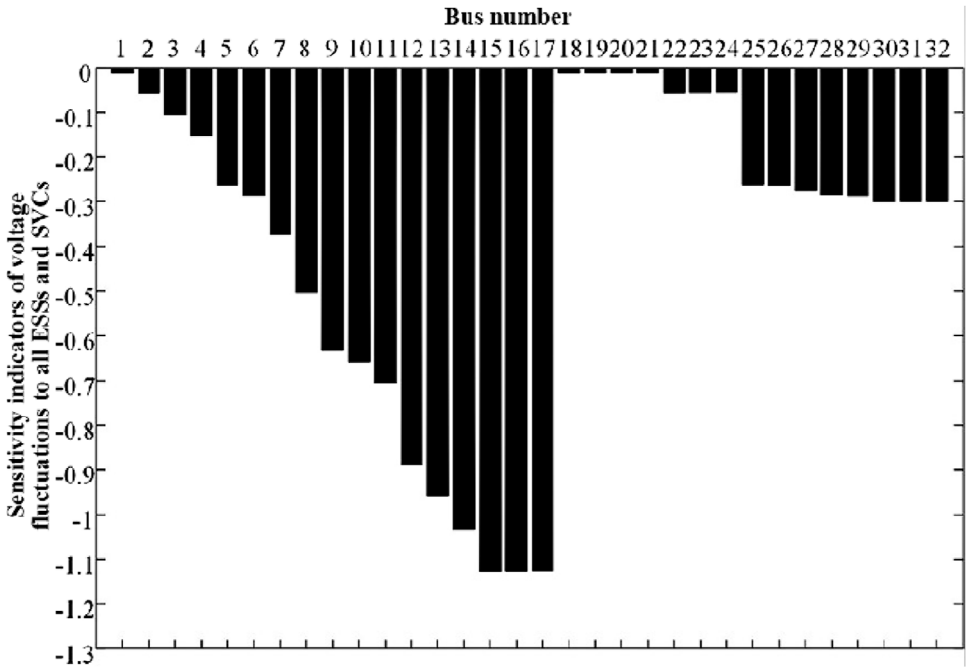

FIGURE 6
Sensitivity indicators of voltage fluctuations to all ESSs and SVCs.

of the levels of voltage fluctuations at buses 17 and 27. Figure 8 shows the interval values of voltages calculated by the two methods.

Then, based on the complex affine voltage of each node in the starting state and the change in voltage fluctuation level in each scene, the proposed method is used to obtain the voltage fluctuation interval after the scene change. Taking nodes 17 and 27 as an example, Figure 8 shows the fluctuation range of the real part of phase A voltage obtained by the two methods in each scenario, including its lower and upper bounds. Figure 9 shows the deviation values of voltage fluctuation level changes in various scenarios.

As can be seen from Figures 7, 8, the change in voltage fluctuation level under each scenario and the voltage fluctuation interval after the scenario change are obtained through the proposed method. The results show that with the gradual increase in the uncertainty level of DG and load in scenarios 1-3, the voltage fluctuation level of each node gradually increases, and the voltage fluctuation range gradually expands; as the ESS and SVC active power in scenarios 4-6 And the gradual increase of the reactive power adjustment range has a certain effect on reducing the voltage fluctuation level, and the voltage fluctuation range gradually decreases.

The results show that with the increase of uncertainty levels of DGs and loads in scenarios 1-3, the levels of voltage fluctuations gradually increase. Meanwhile, with the increase of mitigation levels of ESSs and SVCs in scenarios 4-6, the levels of voltage fluctuations gradually decrease. By comparison, the results obtained by the two methods are very close. The difference can be found after sufficient amplification, which validates the accuracy of the proposed method.

Further, compared with method 2, Figure 9A shows deviations of the variations of the levels of voltage fluctuations obtained by method 1. Figure 9B shows deviations of the lower and upper bounds of voltages obtained by method 1.

It can be seen that as for deviations of voltage fluctuations at buses 17 and 27, the maximum value is within 0.02%. As for deviations of the upper and lower bounds of voltages, the maximum value is within 0.01%. The results further validate the accuracy of the proposed method. Meanwhile, the proposed method avoids the continuous utilization of the power flow algorithm, which guarantees the efficiency of calculation.

5.2.4 Applicability in a large distribution network

To validate the applicability in a large distribution network, the proposed method is tested on the 292-bus distribution system. The topology and technical data can be referred to (Wang and Wang, 2014).

At the initial state, uncertainty levels of DGs and loads, as well as mitigation levels of ESSs and SVCs are set as follows: 1) DG1-DG6 are integrated to buses 15, 50, 93, 110, 216, and 270. The interval of DG active power is [200,300] kW. 2) L1-L4 are the fluctuating loads at buses 13, 208, 230, and 268. The uncertainty level is ± 10%. 3) The interval of ESS active power at bus 15, 50, or 216 is [-60,-20] kW. The interval of ESS active power at bus 93, 110, or 270 is [-60,-20] kW. 4) SVC1-SVC2 are integrated to buses 13 and 208. The intervals of reactive power are [50,90] kvar and [40,50] kvar, respectively.

Considering the variations of multiple factors, sensitivity indicator of the voltage fluctuation at each bus to individual variation is calculated. Figure 10 shows sensitivity indicators of voltage fluctuations to active and reactive power of DG3 and L4. Figure 11 shows sensitivity indicators of voltage fluctuations to power of ESS2, ESS4, SVC1, and SVC2.

From the analysis in Figure 10, it can be seen that considering the changes in DG and load uncertainty fluctuation levels, the single-factor uncertainty sensitivity index curve of the node voltage fluctuation interval shows certain regular

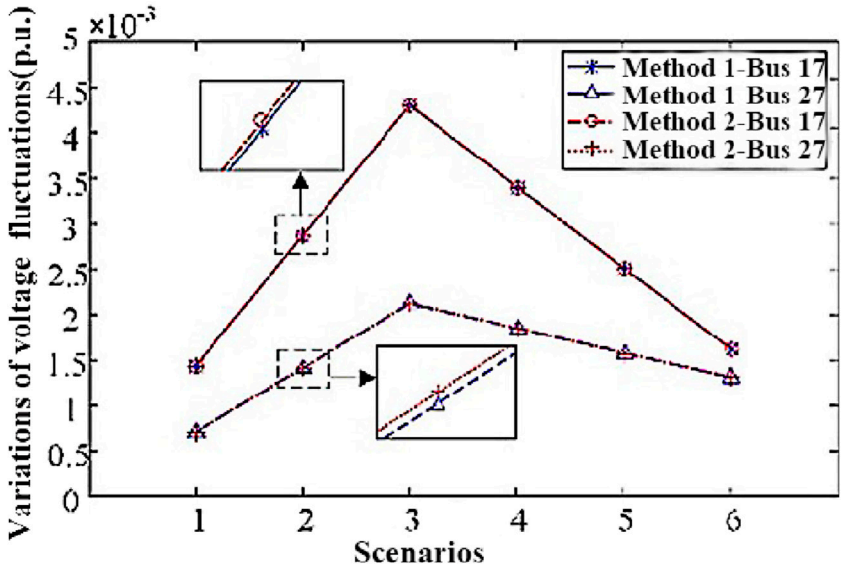

FIGURE 7
Variations of the levels of voltage fluctuations in different scenarios.

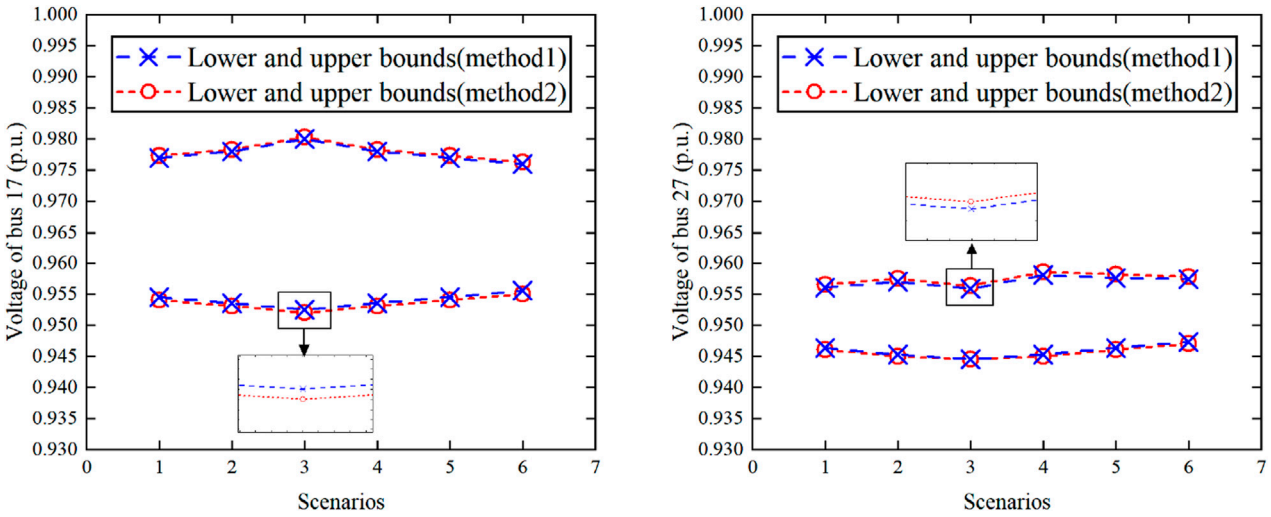

FIGURE 8
Interval values of voltages in different scenarios.

characteristics. First, nodes close to the access location of each uncertainty fluctuation factor have larger sensitivity index values, indicating that they are more sensitive to changes in the uncertainty fluctuation level of this factor; second, the transformers in the network are sensitive to uncertainty fluctuation factors. The impact of change has a certain blocking effect. For example, affected by changes in the uncertainty fluctuation level of load L4 at node 268, the sensitivity index values of nodes 228–292 are larger, and the closer to the node L4, the larger the sensitivity index value, indicating changes in the uncertainty fluctuation level of L4. The more sensitive the reaction. Secondly, the branch where nodes 103–147 are located is directly connected to the branch where L4 is located through node 7. Due to the distance, the sensitivity index value is lower than the index value of nodes 228–292. However, for the nodes on other branches, which are connected to the branch where L4 is located through the transformer at the head end of the branch, the sensitivity index is close to 0, indicating that it is basically not affected by changes in the uncertainty fluctuation level of L4.

From the analysis of Figure 11, it can be seen that in response to changes in the uncertainty reduction levels of ESS and SVC, the single-factor sensitivity indicators of each node's voltage fluctuation range are all negative, indicating that as the uncertainty reduction level

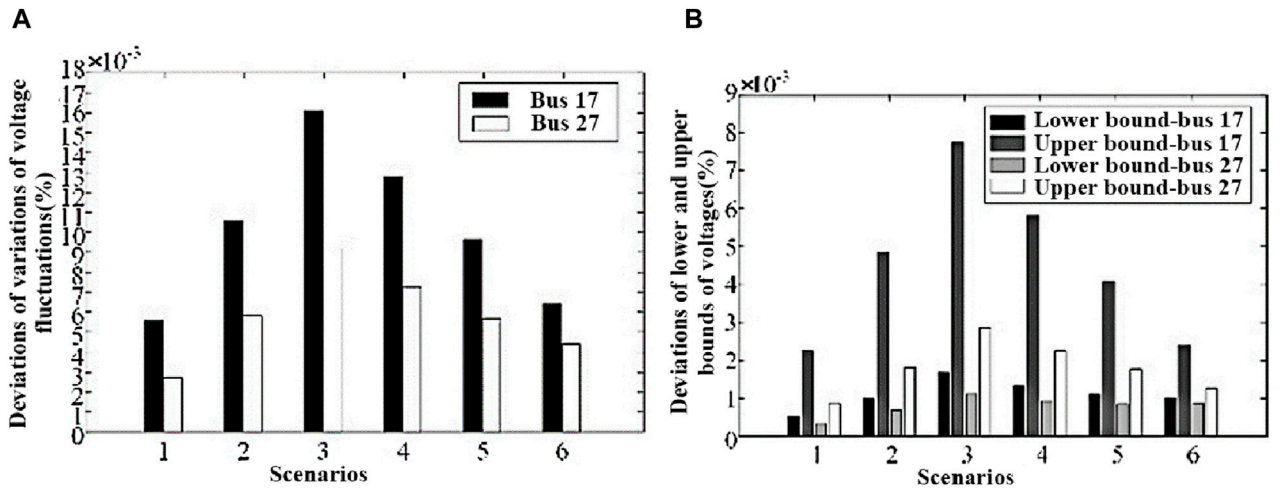

FIGURE 9
Deviations of the proposed method. **(A)** shows the deviation value of the voltage fluctuation level change of nodes 17 and 27 in various scenarios. **(B)** shows the deviation values of the upper and lower bounds of the voltage fluctuation range of nodes 17 and 27 in various scenarios.

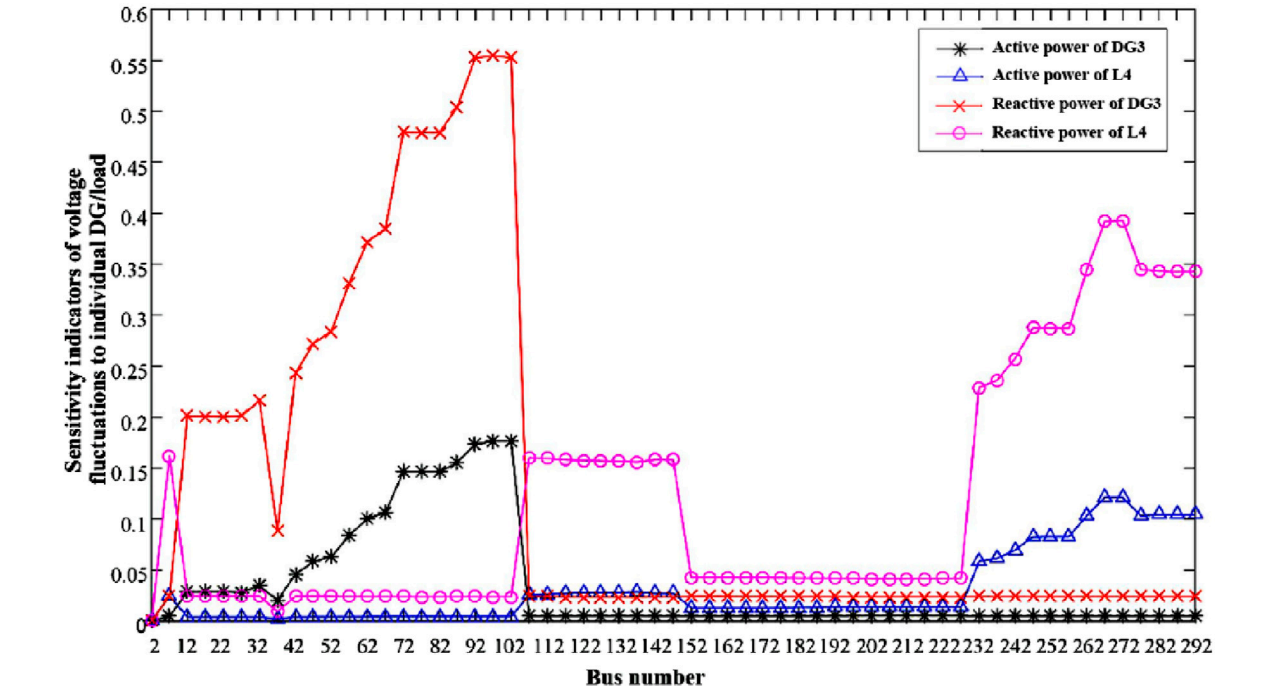

FIGURE 10
Sensitivity indicators of voltage fluctuations to individual DG/load.

increases, the voltage fluctuation level increases. reduced. At the same time, the single-factor sensitivity index curve in the node voltage fluctuation range also shows certain regular characteristics. First, nodes close to the access location of each uncertainty reduction factor have a larger absolute value of the sensitivity index, indicating that they are more sensitive to changes in the uncertainty reduction level of this factor; second, the transformers in the network are sensitive to uncertainty reduction factors. The influence of changes also has a certain blocking effect. For nodes that are far away from the access point of the uncertainty reduction factor and separated by the transformer, the absolute value of the sensitivity index is close to 0, indicating that it is basically not affected by changes in the uncertainty reduction factor. For instance, considering the variation of the uncertainty level of L4 at bus 268, buses 228–292 are more sensitive. However, for buses on other branches, sensitivity indicators are close to 0 due to the blockage of transformers.

In order to better prove the effectiveness and reliability of the method proposed in this article, this paper compares the deviation

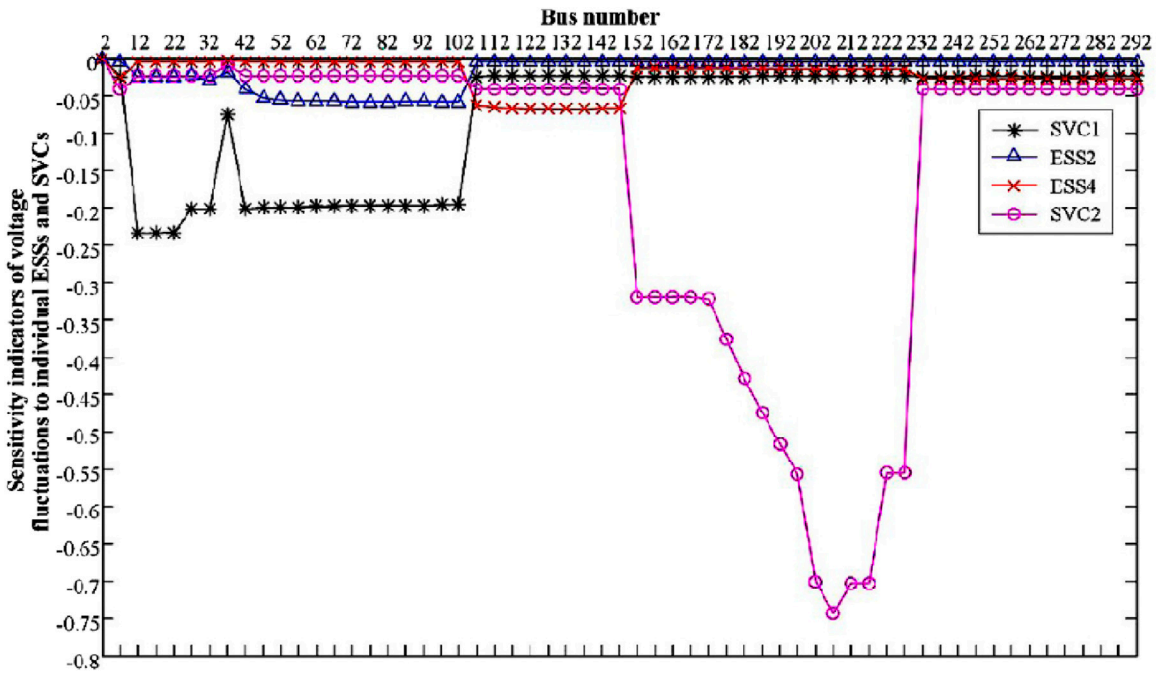

FIGURE 11
Sensitivity indicators of voltage fluctuations to individual ESS/SVC.

TABLE 2 Deviation value of voltage fluctuation level change of node 27 in various scenarios.

	Model 1 (%)	Model 2 (%)	Model 3 (%)	Model 4 (%)
1	0.007	0.019	0.025	0.027
2	0.012	0.022	0.019	0.025
3	0.016	0.024	0.022	0.026
4	0.011	0.022	0.026	0.018
5	0.014	0.018	0.025	0.024
6	0.014	0.022	0.024	0.026

values of the voltage fluctuation level change of the proposed method (Model 1) with the Jacobian matrix method (Model 2), perturb-and-observe, approach (Model 3) and topological analysis method I (Model 4) in six scenarios, and the statistical results are shown in Table 2.

As can be seen from Table 2, the deviation values of the voltage fluctuation level changes of the method proposed in this article are within 0.02% in six scenarios. The deviation value of the results obtained by this method is extremely small, and the deviation value of the results in each scenario is lower than that of other scenarios. The model proposed in this article performs best among the four models, indicating that the model proposed in this article can quantitatively describe the sensitivity of the voltage fluctuation range to the uncertainty fluctuations of various factors, and helps to focus on controlling key nodes and key uncertainty factors.

6 Conclusion

This paper proposes a CAA-based sensitivity analysis method for ADN voltage fluctuation uncertainty. By analyzing the correlation and transitivity of noise symbols, it shows that ESS and SVC can reduce the voltage caused by distributed generation (DG) and load changes. Effectiveness in Fluctuations. This method introduces a new technology to calculate the voltage fluctuation sensitivity index through the micro-increment of coefficients, and an analysis technology to quickly estimate the voltage sensitivity interval value, which can quickly and accurately quantitatively describe the voltage in an uncertain environment. The sensitivity of fluctuations to various factors. Through case analysis in an actual 292-node power distribution system, it is proved that this method not only improves the efficiency and reliability of calculation, but also, in different scenarios, through improved complex affine forward and backward power flow algorithms Compared with the continuous calls, this method avoids repeated calculation of the power flow every time the uncertain factors change, and helps to achieve rapid calculation and online analysis of the node voltage fluctuation range in an uncertain environment. Nonetheless, this method still needs to be in-depth in analyzing the dynamic behavior and long-term stability of the power system. Future research needs to be expanded to dynamic and long-term stability analysis to comprehensively evaluate the long-term benefits of equipment such as ESS and SVC and provide solutions for uncertain environments. The voltage optimization provides a basis for further research.

Data availability statement

The raw data supporting the conclusion of this article will be made available by the authors, without undue reservation.

Author contributions

LQ: Project administration, Writing–original draft. SH: Project administration, Writing–original draft. LM: Project administration, Writing–original draft. LJ: Project administration, Writing–original draft. JW: Project administration, Writing–original draft. WK: Methodology, Project administration, Writing–original draft.

Funding

The author(s) declare financial support was received for the research, authorship, and/or publication of this article. This research was funded by the State Grid Shandong Electric Power Company's science and technology project, including the study of intelligent analysis and disturbance source tracing and control technology for voltage quality in distribution systems with a high proportion of new energy sources(Project Number: 520604220001).

Conflict of interest

Authors LQ, SH, LM, LJ, and JW were employed by State Grid Weifang Electric Power Company.

The remaining author declares that the research was conducted in the absence of any commercial or financial relationships that could be construed as a potential conflict of interest.

The authors declare that this study received funding from State Grid Shandong Electric Power Company's science and technology project. The funder had the following involvement in the study: An affine model of active and reactive power injection was established, and the correlations of noisy symbols was proposed, and the sensitivity indicators of voltage fluctuations were defined based on the transitivity of noise symbols.

Publisher's note

References

Alonso-Travesset, À., Martín, H., Coronas, S., and de la Hoz, J. (2022). Optimization models under uncertainty in distributed generation systems: a review. *Energies* 15 (5), 1932. doi:10.3390/en15051932

Alvarado-Barrios, L., Álvarez-Arroyo, C., Escaño, J. M., Gonzalez-Longatt, F. M., and Martinez-Ramos, J. L. (2020). Two-level optimisation and control strategy for unbalanced active distribution systems management. *IEEE Access* 8, 197992–198009. doi:10.1109/access.2020.3034446

Alzaareer, K., Saad, M., Mehrjerdi, H., Ziad El-Bayeh, C., Asber, D., and Lefebvre, S. (2020). A new sensitivity approach for preventive control selection in real-time voltage stability assessment. *Int. J. Electr. Power & Energy Syst.* 122, 106212. doi:10.1016/j.ijepes.2020.106212

Bai, F., Yan, R., Saha, T. K., and Eghbal, D. (2020). An excessive tap operation evaluation approach for unbalanced distribution networks with high PV penetration. *IEEE Trans. Sustain. Energy* 12 (1), 169–178. doi:10.1109/tste.2020.2988571

Bandler, J., and El-Kady, M. (1980). A unified approach to power system sensitivity analysis and planning, part I: family of adjoint systems. *Proc. IEEE Int. Symp. Circuits Syst.*, 681–687.

Chang, Q., Zhou, C., Valdebenito, M. A., Liu, H., and Yue, Z. (2022). A novel sensitivity index for analyzing the response of numerical models with interval inputs. *Comput. Methods Appl. Mech. Eng.* 400, 115509. doi:10.1016/j.cma.2022.115509

Guerrero, J., Gebbran, D., Mhanna, S., Chapman, A. C., and Verbič, G. (2020). Towards a transactive energy system for integration of distributed energy resources: home energy management, distributed optimal power flow, and peer-to-peer energy trading. *Renew. Sustain. Energy Rev.* 132, 110000. doi:10.1016/j.rser.2020.110000

Gupta, A. R., and Kumar, A. (2022). Deployment of distributed generation with D-FACTS in distribution system: a comprehensive analytical review. *IETE J. Res.* 68 (2), 1195–1212. doi:10.1080/03772063.2019.1644206

Gupta, R., and Paolone, M. Experimental validation of model-less robust voltage control using measurement-based estimated voltage sensitivity coefficients. arXiv preprint arXiv:2304.13638, 2023.

Kersting, W. H. (2001). *Distribution system modeling and analysis*. Boca Raton: CRC Press LLC.

Li, S., Tan, Y., Li, C., Cao, Y., and Jiang, L. (2018). A fast sensitivity-based preventive control selection method for online voltage stability assessment. *IEEE Trans. Power Syst.* 33 (4), 4189–4196. doi:10.1109/tpwrs.2017.2776968

Manson, G. (2005). Calculating frequency response functions for uncertain systems using complex affine analysis. *J. Sound Vib.* 288 (3), 487–521. doi:10.1016/j.jsv.2005.07.004

Meinecke, S., Sarajlić, D., Drauz, S. R., Klettke, A., Lauven, L. P., Rehtanz, C., et al. (2020). Simbench—a benchmark dataset of electric power systems to compare innovative solutions based on power flow analysis. *Energies* 13 (12), 3290. doi:10.3390/en13123290

Mlilo, N., Brown, J., and Ahfock, T. (2021). Impact of intermittent renewable energy generation penetration on the power system networks–A review. . *Technol. Econ. Smart Grids Sustain. Energy* 6 (1), 25. doi:10.1007/s40866-021-00123-w

Munikoti, S., Natarajan, B., Jhala, K., and Lai, K. (2021). Probabilistic voltage sensitivity analysis to quantify impact of high PV penetration on unbalanced distribution system. *IEEE Trans. Power Syst.* 36 (4), 3080–3092. doi:10.1109/tpwrs.2021.3053461

Ruiz-Rodriguez, F. J., Hernandez, J. C., and Jurado, F. (2020). Iterative harmonic load flow by using the point-estimate method and complex affine arithmetic for radial distribution systems with photovoltaic uncertainties. *Int. J. Electr. Power & Energy Syst.* 118, 105765. doi:10.1016/j.ijepes.2019.105765

Shang, L., Zhai, J., and Zhao, G. (2021). Sensitivity analysis of coupled acoustic-structural systems under non-stationary random excitations based on adjoint variable method. *Struct. Multidiscip. Optim.* 64, 3331–3343. doi:10.1007/s00158-021-02978-0

Shuai, C., Deyou, Y., Weichun, G., Chuang, L., Guowei, C., and Lei, K. (2021). Global sensitivity analysis of voltage stability in the power system with correlated renewable energy. *Electr. Power Syst. Res.* 192, 106916. doi:10.1016/j.epsr.2020.106916

Song, S., Han, C., Lee, G. S., McCann, R. A., and Jang, G. (2020). Voltage-sensitivity-approach-based adaptive droop control strategy of hybrid STATCOM. *IEEE Trans. Power Syst.* 36 (1), 389–401. doi:10.1109/tpwrs.2020.3003582

Su, H., Li, P., Li, P., Fu, X., Yu, L., and Wang, C. (2019). Augmented sensitivity estimation based voltage control strategy of active distribution networks with PMU measurement. *IEEE Access* 7, 44987–44997. doi:10.1109/access.2019.2908183

Tang, K., Dong, S., Zhu, C., and Song, Y. (2020). Affine arithmetic-based coordinated interval power flow of integrated transmission and distribution networks. *IEEE Trans. Smart Grid* 11 (5), 4116–4132. doi:10.1109/tsg.2020.2991210

Wang, L., Hou, C., Ye, B., Wang, X., Yin, C., and Cong, H. (2021). Optimal operation analysis of integrated community energy system considering the uncertainty of demand response. *IEEE Trans. Power Syst.* 36 (4), 3681–3691. doi:10.1109/tpwrs.2021.3051720

Wang, S., Liu, Q., and Ji, X. (2018). A fast sensitivity method for determining line loss and node voltages in active distribution network. *IEEE Trans. Power Syst.* 33 (1), 1148–1150. doi:10.1109/tpwrs.2017.2735898

Wang, S., and Wang, C. (2014). *Modern distribution system analysis*. Beijing: Higher Education Press.

Wang, S., Wang, K., Wu, L., and Wang, C. (2019). Polar affine arithmetic: optimal affine approximation and operation development for computation in polar form under uncertainty. *ACM Trans. Math. Softw.* 45 (1), 1–29. doi:10.1145/3274659

Ye, K., Zhao, J., Huang, C., Duan, N., Zhang, Y., and Field, T. E. (2021). A data-driven global sensitivity analysis framework for three-phase distribution system with PVs. *IEEE Trans. Power Syst.* 36 (5), 4809–4819. doi:10.1109/tpwrs.2021.3069009

Zeynali, S., Rostami, N., and Feyzi, M. R. (2020). Multi-objective optimal short-term planning of renewable distributed generations and capacitor banks in power system considering different uncertainties including plug-in electric vehicles. *Int. J. Electr. Power & Energy Syst.* 119, 105885. doi:10.1016/j.ijepes.2020.105885

Zhang, X., Son, Y., Cheong, T., and Choi, S. (2022). Affine-arithmetic-based microgrid interval optimization considering uncertainty and battery energy storage system degradation. *Energy* 242, 123015. doi:10.1016/j.energy.2021.123015

Zhang, Y., Yuan, F., Zhai, H., Song, C., and Poursoleiman, R. (2023). Optimizing the planning of distributed generation resources and storages in the virtual power plant, considering load uncertainty. *J. Clean. Prod.* 387, 135868. doi:10.1016/j.jclepro.2023.135868

frontiers | Frontiers in Energy Research

TYPE Original Research
PUBLISHED 10 April 2024
DOI 10.3389/fenrg.2024.1364528

OPEN ACCESS

EDITED BY
Rufeng Zhang,
Northeast Electric Power University, China

REVIEWED BY
Zhihua Zhang,
China University of Petroleum, China
Xialin Li,
Tianjin University, China
Zhengfa Zhang,
The University of Tennessee, United States

*CORRESPONDENCE
Zhiqi Li,
202234714@mail.sdu.edu.cn

RECEIVED 20 February 2024
ACCEPTED 18 March 2024
PUBLISHED 10 April 2024

CITATION
Wang F, Zhang P, Li J, Li Z, Zhao M, Liang Y, Su G and You X (2024), Multi-feature based extreme learning machine identification model of incipient cable faults.
Front. Energy Res. 12:1364528.
doi: 10.3389/fenrg.2024.1364528

Multi-feature based extreme learning machine identification model of incipient cable faults

Feng Wang[1], Pengping Zhang[1], Jianxiu Li[2], Zhiqi Li[3]*, Mingzhe Zhao[1], Yongliang Liang[3], Guoqiang Su[1] and Xinhong You[1]

[1]State Grid Shandong Electric Power Research Institute, Jinan, China, [2]State Grid Shandong Electric Power Company, Jinan, China, [3]School of Electrical Engineer, Shandong University, Jinan, China

In the operation of medium-voltage distribution cables, the local insulation performance may degrade due to inherent defects, environmental influences, and external forces, leading to consecutive self-recovering latent faults in the cables. If not addressed promptly, these faults may escalate into permanent failures. To address this issue, this paper analyzes the development mechanism and characteristics of latent cable faults. A 10kV low-resistance cable latent fault model based on the Kizilcay arc model is built in the PSCAD/EMTDC platform. Furthermore, the paper analyzes and extracts the time-domain, frequency-domain, and time-frequency domain features of fault current samples. Effective fault feature vectors are constructed using multivariate analysis of variance (MANOVA) and Principal Component Analysis (PCA). Based on the fault feature vectors and Extreme Learning Machine (ELM), an intelligent fault identification model for cable latent faults is developed. The initial parameters of the ELM model are optimized using the Particle Swarm Optimization (PSO) algorithm. Finally, the superiority of the proposed model is validated in terms of classification accuracy, training time, and robustness compared to other machine learning algorithms.

KEYWORDS

cable incipient fault, feature extraction, data-driven, extreme learning machine, particle swarm optimization

1 Introduction

Power cables are commonly buried underground, and with the passage of time, factors such as electrical, thermal, and mechanical stress gradually reduce their insulation strength, eventually leading to permanent faults that jeopardize the safe and reliable power supply of urban distribution networks. Operational experience with medium-voltage cables indicates that, prior to the occurrence of permanent faults, transient and self-recovering arc grounding faults may occur at the same location. Due to their short duration (1/4 to four cycles) and small fault currents, traditional overcurrent protection devices with inverse time characteristics fail to activate. In this paper, such faults are referred to as latent cable faults. Timely detection of latent faults in medium-voltage distribution cables and conducting targeted maintenance can effectively prevent their development into permanent faults, thus ensuring the safe and reliable operation of the power system.

The current research approaches for identifying latent cable faults both domestically and internationally primarily involve extracting fault features, constructing threshold

criteria for identification, and utilizing data-driven algorithms for recognition. Ref (Sidhu and Xu) proposed two detection algorithms, namely, cable latent fault detection and classification rules based on wavelet analysis, as well as the integration of fault currents and negative sequence currents in the time domain, with the latter being more suitable for single-phase cable latent faults. Ref (Zhou et al.) and (Zhang et al., 2017a) analyzed the characteristics of cable overcurrent caused by various disturbance sources, including short circuit faults, capacitor switching and transformer reclosing, load switching, and motor starting. They utilized feature quantities obtained through wavelet transform decom-position to develop overcurrent detection criteria. Furthermore, based on this foundation, feature extraction and grey relational analysis were employed to calculate the correlation between measured samples and reference samples for identifying latent cable faults. Ref (Fothergill et al., 2011) applied wavelet singularity detection and Bayesian change point analysis to detect the current signals of cable latent faults, extract frequency do-main feature vectors, and achieve classification and recognition of cable latent faults using probabilistic neural networks and support vector machines, respectively. In ref (Mousavi and Butler-Purry), the empirical mode decomposition (EMD) method was utilized to extract transient features, and the ant colony algorithm and fuzzy neural network were applied for fault classification in distribution network cables. Ref (Faisal et al., 2012) introduced a latent fault identification method that relies on time-domain characteristics. This method involved obtaining the time-frequency characteristics of fault currents and voltages through S-transform analysis and subsequently detecting latent faults. Ref (Mousavi and Butler-Purry, 2009) proposed a latent fault detection and classification method based on a rule-oriented support vector ma-chine. Addressing the challenge of distinguishing load transients from latent faults, Ref (Mousavi et al., 2003) presented a methodology that employed wavelet packet analysis for extracting waveform features. This approach integrated three signal processing techniques, namely, principal component analysis, linear discriminant analysis, and feature subset classification, in conjunction with the k-nearest neighbor algorithm for fault type identification. Ref (Sidhu and Xu, 2010) introduced two detection algorithms rooted in wavelet analysis and time-domain fault current characteristics. These algorithms established latent fault detection rules and thresholds, enabling the identification and classification of latent faults. Notably, only a limited number of studies have ventured into modeling latent faults. Ref (Mousavi and Butler-Purry, 2010) harnessed self-organizing mapping (SOM) technology for numerical modeling of latent faults. During the modeling process, specific energy features in the wavelet domain were obtained and employed. Ref (Zhang et al., 2017b) adopted the Kizilcay arc model to simulate cable latent faults but did not account for the influence of latent faults on the model.

However, whether it is machine learning algorithms or the more widely used deep learning approaches in recent years, they are fundamentally data-driven algorithms. Data-driven algorithms, especially deep learning algorithms, have higher requirements for the scale and quality of samples. They excessively rely on samples, and when the sample size is insufficient or the quality is poor, they often struggle to achieve desirable results.

In summary, this paper establishes a cable latent fault model based on the Kizilcay arc model in the PSCAD/EMTDC platform, which effectively characterizes the features of cable latent faults. By conducting batch simulations to obtain fault phase current samples, various analyses including time-frequency, frequency-domain, and time-frequency domain are performed to extract multi-dimensional and multi-domain fault features, constructing initial feature vectors. Multivariate analysis of variance is utilized to select features, retaining effective features and constructing feature vectors. Principal Component Analysis is employed to process the feature vectors, significantly reducing the dimensionality while retaining the maximum amount of effective information from the original features. An intelligent diagnosis model based on Extreme Learning Machine (ELM) is established, and the Particle Swarm Optimization (PSO) algorithm is introduced to optimize its generalization capability. Case study results demonstrate that the cable latent fault identification model based on Extreme Learning Machine outperforms other machine learning algorithms in terms of fault recognition performance.

2 Modeling of latent faults in cables based on arc models

2.1 Modeling of latent faults based on the Kizilcay arc model

Latent faults in cables are often characterized by low energy and short duration intermittent arc faults. Therefore, this paper employs the Kizilcay arc model (Kizilcay and Pniok, 2007), (Idarraga et al.) to represent latent faults in cables. The Kizilcay arc model, based on the energy balance theory and control theory, provides a concise and accurate representation of arc fault characteristics, and it has been widely applied in recent research (Wang et al., 2021). This model con-siders the arc ignition process and assumes a constant length for the main arc while the length of the secondary arc linearly increases over time.

The mathematical expression of the Kizilcay arc model is as follows:

$$\frac{dg(t)}{dt} = \frac{1}{\tau}\left(G - g(t)\right) \tag{1}$$

where τ is the time constant, G is the arc static equivalent conductance, which can be understood as the arc conductance value when the current remains stable for a long time under external conditions. It is a function of the arc forward current i_f and the static arc voltage $u_{st}(t)$, as shown in Eq. 2. g is the arc instantaneous conductance and is related to the arc instantaneous resistance according to the quantity relationship de-scribed in Eq. 3.

$$G(t) = \frac{i_f(t)}{u_{st}(t)} \tag{2}$$

$$R_{arc}(t) = \frac{1}{g(t)} \tag{3}$$

The static arc voltage $u_{st}(t)$ satisfies:

$$u_{st}(t) = u_0 + r_0\left|i_f(t)\right| \tag{4}$$

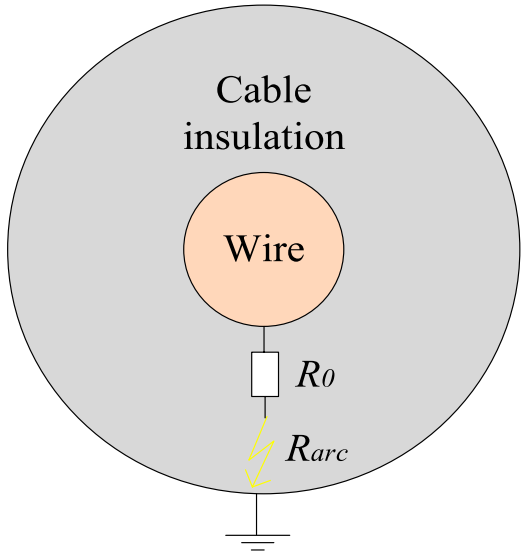

FIGURE 1
Schematic diagram of equivalent model of cable latent fault.

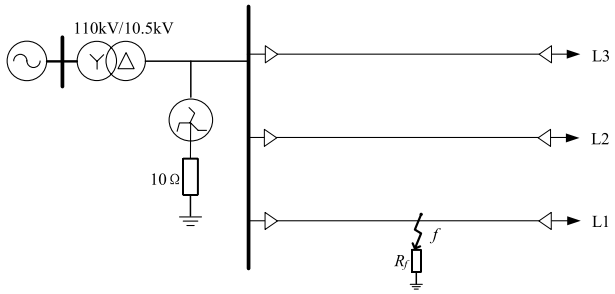

FIGURE 2
Schematic diagram of 10 kV cable distribution system.

where u_0 is the characteristic voltage of the arc, and r_0 is the characteristic resistance of the arc.

Substituting Eqs 2–4 into Eq. 1, the complete formulation of the Kizilcay dynamic arc model can be obtained.

$$\frac{dg(t)}{dt} = \frac{1}{\tau}\left(\frac{|i_f(t)|}{u_0 + r_0|i_f(t)|} - g(t)\right) \tag{5}$$

As mentioned earlier, cable latent faults are often developed from water trees and electrical trees. Using only the arc model is insufficient to accurately characterize the characteristics of latent faults. Therefore, the unburned portions of the water tree and electrical tree channels are equivalently represented as constant resistances, which are connected in series with the arc model to provide a better description of latent faults. The equivalent model of cable latent faults is illustrated in the following figure.

As shown in Figure 1, the latent fault of medium-voltage distribution cables is considered as a series connection of the arc resistance R_{arc} and the equivalent resistance R_0 of the defect channel. Therefore, the model of cable latent faults can be expressed as follows:

$$u_f(t) = i_f(t)(R_0 + R_{arc}(t)) \tag{6}$$

Where u_f is the voltage of the latent fault in the cable, and i_f is the current of the latent fault.

2.2 Modeling of latent cable faults based on PSCAD

This paper establishes a typical low-resistance grounded medium-voltage cable distribution system, as shown in Figure 2, using the Bergeron cable model in the PSCAD platform. The power supply voltage is 110 kV, which is stepped down to 10 kV through a distribution transformer, and connected to three cable feeders. The specific cable parameters are provided in Table 1.

3 Multi-dimensional feature analysis of faults in medium-voltage cables

3.1 Time-domain feature extraction

Time-domain feature statistics include dimensional and dimensionless features, which describe fault characteristics from different perspectives and enable fault classification. In this study, a total of nine time-domain feature statistics were extracted, including five dimensional features and four dimensionless features, as listed in Table 2.

The aforementioned nine statistical features form the time-domain feature vector:

$$C_t = [C_{t1}, C_{t2}, C_{t3}, C_{t4}, C_{t5}, C_{t6}, C_{t7}, C_{t8}, C_{t9}] \tag{7}$$

3.2 Frequency -domain feature extraction

The fault phase current signal is subjected to spectral analysis to obtain the frequency components of the signal, thereby extracting the frequency-domain features. In this paper, a total of four frequency-domain features are extracted, including centroid frequency, average frequency, root mean square frequency, and frequency standard deviation. The specific meanings of each feature are listed in Table 3.

The aforementioned nine statistical features form the time-domain feature vector:

$$C_F = [C_{F1}, C_{F2}, C_{F3}, C_{F4}] \tag{8}$$

3.3 Time-frequency domain feature extraction based on stationary wavelet transform

The stationary wavelet transform, employing the "zero-padding" method during signal decomposition and

TABLE 1 Cable parameters.

Conductor radius R0/m	Insulation radius R1/m	Armour radius R2/m	Shell radius R3/m	Conductor resistivity ρ/Ω	Relative permeability μ	Relative permittivity ε
0.020	0.040	0.044	0.048	1.724e-8	1.2	2.7

TABLE 2 Time-domain feature.

Characteristics	Meaning	Calculation
C_{t1}	Peak-to-peak value	$C_{t1} = \max(x_i) - \min(x_i)$
C_{t2}	Rectified Average	$C_{t2} = \frac{1}{N}\sum_{i=1}^{N}\lvert x_i\rvert$
C_{t3}	Variance	$C_{t3} = \frac{1}{N}\sum_{i=1}^{N}(x_i - \bar{x})^2$
C_{t4}	Standard deviation	$C_{t4} = \sqrt{\frac{1}{N}\sum_{i=1}^{N}(x_i - \bar{x})^2}$
C_{t5}	Root mean square (RMS) value	$C_{t5} = \sqrt{\frac{1}{N}\sum_{i=1}^{N}x_i^2}$
C_{t6}	Skewness	$C_{t6} = \frac{\sum_{i=1}^{N}[(x_i-\bar{x})^3]}{(N-1)(T4)^3}$
C_{t7}	Kurtosis	$C_{t7} = \frac{\sum_{i=1}^{N}[(x_i-\bar{x})^4]}{(N-1)(T4)^4}$
C_{t8}	Peak factor	$C_{t8} = \frac{\max\lvert x_i\rvert}{C_{t5}}$
C_{t9}	Form factor	$C_{t9} = C_{t5}/C_{t2}$

TABLE 3 Frequency-domain feature.

Characteristics	Meaning	Calculation
C_{F1}	Centroid frequency	$C_{F1} = \frac{\sum_{k=1}^{K}s(k)f(k)}{\sum_{k=1}^{K}s(k)}$
C_{F2}	Average frequency	$C_{F2} = \frac{1}{n}\sum_{k=1}^{K}f(k)$
C_{F3}	Root mean square frequency	$C_{F3} = \sqrt{\frac{\sum_{k=1}^{K}f^2(k)s(k)}{\sum_{k=1}^{K}s(k)}}$
C_{F4}	Frequency standard deviation	$C_{F4} = \sqrt{\frac{\sum_{k=1}^{K}(f(k)-F_c)^2s(k)}{\sum_{k=1}^{K}s(k)}}$

TABLE 4 Frequency -domain feature.

Characteristics	Meaning	Calculation
C_{w1}	Energy	$C_{w1} = \sum_{i=1}^{N}s_{ij}^2$
C_{w2}	Energy entropy	$C_{w2} = -\sum_{i=1}^{N}\frac{s_{ij}^2}{E_j}\log_2(\frac{s_{ij}^2}{E_j})$
C_{w3}	Information entropy	$C_{w3} = -\sum_{i=1}^{N}s_{ij}^2\log_2 s_{ij}^2$

reconstruction, exhibits translation invariance, ensuring that the decomposed approximation and detail coefficients at each level have the same length as the original signal. (Wang et al., 2021). This preserves the transient features of the original signal to the maximum extent. Based on this, in this paper, time-frequency domain feature extraction of cable latent faults and other transient disturbances is achieved by calculating the energy and performing statistical analysis on the wavelet coefficients obtained through the stationary wavelet transform (Li, 2021; Wu and Wang, 2022).

The formulas for obtaining the low-frequency approximation coefficients $a_{j,n}$ and high-frequency detail coefficients $d_{j,n}$ at each level through the stationary wavelet transform are as follows:

$$\begin{cases} d_{j,n} = \sum_i g(i-2n)a_{j-1,i} \\ a_{j,n} = \sum_i h(i-2n)a_{j-1,i} \end{cases} \tag{9}$$

10.3389/fenrg.2024.1364528

TABLE 5 Parameter table of 21-dimensional effective features.

Characteristics	F-statistics	p
C_{t1}	200.79	4.44343e-5
C_{t2}	175.18	1.27355e-4
C_{t3}	57.07	5.61522e-3
C_{t4}	174.92	1.45584e-6
C_{t5}	176.45	6.59797e-7
C_{t6}	155.3	1.48556e-3
C_{t7}	215.43	1.80453e-4
C_{t8}	219.14	2.86655e-4
C_{t9}	224.37	2.15367e-5
C_{F1}	218.15	4.69379e--5
C_{F2}	190.39	4.37507e-4
C_{F3}	220.43	1.51552e-5
C_{F4}	219.49	2.41903e-5
$C_{w1(12)}$	157.73	4.47376e-3
$C_{w3(12)}$	182.54	2.12152e-4
$C_{w1(13)}$	108.76	4.91673e-4
$C_{w1(15)}$	83.25	1.55562e-4
$C_{w1(22)}$	158.76	2.69755e-3
$C_{w2(31)}$	76.82	3.95527e-4
$C_{w3(32)}$	191.97	1.99504e-5
$C_{w1(34)}$	51.18	2.75793e-3

$C_{w1(12)}$ represents the energy feature of the second time segment in the first-level subband, and similarly, $C_{w2(31)}$ represents the energy entropy feature of the first time segment in the third-level subband.

In the equations, i is the sample point index within the window, j denotes the level of wavelet coefficients, and n represents the discretization level of the wavelet function.

For the jth level wavelet coefficients $s_j = [s_{1j}, s_{2j}, \ldots s_{Nj}]$ obtained from the stationary wavelet transform, three feature statistics are constructed: energy, energy entropy, and information entropy. The specific meanings of each feature are listed in Table 4.

The above three features constitute the time-frequency domain feature vector.

$$C_w = [C_{w1}, C_{w2}, C_{w3}] \tag{10}$$

Taking the A-phase current of each fault type as an example, the 9-dimensional time-domain feature vector C_{ti} is calculated as described earlier. The 4-dimensional frequency-domain feature vector C_{Fi} is obtained by performing spectral analysis on C_{ti}. The A-phase current is then subjected to 3-level stationary wavelet transform using the dB4 mother wavelet. Each level's subbands are divided into five equal intervals of 0.02s, corresponding to the power frequency period. Within each interval, three feature values are computed, resulting in a total of 60-dimensional time-frequency feature vector C_{wi} By combining the feature vectors from the three domains, a 73-dimensional feature vector [C_{ti}, C_{Fi}, C_{wi}] is constructed for each fault sample. This process is repeated for each fault type, resulting in a fault feature matrix of size (number of fault samples) × 73 for each class of faults.

4 Validation and optimization of fault features

4.1 Feature statistical analysis based on multivariate analysis of variance

Multivariate analysis of variance (MANOVA) is a statistical theory and method for studying the relationships between multiple independent variables and multiple de-pendent variables. It is applicable when the independent variables simultaneously influence two or more dependent variables. MANOVA is used to analyze whether there are significant differences in the means of these dependent variables when the independent variables are at different levels (Wu and Wang, 2022). Furthermore, to specifically analyze the significance levels of each dependent variable, univariate analysis of variance (ANOVA) needs to be conducted for each dependent variable. In univariate ANOVA, the significance of the differences between independent variables and a specific dependent

TABLE 6 Weight results of each component.

Name	Variance contribution rate	Cumulative variance contribution rate	Weight (%)
Principal component 1	0.496	0.496	49.59
Principal component 2	0.269	0.764	26.85
Principal component 3	0.108	0.873	10.84
Principal component 4	0.07	0.943	7
Principal component 5	0.015	0.958	1.51

variable is evaluated using the output parameters p and the test statistic F. Typically, if the F value is large and p < the significance level (usually set at 0.05), the significance level of that dependent variable is considered significant (Liu et al., 2022).

The 73-dimensional features were subjected to individual one-way analysis of variance (ANOVA), resulting in the identification of 21 significant features. The corresponding *p*-values and F-values for each feature are presented in Table 5.

4.2 Feature vector dimensionality reduction optimization based on principal component analysis

Principal Component Analysis (PCA) aims to minimize information loss by per-forming an orthogonal transformation on a set of potentially correlated variables, resulting in a new set of linearly independent variables called principal components. The fundamental idea behind PCA is to represent the amount of information contained in each principal component using their respective variances. A higher variance indicates a greater amount of information contained in the corresponding principal component. The basic steps of PCA involve standardizing the original data, computing the correlation matrix, calculating the eigenvalues and eigenvectors, and determining the variance contribution. Finally, the selection of principal components is made based on these considerations (Huckemann et al., 2010).

The variance of the principal components is an important criterion for selecting the principal components (Huang et al., 2021). The variance contribution rate and cumulative variance contribution rate of the *i*th principal component are defined by Eqs 11, 12 respectively. The variance contribution rate represents the extent to which the principal component reflects the original sample information, with a higher contribution rate indicating a greater reflection of sample information.

$$\lambda_i \Big/ \sum_{k=1}^{M} \lambda_k \tag{11}$$

$$\sum_{k=1}^{i} \lambda_k \Big/ \sum_{k=1}^{M} \lambda_k \tag{12}$$

The 21-dimensional features selected through multivariate analysis of variance were subjected to principal component analysis (PCA) for dimensionality reduction. By considering eigenvalues greater than one and achieving a cumulative

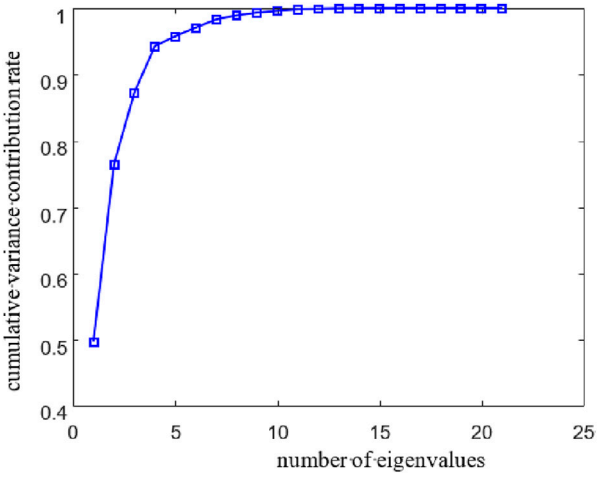

FIGURE 3
The number of eigenvalues and cumulative variance contribution rate of PCA.

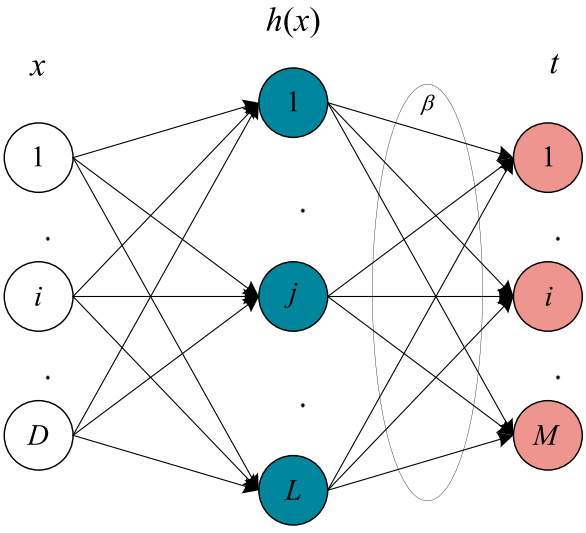

FIGURE 4
Network structure of ELM.

contribution rate of 95%, PCA reduced the feature vectors to five dimensions. The original 21-dimensional feature vectors were replaced by the feature vectors composed of the first five principal components, significantly reducing the dimensionality while retaining the effective information from the original features to the maximum extent. The weights of each principal component and the cumulative variance contribution rate are shown in Table 6 and Figure 3, respectively.

5 A cable latent fault identification model based on extreme learning machine

5.1 Extreme learning machine algorithm

Extreme Learning Machine (ELM) is a machine learning algorithm used for training Single Hidden Layer Feedforward Neural Networks (SLFNs) (Qian et al., 2023). Its basic principles are as follows:

Given input samples $\{(x_i,t_i),i = 1,2, \ldots ,N\}$, where N represents the number of samples, $x_i = \{ x_{i1}, x_{i2}, \ldots , x_{im}\}^{\mathrm{T}}$ and $t_i = \{ t_{i1}, t_{i2}, \ldots , t_{im}\}^{\mathrm{T}}$ denote the input vector and corresponding sample label of the ith sample, respectively (Liu et al., 2023). For a single hidden layer feedforward neural network with L hidden nodes, its network structure is shown in the Figure 4.

5.2 Particle Swarm Optimization-based model for identification of latent cable faults

Particle Swarm Optimization (PSO) algorithm is a population-based intelligent evolutionary computation method that simulates the foraging behavior of birds (Wang P. et al., 2023). It utilizes the collaborative behavior of a bird swarm to achieve optimal population search. In this study, the PSO algorithm is employed to optimize the random initial parameters of the ELM model (Wang D. et al., 2023; Gao, 2023).

The basic steps of the PSO algorithm are as follows:

1. Initialization of particle population: A set of particles is randomly generated, and the initial velocities v_0 and positions x_0 of each particle are randomized
2. Computation of fitness values for each particle: The fitness value of each particle is calculated. Additionally, the individual best (P_{best}) and global best (G_{best}) values are computed and recorded along with the corresponding particle positions.
3. Iterative updates: The velocities and positions of each particle are updated ac-cording to Eqs 13, 14. After each update, the fitness value is recalculated, and the updated particle fitness value is compared with the fitness value at the historical best position to determine the optimal fitness value.

$$V_{id}^{k+1} = wV_{id}^{k} + C_1 rand_1\left(P_{id}^{k} - X_{id}^{k}\right) + C_2 rand_2\left(P_{gd}^{k} - X_{id}^{k}\right) \tag{13}$$

$$X_{id}^{k+1} = X_{id}^{k} + V_{id}^{k+1} \tag{14}$$

Thus, this paper presents a data-driven latent fault identification model based on ELM (Extreme Learning Machine). The overall training process of the model is illustrated in Figure 5.

6 Case study

6.1 Classification results of cable latent faults based on optimized ELM algorithm

The five types of faults described earlier correspond to their respective fault labels, which need to be converted into vector labels when training the ELM model, as shown in Table 7.

After applying principal component analysis (PCA) to the extracted multi-dimensional fault features, the dimension was reduced to 5. Consequently, the ELM model was configured with five input layer nodes and five output layer nodes. The hidden layer activation function was set to the Sigmoid function, and the number of hidden layer nodes was determined as 11. For the output vector, the softmax function was used as the activation function to normalize it, ensuring that each output element in the vector is between 0 and 1. The values represent the probability of the input data be-longing to each fault type. In the PSO optimization algorithm, the learning factors *c1* and *c2* were both set to 1.5, and the number of iterations was set to 1,000. The optimization results are shown in Figure 6. The model training reached its optimal state when the number of iterations reached 815. Initially, due to the random initialization of weights and thresholds in the ELM model, the error was large. However, as the training progressed, the fitness function rapidly decreased.

Figure 7 presents the confusion matrix of the ELM model for fault classification on the training and testing sets, with classification accuracies of 91.02% and 88.87%, respectively. These results demonstrate that the proposed data-driven ELM-based cable latent fault identification model exhibits good classification performance. Although the overall classification accuracy is satisfactory, it can be observed from the classification results that the data-driven model for medium-voltage cable latent fault identification tends to misclassify serious faults such as constant impedance grounding faults as cable latent faults or transient disturbances. This limitation implies that the safety of the model's output results cannot be fully guaranteed, which is an inherent drawback of data-driven algorithms.

6.2 Comparison of machine learning algorithm performance

To validate the effectiveness of the proposed cable incipient fault identification method based on the ELM model, it was compared with the SVM classification model optimized by ten-fold cross-validation and the KNN model.

Similarly, for each type of fault mentioned earlier, 1,200 sets of samples were randomly selected, with 80% of samples used for training and the remaining 20% used for testing. The fault classification based on SVM was implemented using the libSVM software package, while the KNN algorithm was implemented using

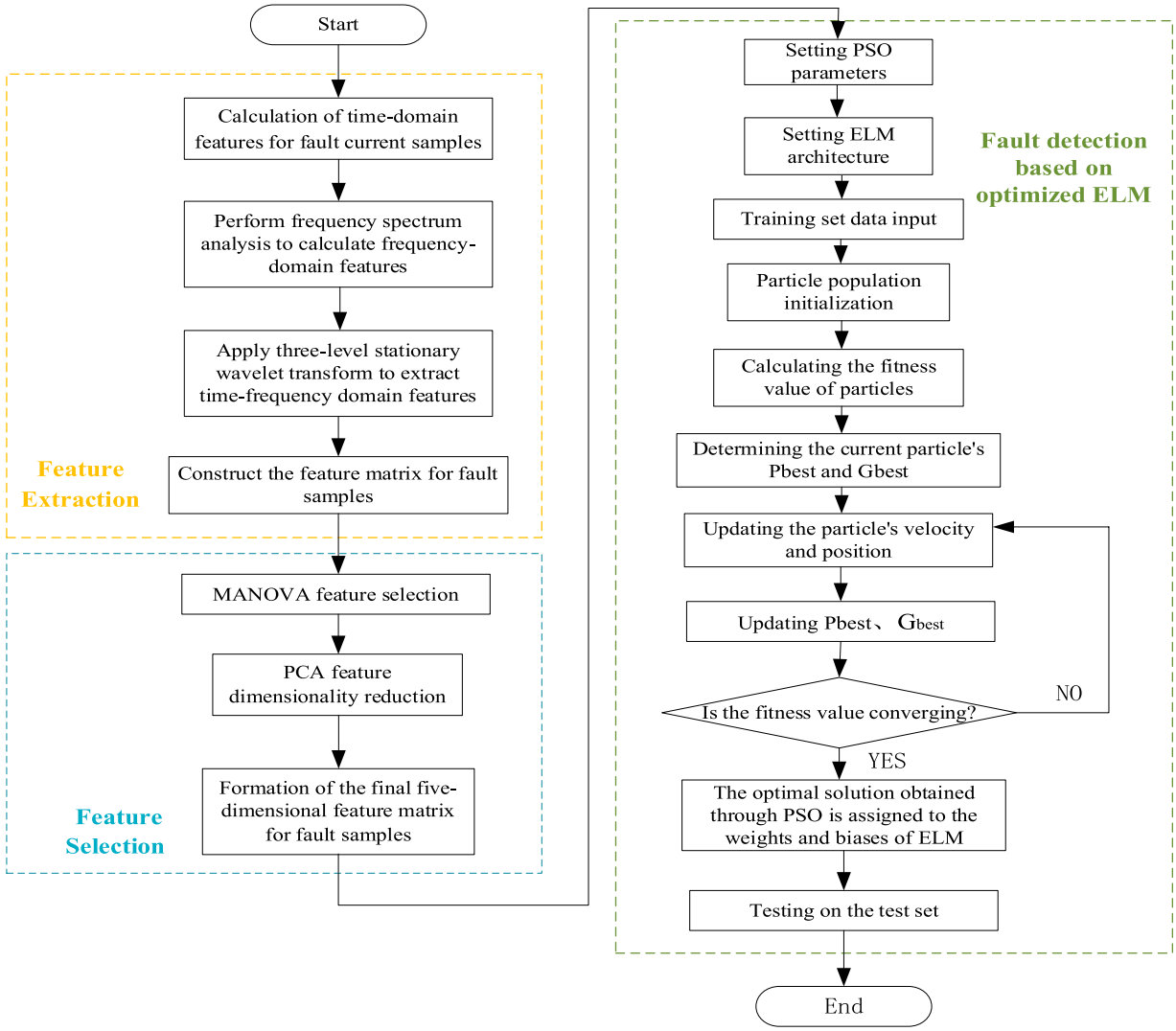

FIGURE 5
Construction process of fault identification model based on data-driven.

TABLE 7 Fault type and its corresponding vector label.

Types of faults	Vector label
Semi-periodic latent cable faults	(1,0,0,0,0)
Multi-periodic latent cable faults	(0,1,0,0,0)
Constant impedance grounding faults	(0,0,1,0,0)
Capacitor switching disturbances	(0,0,0,1,0)
Load transient disturbances	(0,0,0,0,1)

the MATLAB KNN function. The classification accuracies of the three models are shown in Table 8.

From the accuracy values in Table 8, it can be observed that all three classification models achieve classification accuracies above 85% on the test set, validating the effectiveness of the extracted and optimized feature vectors proposed in this study. Furthermore, the ELM model demonstrates higher overall classification accuracy on

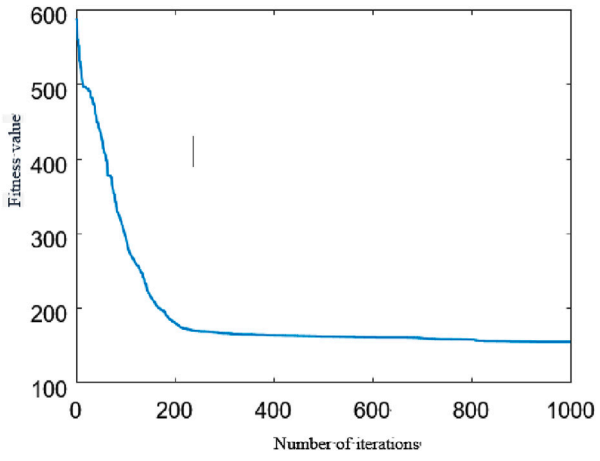

FIGURE 6
Fitness curve of ELM model.

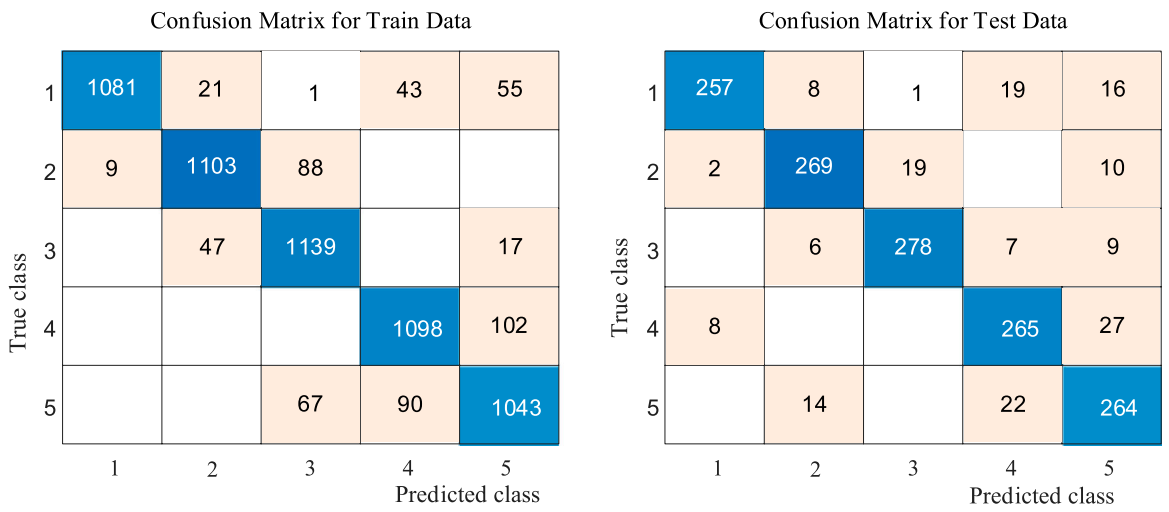

FIGURE 7
Confusion matrix of classification results on training set and test set.

TABLE 8 Comparison of fault classification models based on ELM, SVM and KNN.

Model name	Training set accuracy (%)	Testing set accuracy (%)
ELM model	91.02	88.87
SVM model	83.33	86.67
KNN model	80.62	87.5

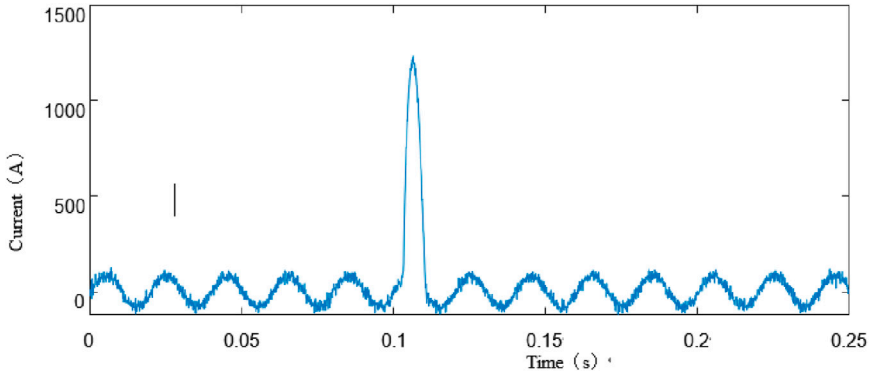

FIGURE 8
Cable latent fault current waveform after adding white noise.

the test set compared to the SVM and KNN-based classification models. Additionally, due to the absence of hidden layer parameter updates, the ELM model exhibits significantly lower training time compared to the SVM and KNN models.

6.3 Noise resistance analysis

To simulate real-world field data, Gaussian white noise with signal-to-noise ratios (SNRs) of 40dB, 30dB, and 20dB was added to the raw data of each fault type to evaluate the model's noise resistance. Figure 8 shows the current signal of the half-wave cable incipient fault with 30dB Gaussian white noise added.

Table 9 presents the accuracy of the three classification models after adding Gaussian white noise with three different signal-to-noise ratios. As observed from the table, the accuracy of all three classification models decreases with decreasing signal-to-noise ratio. This can be attributed to two main factors. Firstly, a lower signal-to-noise ratio indicates a higher level of noise contamination, resulting in more severe distortion of the original signal waveform and

TABLE 9 Comparison of fault classification models based on ELM, SVM and KNN.

Signal-to-noise ratio/dB	ELM (%)	SVM (%)	KNN (%)
0	88.87	86.67	87.50
40	87.25	85.09	84.33
30	85.02	82.21	78.62
20	80.96	78.85	74.93

subsequently masking the under-lying features. Secondly, the transient processes of the five fault types already exhibit relatively small differences, and the introduction of noise further reduces the distinguishability among them, leading to a decrease in the discriminative power of the extracted features.

As shown in Table 9, among the three classification models, KNN exhibits the largest decrease in accuracy, with its accuracy dropping below 75% at a signal-to-noise ratio of 20dB. SVM shows a relatively slower decline in classification accuracy, with its accuracy only falling below 80% under the influence of 20dB signal-to-noise ratio. Although ELM also experiences a decrease in accuracy, its classification performance re-mains superior to the other two neural network models under the same level of noise interference, consistently maintaining an accuracy above 80%.

Considering this evaluation metric, the PSO-optimized ELM model demonstrates good identification performance for cable latent faults even in the presence of signal noise interference.

7 Conclusion

This paper utilizes arc simulation to investigate latent faults in medium-voltage distribution cables. Based on the Kizilcay arc model and utilizing fault samples obtained through batch simulations in PSCAD, the study conducts time-frequency, frequency-domain, and time-frequency domain analyses to extract multi-dimensional and multi-domain fault features. Subsequently, multivariate analysis of variance and Principal Component Analysis are employed to optimize the features. Finally, an intelligent diagnosis model for latent faults in medium-voltage distribution cable networks is established based on Extreme Learning Machine (ELM). The following conclusions are drawn from the analysis and simulation experiments.

(1) The series connection of constant resistors using the Kizilcay arc model effectively simulates the characteristics of latent faults in medium-voltage distribution networks, providing favorable sample conditions for model training.
(2) The optimization and selection of initial feature vectors using multivariate analysis of variance and Principal Component Analysis improve the correlation between features, eliminate redundant information, and reduce the workload of model training and learning.
(3) Particle Swarm Optimization is utilized to optimize the random initial parameters of the ELM model, reducing the number of iterations required for model solution and improving the fitting capability of the model.
(4) Experimental results demonstrate that the Extreme Learning Machine model established in this paper outperforms SVM and KNN models in terms of classification accuracy. Additionally, to simulate actual field data, Gaussian white noise with signal-to-noise ratios of 40dB, 30dB, and 20dB is added to original fault samples to compare the robustness of the three models. The results show that the classification accuracy of the ELM model is consistently higher than that of the SVM and KNN models, confirming the robustness of the fault identification model based on Extreme Learning Machine established in this paper.

Next steps will involve researching fault location on the basis of latent fault identification in cables, aiming to reduce fault repair time and enhance the safety and stability of distribution network operation.

Data availability statement

The original contributions presented in the study are included in the article/Supplementary material, further inquiries can be directed to the corresponding author.

Author contributions

FW: Writing–review and editing. PZ: Writing–review and editing. JL: Writing–review and editing. ZL: Writing–original draft, Writing–review and editing. MZ: Writing–review and editing. YL: Writing–original draft, Writing–review and editing. GS: Writing–review and editing. XY: Writing–review and editing.

Funding

The author(s) declare financial support was received for the research, authorship, and/or publication of this article. This work was supported by State Grid Shandong Electric Power Company Science and Technology Project Funding (520626230044). The funder was not involved in the study design, collection, analysis, interpretation of data, the writing of this article, or the decision to submit it for publication.

Acknowledgments

The authors acknowledge the reviewers for providing valuable comments and helpful suggestions to improve the manuscript.

Conflict of interest

Author JL was employed by State Grid Shandong Electric Power Company.

The remaining authors declare that the research was conducted in the absence of any commercial or financial relationships that could be construed as a potential conflict of interest.

Publisher's note

References

Faisal, M. F., Mohamed, A., and Shareef, H. (2012). Prediction of incipient faults in underground power cables utilizing S-transform and support vector regression. *Int. J. Electr. Eng. Inf.* 4, 186–201. doi:10.15676/ijeei.2012.4.2.1

Fothergill, J. C., Dodd, S. J., Dissado, L. A., Liu, T., and Nilsson, U. (2011). The measurement of very low conductivity and dielectric loss in XLPE cables: a possible method to detect degradation due to thermal aging. *IEEE Trans. Dielectr. Electr. Insulation* 18 (05), 1544–1553. doi:10.1109/tdei.2011.6032823

Gao, L. (2023). Research on reactive power optimization of distribution network with DG based on improved PSO. *Electr. Switchg.* 61 (02), 18–20+25. doi:10.27733/d.cnki.gsxlg.2023.000045

Huang, J. S., Yao, S., and Shu, H. C. (2021). Fault line selection method for distribution networks based on principal component analysis and SVM model. *J. Kunming Univ. Sci. Technol. Nat. Sci. Ed.* 46 (04), 64–75. doi:10.16112/j.cnki.53-1223/n.2021.04.451

Huckemann, S., Hotz, T., and Munk, A. (2010). Intrinsic MANOVA for riemannian manifolds with an application to kendall's space of planar shapes. *IEEE Trans. Pattern Analysis Mach. Intell.* 32 (04), 593–603. doi:10.1109/tpami.2009.117

Idarraga, O. G., Cubillos, D., and Ibanez, L. "Analysis of arcing fault models," in Proceedings of the 2008 IEEE/PES Transmission and Distribution Conference and Exposition: Latin America, Bogota, Colombia, August 2008, 1–5.

Kizilcay, M., and Pniok, T. (2007). Digital simulation of fault arcs in power systems. *Eur. Trans. Electr. Power* 1 (1), 55–60. doi:10.1002/etep.4450010111

Li, Y. K. (2021). *Detection system-on-chip (SoC) and recognition method for low-voltage AC series arc faults based on hardware discrete wavelet transform*. Zhejiang University. doi:10.27461/d.cnki.gzjdx.2021.002031

Liu, K. Y., Zhan, H. Y., and Tan, Y. Y. (2023). Detection of high-resistance ground faults in distribution networks based on improved extreme learning machine. *Power Syst. Technol.* 47 (05), 1886–1899. doi:10.13335/j.1000-3673.pst.2022.1908

Liu, W. B., Qi, J. Y., and Shao, W. Z. (2022). Topological identification of phase relations in low-voltage distribution networks based on principal component analysis and graph theory. *J. Qilu Univ. Technol.* 36 (03), 59–65. doi:10.16442/j.cnki.qlgydxxb.2022.03.009

Mousavi, M. J., and Butler-Purry, K. L. (2009). A novel condition assessment system for underground distribution applications. *IEEE Trans. Power Syst.* 24, 1115–1125. doi:10.1109/tpwrs.2009.2022977

Mousavi, M. J., Butler-Purry, K. L., Gutierrez-Osuna, R., and Najafi, M. (2003). Classification of load change transients and incipient abnormalities in underground cable using pattern analysis techniques. *IEEE PES Transm. Distribution Conf. Expo.* 1, 175–180. IEEE Cat No 03CH37495. doi:10.1109/TDC.2003.1335177

Mousavi, M. J., and Butler-Purry, K. L. (2010). Detecting incipient faults via numerical modeling and statistical change detection. *IEEE Trans. Power Deliv.* 25, 1275–1283. doi:10.1109/tpwrd.2009.2037425

Mousavi, M. J., and Butler-Purry, K. L. "A novel condition assessment system for underground distribution applications," in Proceedings of the IEEE PES T&D 2010, New Orleans, LA, USA, August 2010, 1–1.

Qian, Y. N., Zhao, W., and Zhang, P. C. (2023). Fault localization in distribution networks based on extreme learning machine and wavelet transform. *Inf. Technol.* 47 (03), 177–183. doi:10.13274/j.cnki.hdzj.2023.03.033

Sidhu, T. S., and Xu, Z. "Detection and classification of incipient faults in underground cables in distribution systems," in Proceedings of the 2009 Canadian Conference on Electrical and Computer Engineering, St. John's, NL, Canada, May 2009, 122–126.

Sidhu, T. S., and Xu, Z. (2010). Detection of incipient faults in distribution underground cables. *IEEE Trans. Power Deliv.* 25, 1363–1371. doi:10.1109/tpwrd.2010.2041373

Wang, D., Li, W. H., and Li, S. Z. (2023b). Dynamic optimization method for energy saving and loss reduction in industrial park distribution network based on load measurement. *Ind. Heat.* 52 (06), 49–53. doi:10.3969/j.issn.1002-1639.2023.06.012

Wang, F., Quan, X. Q., and Ren, L. T. (2021). A comprehensive review of research on detection and identification methods for power quality disturbances. *Proc. Chin. J. Electr. Eng.* 41 (12), 4104–4121. doi:10.13334/j.0258-8013.pcsee.201261

Wang, P., Cheng, X. L., and Wang, Y. (2023a). Construction of an intelligent distribution network hierarchical planning model based on hybrid particle swarm optimization. *Electr. Autom.* 45 (03), 68–70+73. doi:10.3969/j.issn.1000-3886.2023.03.021

Wu, C. Y., and Wang, L. T. (2022). Fault location for transmission lines based on stationary wavelet transform. *Electr. Autom.* 44 (03), 100–102. doi:10.3969/j.issn.1000-3886.2022.03.031

Zhang, W., Xiao, X., Zhou, K., Xu, W., and Jing, Y. (2017a). Multicycle incipient fault detection and location for medium voltage underground cable. *IEEE Trans. Power Deliv.* 32 (03), 1450–1459. doi:10.1109/tpwrd.2016.2615886

Zhang, W., Xiao, X., Zhou, K., Xu, W., and Jing, Y. (2017b). Multicycle incipient fault detection and location for medium voltage underground cable. *IEEE Trans. Power Deliv.* 32, 1450–1459. doi:10.1109/tpwrd.2016.2615886

Zhou, C., Zhou, N., Pan, S., et al. "Method of cable incipient faults detection and identification based on wavelet transform and gray correlation analysis," in Proceedings of the 2015 IEEE Innovative Smart Grid Technologies - Asia (ISGT ASIA), Bangkok, Thailand, November 2015, 1–5.

frontiers | Frontiers in Energy Research

TYPE Original Research
PUBLISHED 11 April 2024
DOI 10.3389/fenrg.2024.1373345

OPEN ACCESS

EDITED BY
Michael Carbajales-Dale,
Clemson University, United States

REVIEWED BY
Bin Zhou,
Hunan University, China
Tao Huang,
Polytechnic University of Turin, Italy
Hanbo Zheng,
Guangxi University, China

*CORRESPONDENCE
Nantian Huang,
huangnantian@neepu.edu.cn

RECEIVED 19 January 2024
ACCEPTED 27 March 2024
PUBLISHED 11 April 2024

CITATION
Huang N, Wang X, Wang H and Wang H (2024), Ultra-short-term multi-energy load forecasting for integrated energy systems based on multi-dimensional coupling characteristic mining and multi-task learning.
Front. Energy Res. 12:1373345.
doi: 10.3389/fenrg.2024.1373345

Ultra-short-term multi-energy load forecasting for integrated energy systems based on multi-dimensional coupling characteristic mining and multi-task learning

Nantian Huang*, Xinran Wang, Hao Wang and Hefei Wang

School of Electrical Engineering, Northeast Electric Power University, Jilin, China

To address the challenges posed by the randomness and volatility of multi-energy loads in integrated energy systems for ultra-short-term accurate load forecasting, this paper proposes an ultra-short-term multi-energy load forecasting method based on multi-dimensional coupling feature mining and multi-task learning. Firstly, a method for mining multi-dimensional coupling characteristics of multi-energy loads is proposed, integrating multiple correlation analysis methods. By constructing coupling features of multi-energy loads and using them as input features of the model, the complex coupling relationships between multi-energy loads are effectively quantified. Secondly, an ultra-short-term multi-energy load forecasting model based on multi-task learning and a temporal convolutional network is constructed. In the prediction model construction phase, the potential complex coupling characteristics between multiple loads can be fully explored, and the potential temporal associations and long-term dependencies within data can be extracted. Then, the multi-task learning loss function weight optimization method based on homoscedastic uncertainty is used to optimize the forecasting model, realizing automatic tuning of the loss function weight parameters and further improving the prediction performance of the model. Finally, an experimental analysis is conducted using the integrated energy system of Arizona State University in the United States as an example. The results show that the proposed forecasting method has higher prediction accuracy than other prediction methods.

KEYWORDS

multi-dimensional coupling characteristic mining, multi-task learning, integrated energy systems, ultra-short-term multi-energy load forecasting, homoscedastic uncertainty

1 Introduction

The Integrated Energy System (IES) is a multi-energy supply system that connects multiple independent energy systems through a variety of energy coupling devices to achieve tight coupling, coordination, and complementarity between different energy forms (Alabi et al., 2022). IES can improve the flexibility of various energy systems and achieve full consumption of renewable energy and a reliable supply of multiple energy sources (Zhu

et al., 2022). Therefore, the development and construction of IES is an inevitable choice to solve the energy crisis, improve environmental pollution, improve energy utilization efficiency, and promote the large-scale utilization of renewable energy (Liu et al., 2023). With the development of IES, the potential factors affecting the energy demand of IES users have gradually become more complicated, which brings huge challenges to the ultra-short-term accurate prediction of multi-load, thus affecting the optimal dispatch and demand response strategy formulation of IES (Yan et al., 2024). Therefore, it is necessary to research a more accurate ultra-short-term forecasting method for IES multi-energy loads.

In the construction phase of the input feature set for multi-energy load forecasting in IES, existing research has considered various potential factors that influence IES users' energy consumption habits, and uses correlation analysis methods to screen the strongly correlated features for multi-energy load forecasting. Literature (Wang et al., 2022) considers the impact of meteorological information, holiday information, and temporal features on the multi-energy load when constructing the input feature set. It employs Pearson correlation analysis and Grey Relational Analysis (GRA) to select strongly correlated meteorological features for multi-energy load forecasting, thereby enhancing the forecasting model's accuracy. Similarly, Literature (Zhuang et al., 2023) considers factors such as meteorological information and holiday information in relation to the potential association with the multi-energy load when constructing the input feature set. It utilizes Pearson correlation analysis and correlation analysis methods based on Copula theory to select strongly correlated meteorological features from both linear and nonlinear perspectives for multi-energy load forecasting. In addition, some researchers have constructed strongly correlated features that reflect the latent characteristics of multi-energy loads, achieving high prediction accuracy. For instance, Literature (Tan et al., 2023) introduces a feature selection method based on Synthesis Correlation Analysis (SCA), and constructs a Load Participation Factor (LPF) as an input feature for the prediction model, illustrating the degree of participation of each load in the total load. However, existing multi-energy load forecasting methods for IES have not fully explored the potential complex coupling characteristics between multi-energy loads of the integrated energy system in different dimensions during the input feature set construction phase, thereby leaving room for improvement in the model's prediction accuracy.

In the construction phase of forecasting models for multi-energy loads in IES, some existing studies build separate forecasting models for different types of loads. Literature (Zheng et al., 2023) proposes a multi-energy load forecasting method based on Temporal Convolutional Networks (TCN) and global attention mechanism, forecasting electric, cooling, and heating loads separately. Literature (Ge et al., 2021) introduces a Wavelet Neural Networks (WNN) multi-energy load forecasting model based on Improved Particle Swarm Optimization (IPSO) and Chaos Optimization Algorithm (COA), which forecasts electric, cooling, and heating loads individually. Literature (Liu et al., 2022) presents a multi-energy load forecasting method combining Multivariate Phase Space Reconstruction (MPSR) with Support Vector Regression (SVR), achieving good forecasting results by separately constructing forecasting models for each load. However, there is a complex coupling relationship among the multi-energy loads in IES. The mentioned research method uses historical data of various types of loads, which are strongly correlated with the load to be predicted, as input features for the forecasting model during the construction of the input feature set. This approach only considers the coupling relationship among the multi-energy loads at the construction phase of input feature set construction and fails to fully explore the potential coupling characteristics among the multi-energy loads during the construction phase of the forecasting model. As a result, this leads to the need for improvement in the accuracy of multi-energy load forecasting.

To address this issue, some studies have employed multi-energy load forecasting models based on Multi-Task Learning (MTL), achieving high prediction accuracy. For instance, Literature (Guo et al., 2022) developed a multi-energy load forecasting model based on MTL and Bi-directional Long Short-Term Memory Networks (BiLSTM), effectively extracting potential coupling information between loads. Literature (Wang et al., 2021) used a forecasting model combining MTL with Long Short-Term Memory Networks (LSTM) to forecast the trend curves of decomposed and reconstructed multi-energy loads. Additionally, it employed the Least Squares Support Vector Regression (LSSVR) method to forecast fluctuation curves. The final multi-energy load forecast results were obtained by superimposing the predictions of the two models. However, existing studies on multi-energy load forecasting based on MTL often employ LSTM and their variants to construct the sharing layers in MTL. Although these structures contain temporal memory units, they still face issues with forgetting historical information. Furthermore, their capability to mine potential temporal associations and long-term dependencies within data is relatively weak, limiting the improvement in the accuracy of multi-energy load forecasting.

Selecting appropriate weights for the loss functions of each sub-task in the construction and training process of MTL models is a crucial means of enhancing the overall performance of the model. Current research methods on multi-energy load forecasting in IES using MTL models typically set the weights of each forecasting task's loss function manually without adjustment. For example, Literature (Zhang et al., 2023) manually set the loss function weights for the model when utilizing MTL to construct an electric load forecasting model. Literature (Wu et al., 2022) developed a multi-energy load forecasting model for IES based on MTL and LSTM, where the loss function weights for the MTL model were manually set based on the peak ratio of different types of loads within the IES. However, manually setting the weights of the MTL loss functions during the training process will consume a considerable amount of time for parameter tuning. Additionally, setting model parameters manually may lead to one or more tasks dominating the model training process. This method of parameter configuration fails to balance the losses of the sub-tasks reasonably, lacks scientific rigor, and limits further enhancements in the prediction performance of MTL models.

To address the aforementioned issues, this paper proposes an ultra-short-term multi-energy load forecasting method based on multi-dimensional coupling characteristic mining and multi-task learning. The specific contributions of this paper are as follows:

(1) A multi-dimensional coupling characteristic mining method for multi-energy loads is employed, integrating multiple correlation analysis methods. By utilizing Pearson correlation coefficients, Spearman rank correlation

coefficients, and the Maximum Information Coefficient (MIC), load features that describe the coupling relationships between multi-energy loads are constructed. This effectively quantifies the complex coupling relationships among the historical sequences of IES multi-energy loads, thoroughly mining the potential coupling characteristics from different dimensions in the construction of the input feature set.

(2) An ultra-short-term multi-energy load forecasting model based on MTL and TCN is constructed. During the model construction phase, the sharing layer of MTL is used to fully exploit the potential complex coupling characteristics among multi-energy loads. The use of dilated causal convolutions and residual connections in TCN extracts the latent temporal information of input features, capturing the long-term dependencies of the input time series.

(3) An optimization method for the forecasting model based on homoscedastic uncertainty (HU) for MTL loss function weight optimization is employed. By learning the homoscedastic uncertainty of multiple forecasting tasks, the method automatically tunes the weight parameters of the loss function, saving time on parameter tuning while further enhancing the model's prediction performance.

(4) An experimental analysis is conducted using the IES of Arizona State University as a case study. The results demonstrate that the proposed forecasting method achieves higher prediction accuracy compared to other methods.

2 Multi-energy load characteristic analysis

The various energy subsystems in IES coordinate and complement each other through energy conversion devices, leading to complex coupling relationships among different forms of energy within IES. Simultaneously, changes in external factors such as meteorological conditions can influence the energy consumption habits of IES users, implying that the variation trends of IES multi-energy loads follow certain latent patterns. To fully explore the latent characteristics of IES multi-energy loads, this study analyzes the multi-energy load characteristics using historical data of loads from March 2018 to February 2019 from the IES of the Tempe campus of Arizona State University.

2.1 Analysis of the annual variation trends of multi-energy loads

Figure 1 displays the annual data curves of electric, cooling, and heating loads in IES from March 2018 to February 2019. To facilitate the analysis of the variation trends of multi-energy load sequences in different seasons, the load data from March to May are categorized as Spring data, June to August as Summer data, September to November as Autumn data, and December to the following February as Winter data. As indicated in Figure 1, both electric and cooling loads gradually increase to higher levels in Spring and Summer, with significant fluctuations in these two seasons. The electric load exhibits stronger fluctuations in autumn, while the fluctuations are more subdued in winter. The cooling load remains relatively stable in both autumn and winter. Conversely, the heating load shows an opposite annual trend, gradually decreasing in Spring and Summer with less variability. In Autumn and Winter, the heating load increases to higher levels with more pronounced fluctuations. This demonstrates that for the same load, the variation trends in different seasons are significantly influenced by varying meteorological and other external factors. The differences in load variation trends across different seasons imply that IES users have varying energy consumption habits in different seasons. Ignoring these differences can lead to a failure to fully explore the potential characteristics of multi-energy loads. Therefore, in conducting ultra-short-term forecasting of multi-energy loads, it is crucial to mitigate the negative impact of the differences in load variation trends between seasons on prediction accuracy.

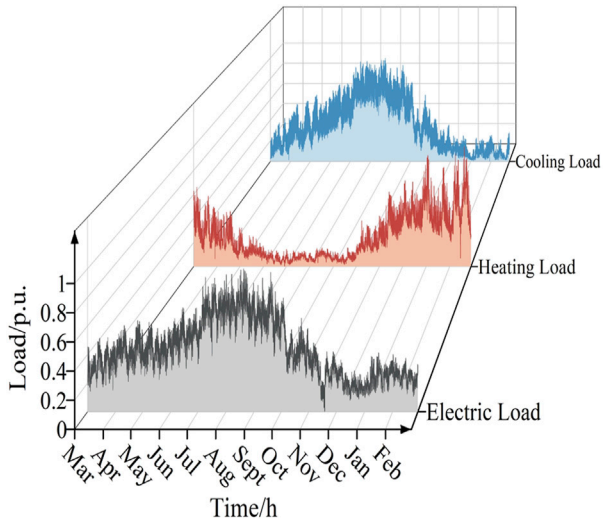

FIGURE 1
The annual historical data curves of multi-energy loads.

2.2 Coupling analysis between multi-energy load

Figure 1 also reveals that within the same season, the variation trends of different loads in IES are either similar or complementary, which preliminarily indicates a tight coupling relationship among IES multi-energy loads. To analyze the coupling among multi-energy loads more intuitively, Figure 2 employs the Pearson correlation analysis method to quantify the correlation of the annual variation trends among different loads. The Pearson correlation coefficient is a statistical metric that measures the degree of linear correlation between two continuous variables, and its specific expression is as follows:

$$\rho = \frac{\sum_{i=1}^{n} (a_i - \bar{a})(b_i - \bar{b})}{\sqrt{\sum_{i=1}^{n} (a_i - \bar{a})^2} \sqrt{\sum_{i=1}^{n} (b_i - \bar{b})^2}} \quad (1)$$

In the formula, a_i and b_i respectively represent the i-th sample of the multi-energy load sequences A and B, while $\bar{a}$ and $\bar{b}$ represent the mean values of the multi-energy load sequences A and B,

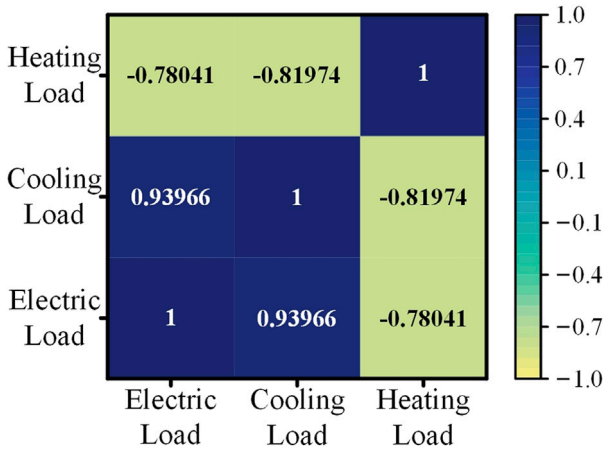

FIGURE 2
Pearson correlation analysis results between multi-energy loads.

respectively. The symbol "n" denotes the total number of samples in the load sequences. The value of ρ ranges from [-1, 1], and a larger value of $|\rho|$ indicates a stronger correlation.

According to Figure 2, there is a positive correlation between the IES electric load and the cooling load, while there is a negative correlation between the heating load and both the cooling and electric load. The absolute values of the Pearson correlation coefficients between the annual electric load, cooling load, and heating load in the IES are all greater than 0.7. This indicates a strong coupling relationship between the various loads in the IES. Therefore, in conducting ultra-short-term forecasts of multiple loads, it is crucial to thoroughly explore the complex coupling characteristics between these loads, as this can significantly enhance the accuracy of the forecasts.

2.3 Multi-energy loads temporal correlation analysis

The Autocorrelation Coefficients Function (ACF) is used to analyze the temporal correlation of multi-energy loads, with the results presented in Figure 3. The calculation formula for ACF is as follows:

$$R(k) = \frac{E[(X_t - \mu)(X_{t+k} - \mu)]}{\sigma^2} \quad (2)$$

In the formula, k represents the time lag, where X_t denotes the load value at time t; μ represents the mean of the historical load sequence, and σ^2 represents the variance of the historical load sequence. The autocorrelation coefficient takes values within the range [-1, 1], where a higher autocorrelation coefficient indicates a stronger correlation.

Figure 3 shows the autocorrelation coefficients of IES multi-energy loads with a 96-h lag, where the shaded area represents the 95% confidence interval. The figure reveals that within each 24-h lag period, the autocorrelation coefficients of the various loads first decrease and then increase, exhibiting a strong daily periodicity. Additionally, the peak values of the autocorrelation coefficients within each 24-h lag period gradually decrease. This indicates that the load values of the IES at a given moment are not only strongly correlated with the load values of adjacent times but also with the load values at the same time on adjacent days. Therefore, when conducting ultra-short-term forecasts of multi-energy loads, it is essential to fully consider the temporal correlation of the loads to achieve accurate ultra-short-term predictions.

3 Multi-dimensional multi-energy load coupling characteristics mining and input feature set construction

Section 2.2 quantifies the coupling relationships between multi-energy loads in the IES using the Pearson correlation analysis method, indicating a strong coupling among the IES multi-energy loads. However, the Pearson correlation analysis method can only describe the linear relationships between two types of load sequences and fails to capture the nonlinear relationships between loads. Therefore, this chapter employs Pearson, Spearman, and MIC correlation analysis methods to construct multi-energy load coupling features. By utilizing multiple correlation analysis methods to quantify various types of linear and nonlinear relationships between multi-energy loads, it is possible to fully

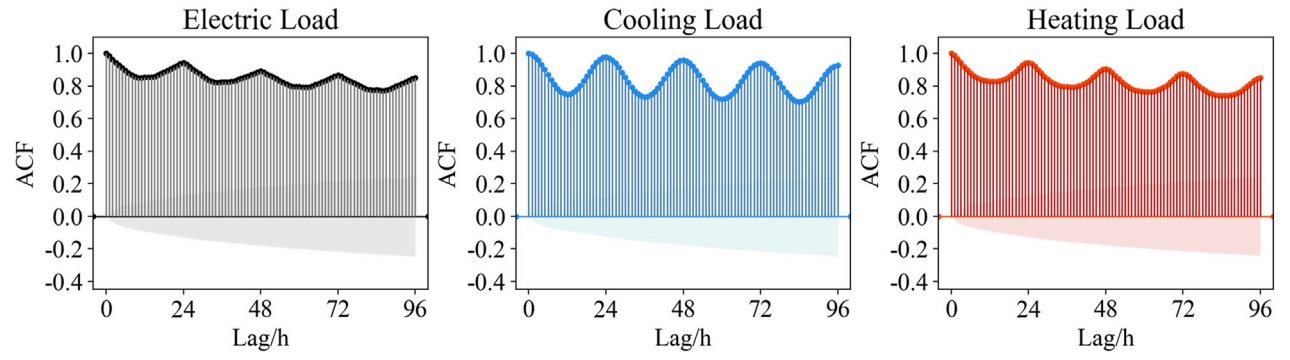

FIGURE 3
Annual multi-energy load autocorrelation coefficient.

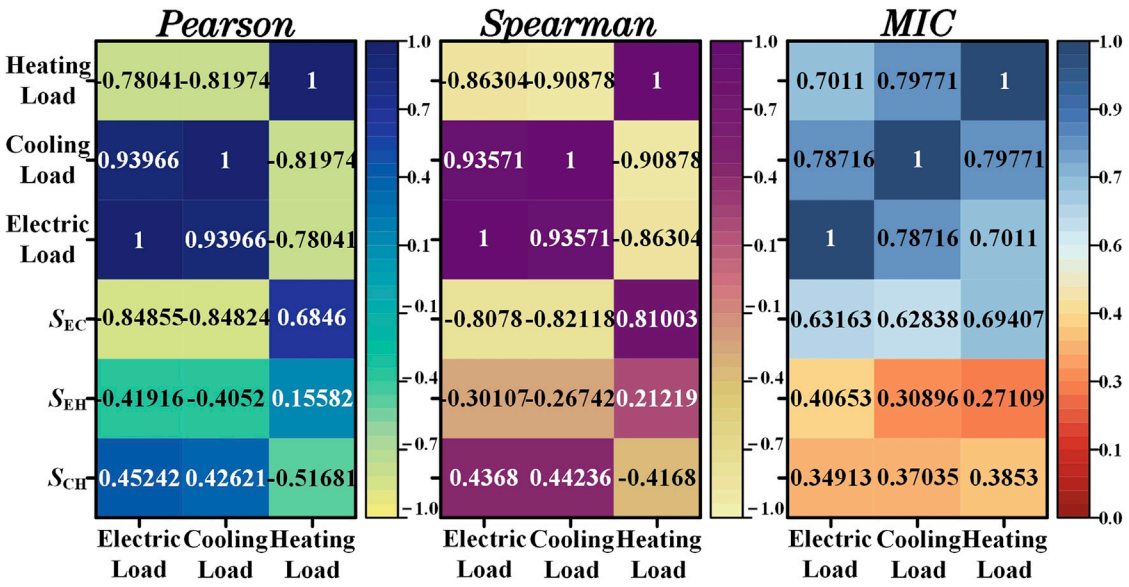

FIGURE 4
Correlation analysis results between coupling features and multi-energy loads.

explore the complex coupling characteristics among multi-energy loads from multiple dimensions. Based on this, considering various potential characteristics of multi-energy loads, an input feature set for the ultra-short-term forecasting model is constructed.

3.1 Multi-dimensional multi-energy load coupling characteristics mining based on the integration of multiple correlation analysis methods

The Spearman's rank correlation coefficient is a non-parametric rank statistic used to measure the strength of the monotonic relationship between two continuous variables. For the multi-energy load sequences A and B, its specific expression is as follows:

$$r = 1 - \frac{6\sum_{i=1}^{n} d_i^2}{n(n^2-1)} \tag{3}$$

In the formula, d_i represents the difference in ranks between the i-th sample a_i and b_i in the multi-energy load sequences A and B. The value of r ranges from [-1,1], and a larger value of $|r|$ indicates a stronger correlation.

MIC measures the linear and nonlinear relationships between two continuous variables by calculating the maximum normalized mutual information under different grid divisions. MIC exhibits robustness to samples containing noise. The mutual information calculation formula between multi-energy load sequences A and B is as follows:

$$I(a;b) = \int p(a,b)\log_2\frac{p(a,b)}{p(a)p(b)}dadb \tag{4}$$

In the formula, $P(a,b)$ represents the joint probability density of multi-energy load sequences A and B, while $P(a)$ and $P(b)$ respectively denote the marginal probability densities of multi-energy load sequences A and B.

A grid is partitioned on the two-dimensional variable (A, B) formed by the multi-energy load sequences A and B, and the mutual information size between each grid is calculated. MIC is the maximum value of the normalized mutual information under different grid partitioning methods. Its calculation formula is as follows:

$$\delta = \max_{m*n<D} \frac{I(a;b)}{\log_2 \min(m,n)} \tag{5}$$

In the formula, m and n respectively represent the number of intervals partitioned in the direction of multi-energy load sequences A and B, D is the total number of grids, typically taken as $D = n^{0.6}$. The value of δ ranges from [0, 1], and a larger value of δ indicates a stronger correlation.

For a multi-energy load sequence of length n, the Pearson correlation coefficient quantifies the linear relationship between multi-energy loads by calculating covariance and standard deviation. The Spearman rank correlation coefficient quantifies simple monotonic nonlinear relationships between multi-energy loads by calculating the correlation coefficients between the ranks of variables. Meanwhile, MIC effectively measures the strength of both linear and nonlinear relationships between multi-energy loads by calculating the maximum normalized mutual information under different grid partitioning methods. Pearson, Spearman, and MIC correlation analysis methods can quantify different types of linear and nonlinear relationships between multi-energy loads. Therefore, combining these three correlation analysis methods to construct multi-energy load coupling features can measure the potential coupling relationships between loads from different dimensions, thereby fully exploring the multi-dimensional coupling characteristics between multi-energy loads.

Therefore, for the forecast moment t, the historical multi-energy load sequences from t-1 to t-s are analyzed using Pearson, Spearman,

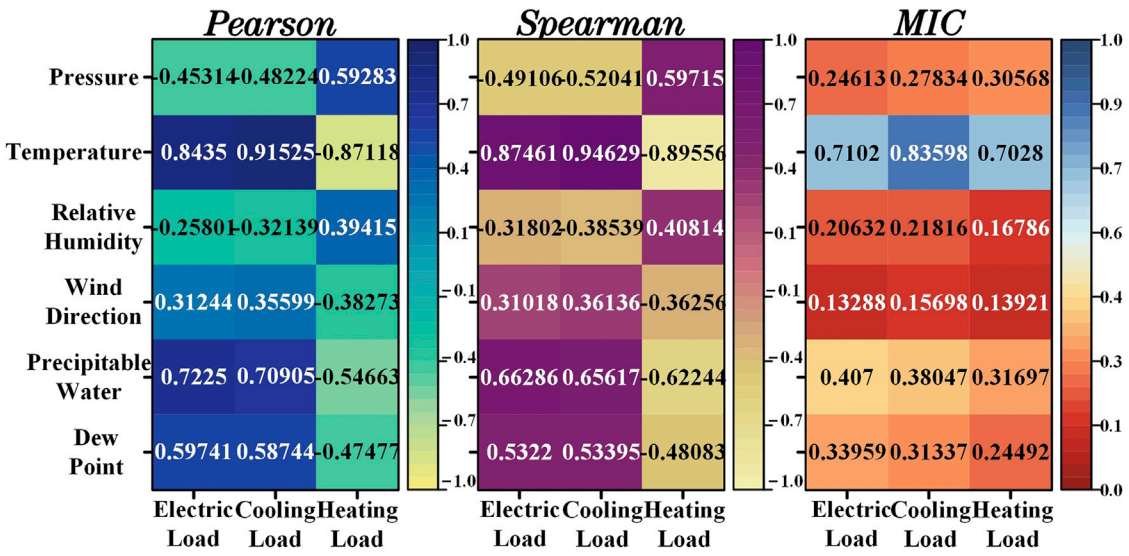

FIGURE 5
Correlation analysis results between meteorological features and multi-energy loads.

TABLE 1 Input feature set for each seasonal forecasting model.

Feature types	Features
Coupling features	S_{EC}, S_{EH}, S_{CH} at time t
Meteorological features	Dew Point, Precipitable Water, Temperature, Pressure at time t
Holiday features	Use 0 to represent weekdays, use 1 to represent weekends, and use 2 to represent important holidays
Time features	Month, Day, Week, Hour
Historical load features	The multi-energy load at time t-1
	The multi-energy load at time t-2
	The multi-energy load at time t-3
	The multi-energy load at time t-24
	The multi-energy load at time t-48
	The multi-energy load at time t-72

and MIC correlation methods. The obtained correlation coefficients are then averaged in a weighted manner according to formula (6), thus obtaining the IES multi-energy load coupling features at time t. These features reflect the coupling characteristics of the historical multi-energy load sequences from t-1 to t-s across different dimensions, effectively quantifying the potential complex coupling relationships between historical IES multi-energy load sequences.

$$S = \frac{|\rho| + |r| + \delta}{3} \tag{6}$$

To analyze the feasibility of the proposed method for mining multi-dimensional multi-energy load coupling characteristics based on the integration of multiple correlation analysis methods, let's consider constructing multi-energy load coupling features using historical multi-energy load data from the month preceding the forecast moment as an example. The constructed multi-energy load coupling features and the load sequences are then analyzed using Pearson, Spearman, and MIC correlation methods, with the results shown in Figure 4. In the figure, S_{EC}, S_{EH}, and S_{CH} represent the coupling features of the electric load with the cooling load, the electric load with the heating load, and the cooling load with the heating load, respectively.

To avoid the one-sidedness of strong correlation features obtained by using a single correlation analysis method, when the constructed coupling feature and a certain type of load in the multi-energy loads simultaneously satisfy formula (7) (Guo et al., 2022; Li et al., 2022; Chen et al., 2023), then that coupling feature is considered a strong correlation feature for the multi-energy loads.

$$\begin{cases} |\rho| > 0.4 \\ |r| > 0.3 \\ \delta > 0.3 \end{cases} \tag{7}$$

As can be seen from Figure 4, when constructing multi-energy load coupling features using the historical load data from the month preceding the forecast moment, S_{EC}, S_{EH}, and S_{CH} can all be considered strong correlation features for multi-energy load prediction. This fully demonstrates the effectiveness of the proposed method for constructing multi-energy load coupling features. Furthermore, analyzing the correlation between multi-energy loads using different correlation analysis methods further indicates the strong coupling relationships within IES multi-energy loads. Using the constructed coupling features as input features for the multi-energy load forecasting model can achieve multi-dimensional mining of potential complex coupling characteristics in the construction phase of input feature set, improving the prediction accuracy of ultra-short-term multi-energy load forecasting.

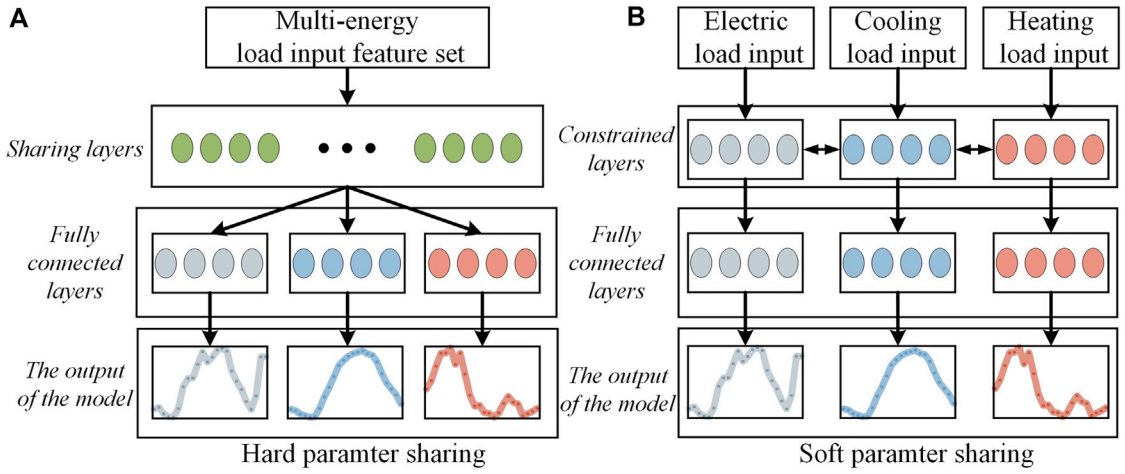

FIGURE 6
The structure of **(A)** hard parameter sharing mechanism and **(B)** soft parameter sharing mechanism.

3.2 Construction of multi-energy load input feature set

To avoid the negative impact of seasonal differences in load variation trends on the accuracy of multi-energy load forecasting,the historical data of loads for the entire year are divided according to different seasons. This seasonal historical data, along with other features, are collectively used as inputs for the model to build ultra-short-term forecasting models for multi-energy loads in different seasons. To fully explore the potential complex coupling relationships between multi-energy loads from multiple dimensions, the constructed coupling features S_{EC}, S_{EH}, and S_{CH} are subjected to correlation analysis with the multi-energy loads. If the correlation analysis results with a certain type of load satisfy Eq. 7, they are considered as input features for the multi-energy load forecasting model. Simultaneously, as meteorological factors can influence users' energy consumption habits, meteorological features whose correlation analysis results with a certain type of load in the multi-energy loads satisfy Eq. 7 are selected as strongly correlated meteorological features for the multi-energy load. The correlation analysis results between atmospheric pressure, temperature, relative humidity, wind direction, precipitable water, dew point, and multi-energy loads are presented in Figure 5.

From Figure 5, it is evident that atmospheric pressure, temperature, precipitable water, and dew point can be considered as strongly correlated meteorological features for multi-energy load forecasting. Additionally holidays information reflecting users' energy usage behaviors, along with time features, are also included as input features for the forecasting model. Since this study uses the IES of Arizona State University in the United States for forecasting research, it adopts the U.S. federal holidays (including New Year's Day, Christmas, Thanksgiving, etc.) as the selection rule for holidays in the dataset. To fully consider the temporal correlation of multi-energy loads, historical load data from moments t-1 to t-3, as well as t-24, t-48, and t-72, are used as historical load features in the forecasting model, thus ensuring thorough mining of the temporal correlations of multi-energy loads.

In summary, for the multi-energy loads at the predicted time t, the input feature set for the ultra-short-term forecasting model of multi-energy loads, considering the potential characteristics of multi-energy loads, is presented as shown in Table 1.

4 Construction of multi-energy load forecasting

This paper develops an ultra-short-term multi-energy load forecasting model based on MTL-TCN-HU. Firstly, an MTL model based on a hard parameter sharing mechanism is employed in the model construction phase to fully mine the coupling characteristics of multi-energy loads. Secondly, the sharing layer based on TCN effectively extracts potential temporal association information from the input features and captures long-term dependencies in the input sequence. Lastly, the use of a homoscedastic uncertainty-based MTL loss function weight optimization method enables the automatic tuning of loss function weight parameters. This approach not only reduces the time cost of model parameter tuning but also further enhances the prediction accuracy of the MTL forecasting model.

4.1 MTL forecasting model based on hard parameter sharing mechanism

For the prediction of IES multi-energy loads, the approach of constructing separate load forecasting models for different types of loads does not deeply explore the potential complex coupling characteristics among various energy loads in the model construction phase. MTL enhances the predictive performance of the model by extracting coupling information from different forecasting tasks. This approach not only facilitates parallel learning of multiple forecasting tasks but also aims to improve the accuracy of the forecasting model and enhance its generalization ability (Zhang and Yang, 2022).

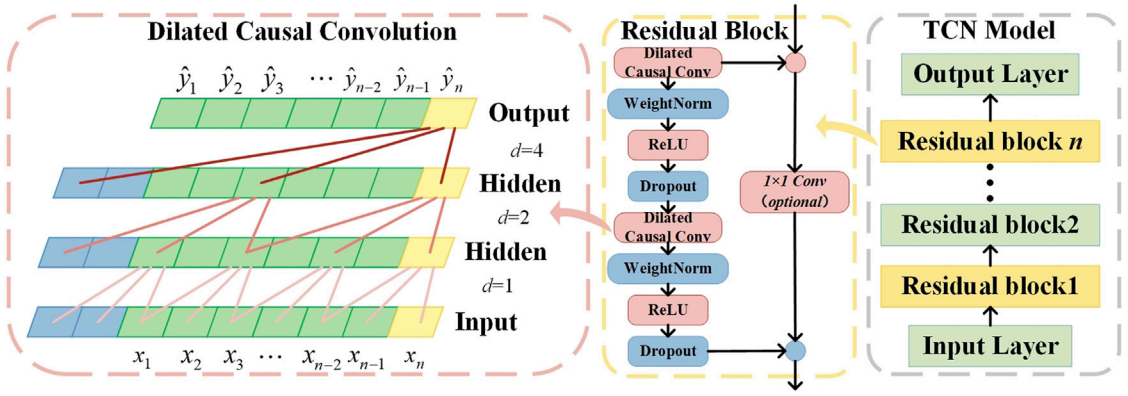

FIGURE 7
The structure of TCN model.

MTL is primarily divided into hard parameter sharing and soft parameter sharing mechanisms based on the type of sharing mechanism. Figure 6 presents the structural diagrams for both soft and hard parameter sharing mechanisms. In the soft parameter sharing mechanism, the models and parameters for each forecasting task are distinct and regularization is required before sharing potential coupling information for each sub-task. The hard parameter sharing mechanism involves different forecasting tasks learning the potential coupling information between sub-tasks directly through the same sharing layer, thereby facilitating joint training of multiple tasks. Given that the soft parameter sharing mechanism has more relaxed constraints compared to the hard parameter sharing mechanism, it is more suitable for multi-energy load forecasting tasks where the sub-tasks have weaker interrelations. In contrast, the hard parameter sharing mechanism, with its common sharing layer for each sub-task, is apt for multi-energy load forecasting tasks where sub-tasks are closely related. Since the IES multi-energy loads under study exhibit strong coupling, this paper opts for a hard parameter sharing mechanism-based MTL method to construct an ultra-short-term multi-energy load forecasting model.

4.2 Construction of MTL sharing layer based on TCN

TCN is a convolutional neural network that integrates Dilated Causal Convolution (DCC) and Residual Connection (RC). DCC includes dilated convolution and causal convolution. In TCN, causal convolution ensures that the forecasting results at earlier time steps do not involve future data information, preventing future information leakage, and making the convolutional network suitable for multi-energy load forecasting models. The dilated convolution in TCN addresses the issue of the limited receptive field in traditional convolution. Introducing a dilation coefficient d, increases the model's receptive field while reducing the computational load, thus enabling the learning of global information. Assuming the model's input sequence is $X = \{x_1, x_2, \cdots, x_n\}$ and the filter is $F = \{f_1, f_2, \cdots, f_{k-1}\}$, the calculation formula for the dilated convolution is as follows:

$$\boldsymbol{F}(\boldsymbol{t}) = \sum_{i=0}^{k-1} \boldsymbol{f}_i \cdot \boldsymbol{x}_{t-d \cdot i} \tag{8}$$

In the formula, k represents the filter size, d is the dilation factor, and $F(t)$ is the result of the dilated convolution for the t-th element in the input sequence.

The residual block of TCN consists of a DCC layer, WeightNorm layer, ReLu activation function, and Dropout layer. The residual block effectively addresses the issue of gradient vanishing in deep network structures and enhances the model's generalization ability. Its core idea is to form an RC by combining the direct mapping of the input with the output of the last layer of the residual module, thereby improving the model's stability and facilitating the construction of deep networks. An example of a DCC structure with $d = 1, 2, 4$, and $k = 3$ is shown in Figure 7. In the figure, $\hat{Y} = \{\hat{y}_1, \hat{y}_2, \cdots, \hat{y}_n\}$ represents the output of the DCC.

From Figure 7, it is evident that TCN can capture long-term dependencies in the input time series while avoiding the problem of gradient vanishing. It possesses a strong capability to mine the potential temporal association information in the input data. Therefore, this paper opts to use TCN to construct the sharing layer of the MTL model.

4.3 Method for optimizing the weight of MTL loss functions based on homoscedastic uncertainty

MTL models achieve parallel learning of multiple sub-tasks through the sharing mechanisms of the model. The loss function of MTL is as shown in Eq. 9:

$$\boldsymbol{L} = \boldsymbol{\lambda}_1 \boldsymbol{L}_1 + \boldsymbol{\lambda}_2 \boldsymbol{L}_2 + \cdots \boldsymbol{\lambda}_r \boldsymbol{L}_r \tag{9}$$

In the formula, L represents the loss function of MTL, r is the number of sub-tasks in MTL, $\{L_1, L_2, \cdots, L_r\}$ denotes the loss functions of each sub-task in the MTL model and $\{\lambda_1, \lambda_2, \cdots, \lambda_r\}$ represents the weights of the loss functions for each sub-task.

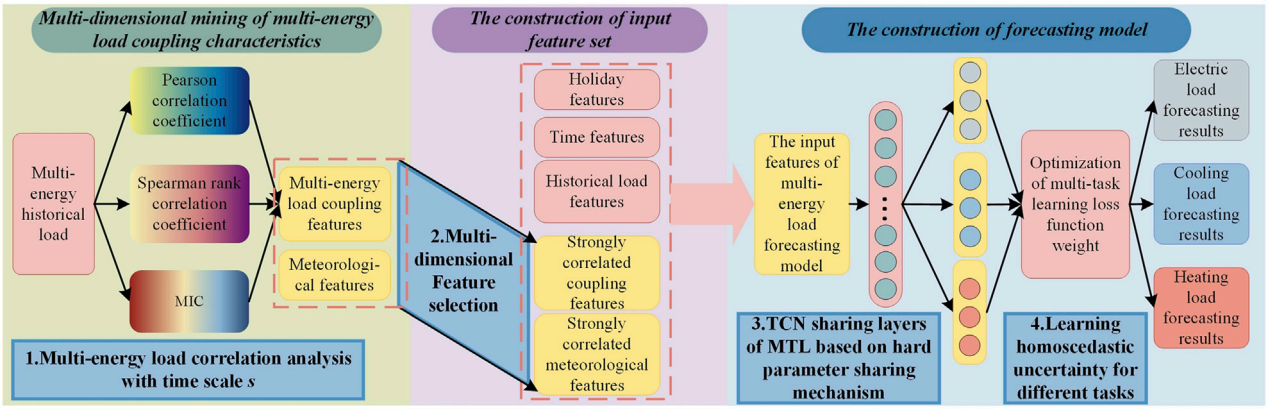

FIGURE 8
The structure of ultra-short-term multi-energy load forecasting model.

According to formula (9), the weights of the loss functions for sub-tasks can affect the training effectiveness of the MTL model. Scientific and rational allocation of weights to the sub-task loss functions can further enhance the performance of the multi-task learning model. Therefore, this paper adopts a homoscedastic uncertainty-based optimization method for the multi-task learning loss function.

Homoscedastic uncertainty refers to the type of uncertainty that is independent of input data. This uncertainty remains constant across all inputs and varies between different tasks, reflecting the inherent learning difficulties of each sub-task in MTL. The optimization method for MTL loss functions based on homoscedastic uncertainty is achieved by learning the homoscedastic uncertainty among different sub-tasks, thereby enabling the automatic tuning of loss function weights. Assuming an MTL model with three sub-tasks has parameters W, and the noise parameters for different tasks are σ_1, σ_2, and σ_3, the total loss function $L(W, \sigma_1, \sigma_2, \sigma_3)$ of MTL can be represented as follows:

$$L(W, \sigma_1, \sigma_2, \sigma_3) = \frac{1}{2\sigma_1^2} L_1(W) + \frac{1}{2\sigma_2^2} L_2(W) + \frac{1}{2\sigma_3^2} L_3(W) + \ln(\sigma_1 \sigma_2 \sigma_3) \quad (10)$$

In the formula, $\sigma_i^2 (i = 1 \cdots 3)$ represents the observation noise, which is used to measure the homoscedastic uncertainty of each forecasting task, and $\ln(\sigma_1 \sigma_2 \sigma_3)$ is the regularization term that restricts the model from learning in the direction of unbounded increase of σ_i^2.

4.4 The overall framework of the forecasting model

The framework of the ultra-short-term multi-energy load forecasting model is shown in Figure 8. It mainly comprises the following three parts:

(1) Multi-dimensional multi-energy load coupling characteristics mining: Selecting the length s of the historical load sequence for correlation analysis, calculating the Pearson correlation coefficient, Spearman correlation coefficient, and MIC between the multi-energy load historical sequences from t-1 to t-s, and using formula (6) to integrate various correlation analysis methods to construct the multi-energy load coupling features at time t. This approach quantifies the complex coupling relationships between multi-energy loads and enables in-depth multi-dimensional mining of potential couplings in the construction phase of the multi-energy load input feature set.

(2) Construction of multi-energy load input feature set: Dividing the annual historical data of multi-energy loads by different seasons, to construct ultra-short-term forecasting models for multi-energy loads in various seasons. Various correlation analysis methods are used to select strongly correlated features from coupling and meteorological features, which are then combined with holiday features, time features, and historical load features to form the multi-energy load input feature set. This method comprehensively considers various factors affecting the energy usage habits of IES users and deeply mines the potential characteristics of multi-energy loads.

(3) Construction of multi-energy load forecasting model: An ultra-short-term multi-energy load forecasting model based on MTL-TCN-HU for IES is constructed. The MTL model based on a hard parameter sharing mechanism extracts coupling information between sub-tasks through the sharing layer, enabling in-depth mining of potential complex coupling characteristics among multi-energy loads during the model construction phase. TCN, using DCC and RC, extracts potential temporal association information from input features and captures long-term dependencies in the input time series. The HU multi-task learning loss function weight optimization method, by learning the homoscedastic uncertainty of different tasks, achieves automatic tuning of loss function weight parameters, thereby saving time in model tuning and further enhancing the accuracy of multi-energy load forecasting.

TABLE 2 Experimental input features and model parameters for selecting load sequence length used in constructing coupling features.

Sequence length	1 week	2 weeks	3 weeks	1 month	2 months	3 months
Type of input feature	According to Table 1, the feature set of multi-energy load input was constructed					
Coupling features	S_{CH}	S_{EH}, S_{CH}	S_{EC}, S_{EH}, S_{CH}	S_{EC}, S_{EH}, S_{CH}	S_{EH}, S_{CH}	S_{EH}, S_{CH}
Model	MTL-TCN-HU					
Hyper-parameter of the model	Batch size	128				
	Number of filters	32				
	Size of the filter	3				
	Dropout	0.1				
	Dilation factor	1,2,4,8,16				
	Number of iterations	200				
	Learning rate	0.001				
	Number of residual blocks	1				
	Number of fully-connected units	16				
	Number of fully-connected layers	1				

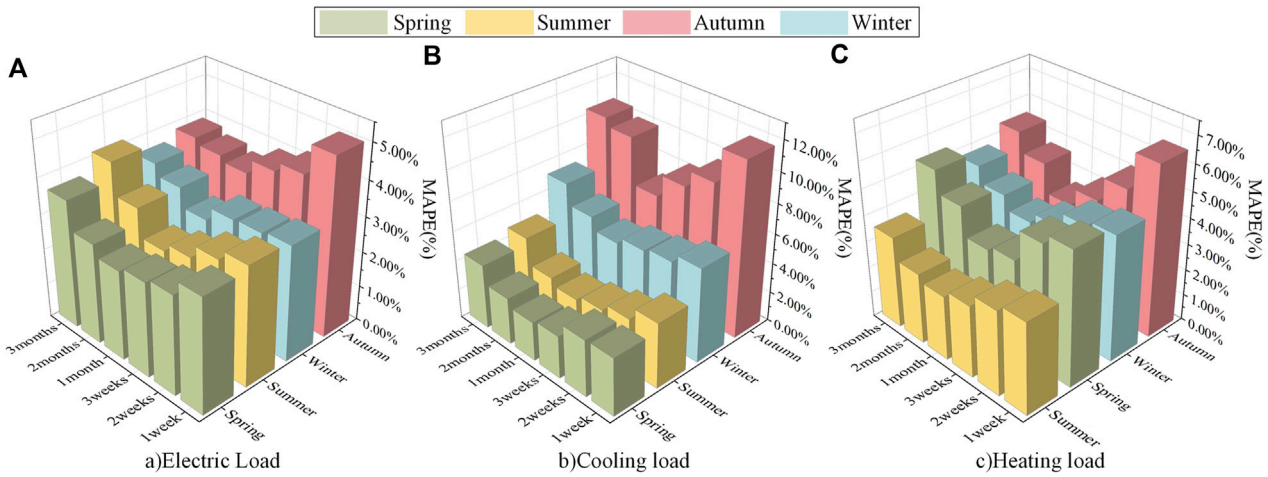

FIGURE 9
Comparative MAPE chart for the experiment on selecting load sequence length used in constructing coupling features.

5 Case study

5.1 Data source and evaluation index

This paper selects historical data on electric, cooling, and heating loads from the comprehensive energy system of Arizona State University's Tempe campus, spanning from 1 March 2018, to 28 February 2019, for training the ultra-short-term forecasting model. The multi-energy load data are divided according to different seasons, and then each season's load data are split into training, validation, and test sets in the ratio of 8:1:1. The meteorological data are sourced from the National Solar Radiation Database of the United States.

This paper selects Mean Absolute Error (MAE), Mean Absolute Percentage Error (MAPE), Root Mean Square Error (RMSE), and Weighted Mean Absolute Percentage Error (WMAPE) as the forecasting error evaluation metrics, and their calculation formulas are as follows:

$$MAE = \frac{1}{n}\sum_{i=1}^{n}|y_i - \hat{y}_i| \tag{11}$$

$$MAPE = \frac{1}{n}\sum_{i=1}^{n}\left|\frac{y_i - \hat{y}_i}{y_i}\right| \times 100\% \tag{12}$$

$$RMSE = \sqrt{\frac{1}{n}\sum_{i=1}^{n}(y_i - \hat{y}_i)^2} \tag{13}$$

$$WMAPE = \theta_E MAPE_E + \theta_C MAPE_C + \theta_H MAPE_H \tag{14}$$

TABLE 3 Ablation experiment input features and model parameters.

Model number	Model0	Model1	Model2	Model3	Model4
Type of input feature	According to the results of correlation analysis, the strong correlation features of each load were selected. The coupling features of multiple loads are not considered.	According to the results of correlation analysis, the strong correlation features of each load were selected. The feature types are the same as Table 1.		Same as Table 2	
Forecasting model	LSTM		TCN	MTL-TCN	MTL-TCN-HU
Hyper-parameter of the model	Number of hidden layers	2	Same as Table 2	The loss function weight of the multitask learning model is 0.4, 0.4, 0.2. The other model hyperparameters are the same as Table 2	Same as Table 2. use HU to adjust loss function weight automatically
	Number of hidden layer units	32			
	The other model hyperparameters are the same as Table 2				

In the formula, y_i represents the actual load value, $\hat{y}_i$ denotes the forecasting load value, and n indicates the number of samples. θ_E, θ_C, and θ_H represent the prediction error weights for electric, cooling, and heating loads, respectively. They are set to 0.4, 0.4, and 0.2 (Wu et al., 2022), respectively. $MAPE_E$, $MAPE_C$, and $MAPE_H$ represent the MAPE for electric, cooling, and heating loads. Lower values of MAE, MAPE, and RMSE imply higher accuracy of the model's predictions.

5.2 Experimental platform and data preprocessing

The construction and training of the forecasting model are based on the Pytorch deep learning framework. The hardware configuration of the experimental platform includes an Intel(R) Core (TM) i7-12700H CPU, with acceleration provided by an NVIDIA GeForce RTX3060 Laptop GPU.

The 3 σ rule is used to filter out anomalies in the historical multi-energy load data, treating these anomalies as missing data, which are then filled using cubic spline interpolation. To eliminate the impact of input feature dimensions on the forecasting model, max-min normalization is applied to ensure that the input data range is between [0,1].

TABLE 4 Comparison of prediction errors in electric load forecasting results of different models.

Season model		Spring	Summer	Autumn	Winter
Model0	MAPE	4.014%	3.952%	5.140%	4.570%
	RMSE	1142.542	1449.89	1190.07	945.592
	MAE	950.643	1202.68	1030.03	820.507
Model1	MAPE	3.490%	3.435%	4.506%	3.872%
	RMSE	1035.59	1331.17	1072.03	818.780
	MAE	857.682	1042.37	896.725	694.082
Model2	MAPE	3.272%	3.094%	4.152%	3.434%
	RMSE	1013.40	1199.50	1007.00	759.829
	MAE	778.181	947.146	867.486	620.585
Model3	MAPE	2.890%	2.751%	3.760%	2.998%
	RMSE	882.260	1069.68	926.778	696.124
	MAE	687.800	877.501	746.664	533.179
Model4	MAPE	**2.543%**	**2.475%**	**3.521%**	**2.749%**
	RMSE	**787.7014**	**963.5569**	**877.0918**	**650.5965**
	MAE	**607.003**	**782.2664**	**714.5630**	**494.145**

5.3 Comparative analysis of forecasting methods

5.3.1 Selection of load sequence length for constructing coupling features

The method of mining multi-dimensional multi-energy load coupling characteristics based on the integration of multiple correlation analysis methods involves analyzing the correlation of the historical multi-energy load sequences from t-1 to t-s to construct the coupling features of multi-energy loads at time t. Therefore, it is crucial to appropriately select the length of the multi-energy load historical sequence used for constructing coupling features. If a shorter load sequence is chosen to construct coupling features, the randomness and volatility of the multi-energy loads may result in significant changes in coupling features between adjacent time steps. The strong fluctuations in the sequence prevent the coupling feature sequence from fully reflecting the potential coupling relationships among multi-energy loads. On the other hand, if a longer load sequence is chosen to construct coupling features, the changes in coupling features between adjacent time steps are relatively small. Consequently, the sequence of coupling features for multi-energy loads exhibits a more gradual change trend, also failing to capture the potential coupling relationships. To select an appropriate length for the multi-energy load sequence to construct coupling features, experiments are conducted using historical load data from 29 November 2017, to 28 February 2019.

Different lengths of multi-energy load sequences, specifically 1 week, 2 weeks, 3 weeks, 1 month (31 days), 2 months (61 days),

TABLE 5 Comparison of prediction errors in cooling load forecasting results of different models.

Season model		Spring	Summer	Autumn	Winter
Model0	MAPE	5.963%	6.087%	13.278%	7.970%
	RMSE	689.712	1106.31	553.570	283.108
	MAE	576.056	939.455	485.663	236.215
Model1	MAPE	3.801%	4.224%	11.337%	7.114%
	RMSE	449.771	669.713	506.408	261.672
	MAE	347.180	568.314	434.940	213.595
Model2	MAPE	3.378%	3.716%	9.942%	6.585%
	RMSE	388.592	634.589	488.733	223.868
	MAE	304.066	515.800	417.852	187.785
Model3	MAPE	2.895%	3.068%	8.001%	5.621%
	RMSE	333.329	519.307	413.671	217.304
	MAE	252.306	422.211	340.658	170.274
Model4	MAPE	**2.637%**	**2.583%**	**6.843%**	**4.987%**
	RMSE	**287.6244**	**448.215**	**360.527**	**184.807**
	MAE	**226.131**	**359.368**	**294.187**	**146.175**

TABLE 6 Comparison of prediction errors in heating load forecasting results of different models.

Season model		Spring	Summer	Autumn	Winter
Model0	MAPE	6.854%	4.403%	8.587%	7.461%
	RMSE	0.442	0.266	0.907	0.878
	MAE	0.388	0.220	0.812	0.766
Model1	MAPE	5.446%	3.917%	6.134%	5.969%
	RMSE	0.363	0.239	0.699	0.726
	MAE	0.306	0.197	0.589	0.620
Model2	MAPE	4.428%	3.339%	5.263%	5.206%
	RMSE	0.307	0.214	0.596	0.654
	MAE	0.250	0.169	0.490	0.545
Model3	MAPE	3.703%	2.904%	4.419%	4.216%
	RMSE	0.276	0.196	0.532	0.544
	MAE	0.209	0.146	0.414	0.442
Model4	MAPE	**3.387%**	**2.480%**	**3.629%**	**3.536%**
	RMSE	**0.248**	**0.178**	**0.446**	**0.520**
	MAE	**0.190**	**0.127**	**0.342**	**0.402**

and 3 months (92 days), are selected to construct coupling features as input features for the forecasting model. The ultra-short-term prediction accuracy of multi-energy loads is compared and analyzed using the MAPE. To facilitate the construction of multi-energy load coupling features and to ensure that the selected sequence lengths effectively reflect the potential coupling relationships of multi-energy loads 1 month, 2 months, and 3 months prior to the predicted moment, the load sequence lengths for 1 month, 2 months, and 3 months were defined as the number of days with the highest occurrence frequency for 1 month, 2 months, and 3 months, respectively, in the dataset from March 2018 to February 2019, which are 31 days, 61 days, and 92 days, respectively. The related parameters of the experiment are presented in Table 2. To comprehensively assess the prediction effects of different sequence lengths, data from 1 week in different seasonal test sets are used for ultra-short-term multi-energy load forecasting, with specific experimental results shown in Figure 9.

As Figure 9 indicates, when multi-energy load coupling features are constructed using historical sequence lengths of 1 week, 2 weeks, 3 weeks, and 1 month, the prediction error of the models for each season decreases with the increase in the length of the load sequence used for constructing coupling features. However, when using 1 month, 2 months, and 3 months as the historical sequence lengths, the prediction error increases with the length of the load sequence. The MAPE, RMSE, and MAE of the forecasting models are the lowest when a 1-month multi-energy historical load sequence is used for constructing coupling features. This suggests that coupling features constructed with a 1-month load sequence effectively quantify the complex coupling relationships between multi-energy loads. Therefore, the historical multi-energy load sequence length of 1 month prior to the forecast moment is chosen for constructing the coupling features at the forecast moment, making it the input feature of the model, thereby better achieving in-depth multi-dimensional mining of the potential coupling characteristics of multi-energy loads.

5.3.2 Ablation experiment

To validate the effectiveness of each component of the proposed forecasting method, comparative experiments are designed as shown in Table 3. Models 0, 1, and 2 all use the approach of constructing separate forecasting models for different types of loads and select strongly correlated features as input features for each load forecasting model. Among these, Model 0 does not include coupling features as input for the forecasting model, and Model 1 does not use the TCN model for multi-energy load prediction. Models 3 and 4 both employ MTL models for prediction. Model 3 does not use the homoscedastic uncertainty-based MTL loss function weight optimization method, and its loss function weights are manually set (Wu et al., 2022). Model 4 represents the multi-energy load forecasting method proposed in this paper. Data from 1 week in different seasonal test sets are used for ultra-short-term multi-energy load forecasting, and the forecasting results of each model for different seasons are evaluated using MAPE, RMSE, and MAE. The forecasting results of each model are presented in Tables 4–6.

From Tables 4–6, it is evident that Model 4 achieves the highest ultra-short-term prediction accuracy for multi-energy loads across different seasons. Additionally, there is a gradual increase in the ultra-short-term prediction accuracy of multi-energy loads from Model 0 to Model 4. Compared to Model 0, Model 1 shows a decrease in the MAPE of electric load by 12.330%–15.273%, cooling load by 10.740%–36.257%, and heating load by 11.106%–28.566% across different seasons. This demonstrates that the proposed

10.3389/fenrg.2024.1373345

TABLE 7 Comparison of experimental input features and model parameters between different forecasting models.

Forecasting model	SVR		RF	CNN-BiGRU		MTL-BiGRU	MTL-TCN-HU
Type of input feature	According to the results of correlation analysis, the strong correlation features of each load were selected. The feature types are the same as in Table 1.					Same as Table 2	
Hyper-parameter of the model	Kernel function	RBF	Number of trees	200	Number of convolutional layers	2	The loss function weight of the multitask learning model is 0.4, 0.4, 0.2. The other model hyperparameters are the same as Model0 in Table 2	Same as Table 2. use HU to adjust loss function weight automatically
	Penalty coefficient	10	Maximum depth	10	Number of filters	16		
	Gamma	0.01			Size of the filter	3		

method for mining multi-dimensional multi-energy load coupling characteristics based on the integration of multiple correlation analyses can effectively quantify the complex coupling relationships between multi-energy loads. It achieves in-depth mining of potential coupling characteristics from various dimensions in the construction phase of the input feature set, significantly enhancing the prediction accuracy of multi-energy loads. Compared to Model 1, Model 2 shows a reduction in the MAPE of electric load by 6.246%–11.313%, cooling load by 7.436%–12.305%, and heating load by 12.783%–18.693%. This indicates that the TCN model effectively extracts potential temporal association information from input features and captures long-term dependencies in the input time series, thereby improving the accuracy of multi-energy load prediction. Compared to Model 2, Model 3 shows a reduction in the MAPE of electric load by 9.44%–12.696%, cooling load by 14.298%–19.523%, and heating load by 13.028%–19.016%. This suggests that the MTL model based on a hard shared parameter mechanism can fully mine the potential complex coupling characteristics between multi-energy loads during the model construction phase, further reducing the prediction error of the model. Compared to Model 3, Model 4 shows a decrease in the MAPE of electric load by 6.356%–12.007%, cooling load by 8.912%–15.808%, and heating load by 8.533%–17.877%. This indicates that the homoscedastic uncertainty-based MTL loss function weight optimization method can automatically tune the loss function weights by learning the homoscedastic uncertainty of different tasks, further enhancing the model's prediction performance. Overall, each component of the proposed multi-energy load forecasting method significantly improves the prediction accuracy of multi-energy loads.

5.3.3 Comparative analysis of different prediction models

To further evaluate the prediction accuracy of the proposed model, this study compares its performance with commonly used models in existing research, including Random Forest (RF), Support Vector Regression (SVR), CNN-BiGRU, and MTL-BiGRU forecasting models. The input features and related parameters for the experiment are shown in Table 7.

Data from 1 week in different seasonal test sets are used for ultra-short-term multi-energy load forecasting. The MAPE prediction errors of each forecasting model in different seasons are shown in Figure 10, and the prediction result curves for each model in different seasons are presented in Figure 11. The WMAPE prediction errors of each forecasting model in different seasons are shown in Table 8. Tables 8; Figures 10, 11 reveal that in different seasons, the prediction curves of the SVR and RF models have a poor fit with the actual values. The CNN-BiGRU model can extract latent feature information and temporal associations reflecting load changes (Niu et al., 2022), but it fails to fully extract the long-term dependencies of input features and does not adequately mine the potential complex coupling characteristics between multi-energy loads, resulting in lower prediction accuracy. The MTL-BiGRU model also cannot learn long-term dependencies of input features and does not employ a scientific MTL loss function weight optimization method, leading to poor prediction performance. In contrast, the proposed forecasting model not only uses TCN to thoroughly mine potential temporal associations and long-term

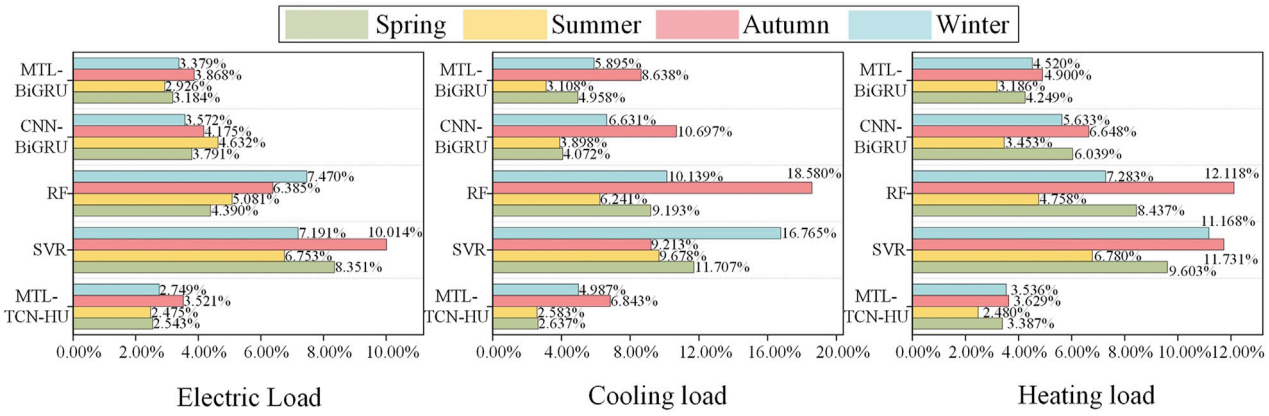

FIGURE 10
MAPE comparison chart of different forecasting models.

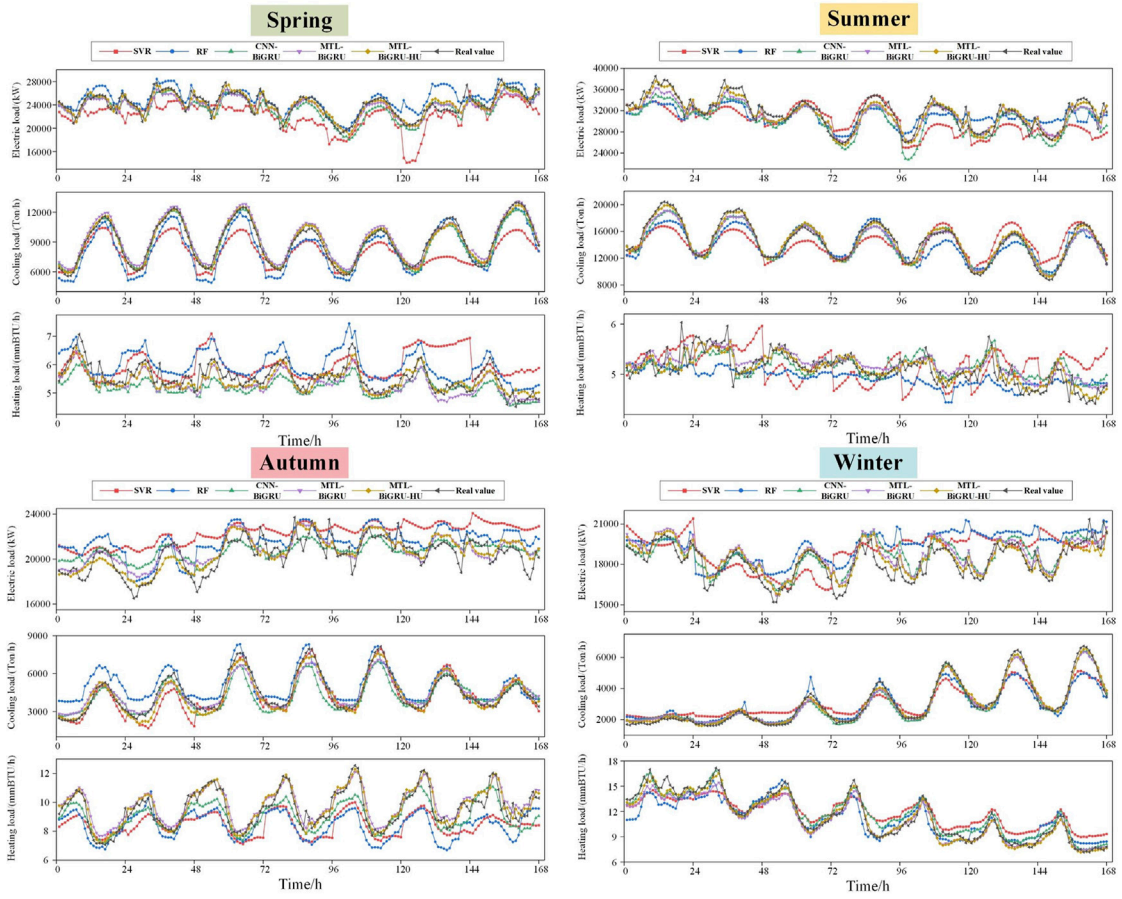

FIGURE 11
Forecast results of each model in different seasons.

dependencies in the input data but also explores the potential coupling characteristics between multi-energy loads through an MTL model based on a hard parameter sharing mechanism. Additionally, it achieves scientific parameter optimization through a homoscedastic uncertainty-based MTL loss function weight optimization method. Therefore, the proposed forecasting model exhibits the highest prediction accuracy across different seasons.

TABLE 8 Comparison of WMAPE for different forecasting models.

Season model		Spring (%)	Summer (%)	Autumn (%)	Winter (%)
MTL-BiGRU	WMAPE	4.107	3.051	5.982	4.614
CNN-BiGRU	WMAPE	4.353	4.103	7.278	5.208
RF	WMAPE	7.121	5.480	12.410	8.500
SVR	WMAPE	9.944	7.928	10.037	11.816
MTL-TCN-HU	WMAPE	**2.749**	**2.519**	**4.871**	**3.802**

6 Conclusion

This paper proposes an ultra-short-term multi-energy load forecasting method based on multi-dimensional coupling characteristic mining and multi-task learning. Firstly, a multi-dimensional multi-energy load coupling characteristics mining method, integrating multiple correlation analysis methods, is employed to construct load coupling features. This effectively quantifies the complex coupling relationships between IES multi-energy loads and thoroughly mines potential coupling characteristics from various dimensions in the input feature set construction phase. Case studies show that using this method in different seasons results in a decrease in the MAPE of electric load by 12.330%–15.273%, cooling load by 10.740%–36.257%, and heating load by 11.106%–28.566%.

Then, an ultra-short-term multi-energy load forecasting model based on MTL and TCN is constructed, which mines the potential complex coupling characteristics between multi-energy loads during the model construction phase. The TCN is used to mine potential temporal association information from input features and capture long-term dependencies in the input time series. Case studies indicate that employing MTL reduces the MAPE of electric load by 9.44%–12.696%, cooling load by 14.298%–19.523%, and heating load by 13.028%–19.016% in different seasons. Using TCN results in a decrease in the MAPE of electric load by 6.246%–11.313%, cooling load by 7.436%–12.305%, and heating load by 12.783%–18.693%.

Moreover, a homoscedastic uncertainty-based MTL loss function weight optimization method is adopted to automatically tune the loss function weight parameters, saving time in model tuning while further enhancing the model's prediction performance. Case studies show that employing this method results in a decrease in the MAPE of electric load by 6.356%–12.007%, cooling load by 8.912%–15.808%, and heating load by 8.533%–17.877% in different seasons.

Finally, a comparative analysis of different forecasting models is conducted using the comprehensive energy system of Arizona State University in the United States as a case study. The results indicate that the proposed forecasting method has higher prediction accuracy compared to other methods.

Data availability statement

Publicly available datasets were analyzed in this study. This data can be found here: https://nsrdb.nrel.gov/data-viewer, http://cm.asu.edu/.

Author contributions

NH: Conceptualization, Data curation, Formal Analysis, Supervision, Writing–original draft. XW: Data curation, Investigation, Methodology, Validation, Writing–original draft. HaW: Methodology, Project administration, Software, Writing–review and editing. HeW: Resources, Software, Visualization, Writing–review and editing.

Funding

The author(s) declare that financial support was received for the research, authorship, and/or publication of this article. This research was funded by China's National Key Development Plan, grant number 2022YFB2404002.

Conflict of interest

The authors declare that the research was conducted in the absence of any commercial or financial relationships that could be construed as a potential conflict of interest.

Publisher's note

All claims expressed in this article are solely those of the authors and do not necessarily represent those of their affiliated organizations, or those of the publisher, the editors and the reviewers. Any product that may be evaluated in this article, or claim that may be made by its manufacturer, is not guaranteed or endorsed by the publisher.

References

Alabi, T. M., Aghimien, E. I., Agbajor, F. D., Yang, Z., Lu, L., Adeoye, A. R., et al. (2022). A review on the integrated optimization techniques and machine learning approaches for modeling, prediction, and decision making on integrated energy systems. *Renew. Energy* 194, 822–849. doi:10.1016/j.renene.2022.05.123

Chen, H., Zhu, M., Hu, X., Wang, J., Sun, Y., and Yang, J. (2023). Research on short-term load forecasting of new-type power system based on GCN-LSTM considering multiple influencing factors. *Energy Rep.* 9, 1022–1031. doi:10.1016/j.egyr.2023.05.048

Ge, L., Li, Y., Yan, J., Wang, Y., and Zhang, N. (2021). Short-term load prediction of integrated energy system with wavelet neural network model based on improved Particle Swarm optimization and Chaos optimization Algorithm. *J. Mod. Power Syst. Clean. Energy* 9 (6), 1490–1499. doi:10.35833/mpce.2020.000647

Guo, Y., Li, Y., Qiao, X., Zhang, Z., Zhou, W., Mei, Y., et al. (2022). BiLSTM multitask learning-based combined load forecasting considering the loads coupling relationship for multienergy system. *IEEE Trans. Smart Grid* 13 (5), 3481–3492. doi:10.1109/tsg.2022.3173964

Li, C., Li, G., Wang, K., and Han, B. (2022). A multi-energy load forecasting method based on parallel architecture CNN-GRU and transfer learning for data deficient integrated energy systems. *Energy* 259, 124967. doi:10.1016/j.energy.2022.124967

Liu, H., Tang, Y., Pu, Y., Mei, F., and Sidorov, D. (2022). Short-term load forecasting of multi-energy in integrated energy system based on multivariate phase Space reconstruction and support vector regression mode. *Elect. Power Syst. Res.* 210, 108066. doi:10.1016/j.epsr.2022.108066

Liu, Y., Li, Y., Li, G., Lin, Y., Wang, R., and Fan, Y. (2023). Review of multiple load forecasting method for integrated energy system. *Front.Energy Res.* 11. doi:10.3389/fenrg.2023.1296800

Niu, D., Yu, M., Sun, L., Gao, T., and Wang, K. (2022). Short-term multi-energy load forecasting for integrated energy systems based on CNN-BiGRU optimized by attention mechanism. *Appl. Energy* 313, 118801. doi:10.1016/j.apenergy.2022.118801

Tan, M., Liao, C., Chen, J., Cao, Y., Wang, R., and Su, Y. (2023). A multi-task learning method for multi-energy load forecasting based on synthesis correlation analysis and load participation factor. *Appl. Energy* 343, 121177. doi:10.1016/j.apenergy.2023.121177

Wang, C., Wang, Y., Ding, Z., Zheng, T., Hu, J., and Zhang, K. (2022). A transformer-based method of multienergy load forecasting in integrated energy system. *IEEE Trans. Smart Grid* 13 (4), 2703–2714. doi:10.1109/tsg.2022.3166600

Wang, S., Wu, K., Zhao, Q., Wang, S., Feng, L., Zheng, Z., et al. (2021). Multienergy load forecasting for regional integrated energy systems considering multienergy coupling of variation characteristic curves. *Front.Energy Res.* 9. doi:10.3389/fenrg.2021.635234

Wu, K., Gu, J., Meng, L., Wen, H., and Ma, J. (2022). An explainable framework for load forecasting of a regional integrated energy system based on coupled features and multi-task learning. *Prot. Control Mod. Power Syst.* 7 (1), 24. doi:10.1186/s41601-022-00245-y

Yan, Q., Lu, Z., Liu, H., He, X., Zhang, X., and Guo, J. (2024). Short-term prediction of integrated energy load aggregation using a bi-directional simple recurrent unit network with feature-temporal attention mechanism ensemble learning model. *Appl. Energy* 355, 122159. doi:10.1016/j.apenergy.2023.122159

Zhang, S., Chen, R., Cao, J., and Tan, J. (2023). A CNN and LSTM-based multi-task learning architecture for short and medium-term electricity load forecasting. *Elect. Power Syst. Res.* 222, 109507. doi:10.1016/j.epsr.2023.109507

Zhang, Y., and Yang, Q. (2022). A survey on multi-task learning. *IEEE Trans. Know. Data Eng.* 34 (12), 5586–5609. doi:10.1109/tkde.2021.3070203

Zheng, Q., Zheng, J., Mei, F., Gao, A., Zhang, X., and Xie, Y. (2023). TCN-GAT multivariate load forecasting model based on SHAP value selection strategy in integrated energy system. *Front. Energy Res.* 11. doi:10.3389/fenrg.2023.1208502

Zhu, J., Dong, H., Zheng, W., Li, S., Huang, Y., and Xi, L. (2022). Review and prospect of data-driven techniques for load forecasting in integrated energy systems. *Appl. Energy* 321, 119269. doi:10.1016/j.apenergy.2022.119269

Zhuang, W., Fan, J., Xia, M., and Zhu, K. (2023). A multi-scale spatial-temporal graph neural network-based method of multienergy load forecasting in integrated energy system. *IEEE Trans. Smart Grid*, 1. doi:10.1109/tsg.2023.3315750

frontiers | Frontiers in Energy Research

TYPE Original Research
PUBLISHED 23 May 2024
DOI 10.3389/fenrg.2024.1378067

OPEN ACCESS

EDITED BY
Rufeng Zhang,
Northeast Electric Power University, China

REVIEWED BY
Dongliang Xiao,
South China University of Technology, China
Jintao Han,
Opal-Rt Technologies, Canada
Fei Zhang,
Southeast University, China
R. Kiranmayi,
Jawaharlal Nehru Technological University Anantapur, India

*CORRESPONDENCE
Yi Zhong,
yizhong20232023@163.com

RECEIVED 29 January 2024
ACCEPTED 23 April 2024
PUBLISHED 23 May 2024

CITATION
Yin Y, Zhong Y, He Y, Li G, Li Z and Pan S (2024), Online modeling method for composite load model including EVs and battery storage based on measurement data.
Front. Energy Res. 12:1378067.
doi: 10.3389/fenrg.2024.1378067

Online modeling method for composite load model including EVs and battery storage based on measurement data

Yanhe Yin[1], Yi Zhong[1]*, Yi He[1], Guohao Li[1], Zhuohuan Li[2] and Shixian Pan[2]

[1]Zhongshan Power Supply Bureau of Guangdong Power Grid Co., Ltd., Zhongshan, Guangdong, China, [2]Digital Grid Research Institute, China Southern Power Grid, Guangzhou, Guangdong, China

Load models have a significant influence on power system simulation. However, current load modeling approaches can hardly satisfy the diversity and time-varying characteristics of loads [including electric vehicles (EVs) and battery storage] in terms of model accuracy and computing efficiency. An online modeling method for composite load models based on measurement information is proposed in this paper. Firstly, the dominant factors in load model output are analyzed based on the active subspace of parameter space. Then the clustering algorithm is applied to cluster the large number of underlying loads based on the characteristics of load daily output curves. Finally, the underlying loads are equivalently aggregated from the low voltage levels to the high voltage levels to construct the composite load model. Simulation results obtained based on PSCAD/EMTDC demonstrate that the load model constructed by the proposed approach can accurately reflect the actual load characteristics of a power system.

KEYWORDS

load modeling, measurement data, composite load model, equivalent aggregation, electric vehicles (EVs), battery storage

1 Introduction

Simulation analysis is an important means to study the steady state and transient characteristics of the power system, which is carried out through the establishment of the power system source, network, and load simulation model, taking the initial trend results as a starting point, and using numerical methods to iteratively solve for each state response quantity of the system so as to carry out the inversion of accidents or fault preview (Zhang et al., 2022). Therefore, the accuracy of the simulation model is an important guarantee for the reliability of the simulation analysis results (Zhang et al., 2021; Qian et al., 2023).

However, the models used in the current simulation analysis have not been able to accurately reflect the real characteristics of complex power systems, and it is difficult to accurately invert and reproduce the real faults occurring in some actual power grids by means of simulation (Zhang et al., 2017). Among them, the accuracy of the load model is doubtful, which is an important reason affecting the simulation results, and the diversity of the power system network structure and the expansion of the scale of new load access further increase the difficulty of load modeling (Xu et al., 2023). Compared with traditional vehicles, new energy vehicles have the advantages of low pollution, high

energy efficiency, and low operating costs. The operation benefit of order charging is verified by constructing order charging on the power grid side.

Currently, a large number of studies have been carried out for load modeling. The comprehensive load model composed of static constant impedance, constant current, constant power components, and dynamic induction motor components is widely used in power system simulation due to its good generalization ability (Overbye, 1994; Zalok and Eduful, 2013; Camille et al., 2021). On this basis, related studies have proposed model construction and parameter identification methods, which can be mainly categorized into two types based on constituent components (Chen et al., 1997; Zhang et al., 2023) and measurement information (Ma et al., 2008; Zhang et al., 2020a). Component-based methods divide the loads according to types and then characterize different types of loads with typical static loads or motor loads, but the statistical work efficiency is low and the dynamic changes of loads are ignored. The method based on measurement information regards all kinds of loads as a black box model and makes the simulation response output consistent with the measured response by identifying its parameters so as to reflect the real dynamic characteristics of the system and be used for power system simulation analysis, but the complex structure of the load model and its high-dimensional nonlinear parameter space lead to computational speed and efficiency that are still low. The vigorous development of electric vehicles is of the utmost significance to adjust the optimal design of industrial structures and promote the sustainable development of industry. In view of the problems existing in the development of electric vehicles at the present stage, the state focuses on the research and development of charging problems for electric vehicles and carries out research on the safety and power supply of charging equipment at the present stage so as to form a safe and effective charging safety system.

In order to reduce the complexity of load modeling, literature (Zhang et al., 2021b) proposes a comprehensive load simplification model based on the dominant parameter selection, which transforms the induction motor model into a second-order equation of state; literature (Han et al., 2022) proposes a fast calculation method for the parameters of the comprehensive load model based on the sensitivity analysis; and some researchers use intelligent optimization algorithms (Wang et al., 2018; Hu et al., 2022) or machine learning algorithms (Cui et al., 2019; Bu et al., 2020; Hu et al., 2023) for the overall identification of the model parameters. These studies aim to reduce the parameter space of the load model or increase the parameter calculation rate to simplify the complexity of load modeling. However, the electrical quantity measurement is usually targeted at nodes of higher voltage levels, and it is difficult to obtain all the underlying load information of the lower voltage levels of the distribution network, and its iterative or training process often requires sample labels, i.e., the exact values of the parameters to be measured corresponding to the observed quantities, which are usually difficult to know in advance in practical applications especially in the transmission system (Tsekouras et al., 2007; Zhang et al., 2020b; Zhang et al., 2020c; Zhang et al., 2021c).

Aiming at the above problems, this paper proposes an online modeling method for integrated load models based on measurement information. On the basis of analyzing and identifying the dominant factors of the external characteristics of the comprehensive load model, the bottom load is clustered according to the load curve, and the comprehensive load equivalent aggregation model is constructed by aggregating equivalently from the low voltage level to the high voltage level step by step. The proposed method is simulated, analyzed, and validated based on the PSCAD/EMPDC platform.

2 Identification of dominant factors for external characterization of integrated load models

2.1 Activation subspace of the parameter space

The integrated load model generally refers to a load model composed of induction motors and static loads in a certain proportion. Obviously, the external characteristics of the integrated load model are related to the composition ratio of each type of load and the parameters of its internal model, and it is necessary to analyze and identify the dominant factors affecting the external characteristics of the integrated load model before carrying out the integrated load equivalent modeling. This section identifies the dominant factors in the characteristics of the integrated load model based on the activation subspace approach. The activation subspace is a low-dimensional linear subspace of the parameter space that allows for a global assessment of the sensitivity of the output variables with respect to the parameters.

Consider a parameterization function that maps the parameters of the system to the scalar output of interest, where C denotes the canonical set of parameter values:

$$C = \int_{\chi} \left(\nabla_{\bar{\theta}} g(\bar{\theta})\right)\left(\nabla_{\bar{\theta}} g(\bar{\theta})\right)^{T} \rho(\bar{\theta}) d\bar{\theta} \tag{1}$$

$$\bar{\theta} \in \chi = \{x \in \mathrm{i}^{m} \mid -1 \le x_i \le 1, i = 1, K, m\} \tag{2}$$

In Eq. 3, the joint probability function of the parameters satisfies:

$$\int_{\chi} \rho(\bar{\theta}) d\bar{\theta} = 1 \tag{3}$$

For any smooth function, in the reduced-dimensional case, the matrix C is called the average generalized derivative, which weights the input values according to the density. A single normalization parameter is a random variable with values in the range [−1, 1] that represents a parameter in the original model. The matrix C is the average of the gradient and its own outer product.

From Eq. 1, the elements of C are the average of the product of partial derivatives, which can be regarded as the parameter sensitivity:

$$C_{ij} = \int_{\chi} \left(\frac{\partial g}{\partial \bar{\theta}_i}\right)\left(\frac{\partial g}{\partial \bar{\theta}_j}\right) \rho d\bar{\theta}, i, j = 1, K, m \tag{4}$$

In (4), C_{ij} is the (i,j) element of C and m denotes the number of parameters. Since the matrix C is symmetric, the spectral eigen-decomposition can be performed, as shown in Eq. 5.

$$C = W\Lambda W^T \tag{5}$$

where W is a column of the orthogonal matrix, is the standard orthogonal eigenvector of C, $\Lambda = \mathrm{diag}([\lambda_1, K, \lambda_m])$ and $\lambda_1 \geq K \geq \lambda_m$. λ_1, λ_m are the largest and smallest eigenvalues of the matrix C.

It can be seen that the eigenvalue of matrix C is the mean square directional derivative in the direction of the corresponding eigenvector. If the eigenvalue is very small, it indicates insensitivity in the direction of the corresponding eigenvector. On the contrary, the larger the eigenvalue, the more significant the change in the direction of the corresponding eigenvector.

The eigenvalues can be separated from the eigenvectors based on the magnitude of the eigenvalues, shown in Eq. 6:

$$\Lambda = \begin{bmatrix} \Lambda_1 & 0 \\ 0 & \Lambda_2 \end{bmatrix}, W = \begin{bmatrix} W_1 & 0 \\ 0 & W_2 \end{bmatrix} \tag{6}$$

where Λ_1 and W_1 contains the first n larger eigenvalues and corresponding eigenvectors, Λ_2 and W_2 contains the other m-n smaller eigenvalues. To determine this separation, the spectral gap between the nth and $(n + 1)^{th}$ eigenvalues can be found on the log-log plot in order of magnitude. It is worth noting that the presence of a spectral gap directly indicates the presence of an activation subspace.

The integrated load model in our study includes parameters like Distributed Network Reactance, Inductive Motor Active Power Proportion, Load Ratio, Stator Reactance, Constant Reactance Load Proportion, Direct Current Side Capacitor, and Photovoltaic Output Equivalent Reactance. These parameters significantly shape the external characteristics of the load model and should be compared with the model discussed in this paper.

Since W is orthogonal, any parameter vector can be expressed as:

$$\theta = WW^T\theta = W_1W_1^T\theta + W_2W_2^T\theta \tag{7}$$

In Eq. 7, θ represents the parameter vector in the model.

Then any parameter vector-sensitive output is shown in Eq. 8:

$$g(\theta) = W_1\theta_1 + W_2\theta_2 \tag{8}$$

From the definitions of W_1 and W_2, it can be seen that a small perturbation has little effect on the value of On the contrary, small perturbations can significantly change Based on this property, the range of W_1 is defined as the activation subspace, and the range of W_2 is defined as the corresponding inactivation subspace of the model. The above subspaces describe the sensitivity of the model outputs to parameter changes.

Distributed Network Reactance affects the load's impedance, while Inductive Motor Active Power Proportion and Load Ratio determine the proportion of induction motors and static loads, influencing dynamic behavior. Stator Reactance and Constant Reactance Load Proportion impact impedance and power consumption, and the Direct Current Side Capacitor and Photovoltaic Output Equivalent Reactance represent auxiliary component influences. By analyzing these parameters alongside our model, the sensitivity can be extended to understand their impact on external behavior. This comparative approach enhances our understanding and informs system design. Incorporating these parameters allows for a comprehensive comparison, identifying key factors influencing the load model's behavior.

2.2 Key parameters identification

The integrated load model is accessed in the WSCC-9 node system and tested based on the Python-PSASP simulation platform. The test parameters are the internal parameters of the static load or the induction motor load and their composition ratios, and all parameters are uniformly distributed by default. The voltage, active power, and reactive power of the observation point are used as the response output trajectory, and the change of the internal parameters of the integrated load model under the observation point will cause the change of the response trajectory. The degree of change of the dynamic trajectory after the parameter change is used as the sensitivity index, and a sample contains the numerical sensitivity of all the parameters at a randomized point in the parameter space (which is a composite index after the average of the voltage and the power), and the set of the sample set is 2,000.

Among the 2,000 samples generated at the end of the simulation, noisy samples due to transient instability (the model is prone to instability under certain parameter compositions) are sifted out by analysis, and for the column vectors of sensitivity in the samples the corresponding variational generalized function matrices are computed and the mean value C is found in Eq. 9:

$$C = \frac{1}{2000}\sum_{i}^{2000}\left(\nabla_{\bar{\theta}}g(\bar{\theta})\right)\left(\nabla_{\bar{\theta}}g(\bar{\theta})\right)^T \tag{9}$$

In this paper, the method for separating eigenvalues from eigenvectors is called the "Variational Generalized Function Matrices Approach."

The eigendecomposition of C is performed to calculate the eigenvalues and eigenvectors of C. If C can be understood as a variational generalized function matrix with the parameter space as the independent variable, the parameter's own sensitivity, and the correlation between the parameters as the dependent variable, then there must be a parameter space that has a high sensitivity distribution under a certain subspace after some kind of linear transformation. The diagonal array of eigenvalues generated by the eigendecomposition of C is understood as a new function space transformed by the coordinates of these eigenvectors. These eigenvectors after the coordinate transformation of the new function space, these eigenvectors for the function space of the coordinate axes, the function space of the function value, are also the correlation coefficient and the parameter's own sensitivity to the size of the numerical value, except that the corresponding independent variable is no longer a parameter value of physical significance but the parameter space after the coordinate transformation of some kind of independent variable. Obviously, the 1st eigenvalue of C is much larger than the other eigenvalues, i.e., in the transformed function space, the change of the function value in the direction represented by the first eigenvector is much larger than that in the direction pointed by the other eigenvectors; therefore, the activation subspace of C is a 1-dimensional space, and the value of eigenvectors corresponding to the 1st eigenvalue multiplied by the parameter vectors is the coordinate of the parameter vectors on this space. The distribution of eigenvectors corresponding to the first eigenvalue is shown in Figure 1. The analysis reveals that the composition ratios of static load and induction motor exhibit larger sensitivity weights compared to the internal parameters of the model. Thus, the primary factors influencing the external characteristics of the integrated composite

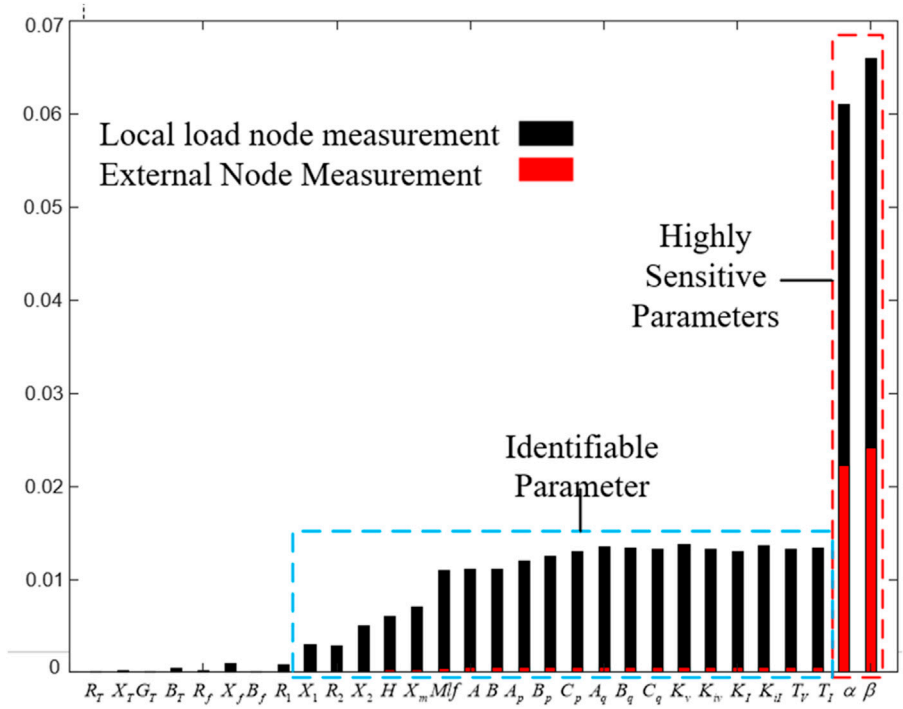

FIGURE 1
Sensitivity weights corresponding to different parameters.

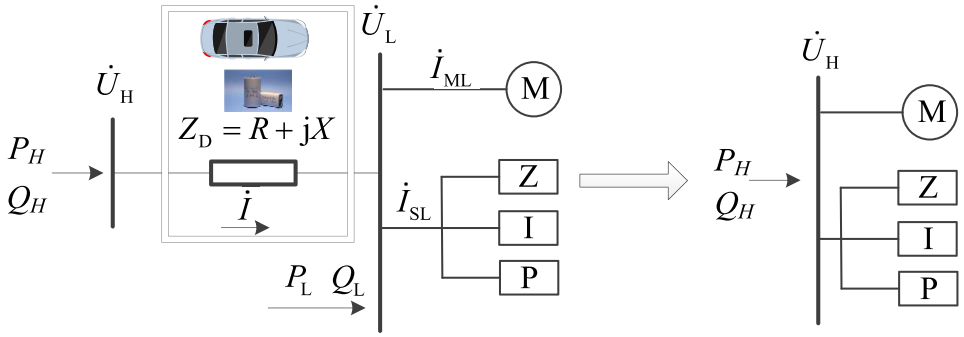

FIGURE 2
Diagram of converting load model to high-voltage side considering the EVs and fuel betteries.

model are identified as the composition ratios of static load and induction motor load. Diagram of converting load model to highvoltage side considering the EVs and fuel betteries is shown in Figure 2 and structure of the simulation system is depicted in Figure 3.

2.3 Exploration of advanced modeling techniques

In this section, we delve into the integration of advanced modeling techniques to augment the accuracy and robustness of integrated load models. Specifically, we adopt deep learning architectures, including deep neural networks (DNNs), recurrent neural networks (RNNs), and convolutional neural networks (CNNs), alongside data-driven parameter estimation techniques. Our choice of these methodologies is driven by their capacity to capture intricate nonlinear relationships within load dynamics and to accurately estimate model parameters based on historical operational data. By leveraging the capabilities of these advanced techniques, we aim to refine load modeling accuracy and contribute to the advancement of computational methodologies in this domain.

With the rapid advancement in computational methodologies, exploring advanced modeling techniques becomes imperative for

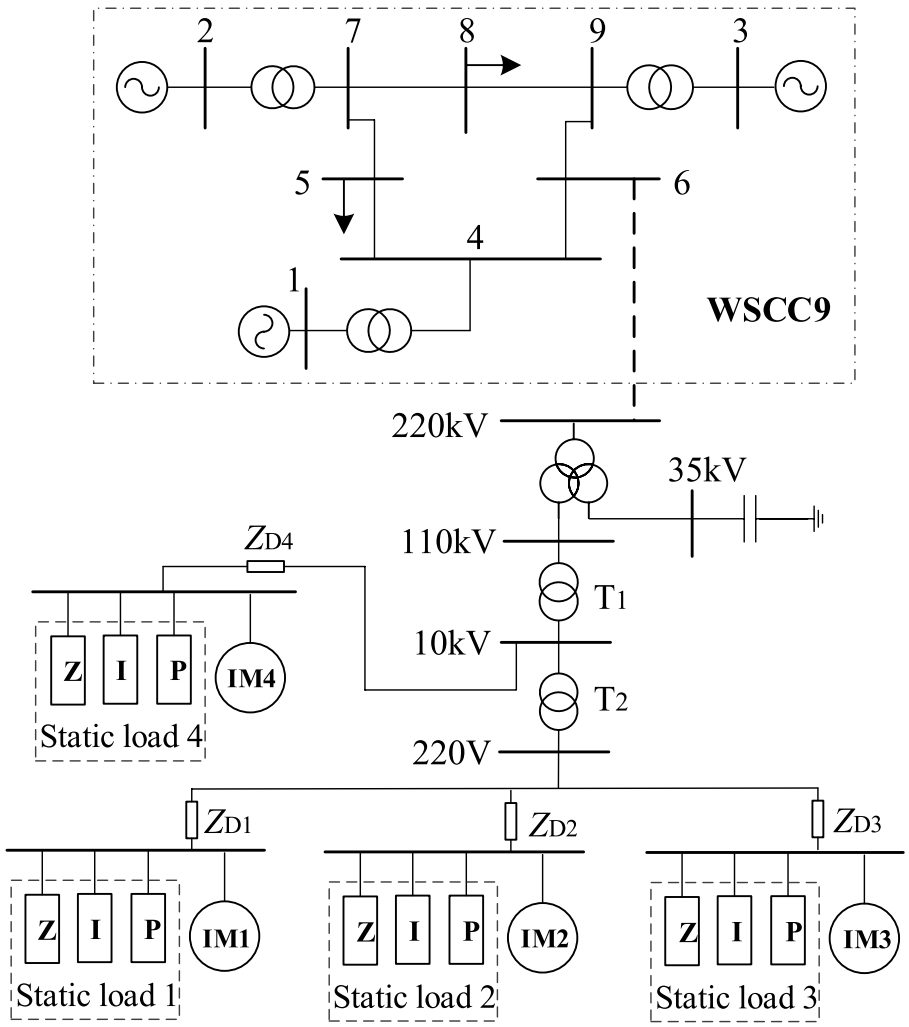

FIGURE 3
Structure of the simulation system.

refining the accuracy and robustness of integrated load models. One promising avenue is the incorporation of machine learning algorithms, particularly deep learning architectures, to capture intricate nonlinear relationships within the load dynamics. Deep neural networks (DNNs) offer unparalleled capabilities in handling complex data structures and learning high-dimensional mappings, which could significantly enhance the fidelity of load modeling.

2.3.1 Integration of deep learning models

To leverage the potential of deep learning, integrating DNNs within the integrated load modeling framework presents an intriguing prospect. By training DNNs on extensive datasets comprising diverse operational scenarios and load profiles, these models can learn intricate patterns and correlations, thus enabling more accurate predictions of load behavior. Moreover, recurrent neural networks (RNNs) and convolutional neural networks (CNNs) can capture temporal dependencies and spatial features, respectively, further enriching the modeling capabilities.

2.3.2 Data-driven parameter estimation

Another avenue for enhancing integrated load modeling is through data-driven parameter estimation techniques. By leveraging historical operational data and advanced optimization algorithms such as genetic algorithms or Bayesian inference methods, accurate estimation of model parameters can be achieved. These data-driven approaches offer a pragmatic means to calibrate model parameters in real-time, thereby ensuring adaptability to evolving system dynamics and load characteristics.

3 Online modeling method of integrated load based on measurement information

3.1 Load clustering based on output curves

Since the dominant factor affecting the external characteristics of the integrated load model is the load composition ratio, it can be assumed that users with similar daily load profiles have similar load

composition ratios. After clustering the loads using the clustering algorithm, the typical load composition ratio at the center of the clusters is used to characterize the composition of the loads in the class. The specific steps are as follows: 1) The load clustering process involves the following steps:

1) Processing the load data into daily load profiles and normalizing them based on Eq. 9 to create a library of daily load profiles:

$$x_i^{'} = \frac{x_i - \min(X)}{\max(X) - \min(X)} \tag{10}$$

In Eq. 10 x_i denotes the ith daily load profile sampling point data and X denotes all sampling point data of the daily load profile There are two common Copula families, the Archimedes Copula and the Elliptic Copula. The three most common types of Archimedes Copula functions are Gumbel Copula, Clayton Copula and Frank Copula, and elliptic Copula functions mainly include normal Copula and t-Copula. Because t-Copula is extremely time-consuming to fit multidimensional random variables and the Gumbel-Copula form is complex, only the remaining three Copula functions are considered in this paper.

2) Clustering the daily load profiles of a large number of users using the k-means algorithm (Zhang et al., 2020b), for a given N daily load profile data, k cluster centers are randomly generated, the Euclidean distances of all the load profiles to the k cluster centers are calculated, respectively, and the cluster centers with the closest distances are selected as the groups to which they belong.
3) Recalculate the center of clustering for each cluster, i.e., average all load profiles in the load cluster and use it as the center of clustering for the next iteration;
4) Repeat the above steps until the center of clustering does not change anymore or the clustering reaches the convergence condition, which here corresponds to the mathematical problem of minimizing the number of 2-parameters:

$$\min E = \sum_{i=1}^{k} \sum_{\boldsymbol{x} \in C_i} \left\| \boldsymbol{x} - \mu_i \right\|_2 \tag{11}$$

In Eq. 11, C_i denotes the ith user group, μ_i is the clustering center of user group C_i.

3.2 Load model equivalent aggregation

For loads within the same cluster, they are aggregated equivalently to characterize the underlying large number of user loads in terms of a typical load model.

3.2.1 Induction motor load aggregation

In the actual power system, not all induction motors under the same bus may be in a working state, and one motor may correspond to multiple working states. Therefore, there are uncertainties and time-varying characteristics of load aggregation, and the model established based on the traditional capacity weighting method is single and fixed, which cannot reflect the real-time state and time-varying characteristics of load. In this paper, the real-time measured power of nodes is used instead of capacity for weighted aggregation, and the weighting coefficients are calculated according to Eq. 11:

$$\sigma_i = \frac{P_i}{\sum_{i=1}^{n} P_i} \tag{12}$$

In Eq. 12, Pi denotes the real-time measured power of the ith single motor load node. Following the calculation of weight coefficients using real-time measured power, Eqs 13, 14 are utilized to compute the inertia time constant of the aggregation model and the conductance of each branch of the equivalent circuit:

$$T' = \sum_{i=1}^{n} \sigma_i T_i \tag{13}$$

$$\frac{1}{Z'} = \sum_{i=1}^{n} \sigma_i \frac{1}{Z_i} \tag{14}$$

where T_i and Z_i are the inertia time constant and branch impedance of the ith individual motor load, respectively, and the specific form of resistance and reactance of Zi varies depending on whether it is a stator branch, rotor branch, or excitation branch that is being expressed.

3.2.2 Static load aggregation

The static load is usually described by a polynomial consisting of constant impedance, constant current, and constant power as shown in Eq. 15:

$$\begin{cases} P = P_0 \left[a_p (U/U_0)^2 + b_p (U/U_0) + c_p \right] \\ Q = Q_0 \left[a_q (U/U_0)^2 + b_q (U/U_0) + c_q \right] \end{cases} \tag{15}$$

where P_0 and Q_0 denote the rated active and reactive power consumed by the load, U and U_0 denote the actual and rated voltage of the load bus, respectively, and a_p, b_p, c_p, and a_q, b_q, c_q denote the active and reactive power coefficients of each part of the model, respectively.

$$\begin{cases} a_p^{'} = \left(a_{p1} P_{01} + a_{p2} P_{02} + \cdots + a_{pn} P_{0n} \right) / P_0 \\ b_p^{'} = \left(b_{p1} P_{01} + b_{p2} P_{02} + \cdots + b_{pn} P_{0n} \right) / P_0 \\ c_p^{'} = 1 - a_p^{'} - b_p^{'} \end{cases} \tag{16}$$

In Eq. 16, P_0 denotes the rated active power consumed by the single static load, a_p, b_p, c_p denote the active power coefficients of each part of the model, and the subscripts 1-n denote the serial number of the single static load.

3.3 Load modeling step-by-step equivalence

When simulating and analyzing the power system, the load model is difficult to cover the lower voltage levels of the distribution network and is often connected to the higher voltage level buses, such as 110 kV or even 220 kV for simulation. Taking EVs and batteries into consideration, from the point of view of vehicle charging, to provide more electricity in the shortest time, the equipment needs to be optimized. The safety problems of charging on the side of the charging vehicle are mainly the adverse effects of the charging behavior of the electric vehicle on

the battery or battery management system, including BMS (Battery Management System) safety protection measures out of control, poor consistency of the BMS communication protocol, poor collision coefficient, and leakage. Therefore, reasonable planning and selection of charging facilities increase battery safety and the anti-collision safety factor. From the point of view of an electric vehicle power collision, not only the voltage will change, but also the shape will deform and lead to the battery. The electrolyte of the part is splashed. Therefore, after the load model is aggregated, it is necessary to equate it step by step from the low voltage level to the high voltage level, as shown in the figure below:

In the figure, and denote the bus voltage of HV side and LV side, respectively, PH and PL denote the active power flowing into HV side and LV side, respectively, QH and QL denote the reactive power flowing into HV side and LV side, respectively, and denote the current of HV side, the current flowing into the motor load and the static load, respectively, and ZD is the equivalent impedance. The increasing charging load and the discordance in structure design increase the operating pressure of the power grid, but compared with fuel vehicles, electric vehicles have energy savings and emission reductions to maximize the benefits.

3.3.1 Induction motor load equivalence

The following mathematical relationships of electrical quantities can be written as below:

$$\begin{cases} \dot{U}_{\mathrm{H}} = Z_{\mathrm{D}}\left(\dot{I}_{\mathrm{ML}} + \dot{I}_{\mathrm{SL}}\right) + \dot{U}_{\mathrm{L}} \\ \dot{I}_{\mathrm{SL}} = \dot{U}_{\mathrm{L}} Y_S = \dot{U}_{\mathrm{L}} (Y_Z + Y_I + Y_P) \\ \dot{I} = \dot{I}_{ML} + \dot{I}_{SL} \end{cases} \tag{17}$$

Where: Y_Z, Y_I and Y_P denote the conductance of the constant impedance, constant current and constant power parts of the static load, respectively.

$$\dot{U}_{\mathrm{L}} = \frac{1}{Z_{\mathrm{D}}(Y_Z + Y_I + Y_P) + 1}\left(\dot{U}_{\mathrm{H}} - Z_{\mathrm{D}}\dot{I}_{\mathrm{ML}}\right) \tag{18}$$

According to the third order model of induction motor, it can be expressed as:

$$\dot{U}_L = \dot{E}' + (R_{\mathrm{s}} + \mathrm{j}X')\dot{I}_{ML} \tag{19}$$

where: Rs is the stator resistance, and is the short circuit reactance when the slew rate is zero.

The joint solution of Eqs 17, 18 can be obtained:

$$\dot{U}_{\mathrm{H}} = \left[\frac{Z_{\mathrm{D}}}{Z_{\mathrm{D}}Y_{\mathrm{S}} + 1} + (R_{\mathrm{s}} + \mathrm{j}X')\right](Z_{\mathrm{D}}Y_{\mathrm{S}} + 1)\dot{I}_{\mathrm{ML}} + (Z_{\mathrm{D}}Y_{\mathrm{S}} + 1)\dot{E}' \tag{20}$$

Order is shown in Eq. 21:

$$\begin{cases} Z_D/(Z_D Y_S + 1) = \lambda_1 + j\lambda_2 \\ Z_D Y_S + 1 = \dot{\lambda}_3 \\ \dot{E}_H^{'} = \dot{\lambda}_3 \dot{E}' \\ \dot{I}_{MH} = \dot{\lambda}_3 \dot{I}_{ML} \\ R_{sH} + jX_H^{'} = (R_s + \lambda_1) + j(X' + \lambda_2) \end{cases} \tag{21}$$

Substituting Eq. 20 into Eq. 19 yields the high voltage side bus voltage shown in Eq. 22:

$$\dot{U}_H = \dot{E}'_H + \left(R_{sH} + jX_H^{'}\right)\dot{I}_{MH} \tag{22}$$

Substituting Eq. 20 into the low voltage side motor transient electromotive force equation Eq. 23:

$$\frac{d\dot{E}'_H}{dt} = j\omega_0(\omega - 1)\dot{E}'_H - \frac{1}{T'_{0H}}\left[\dot{E}'_H - j\left(X_H - X_H^{'}\right)\dot{I}_{MH}\right] \tag{23}$$

This gives the equivalent to the high voltage side induction motor excitation reactance, stator reactance, and rotor resistance and rotor reactance, as shown in Eq. 24:

$$\begin{cases} X_{mH} = X_m \\ X_{sH} = X_s + \lambda_2 \\ R_{rH} + jX_{rH} = R_r + jX_r \end{cases} \tag{24}$$

Substituting Eq. 20 into the low voltage side induction motor electromagnetic moment equation yields the equivalent motor electromagnetic moment on the high voltage side as shown in Eq. 25:

$$T_{EH} = \mathrm{Real}\left(\dot{E}'_H \dot{I}_H^{*}\right) = \lambda_3^2 T_E \tag{25}$$

Then the time constant of inertia of the induction motor load equaled to the high-voltage side is shown in Eq. 26:

$$H_H = \lambda_3^2 H \tag{26}$$

3.3.2 Static load equivalence

From the circuit relationship, it can be obtained Eq. 27:

$$\dot{I} = \dot{I}_{ML} + \dot{U}_L Y_S = \frac{1}{Z_D Y_S + 1}\dot{I}_{MH} + \left(\dot{U}_H - Z_D\dot{I}\right)Y_S \tag{27}$$

Simplification leads to Eq. 28:

$$\dot{I}_{MH} = (Z_D Y_S + 1)\left[\dot{I} - \left(\dot{U}_H - Z_D\dot{I}\right)Y_S\right] \tag{28}$$

Therefore, the static load conductance equated to the high-voltage side can be calculated by Eq. 29, where the proportion of constant impedance, constant current, and constant power components is determined according to the typical load composition in the clustering.

$$Y_H = Y_S(Z_D Y_S + 1) - Z_D Y_S(Z_D Y_S + 2)\frac{P - jQ}{U_H^2} \tag{29}$$

4 Case study

Based on the WSCC-9 node system in PSCAD/EMTDC, the example system is built, and a distribution network containing integrated load models of low voltage levels is accessed at node 6, and each integrated load model characterizes a class of customer loads. The specific parameters of the load model and the example system are shown in the Tables 1-4.

The method of this paper and the traditional overall measurement and discrimination method are used to construct the integrated load model of the high-voltage side, in which the method of this paper aggregates the loads of each voltage level of the low-voltage side and equates them step by step to the nodes of the 110 kV buses, and the overall measurement and discrimination method is based on the

TABLE 1 Parameters of the generalized SLM.

Parameter name	Parameter symbols
Distributed Network Reactance	X_{D}
Inductive Motor Active Power Proportion	P_{MP}
Load Ratio	K_L
Stator Reactance	X_s
Constant Reactance Load Proportion	K_Z
Direct Current Side Capacitor	C
Photovoltaic Output Equivalent Reactance	X_{PV}

TABLE 2 Model parameters of the induction motor load.

	R_s	X_s	X_m	R_r	X_r	H
IM1	0.023	0.126	3.39	0.0136	0.126	1.07
IM2	0.032	0.096	2.69	0.032	0.096	0.50
IM3	0.083	0.095	2.10	0.046	0.095	0.47
IM4	0.018	0.117	3.60	0.009	0.117	1.40

measurement information of the 110 kV nodes, and the optimization algorithm is used for the overall optimization of the load parameters under the nodes. Some of the parameters of the high-voltage side equivalent aggregated load model obtained by the method of this paper and the overall measurement and discrimination method (control) are shown in the Tables 5-7.

From the above table, it can be seen that there is not much difference in the parameters of the equivalent integrated load model obtained by the two methods. However, the overall measurement method cannot track and reflect the real-time changes in the system state and load. If the load model 1 of the load model of the system is cut off, the model parameters obtained by the overall measurement method remain fixed, while the model parameters obtained by the method of this paper will be changed accordingly, as shown in the table below:

These tables reflect the proportion of the induction motor before and after the load change. When the load composition changes, the identification result of this paper's method for the induction motor is adjusted from 43.0% to 41.4%, while the identification result of the control method remains unchanged at 41.0%. It can be seen that the method of this paper can track the real load changes compared with the overall measurement and identification method, and the error of the identification results of the load proportion of the induction motor is relatively small. When the battery is overcharged, the electrode materials with different chemical properties will have different effects. At the beginning of charging, most of the electric energy is stored by a reversible reaction, and the heating power is small. But in the later stage of charging, because of the irreversible chemical reaction, the electric energy becomes heat energy. Causing the battery temperature to rise rapidly, resulting in a series of chemical reactions. The following reactions occur when the battery is out of control: the battery cathode material loses lithium and releases oxygen to oxidize the electrolyte, and the

TABLE 3 Parameters of static load and impedance.

	$Z\%$	$I\%$	$P\%$	R_D	X_D	$M\%$
load1	0.33	0.32	0.35	0.002	0.042	0.35
load2	0.20	0.50	0.30	0.001	0.04	0.20
load3	0.20	0.55	0.25	0.001	0.04	0.45
load4	0.10	0.85	0.05	0.003	0.04	0.60

TABLE 4 Parameters of static load and impedance.

	R_s	X_s	X_m	R_r	X_r	H
Article	0.034	0.152	3.166	0.020	0.113	1.05
Contrast	0.027	0.116	3.302	0.019	0.116	1.25

battery negative electrode cannot be embedded with lithium due to the decomposition of the diaphragm, which is deposited into lithium metal. These processes release heat accumulation beyond heat dissipation. Therefore, electric vehicles and the power grid are in a state of balance in order to protect the charging safety of electric vehicles.

Setting a short-time ground fault based on the load model obtained by different modeling methods, the simulation response curve of the relevant electrical quantities at the 110 kV node is shown in Figure 4. From the response curves of node voltage and active power, it can be seen that the simulation curves obtained from the load model established based on the method of this paper are closer to the actual real response and can more accurately reflect the real-time operation status and dynamic changes of the system load. The average errors of nodal voltage and active power are 1.88% and 2.17%, respectively, and the average errors of the simulation curves obtained from the load model based on the overall measurement and discrimination method are larger, 3.16% and 3.54%, respectively. The random charging of electric vehicles on a large scale is bound to cause the conventional load of the power grid to be "peak plus peak." If electric vehicle charging is introduced and an effective charging control strategy is formulated to charge the electric vehicle at a relatively low power grid load, this will play a positive role in cutting the peak and filling the valley. To reduce the variance of the load curve and reduce the peak load as the charging target of the power grid side to manage the charging load of electric vehicles. A safety assessment model is established to analyze the charge-discharge process of electric vehicles and study the interaction characteristics of power batteries, charge and discharge equipment, and power supply equipment. At present, the mainstream charging modules on the market usually use a Vienna rectifier circuit because of the advantages of low cost, high power density, and a simple control strategy.

5 Conclusion

This paper proposes an online modeling method for a comprehensive load model (including electric vehicles (EVs) and battery storage) based on measurement information, based on the

TABLE 5 Parameters of static load and impedance.

	R_s	X_s	X_m	R_r	X_r	H
Article	0.034	0.152	3.166	0.020	0.113	1.05
Contrast	0.027	0.116	3.302	0.019	0.116	1.25

TABLE 6 Model parameters after load changes.

R_s	X_s	X_m	R_r	X_r	H
0.034	0.150	3.174	0.021	0.116	1.09
22.1	3	5	2	8	2
24.72	0.24	0.50	0.26	16.21	0.414

TABLE 7 Ratio of induction motors before and after load changes.

	$R_{s\ (\%)}$	X_s before (%)	X_m after (%)
Real load	43.6	41.9	43.6
Article	43.0	41.4	43.0
Contrast	41.0	41.0	41.0

analysis and identification of the dominant factors of the external characteristics of the comprehensive load model, clustering the bottom load according to the load curve, and constructing the comprehensive load isoaggregation model by stepwise isoaggregation from the low voltage level to the high voltage level. The load model based on the proposed method can track and reflect the real-time changes of the system load and can reflect the real characteristics of the load more accurately than the traditional overall measurement and classification methods. The charging of electric vehicles affects the power quality of the power network and produces about 6 k harmonics, which lead to the loss of the power network, affect the life of the equipment, interfere with the circuit, and then affect the normal operation of the equipment. Therefore, only by avoiding these effects can the impact of electric vehicles on the power grid be minimized. However, the proposed method is only oriented toward the integrated load model composed of static loads and induction motor loads and does not consider the characteristics of new types of loads, such as distributed new energy.

This study elucidated the critical factors influencing the external characteristics of integrated load models, emphasizing the significance of load composition ratios and parameter sensitivities. Through the activation subspace approach and spectral analysis, we identified the

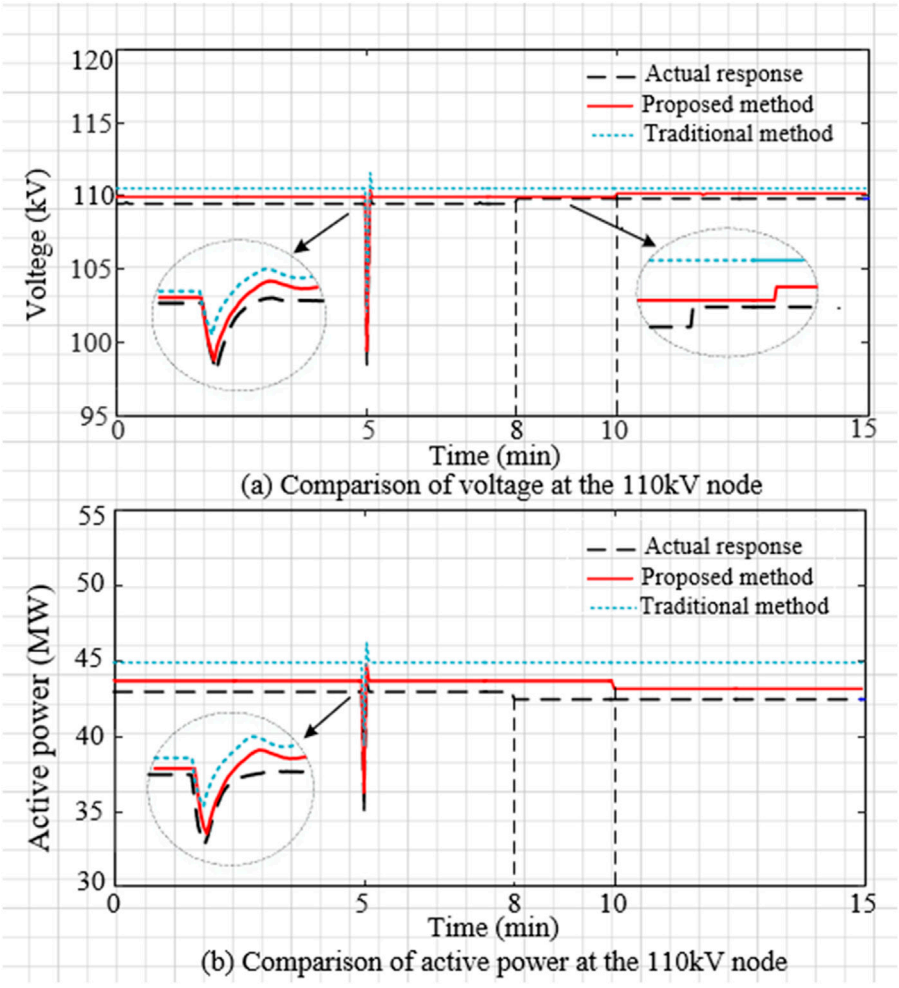

FIGURE 4
Comparison of simulation curves of electrical variables.

dominant factors shaping integrated load behavior, laying the groundwork for more comprehensive modeling techniques.

With a large number of new types of loads connected to the power system, the load characteristics are more complex and variable. The electric vehicle is connected to the distribution side of the power grid, which has the characteristics of random and extensive access. The performance and charging mode of each vehicle are different, and there will be different characteristics in the management of the dispatching center. Considering the future, electric vehicle ownership will be considerable. In order to access any electric vehicle randomly on a large scale, a hierarchical architecture is adopted to construct the integrated structure of intelligent charging, charging, and power monitoring.

The grid voltage is divided into several grades in the stratified area, and the power supply capacity is divided into several power supply areas at different structural levels. The supply is carried out in each area according to the different power loads. The high-dimensional nonlinear characteristics of the model parameters are more prominent, so how to consider this factor to construct a more accurate integrated load model is the focus of the next research work.

Looking ahead, future research directions encompass the exploration of advanced modeling techniques, including deep learning and data-driven parameter estimation, to further refine the accuracy and adaptability of integrated load models. Additionally, efforts should be directed towards integrating these advanced models into practical power system applications, facilitating enhanced load forecasting, grid optimization, and resilience analysis in the face of evolving energy landscapes and demand patterns.

Data availability statement

The original contributions presented in the study are included in the article/Supplementary material, further inquiries can be directed to the corresponding author.

Author contributions

YY: Formal Analysis, Project administration, Investigation, Writing–original draft. YZ: Investigation, Writing–original draft. YH: Data curation, Writing–review and editing. GL: Data curation, Writing–review and editing. ZL: Validation, Writing–review and editing. SP: Methodology, Writing–review and editing.

Funding

The author(s) declare that financial support was received for the research, authorship, and/or publication of this article. This research was Supported by the Science and Technology Project of China Southern Power Grid Co., Ltd. (032000KK52220006(GDKJXM20220163)). The funder was not involved in the study design, collection, analysis, interpretation of data, the writing of this article, or the decision to submit it for publication.

Conflict of interest

Authors YY, YZ, YH, and GL were employed by Zhongshan Power Supply Bureau of Guangdong Power Grid Co., Ltd.

The remaining authors declare that the research was conducted in the absence of any commercial or financial relationships that could be construed as a potential conflict of interest.

Publisher's note

References

Bu, F., Ma, Z., Yuan, Y., and Wang, Z. (2020). WECC composite load model parameter identification using evolutionary deep reinforcement learning. *IEEE Trans. Smart Grid* 11 (6), 5407–5417. doi:10.1109/tsg.2020.3008730

Camille, C., Hewage, D. K., Mirza, O., Mashiri, F., Kirkland, B., and Clarke, T. (2021). Performance behaviour of macro-synthetic fibre reinforced concrete subjected to static and dynamic loadings for sleeper applications. *Constr. Build. Mater.* 270, 121469. doi:10.1016/j.conbuildmat.2020.121469

Chen, C. S., Hwang, J. C., and Huang, C. W. (1997). Application of load survey systems to proper tariff design. *IEEE Trans. power Syst.* 12 (4), 1746–1751. doi:10.1109/59.627886

Cui, M., Khodayar, M., Chen, C., Wang, X., and Zhang, Y. (2019). Deep learning-based time-varying parameter identification for system-wide load modeling. *IEEE Trans. Smart Grid* 10 (6), 6102–6114. doi:10.1109/tsg.2019.2896493

Han, R., Hu, Q., Cui, H., Chen, T., Quan, X., and Wu, Z. (2022). An optimal bidding and scheduling method for load service entities considering demand response uncertainty. *Appl. Energy* 328 (1), 120167. doi:10.1016/j.apenergy.2022.120167

Hu, Q., Guo, Z., and Li, F. (2023). Imitation learning based fast power system production cost minimization simulation. *IEEE Trans. Power Syst.* 38 (3), 2951–2954. doi:10.1109/tpwrs.2023.3237398

Hu, Q., Han, R., Quan, X., Wu, Z., Tang, C., Li, W., et al. (2022). Grid-forming inverter enabled virtual power plants with inertia support capability. *IEEE Trans. Smart Grid* 13 (5), 4134–4143. doi:10.1109/tsg.2022.3141414

Ma, J., Han, D., He, R., Dong, Z. Y., and Hill, D. J. (2008). Reducing identified parameters of measurement-based composite load model. *IEEE Trans. Power Syst.* 23 (1), 76–83. doi:10.1109/tpwrs.2007.913206

Overbye, T. J. (1994). Effects of load modelling on analysis of power system voltage stability. *Int. J. Electr. Power and Energy Syst.* 16 (5), 329–338. doi:10.1016/0142-0615(94)90037-x

Qian, T., Ming, W., Shao, C., Hu, Q., Wang, X., Wu, J., et al. (2023). An edge intelligence-based framework for online scheduling of soft open points with energy storage. *IEEE Trans. Smart Grid* 15, 2934–2945. doi:10.1109/TSG.2023.3330990

Tsekouras, G. J., Hatziargyriou, N. D., and Dialynas, E. N. (2007). Two-stage pattern recognition of load curves for classification of electricity customers. *IEEE Trans. Power Syst.* 22 (3), 1120–1128. doi:10.1109/tpwrs.2007.901287

Wang, C., Wang, Z., Wang, J., and Zhao, D. (2018). SVM-based parameter identification for composite ZIP and electronic load modeling. *IEEE Trans. Power Syst.* 34 (1), 182–193. doi:10.1109/tpwrs.2018.2865966

Xu, T., Chen, T., Gao, C., and Hui, H. (2023). Intelligent home energy management strategy with internal pricing mechanism based on multiagent artificial intelligence-of-things. *IEEE Syst. J.* 17 (4), 1–12. doi:10.1109/JSYST.2023.3324795

Zalok, E., and Eduful, J. (2013). Assessment of fuel load survey methodologies and its impact on fire load data. *Fire Saf. J.* 62, 299–310. doi:10.1016/j.firesaf.2013.08.011

Zhang, W., Remon, D., and Rodriguez, P. (2017). Frequency support characteristics of grid-interactive power converters based on the synchronous power controller. *IET Renew. Power Gener.* 11 (4), 470–479. doi:10.1049/iet-rpg.2016.0557

Zhang, Y., Meng, X., Malik, A., and Wang, L. (2022). The use of analytical converter loss formula to eliminate DC slack/droop bus iteration in sequential AC-DC power flow algorithm. *Int. J. Electr. Power and Energy Syst.* 137, 107596. doi:10.1016/j.ijepes.2021.107596

Zhang, Y., Meng, X., Shotorbani, A. M., and Wang, L. (2020c). Minimization of AC-DC grid transmission loss and DC voltage deviation using adaptive droop control and improved AC-DC power flow algorithm. *IEEE Trans. Power Syst.* 36 (1), 744–756. doi:10.1109/tpwrs.2020.3020039

Zhang, Y., Mohammadpour Shotorbani, A., Wang, L., and Mohammadi-Ivatloo, B. (2021b). Enhanced PI control and adaptive gain tuning schemes for distributed secondary control of an islanded microgrid. *IET Renew. Power Gener.* 15 (4), 854–864. doi:10.1049/rpg2.12074

Zhang, Y., Qian, W., Ye, Y., Li, Y., Tang, Y., Long, Y., et al. (2023). A no*vel non*-intrusive load monitoring method based on ResNet-seq2seq networks for energy disaggregation of distributed energy resources integrated with residential houses. *Appl. Energy* 349, 121703. doi:10.1016/j.apenergy.2023.121703

Zhang, Y., Shotorbani, A. M., Wang, L., and Li, W. (2020b). Distributed voltage regulation and automatic power sharing in multi-terminal HVDC grids. *IEEE Trans. Power Syst.* 35 (5), 3739–3752. doi:10.1109/tpwrs.2020.2986168

Zhang, Y., Shotorbani, A. M., Wang, L., and Li, W. (2021c). A combined hierarchical and autonomous DC grid control for proportional power sharing with minimized voltage variation and transmission loss. *IEEE Trans. Power Deliv.* 37 (4), 3213–3224. doi:10.1109/tpwrd.2021.3125254

Zhang, Y., Shotorbani, A. M., Wang, L., and Mohammadi-Ivatloo, B. (2021a). Distributed secondary control of a microgrid with a generalized PI finite-time controller. *IEEE Open Access J. Power Energy* 8, 57–67. doi:10.1109/oajpe.2021.3056507

Zhang, Y., Wang, L., and Li, W. (2020a). Autonomous DC line power flow regulation using adaptive droop control in HVDC grid. *IEEE Trans. Power Deliv.* 36 (6), 3550–3560. doi:10.1109/tpwrd.2020.3044978

frontiers | Frontiers in Energy Research

TYPE Original Research
PUBLISHED 14 June 2024
DOI 10.3389/fenrg.2024.1375210

OPEN ACCESS

EDITED BY
Yumin Zhang,
Shandong University of Science and Technology, China

REVIEWED BY
Haotian Ge,
Hainan Normal University, China
Pengfei Li,
Hebei University of Engineering, China
Xiao Hu,
Northeast Electric Power University, China

*CORRESPONDENCE
Guangzeng You,
yunnanguihua@163.com

RECEIVED 23 January 2024
ACCEPTED 22 May 2024
PUBLISHED 14 June 2024

CITATION
Sun N, You G, Zhu X, Liu Y, Wu J and Zhu H (2024), A multi-time-scale optimization dispatching strategy for the regional DN–MG systems.
Front. Energy Res. 12:1375210.
doi: 10.3389/fenrg.2024.1375210

A multi-time-scale optimization dispatching strategy for the regional DN–MG systems

Ning Sun[1], Guangzeng You[2]*, Xiaoli Zhu[1], Yong Liu[1], Junhong Wu[1] and Huiqiong Zhu[1]

[1]Chuxiong Power Supply Bureau of Yunnan Power Grid Co, Chuxiong, China, [2]Planning and Construction Research Center of Yunnan Power Grid Corporation Kunming, Kunming, China

The optimization dispatching problem of the regional distribution network (DN) interconnection with the microgrid (MG) is studied in this paper. By installing flexible interconnection devices based on the soft open point (SOP) at the boundaries of DNs, the flexible interconnection can be achieved between distribution networks, and the distribution zoning model is established. A multiobjective DN–MG system optimization dispatching model for multi-area DNs considering distributed resources is established based on the distribution zoning model. By introducing intermediate coupling variables, the optimization dispatching problem of the DN–MG system is decomposed into MG sub-area optimization problems and DN sub-area optimization problems. On the basis of the above, a method based on the alternating direction method of multipliers (ADMM) is proposed to solve the optimization dispatching model. Finally, simulation verification shows that by application of the proposed method, the economic efficiency of the DN–MG system is improved effectively.

KEYWORDS

distribution network, microgrid, soft open point, flexible load, alternating direction method of multipliers

1 Introduction

With the development of power systems, cooperation between different distribution networks (DNs) will be applied to achieve complementary power support between DNs. The power supply reliability will be improved, and it will promote local consumption of distributed power sources (Tabandeh A, 2022; Li T, 2023a; Xu J, 2024). The collaboration between microgrids (MGs) and DNs can not only alleviate the operational pressure of DNs but also reduce the operating costs of MGs (Li Z, 2023b; Chen X, 2023). In this background, realizing reasonable control of power generation and flexible interconnection devices within a flexible interconnected AC/DC distribution system between different regions is an urgent problem that needs to be solved in the economic operation of DN–MG. Domestic and foreign experts and scholars have also conducted relevant research on such optimization problems.

However, currently, soft open points (SOPs) are mostly applied for flexible connection of distributed generation (DG), flexible loads, energy storage (ES), electric vehicles (EVs), and other equipment (Aithal A, 2018; Yao C, 2018; Zhang J, 2021). In order to enhance network performance and flexibility, the rapid development of flexible interconnection technology based on SOPs realized flexible interconnection between feeders. Ebrahimi H (2024a) proposed that SOPs can be installed in the end feeders of the distribution network

to improve network performance. Harmonic distortion, voltage imbalance, and active power loss can be minimized through active and reactive power control and selective harmonic current injection. The optimal active and reactive power control of the location and hourly control of SOPs in a distribution network can achieve minimum harmonic distortion and voltage unbalance. The regional interconnection between DNs has not been realized. In order to improve the flexibility of the power grid, Ehsanbakhsh M (2023) used SOPs to change the topology structure of the distribution network to improve the flexibility of the distribution network. The penetration capability range of renewable energy sources (RESs) is defined as an indicator for evaluating the flexibility of active distribution networks (ADNs). The optimal site and size of SOPs, the final network topology, and the penetration capability range of the RES are determined by solving a multiobjective robust optimization model and adopting flexibility improvement methods. Kamel T (2022) proposed a strategy to interconnect the railway electrification system with the local DN through SOPs, which achieved energy transmission at different power levels between the two systems. The flexibility and reliability of the two systems were improved. However, the direction of energy flow was not changed. Saboori H (2023) proposed a segmentation model based on SOPs to improve the resilience of DNs. This method effectively solved the internal topology reconstruction problem of DNs. However, the issue of improving resilience through collaboration between DNs has been ignored.

In order to address the negative impact of renewable energy on the power system, flexible operation of DN was realized to control the active power, reactive compensation, and voltage regulation by the application of SOPs (Rezaeian-Marjani S, 2022). However, the local consumption level of DG will be limited. The distribution network can flexibly exchange power through multi-terminal intelligent soft switches, provide local reactive power, and alleviate voltage exceeding limits. By the application of SOPs, the distribution network has gradually evolved into a highly controllable flexible interconnection architecture (Li P, 2022).

The DN can flexibly exchange power through multiple SOPs and provide local reactive power. The distribution network gradually evolved into a highly controllable flexible interconnection architecture through the connection of multiple SOPs. In order to alleviate the fluctuation of feeder power flow and load imbalance in DNs, an SOP was applied to provide accurate control of active and reactive power to realize flexible connection of feeders (Ji H, 2017). In order to determine the installation location of an SOP, a classic scenario was constructed based on Wasserstein distance metric to optimize the configuration method for SOPs (Wang C, 2016). However, this configuration method is only applicable to the optimized configuration of SOPs within a single DN.

At the same time, the uncertainty of renewable energy output and the uncertainty of multi-load demand significantly will increase the complexity of regional energy system optimization scheduling (Ma X, 2023). Ma X (2023) proposed a rolling mechanism based on the flexible loads to reduce the impact of DG on the power system. In addition, a two-stage multiobjective framework is proposed to manage the energy of MG (Karimi H, 2023). However, this article only studied from the perspective of MG and did not consider the operational status of the distribution network. (Li Z (2023c) proposed a multi-time-scale coordinated control strategy where EVs were modeled as the flexible loads to participate in multi-region dispatching tasks in the DN in the day-ahead stage. In the real-time stage, the charging load was defined as a controllable load to compensate for power errors caused by DG. Han C (2023) proposed a new SOP management strategy based on the model predictive control (MPC) framework. The proposed method corresponds to the factory modeling of voltage and network losses as a linear time-varying system, which provides better performance than traditional MPC methods in reducing network losses and improving voltage distribution based on the data clustering technology; Ebrahimi H (2024b) proposed a method to handle uncertain factors. By optimizing the installation position of SOPs, the expected values of active power loss and voltage deviation were reduced.

In the above research, the application of SOPs and the optimization dispatching problem of multiple time scales were studied, but the collaboration between DNs and MGs was not considered. In response to the current research shortcomings, the main contributions of this article are as follows:

(1) A regional optimization model is constructed based on the zoning of the distribution system. The interconnection between DNs is realized through SOPs. Based on the TOU, the power flow between DNs can be coordinated by the application of SOPs. Under the background of ensuring the safe and stable operation of a DN, collaborative support between DNs is realized. In addition, the operating cost of the DN is reduced.
(2) An optimized dispatching model for the DN–MG collaboration is proposed. While the MG ensures its own economic operation, the MG responds to TOU and the operating status of the DN. The flexible load within the microgrid can be adjusted according to TOU. By reducing the operating cost of MG through flexible load shifting, the purchase of electricity during various periods of MG is adjusted. Thereby, the operational pressure during peak load periods of the DN is alleviated.
(3) A multi-time-scale optimization method based on the alternating direction method of multipliers (ADMM) is proposed. On the basis of adopting multi-time-scale rolling optimization, the optimization problem is decomposed into several sub-problems. These sub-problems are solved by the ADMM. The simulation results show that the strategy proposed in this paper can effectively reduce the operating costs of the DN and MG.

2 Regional optimization model

2.1 Distribution network zoning

The active distribution network (ADN) structure with the MG is shown in Figure 1. In addition to fixed topology parameters, the DN also includes local loads and DG. The distribution network is connected to the microgrid through a point of common coupling (PCC). The MG directly combines the DG with local user loads in a certain area. The DG will prioritize supplying power to the local load within the MG. When the DG in the MG is excessive or insufficient, the MG will interact with the DN for power. The MG can include

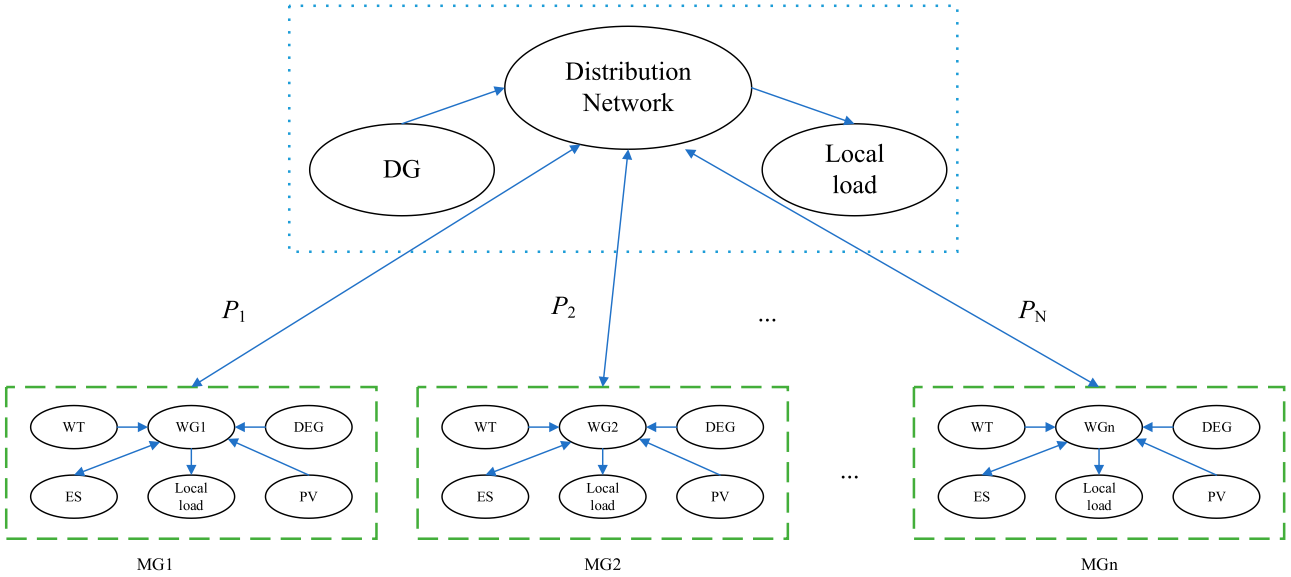

FIGURE 1
Distribution network structure with microgrids.

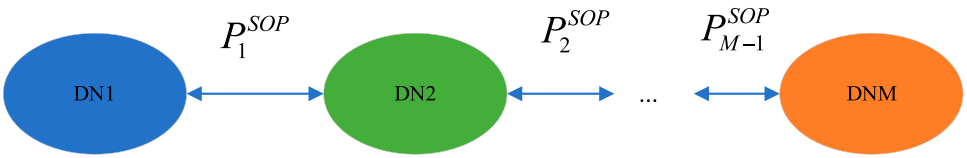

FIGURE 2
Interconnection architecture of the distribution network.

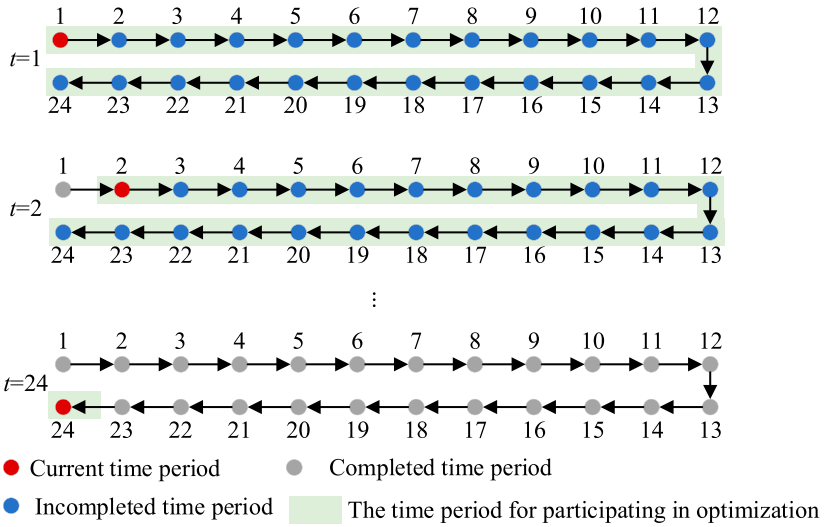

FIGURE 3
Multi-time-scale dispatching architecture.

diesel generators (DEG), photovoltaics (PV), wind power generation (WG), energy storage (ES), and local load. In addition, the local load can be flexibly adjusted to participate in demand response.

At the same time, DNs are interconnected through SOPs. Power interaction between the DNs is realized by controlling the flexible interconnection devices. The interconnection

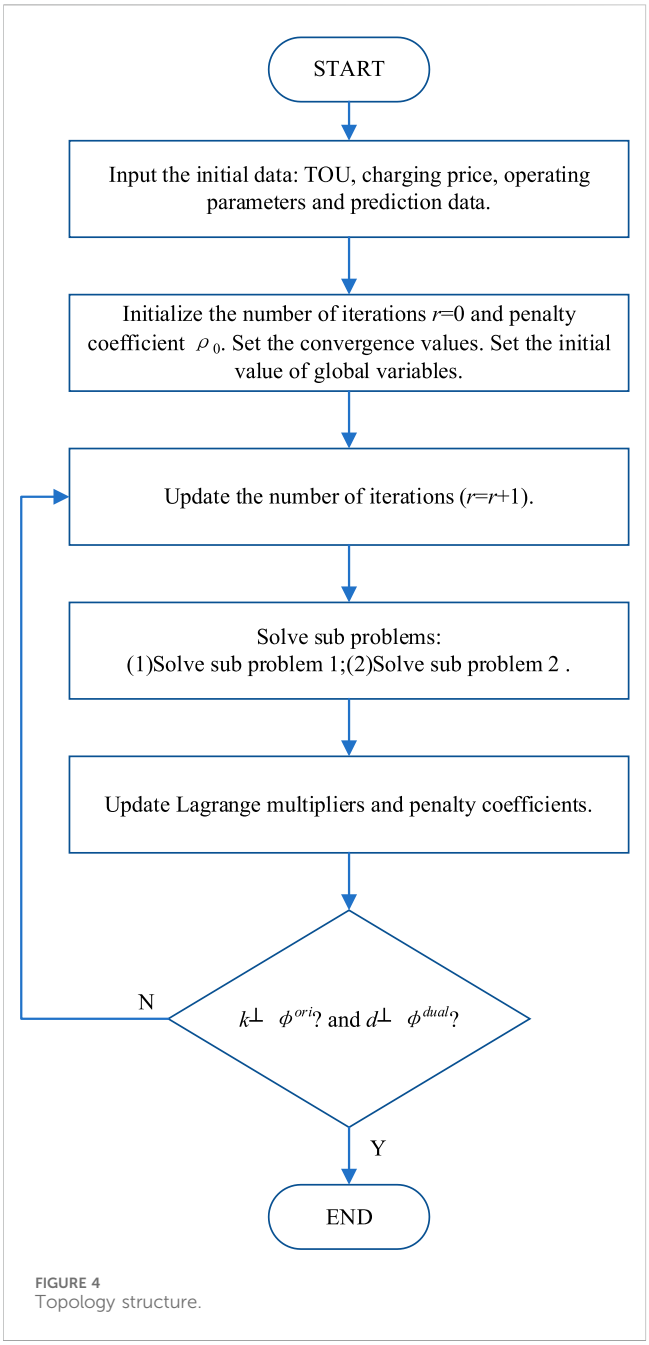

FIGURE 4
Topology structure.

architecture of the distribution network is shown in Figure 2. DNs can be divided into several sub-DNs. Flexible interconnection between sub-DNs can be achieved through SOPs.

2.2 DN operation constraints

In this paper, the DistFlow model is applied to constrain the power flow of the DN:

$$U_{\min}^{2} \le V_{i,t} \le U_{\max}^{2}, i \in \mathfrak{R}. \quad (1)$$

$$0 \le l_{ij,t} \le l_{ij,\max}. \quad (2)$$

$$P_{ij,t} + \sum_{i_{DEG}=1}^{N_{DEG}} \kappa_j P_{t,i_{DEG}} = r_{ij} l_{ij,t} + p_{j,t} + \sum_{j:\ j-k} P_{jk,t} + \sum_{i_{SOP}=1}^{N_{SOP}} \upsilon_j P_{t,i_{SOP}}. \quad (3)$$

$$Q_{ij,t} + \sum_{i_{DEG}=1}^{N_{DEG}} \kappa_j Q_{t,i_{DEG}} = x_{ij} l_{ij,t} + q_{j,t} + \sum_{j:\ j-k} Q_{jk,t}. \quad (4)$$

$$V_{i,t} + l_{ij,t}\left(r_{ij}^2 + x_{ij}^2\right) = 2\left(r_{ij} P_{ij,t} + x_{ij} Q_{ij,t}\right) + V_{j,t}. \quad (5)$$

$$\left\| \begin{matrix} 2P_{ij,t} \\ 2Q_{ij,t} \\ V_{i,t} - l_{ij,t} \end{matrix} \right\|_2 \le V_{i,t} + l_{ij,t}. \quad (6)$$

Here, $\mathfrak{R}$ is the node set of the DN; i and j are the node ID of the DN; t is the time interval; $P_{ij,t}$ is the active power of branch ij in t; $Q_{ij,t}$ is the reactive power of branch ij in t; $V_{i,t}$ is the square of voltage amplitude; $U_{\max}$ and $U_{\min}$ are maximum and minimum values of voltage amplitude, respectively; $l_{ij,t}$ is the square of the current amplitude; $l_{ij,\max}$ is the maximum values of $l_{ij,t}$; r_{ij} is the resistance value of the branch ij; x_{ij} is the reactance value of the branch ij; N_{DEG} is the number of DEGs; $P_{t,i_{DEG}}$ is the active power of DEGs; $Q_{t,i_{DEG}}$ is the reactive power of DEGs; κ_j is a binary variable that indicates whether the DEG is installed at node j; $p_{j,t}$ is the active load at node j; $q_{j,t}$ is the reactive load at node j; υ_j is a binary variable that indicates whether the SOP is installed at node j; $P_{t,i_{SOP}}$ is the active power of the SOP.

At the same time, the DEG needs to meet the constraints of power upper and lower limits and the constraints of ramp rate:

$$P_{i_{DEG},\min} \le P_{t,i_{DEG}} \le P_{i_{DEG},\max}. \quad (7)$$

$$Q_{i_{DEG},\min} \le Q_{t,i_{DEG}} \le Q_{i_{DEG},\max}. \quad (8)$$

$$\left|P_{t,i_{DEG}} - P_{t-1,i_{DEG}}\right| \le \varepsilon_{DEG}. \quad (9)$$

Here, $P_{i_{DEG},\max}$ and $P_{i_{DEG},\min}$ are the maximum and minimum values of DEG active power output, respectively; $Q_{i_{DEG},\max}$ and $Q_{i_{DEG},\min}$ are the maximum and minimum values of DEG reactive power output, respectively; ε_{DEG} is the ramp rate of the DEG.

2.3 MG operation constraints

The MG can include DEG, PV, WG, ES, and local electricity loads. Among them, the local electricity load can be adjusted flexibly, which can be powered by time-series translation. Therefore, the operational constraints of the MG are as follows:

$$P_t^{DEG} + P_t^{PV} + P_t^{WG} + P_t^{grid} = P_t^{ES} + P_t^{load}, \quad (10)$$

where P_t^{DEG} is the active power of DEG in the MG; P_t^{PV} is the active power of PV in the MG; P_t^{WG} is the active power of WG in the MG; P_t^{grid} is the electricity purchased from the DN; P_t^{ES} is the active power of ES in the MG; P_t^{load} is the load of the MG.

$$P^{load} = \sum_{t=1}^{T} P_t^{load}. \quad (11)$$

$$P_{t,\min}^{load} \le P_t^{load} \le P_{t,\max}^{load}. \quad (12)$$

Here, P^{load} is the total load of the MG within a day; $P_{t,\max}^{load}$ and $P_{t,\min}^{load}$ are the maximum and minimum values of P_t^{load}, respectively.

The constraints of DEG in MGs are similar to those of DNs and will not be elaborated here.

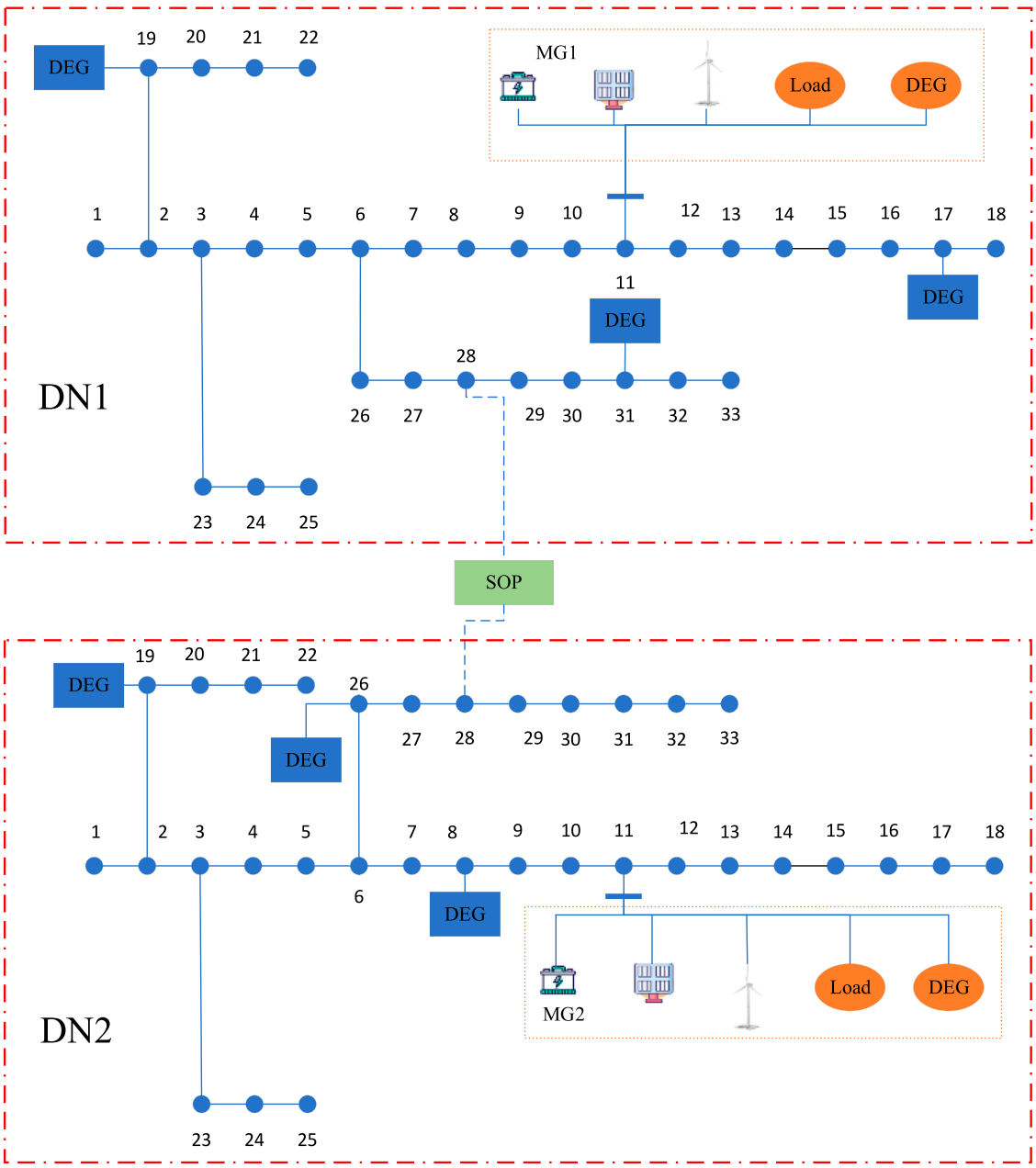

FIGURE 5
Topology structure.

$$-P_{t,\max}^{ES} \le P_t^{ES} \le P_{t,\max}^{ES}. \quad (13)$$

$$S_{\min}^{ES} \le S_t^{ES} \le S_{\max}^{ES}. \quad (14)$$

$$S_t^{ES} = S_{t-1}^{ES} + P_t^{ES}. \quad (15)$$

Here, $P_{t,\max}^{ES}$ is the maximum value of P_t^{ES}; S_t^{ES} is ES capacity; $S_{\max}^{ES}$ and $S_{\min}^{ES}$ are the maximum and minimum values of S_t^{ES}, respectively.

2.4 SOP model

The DNs are flexibly interconnected through SOPs with DC charging devices. The upper control center can achieve power flow direction control through voltage source converters (VSCs) on both sides of the SOP. In order to realize the regional division, the DC charging device and DN are the same optimized area. In addition, information exchange is carried out point-to-point with the adjacent DN side. The decoupled interaction power relationship is as follows:

$$P_t^{vsc_i} - P_{t,sale_i} = P'_{t,vsc_i}. \quad (16)$$

$$P_t^{vsc_{i+1}} = P'_{t,vsc_{i+1}}, \quad (17)$$

where $P_t^{vsc_i}$ is the power on the VSC AC side at the boundary of the DN; $P_{t,sale_i}$ is the power of the DC charging load; P'_{t,vsc_i} and $P'_{t,vsc_{i+1}}$ are the amounts of power interaction information

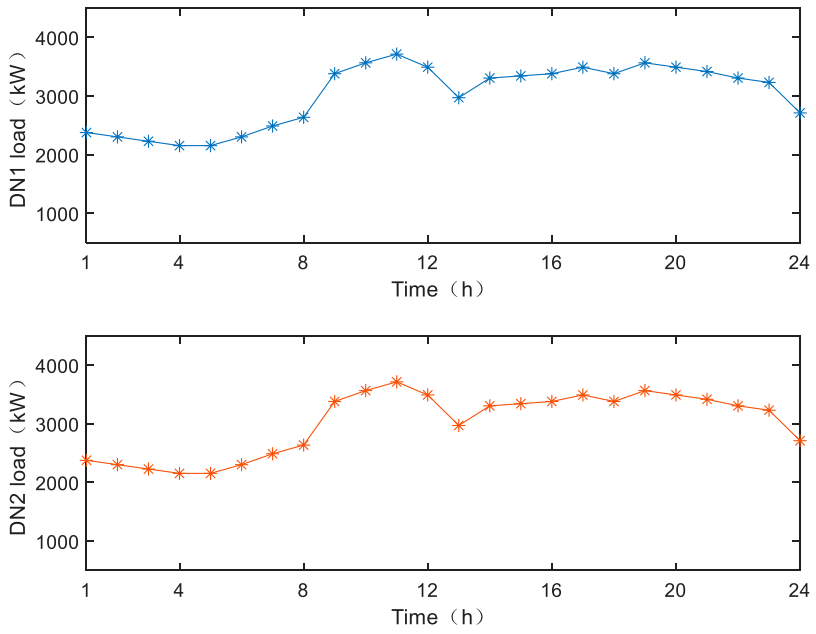

FIGURE 6
Load data of the distribution network.

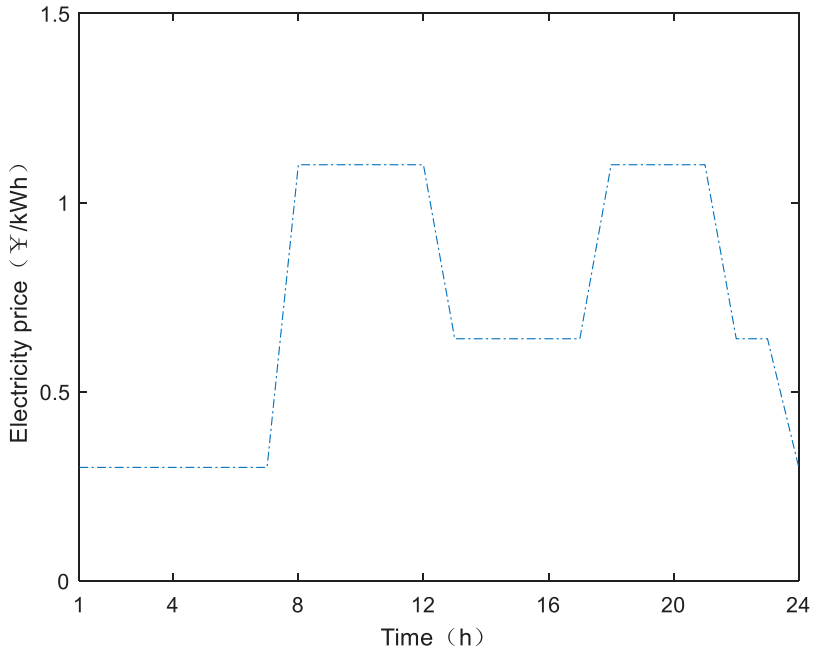

FIGURE 7
TOU of the distribution network.

between adjacent active distribution networks; $P_t^{vsc_{i+1}}$ is the power on the VSC AC side at the boundary of the DN.

At the same time, the upper limit constraint of interaction power is as follows:

$$P_t^{vsc_i} - P_{t,sale_i} \le P_{t,sop}^{\max}, \tag{18}$$

where $P_{t,sop}^{\max}$ is the maximum value of P_{t,vsc_i}'.

2.5 PCC model

The MG and DN are connected through a PCC. They are coupled and interconnected. In order to achieve partition calculation, the DN area in the coupling area between the DN and MG is defined as region H, and the MG area is defined as region L. The PCC will be decoupled into two independent regions. The

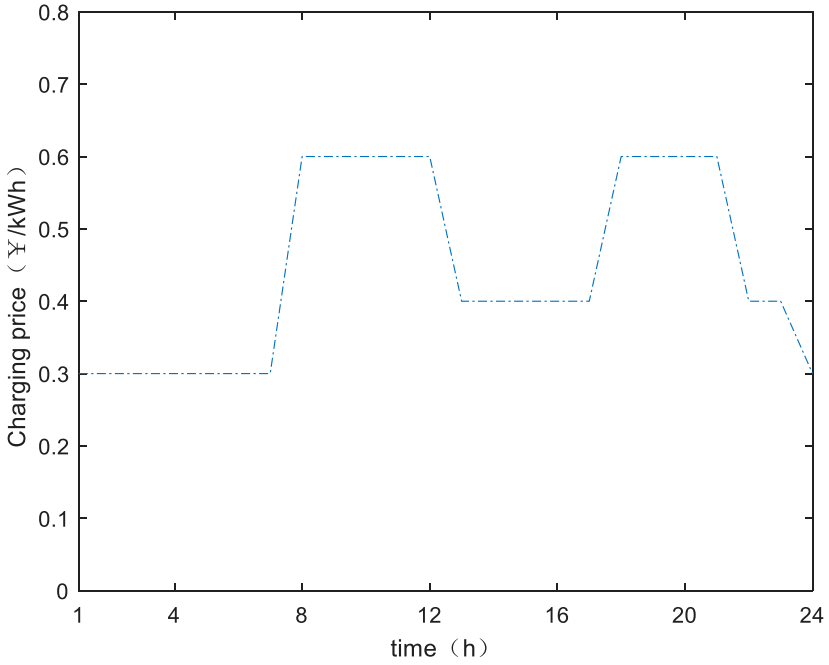

FIGURE 8
Charging price.

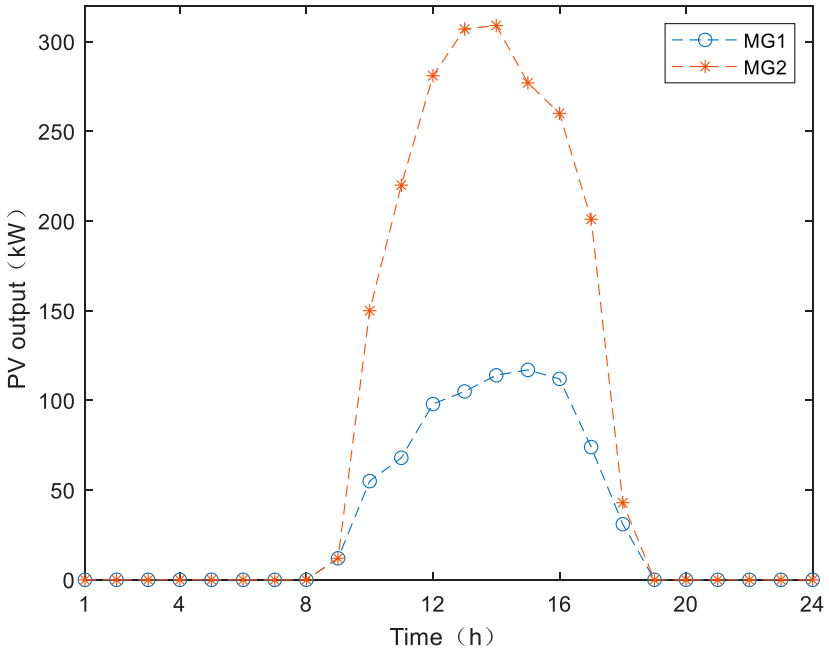

FIGURE 9
PV output of MGs.

relationship between the variables decoupled from two independent regions is as follows:

$$P_{t,DN} = P'_{t,DN,H}. \quad (19)$$

$$P_{t,MG} = P'_{t,MG,L}. \quad (20)$$

Here, $P_{t,MG}$ is the power value of the MG area at the PCC; $P_{t,DN}$ is the power value of the DN area at the PCC; $P'_{t,DN,H}$ is the replication area variable of the DN; $P'_{t,MG,L}$ is the replication area variable of the DN.

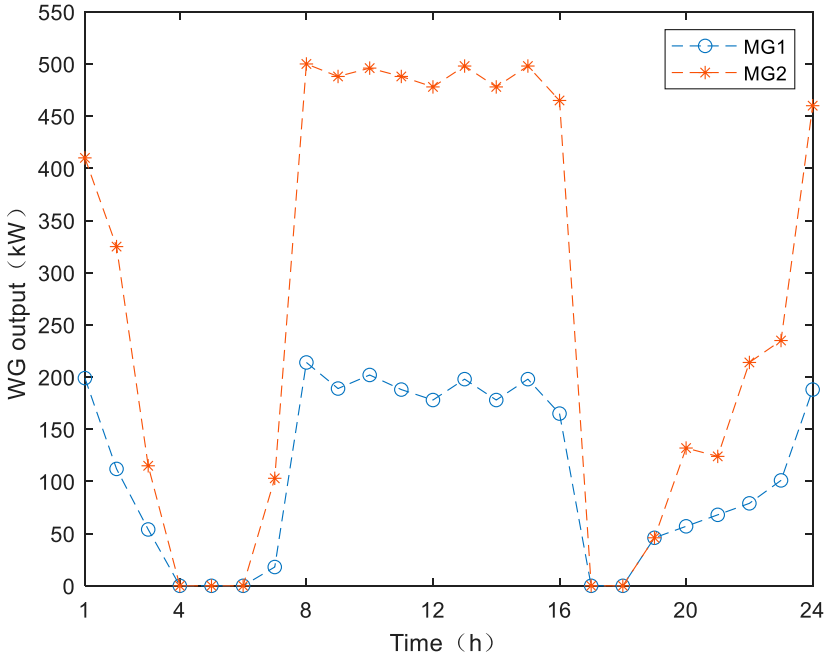

FIGURE 10
WG output of MGs.

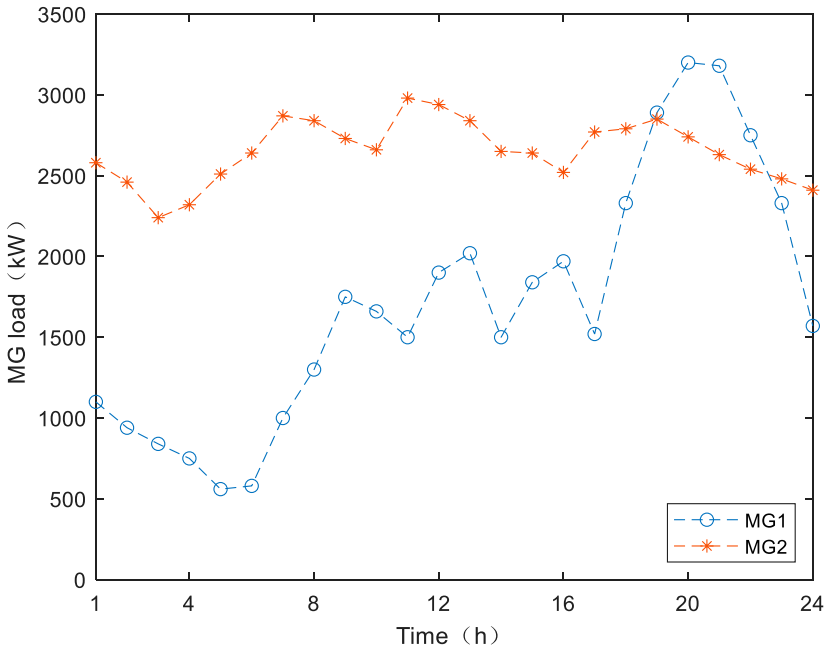

FIGURE 11
MG load curve.

3 Optimal dispatching model

Based on the regional optimization model, the optimal dispatching model is established to realize economic optimization, and a rolling optimization dispatching model with multiple time scales is established.

The multi-time-scale dispatching architecture is shown in Figure 3. Due to fluctuations of the PV and WG, rolling optimization dispatching can effectively ensure the accuracy of optimization dispatching. The participating optimization period includes the current period and all the remaining unfinished periods to ensure that the optimization results of the current period are optimal.

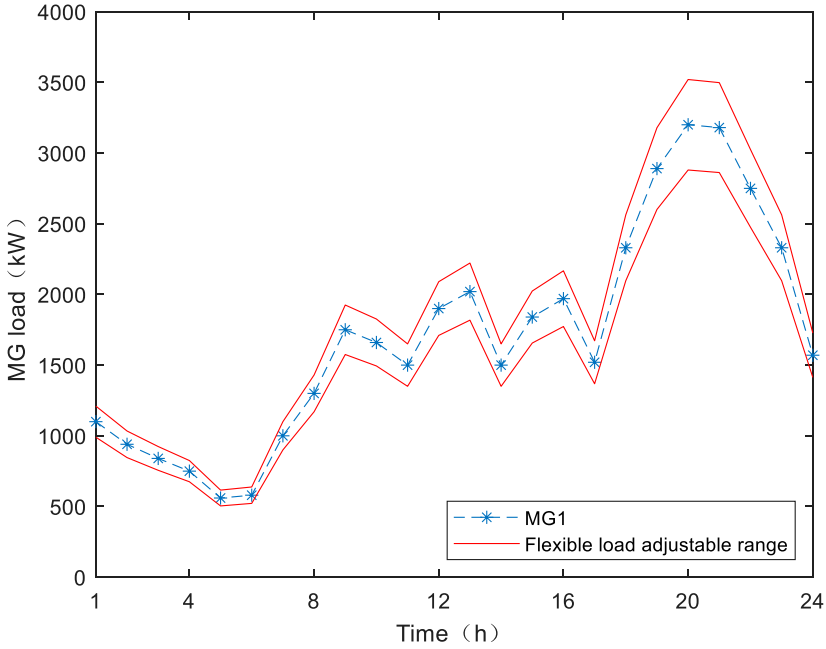

FIGURE 12
MG1 flexible load adjustable range.

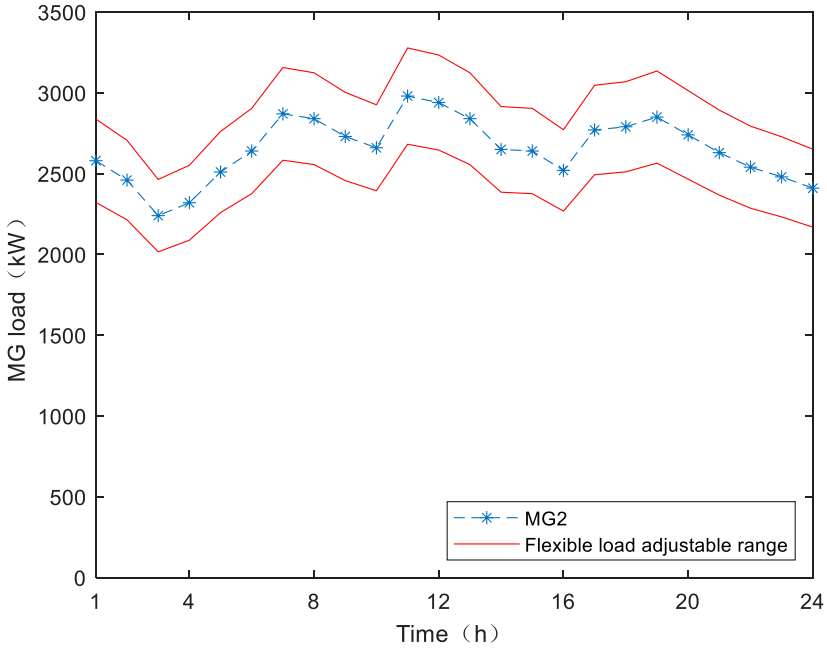

FIGURE 13
MG2 flexible load adjustable range.

It can be seen from Figure 3 that the dispatching strategy is divided into the completed time period and the period for participating in optimization. The completed time period is time-varying. The period for participating in optimization is also time-varying. The sum of the two time periods is fixed. The size of the completed time period increases sequentially from 1 to 24. The size of the period for participating in optimization decreases sequentially from 1 to 24. Therefore, the dispatching strategy has 24 calculation time scales.

The optimization dispatching models for each region are as follows:

$$\min\ C = C_{DN} + C_{MG} - C_{sale}, \tag{21}$$

TABLE 1 WG parameters for MG1.

WG ID	Maximum value of active power output (kW)	Maximum value of active power output (kW)
1	1,500	450
2	1,500	450

TABLE 2 ES parameters for MG1.

ES ID	ES capacity (kWh)	Maximum value of active power output (kW)	Maximum value of active power output (kW)
1	500	60	−60
2	500	60	−60

TABLE 3 WG parameters for MG2.

WG ID	Maximum value of active power output (kW)	Maximum value of active power output (kW)
1	1,500	450
2	1,500	450

TABLE 4 ES parameters for MG2.

ES ID	ES capacity (kWh)	Maximum value of active power output (kW)	Maximum value of active power output (kW)
1	500	60	−60
2	500	60	−60

TABLE 5 Scenario setting.

Scenario ID	SOP	Flexible load
Scenario 1	√	√
Scenario 2	√	-
Scenario 3	-	√
Scenario 4	-	-

TABLE 6 SOP parameters.

Maximum value of SOP transmission power	Minimum value of SOP transmission power (kW)
1,000 kW	−1,000

where C represents the total operating cost during the optimization period; C_{DN} represents the operating cost of the DN during the optimization period; C_{MG} represents the operating cost of the MG during the optimization period; C_{sale} represents the revenue from the DC charging devices.

The objective of the DN_i regional economic optimization model is to optimize the economic efficiency of DN_i and its regional boundaries, including the output cost of DEGs, the PCC at the partition boundary, and the interaction cost at the SOP.

$$\min C_{DN_i} = \sum_{t=1}^{T}\left[a\left(P_{t,DN_i}^{DEG}\right)^2 + bP_{t,DN_i}^{DEG} + c\right] - \mu\sum_{t=1}^{T}P_t^{VSC_i} - \mu\sum_{t=1}^{T}P_{t,DN_i}, \tag{22}$$

where C_{DN_i} is the total operating cost of the DN_i; a, b, and c are the fuel consumption parameters of DEGs; P_{t,DN_i}^{DEG} is the active power of DEG in the DN_i; μ is the TOU for purchasing and selling between regions.

The optimization objective of the regional economic optimization model for the MG is to minimize the operating costs of microgrids, including the output cost of the DEGs, the charging and discharging cost of the ES, and the interaction cost at the PCC of the partition boundary.

$$\min C_{MG_i} = \sum_{t=1}^{T}\left[a\left(P_{t,MG_i}^{DEG}\right)^2 + bP_{t,MG_i}^{DEG} + c\right] - \gamma\sum_{t=1}^{T}P_t^{ES} - \mu\sum_{t=1}^{T}P_{t,MG_i}, \tag{23}$$

where C_{MG_i} is the total operating cost of MG_i; γ is the cost coefficient for charging and discharging of ES; P_{t,MG_i}^{DEG} is the active power of DEG in MG_i.

The economic optimization model of the DC charging device at the SOP is as follows:

$$\min C_{sale_i} = \mu_{sale}\sum_{t=1}^{T}P_{t,sale_i}, \tag{24}$$

where μ_{sale} is the charging price of EVs.

4 Optimization dispatching based on the ADMM

The ADMM is an iterative algorithm used to solve convex optimization problems. This algorithm is suitable for large-scale data and distributed computing environments. The ADMM algorithm has the following advantages:

(1) ADMM can decompose large optimization problems into multiple smaller sub-problems to make the problem easier to solve.
(2) This algorithm is suitable for distributed computing environments. In addition, it allows multiple computing nodes to participate in the problem-solving process to improve the computational efficiency.
(3) ADMM usually has good convergence performance and can find near-optimal solutions within a finite number of iterations.
(4) During the iteration process, each sub-problem can independently perform sparse reconstruction and noise reduction operations to achieve high reconstruction accuracy.

Based on the optimization architecture and model mentioned above, an optimization dispatching method based on the ADMM is

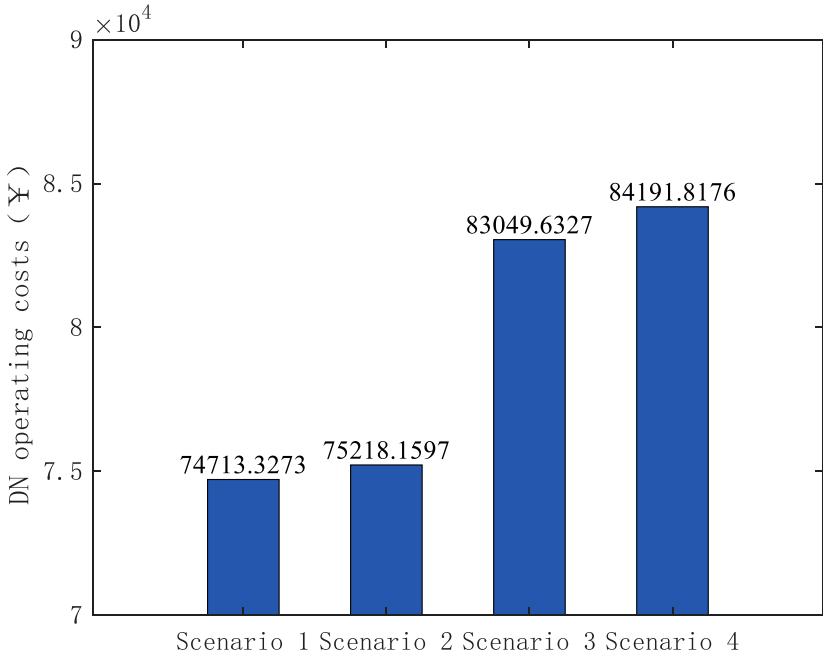

FIGURE 14
DN 1 operating cost.

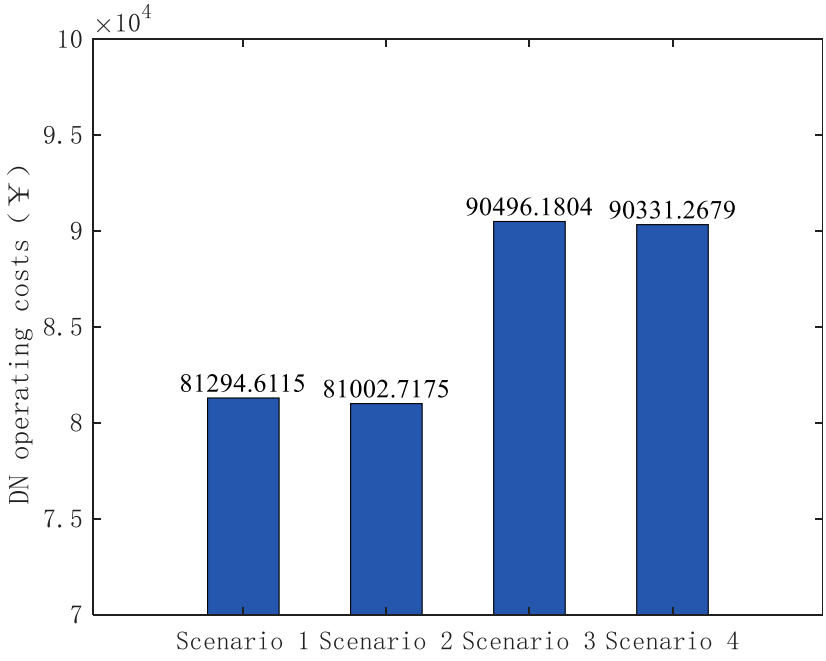

FIGURE 15
DN 2 operating cost.

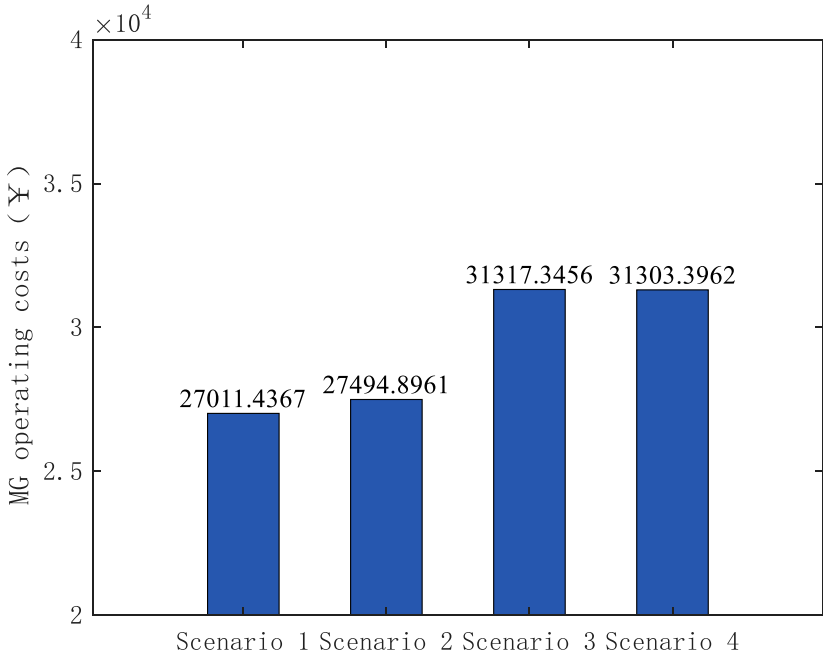

FIGURE 16
MG 1 operating cost.

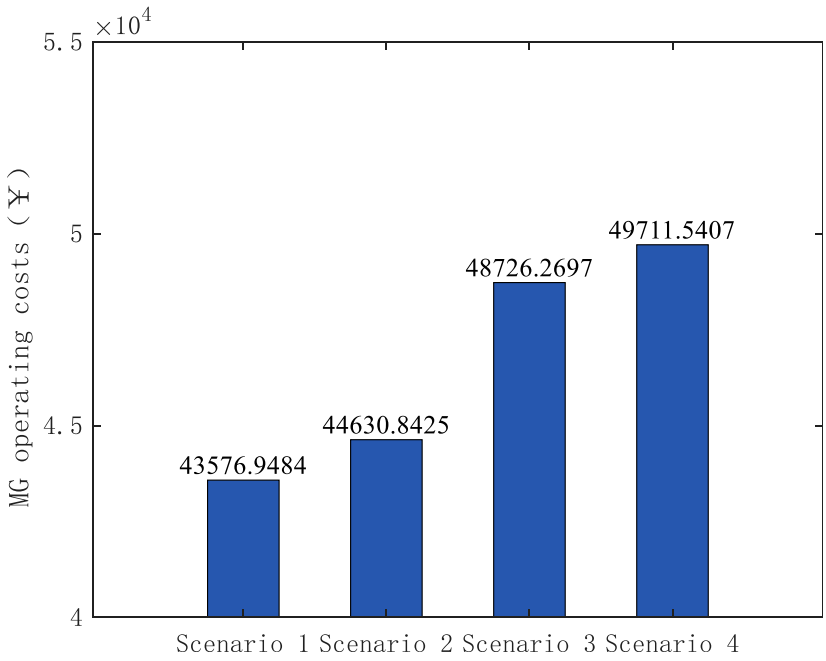

FIGURE 17
MG 2 operating cost.

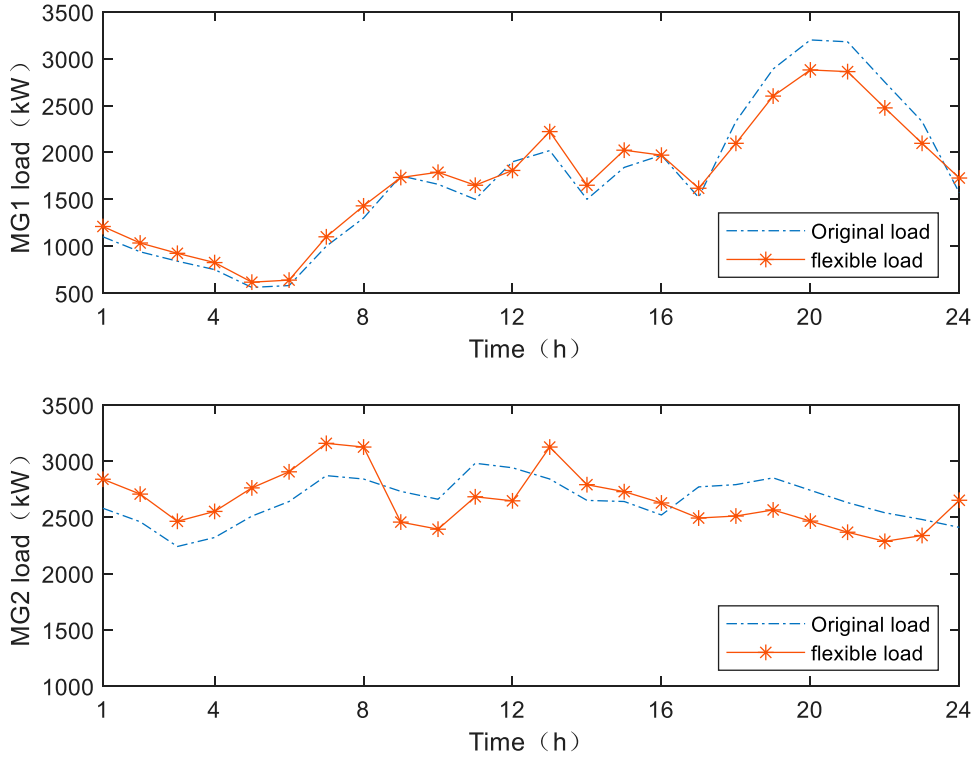

FIGURE 18
MG load for scenario 1

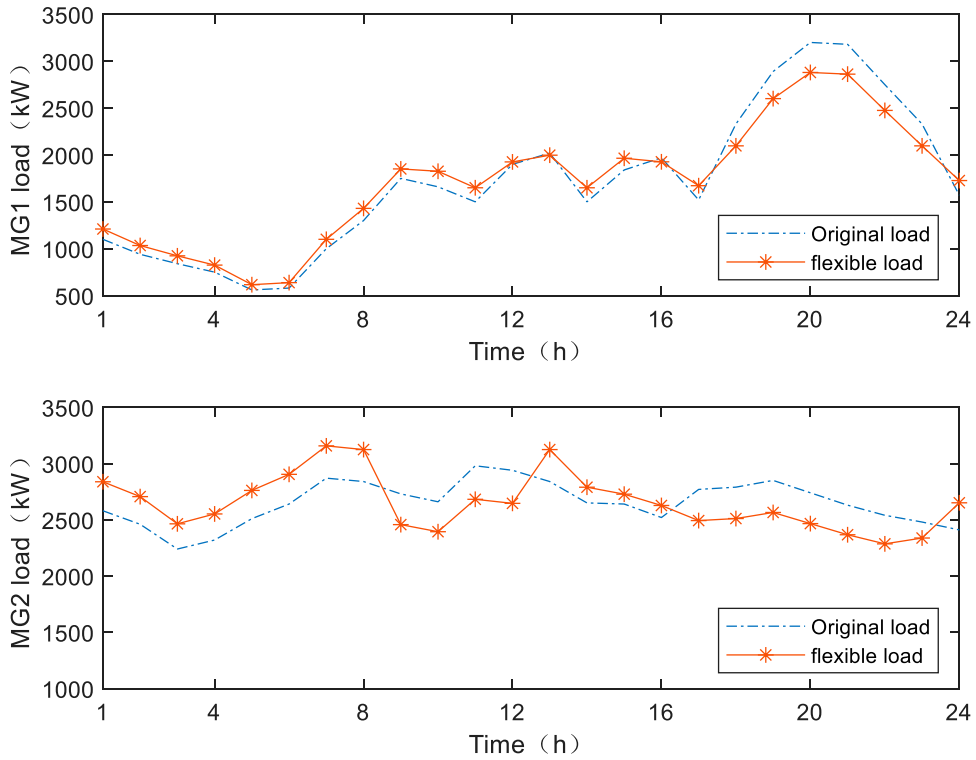

FIGURE 19
MG load for scenario 3

proposed. An augmented Lagrangian function is constructed, and the sub-problems are divided according to the framework structure of the optimization model.

$$\begin{aligned} L = & \sum_{i=1}^{I} C_{DN_i} + \sum_{i=1}^{I}\sum_{j=1}^{J} C_{MG_{j,i}} - \sum_{i=1}^{I} C_{sale,i} \\ & + \sum_{i=1}^{I}\sum_{t=1}^{T} \lambda_i \left(P_t^{VSC_i} - P_{t,sale_i} - P_t^{VSC_{i+1}}\right) \\ & + \frac{\rho}{2}\left\|P_t^{VSC_i} - P_{t,sale_i} - P_t^{VSC_{i+1}}\right\|_2^2 \\ & + \sum_{i=1}^{I}\sum_{t=1}^{T} \lambda_i \left(P_t^{VSC_{i+1}} - P_t^{VSC_i} + P_{t,sale_i}\right) \\ & + \frac{\rho}{2}\left\|P_t^{VSC_{i+1}} + P_{t,sale_i} - P_t^{VSC_i}\right\|_2^2 + \sum_{i=1}^{I}\sum_{j=1}^{J}\sum_{t=1}^{T} \lambda_{j,i}\left(P_{t,MG_{j,i}} - P_{t,DN_i}\right) \\ & + \frac{\rho}{2}\left\|P_{t,MG_{j,i}} - P_{t,DN_i}\right\|_2^2, \end{aligned} \tag{25}$$

where I is the number of DNs; J is the number of MGs; λ_i and $\lambda_{j,i}$ are dual variables; ρ is the penalty coefficient; L is the Lagrangian function.

4.1 Sub-problem 1: solving the DN and SOP optimization problems

Sub-problem 1 can be decomposed into two local sub-problems; namely, the optimization of DN_i and DN_{i+1}. The decision variables within the DN can be optimized by solving local sub-problems using the ADMM. The SOP serves as the boundary between two DN areas, and its injection power is optimized as an interaction variable during the calculation process.

For DN_i

$$\begin{aligned} L_{DN_i}^{ADMM} = & C_{DN_i} - C_{sale_i} + \lambda_i \sum_{t=1}^{T} \left(P_t^{VSC_i} - P_{t,sale_i} - P'_{t,VSC_{i+1}}\right) \\ & + \frac{\rho}{2}\left\|P_t^{VSC_i} - P_{t,sale_i} - P'_{t,VSC_{i+1}}\right\|_2^2. \end{aligned} \tag{26}$$

For DN_{i+1}:

$$L_{DN_{i+1}}^{ADMM} = C_{DN_{i+1}} + \lambda_i \sum_{t=1}^{T} \left(P_t^{VSC_{i+1}} - P'_{t,VSC_i}\right) + \frac{\rho}{2}\left\|P_t^{VSC_{i+1}} - P'_{t,VSC_i}\right\|_2^2. \tag{27}$$

Here, $L_{DN_i}^{ADMM}$ and $L_{DN_{i+1}}^{ADMM}$ are the Lagrangian functions.

The original residual error, dual residual error, and iterative update mechanism for sub-problem 1 are as follows:

$$\begin{cases} k_i^r = \left\|P_t^{VSC_i,r} - P_{t,sale_i}^r - P'^r_{t,VSC_{i+1}}\right\|_2^2 \\ k_{i+1}^r = \left\|P_t^{VSC_{i+1},r} - P'^r_{t,VSC_i}\right\|_2^2 \end{cases}. \tag{28}$$

$$\begin{cases} d_i^r = \left\|P_t^{VSC_{i+1},r} - P_{t,sale_i}^r - \left(P_t^{VSC_{i+1},r-1} - P_{t,sale_i}^{r-1}\right)\right\|_2^2 \\ d_{i+1}^r = \left\|P_t^{VSC_{i+1},r} - P_t^{VSC_{i+1},r-1}\right\|_2^2 \end{cases}. \tag{29}$$

$$\begin{cases} \lambda_i^{r+1} = \lambda_i^r + \frac{\rho}{2}\left(P_t^{VSC_i,r} - P_{t,sale_i}^r - P'^r_{t,VSC_{i+1}}\right) \\ \lambda_{i+1}^{r+1} = \lambda_{i+1}^r + \frac{\rho}{2}\left(P_t^{VSC_{i+1},r} - P'^r_{t,VSC_i}\right) \end{cases}. \tag{30}$$

Here, r is the number of iterations; k is the original residual; d is the dual residual.

4.2 Sub-problem 2: solving the MG and PCC optimization problems

$$L_{MG_{j,i}}^{ADMM} = C_{MG_{j,i}} + \lambda_{j,i} \sum_{t=1}^{T} \left(P_{t,MG_{j,i}} - P'_{t,DN_i}\right) + \frac{\rho}{2}\left\|P_{t,MG_{j,i}} - P'_{t,DN_i}\right\|_2^2. \tag{31}$$

$$k_{j,i}^r = \left\|P_{t,MG_{j,i}}^r - P'^r_{t,DN_i}\right\|_2^2. \tag{32}$$

$$d_{j,i}^r = \left\|P_{t,MG_{j,i}}^r - P_{t,MG_{j,i}}^{r-1}\right\|_2^2. \tag{33}$$

$$\lambda_{j,i}^{r+1} = \lambda_{j,i}^r + \frac{\rho}{2}\left(P_{t,MG_{j,i}}^r - P'^r_{t,DN_i}\right). \tag{34}$$

Here, $L_{MG_{j,i}}^{ADMM}$ is the Lagrangian function.

The selection of the penalty coefficient will affect the convergence speed of the algorithm. By balancing the original residual error and the dual residual error, the penalty coefficient can be adaptively adjusted according to the residual error, which can accelerate the convergence speed of the algorithm.

$$\rho^{r+1} = \begin{cases} \dfrac{\rho^r}{1 + \lg\dfrac{d^r}{k^r}} & k^r < 0.1d^r \\ \rho^r\left(1 + \lg\dfrac{k^r}{d^r}\right) & k^r > 10d^r \\ \rho^r & \text{others} \end{cases}. \tag{35}$$

The decision variables are divided into two parts: 1) the interaction variables within the flexible interconnection devices of the DN; 2) the interaction variables between the PCC coupling part of the DN and MG. The optimization process is shown in Figure 4.

The detailed optimization process is as follows:

Step 1: input the initial data. Input the TOU for regional purchase and sale, DC charging price for EVs, user flexible load, operating parameters of the DN and MG, and rolling prediction data for the PV and WG.

Step 2: initialize the number of iterations $r = 0$ and penalty coefficient ρ_0. Set the convergence values of the original residual and the dual residual (φ^{ori} and φ^{dual}). The initial settings for dual variables, original residuals, and dual residuals are all set to 0. Set the initial value of the global variables (P'_{t,VSC_i}, $P'_{t,VSC_{i+1}}$, and P'_{t,DN_i}).

Step 3: update the number of iterations ($r = r + 1$).

Step 4: solving sub-problems.

(1) Solve sub-problem 1. At the flexible interconnection device SOP, the interaction data received by DN_i from DN_{i+1} are $P'^{r+1}_{t,VSC_{i+1}} = P_t^{VSC_{i+1},r}$. The interaction data received by DN_{i+1} from DN_i are $P'^{r+1}_{t,VSC_{i+1}} = P_t^{VSC_{i+1},r} - P_{t,sale_i}^r$.

(2) Solve sub-problem 2. The interaction variables between the microgrid area and the connected distribution network are obtained through the PCC ($P'^{r+1}_{t,DN_i} = P^r_{t,DN_i}$).

Step 5: Update Lagrange multipliers and penalty coefficients.

Step 6: Residual update and iteration termination determination. When $k \le \varphi^{ori}$ and $d \le \varphi^{dual}$, the algorithm ends and outputs the result. Otherwise, return to step 3 to continue iterating until the convergence condition is met.

5 Case study

5.1 Case data

In order to verify the effectiveness of the optimization strategy, this paper selected two IEEE 33 node systems and two MGs as a study case. The topology structure is shown in Figure 5, and the load data of the DN are shown in Figure 6.

In this paper, a multiple time-scale rolling optimization strategy is proposed to achieve a full-day optimization calculation. TOU is applied for purchasing and selling electricity between the regions, and the charging price for EVs is set based on TOU. The TOU is shown in Figure 7, and the charging price is shown in Figure 8.

The PV output is shown in Figure 9.

The WG output is shown in Figure 10.

The MG load curve is shown in Figure 11, and the adjustable range of the flexible load is shown in Figure 12 and Figure 13. The WG parameters and ES parameters are shown in Table 1, Table 2, Table 3, Table 4.

The comparison of the scenario settings is shown in Table 5. For scenario 1, SOP and flexible load are available. For scenario 2, SOP is available, but flexible load is not available. For scenario 3, flexible load is available, but SOP is not available. For scenario 4, flexible load and SOP are not available. The SOP parameters are shown in Table 6.

5.2 Optimization results of the DN

The operating costs for DN1 and DN2 for different scenarios are shown in Figure14 and Figure 15. For DN1, when the SOP is coordinated with flexible loads, the operating cost of DN1 is the lowest. Compared with scenario 2, the operating cost of DN1 has significantly decreased. Compared with scenario 3, due to the lack of an SOP interconnection between DN1 and DN2, there is no power interaction. These two DNs will operate independently of each other and lack collaborative assistance, which, to some extent, increases the operating cost of the DN. Comparison of scenario 2 with scenario 4 shows that due to the lack of an SOP interconnection between DN1 and DN2, the two networks are unable to interact with each other based on their operating status. The operating cost of DN1 is increased. On comparing scenario 3 with scenario 4, when the internal load of the MG can be flexibly controlled, the load can be adjusted based on TOU, and the operating cost of the DN is reduced.

The operating cost of DN2 in scenario 1 is ¥291.894 yuan higher than that of DN2 in scenario 2. The operating cost of DN2 has increased, but the operating cost of DN1 has decreased by ¥504.8324. The overall operating cost of the DN has reduced.

5.3 Optimization results of the MG

The comparison of the operating costs between MG1 and MG2 is shown in Figure 16 and Figure 17, respectively. According to Figure 16, it can be seen that the overall load of MG2 is greater than the overall load of MG1. Therefore, the operating costs of MG2 are higher than those of MG1. In scenario 2, due to the non-flexible regulation of load, the MG will purchase electricity from the DN according to the original plan during the peak load period of the DN. When the amount of load access is adjusted flexibly, MGs can adjust the time shift access of the load to reduce the operating costs and meet the demand for load access. In scenario 4, due to the lack of power interaction with the upper level DNs, MGs will increase the output power of the DEG to meet the load demand of the microgrid. When scenario 3 is adopted, the MG load can achieve time-shift access to reduce the purchase of electricity from the DN during weak DN periods and the peak time of TOU. At the same time, the power generation of DEGs is adjusted to optimize the operating costs of the MG.

The flexible load regulation curves of MG1 and MG2 are shown in Figure 18 and Figure 19, respectively. MG1 increases load during low load periods and reduces the load during peak load periods. The load fluctuations have been suppressed. The operational pressure during peak load periods has been alleviated. MG2 has a larger load access volume than that of MG1. That will be more evident in flexible load regulation. MG2 will increase load access volume during periods of low electricity prices in the DN, and MG2 will reduce load access volume during periods of high electricity prices to meet the demand for flexible loads.

6 Conclusion

In this paper, the optimization dispatching problem of DN interconnection and DN–MG systems is studied. The flexible interconnection between DNs is realized by the application of the SOP, and the optimization dispatching of the DN–MG system is realized based on flexible loads. An optimization solution method based on the ADMM is proposed, which reduces the overall operating costs of DNs and MGs, and the operational efficiency of the DN–MG system is improved.

Data availability statement

The original contributions presented in the study are included in the article/Supplementary Material; further inquiries can be directed to the corresponding author.

Author contributions

NS: conceptualization, resources, software, and writing–original draft. GY: conceptualization, methodology, project administration, writing–original draft, and writing–review and editing. XZ: funding acquisition, writing–original draft, and writing–review and editing. YL: writing–original draft and writing–review and editing. JW: writing–original draft and writing–review and editing. HZ: writing–original draft and writing–review and editing.

Funding

The author(s) declare that no financial support was received for the research, authorship, and/or publication of this article.

Conflict of interest

Authors NS, XZ, YL, JW, and HZ were employed by Chuxiong Power Supply Bureau of Yunnan Power Grid Co.

Author GY was employed by the Planning and Construction Research Center of Yunnan Power Grid Corporation, Kunming.

Publisher's note

All claims expressed in this article are solely those of the authors and do not necessarily represent those of their affiliated organizations, or those of the publisher, the editors, and the reviewers. Any product that may be evaluated in this article, or claim that may be made by its manufacturer, is not guaranteed or endorsed by the publisher.

References

Aithal, A., Li, G., Wu, J., and Yu, J. (2018). Performance of an electrical distribution network with Soft Open Point during a grid side AC fault. *Appl. Energy* 227, 262–272. doi:10.1016/j.apenergy.2017.08.152

Chen, X., Zhai, J., Jiang, Y., Ni, C., Wang, S., and Nimmegeers, P. (2023). Decentralized coordination between active distribution network and multi-microgrids through a fast decentralized adjustable robust operation framework. *Sustain. Energy, Grids Netw.* 34, 101068. doi:10.1016/j.segan.2023.101068

Ebrahimi, H., Galvani, S., Talavat, V., and Farhadi-Kangarlu, M. (2024a). Optimal parameters setting for soft open point to improve power quality indices in unbalanced distribution systems considering loads and renewable energy sources uncertainty. *Electr. Power Syst. Res.* 229, 110155. doi:10.1016/j.epsr.2024.110155

Ebrahimi, H., Galvani, S., Talavat, V., and Farhadi-Kangarlu, M. (2024b). A conditional value at risk based stochastic allocation of SOP in distribution networks. *Electr. Power Syst. Res.* 228, 110111. doi:10.1016/j.epsr.2023.110111

Ehsanbakhsh, M., and Sepasian, M. S. (2023). Bi-objective robust planning model for optimal allocation of soft open points in active distribution network: a flexibility improvement approach. *Electr. Power Syst. Res.* 224, 109780. doi:10.1016/j.epsr.2023.109780

Han, C., Cho, S., Song, S. G., and Rao, R. R. (2023). Regression model-based adaptive receding horizon control of soft open points for loss minimization in distribution networks. *Int. J. Electr. Power & Energy Syst.* 151, 109130. doi:10.1016/j.ijepes.2023.109130

Ji, H., Wang, C., Li, P., Zhao, J., Song, G., Ding, F., et al. (2017). An enhanced SOCP-based method for feeder load balancing using the multi-terminal soft open point in active distribution networks. *Appl. energy* 208, 986–995. doi:10.1016/j.apenergy.2017.09.051

Kamel, T., Tian, Z., Zangiabadi, M., Wade, N., Pickert, V., and Tricoli, P. (2022). Smart soft open point to synergically improve the energy efficiencies of the interconnected electrical railways with the low voltage grids. *Int. J. Electr. Power & Energy Syst.* 142, 108288. doi:10.1016/j.ijepes.2022.108288

Karimi, H., Gharehpetian, G. B., Ahmadiahangar, R., and Rosin, A. (2023). Optimal energy management of grid-connected multi-microgrid systems considering demand-side flexibility: a two-stage multi-objective approach. *Electr. Power Syst. Res.* 214, 108902. doi:10.1016/j.epsr.2022.108902

Li, P., Wei, M., Ji, H., Xi, W., Yu, H., Wu, J., et al. (2022c). Deep reinforcement learning-based adaptive voltage control of active distribution networks with multi-terminal soft open point. *Int. J. Electr. Power & Energy Syst.* 141, 108138. doi:10.1016/j.ijepes.2022.108138

Li, T., Han, X., Wu, W., and Sun, H. (2023a). Robust expansion planning and hardening strategy of meshed multi-energy distribution networks for resilience enhancement. *Appl. Energy* 341, 121066. doi:10.1016/j.apenergy.2023.121066

Li, Z., Sun, Y., Yang, H., Wang, S., Shen, Y., Wang, X., et al. (2023c). A multi-time scale coordinated control and scheduling strategy of EVs considering guidance impacts in multi-areas with uncertain RESs. *Int. J. Electr. Power & Energy Syst.* 154, 109444. doi:10.1016/j.ijepes.2023.109444

Li, Z. L., Li, P., Xia, J., and Yuan, Z. P. (2023b). Cyber-physical-social system scheduling for multi-energy microgrids with distribution network coordination. *Int. J. Electr. Power & Energy Syst.* 149, 109054. doi:10.1016/j.ijepes.2023.109054

Ma, X., Peng, B., Ma, X., Tian, C., and Yan, Y. (2023). Multi-timescale optimization scheduling of regional integrated energy system based on source-load joint forecasting. *Energy* 283, 129186. doi:10.1016/j.energy.2023.129186

Rezaeian-Marjani, S., Talavat, V., and Galvani, S. (2022). Impact of soft open point (SOP) on distribution network predictability. *Int. J. Electr. Power & Energy Syst.* 136, 107676. doi:10.1016/j.ijepes.2021.107676

Saboori, H., and Heshmati, Y. (2023). Novel load partitioning and prioritization for distribution restoration with storage integrated-soft open point and energy-constrained resources. *Electr. Power Syst. Res.* 214, 108947. doi:10.1016/j.epsr.2022.108947

Tabandeh, A., Hossain, M. J., and Li, L. (2022). Integrated multi-stage and multi-zone distribution network expansion planning with renewable energy sources and hydrogen refuelling stations for fuel cell vehicles. *Appl. Energy* 319, 119242. doi:10.1016/j.apenergy.2022.119242

Wang, C., Song, G., Li, P., Ji, H., Zhao, J., and Wu, J. (2016). Optimal configuration of soft open point for active distribution network based on mixed-integer second-order cone programming. *Energy Procedia* 103, 70–75. doi:10.1016/j.egypro.2016.11.251

Xu, J., Liu, J., Wu, Z., Jiang, W., and Wu, Q. (2024). Multi-area state estimation for active distribution networks under multiple uncertainties: an affine approach. *Int. J. Electr. Power & Energy Syst.* 155, 109632. doi:10.1016/j.ijepes.2023.109632

Yao, C., Zhou, C., Yu, J., Xu, K., Li, P., and Song, G. (2018). A sequential optimization method for soft open point integrated with energy storage in active distribution networks. *Energy Procedia* 145, 528–533. doi:10.1016/j.egypro.2018.04.077

Zhang, J., Foley, A., and Wang, S. (2021). Optimal planning of a soft open point in a distribution network subject to typhoons. *Int. J. Electr. Power & Energy Syst.* 129, 106839. doi:10.1016/j.ijepes.2021.106839

frontiers | Frontiers in Energy Research

TYPE Original Research
PUBLISHED 25 June 2024
DOI 10.3389/fenrg.2024.1342516

OPEN ACCESS

EDITED BY
Haifeng Qiu,
Nanyang Technological University, Singapore

REVIEWED BY
Xin Lu,
the University of Sydney, Australia
Feixiang Peng,
Anhui University, China

*CORRESPONDENCE
Xuguang Wu,
xuguang0401@163.com

RECEIVED 22 November 2023
ACCEPTED 31 May 2024
PUBLISHED 25 June 2024

CITATION
Wu X, Ye Q, Chen L, Liao H and Wang W (2024), Electricity market clearing for multiple stakeholders based on the Stackelberg game. *Front. Energy Res.* 12:1342516.
doi: 10.3389/fenrg.2024.1342516

Electricity market clearing for multiple stakeholders based on the Stackelberg game

Xuguang Wu*, Qingquan Ye, Liyuan Chen, Hongtu Liao and Wanhuan Wang

State Grid Pingyang Power Supply Company, Wenzhou, Zhejiang, China

In order to improve the operating benefits of the distribution network and reduce the energy consumption costs of small–micro-industrial parks, an electricity market clearing considering small–micro-industrial parks is proposed based on the Stackelberg game. First, an optimal operating model of multiple stakeholders is established for integrated energy suppliers, the electricity market, and small–micro-industrial parks. In this model, an optimal electricity supply model for integrated energy suppliers is established with the goal of maximizing the operating benefits. A market clearing optimization model is established for the electricity market with the goal of maximizing the social surplus profit. In addition, an energy utilization optimization model is established for the small–micro-industrial parks with the goal of minimizing the energy procurement costs. Second, with the electricity market as the leader, the integrated energy suppliers and the small–micro-industrial parks as the followers, a leader–follower game strategy is proposed based on the Stackelberg game theory to achieve the maximizing benefits for multiple stakeholders. Finally, the simulation indicates that the proposed strategy can find the best profit point during the game process and achieve a balance between supply and demand.

KEYWORDS

electricity market, multiple stakeholders, Stackelberg game, small–micro-industrial parks, distribution network

1 Introduction

In recent years, small and micro-enterprises have developed rapidly in Zhejiang Province, China. In order to facilitate the prosperous development of such enterprises, Zhejiang Province has standardized and renovated the existing small–micro-industrial parks (SMIPs) based on the actual operation. However, the SMIPs do not dispatch enough power generation and energy storage (ES) devices, which results in a low capacity to withstand the operating risks. With the rapid development of SMIPs, the demand for electricity trading between SMIPs and distribution networks (DNs) is constantly increasing. On one hand, trading electricity with the DNs can help the SMIPs withstand operating risks. On the other hand, an optimal trading electricity strategy can help the SMIPs save operating costs. Then, how to optimize the electricity trading between the DNs and SMIPs is currently a highly important issue.

As the electricity market (EM) continues to open up, operators and agents in the DNs gradually participate in the competition within the EM (He et al., 2021). As a user-side autonomous system, SMIPs can participate in power trading in the EM under the

management of operators (Davoudi and Moeini-Aghtaie, 2022), which can deepen the hierarchical structure of the EM trading framework (Pownall et al., 2021). Meanwhile, agents, as the link between SMIP operators and the EM, directly affect the energy costs of these parks. Talaeizadeh et al. (2022) explored the procurement of flexibility services in the power system by the collaboration between distribution system operators and transmission system operators. With the coordination among the operators, the flexibility sources were exploited to procure flexibility services. Anwar et al. (2022) introduced an electricity market and investment suite-agent-based simulation, which modeled the evolution of the electricity generation mix under various market structures while explicitly capturing the aforementioned investment factors and imperfect information. To improve power generation profits, Yuan et al. (2022) proposed an optimized scheduling model for cascade hydropower plants, simultaneously participating in both the day-ahead spot market and the daily contract market. Considering the characteristic that natural gas can blend with hydrogen, Ding et al. (2023) proposed a multi-agent electricity–heat–hydrogen trading model by taking hydrogen produced on the load side. Tan et al. (2022) treated carbon as a direct trading object and proposed an internal multi-energy trading mechanism, which adopts an auction based on the demands for cooling, heating, electricity, and carbon. To further explore the multi-energy coupling capacity and carbon reduction potential of the integrated energy systems, Yang et al. (2023) proposed a cooling–heat–electricity–gas collaborative optimization model of integrated energy systems given a ladder carbon trading mechanism and multi-energy demand response. Li et al. (2023) proposed a medium-term multi-stage distributionally robust optimization scheduling approach for a price-taking of hydro–wind–solar complementary systems in the EM. A multi-agent deep reinforcement learning approach combining the multi-agent actor–critic algorithm with the twin delayed deep deterministic policy gradient algorithm was proposed by Chen et al. (2022), and the proposed approach can handle the high-dimensional continuous action space and aligns with the nature of peer-to-peer energy trading. Yang et al. (2022) analyzed the impact of different bidding decisions on the distribution of wind farm revenues in a process where the interest of two markets is played against each other. Khaligh et al. (2022) introduced a stochastic agent-based model for the coordinated scheduling of multi-vector microgrids considering interactions between electricity, hydrogen, and gas agents. Considering the power loss, flexible load demand, and other operating indicators to maximize the user and supplier benefits, the real-time transaction electricity price model of the user side and the power supply side was constructed by Lyu et al. (2022). In the EM trading that SMIPs participate in, how to coordinate the benefit relationship between agents and operators (Green and Newman, 2017), increasing the profit of agents while reducing the electricity costs for the operators (Zare et al., 2015), has become a hotspot in the research direction of the EM.

In EM trading, the optimization goals of multiple stakeholders are different (Yu and Hong, 2016), but there exists a coupling relationship among the optimization models (Mahdavi et al., 2018). Finding a point of balanced benefits has become a key factor for the stability of the alliances in EM trading (Cao et al., 2021). Stackelberg game theory is frequently employed as an effective tool in solving optimization problems within the electricity market (Du et al., 2022). To solve the inherent conflict among the players, a Stackelberg game-based technique is proposed by Haghifam et al. (2020). To achieve comprehensive optimal benefits for different stakeholders, Liu et al. (2018) established a two-layer optimization model considering the involvement of different stakeholders, and the stakeholders achieve the maximization of the overall benefits by aggregating the generation units within microgrids. However, in this method, the electricity price during the trading process is a fixed time-of-use price, which cannot reflect the flexibility of EM trading. Cherukuri and Cortes (2020) proposed a bidding iterative auction mechanism in the EM but did not analyze the factors affecting the electricity price of the agents. Furthermore, the operation of the generation units can only be optimized after obtaining the market clearing results, so it has lower flexibility. A trading model based on the Stackelberg game model is proposed by Wei et al. (2022) to balance the interests of the supply side and demand side and reduce the carbon emissions. To solve the problems of environmental pollution and conflict of interests among multiple stakeholders in the integrated energy system, Wang et al. (2022) proposed a novel collaborative optimization strategy for a low-carbon economy in the integrated energy system based on the carbon trading mechanism and Stackelberg game theory. Envelope et al. (2022) proposed a Stackelberg game-based optimal scheduling model for electro–thermal integrated energy systems, which seeks to maximize the revenue of the integrated energy operator and minimize the cost of users. Pu et al. (2023) constructed a two-stage supply chain consisting of a manufacturer and a retailer based on a dual-credit policy, considering three different power structure models, namely, the vertical Nash game model, the manufacturer Stackelberg game model, and the retailer Stackelberg game model, and explored the operational strategy issues of new energy vehicle enterprises under the dual-credit policy. Zhang et al. (2022) took the integrated energy system operator as the leader and each integrated energy system as the follower to construct the Stackelberg operation model, and the proposed model is constructed and solved by the double mutation differential evolution algorithm. Hua et al. (2023) proposed a framework of local energy markets to manage this transactive energy and facilitate the flexibility provision, the decision-making, and interactions between a DN operator, and multiple microgrid traders are formulated as the Stackelberg game-theoretic problem. Fattaheian et al. (2022) applied the Stackelberg game to model the incentivizing resource scheduling optimization under post-contingency conditions, and a strong duality condition is used to re-cast the preliminary bi-level model into a one-level mathematical problem. The pricing mechanisms in existing research are mainly day-ahead fixed pricing mechanisms; as SMIP types participate in market trading in the future, fixed pricing strategies will not be able to adapt to the increasingly flexible EM. In this context, it is highly necessary to study the dynamic pricing strategies for EM trading to enhance the economic operation of the multiple stakeholders in the power system.

In light of the abovementioned strategies, an EM clearing considering SMIP is proposed based on the Stackelberg game. The main contributions of this paper are summarized as follows:

(1) To improve the DN operating benefits, as well as reduce the energy costs of SMIPs, an optimal operating model for

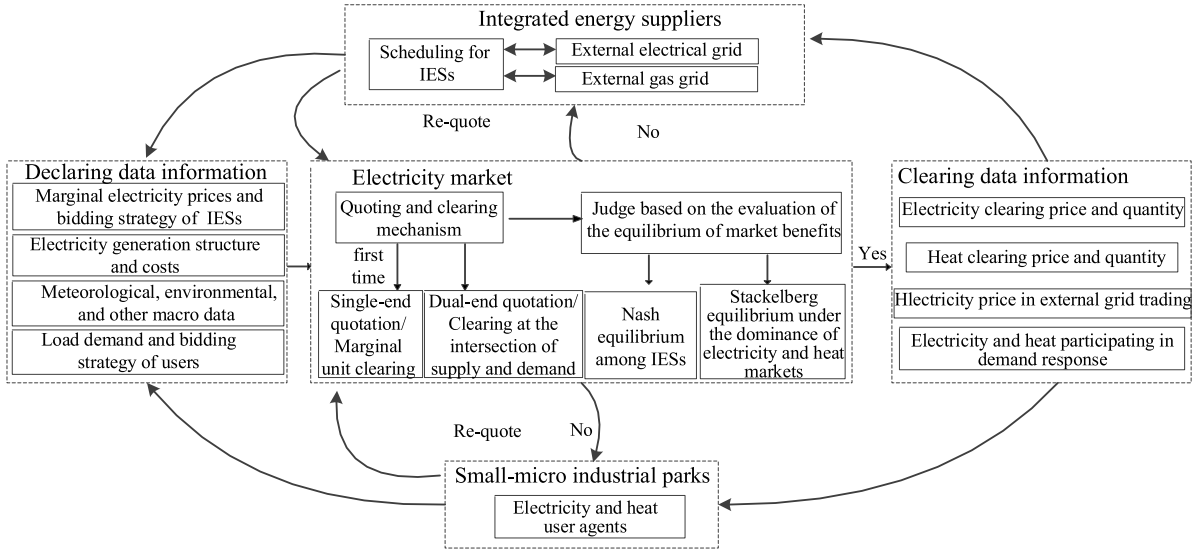

FIGURE 1
EM clearing framework.

multiple stakeholders in the EM clearing is established, which contains an optimal electricity supply model for integrated energy suppliers (IESs), a market clearing optimization model for the EM, and an energy utilization optimization model for the SMIPs.

(2) To characterize the benefit relationship among multiple stakeholders, with the EM as the leader and the IESs and SMIPs as the followers, a leader–follower game model based on the Stackelberg game is proposed to maximize the benefits for multiple stakeholders.

(3) To find the balanced benefits, an iterative optimization method is proposed to solve the leader–follower game model. In addition, by the iterative optimization among the multiple stakeholders, the best profit point during the game process can be found, and a dynamic optimal pricing strategy for EM trading is obtained.

The remainder of this paper is organized as follows: an EM clearing framework for multiple stakeholders is proposed in Section 2; an optimized operating model for multiple stakeholders in the EM clearing is introduced in Section 3; in Section 4, a leader–follower game strategy is proposed for multiple stakeholders; in Section 5, the case study is analyzed; and the conclusion is given in Section 6.

2 The EM clearing framework for multiple stakeholders

The EM clearing framework for bilateral bidding between IESs and SMIPs is shown in Figure 1. The IESs have their own scheduling strategies and market quotation–bidding strategies. The SMIPs offer quotations to the market through an agency and engage in bidding with IESs.

At the beginning of the first quotation, the IESs and SMIPs declare the prices to the market side, and then the declared prices are processed according to the quotation clearing mechanism. The price clearing data are prepared by the evaluation of the market benefits. If the equilibrium of benefits does not meet the standard, the IESs and SMIPs will carry on a re-quote based on the latest clearing results. When the equilibrium of benefits meets the standard, the final clearing data will be exported and transmitted to the IESs and SMIPs.

3 The optimal operating model for multiple stakeholders

The optimal operating model for multiple stakeholders in the EM clearing contains an optimal electricity supply model for IESs, a market clearing optimization model for the EM, and an energy utilization optimization model for the SMIPs.

3.1 The optimal electricity supply model for IESs

The electricity supply of IESs should consider the income from selling energy F_{sell}, trading costs with external electricity grids F_{util}, and various energy supply costs. The energy supply costs include the natural gas fuel cost F_{f} and the equipment maintenance cost F_{om}. The optimal electricity supply model is as follows:

$$\max F = F_{\text{sell}} - (F_{\text{f}} + F_{\text{util}} + F_{\text{om}}). \quad (1)$$

The IESs can earn profits by selling the produced electricity and heat to SMIPs. The price and power of the sold energy are obtained based on the electricity market clearing. Then, the income from selling energy F_{sell} is given as follows:

$$F_{\text{sell}} = \sum_{t=1}^{\text{T}} P_{el}(t) C_e(t) + \sum_{t=1}^{\text{T}} Q_{hl}(t) C_h(t), \tag{2}$$

where $P_{el}(t)$ and $Q_{hl}(t)$ represent the electricity power and heat power, respectively, at time t under the response to the demand of the SMIPs. $C_e(t)$ and $C_h(t)$ represent the electricity prices and heat prices, respectively, at time t cleared by the EM. T represents the optimization time.

IESs can arbitrage through trading with external grids. When the electricity price of the power grid is low, the IESs purchase the electricity and sell electricity when its price is high, and then the profits can be obtained. The trading costs with the external electricity grid F_{util} is given as follows:

$$F_{\text{util}} = \sum_{t=1}^{\text{T}} P_{util}(t) C_{util}(t), \tag{3}$$

where $P_{util}(t)$ is the interactive power between the IESs and the external electricity grid at time t. When $P_{util}(t) > 0$, it means that the IESs purchase electricity from the external electricity grid. When $P_{util}(t) < 0$, it means that the IESs sell electricity from the external electricity grid. $C_{util}(t)$ is the interactive electricity price between the IESs and the external electricity grid at time t.

The energy provided by IESs is divided into two categories. The first category is wind turbines (WTs) and photovoltaic (PV) power generation, and this type of energy does not need to be purchased. The second category is gas turbines and gas boilers, which burn natural gas to generate electricity and heat, respectively. For this category, the purchasing cost of natural gas needs to be included in the cost, which is called fuel cost. The fuel cost F_{f} is given as follows:

$$F_f = \frac{C_{gas}}{L} \cdot \sum_{t=1}^{\text{T}} \left[\frac{P_{GT}(t)}{\eta_{GT}} + \frac{Q_{GB}(t)}{\eta_{GB}} \right], \tag{4}$$

where C_{gas} is the price of natural gas and L is the low calorific value of natural gas, which represents the heat released by burning a certain volume of natural gas. $P_{GT}(t)$ and $Q_{GB}(t)$ represent the output powers of the gas turbine and gas boiler at time t, respectively. η_{GT} and η_{GB} represent the efficiencies of the gas turbine and gas boiler, respectively.

The distributed energy equipment in the system needs maintenance, and the equipment maintenance cost F_{om} is given as follows:

$$F_{om} = \sum_{i=1}^{\text{I}} \sum_{t=1}^{\text{T}} \xi_i^S P_{DGi}(t), \tag{5}$$

where I is the number of power generation equipment. ξ_i^S is the cost coefficient of the *ith* power generation equipment. $P_{DGi}(t)$ represents the supply power of the *ith* power generation equipment at time t. In the IES optimization model, the constraints of various parameters are given as follows:

(1) Constraints on electricity and heat power balance

$$P_{el}(t) = \sum_{i=1}^{\text{I}} P_{DGi}(t) + P_{GT}(t) + P_{util}(t), \tag{6}$$

$$P_{el}(t) = L_e(t) + P_{EDR}(t), \tag{7}$$

$$Q_{hl}(t) = Q_{WH}^{out}(t) + Q_{GB}^{h}(t), \tag{8}$$

$$Q_{hl}(t) = L_h(t) + Q_{HDR}(t). \tag{9}$$

Formulas 6, 7 are the constraints on electricity power balance, and Formulas 8, 9 are the constraints on heat power balance. $L_e(t)$ and $L_h(t)$ represent the original electricity and heat loads of SMIPs at time t, respectively. $Q(t)$ is the heat power recovered from the gas boiler at time t. $P_{EDR}(t)$ and $Q_{eHDR}(t)$ represent the electricity and heat load responding to the demand of SMIPs at time t, respectively.

(2) Constraints on the output of distributed energy generation equipment

$$P_{DGi,\min} \le P_{DGi}(t) \le P_{DGi\max}, \tag{10}$$

where $P_{i\ \min}(t)$ and $P_{i\ \max}(t)$ represent the upper and lower limits of the power of the *ith* distributed energy equipment, respectively.

(3) Constraints on the power exchange with the external electricity grid

$$P_{\max}^{sell} \le P_{util}(t) \le P_{\max}^{buy}, \tag{11}$$

where $P_{\max}^{sell}$ and $P_{\max}^{buy}$ are the upper limits of the power sold to and bought from the external electricity grid by the IESs, respectively.

(4) Constraints on the power of energy equipment participating in the electricity market clearing

$$P_{k,e}^{'}(t) \le P_{k,e}(t), \tag{12}$$

$$Q_{s,h}^{'}(t) \le Q_{s,h}(t), \tag{13}$$

where $P_{k,e}^{'}(t)$ and $Q_{s,h}^{'}(t)$ represent the powers cleared in the EM for each electric and thermal unit at time t, respectively. $P_{k,e}(t)$ and $Q_{s,h}(t)$ represent the actual power generated by each electric and thermal unit at time t, respectively.

3.2 The energy utilization optimization model for the SMIPs

The energy utilization optimization model of SMIPs takes minimizing the energy purchase cost as the objective function. In addition to paying the energy purchase fee F_{sell} to the IESs, SMIPs can also obtain income compensation F_{DR} by reducing a certain amount of load through demand response. Therefore, the objective function is established as follows:

$$\min F_{user} = F_{sell} - F_{DR}, \tag{14}$$

$$F_{sell} = \sum_{t=1}^{\text{T}} [L_e(t) + P_{EDR}(t)] \cdot C_e(t) + \sum_{t=1}^{\text{T}} [L_h(t) + Q_{HDR}(t)] \cdot C_h(t), \tag{15}$$

$$F_{DR} = \sum_{t=1}^{\text{T}} [v_e P_{EDR}(t)] + \sum_{t=1}^{\text{T}} [v_h Q_{HDR}(t)], \tag{16}$$

where v_e and v_h represent the reduction compensation coefficients for the electricity and heat demand response of

SMIPs, respectively. For the demand response to SMIPs, various constraints need to be considered as follows:

(1) Constraints on the income of SMIPs

The benefits of users after demand response F_{user}^{DR} should be greater than the benefits before the response F_0. The mathematical formula is

$$F_{user}^{DR} \geq F_0. \tag{17}$$

(2) Constraints on the power of load transfer

During the optimization process, the SMIPs can participate in price-based demand response. Thus, the power of electricity and heat load transfer cannot exceed the limit value ${P_{EDR}}^{max}$ and ${Q_{HDR}}^{max}$. The mathematical formula is

$$P_{EDR}(t) \leq P_{EDR}^{\max}, \tag{18}$$

$$Q_{HDR}(t) \leq Q_{HDR}^{\max}. \tag{19}$$

3.3 The market clearing optimization model for the EM

The EM aims at maximizing the social surplus profit, which reflects the balance of benefits between the supply and demand. The maximum social surplus profit in this paper consists of the profit surplus of IESs and profit surplus of the users. The objective function of the model is established as follows:

$$\max H = \sum_{t=1}^{T} [H_{emo}(t) + H_{user}(t)], \tag{20}$$

$$H_{emo}(t) = \sum_{k=1}^{K} \left[(C_e(t) - C_{e,\min}(t)) P'_{k,e}(t) \right] + \sum_{s=1}^{S} \left[(C_h(t) - C_{h,\min}(t)) Q'_{s,h}(t) \right], \tag{21}$$

where $H_{emo}(t)$ and $H_{user}(t)$ represent the surplus profits of the IESs and the surplus profits of SMIPs at time t, respectively. K represents the number of electricity power generation equipment. S represents the number of heat power generation equipment. $C_{e,\min}(t)$ and $C_{h,\min}(t)$ represent the lower limits of the electricity and heat bidding prices of the IESs, respectively. $C_{e,\max}(t)$ and $C_{h,\max}(t)$ represent the upper limits of electricity and heat bidding prices of SMIPs, respectively.

The price and power of the electricity and heat cleared by the EM need to be constrained to ensure that the clearing data are within a reasonable range. The formulas are as follows:

$$P'_{e,\min}(t) \leq P'_e(t) \leq P'_{e,\max}(t), \tag{22}$$

$$Q'_{h,\min}(t) \leq Q'_h(t) \leq Q'_{h,\max}(t), \tag{23}$$

$$C_{e,\min}(t) \leq C_e(t) \leq C_{e,\max}(t), \tag{24}$$

$$C_{h,\min}(t) \leq C_h(t) \leq C_{h,\max}(t), \tag{25}$$

where $P'_{k.e}(t)$ represents the electricity power cleared by the EM. $Q'_{s.h}(t)$ represents the heat power cleared by the EM. $P'_{e,\min}(t)$ represents the essential need of electricity load. $Q'_{s.h}(t)$ represents the essential need of heat load. $P'_{e,\max}(t)$ represents the electricity load after the demand response. $Q'_{h,\max}(t)$ represents the heat load after the demand response. To solve the proposed optimal electricity supply model for IESs, the energy utilization optimization model for the SMIPs, and the market clearing optimization model for the EM, an improved particle swarm optimization algorithm (Xiao et al., 2017) is utilized to conduct the optimization.

4 The leader–follower game strategy for the multiple stakeholders

4.1 The leader–follower game model for the multiple stakeholders

To characterize the benefit relationship among multiple stakeholders, a leader–follower game model based on the Stackelberg game is proposed in this paper to maximize benefits for multiple stakeholders. In the proposed leader–follower game mode, there are three stakeholders: the EM, SMIPs, and the IESs. The EM is the leader in the game, while the SMIPs and IESs are followers. The SMIPs and the IESs respond to the decisions of the EM and adjust the strategy according to their objective functions. The EM aims to maximize social surplus profits, and the strategy set includes clearing electricity power, heat power, and energy prices to the SMIPs and the IESs. The IESs aim to maximize operating benefits, and the strategy set includes energy equipment output, external grid trading amount, and energy storage management. The SMIPs aim to minimize energy procurement costs, and the strategy set includes the electricity loads for the demand response and heat loads for the demand response. The interactive framework of the leader–follower game is shown in Figure 2.

For the Stackelberg equilibrium of a non-cooperative game, when Eq. 26 is satisfied, it indicates that the game has reached equilibrium. At this point, the followers make the best response according to the strategy of the leader. In addition, each stakeholder cannot obtain more profits by changing their own strategy set.

$$\begin{cases} E_{mar}[I_{mar}, F^*_{emo}, L^*_{user}] \leq E_{mar}[I^*_{mar}, F^*_{emo}, L^*_{user}] \\ E_{user}[I^*_{mar}, F_{emo}, L^*_{user}] \leq E_{user}[I^*_{mar}, F^*_{emo}, L^*_{user}] \\ E_{emo}[I^*_{mar}, F^*_{emo}, F_{emo}] \leq E_{emo}[I^*_{mar}, F^*_{emo}, F^*_{emo}] \end{cases}, \tag{26}$$

where E_{mar} represents the profits of the EM. E_{user} represents the profits of the SMIPs. E_{emo} represents the profits of the IESs. L_{user}, F_{emo}, and I_{mar} represent the strategy sets for the SMIPs, the IESs, and the EM, respectively. L^*_{user}, F^*_{emo}, and I^*_{mar} represent the optimal strategy sets for the SMIPs, the IESs, and the EM, respectively.

4.2 The solution process of the proposed method

To solve the proposed method, an iteration search method proposed by Chuang et al. (2001) is employed to find the Nash equilibrium point. The solution of the proposed scheduling model is summarized as follows:

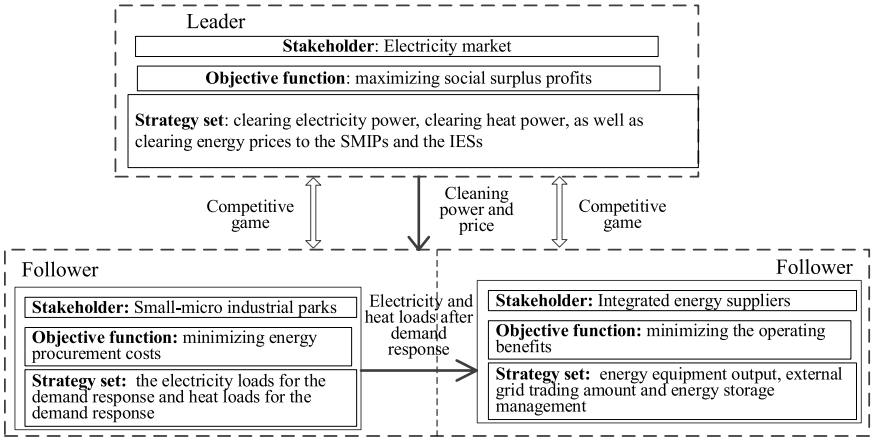

FIGURE 2
Leader–follower game interaction framework.

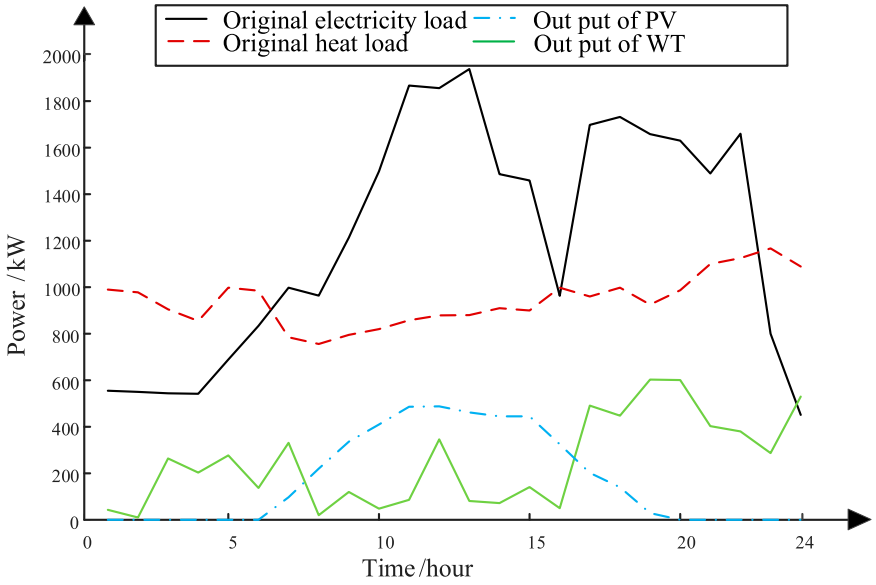

FIGURE 3
Loads and renewable energy outputs.

Step 1. The strategies of all the stakeholders are initialized as $\mathbf{D}^{old} = [I^0_{mar}, L^0_{user}, E^0_{emo}]$, and the profits of all stakeholders are calculated as $\mathbf{F}^{old} = [E^0_{mar}, E^0_{user}, E^0_{emo}]$.

Step 2. The scheduling model for each stakeholder is solved based on the exchanged game strategies from other stakeholders.

Step 3. The game strategy of each stakeholder is updated as $\mathbf{D}^{new} = [I^1_{mar}, L^1_{user}, F^1_{emo}]$, and the operating cost of all stakeholders is calculated as $\mathbf{F}^{new} = [E^1_{mar}, E^1_{user}, E^1_{emo}]$.

Step 4. The operating cost difference of $\mathbf{F}^{new}$ and $\mathbf{F}^{old}$ is calculated. If the cost difference is smaller than its threshold, the procedure is terminated, and the new strategies $\mathbf{D}^{new}$ is output. Otherwise, $\mathbf{D}^{old}$ is reset as $\mathbf{D}^{new}$, and Step 2 onwards is repeated.

5 Case study

5.1 Basic data of the case study

This paper conducted a simulation analysis of the day-ahead EM clearing with SMIPs as an example. The WT and PV forecast data, as well as the electricity and heat load power of users, are shown in Figure 3. Table 1 shows the time-of-use energy prices of the electricity and gas grids. Table 2 shows the parameters for IESs and SMIPs.

TABLE 1 Time-of-use energy price for electricity and gas grids.

Time	Trading price with the electricity grid/¥	Trading price with the heat grid/¥
1:00–7:00	0.38	0.21
8:00–10:00 and 23:00–24:00	0.85	0.33
11:00–22:00	1.32	0.41

TABLE 2 Parameters of the IESs and SMIPs.

Equipment type	Parameter	Value	Equipment type	Parameter	Value
Gas turbine	Maximum output power	1,000 kW	Gas boiler	Heating efficiency	0.89
	Minimum output power	50 kW		Maintenance costs	0.023 kW/¥
	Electricity generation efficiency	0.3	PV	Rated power	500 kW
	Heat generation efficiency	0.345		Maintenance costs	0.03 kW/¥
	Maintenance costs	0.025 kW/¥	WT	Rated power	600 kW
Gas boiler	Rated power	200 kW		Maintenance costs	0.035 kW/¥

TABLE 3 Comparison of the three scenarios.

Scenario	Social surplus profit/¥	Profit of the IES/¥	Cost of SMIP/¥	Operation and maintenance costs of each unit/¥	Energy storage scheduling cost/¥
1	5,642	3,631	8,021	1,034	1,615
2	6,354	3,171	7,365	996	1,170
3	8,324	4,886	6,832	728	665

In order to analyze the advantages of the proposed method, three scenarios are set up. In scenario 1, the objective function of the operation is maximizing the profits of IESs, electricity and heat prices are fixed, and users do not participate in the demand response. In scenario 2, the objective function of the operation is still maximizing the profits of IESs, but the user side will actively respond according to the change in energy prices. In scenario 3, the EM, IES, and SMIP carry out the operation with the proposed strategy of this paper, and the power and price of energy are determined by market clearing through market-side quoting and bidding.

5.2 Analysis of the case study

Table 3 shows the operation results of the three scenarios. It shows that under the proposed method, there have been varying degrees of improvement in social surplus profits, profits of the IESs, and profits of the SMIPs, with the most notable increase in social surplus profits.

Compared to scenario 1, in scenario 2, the social surplus increase in the profits of the IES decrease slightly, and the energy purchase costs for SMIPs decrease significantly. This is because through price-based demand response, the user side can peak-shave and valley-fill to smooth the electricity and heat load curves, thereby obtaining extra compensation benefits. As the load demand curve becomes smoother, the arbitrage space obtained by IESs through energy storage will be correspondingly reduced, leading to a decrease in profits. As the load demand becomes flat, the marginal cost of the energy equipment output is reduced, and the social surplus profits increase. In scenario 3, the profits of all stakeholders increase significantly, and the energy purchase costs of SMIPs have been reduced. This is because under the guidance of the EM mechanism, the energy trading price between IESs and SMIPs is determined based on the clearing of the supply and demand relationship at each moment. Thus, the price can better reflect the degree of energy surplus or scarcity within the SMIPs. The proposed method can also increase efficiency in energy storage arbitrage and trading with the external electricity grid, as well as improve the precision of user demand response.

Figure 4 shows the convergence diagram of profits for each stakeholder in scenario 3. It well reflects the game process between various stakeholders throughout the entire iteration process, and finally, equilibrium is achieved at about 80 iterations, which takes 16.3 min. In the game process, the declared energy power and prices from other stakeholders are constantly cleared by the EM. In addition, the EM, as the leader in the entire game process, shows a gradual upward trend in its profits. The SMIPs and IESs adjust their own strategy sets continuously and rationally based on the clearing results of the EM. The SMIPs and IESs, as followers, also engage in game interaction at the same time and finally reach

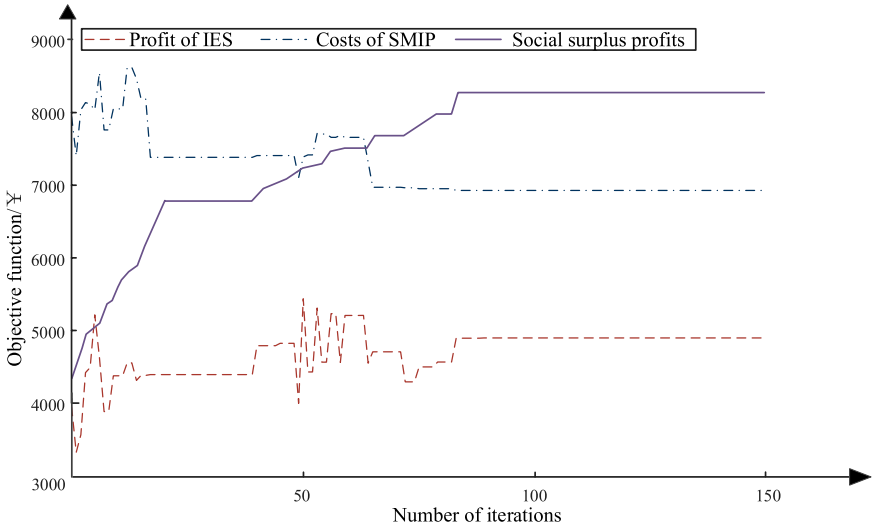

FIGURE 4
Convergence diagram of profits for each stakeholder.

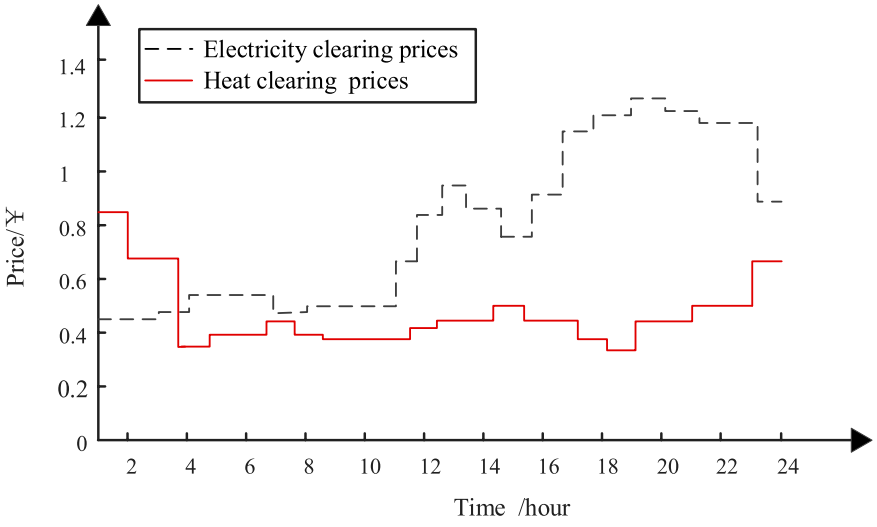

FIGURE 5
Energy clearing prices.

convergence. When the leader and two followers reach the Stackelberg equilibrium, their strategy sets no longer change.

The energy clearing prices are shown in Figure 5. The electricity clearing price in the EM peaks from 18:00 to 22:00. During this period, the PV output is low, and the demand for electricity load is high. To meet the demand, the IES will utilize more gas turbines. At the same time, the gas turbines have the highest marginal cost among all units, so their prices are the highest. Meanwhile, the demand response from the SMIPs is low, and the electric load demand curve is flat. Therefore, the EM will clear the electricity generated by gas turbines at high prices. The heat clearing price in the EM shows a significant peak from 00:00 to 04:00. Therefore, during this period, the output of gas boilers needs to be scheduled to meet the heat needs of the SMIPs. The cost of gas boilers is higher than that of other heat sources, so the heat clearing price in the EM shows a short-term peak.

Figure 6 shows the comparison of the before and after demand response of the SMIPs under the proposed strategy. It indicates that the fluctuations in electricity and heat loads have been significantly reduced, and the effects of peak-shaving and valley-filling are obvious. SMIPs respond more accurately to the energy price in the EM clearing, which brings a lot of hidden benefits to the DN. After the demand response, the electricity and heat load curves are smoothed within an appropriate range, and the energy purchase costs on the user side are reduced. At the same time, the energy supply pressure of the IESs is eased.

The final optimized electricity and heat power of the IESs are shown in Figures 7, 8. According to the following optimization

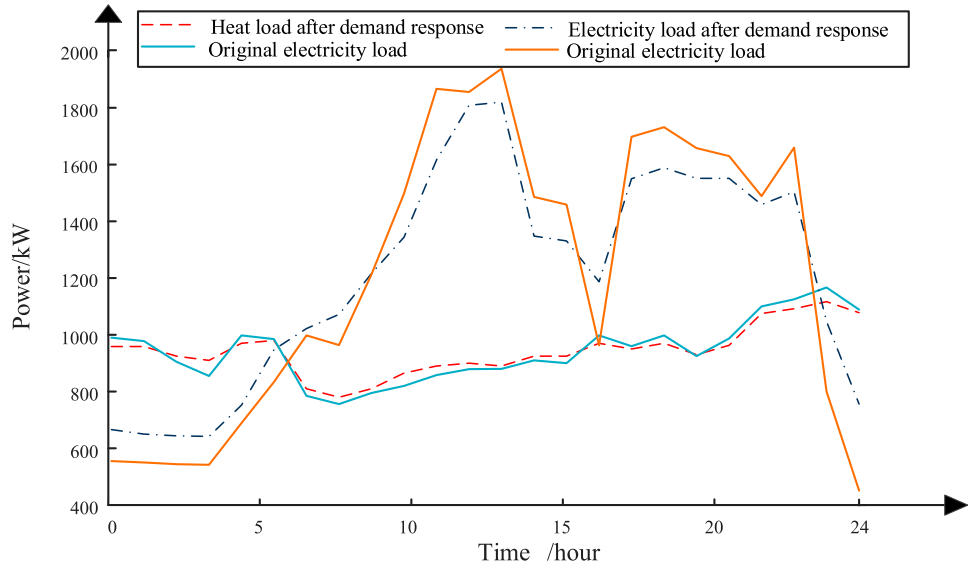

FIGURE 6
Demand response of SMIPs.

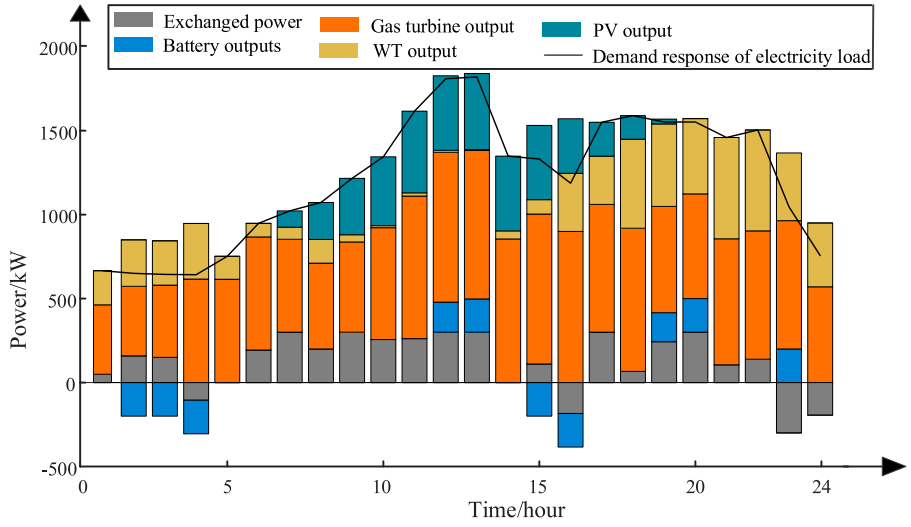

FIGURE 7
Optimized electricity power of the integrated energy supplier.

results, several key time periods with obvious characteristics are analyzed:

1) From 0:00 to 9:00, the electric load demand is low. During this period, the electricity clearing price of the EM is low, so the SMIPs follow the price-based demand response and increase electricity usage when the electricity price is low. The output of the WT is relatively high, and only a minimal amount of gas turbine output is needed to supplement the electricity supply alongside the WT. At the same time, the energy prices of the upper-layer electricity and gas grids are relatively low. Therefore, with the complete consumption of the WT, the IESs can use a small amount of gas turbine power while purchasing electricity from the external electricity grid. Then, the electrical energy is stored under the premise of meeting the electrical load demand.
2) From 10:00 to 13:00, the electricity load demand is at its peak. During this period, the electricity clearing price in the EM is relatively high, so the SMIPs follow a price-based demand response and reduce electricity consumption. The output of the PV increases, the output of the WT is very low, and the output of gas turbines needs to be increased to meet the electrical load. At the same time, the energy prices of the electricity and gas grids are relatively high. With the complete consumption of the WT, the IESs need to increase the output of the gas turbines to meet the load demand. If the load

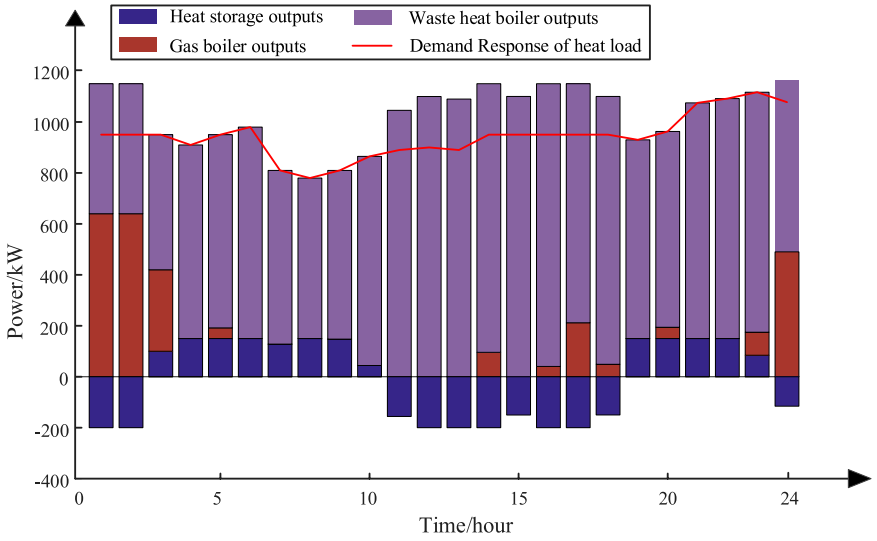

FIGURE 8
Optimized heat power of the IESs.

demand failed to be met, electricity needs to be purchased from the external electricity grid, and the battery power is released to complete the supply.

3) From 17:00 to 22:00, the electricity and heat load demands are both high. During this period, the electricity and heat clearing prices in the EM are relatively high, so users follow a price-based demand response and reduce electricity and heat usage. The outputs of the WT are very high, the outputs of the PV decreased significantly, and the output of the gas turbines needs to be increased to meet the electrical load demand. The heat outputs of the waste heat boiler are relatively high and can basically meet the heat load demands of SMIPs. During this period, the energy prices of the electricity and gas grids are both relatively high. Therefore, with the complete consumption of the WT, IESs can choose to increase the output of gas turbines to meet the electrical load demand. If the load demand is still unable to be met, electricity needs to be purchased from the external electricity grid, and the battery power is released to complete the electric load supply.

6 Conclusion

In order to improve the flexibility of SMIPs to participate in market trading, a Stackelberg game-based EM clearing is proposed for multiple stakeholders in DNs. First, an optimal operating model for multiple stakeholders is established, which contains an optimal electricity supply model for the IES, a market clearing optimization model for the EM, and an energy utilization optimization model for the SMIPs. With the EM as the leader, and the IESs and the SMIPs as the followers, a leader–follower game model is proposed to achieve the maximizing benefits for multiple stakeholders. Finally, an iterative optimization method is proposed to find a point of balanced benefits of multiple stakeholders. The proposed strategy can enhance the benefits of all participating stakeholders and achieve a balance between supply and demand. It should be noted that the uncertainty of WTs, PVs, and loads in the operation is not considered. In the future, considering the uncertainty, the real-time quoting and clearing will be conducted in the EM.

Data availability statement

The original contributions presented in the study are included in the article/Supplementary Material; further inquiries can be directed to the corresponding author.

Author contributions

XW: writing–original draft. QY: writing–review and editing. LC: writing–review and editing. HL: writing–review and editing. WW: writing–review and editing.

Funding

The authors declare that financial support was received for the research, authorship, and/or publication of this article. The study in this paper was supported by the project supported by Zhejiang Electric Power Industry Corporation Technology Project (CF058810002022001).

Conflict of interest

Authors XW, QY, LC, HL, and WW were employed by State Grid Pingyang Power Supply Company.

The authors declare that this study received funding from the Zhejiang Electric Power Industry Corporation. The funder had the following involvement in the study design, collection, analysis, the writing of this article.

Publisher's note

References

Anwar, B., Stephen, G., Dalvi, S., Frew, B., Ericson, S., Brown, M., et al. (2022). Modeling investment decisions from heterogeneous firms under imperfect information and risk in wholesale electricity markets. *Appl. Energy* 306, 117908. doi:10.1016/j.apenergy.2021.117908

Cao, S., Zhang, H., Cao, K., Chen, M., Wu, Y., and Zhou, S. (2021). Day-ahead economic optimal dispatch of microgrid cluster considering shared energy storage system and P2P transaction. *Front. Energy Res.* 9 (9), 645017. doi:10.3389/fenrg.2021.645017

Chen, T., Bu, S., Liu, X., Kang, J., Yu, F. R., and Han, Z. (2022). Peer-to-peer energy trading and energy conversion in interconnected multi-energy microgrids using multi-agent deep reinforcement learning. *IEEE Trans. Smart Grid* 13 (1), 715–727. doi:10.1109/tsg.2021.3124465

Cherukuri, A., and Cortes, J. (2020). Iterative bidding in electricity markets: rationality and robustness. *IEEE Trans. Netw. Sci. Eng.* 7 (3), 1265–1281. doi:10.1109/tnse.2019.2921056

Chuang, A., Wu, F., and Varaiya, P. (2001). A game-theoretic model for generation expansion planning: problem formulation and numerical comparisons. *IEEE Power Eng. Rev.* 21 (10), 63. doi:10.1109/mper.2001.4311103

Davoudi, M., and Moeini-Aghtaie, M. (2022). Local energy markets design for integrated distribution energy systems based on the concept of transactive peer-to-peer market. *IET Generation, Transm. Distribution* (1), 16. doi:10.1049/gtd2.12274

Ding, J., Gao, C., Song, M., Yan, X., and Chen, T. (2023). Optimal operation of multi-agent electricity-heat-hydrogen sharing in integrated energy system based on Nash bargaining. *Int. J. Electr. Power Energy Syst.* 148 (6), 108930. doi:10.1016/j.ijepes.2022.108930

Du, X., Li, X., Hao, Y., and Chen, L. (2022). Sizing of centralized shared energy storage for resilience microgrids with controllable load: a bi-level optimization approach. *Front. Energy Res.* 10 (10), 954833. doi:10.3389/fenrg.2022.954833

Envelope, L., Envelope, R., Envelope, Y., and Xu, C. (2022). Stackelberg game-based optimal scheduling of integrated energy systems considering differences in heat demand across multi-functional areas. *Energy Rep.* 8, 11885–11898. doi:10.1016/j.egyr.2022.08.199

Fattaheian, S., Tavakkoli, M., Abbaspour, A., Fotuhi-Firuzabad, M., and Lehtonen, M. (2022). Optimal energy management of distribution networks in post-contingency conditions. *Int. J. Electr. Power Energy Syst.* 141 (11), 108022. doi:10.1016/j.ijepes.2022.108022

Green, J., and Newman, P. (2017). Citizen utilities: the emerging power paradigm. *Energy Policy* 105, 283–293. doi:10.1016/j.enpol.2017.02.004

Haghifam, S., Zare, K., Abapour, M., Muñoz-Delgado, G., and Contreras, J. (2020). A Stackelberg game-based approach for transactive energy management in smart distribution networks. *Energies* 13 (14), 3621. doi:10.3390/en13143621

He, C., Tang, J., Zhang, W., Zhang, Z., Lin, Z., Li, Y., et al. (2021). Optimal planned electricity allocation model for power exchange under the plan-market double-track mechanism. *Front. Energy Res.* 9 (9), 679365. doi:10.3389/fenrg.2021.679365

Hua, W., Xiao, H., Pei, W., et al. (2023). Transactive energy and flexibility provision in multi-microgrids using Stackelberg game. *CSEE J. Power Energy Syst.* 9 (2), 505–515. doi:10.17775/CSEEJPES.2021.04370

Khaligh, V., Ghezelbash, A., Mazidi, M., Liu, J., Ryu, J. H., and Na, J. (2022). A stochastic agent-based cooperative scheduling model of a multi-vector microgrid including electricity, hydrogen, and gas sectors. *J. Power Sources* 546 (10), 231989–232014. doi:10.1016/j.jpowsour.2022.231989

Li, Z., Yang, P., Guo, Y., and Lu, G. (2023). Medium-term multi-stage distributionally robust scheduling of hydro–wind–solar complementary systems in electricity markets considering multiple time-scale uncertainties. *Appl. Energy* 347, 121371. doi:10.1016/j.apenergy.2023.121371

Liu, Y., Guo, L., and Wang, C. (2018). Economic dispatch of microgrid based on two stage robust optimization. *Proc. CSEE* 38 (14), 4013–4022. doi:10.13334/j.0258-8013.pcsee.170500

Lyu, Z., Lai, Y., Yang, X., Li, Y., and Yi, J. (2022). Cooperative game consistency optimal strategy of multi-microgrid system considering flexible load. *Energy Sources.* 44 (3), 7378–7399. doi:10.1080/15567036.2022.2109779

Mahdavi, S., Hemmati, R., and Jirdehi, M. (2018). Two-level planning for coordination of energy storage systems and wind-solar-diesel units in active distribution networks. *Energy* 151, 954–965. doi:10.1016/j.energy.2018.03.123

Pownall, T., Soutar, I., and Mitchell, C. (2021). Re-designing GB's electricity market design: a conceptual framework which recognises the value of distributed energy resources. *Energies* 14 (4), 1124. doi:10.3390/en14041124

Pu, J., Chun, W., Wang, Z., and Chen, W. (2023). Operation strategy for new energy vehicle enterprises based on dual credit policy. *J. Industrial Manag. Optim.* 19 (8), 5724–5748. doi:10.3934/jimo.2022192

Talaeizadeh, V., Aghaei, J., and Shayanfar, H. (2022). Day-ahead flexibility market clearing mechanism for interactive collaboration of transmission and distribution system operators. *IET Generation, Transm. Distribution* 16 (13), 2587–2599. doi:10.1049/gtd2.12474

Tan, J., Li, Y., and Zhang, X. (2022). Optimization and trading of district multi-energy system in university community considering carbon emission. *Int. J. Electr. Power Energy Syst.* 137 (5), 107450. doi:10.1016/j.ijepes.2021.107450

Wang, R., Cheng, S., Zuo, X., and Liu, Y. (2022). Optimal management of multi stakeholder integrated energy system considering dual incentive demand response and carbon trading mechanism. *Int. J. Energy Res.* 46 (5), 6246–6263. doi:10.1002/er.7561

Wei, M., Deng, Y., Long, M., Wang, Y., and Li, Y. (2022). Transaction model based on Stackelberg game method for balancing supply and demand sides of multi-energy microgrid. *Energies* 15 (4), 1362–1420. doi:10.3390/en15041362

Xiao, C., Zhao, B., Ding, M., Li, Z., and Ge, X. (2017). Zonal voltage control combined day-ahead scheduling and real-time control for distribution networks with high proportion of PVs. *Energies* 10 (10), 1464. doi:10.3390/en10101464

Yang, M., Liu, Y., Lund, H., et al. (2023). Research on multi-energy collaborative operation optimization of integrated energy system considering carbon trading and demand response. *Energy* 283, 129117. doi:10.1016/j.energy.2023.129117

Yang, X., Fan, L., Gao, X., and Liu, H. (2022). Analysis of wind farm participation in frequency regulation considering multi-market interests. *J. Renew. Sustain. Energy* 14 (1), 013304. doi:10.1063/5.0073140

Yu, M., and Hong, S. H. (2016). Supply–demand balancing for power management in smart grid: a Stackelberg game approach. *Appl. Energy* 164, 702–710. doi:10.1016/j.apenergy.2015.12.039

Yuan, W., Zhang, S., Su, C., Wu, Y., Yan, D., and Wu, Z. (2022). Optimal scheduling of cascade hydropower plants in a portfolio electricity market considering the dynamic water delay. *Energy* 252, 124025. doi:10.1016/j.energy.2022.124025

Zare, K., Abapour, S., and Mohammadi-Ivatloo, B. (2015). Dynamic planning of distributed generation units in active distribution network. *Generation Transm. Distribution Iet* 9 (12), 1455–1463. doi:10.1049/iet-gtd.2014.1143

Zhang, Y., Zhao, H., Li, B., and Wang, X. (2022). Research on dynamic pricing and operation optimization strategy of integrated energy system based on Stackelberg game. *Int. J. Electr. Power Energy Syst.* 143 (12), 108446. doi:10.1016/j.ijepes.2022.108446

frontiers | Frontiers in Energy Research

TYPE Original Research
PUBLISHED 14 August 2024
DOI 10.3389/fenrg.2024.1387670

OPEN ACCESS

EDITED BY
Hao Wang,
Monash University, Australia

REVIEWED BY
Xiangmin Xie,
Qingdao University, China
Yi Liu,
Tiangong University, China

*CORRESPONDENCE
Xingjian Zhao,
202134949@mail.sdu.edu.cn

RECEIVED 18 February 2024
ACCEPTED 12 June 2024
PUBLISHED 14 August 2024

CITATION
Li Y, Li Y, Zhao X, Gao F and Xu T (2024), An adaptive power control method for soft open points based on virtual impedance.
Front. Energy Res. 12:1387670.
doi: 10.3389/fenrg.2024.1387670

An adaptive power control method for soft open points based on virtual impedance

Yan Li[1], Yang Li[1], Xingjian Zhao[2]*, Feng Gao[2] and Tao Xu[2]

[1]State Grid Intelligence Technology Co., Ltd., Jinan, China, [2]School of Control Science and Engineering, Shandong University, Jinan, China

The fluctuations in power output from distributed power sources are rapid and dramatic, causing voltage fluctuations in the distribution network that threaten the safety of electricity consumption. Soft open points (SOPs) can replace traditional contact switches and are expected to suppress voltage fluctuations. However, traditional power regulation methods based on the reference values are unable to address rapid and large voltage fluctuations. Therefore, this paper proposes an adaptive power control method for SOPs based on virtual impedance. The SOP is modeled as a series link of adjustable impedance and a voltage source. Then, the voltage difference component is used to calculate the reference for the DQ domain to regulate the power flow in real time automatically. By doing so, the proposed method can smooth the voltage fluctuations in the distribution network. Additionally, the virtual impedance is also optimized to minimize the power loss. Finally, the method is validated through simulation and experiments, demonstrating that this method can automatically regulate power and significantly reduce voltage fluctuations.

KEYWORDS

soft open point, virtual impedance, adaptive power control, voltage fluctuations, PSO

1 Introduction

At present, wind power and solar power are representatives of the rapid development of distributed generation (DG) and have several points of access to the distribution network to help realize the effective measures for the carbon peak and neutrality targets. However, the large and rapid fluctuations in the output of DG lead to rapid and drastic voltage fluctuations in the distribution network, which seriously threatens the safety of electricity consumption (Bloemink and Green, 2013; Ren, 2021).

In order to realize effective control of rapid power and voltage fluctuations, a variety of new power electronic devices represented by soft open points (SOPs) have been rapidly developed and widely used in the optimized operation and scheduling of active distribution networks and have achieved good results. An SOP is an emerging piece of power electronic equipment, and it can replace the tie switch in the traditional distribution network. SOPs can significantly enhance the traditional distribution network's connection situation, expanding its operational capabilities beyond simple on and off states. Moreover, SOPs can also improve the traditional contact switch work casting process that leads to power failure and closing impact situation (Yang Huan, 2018). By placing the SOP in the distribution network, power mutualization between different feeders is realized, while the disadvantage of the lack of isolation between feeders is eliminated (Bloemink and Green, 2010; Wang, 2017). Its connection in the distribution network is shown in Figure 1.

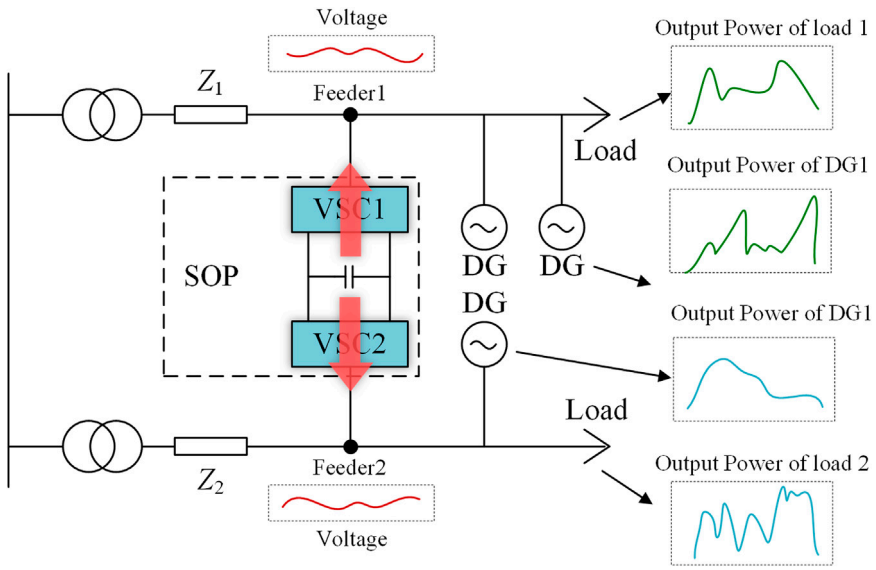

FIGURE 1
Simplified schematic diagram of the distribution network with SOPs.

DG is the distributed power source connected to the distribution grid, and Z_1 and Z_2 are the line impedance of the distribution grid. The distribution grid above the SOP is defined as the feeder 1 system, and the distribution grid below the SOP is defined as the feeder 2 system. As shown in Figure 1, the power fluctuations of the load and the DG cause the voltage on feeder 1 and feeder 2 to fluctuate.

At present, many experts and scholars have paid attention to the research and application of the SOP, and its topology has been more mature, but research on its control strategy is still in its infancy. Wang et al. (2015) provided a detailed introduction to the basic functions and principles of a SOP and compared three topological models of SOPs, proving that the topology of the back-to-back voltage source converter has a greater advantage. Shen et al. (2012) and Xiong et al. (2020) provided a detailed introduction of the operation principle of the back-to-back voltage source converter and the PQ-V_{dc}Q control strategy. Aithal et al. (2016) and Dong et al. (2018) provided a detailed analysis of the operation modes and basic control strategies of a SOP. Li et al. (2019), Meng et al. (2019), Zhang et al. (2020), and Liu et al. (2022) optimized distribution networks containing multi-port flexible switches to achieve the regulation of active and reactive power. Related studies have shown that an SOP can effectively improve the power quality of distribution networks and optimize the system current. However, the traditional control strategy cannot realize the automatic regulation of the system current.

Based on the above research, this paper proposes an adaptive power control method to realize the adaptive regulation of SOPs to a distribution network. The method equates the SOP as a link with impedance in the series with the voltage source. It takes the voltage difference at the feeder end as the input to the control loop and adjusts the value of the equivalent impedance through the feedback link. The virtual impedance is also optimized to minimize the power loss. This method enables automatic control of system currents and node voltages without adding additional controllers. Finally, the effectiveness of the proposed method is verified by MATLAB/Simulink simulation and the built experimental platform.

2 Structure and working mode of SOPs

SOPs are mainly composed of fully controlled power electronics, and their common topology is a back-to-back voltage source converter, which is characterized by connecting two converters back-to-back using a capacitor (Li et al., 2013; Chengshan et al., 2022; Xie et al., 2024), as shown in Figure 2.

Due to its special structure and function, the SOP needs to maintain the stability of the DC chain voltage during operation, so the voltage source converter on one side of it needs to work in the rectifier mode. As shown in Figure 2, the converter on feeder 1 operates in the rectified state. This feeder mainly maintains the stability of the DC voltage. First, the acquired AC voltage and AC current signals are converted by abc/dq to the output DC signals $u_{1,2}^{d,q}$ and $i_{1,2}^{d,q}$ under the dq axis. Then, $u_{1,2}^{d,q}$ and the reference signals U_{dcref} and Q_{ref} are input to the PI controller of the outer loop, and $i_{1,2}^{d,q}$ are input to the PI controller of the inner loop. Finally, after the dq/abc conversion and SPWM link, it can realize the control of DC voltage. The converter on feeder 2 operates in the inverter state. This feeder is mainly used to realize the regulation of power flow. The input signals for its control link are the active power reference value P_{ref} and the reactive power reference value Q_{ref}. Its specific control strategies are adjusted according to the current operating status of the distribution network, mainly V_{dc}Q-PQ control for power regulation and V_{dc}Q-V_{ac}f control for maintaining load voltage stabilization (Wang et al., 2015; Wang et al., 2016).

The control strategy mentioned in the previous section is capable of realizing the regulation of power flow and uninterrupted power supply under the fault condition according to the input signals. However, it has the following shortcomings: (1) it needs to get the actual power consumed by the load and the power supplied by the DG in advance. (2) The reference value of active power P_{ref} cannot be automatically adjusted according to the actual load power. It needs to be calculated and artificially input to the control link, resulting in a waste of human resources. Due to the above shortcomings, the traditional control method cannot achieve

10.3389/fenrg.2024.1387670

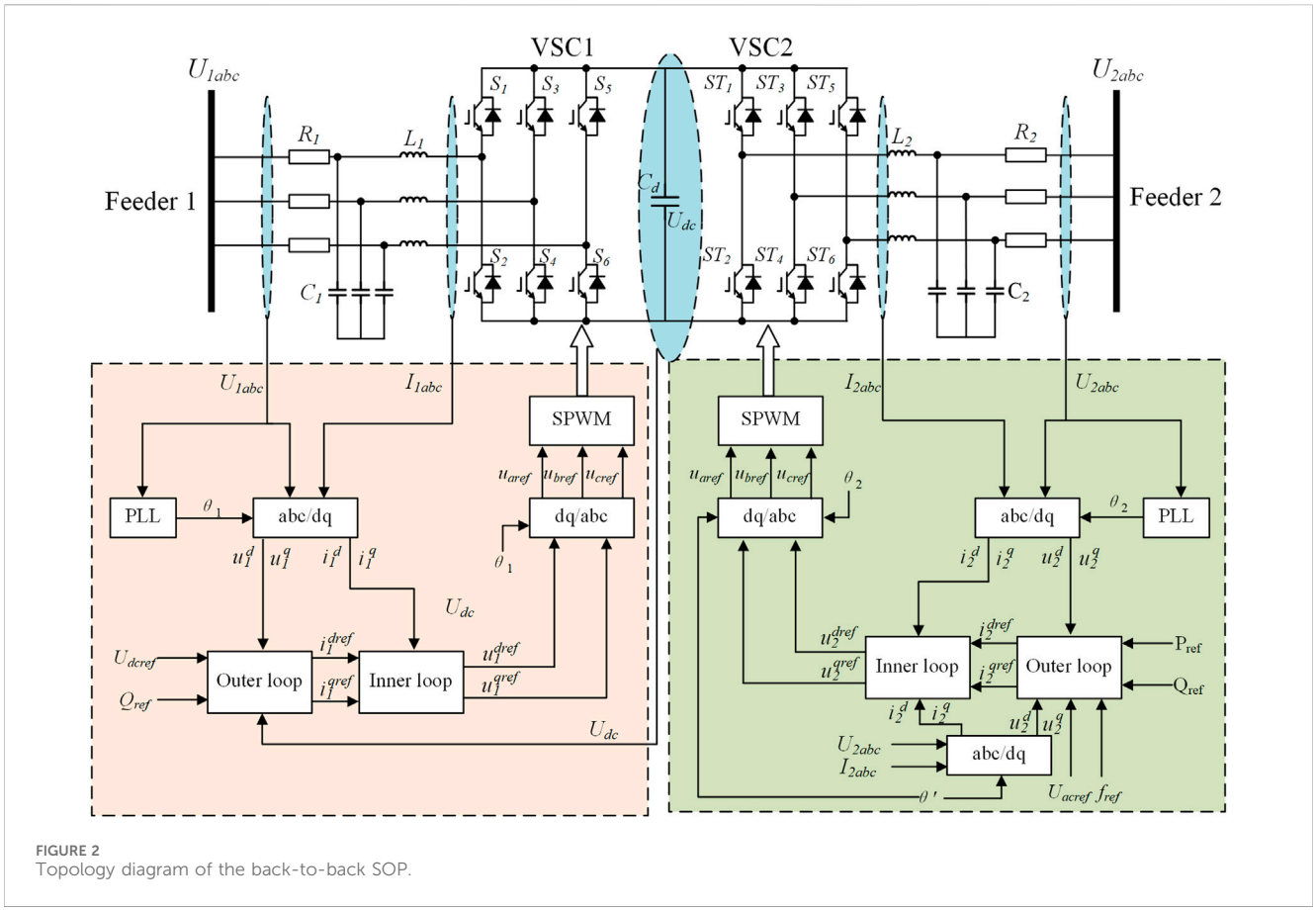

FIGURE 2
Topology diagram of the back-to-back SOP.

real-time, automatic control. In particular, in the case of several new energy sources with a high proportion of new energy, it is difficult to realize real-time adaptive regulation, following the rapid and drastic power and voltage changes.

3 Power adaptive regulation strategy based on virtual impedance

At the distribution network, the loads and DG connected to different feeders are not equal, so the voltage at the end of the loads in different feeders and different locations are not equal, which makes the operating voltage of the user loads fluctuate with the distribution network. The distribution system connected through an SOP is able to regulate the power flow by adjusting the control strategy, which, in turn, affects the voltage at the load terminals on both sides (Zhang et al., 2021; Wang et al., 2016). However, as mentioned earlier, the traditional control strategies do not realize adaptive regulation.

3.1 Operation criteria

When the transformer ratios and capacities accessed on both sides of the distribution network are the same and SOPs are accessed on both sides of the distribution network at similar locations, then, the ideal operation state is the same voltage at the access points on both sides. Therefore, SOPs can be equipotential virtual impedance

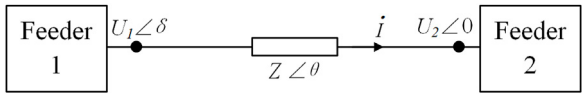

FIGURE 3
SOP is equivalent to impedance.

link representations and can be adjusted through the virtual impedance value to change the voltage difference between the two sides to realize the power transfer. The 1-side system and the 2-side system do not change due to the change of impedance; only the voltage of node 1 and node 2 changes. Therefore, node 1 and node 2 can be considered two AC sources and represented as phase quantities, as shown in Figure 3. Here, U_1 and U_2 denote the RMS values of the AC voltages on both sides, δ denotes the phase difference between the AC voltages on both sides, and θ denotes the impedance angle of the equivalent impedance.

$$\begin{bmatrix} u_\alpha \\ u_\beta \end{bmatrix} = \frac{2}{3}\begin{bmatrix} U_A - U_B\cos\left(\frac{\pi}{3}\right) - U_C\cos\left(\frac{\pi}{3}\right) \\ U_B\cos\left(\frac{\pi}{6}\right) - U_C\cos\left(\frac{\pi}{6}\right) \end{bmatrix} = \frac{2}{3}\begin{bmatrix} 1 & -\frac{1}{2} & -\frac{1}{2} \\ 0 & \frac{\sqrt{3}}{2} & -\frac{\sqrt{3}}{2} \end{bmatrix}\begin{bmatrix} U_a \\ U_b \\ U_c \end{bmatrix}, \quad (1)$$

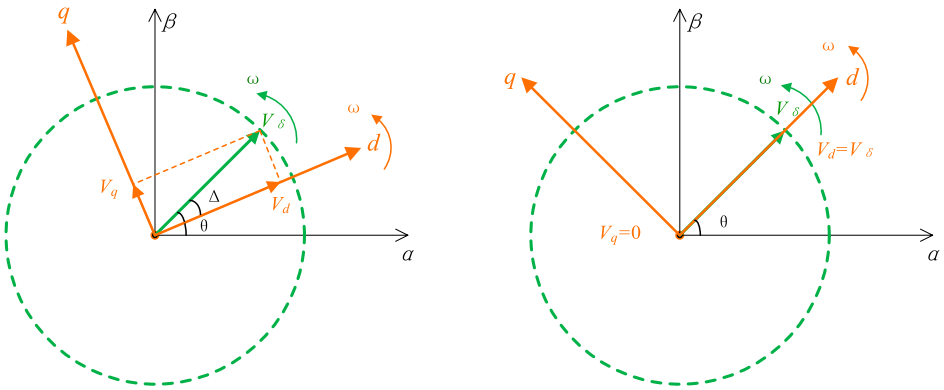

FIGURE 4
Schematic diagram of the dq coordinate system.

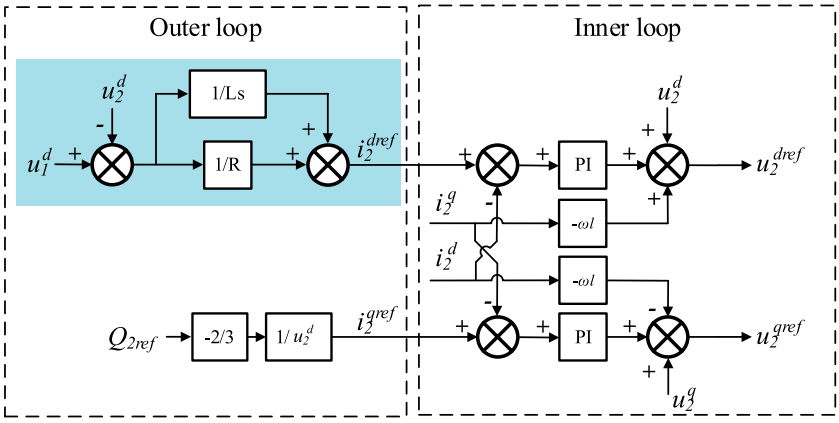

FIGURE 5
Control block diagram based on virtual impedance when the SOP is equivalent to impedance.

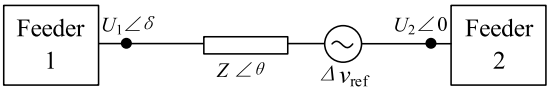

FIGURE 6
SOP is equivalent to a series connection of impedance and voltage source.

$$\begin{bmatrix} u_d \\ u_q \end{bmatrix} = \begin{bmatrix} u_\alpha \cos(\theta) + u_\beta \sin(\theta) \\ -u_\alpha \sin(\theta) + u_\beta \cos(\theta) \end{bmatrix} = \begin{bmatrix} \cos(\theta) & \sin(\theta) \\ -\sin(\theta) & \cos(\theta) \end{bmatrix} \begin{bmatrix} u_\alpha \\ u_\beta \end{bmatrix}. \quad (2)$$

In the PLL link, when the d-axis is used as the directional axis, as shown in Figures 3, 4, the phase difference is constant Δ when the dq-axis is rotating with the reference synthesized vector V_δ at a synchronous rotational speed ω. To achieve Δ = 0, it is necessary to satisfy that the d-axis is coincident with the reference synthesized vector V_δ, at which time, there is $V_d = V_\delta$, $V_q = 0$. When the d-axis is used as the directional axis, the active power is positively correlated with the d-axis component and the voltage magnitude. The q-axis is related to the reactive power and the voltage phase difference. Similarly, when the q-axis is the directional axis, the q-axis represents the active power and the d-axis represents the reactive power.

According to the basic principles of the power system, in the high-voltage transmission lines, the line reactance value is much larger than the resistance value, and the resistance value can be regarded as zero. Then, the voltage amplitude is related to the reactive power, and the voltage phase is related to the active power. In the low-voltage distribution network, the line resistance value is greater than the reactance value, and the reactance value can be regarded as zero, that is, when the line is resistive, the voltage amplitude and active power, voltage phase, and reactive power. Therefore, in the low-voltage distribution network, when the d-axis is the directional axis, the d-axis component is related to the voltage magnitude.

In summary, the dq-axis component in the rotating coordinate system obtained based on the Park transform realizes that the sinusoidal quantity of AC can be changed into DC signal for

10.3389/fenrg.2024.1387670

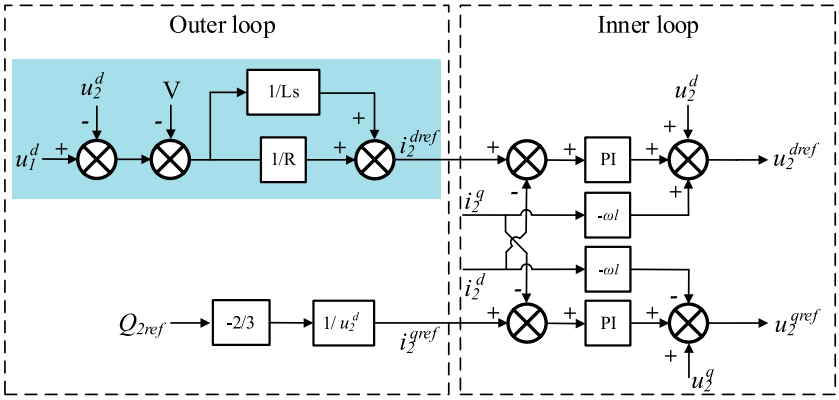

FIGURE 7
Control block diagram when the SOP is equivalent to a series connection of impedance and voltage source.

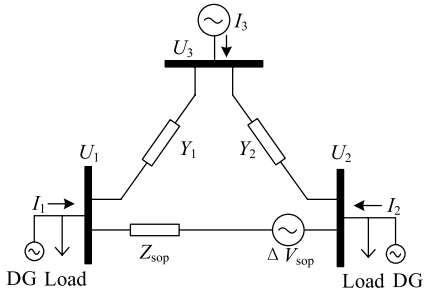

FIGURE 8
Equivalent model for optimizing the virtual impedance and virtual voltage source.

comparison, and it can reflect the change in the voltage in real time, which is very suitable to be used as the input signal of the control loop. Moreover, because of the DC state, it can be controlled by the PI controller. Therefore, the AC voltage on both sides can be changed into DC flow in the DQ domain by the Park transformation, and then, the difference of DC flow can be carried out for negative feedback control.

Therefore, the active power is mainly related to the voltage magnitude, and the reactive power is mainly related to the voltage phase angle difference. The current flowing through the equivalent impedance link at this time is expressed as follows:

$$i = \frac{\Delta u}{R} + \frac{1}{L}\int \Delta u \mathrm{d}t, \tag{3}$$

where Δu denotes the voltage difference between feeder 1 and feeder 2, R denotes the resistance value of the virtual impedance, and L denotes the inductance value of the virtual impedance.

Using PLL and Park transformation, the AC volume is converted to a direct flow in the dq coordinate system, which can be obtained as follows:

$$i_{\mathrm{d}}(t) = \frac{u_1^{\mathrm{d}}(t) - u_2^{\mathrm{d}}(t)}{R} + \frac{1}{L}\int \left(u_1^{\mathrm{d}}(t) - u_2^{\mathrm{d}}(t)\right)\mathrm{d}t. \tag{4}$$

Furthermore, it can be expressed in the frequency domain as follows:

$$i_{\mathrm{d}}(s) = \left(\frac{1}{R} + \frac{1}{Ls}\right)\cdot\left(u_1^{\mathrm{d}}(s) - u_2^{\mathrm{d}}(s)\right). \tag{5}$$

Since the d-axis component in the DQ domain is positively correlated with the amplitude of the sinusoidal AC voltage (Kupzog et al., 2007), the d-axis component is used as the input signal for the power control. The virtual impedance control link is obtained according to Equation 5, as shown in the dashed box of Figure 5, and the overall control strategy of the node virtual impedance-based power control is shown in Figure 5.

3.2 The control strategy of SOPs based on virtual impedance and virtual power supply

When the transformer ratios accessed on both sides of the distribution network are different, or when the positions of node 1 and node 2 of SOPs accessed to the distribution network differ greatly relative to the loads and DGs, the load terminal voltages on both sides should be different in the ideal case. In this case, the SOP in Figure 3 can be represented by a link of impedance series voltage source, where Z denotes the impedance, as shown in Figure 6.

The voltage difference between the two sides can be expressed as follows:

$$U_1\angle\delta - U_2\angle 0 = \Delta u = I\cdot Z\angle\theta + \Delta v_{\mathrm{ref}}. \tag{6}$$

The current flowing through the SOP at this time is expressed as follows:

$$I = \frac{\Delta u - \Delta v_{\mathrm{ref}}}{R} + \frac{1}{L}\int (\Delta u - \Delta v_{\mathrm{ref}})\mathrm{d}t, \tag{7}$$

Using PLL and Park's transformation, the AC volume is converted to a direct flow in the dq coordinate system, which can be obtained:

$$i_{\mathrm{d}}(t) = \frac{u_1^{\mathrm{d}}(t) - u_2^{\mathrm{d}}(t) - \triangle v_{\mathrm{ref}}}{R} + \frac{1}{L}\int \left(u_1^{\mathrm{d}}(t) - u_2^{\mathrm{d}}(t) - \triangle v_{\mathrm{ref}}\right)\mathrm{d}t, \tag{8}$$

Further, it can be expressed in the frequency domain as:

$$i_{\mathrm{d}}(s) = \left(\frac{1}{R} + \frac{1}{Ls}\right)\cdot\left(u_1^{\mathrm{d}}(s) - u_2^{\mathrm{d}}(s)\right) - \left(\frac{1}{R} + \frac{1}{Ls}\right)\cdot\triangle v_{\mathrm{ref}}. \tag{9}$$

TABLE 1 Power stages and probability.

Power stage	P_{11} Q_{11} P_{21} Q_{21}	P_{12} Q_{12} P_{22} Q_{22}	P_{13} Q_{13} P_{23} Q_{23}	.....	P_{19} Q_{19} P_{29} Q_{29}	P_{110} Q_{110} P_{210} Q_{210}
Probability	Pro_1	Pro_2	Pro_3	.....	Pro_9	Pro_{10}

The power loss for each particle is calculated here.

TABLE 2 Simulation parameters.

Parameter	Value	Parameter	Value
One-side AC voltage/V	220	Inner loop k_{pi}	1.2
Two-side AC voltage/V	220	Inner loop k_{ii}	200
DC voltage reference/V	800	Switching frequency/kHz	10
Outer loop k_{pi}	0.2	Sampling frequency/kHz	10
Outer loop k_{ii}	50	Filter inductors/mH	2.5
Two-side virtual impedance R	0.2	Filter capacitor/μF	10
Two-side virtual impedance L	50	Loading power/kW	10–100

Again, using the d-axis voltage component under the DQ domain as the input signal, the corresponding control block diagram shown in Figure 7 can be obtained from Equation 9, as shown below:

4 The general method to optimize the parameters

The general method to calculate the virtual impedance and the virtual voltage source.

In the last section, the adaptive control method has been proposed. The power flow through the SOP is determined by two side-grid voltages. A simplified diagram of the system of the SOP connected to the distribution grid is shown in Figure 8, where the AC source voltages U_1 and U_2 on both sides denote the voltages intervening in the distribution grid, Y_1 and Y_2 denote the line admittance, Z_{sop} denotes the virtual impedance link of the SOP, and $\triangle V_{sop}$ denotes the virtual voltage source link. U_3 indicates the voltage of the utility grid. As mentioned before, the regulation of the system power flow is realized by adjusting the values of Z_{sop} and $\triangle V_{sop}$. Among them, when the value of z is small enough, the power flow regulation on both sides is more flexible and flows more frequently, and any small voltage deviation will cause the power balance, which increases the power flowing through the SOP, and the loss generated by the SOP itself increases. In addition, when the value of z is large, the sensitivity to the voltage difference between the two sides decreases and the power flow regulation threshold rises, decreasing the losses generated by the SOP. Therefore, how to design the values of Z_{sop} and $\triangle V_{sop}$ such that the SOP can automatically regulate the power flow, balance the voltage difference between the two sides, and also take into account the loss due to the SOP power regulation is the key to the realization of the control strategy proposed in this paper.

The goal in this section is to find the virtual impedance and virtual voltage for a specific purpose; for example, for minimizing the power loss. The virtual impedance and virtual voltage are given as follows:

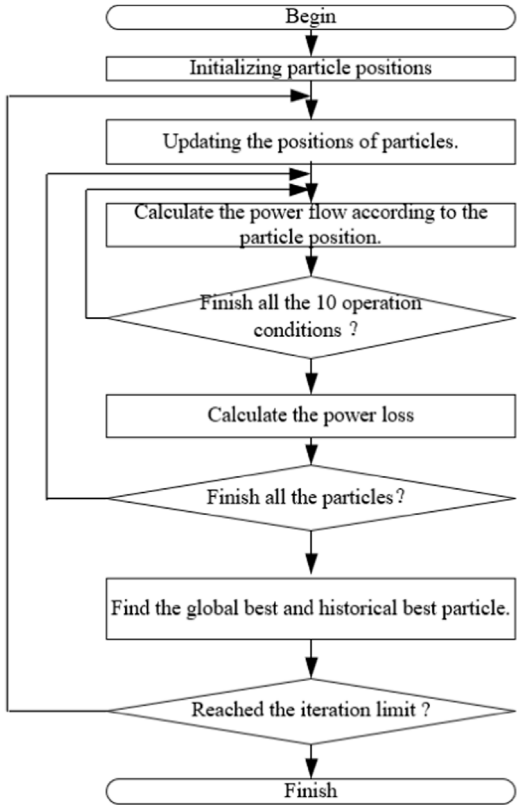

FIGURE 9
Flowchart of parameter optimization.

$$\Delta \dot{V}_{sop} = \Delta V_{sop} e^{j\theta_{sop}} \frac{1}{Z_{sop}} = Y_{sop} = G_{sop} + jB_{sop}, \tag{10}$$

where $\triangle V_{sop}$ and θ_{sop} are the magnitude and phase angle of the virtual voltage source, respectively. G_{sop} and B_{sop} are the conductance and susceptance, respectively. In this article, the objective function is to minimize the power loss. For other objective functions, the method can still be used. The objective function is given as follows:

$$\begin{aligned} \min \quad & P_{loss}\left(Y_{sop}, \Delta \dot{V}_{sop}, P_1, Q_1, P_2, Q_2\right) = P_{loss1} + P_{loss2} + P_{loss\_sop}, \\ & P_{loss1} = real\left[(U_3 - U_1)[Y_1(U_3 - U_1)]^*\right], \\ & P_{loss2} = real\left[(U_3 - U_2)[Y_2(U_3 - U_2)]^*\right], \\ & P_{loss\_sop} = P_{sop\_semi}\left(P_{sop}, Q_{sop}\right) + P_{sop\_ind}\left(P_{sop}, Q_{sop}\right). \end{aligned} \tag{11}$$

The power loss mainly contains the losses caused by the transformers and line impedance, which are indicated by P_{loss1} and P_{loss2}, respectively. Additionally, the power loss of the SOP, which is indicated by P_{loss_sop}, is also included. Unlike traditional line losses, SOP losses require calculating power device losses and inductor losses based

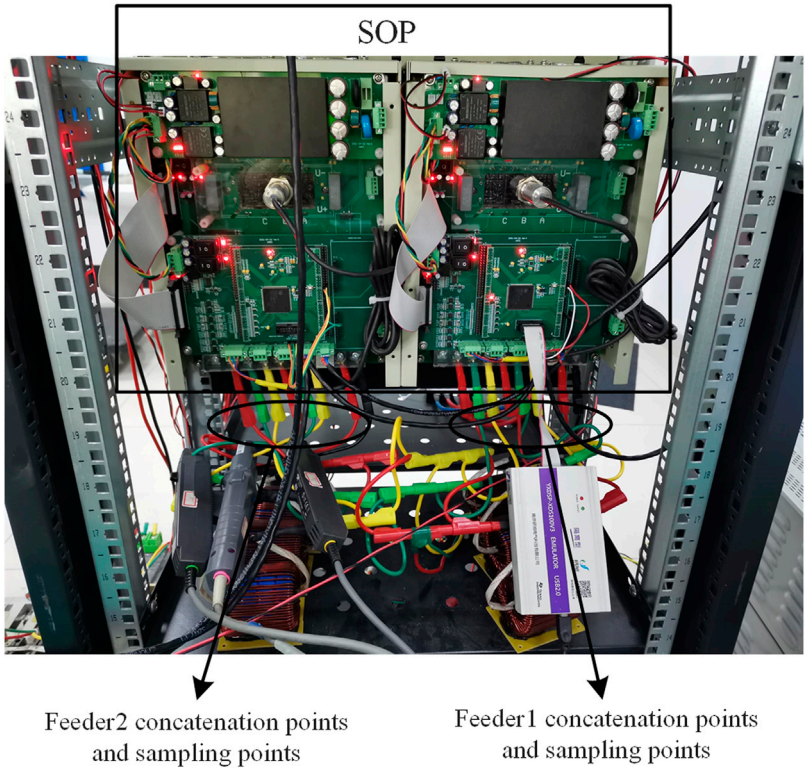

FIGURE 10
SOP experiment platform.

on the power flowing through the SOP. The constraints of the objective function are the power flow distribution. The complexity of the constraints and the nonlinearity of the objective function make the optimization difficult to solve. So, an artificial intelligent optimization method, such as particle swarm optimization (PSO), can be employed. The details of the solving processes are given in the following sections.

(1) The particles are initialized as follows:

$$\begin{aligned}&\mathbf{Par}_x(0)=\left[\Delta V_{\mathrm{sop},x}(0),\theta_{\mathrm{sop},x}(0),G_{\mathrm{sop},x}(0),B_{\mathrm{sop},x}(0)\right],\\&\Delta V_{\mathrm{sop},x}(0)=\mathrm{rand}([0,0.1])\ \ \theta_{\mathrm{sop},x}(0)=\mathrm{rand}([-10^{\circ},10^{\circ}]),\\&G_{\mathrm{sop},x}(0)=\mathrm{rand}([0,0.1])\quad B_{\mathrm{sop},x}(0)=\mathrm{rand}([0,0.1]),\end{aligned}\tag{12}$$

where the subscript x indicates the number of particles. rand() denotes the random value. $\mathbf{Par}_x$ indicates the position of particle x, where the dimension of $\mathbf{Par}_x$ is 4.

(2) The main purpose of flexible interconnection equipment is to facilitate the transfer of power imbalances. Considering the variability of real-world operating conditions, traversing all operating conditions would consume a significant amount of resources. Therefore, different operating conditions are separated into a finite number of intervals.

$$P_{\mathrm{loss},x}=P_{\mathrm{loss}}(\mathbf{Par}_x)=\sum_{n=1}^{10}pro_nP_{\mathrm{loss}}(\mathbf{Par}_x,P_{1n},Q_{1n},P_{2n},Q_{2n}).\tag{13}$$

The parameters in Eq 13 can be calculated according to the power flow. For each combination of P and Q, the power flow can be calculated according to Equs 14–16.

According to Figure 8, the admittance matrix is given as follows:

$$\begin{bmatrix}\dot{I}_1\\ \dot{I}_2\\ \dot{I}_3\end{bmatrix}=\begin{bmatrix}Y_{11}&Y_{12}&Y_{13}\\ Y_{21}&Y_{22}&Y_{23}\\ Y_{31}&Y_{32}&Y_{33}\end{bmatrix}\begin{bmatrix}\dot{U}_1\\ \dot{U}_2\\ \dot{U}_3\end{bmatrix}+\Delta\dot{V}_{\mathrm{sop}}\begin{bmatrix}-Y_{\mathrm{sop}}\\ +Y_{\mathrm{sop}}\\ 0\end{bmatrix},\tag{14}$$

$$\begin{bmatrix}Y_{11}&Y_{12}&Y_{13}\\ Y_{21}&Y_{22}&Y_{23}\\ Y_{31}&Y_{32}&Y_{33}\end{bmatrix}=\begin{bmatrix}Y_1+Y_{\mathrm{sop}}&-Y_{\mathrm{sop}}&-Y_1\\ -Y_{\mathrm{sop}}&Y_2+Y_{\mathrm{sop}}&-Y_2\\ -Y_1&-Y_2&Y_1+Y_2\end{bmatrix}$$

where

$$Y_{ij}=G_{ij}+jB_{ij}\quad \dot{U}_i=U_ie^{j\theta_i}.\tag{15}$$

Substituting the power in Table 1 into the formula to obtain the power flow equation, we obtain:

$$\begin{cases}P_{1n}+jQ_{1n}=\dot{U}_1\overset{*}{I}_1=U_1e^{j\theta_1}\sum_{j=1}^{n}\left(G_{ij}-jB_{ij}\right)U_ie^{-j\theta_j}-\Delta\dot{V}_{\mathrm{sop}}Y_{\mathrm{sop}}\\ P_{2n}+jQ_{2n}=\dot{U}_2\overset{*}{I}_2=U_2e^{j\theta_2}\sum_{j=1}^{n}\left(G_{ij}-jB_{ij}\right)U_ie^{-j\theta_j}+\Delta\dot{V}_{\mathrm{sop}}Y_{\mathrm{sop}}\end{cases}.\tag{16}$$

According to the above equation, $\dot{U}_1$ and $\dot{U}_2$ can be obtained using the Newton–Raphson method. So far, the power in Eq 13 can be calculated. All the possible operation conditions can be covered by repeating the power loss calculation 10 times.

(3) The results are compared to find the historical best and the global best. The historical best of each particle is $\mathrm{Par}_{\mathrm{xb}}$. The global best is $\mathrm{Par}_{\mathrm{gb}}$.
(4) The update of the particles is expressed as follows:

10.3389/fenrg.2024.1387670

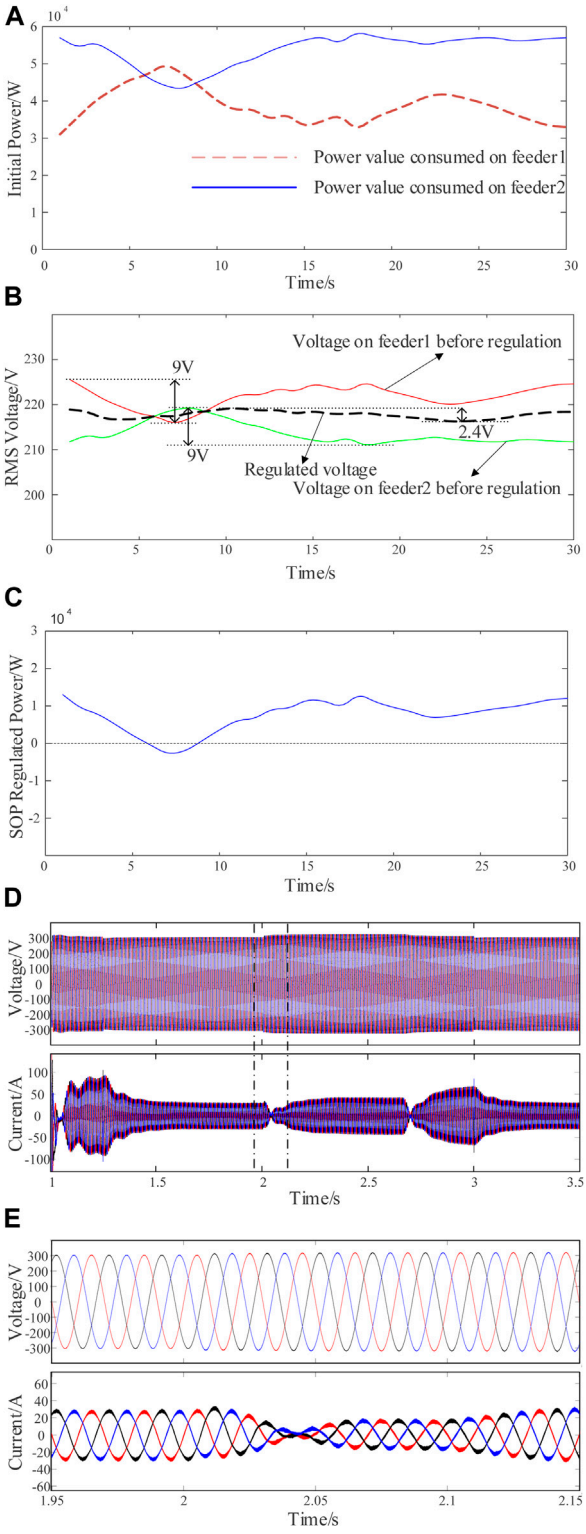

FIGURE 11
Simulation results diagram when the SOP is equivalent to impedance. **(A)** Initial net power consumption trajectory; **(B)** RMS voltage trajectory; **(C)** SOP regulated power trajectory; **(D)** Voltage and current waveform on long time scales for feeder1; **(E)** Voltage and current waveform on short time scales for feeder1.

$$\begin{aligned}\mathbf{v}_x(c) &= \left\{\begin{array}{l}\mathbf{v}_x(c-1) + a_1 \cdot \mathrm{rand}_1([0,1]) \cdot (\mathbf{Par}_{xb} - \mathbf{Par}_x(c-1)) \\ +a_2 \cdot \mathrm{rand}_2([0,1]) \cdot \left(\mathbf{Par}_{gb} - \mathbf{Par}_x(c-1)\right)\end{array}\right\}. \\ \mathbf{Par}_x(0)(c) &= \mathbf{Par}_x(0)(c-1) + \mathbf{v}_x(c)\end{aligned} \tag{17}$$

(5) Repeat steps (2)–(4) until the into English is “iteration limit. The flowchart of the above method is given in Figure 9.

5 Simulation and experimental verification

A simulation model of the distribution network shown in Figure 1 is built in MATLAB/Simulink, and to simplify the model without affecting the simulation results, the line impedance Z on both sides is taken as 1 Ω. The parameters of the simulation model are shown in Table 2.

The DG and load connected on both sides are equated as load 1 and load 2, respectively, and the power absorbed/released by the load from the distribution network is defined as the net consumed power, in which both are of 10 kW–100 kW level; the reference quantity of DC chain voltage is 800 VDC, the output voltage of the transformer is 220 V/50 Hz, the R value of the virtual impedance link is taken as 0.2, the L value is taken as 50, the parameter of the PI control ring is taken as kp 1.2, and ki is 200, and the simulation verifies the effectiveness of the virtual impedance-based SOP power adaptive regulation method. In addition, the experimental platform of the SOP is also built for verification. Under the laboratory conditions, the output voltage of the transformer is 35 V/50 Hz, the DC chain voltage reference quantity is 100 VDC, and the loads on both sides are of kW level; the built experimental platform is shown in Figure 10.

In the simulation experiment in which the smart soft switch is connected to the same position on both sides of the distribution network, the smart soft switch is equated to a virtual impedance link. The 1-side and 2-side systems have large fluctuations in the total net consumed power due to the access of the distributed power sources, as shown in Figure 11A. At this time, the voltage RMS of both sides accessed to the load terminal fluctuates largely with the power fluctuation, as shown by the solid line in Figure 11B. After adding the regulation method proposed in this paper, the waveform of the RMS voltage at the load terminal on both sides is shown as the dotted line in Figure 11B, and at this time, the RMS voltages on both sides are equal, and the fluctuation amplitude is smaller. The power flow regulated by the SOP is shown in Figure 11C, where the part greater than 0 indicates that the power flows from side 1 to side 2, and the part less than 0 indicates that the power flows from side 2 to side 1.

In the simulation experiments where the positions of the two sides of the SOP access to the distribution network differ greatly, the SOP is equivalent to an impedance series-connected voltage source link. The total net power consumption of the 1-side and 2-side system access is shown in Figure 12A, and the RMS values of the voltages at the access point of the SOP to the distribution network are, respectively, shown as the solid lines in Figure 12B, at which time the voltages fluctuate rapidly and with a large

10.3389/fenrg.2024.1387670

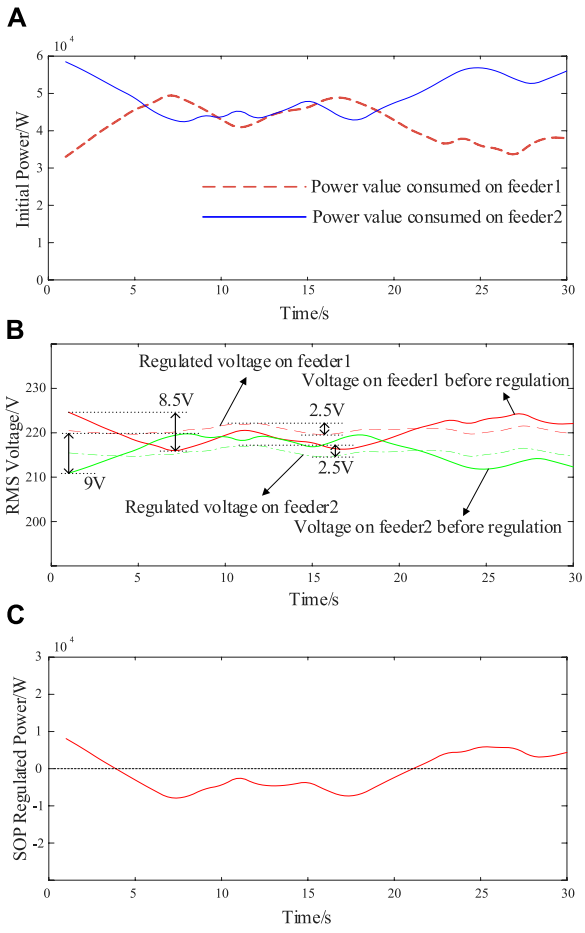

FIGURE 12
Simulation results when the SOP is equivalent to a series connection of impedance and voltage source. **(A)** Initial net power consumption trajectory; **(B)** RMS voltage trajectory; **(C)** SOP regulated power trajectory.

fluctuation amplitude. After adding the regulation method proposed in this paper, the waveform of the RMS voltage at the access point of the SOP is shown as the dotted line in Figure 12B, at which time, the voltage difference between the two sides follows the change in the control quantity, and the voltage fluctuation between the two sides becomes smaller. The power flow regulated by the SOP is shown in Figure 12C, where the part greater than 0 indicates that the power flows from side 1 to side 2, and the part less than 0 indicates that the power flows from side 2 to side 1. The simulation experiment can prove that the power adaptive regulation method of the SOP based on virtual impedance proposed in this paper can realize the regulation of power and voltage in a distribution network.

Under the experimental conditions of an AC voltage of 35 V/50 Hz, DC voltage of 100 VDC, and load power of kW class, the waveforms measured by an oscilloscope are shown in Figure 11, where the upper side of Figure 13 shows the current waveforms of the long time-scale on the 2-side of SOP, and the lower side of Figure 13 shows the current waveforms of the short time-scale after the addition of the regulation strategy. From the long time-scale current waveforms, it can be seen that

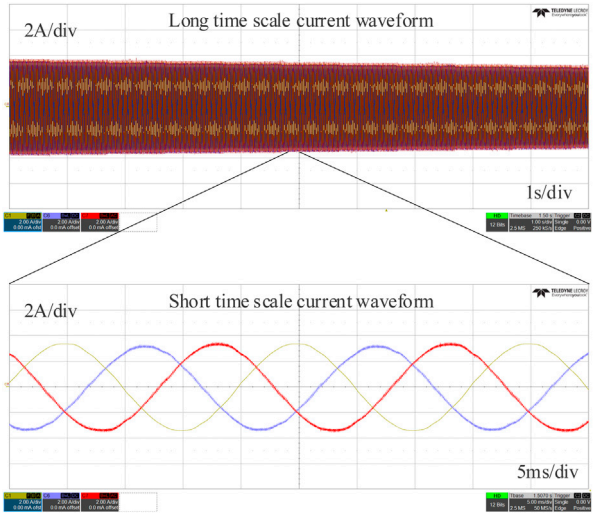

FIGURE 13
Experimentally measured current waveform.

the current amplitude of this side of the overall downward trend with the power changes, which can realize the adaptive regulation; from the short time-scale current waveforms, it can be seen that after the regulation of the SOP, the three-phase current frequency, phase stability in line with the requirements of the grid, and the experimental platform can realize the proposed regulation method.

6 Conclusion

In this paper, an adaptive regulation method based on virtual impedance is proposed for the power of SOPs. This method equates SOPs as virtual impedance and power source links and determines the equivalent impedance value of SOPs with the voltage component in the DQ domain. The adaptive control of power flow and voltage is realized by adding the virtual impedance and the power supply link in the control loop.

Simulation and experimental results show that the proposed method can quickly regulate the power flow, effectively reduce the voltage fluctuation, and improve the operational efficiency and stability of the distribution network.

Data availability statement

The original contributions presented in the study are included in the article/Supplementary material; further inquiries can be directed to the corresponding authors.

Author contributions

YL: data curation, validation, and writing–review and editing. YL: investigation, resources, and writing–review and editing. XZ: writing–original draft and data curation. FG: supervision and

writing–review and editing. TX: writing–original draft, writing–review and editing, and conceptualization.

Funding

The author(s) declare that no financial support was received for the research, authorship, and/or publication of this article.

Conflict of interest

Authors YL and YL were employed by the State Grid Intelligence Technology Co., Ltd.

The remaining authors declare that the research was conducted in the absence of any commercial or financial relationships that could be construed as a potential conflict of interest.

Publisher's note

All claims expressed in this article are solely those of the authors and do not necessarily represent those of their affiliated organizations, or those of the publisher, the editors, and the reviewers. Any product that may be evaluated in this article, or claim that may be made by its manufacturer, is not guaranteed or endorsed by the publisher.

References

Aithal, A., Long, C., Cao, W., Wu, J., and Ugalde-Loo, C. E. (2016). Impact of soft open point on feeder automation. *2016 IEEE Int. Energy Conf.*, 1–6. doi:10.1109/ENERGYCON.2016.7514101

Bloemink, J. M., and Green, T. C. (2010). Increasing distributed generation penetration using soft normally-open points. *IEEE PES General Meet.*, 1–8. doi:10.1109/PES.2010.5589629

Bloemink, J. M., and Green, T. C. P. (2013). Benefits of distribution-level power electronics for supporting distributed generation growth. *IEEE Trans Power Deliv.* 28 (2), 911–919. doi:10.1109/tpwrd.2012.2232313

Chengshan, W., Ji, J., Ji, H., Yu, H., and Wu, J. (2022). Technologies and application of soft open points in distribution networks. *Automation Electr. Power Syst.* 46 (4), 1–14. doi:10.7500/AEPS20210514005

Dong, X., Liu, Z., Li, P., Song, G., Wu, Z., and Chen, L. (2018). Intelligent distribution network control technology based on multi-terminal flexible distribution switch. *Proc. CSEE* 38 (1), 86–92. doi:10.13334/j.0258-8013.pcsee.172359

Kupzog, F., Brunner, H., Pruggler, W., Pfajfar, T., and Lugmair, A. (2007). Dg demonet-concept – a new algorithm for active distribution grid operation facilitating high dg penetration. *2007 5th IEEE Int. Conf.* (2), 1197–1202. doi:10.1109/INDIN.2007.4384946

Li, P., Ji, H., Yu, H., Zhao, J., Wang, C., and Song, G. (2019). Combined decentralized and local voltage control strategy of soft open points in active distribution networks. *Appl. Energy*, 241.613–624. doi:10.1016/j.apenergy.2019.03.031

Li, Z., et al. (2013). Dual closed-loop control of soft normally open points and its application in distribution networks. *Smart Grid* 1 (1), 49–55.

Liu, Y. J., Xuan, X. F., Zou, X. S., Xiong, W., Tan, Z. K., and Xu, Y. T. (2022). Review of distributed power supply dissipation technology based on soft open point. *Electr. Meas. Instrum.* 59 (7), 1–8. doi:10.19753/j.issn1001-1390.2022.07.001

Meng, M., Wei, Y., Zhu, G. L., and Zhang, J. S. (2019). Research on optimal control strategy of AC/DC active distribution networks based on soft open point. *Mod. Electr. Power* 36 (2), 1–7. doi:10.3969/j.issn.1007-2322.2019.02.001

Ren, P. (2021) "Research on hybrid energy storage control strategy for PV microgrid," in *Shanxi*. China: North University of China Master's Degree Thesis.

Shen, Y., Peng, X., and Sun, Y. (2012). Study on cooperative control strategies of back-to-back dual-PWM Converter. *Power Syst. Technol.* 36 (1), 146–152. doi:10.13335/j.1000-3673.pst.2012.01.031

Wang, C. S., Sun, C. B., Li, P., and Wu, J. Z. (2015). SNOP-based operation optimization and analysis of distribution networks. *Automation Electr. Power Syst.* 39 (9), 82–87. doi:10.7500/AEPS20140828002

Wang, C. S., Song, G. Y., Li, P., Yu, H., Zhao, J. L., and Wu, J. Z. (2016). Research andprospect for soft open point based flexible interconnection technology for smartdistribution network. *Automation Electr. Power Syst.* 40 (22), 168–175. doi:10.7500/AEPS20160620009

Wang, J., et al. (2021). Overview of typical control methods for grid-connected inverters of distributed generation. *Proceeding CSU-EPSA* 24 (2), 12–20.

Wang, P. (2017) "Electromagnetic transient modeling and fast simulation of soft open points in active distribution network," in *Tianjin*. China: Tianjin University Master's Degree Thesis.

Xie, X., Sun, Y., and Fan, J. X. (2024). A measurement-based dynamic harmonic model for single-phase diode bridge rectifier-type devices. *IEEE Trans. Instrum. Meas.* 73, 1–13. doi:10.1109/tim.2024.3370782

Xiong, Z. Y., Miao, H., and Zeng, C. B. (2020). Operation optimization of active distribution network based on smart soft open point and energy storage system. *Electr. Meas. Instrum.* 57 (13), 33–39. doi:10.19753/j.issn1001-1390.2020.13.007

Yang, H., Cai, Y. Y., Qu, Z. S., Deng, Y., Lu, Y., and Zhao, R. X. (2018). Key techniques and development trend of soft open point for distribution network. *Automation Electr. Power Syst.* 42 (7), 153–165. doi:10.7500/AEPS20171031018

Zhang, B., Liu, S. Y., Lin, Z. Z., Yang, L., Gao, Q., and Xu, H. (2021). Distribution network reconfiguration with high penetration of renewable energy considering demand response and soft open point. *Automation Electr. Power Syst.* 45 (8), 86–94. doi:10.7500/AEPS20190930004

Zhang, G. R., Luo, L., Peng, B., Lu, Y., Wang, C. L., and Xu, F. (2020). Bi-level optimization method for active distribution network based on soft open point. *Electr. Meas. Instrum.* 57 (24), 58–65. doi:10.19753/j.issn1001-1390.2020.24.008

Frontiers in
Energy Research

Advances and innovation in sustainable, reliable and affordable energy

Explores sustainable and environmental developments in energy. It focuses on technological advances supporting Sustainable Development Goal 7: access to affordable, reliable, sustainable and modern energy for all.

Discover the latest Research Topics

See more →

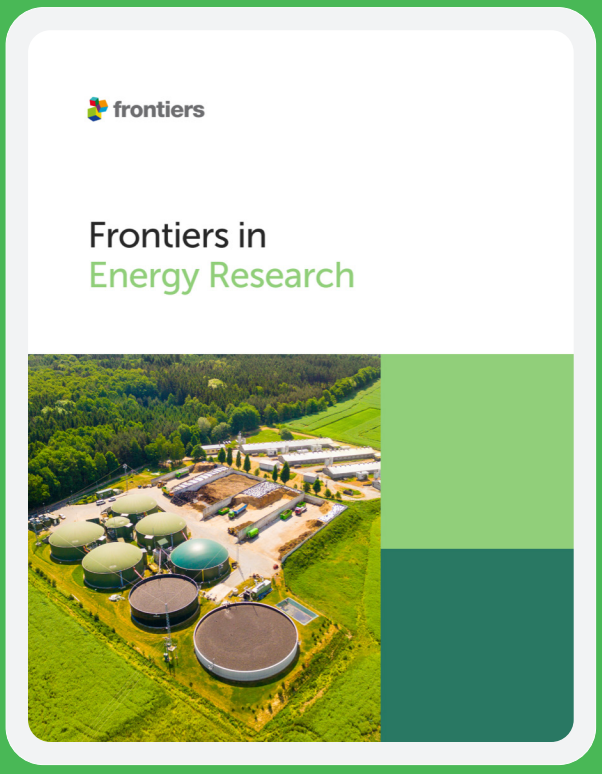

Frontiers

Avenue du Tribunal-Fédéral 34
1005 Lausanne, Switzerland
frontiersin.org

Contact us

+41 (0)21 510 17 00
frontiersin.org/about/contact